PSFC/RR-11-14 DOE/ET-54512-376

Experimental Tests of Parallel Impurity Transport Theory in Tokamak Plasmas

M.L. Reinke

December, 2011

Plasma Science and Fusion Center
Massachusetts Institute of Technology
Cambridge MA 02139 USA

This work was supported by the U.S. Department of Energy, Grant No. DE-FC02-99ER54512 Reproduction, translation, publication, use and disposal, in whole or in part, by or for the United States government is permitted.

Experimental Tests of Parallel Impurity Transport Theory in Tokamak Plasmas

by

Matthew Logan Reinke

B.S., University of Wisconsin (2004)

Submitted to the Department of Nuclear Science and Engineering
in partial fulfillment of the requirements for the degree of

Doctor of Philosophy

at the

MASSACHUSETTS INSTITUTE OF TECHNOLOGY

December 2011

Author .....
Department of Nuclear Science and Engineering
December 15, 2011

Certified by .....
Ian H. Hutchinson
Professor
Thesis Supervisor

Certified by .....
Jim Terry
Principal Research Scientist
Thesis Reader

Accepted by .....
Prof. Mujid S. Kazimi
Professor of Nuclear Science & Engineering
Chair, Department Committee on Graduate Students

Experimental Tests of Parallel Impurity Transport Theory in Tokamak Plasmas

by

Matthew Logan Reinke

Submitted to the Department of Nuclear Science and Engineering
on December 15, 2011, in partial fulfillment of the
requirements for the degree of
Doctor of Philosophy

Abstract

In realistic reactor scenarios, high temperature plasmas will be composed of not only the fusion reactants and products, but also impurities introduced purposefully or unintentionally from plasma facing materials. In tokamaks it is often assumed, sometimes erroneously, that surfaces of constant main ion pressure are also surfaces of constant impurity pressure. Although the same underlying physics determine impurity momentum balance along closed magnetic field lines, the increased mass and charge of high-Z impurities weights terms differently. Their large mass enhances inertial effects like the centrifugal force from toroidal rotation, and can lead to accumulation of heavy impurities on the outboard side of a flux surface. Their high charge enhances ion-impurity friction and makes impurities sensitive to small poloidal variations in the electrostatic potential.

In Alcator C-Mod, 2D (R,Z) measurements of photon emission from high-Z impurities reveal significant variations of impurity density on a flux surface. Poloidal variations, normalized to the flux surface average, $|\tilde{n}_z/\langle n_z\rangle|$, have been measured up to $\sim 1/3$, and separate cases of impurities accumulating on the inboard and outboard side of a flux surface are observed, depending on local plasmas conditions. Experiments demonstrate that these asymmetries are due to a combination of inertia, poloidal electric fields and ion-impurity friction, and measurements are compared to existing neoclassical parallel impurity transport theory. This is the first time centrifugal force has been observed to cause a substantial asymmetry in a plasma with no external momentum input and where the flow is entirely self-generated. Magnetically trapped fast ions, sustained by ion cyclotron waves, create a poloidally varying electrostatic potential which causes high-Z impurities to accumulate on the inboard side. Existing theory is extended to include this effect by incorporating a species that has an anisotropic pressure tensor. Experimental measurements in plasmas where the minority resonance layer is scanned show good qualitative and quantitative agreement with this extended theory. The sensitivity of $\tilde{n}_z/\langle n_z\rangle$ to fast-ions demonstrates the opportunity for the impurity asymmetry to be used as a novel diagnostic tool and calls into question prior work on in/out asymmetries in neutral beam heated

plasmas. Measured up/down asymmetries in the banana regime are unable to be explained by ion/impurity friction in the trace limit, $n_z Z^2/n_i \ll 1$. The sensitivity of such asymmetries to main ion poloidal rotation, which depends on impurity density when $n_z Z^2/n_i \sim 1$, suggests explaining up/down asymmetries requires a more complex model which couples the parallel force balance of main ions and multiple impurity species. Additionally, the connection between impurity poloidal flow and poloidal density variation is highlighted. Since they are the result of the same parallel transport equation, predictions for both need to match measurements in order to validate friction-based asymmetry theory.

Thesis Supervisor: Ian H. Hutchinson
Title: Professor

Thesis Reader: Jim Terry
Title: Principal Research Scientist

Acknowledgments

One of the things I love about working on an experiment like C-Mod is the sense of community I feel everyday I step into the lab. No one person can be an expert in all of the areas needed to succeed in this field, and so we come together to design, build, plan and execute our lofty goals. From engineers to experimentalists, from theorists to technicians, we fail together and we triumph together. The inevitable acrimony that arises when passionate people, working long hours in close quarters while fighting over limited resources is not that of enemies, but that of family.

To start with, I would like to thank those that directly contributed analysis or data to this research. Many thanks to Steve Wolfe, not only for all he does making sure C-Mod is running smoothly, but since without his overseeing the EFIT tools at C-Mod, there would be no flux-surfaces for which I could spend the next few hundred pages discussing how impurities are not constant over them. I would like to thank Nathan Howard for helping me with the TRANSP simulations that help give Chapter 5 that extra punch. The background plasma profiles used in comparisons to theory are provided by Thomson Scattering (Jerry Hughes, John Walk and Yunxing Ma), ECE (Amanda Hubbard) and HIREXSR (Y. Podpaly and the entire HIREXSR team), and the fiTS software (Darin Ernst) was used in analyzing the data.

After the end of the campaign in April 2011 when I begin exploring the data in more detail, it became apparent that my runs did not test the correct physics behind the asymmetries. I'd like to thank the many session leaders for running excellent controlled experiments that allowed their run days to be useful beyond their immediate goals: John Rice (1101208), Amanda Hubbard (1101209), Catherine Fiore (1110105), Yunxing Ma (1110114) and Jerry Hughes (1110201). I would also like to thank members of the ICRF and energetic particle groups at C-Mod, Steve Wukitch, Yijun Lin, Aaron Bader, David Pace and Paul Bonoli, for helping me with the minority heating and fast-ion physics.

I number of people helped to design and deploy the pinhole camera diagnostics used in this research. Thanks to Ned Mucic and Henry Savelli for assistance with the

KLIM enclosure and the wall boxes design, respectively, and also to Rui Vieira for his guidance and support over the years. Thanks to Ed Fitzgerald and everyone in the machine shop, especially Charlie, Richie and Eric, as well as master welder Dave Arsenault. I can't remember the times the guys in the vacuum shop have rescued me from my poor planning when I needed something passivated, baked or cleaned on short notice. Tommy Toland and Ronnie Rosati have been a great help over the years not just with the bolometry tools but also with my spectroscopy side-projects. Sam Pierson has also been invaluable as my hands and eyes inside the vessel. Sam is a pleasure to work with and always seems to have a smile on his face, even after spending a whole in day in the tokamak on only a few hours of sleep. I would also like to thank the number graduate students who helped in the in-vessel calibration of these cameras, including Rachael McDermott, Michael Churchill, Geoff Olynyk, Roman Ochoukov and Aaron Bader. Thanks to Bill Parkin, Dave Bellofatto, Wade Cook and Maria Silveira for help with cables and amplifiers construction. Lastly, I'd like to thank the magicians of the C-Mod, Josh Stillerman and Tom Fredian, as their constant work on MDSPlus prevent a lot of headaches for the rest of us.

I'd also like to thank those people who have been critical in guiding my development as a scientist. John Rice has been a great mentor and a dear friend, helping me to make sure I don't take myself too seriously. A young researcher couldn't ask for a better role model, both in and out of the lab, than Jerry Hughes, and I'm looking forward to our working together in the near future. The last few years, I have always been able to count on Steve Wolfe's criticism and support to help make anything I work on simply better. Manfred Bitter, John Rice, Jim Terry and Bruce Lipschultz have all been generous with their time, teaching me everything there is to know about plasma spectroscopy. I would also like to thank Ray Fonck at Pegasus for his role in bringing me into the field of plasma physics and giving me the background that helped me succeed at MIT. Ian Hutchinson has been a wonderful adviser, giving me the freedom to explore all that C-Mod has to offer, while being available whenever I needed a sounding board. His ability to instantaneously deconstruct a theory or an experimental result and find its flaws has to be one of Ian's most inspiring and

irritating traits. My quixotic attempts trying to prove Ian wrong over the years have sharpened both my mind and my wit. I have thoroughly enjoyed this past year working closely with him on my thesis. Thanks to those that work behind the scenes, the administrators, the technicians, the students and the staff that allow me to selfishly spend most of my day thinking about plasmas physics.

I would also like to thank my family and friends for their support these past few years. Thanks to Craig, Dusty and all the people to inhabit 5 Michael Way over the years who have helped me to enjoy those few hours outside the lab. Thanks to my parents for supporting me and showing me how working hard can help me achieve my dreams. To Dr. Ashley A. Reinke, I don't know what your rush was, but I couldn't be prouder to come in second place to you. Lastly, I couldn't have made it through this past year without Paula, my kindred inquisitive spirit. If I had come to Boston simply to meet you, these years would have been worth it. This PhD business is just a nice bonus.

Contents

List of Figures

List of Tables

Chapter 1

Introduction

On November 21st, 2006, officials from China, the European Union, India, Japan, Korea, Russia and the United States gathered at the Elysee Palace in Paris to sign the ITER Agreement [1]. This act represented the culmination of decades of research in plasma physics and fusion science necessary to develop a magnetically confined plasma where power generated from fusion reactions exceeds the input power. ITER, designed to reach this break-even level and beyond, should provide much of the physics basis necessary to move onward to a demonstration reactor and, eventually, commercial generation of power from thermonuclear fusion. It is clear that significant physics and engineering work still needs to be done to insure the success of ITER and future reactors, motivating research efforts around the world, including experiments on the Alcator C-Mod tokamak at the Massachusetts Institute of Technology.

The core of a plasma used in generation of net power from fusion will contain deuterium and tritium fuel sources with temperatures reaching 10-20 keV or approximately 100-200 million degrees Kelvin. This represents the ideal conditions for the D-T fusion reaction,

$$\mathrm{D} + \mathrm{T} =^4 \mathrm{He} + n + 17.6\mathrm{MeV}, \tag{1.1}$$

to take place. The 17.6 MeV is split between the ^{4}He and n products according to conservation of momentum, with 3.5 MeV going to ^{4}He and 14.1 MeV going to the neutron [2]. The energy given to the neutron leaves the plasma, deposits its energy in

blanket materials around the reactor and will be used to generate electricity. The ^{4}He product, commonly called ash, is confined in the plasma, transferring its energy to the electrons and hydrogenic ions allowing the next fusion reaction to occur. This is referred to as the burning plasma state, where the reaction is self-sustaining, requiring external input power only to maintain stability and control.

Another class of particles likely to be present are impurities, which can refer to any ion besides the fusion reactants and products, and exist in fractions ranging from a few percent to a few parts per million. These can be introduced into the plasma deliberately or come from the surrounding structures. The presence of significant impurities represents a fundamental limitation to the efficiency of a reactor. Too many light impurity ions will dilute the plasma of hydrogenic fuel, and too many heavy impurities will increase power losses via photon radiation, removing energy from the core plasma necessary to maintain high temperatures. Conversely, impurities can also be used as tracers to gain insight into the plasma state, and their radiative properties are used to form boundary layers which help to maintain engineering limits by spreading out exhaust power. The capacity exists for impurities to be both beneficial and harmful to a fusion reactor and a thorough understanding of how they interact with high-temperature plasmas is an ongoing investigation. This thesis strives to validate and extend existing theoretical models that describe how impurities maintain equilibrium along closed magnetic field lines in a tokamak plasma.

1.1 Confining a Plasma Inside a Torus: the Tokamak

Confining the plasma energy long enough and at densities high enough for fusion power generation has been explored for over half a century. The method proven most effective is referred to as a tokamak, a transliteration of a Russian phrase meaning "toroidal chamber with axial magnetic field" [3]. Although modern tokamaks can confine heat and particles much better than their early predecessors [4], the basic

design of the device remains unchanged [5]. Its major components can be understood as correcting for various ways heat and particles can escape from magnetic fields.

The Lorentz force acting on a charged particle causes it to gyrate around a magnetic field line but allows unhindered movement along the field line. When trying to confine charged particles with a simple Helmholtz coil configuration any energy given to the particles quickly escapes out of the ends (along with the particles). This cylindrical geometry can then be wrapped into a torus, seemingly allowing the heat and particles to be confined indefinitely. But, the act of bending the magnetic field lines creates gradients and curvature in the magnetic field. As a charged particle gyrates around the magnetic field line, it samples regions of different magnetic field strength. Evaluating the kinematics of this process shows that the particles drift vertically off the field lines, deconfining the charged particles. If current is driven toroidally in the plasma a poloidal field is produced, making the field lines wrap helically around the torus. Now, as a particle moves along the field the vertical drifts are directed both radially inward and outward and the net motion is eliminated. This toroidal current loop is unstable, wanting to expand to larger radii, and so a vertical magnetic field is used to provide an inward $\mathbf{J} \times \mathbf{B}$ force. Figure 1-1 shows, schematically, these major components of a tokamak.

This combination of currents driven in the plasma and externally imposed fields results in the axisymmetric magnetic field, $\mathbf{B}$, of the form,

$$\mathbf{B} = I(\psi)\nabla\phi + \nabla\phi \times \nabla\psi = \mathbf{B}_t + \mathbf{B}_p \tag{1.2}$$

where $\nabla\phi = R\hat{\phi}$ and $\psi = 1/2\pi \int \mathbf{B}_p \cdot d\mathbf{A}$ the poloidal flux [6]. The first term in (1.2) is the toroidal magnetic field, $\mathbf{B}_t$, directed the long way around the torus, and the second is the poloidal field, $\mathbf{B}_p$, directed the shorter way. These fields add together to form the helical magnetic field lines that can be shown to lie on surfaces of constant poloidal flux, referred to as flux surfaces. In a tokamak, the toroidal field is stronger than the poloidal field and so the magnitude of $\mathbf{B}$ on a flux surface is determined mostly by $\mathbf{B}_t$, which varies like $1/R$. This introduces the concept of the high-field

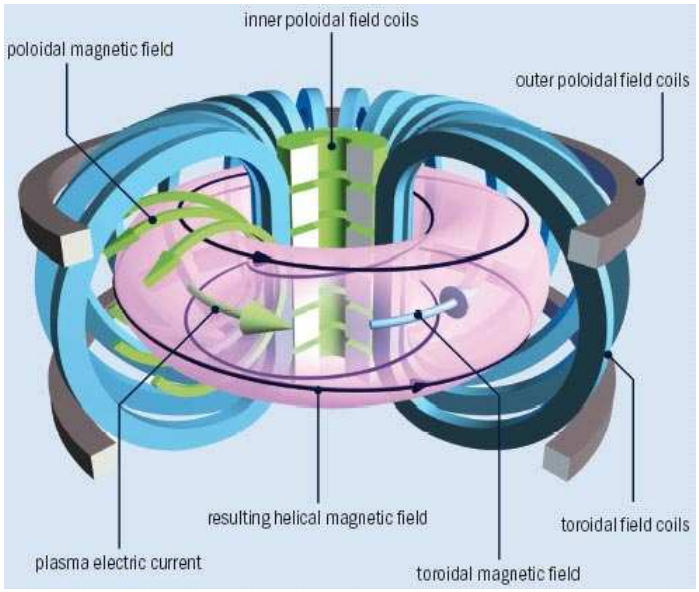

Figure 1-1: Schematic of basic tokamak components (http://www1.cfi.lu.lv/teor/main.html)

side (HFS) of a tokamak at small major radii and a low-field side (LFS) of a tokamak at large major radii.

The structure of flux surfaces, $\psi(R, Z)$ is found from the macroscopic force balance between the plasma pressure and the confining magnetic fields, and is known as the Grad-Shafranov equation [6].

$$R\frac{\partial}{\partial R}\left(\frac{1}{R}\frac{\partial \psi}{\partial R}\right) + \frac{\partial^2 \psi}{\partial Z^2} = -\mu_o R^2 \frac{\partial p}{\partial \psi} - I\frac{\partial I}{\partial \psi} \tag{1.3}$$

Both $p(\psi)$, the plasma pressure, and $I(\psi)$ are free functions that are constant on a flux surface. These surfaces are also commonly assumed to be contours of constant impurity pressure, but, as will be discussed throughout this work, variation of the impurity density on a flux surface is both predicted theoretically and observed experimentally. The goal of this thesis is determine if existing theories accurately predict the poloidal distribution of high-Z impurities.

1.2 The Alcator C-Mod Tokamak

Alcator C-Mod is a compact, high-field tokamak [7] built to study a variety of plasma physics and fusion engineering topics in support of the world-wide research effort to develop magnetic confinement fusion as an energy source. Figure 1-2 shows a cross-section of the entire tokamak with a typical last plasma boundary shown in magenta. Major and minor radii of typical plasmas are 0.68 m and 0.21 m, respectively, with plasma volumes $\sim$1 m^3 and surface areas of $\sim$7 m^2. Figure 1-3a shows details of the vacuum chamber and plasma facing components, as well as contours of constant ψ found by solving (1.3) constrained by magnetics measurements. The thicker red line is the boundary between closed and open field lines and is referred to as the last closed flux surface (LCFS) or separatrix. Also shown in 1-3a are the magnetics diagnostics used to constrain the equilibrium reconstruction, the green dots being flux loops sensitive to B_ϕ, and the cyan bars being poloidal field coils [8] sensitive to B_z. Figure 1-3b is a image of the same plasma captured using a video camera sensitive only to visible light, viewing radially into vacuum chamber. The intense emission in the lower part of the chamber, the divertor region, is actually coming from the colder part of the plasma where hydrogenic atoms are emitting visible radiation during recombination. The core of the plasma is so hot that photon emission is in the ultraviolet and soft x-ray range, 1-100 nm, and requires custom-built instrumentation to measure.

On-axis toroidal magnetic fields from $2.7 < B_t < 8.0$ T can be orientated, looking from the top down, in both the clockwise (normal-field) or counter-clockwise (reversed-field) direction. This has the effect of changing the direction of the cross-field particle drifts. When the toroidal field is in the normal direction, the ion $B \times \nabla B$ drift, the so-called ∇B drift, is pointed downward, while the opposite is true for reversed field. Plasma current, I_p, is always aligned with the magnetic field to maintain the same helicity, and ranges from 300 kA to 2.0 MA. Typical pulses last approximately 2 seconds with $\sim$1 second of constant current, also referred to as "flattop". Both hydrogen, deuterium and helium can all used as the main-ion species. Line-averaged electron densities of $0.3 < \bar{n}_e < 6.0\ 10^{20}$ m^{-3} and core electron temperatures,

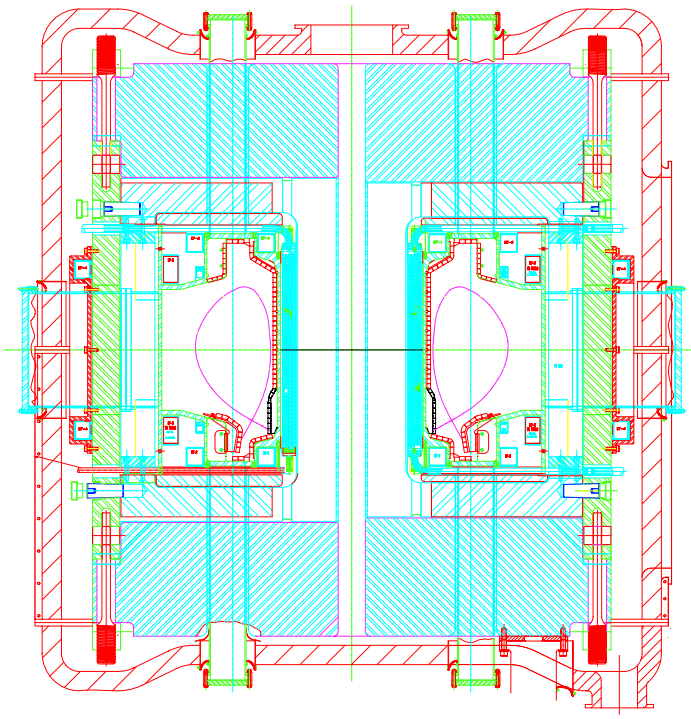

Figure 1-2: Engineering cross-section of the Alcator C-Mod tokamak

$T_{e,o}$, up to 9 keV have been achieved in deuterium plasmas.

The primary mechanism to heat the plasma is to drive current inductively using the Ohmic transformer. Auxiliary heating is provided by electromagnetic waves in the ion-cyclotron range of frequencies (ICRF), and both minority and mode-conversion heating schemes can be used. In minority heating, cyclotron waves travel through the plasma and damp on a small, < 10 %, fraction of a minority ion which then transfers energy via Coulomb collisions to both electrons and ions. Both D(H) and D(^{3}He) majority(minority) have been explored in C-Mod. A single four-strap antenna operates at frequencies from 50-78 MHz and powers up to 3 MW, and two dipole antennas at 80 and 80.5 MHz each provide up to 1.5 MW of input power, for a total of $\sim$6 MW [9].

Heat and particles exhausted from the plasma are directed to molybdenum plasma facing components (PFCs) in both limited and diverted geometries. Small, $\sim$1 inch tiles make up the armor of the divertor, inner wall and outer limiters as seen in Figure 1-3. The plasma flux causes sputtering and an intrinsic molybdenum impurity

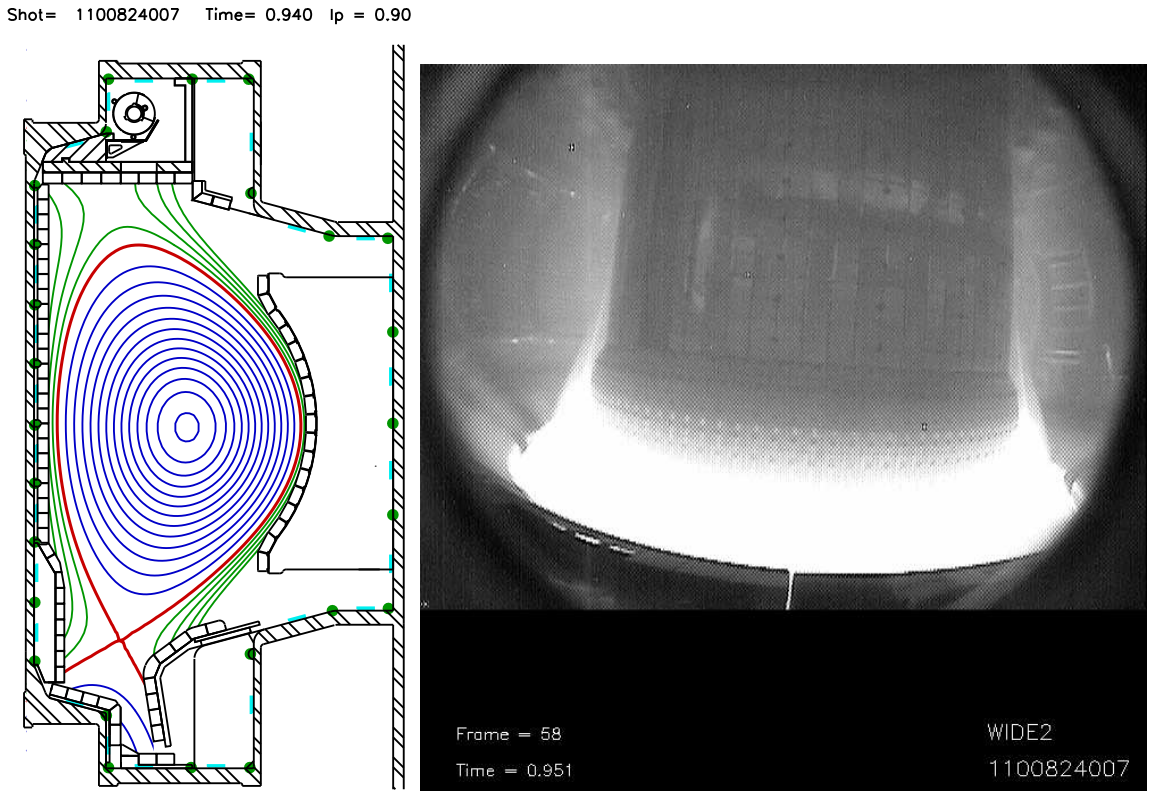

(a) (b)

Figure 1-3: Cross-section of the vacuum chamber showing flux surfaces (a) and a visible camera view of C-Mod during a plasma (b)

is present in all C-Mod plasmas, with n_{Mo}/n_e from 10^{-5} $\rightarrow 10^{-3}$. The use of ICRF is correlated with an increase in Mo concentration. Deposition of a thin boron layer on the surfaces, via a low-temperature cyclotron discharge seeded with diborane, D_2B_6, is used to temporarily reduce the level of molybdenum and leads to intrinsic B impurity estimated to be at the 1% level. More comprehensive information on the design, operation, diagnostics and research of the Alcator C-Mod tokamak can be found in [7],[10] and [11].

1.3 The Impact of Impurities in Fusion Plasmas

Production and transport of impurities have been studied both experimentally and theoretically since the beginning of tokamak research. Early tokamaks observed contamination of plasmas from PFCs [12][13], and it was observed that operating regimes which are good at confining energy also tend to be good at confining high-Z impurities [14][15]. Impurities are not simply an efficiency issue for future reactors to worry about, but represent a day-to-day challenge in performing controlled experiments on modern tokamaks.

Low-Z ions, typically thought of as ions with atomic mass Z $\leq$ 10 are fully ionized in the core of most tokamak plasmas. In a fusion plasma, low-Z ions dilute the core and reduce the DT reaction rate, starving the plasma of heat. The effective charge of the plasma, $Z_{eff} = \sum n_j Z_j^2/n_e$, is increased along with the power loss due inelastic electron-ion collisions, also referred to as bremsstrahlung. High-Z impurities, Z $>$ 10, tend to remain only partially ionized. In these cases, electron-ion collisions elevate bound electrons to excited states which quickly decay, releasing the collision energy as photon emission which, in most cases, promptly leaves the plasma. Refractory metals such as molybdenum and tungsten are used as PFCs due to their high melting temperatures, but since ionization energies scale as Z^2, these atoms will remain only partially ionized for all DT burning plasmas. Small influxes of high-Z impurities such as tungsten quickly convert plasma thermal energy into radiation, and, in some cases the large radiative losses can change pressure profiles enough to destabilize the plasma

and terminate the discharge.

Examining 0-D power balance, it is straightforward to estimate the typical fractions of each type of impurity that will impact the operation of the tokamak fusion reactor. In steady state,

$$\frac{W_{th}}{\tau_E} = P_\alpha + P_{ext} - P_{rad} \tag{1.4}$$

where P_α is the power supplied to the plasma by α particles from fusion reactions, P_{ext} is the power provided by external heating mechanisms and P_{rad} is the power lost due to radiation. The total fusion power, P_{fus}, is the sum of the α heating and the power going to the neutrons. Modeling of the T_e-dependent radiation physics for impurities is taken from [16]. W_{th} is the thermal stored energy density, $3/2(n_i T_i + n_e T_e + n_z T_z)$, integrated over the plasma volume, and τ_E is energy confinement time which characterizes the energy loss through radial heat conduction. Both $Q = P_{fus}/P_{ext} = 10$ and $T_e = T_i$ are assumed, reasonable estimates for an ITER-like burning plasma. Reorganizing (1.4) allows for the $n_e\tau_E$ required to maintain steady-state to be plotted versus T for different levels of impurities. In Figure 1-4a, this relationship is plotted for tungsten and Figure 1-4b for carbon, another common PFC material. Very small fractions of tungsten, from 10^{-5} to 10^{-4}, quickly raise $n_e\tau_E$, while much larger amounts of carbon, 4-8%, are needed to have the same effect. Increasing both $n_e\tau_E$ and T are serious challanges for tokamaks, and can be overcome by increasing the size of the device and thus the cost, or by moving closer to stability limits, risking the integrity of the reactor. The required $n_e\tau_E$ will be pushed even higher when including a realistic amount of He ash. To ensure the best chance of success for ITER and other burning plasmas, an empirical, if not a comprehensive theoretical, understanding of impurities in tokamaks is necessary.

1.4 Impurity Transport in Tokamaks

The global picture of impurities in tokamaks involves a variety of physical processes over a wide range of densities, temperatures, length and time scales. For intrinsic impurities, it starts with knowing how plasma interacts with material surfaces at the

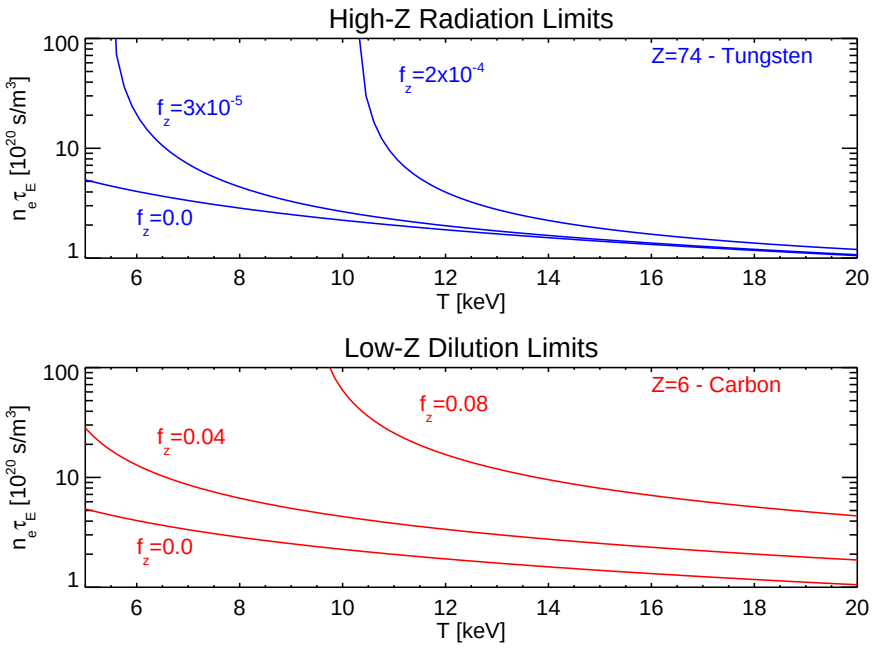

Figure 1-4: $n_e\tau_E$ required at Q=10 for non-zero high-Z (a) and low-Z (b) impurity fraction

atomic level to erode and sputter impurities into the plasma. For both intrinsic and deliberately introduced impurities, it then becomes the study of how the impurities are ionized and transported along and across open field lines in the plasma scrape-off layer and divertor. Once inside the confined plasma, the focus is on how the impurities reach equilibrium along the field and what influences their transport across flux surfaces. All of these topics are part of on-going investigations at both Alcator C-Mod and most of the world's tokamak facilities, but the focus of this research is transport inside the confined plasma.

The neoclassical theory of radial impurity transport is well developed [17] but decades of experimental measurements on many tokamaks have shown cross-field impurity fluxes to be significantly higher than this theory would predict [18][19][20][21][22]. Historically referred to as anomalous transport, this is thought to be due to plasma turbulence and is still an area of active research.

Theories describing parallel impurity transport predict that the impurity density can vary along the magnetic field in situations where the ions can still be assumed

to be evenly distributed (see Table 2.1). This poloidal variation is attributed to the impurity's high charge and large mass. The large mass enhances inertial effects like the centrifugal force arising from toroidal rotation, and can lead to accumulation of heavy impurities on the outboard side of a flux surface. The high charge enhances ion-impurity friction and makes impurities sensitive to small poloidal variations in the electrostatic potential. While experimental measurements have observed poloidal asymmetries in impurity density on a number of tokamaks (see Table 2.2), a validation [23] effort of the most comprehensive theoretical work [24] has not been completed. In this research, measurements of poloidal impurity density variation in Alcator C-Mod plasmas are compared to existing theories of neoclassical transport along closed magnetic field lines.

1.5 Motivation for Studying Parallel Impurity Transport

While significant attention has been devoted to radial impurity transport over the past decades, a comparatively small amount of effort has been devoted to the study of parallel impurity transport. This can understood by the relative success and failure of neoclassical theory describing the two processes. While radial impurity transport is much higher than theoretical predictions, early efforts at examining the direction and magnitude of poloidal asymmetries of impurities [25] seemed to be in much better agreement and thus, justifiably, attention was diverted to empirical characterization of anomalous radial impurity transport. Recently, turbulent impurity transport has been computed using linear [26][27] and non-linear gyro-kinetic codes [28], and when compared to measurements, much closer agreement is found relative to neoclassical predictions. In the effort to demonstrate our understanding of impurity transport in tokamaks we should revisit the topic of parallel impurity transport as discrepancies between gyro-kinetic modeling and experiment are reduced to levels where accurately including poloidal asymmetries can be quantitatively important.

1.5.1 Influence on Radial Impurity Transport

The impurity force balance along the field determines the poloidal variation of n_z, which in turn is used to compute the flux-surface averaged radial particle flux, $\langle \nabla\psi \cdot \vec{\Gamma}_z \rangle$ for both neoclassical and anomalous processes. Knowing the physics that controls the impurity flux, $\vec{\Gamma}_z = n_z \vec{v}_z$, will help to confidently explore burning plasma scenarios that can avoid an impurity-driven demise.

The neoclassical effects of n_z asymmetries on radial flux can be qualitatively explained by looking at the orientation of cross-field drifts. The ∇B drift always points in one direction and, for the toroidal field in the clockwise direction, viewed from above, the ions will tend to drift towards the core when above the magnetic axis, and away from the core when below it. If a poloidal variation of the density has a $\sin\theta$ term, then more particles will drift in than out, creating a pinch effect.

Heuristic descriptions of neoclassical particle diffusion explain radial transport driven by unlike particle collisions with $D_{\perp,a} \sim \frac{1}{2}\nu_{ab}\rho_a^2$. If, for example, the impurities accumulate on the outboard side, more ion-impurity ($a = i$, $b = z$) collisions will occur where the magnetic field is weaker and ρ_i is larger, increasing $D_{\perp,i}$ [29]. In cases where the radial electron flux is small, the non-ambipolar nature of radial particle transport in tokamaks can lead to $\Gamma_i = -Z\Gamma_z$, and the impurity transport influence the ion transport when $Zn_z/n_i \sim 1$.

Wong explored the effect of spatial asymmetries in impurity density for the collisionless main-ion regime, deriving the sensitivity of the impurity particle transport in a rotating plasma where centrifugal force moves heavy impurities to the outboard side of a flux surface [30]. The neoclassical radial impurity particle flux (1.5) is proportional to gradients in particle density and temperature, and the coefficients C_{11} and C_{12} are shown to be sensitive to toroidal rotation.

$$Z\Gamma_z = C_{11}\left(\frac{1}{Z_i}\frac{n_i'}{n_i} - \frac{1}{Z_z}\frac{n_z'}{n_z}\right) + C_{12}\frac{T'}{T} \tag{1.5}$$

Figure 1-5 from [30] shows the change in C_{11} and C_{12} for a trace amount of Ar versus toroidal velocity, $U = \omega_\phi R_o$, normalized to the main ion thermal speed, $\bar{v}_i$.

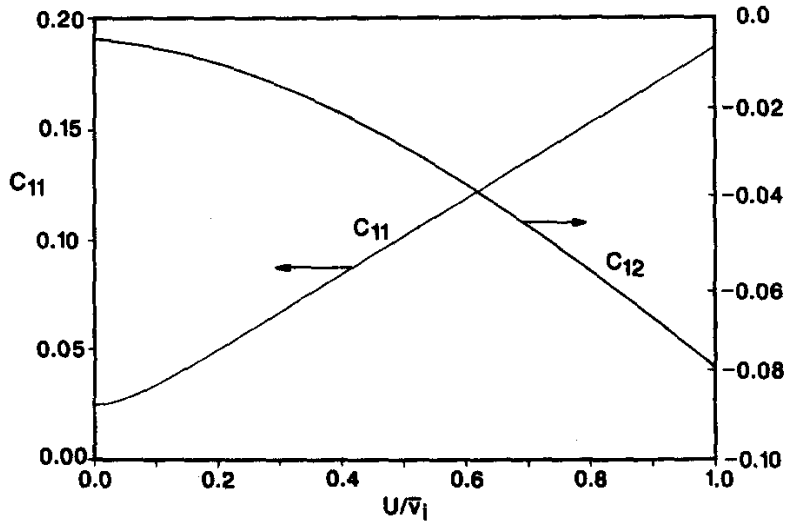

FIG. 5. The transport coefficients C_{11},C_{12} for a trace amount (0.1%) of Ar^{+18} ions in a hydrogen plasma, measured in units of $n_i\sqrt{\delta}\rho_{\theta i}^2/\tau_i$.

Figure 1-5: Neoclassical impurity flux coefficients versus main ion rotation (from [30])

Significant changes in both constants are seen even for moderate changes in $U/\bar{v}_i$.

Fülöp and Helander examined the impact of poloidal asymmetries driven by ion-impurity friction on the radial impurity flux [24]. Illustrated in Figure 1-6, $\langle \nabla\psi \cdot \vec{\Gamma}_z \rangle$ is nonlinear in the parameter g, proportional to a combination of the radial gradients in the main-ion temperature and density. A flux-gradient relationship like this which exhibits local maxima and minima implies the possibility of bifurcation between states with equal flux but steep or weak gradients [31].

For anomalous transport, the impact of poloidal impurity asymmetries on radial transport is only starting to be explored. The electrostatic potential fluctuations and the resulting $\mathbf{E} \times \mathbf{B}$ particle flux have been predicted to be poloidally asymmetric with a larger intensity on the outboard side [32], consistent with ballooning-type instabilities in the bad magnetic curvature region. In/out [33] and up/down [34] asymmetries of these types of fluctuations have also been observed experimentally. In turbulent transport, the zero flux gradient scale length, L_{nz}^0 is the impurity density gradient calculated to make the radial particle flux equal to zero, implying a steady state. Initial calculations show L_{nz}^0 sensitive to the orientation and magnitude of

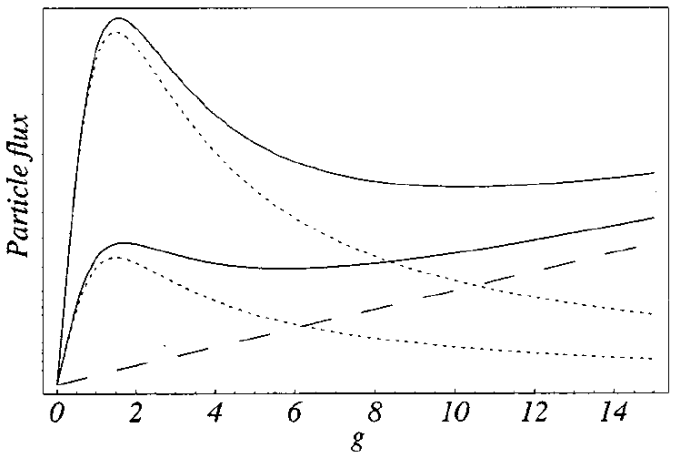

FIG. 3. Ion particle fluxes versus normalized gradient g in a large-aspect-ratio tokamak with circular cross section, $\epsilon \ll 1$, $\alpha = 0.5$, $q = 3$. The dashed line is the classical flux, the dotted lines are neoclassical fluxes, and the solid lines represent the sum of classical and neoclassical fluxes. The lower pair of dotted and solid lines are for vanishing toroidal rotation, $M_0^2 = 0$, and the upper pair for impurity Mach number $M_0^2 = 1$. Note that the neoclassical fluxes are enhanced by finite rotation and suppressed by large gradients.

Figure 1-6: Neoclassical impurity flux coefficients driven by friction (from [24])

the poloidal asymmetry. Figure 1-7, reproduced from [35] models the variation as $n_z(\theta)/\langle n_z \rangle = (\cos[(\theta - \delta)/2])^{2n}$ and plots the change in L_{nz}^0 for various values of n and δ. For $\delta = \pi$, impurities accumulate on the inboard side of a flux surface, and the zero flux density scale length decreases as n increases, implying flatter radial impurity density profiles. For $\delta = 0$, impurities accumulate is on the outboard side, and L_{nz}^0 increases with n, implying more peaked impurity density profile, an undesirable result for a reactor.

These examples demonstrate a sensitivity of radial impurity transport to the details of the flux surface distribution of the impurities. In order to confirm our understanding of cross-field transport, neoclassical or anomalous, the effects of parallel impurity transport must be included.

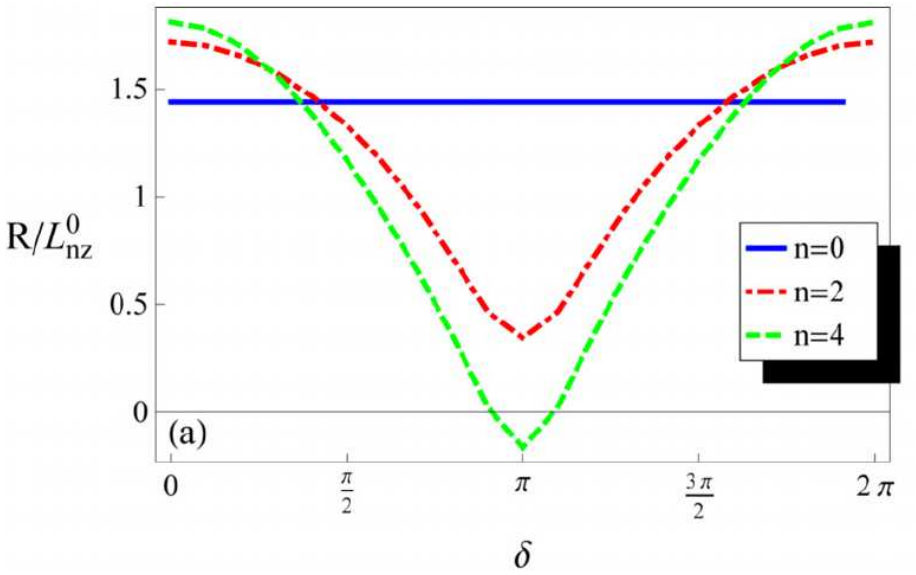

(a)

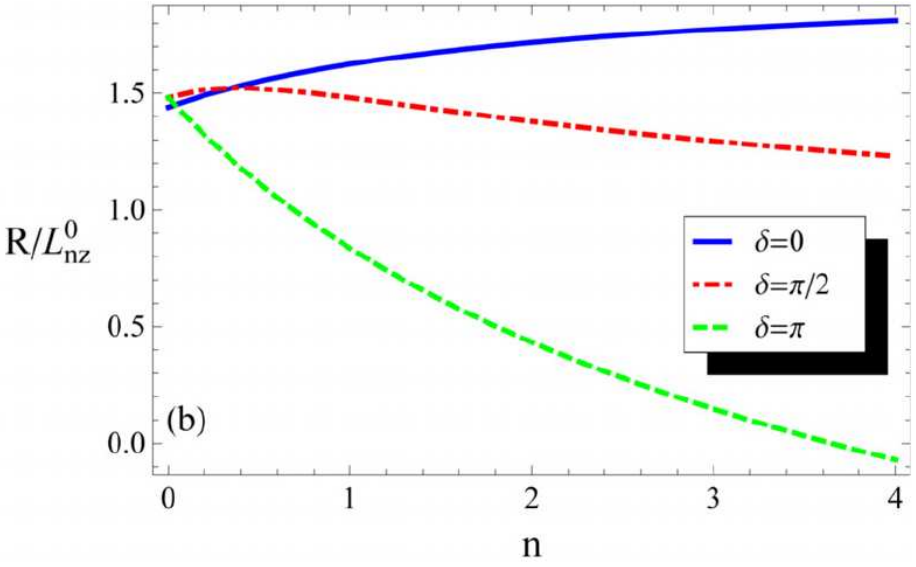

(b)

Figure 1-7: Zero flux impurity density scale length sensitivity to magnitude and type of asymmetry (from Fülöp and Moradi [35])

1.5.2 Impact on Diagnostic Interpretation

The accuracy of modern plasma diagnostics also benefits from a predictive understanding of parallel impurity transport. Tools that measure radiation from impurities typically do so by integrating through a volumetric emitter that varies as a function of space. These projections, or line-integrated measurements, are typically inverted to find local plasma quantities using standard tomographic techniques. The restricted diagnostic access in a tokamak often means the inversion is done with less information than desired and a variety of techniques are used to constrain the results. Qualitative understanding of parallel impurity transport can reduce the complexity of the inversion problem and motivate design choices to avoid sensitivity to asymmetries. If the theory can be shown to get the poloidal scale length correct, then this can be added as *a priori* information to help constrain the inversion. These diagnostic tools are usually the same ones that are used for radial impurity transport studies, and systematic errors in transport coefficients can come from ignoring poloidal structure. If not properly accounted for, this will limit the accuracy of experimental measurements used to validate anomalous impurity transport models.

A relevant example of this is shown for calculations of the volume-averaged radiated power, P_{RAD}, in Alcator C-Mod. The radiated power density profile, [MW/m^3], is found on the outboard midplane [36] and assumed to be constant on a flux surface when determining P_{RAD}. Figure 1-8 shows the consequence of having an in/out asymmetry, $\varepsilon = \langle\varepsilon\rangle + \varepsilon_c \cos\theta$, using a typical H-mode emissivity profile, and assuming an asymmetry similar to those dominated by the centrifugal force at levels relevant for C-Mod. As the peak $\varepsilon_c / \langle\varepsilon\rangle$ increases, the calculated radiated power is above the actual P_{RAD} due to impurities accumulating on the outboard midplane. If parallel theory is shown to be accurate, and inertia is all that determines $n_z(\theta)$, then by measuring the rotation profile the centrifugal force can be calculated and the error in P_{RAD} reduced without going through the effort and expense of measuring the full 2D radiation profile.

In cases where quantitative accuracy can be demonstrated it reduces the complex-

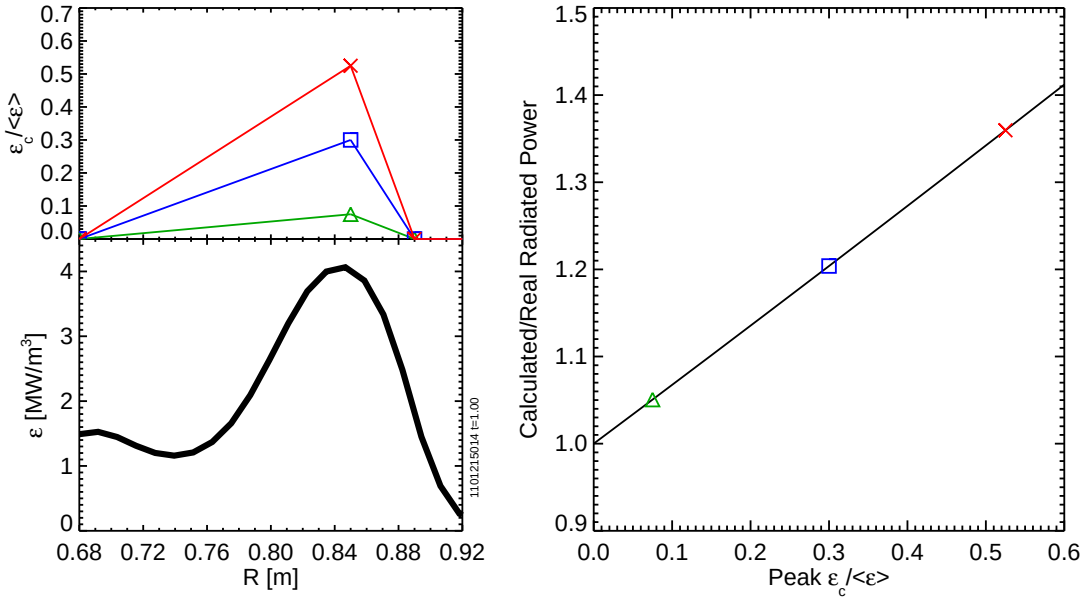

Figure 1-8: Overestimation of radiated power due to an in/out asymmetry

ity of the problem back to 1-D with the poloidal variation predicted from background plasma profiles. For some diagnostics, like soft x-ray tomography, the cost to add more detectors is relatively low and systems with extensive coverage are common to most tokamaks. For other tools, like soft x-ray Doppler tomography [37] used to measure flows and ion temperature, the ability to reduce a 2-D tomography problem to 1-D presents significant cost savings. If poloidal variation is simply left unaccounted for, errors in the calculated profiles can occur and estimates show that even an unaccounted for $\sim$10% variation in the impurity density can significantly alter the derived density and temperature profiles. Details on this topic are discussed in Section 7.3.

It is very difficult to measure the flow and temperature profiles of the main ions because they are fully ionized and so measurements of these quantities in the impurity species are done using charge exchange recombination spectroscopy (CXRS) and soft x-ray Doppler spectroscopy. When impurities are used in this manner as tracers to measure properties of the plasma, the underlying physics describing the coupling of the impurities to the ions becomes important. In fusion-grade plasmas, the difference between the ion and impurity temperature is usually negligible due to strong collisional energy transfer between the two species, and $T_i = T_z$ is a valid assumption. For

flows, there are important differences in both diamagnetic flow and poloidal rotation, v_θ. In fact, it is the solution of the parallel impurity transport equation under investigation in this research that allows the ion velocity to be predicted from the impurity velocity. Section 6.5 describes in more detail the important coupling between parallel flow and flux surface asymmetries of density.

1.6 Organization of the Thesis

In Chapter 2, the evolution and current state of parallel impurity transport theory are reviewed, and a comprehensive overview of previous experimental measurements of poloidal impurity density asymmetries, both on Alcator C-Mod and other tokamaks, is presented. Chapter 3 describes the tools and analysis methods used to infer poloidal variation of impurity density, as well as those necessary to compare measurements to the theories discussed in Chapter 2. Chapters 4, 5 and 6 present the experimental results with each chapter focusing on the influence of specific physical mechanism in parallel force balance. Chapter 4 deals with in/out asymmetries driven by centrifugal force in collisionless plasmas, and shows how this force cannot fully explain C-Mod measurements. Chapter 5 discusses how the in/out asymmetry is modified by the poloidal electric field from ion cyclotron heated minority ions. Theory discussed in Chapter 2 is extended to include this effect, which compares well with experimental data. Chapter 6 explores up/down and in/out asymmetries driven by ion-impurity friction, showing disagreement between measured up/down asymmetries and predictions from theory in the trace impurity limit. Chapter 7 discusses the implications of this research for the tokamak community and suggests topics for future investigations into parallel impurity transport. Choosing to err "on the side of comprehensiveness rather then brevity" [38], Appendices A, B and C are included to discuss in gruesome detail some of the diagnostic and code verification efforts completed as part of this research, while Appendix D presents initial results on an up/down asymmetry possibly linked to anomalous transport.

1.7 Summary of Primary Results

The following are the most significant contributions this research has made, both to the Alcator C-Mod group and the plasma physics community as a whole.

1. **Demonstrating a large $\tilde{n}_z/\langle n_z \rangle \sim 0.3$ in/out asymmetry due to intrinsic rotation on Alcator C-Mod**

   Previously, in/out asymmetries due to the centrifugal force have only been observed in neutral beam-heated plasmas using significant external torque. This research shows that flux surface asymmetries in high-Z impurity density can develop in cases of self-generated flows. For Alcator C-Mod, these asymmetries are robustly produced in all high confinement plasmas, but have remained undiagnosed until now.

2. **Establishing the impact of fast ion pressure anisotropy on parallel impurity transport**

   Ion cyclotron heating is known to create poloidal variations in minority density by increasing magnetic trapping, but the influence this has on parallel impurity transport has not been firmly established experimentally or thoroughly investigated analytically. Existing parallel transport theory is extended to include effects from particle distributions exhibiting a pressure anisotropy. Measurements on C-Mod conclusively show a link between ICRH and inboard accumulation of impurities, and initial calculations using the extended theory agree well with experimental results. The sensitivity of the impurity asymmetry to small poloidal potential variations also demonstrates its effectiveness as a measure of the poloidal electric field, E_θ, and/or a simple fast-ion diagnostic.

3. **Defining a more rigorous experimental test of ion/impurity friction, linking asymmetries and poloidal rotation**

   Measurements of up/down asymmetries driven by ion/impurity friction are shown to disagree with theory in the trace impurity limit, $n_z Z^2/n_i \ll 1$. In practice, background impurities and/or the impurity whose asymmetries are

being measured can have $n_z Z^2/n_i \sim 1$, where ion/impurity friction will begin to affect the main ions. Unlike when inertial or electrostatic forces dominate, this cannot be handled by including a Z_{eff} term, and finding the impurity asymmetry requires solving a coupled set of differential equations for the main-ions and all impurity species. The friction also plays a role in defining the impurity poloidal rotation, $v_{\theta,z}$, found by solving the 1-D parallel transport problem. Thus, to fully validate parallel impurity transport theory when friction is involved, the flux surface asymmetries and $v_{\theta,z}$ must be correctly predicted.

4. **Reviewing impurity asymmetry theory**

   When reviewing the published works on neoclassical parallel impurity transport it is clear that there is not an authoritative reference as for radial impurity transport in Hirschman and Sigmar [17]. In some instances, similar results had been derived by multiple authors, decades apart without any apparent reference or knowledge. The overview and comparison of these theories should serve as a useful contribution to the plasma physics community.

5. **Expanding the use of spatially-resolved soft x-ray crystal spectroscopy for $\mathbf{T}_i$ and ω_ϕ profiles**

   In order to compare the measured asymmetries with theory, accurate ion temperature and rotation profiles were necessary. Significant effort was spent on advancing the quality of the spectral fitting and Doppler tomography codes used to analyze data from the imaging x-ray crystal spectrometer diagnostic. These contributions have enabled the use of this instrument, the first of its kind, in a wide variety of C-Mod research efforts.

Chapter 2

Background

This chapter discusses prior theoretical and experimental investigations into parallel impurity transport in tokamak plasmas. The first experimental measurements were done in 1977 on Alcator-A and since then there has been infrequent, albeit continual, production of measurements and advancements in analytical theory. In Section 2.2, the historical development of asymmetry theory will be briefly discussed, and details of the most comprehensive parallel transport theories will be presented, focusing on predictions for the impurity density variation on a flux surface in the low collisionality regime. The most current theories have yet to be validated by experimental results and are a central focus of this research. Section 2.3 briefly discusses computational implementation of parallel impurity transport. In Section 2.4, experimental measurements of both up/down and in/out asymmetries are reviewed, organized by experimental facility, with important previously published results included. Table 2.1 and 2.2 provide a comprehensive overview of the theoretical and experimental research on parallel impurity impurity transport published over the last 30+ years.

2.1 Neoclassical Transport Theory

Classical transport, reviewed in [39] [40], deals with the transport of heat, momentum and particles parallel and perpendicular to straight magnetic field lines. Neoclassical transport theory [39] [41] expands classical transport to include the effects of curved

magnetic field lines. For an axisymmetric system like the tokamak, this is driven primarily by the inhomogeneity of the magnetic field, but spatial derivatives of unit vectors also play a role, creating effects such as the centrifugal force due to toroidal rotation.

In order to understand changes in the macroscopic plasma properties, neoclassical theory applies simplifying assumptions to the underlying Fokker-Planck equation governing the evolution of each particle's distribution function. These are referred to as transport orderings or drift-kinetic orderings. Collisional frequencies are assumed to be much smaller than the gyro frequency, $\nu \ll \Omega$, allowing this motion to be averaged over. The macroscopic scale lengths, L, are assumed to be small large relative to the Larmor radius, $\delta = \rho/L$, making the particle sample a homogeneous plasma over the gryo motion. This has the significant impact of making the particle distribution functions Maxwellian to lowest order in δ. In most regions of the plasma this is valid but in edge transport barriers of typical H-mode plasmas, $\delta \sim 1$ has been observed [42]. Analytical theory is just beginning to probe this region [43].

Assuming an axisymmetric system, these simplifications and knowledge of the cross-field particle drifts it can be used to show that in order for the particle flux to be divergence free, the velocity of each particle species must have the form,

$$\mathbf{V}_a = -\left(\frac{\partial \Phi}{\partial \psi} + \frac{1}{Z_a e n_a}\frac{\partial p_a}{\partial \psi}\right) R\hat{\phi} + \frac{K_a(\psi)}{n_a}\mathbf{B} \tag{2.1}$$

where Φ is the electrostatic potential and K_a is a flux-function specified by solving the parallel force balance equation. This is also commonly written in the form,

$$\mathbf{V}_a = \omega_a(\psi)\, R\hat{\phi} + u_a(\psi)\,\mathbf{B} \tag{2.2}$$

where ω_a can be thought of as the solid-body toroidal rotation frequency, and u_a is related to purely poloidal rotation, $v_\theta = u_a B_\theta$.

Another simplification that is often used to make further progress is the small inverse aspect ratio approximation, $\epsilon \ll 1$. This can hold in the core as $r/a \to 0$ but closer to the edge of conventional tokamaks, $\epsilon = r/R_o \sim 1/3$. Since it is not employed

universally and can be violated in C-Mod experiments, it will be noted when $\epsilon \ll 1$ is used. When this is assumed, the $\rho/L \ll 1$ assumption must be made more stringent and a small poloidal Larmor radius, $\delta_\theta = \rho_\theta/L \ll 1$, is required [39].

Neoclassical theory is broken down further into different regimes depending upon the frequency of charged particle collisions, ν, relative to the their transit frequency, $\omega_{tr} = v_{th}/qR_o$, around the tokamak. There is the Pfirsch-Schlüter regime, also referred to as collisional or short mean-free path regime, where $\nu/\omega_{tr} \gg 1$, the plateau-regime where $\epsilon^{3/2} < \nu/\omega_{tr} < 1$ and the banana regime, also referred to as collisionless or long mean-free path regime, where $\nu/\omega_{tr} \ll \epsilon^{3/2}$. In the Pfirsch-Schlüter regime, the charged particles sample only local conditions. As the collisions become more infrequent, a particle experiences more of the inhomogeneity of the tokamak and can become trapped in the magnetic well on the outboard side rather than move completely around the torus. Each collisionality regime requires a different approach in solving the underlying kinetic equation to take these effects into account.

Although there have been observations of radial impurity transport consistent with neoclassical theory in edge [44] and internal [45] transport barriers, the regions of the plasma that are studied in this work exhibit significantly larger cross-field impurity flux, often referred to as anomalous transport. This is worth noting in the context of the current research because the theory that will be discussed in the next section assumes that equilibrium is reached along the field much faster than that across the field, $\tau_\parallel \ll \tau_\perp$. This is certainly consistent with the drift-kinetic orderings, but experimental observations show radial flux to be >10 times higher than is assumed in the derivations. The prospect of violating this assumption is discussed in section 2.2.6.

2.2 Parallel Impurity Transport Theory

Often it is assumed, sometimes incorrectly, that transport along the magnetic field is strong enough to make the density and temperature of all species flux-functions to first order in δ. But, as has been pointed out by several authors (see Table 2.1), it is

possible to sustain gradients in impurity pressure along the field, even while retaining the nominal flux-surface symmetry of the main-ion and electron species. Although the basic parallel momentum balance equations are the same for ions and impurities, the charge and mass of the impurities weight terms differently. The large impurity mass enhances inertial effects like the centrifugal force, tending to push impurities to the low-field side of a flux surface in cases of significant toroidal rotation, ω. The high charge of the impurity amplifies any small poloidal variation of the electrostatic potential and the impurities respond in a Boltzmann-like manner to $\Phi(\theta)$ along the field. When the impurity density is small, $n_z Z^2/n_i \ll 1$, self-collisions are negligible and collisional processes with the main-ion species dominate, and may lead to to an impurity density asymmetry that is driven by the poloidally varying ion-impurity friction.

Examining the body of work as whole there are common themes that are observed. The starting equations are essentially the same and the differences lie mainly in the simplifying assumptions and solution methods. To determine the poloidal variation of the impurity density, their source free, steady-state particle conservation (2.3) and momentum balance (2.4) equations for are used. Due to their higher charge and mass, impurities are assumed to be in the collisional regime, and the fluid equations for the impurities are employed nearly universally throughout the literature.

$$\nabla \cdot (n_Z \mathbf{V}_Z) = 0 \tag{2.3}$$

$$n_Z m_Z (\mathbf{V}_Z \cdot \nabla) \mathbf{V}_z + \nabla p_Z + \nabla \cdot \pi_Z + Z n_Z \nabla \Phi + Z n_Z (\mathbf{V}_Z \times \mathbf{B}) = \mathbf{R_Z} \tag{2.4}$$

Here, $\mathbf{R}_Z$ is the sum of the friction forces and π_Z is the viscosity tensor. The energy conservation can be ignored if the impurity-ion equilibration timescale, τ_{zi}, is significantly less than the parallel momentum equilibration timescale, $\tau_{\|}$, making $T_z = T_i$.

$$\tau_{ii} = \frac{12\pi^{3/2}}{\sqrt{2}} \frac{m_i^{1/2} T_i^{3/2} \epsilon_0^2}{n_i Z_i^4 e^4 \ln \Lambda} \tag{2.5}$$

$$\tau_{zi} = \tau_{ii} \frac{\sqrt{m_z} Z_i^2}{\sqrt{m_i} Z_z^2} \tag{2.6}$$

In order to decouple the parallel and perpendicular transport to simplify the problem, $\tau_{\|} \ll \tau_{\perp}$ is assumed to be valid and explored further in Section 2.2.6. For trace impurity species, $n_z Z^2/n_i \ll 1$, the ion and electron dynamics are independent of the impurities and requires a solution of the two species' coupled fluid or kinetic equations, depending on the assumed collisionality. The electron and ion density are used to determine the poloidal potential variation, $\hat{b} \cdot \nabla \Phi$ and the ion-impurity collisional terms, $\hat{b} \cdot \mathbf{R}_z$ and $\hat{b} \cdot (\nabla \cdot \pi_z)$. The electron-impurity collisional effects are ignored as they are $\sqrt{m_e/m_i}$ smaller. As the impurity density increases, ion-impurity collisions can influence the ion equation, and the impurity density must be included in the electrostatic potential when solving for quasi-neutrality. This couples all species together, increasing the complexity of the asymmetry physics.

Table 2.1 outlines nearly all of the theoretical work done on parallel impurity transport, displaying which terms in (2.4) are included and what main-ion collisionality and impurity strength parameter, $\alpha_z = n_z Z^2/n_i$, are assumed. The next sections describe the theoretical development of parallel impurity transport theory, focusing on the physics behind the asymmetries driven by inertia (2.2.1), ion-impurity friction (2.2.2) and externally sustained potential variations (2.2.3). Comprehensive theories that include a balance of multiple forces are discussed in 2.2.4 and will be used for comparison to experimental data.

2.2.1 Asymmetry due to Centrifugal Force

The effect of strong toroidal rotation on ion density profiles has been known since early work on transport theory [41]. In Hazeltine and Ware [46] the effect on the impurity density was first explored, acknowledging that the impurity's large mass enhances the centrifugal force. An explicit equation for $n_z(\psi, \theta)$ was not presented as their focus was on the response of the main-ions to the poloidal potential variation generated by the asymmetric impurities. Wong [30] derived the first expression for $n_z(\theta)$, a result that was rediscovered in the next decade by Wesson [56] and Helander

SOURCE	YEAR	n_Z FORCE			$\lambda_{i,mfp}/L_\parallel$			α
		inertia	fric.	visc.	$\gg 1$	$\simeq 1$	$\ll 1$	
Hazeltine and Ware [46]	76	X				X		$\simeq$Z
Burrell and Wong [25]	79		X				X	$\ll 1$
Tendler [47]	80		X				X	≥ 1
Chang and Hazeltine [48]	80		X				X	$\gg 1$
Burrell, Ohkawa & Wong [49]	81	X	X		X	X	X	$\ll 1$
Brau, Suckewer& Wong [50]	83		X		X	X	X	$\ll 1$
Stacey [51]	86	X	X	X	X	X	X	arb
Wong [30]	87	X			X			arb
Feneberg [52]	89	X	X	X	X	X	X	$\ll 1$
Hsu and Sigmar [53]	90	X	X	X			X	arb
Stacey [54]	92	X	X	X	X	X	X	arb
Rozhansky and Tendler [55]	96		X			X		$\simeq$1
Wesson [56]	97	X					X	arb
Helander [29]	98	X			X			$\ll$1
Romanelli and Ottaviani [57]	98	X	X				X	$\ll$1
Helander [31]	98		X		X			$\simeq$1
Fülöp and Helander [24]	99	X	X		X			arb
Fülöp and Helander [58]	01		X				X	arb
Stacey [59]	02	X	X	X	X	X	X	arb
Landreman [60]	11		X			X		arb

Table 2.1: Theoretical work on parallel impurity transport, organized chronologically.

[29]. There are actually two terms at work for the asymmetry driven by centrifugal force, the inertial and electrostatic forces. In a pure plasma, the inertia will effect the main-ions and electrons differently, and a small poloidal electric field is necessary to maintain quasineutrality. The large charge of the impurities amplifies this variation and for highly ionized, heavy impurities, $Z/m_Z \sim 2$, making both terms the same order.

Taking the parallel dot product of the momentum equation (2.4) and keeping the inertia, self-pressure and electric field terms, the poloidal variation of n_z is straightforward to compute since the only ion-impurity coupling is through quasi-neutrality. Assuming that the rotation is dominated by $\mathbf{E} \times \mathbf{B}$ flow and the poloidally varying pressure is due to density, i.e. $\tilde{p}_z = T_z \tilde{n}_z$, the parallel component of 2.4 becomes,

$$\frac{m_z n_z \omega^2}{2} \nabla_\parallel R^2 + Z n_z e \nabla_\parallel \Phi + T_z \nabla_\parallel n_z = 0 \tag{2.7}$$

where $\nabla_\parallel = \hat{b} \cdot \nabla$. By assuming subsonic main-ion flow, $M_i^2 = (v_i/v_{th_i})^2 \ll 1$, and ignoring inertial effects for electrons as $m_e/m_i \ll 1$, quasineutraility, $Zn_z + n_i - n_e = 0$ can be used to find the parallel gradient of the electrostatic potential,

$$\frac{e\nabla_\parallel \Phi}{T_e} = \left(n_{e,o} + n_{i,o}\frac{T_e}{T_i} \right) \nabla_\parallel \left(Zn_z + n_{i,o}M_i^2 \right) \tag{2.8}$$

For a small impurity level, $Zn_z \ll n_i$, using (2.8) equation (2.7) is simplified to

$$\frac{n_z}{n_{z,0}} = \exp\left[\frac{m_z\omega^2 R_0^2}{2T_z} \left(\frac{R^2}{R_0^2} - 1 \right) \left(1 - \frac{Zm_i}{m_z}\frac{T_e}{T_e + T_i} \right) \right] \tag{2.9}$$

where $n_{z,0}$ is the impurity density at a reference major radius $R = R_0$. In the circular, small inverse-aspect ratio limit, the lowest order Fourier expansion of (2.9) results in an in/out asymmetry of $n_z/\langle n_z \rangle = 2\epsilon M_o^2 \cos\theta$, where

$$M_o^2 = \frac{m_z\omega^2 R_o^2}{2T_z} \left(1 - \frac{Zm_i}{m_z}\frac{T_e}{T_e + T_i} \right) \tag{2.10}$$

Wesson [56] also includes useful extensions to (2.7) for a plasma with multiple impurities, one trace impurity of interest and another non-trace. In this case, the centrifugal force acting on the non-trace impurity will increase the poloidal potential at the outboard side, reducing the in/out asymmetry for the trace impurity. Assuming $Z/m_z \sim 1/2$ for the non-trace impurity,

$$\frac{n_z}{n_{z,o}} = \exp\left[\frac{m_z\omega^2 R_o^2}{2T_z} \left(\frac{R^2}{R_o^2} - 1 \right) \left(1 - \frac{Zm_i}{m_z}\frac{Z_{eff}T_e}{Z_{eff}T_e + T_i} \right) \right] \tag{2.11}$$

2.2.2 Asymmetry due to Ion-Impurity Friction

The first derivation of a poloidal variation of impurity density due to friction was from Burrell and Wong [25] which sought to explain the up/down asymmetry measurements from PLT and Alcator-A. Brau [50] expanded on this analysis to include all collisionality regimes. The self-pressure, electric field and friction terms are kept

from the general parallel impurity force balance equation (2.4).

$$T_z \nabla_\parallel n_z + n_z Z e \nabla_\parallel \Phi = R_{z,\parallel} \tag{2.12}$$

A trace level of impurities with $T_z = T_i$ was assumed and in the circular, low inverse aspect ratio limit, the impurity density can be expressed as $n_z(\theta, r) = n_{z,o}(r)(1+ \eta_{qf} \sin\theta)$. The asymmetry term, η_{qf}, is

$$\eta_{qf} = \frac{2\sqrt{2} R m_i q^2 Z^2}{e B_t \tau_i} \left[\frac{n_i'}{n_i} + \left(1 - \xi - \frac{1}{Z}\right) \frac{T_i'}{T_i} \right] - A q \rho_i \frac{T_e}{T_e + T_i} \frac{T_i'}{T_i} \tag{2.13}$$

with ξ and A dependent upon collisionality [50]. In the collisional, plateau and collisionless regimes, ξ is 1, -0.75 and 1.5, respectively while,

$$A = \begin{cases} \frac{1.3}{\omega_{tr}\tau_{ii}} & \text{Pfirsch-Slüter} \\ \frac{\sqrt{\pi}}{2} & \text{plateau} \\ 1.28\nu_* & \text{banana} \end{cases} \tag{2.14}$$

where $\nu_* = \nu_{ii}/(\omega_{tr,i}\epsilon^{3/2})$. Tendler [47] was the first to demonstrate that the friction would also lead to an in/out asymmetry, with a build-up of impurities on the high-field side. Hsu and Sigmar [53] described this in more detail for a circular, collisional, isothermal plasma defining an ordering parameter,

$$\Delta \equiv \frac{\delta_{\theta,i} Z^2 \nu_{ii} \sqrt{2}}{\omega_{tr,i}} \tag{2.15}$$

A distinction was made between the weak ordering, $\Delta \sim \delta_{\theta,i}$ and strong ordering, $\Delta \sim 1$. It was argued that while earlier theories identified the correct physics, the nonlinear consequences of $\Delta \sim 1$ were not identified [61]. For example, the up/down asymmetry in (2.13) increases monotonically as the radial gradients or the Z of the impurity increases, while Hsu and Sigmar showed the asymmetry would eventually decrease back to zero and in/out asymmetry would develop.

The work of Helander [31], Fülöp [58] and Landreman [60] extended the analysis in

[53] to include ion temperature gradients and describe all three collisionality regimes. Helander showed that viscosity, $\nabla \cdot \pi$, could be ignored relative to friction [31]. For the collisional [58] and collisionless [31] regimes, an identical 1-D differential equation for $n = n_z/\langle n_z \rangle$ as a function of poloidal angle is derived with,

$$(1 + \alpha_z n) \frac{\partial n}{\partial \vartheta} = g \left[n - b^2 + \gamma \left(n - \langle n b^2 \rangle \right) b^2 \right] \tag{2.16}$$

where $b^2 = B^2/\langle B^2 \rangle$ and the g and γ values are dependent on the collisionality regime and $\alpha_z = Z^2 \langle f_z \rangle / (T_i/T_e + n_i/n_e)$. The poloidal variable ϑ is referred to as the modified poloidal angle and is related to the conventional θ via,

$$\frac{d\vartheta}{d\theta} \equiv \frac{\langle \vec{B} \cdot \nabla \theta \rangle}{\vec{B} \cdot \nabla \theta} \tag{2.17}$$

For the Pfirsch-Schlüter regime [58],

$$g = -\frac{m_i Z^2 I}{e \tau_{ii} \langle \mathbf{B} \cdot \nabla \theta \rangle} \frac{1}{n_i} \frac{\partial n_i}{\partial \psi} \tag{2.18}$$

$$\gamma = 2.8 \frac{n_i}{T_i} \frac{\partial T_i/\partial \psi}{\partial n_i/\partial \psi} \tag{2.19}$$

where $I(\psi)$ is the flux function described in the toroidal field in (1.2). For the banana regime [31],

$$g = -\frac{m_i Z^2 I}{e \tau_{ii} \langle \mathbf{B} \cdot \nabla \theta \rangle} \left(\frac{1}{n_i} \frac{\partial n_i}{\partial \psi} - 0.5 \frac{1}{T_i} \frac{\partial T_i}{\partial \psi} \right) \tag{2.20}$$

$$\gamma g = -\frac{m_i Z^2 I f_c}{3 e \tau_{ii} \langle \mathbf{B} \cdot \nabla \theta \rangle} \frac{1}{T_i} \frac{\partial T_i}{\partial \psi} \tag{2.21}$$

where f_c is the fraction of circulating ions and the product of g and γ specified in (2.21) for clarity. Note that this value of γ is for the trace limit,$\alpha_z = 0$, while more general expressions can be found in [24].

In the limit of $g \gg 1$, (2.16) describes an in/out asymmetry with n varying like the magnetic field strength squared.

$$n = \frac{\gamma}{1 - \langle (1 + \gamma b^2)^{-1} \rangle} \frac{b^2}{1 + \gamma b^2} \tag{2.22}$$

In the trace, small inverse aspect ratio circular limit, n can be Fourier expanded and (2.16) used to find the $m = 1$ components describing the up/down (n_s) and in/out (n_c) asymmetry.

$$n_s = \frac{2\epsilon g}{1 + (1+\gamma)^2 g^2} \tag{2.23}$$

$$n_c = -\frac{2\epsilon (1+\gamma) g^2}{1 + (1+\gamma)^2 g^2} \tag{2.24}$$

For small values of g an up/down asymmetry develops with the direction depending upon the sign of g but diminishes as g increases as described in [53]. For collisional plasmas (2.18), g can only change sign when the magnetic field configuration is changed, but for collisionless plasmas (2.20), g can switch sign depending on the relative magnitude of the density and temperature scale lengths.

For the plateau regime [60], Landreman follows a similar path, but an additional term describing the poloidal variation of the main ions must be included. The details of this derivation are not included here, in part due to theory being published very recently. Results in the plateau regime will be discussed only qualitatively in Section 6.2, where the relevant detail is that the g term becomes,

$$g = -\frac{m_i Z^2 I}{e\tau_{ii}\langle \mathbf{B}\cdot\nabla\theta\rangle}\frac{1}{p_i}\frac{\partial p_i}{\partial \psi} \tag{2.25}$$

in the plateau regime.

2.2.3 Asymmetry due to Externally Sustained Poloidal Electric Field

The parallel gradient of the electrostatic potential is included in all theories where the forces that impact the impurities also impact the electrons and ions, and quasi-neutrality is needed to solve for $\Phi(\theta)$. The electrons will have a Boltzmann response and the poloidal variation of the ions comes from its parallel force balance equation. Although very small, $e\tilde{\Phi}/T_e \ll \epsilon$, this poloidal potential variation is amplified by the high charge of the impurity.

External input of energy via waves [62],[63] and neutral particle beams [64] are also expected to sustain poloidal electric fields. Changes in the distribution function can alter the trapped/passing fractions, creating a small poloidal density variation which must be taken into account. For cyclotron heating, the perpendicular velocity of a particle is increased and the fraction of that particle species that is trapped on the low-field side (LFS) magnetic well increases. In electron cyclotron heating, this creates a negative charge accumulation on the outboard side, increasing the LFS abundance of high-Z impurities. When using ion-cyclotron waves, the power is typically absorbed in a minority species, $f_m \leq 10\%$, creating a positive outboard charge accumulation, pushing the high-Z impurities to the high-field side (HFS) [62]. Neutral beams inject high energy, 10-500 keV, particles and their geometry relative to the tokamak determines their impact on $\tilde{\Phi}$. Beams aligned to be tangent to the magnetic axis, used to drive toroidal rotation and plasma current, inject particles with a large $v_{\|}$ into passing orbits, but have a small, but non-negligable, impact on the poloidal electric field. Perpendicular beams inject particles with a large $v_{\perp}$ and a substantial fraction will be introduced directly into trapped orbits [64]. Pondermotive forces due to the electric field of the waves themselves have also been discussed [65] but this effect is not considered here. It has also been noted in [66] that the parallel electric field due to Ohmic heating is a smaller force than electron-ion friction, which itself is smaller than ion-impurity friction and therefore is ignored as well.

Parallel impurity transport theory due to $\Phi(\theta)$ from wave or beam heating is essentially non-existent. Only a lab technical report exists [51] on this subject where a poloidal potential variation $\tilde{\Phi} \sim \epsilon$ was inserted artificially, with the motivation that cyclotron heating could cause such an effect. For cases of practical interest, the neutral beam ions or particles absorbing the cyclotron wave energy can be assumed to not interact directly with the impurity species. Thus, the task of including the poloidal electric field effect only comes in when using quasi-neutrality to solve for $\Phi(\theta)$. This is outlined in Section 5.1 in an effort to explain experimental Alcator C-Mod measurements in plasmas heated with ion cyclotron waves.

2.2.4 Combined Impurity Momentum Balance in Collisionless Plasmas

A few authors have solved the parallel force balance equations for ions and impurities including both friction and inertial forces in the banana regime which describes the core of C-Mod and other fusion plasmas. As shown in Table 2.1, Hsu [53] and Romanelli [57] included friction but only assumed collisional main-ions with [57] dramatically oversimplifying the ion-impurity friction.

From Table 2.1, the work of Stacey [54][59] seems promising and also included the ability to specify external momentum and particle sources. But, in [59] the radial electric field is calculated from theory using neoclassical gyro-viscous stress which has been proven to be incorrect [67][68]. Earlier work [54] left the E_r to be specified, but presented the reader with a series of coupled, nonlinear differential equations for the ion, impurity and electron density variation. Little to no simplification from the starting equations is offered and the complexity of deriving solutions is immense. In addition results discussed in [54] show what appear to be unphysical solutions to the rotation-induced in/out asymmetry for impurity and ion density, $\tilde{n}_I^c$ and $\tilde{n}_i^c$. For a non-trace, $\alpha = 1.8$ carbon impurity, as $v_{\phi I}/v_{th,I}$ is increased to 0.7, $\tilde{n}_i^c$ increases to $\sim$0.6 and $\tilde{n}_I^c$ decreases to -1.1, indicating an accumulation of impurities on the inboard side. This is in contrast to every other theory which predicts LFS accumulation of impurities due to toroidal rotation of order $v_{\phi I}/v_{th,I} \sim 1$. For these reasons, [54] and [59] are omitted from the current validation exercise discussed in this thesis.

Burrell [49] was the first to combine friction and inertia, deriving relations for both the in/out and up/down asymmetries assuming a small inverse aspect ratio and circular geometry. Feneberg [52] also developed a parallel impurity transport theory including viscosity along with inertia and friction forces, although the poloidal ion flow was not constrained using neoclassical theory. The basic form of the velocity in (2.1) was used to derive the difference between ion and impurity flows for use in the friction, but left $v_{z,\phi}$ and $v_{z,\theta}$ to be specified. In both cases, poloidal electric field effects were ignored recognizing, correctly, that $e\tilde{\phi}/T_e$ is small but failing to realize

that $Ze\tilde{\phi}/T_e$ is what enters into the impurity force balance. As shown in Section 2.2.1, this is an important piece of the asymmetry driven by the centrifugal force.

The work by Fülöp and Helander [24] combined the results derived in [29] and [31]. The circular, $\varepsilon \ll 1$ limit is derived, but a general differential equation for use with shaped tokamaks is also given. This represents the most comprehensive parallel impurity transport theory for collisionless main ions, and will be used to model asymmetries for comparisons to experimental data on Alcator C-Mod. Important points are summarized here, but the reader is strongly encouraged to review [24] for details of the derivation. As expected from discussion in Section 2.2.1 and 2.2.2, the starting momentum balance equation is,

$$\frac{m_z n_z \omega^2}{2} \nabla_\parallel R^2 + Z n_z e \nabla_\parallel \Phi + T_z \nabla_\parallel n_z = R_{z,\parallel} \tag{2.26}$$

This leads to a 1-D differential equation describing the poloidal density variation, $n = n_z/\langle n_z \rangle$ as a function of modified poloidal angle (2.17),

$$\left(1 + \alpha_z n\right) \frac{\partial n}{\partial \vartheta} = g \left[n + \gamma \left(n - \frac{K_z}{\langle n_z \rangle u_i} \right) b^2 \right] + \frac{\partial M^2}{\partial \vartheta} n \tag{2.27}$$

where K_z is determined from the constraint that $n(0) = n(2\pi)$, g and γg are (2.20) and (2.21), respectively, and $M^2 = M_o^2 R^2 / R_o^2$ with M_o the same as in (2.10). The variable u_i is related to the ion poloidal flow, and in the trace ($\alpha_z \ll 1$) and $\epsilon \ll 1$ limit is,

$$u_i = -\frac{I f_c}{3e\langle B^2 \rangle} \frac{\partial T_i}{\partial \psi} \tag{2.28}$$

The basic structure of the poloidal asymmetries can be found by expanding n in a low-order Fourier series, assuming a circular cross-section, to find the leading order (in $\epsilon = r/R_o$) $m = 1$ terms with $n = 1 + n_c \cos\theta + n_s \sin\theta$.

$$n_c = 2 \frac{r}{R_o} \frac{\left(1 + \alpha_z\right) M_0^2 - \left(1 + \gamma\right) g^2}{\left(1 + \alpha_z\right)^2 + \left(1 + \gamma\right)^2 g^2} \tag{2.29}$$

$$n_s = 2g \frac{r}{R_o} \frac{\left(1 + \alpha_z\right) + \left(1 + \gamma\right) M_0^2}{\left(1 + \alpha_z\right)^2 + \left(1 + \gamma\right)^2 g^2} \tag{2.30}$$

Note that setting $\alpha_z = 0$ and either $M_o^2 = 0$ or $g = 0$ recovers the respective friction or inertia dominated limits discussed earlier.

The equations for n_c and n_s reveal an asymmetry structure with a complicated dependence on the background plasma profiles. The in/out asymmetry now becomes a competition between centrifugal force pushing high-Z impurities to the outboard side of a flux surface and friction pushing them to the inboard side. The magnitude of the up/down asymmetry now also has a component driven by the centrifugal force, M_o^2, yet the direction is still determined by g. Both terms decreases to zero for large values of γ.

2.2.5 Form of Solution in the Trace Limit

The above derivations for n_c and n_s are done for a low inverse aspect ratio, circular plasma where the poloidal variation can be expanded in a Fourier series. In order to compare to experiments that use shaped plasmas, a numerical solution to the parallel force balance equation must be found. For the trace limit, (2.27) from [24] shows the poloidal density variation, $n = n_z/\langle n_z \rangle$, to be of the form,

$$\frac{\partial n\left(\theta\right)}{\partial \theta} + X\left(\theta\right) n + K_z Y\left(\theta\right) = 0 \tag{2.31}$$

where K_z is found from the requirement that n is periodic, $n\left(0\right) = n\left(2\pi\right)$. The solution to this 1-D inhomogeneous linear differential equation can be determined by using an integrating factor, $\exp\left(\mu\right) = \exp\left(\int_0^\theta X\left(\theta\right)\, d\theta\right)$. This allows (2.31) to be written as,

$$\frac{\partial}{\partial \theta}\left[\exp\left(\mu\left(\theta\right)\right) n\left(\theta\right)\right] = -K_z Y\left(\theta\right) \exp\left(\mu\left(\theta\right)\right) \tag{2.32}$$

Integrating and applying the periodic boundary condition allows $n\left(\theta\right)$ to be expressed as,

$$\frac{n\left(\theta\right)}{n\left(0\right)} = \exp\left(-\mu\left(\theta\right)\right)\left(1 - \frac{1-\alpha}{\beta}\int_0^\theta Y\left(\theta\right)\exp\left(\mu\left(\theta\right)\right)\, d\theta\right) \tag{2.33}$$

where $\alpha = \exp\left(-\mu\left(2\pi\right)\right)$ and $\beta = \int_0^{2\pi} Y\left(\theta\right)\exp\left(\mu\left(\theta\right)\right)\, d\theta$. A code has been written in the Interactive Data Language (IDL) that solves (2.33) using experimental magnetic

reconstructions and kinetic profiles to calculate $X(\theta)$ and $Y(\theta)$. The details of the verification of this code is outlined in Appendix A, where numerical solutions are compared to various analytical limits.

2.2.6 Impact of Anomalous Radial Transport on Parallel Transport

In reality, radial transport is larger then the neoclassical levels assumed in the above derivations, raising the possibility of turbulent radial transport affecting parallel transport. There are two measures of the parallel transport time for the impurities. If they are assumed to be in the Pfirsch-Schlüter regime, the mean free path is small and there is no streaming along the field at the thermal velocity. Instead perturbations along the field are relaxed diffusively with $D_{z,\|} = v_{th,z}^2/\nu_{zi}$, assuming that ion-impurity collisions dominate over self or impurity-impurity collisions. This results in a parallel impurity relaxation time, $\tau_\|$, of,

$$\tau_\| \sim \nu_{zi} \left(\frac{qR_o}{v_{th,z}} \right)^2 \tag{2.34}$$

where $\nu_{zi} = 2\sqrt{\pi}/(4\tau_{zi})$. If there is solidbody rotation, then convection can work to symmetrize isolated particle sources introduced in the lab frame such as an injection, but this does work to symmetrize transport which occurs in the rest frame of the plasma like the ∇B drift. Parallel equilibration can also be driven by convection due to flow which does occur the rest frame like the poloidal rotation. This results in parallel diffusion time of $\tau_\| = L_\|/uB$, although in practice this is difficult to calculate since v_θ is generally not measured with sufficient accuracy.

The parallel transport theory developed in the Section 2.2 assumes that $\tau_\|$ is much smaller than the time it takes to diffuse across field lines according to neoclassical theory,

$$\tau_{\perp,D}^{NC} \sim \frac{L_\perp^2}{\nu_{zi}\rho_z^2 q^2} \tag{2.35}$$

This allows the parallel transport problem to be solved independent of radial trans-

port, keeping it a 1-D problem. While this *ansatz* is consistent with the derivations as pointed out by [31], the neoclassical restriction should in reality be a bit more stringent. Although the combination of the ∇B and curvature drift, v_{dr}, does not produce a net radial flow when averaged over the flux surface, $\tau_{\|}$ must be sufficiently small to symmetrize this poloidally varying source.

$$\tau_{\perp,dr}^{NC} \sim \frac{L_\perp}{v_{dr}} \sim \frac{2ZeR_oB_\phi L_\perp}{m_z v_{th,z}} \tag{2.36}$$

In addition, the observed perpendicular transport is much faster than neoclassical predictions, with the radial particle flux commonly expressed as $\Gamma_z = D_\perp^{an}\nabla n_z + v^{an} n_z$. Empirical measures of these transport coefficients can be used to determine anomalous perpendicular transport time scales.

$$\tau_{\perp,D}^{an} \sim \frac{L_\perp^2}{D_\perp^{an}} \tag{2.37}$$

$$\tau_{\perp,v}^{an} = \frac{L_\perp}{v_\perp^{an}} \tag{2.38}$$

In order for experimental asymmetry measurements to be properly used to verify the theory discussed in this section, $\tau_{\|}$ must be much faster than all the perpendicular time scales. In addition, if significant disagreements between theory and experiment arise in situations when $\tau_\perp \sim \tau_{\|}$, this is an indication that the parallel transport problem may becoming 2-D. When computing outputs of the code discussed in Section 2.2.4, these τ's will also be determined using experimental data.

2.3 Computational Impurity Transport

Computational tools have been developed to numerically solve the coupled multi-species heat and particle transport equations. Many of these have simplifying assumptions in the ordering of the parallel impurity momentum balance and it remains unclear what physics is retained. Certainly for the NCLASS code [69], commonly used to calculate neoclassical poloidal flows, the impurity density is forced to be a

flux function. The NEO [70] and GTC-NEO [71] codes solve the drift-kinetic equation for ions and impurities up to second order in ρ_i/a where ion-impurity collisional effects are not included in the highest order impurity momentum balance. This ordering for the impurities is similar to the weak ordering discussed by Hsu and Sigmar, thus, it's unclear if such codes could accurately produce asymmetries driven by friction. While NEO accounts for the centrifugal force, allowing for in/out asymmetries, no poloidal electric fields due to cyclotron or beam heating are included. A verification effort of these codes in the circular low-aspect ratio limit is suggested as future work,while the focus of this research is on validation of analytical theory against experiments.

2.4 Experimental Observations of Impurity Asymmetries

The experimental observation of poloidal impurity density variation is extremely robust, having been demonstrated on a wide range of tokamaks (see Table 2.2) starting with Alcator-A in 1977. Although theory can selectively include physics which drives different asymmetries, experiments measure their sum. If different terms in the parallel force balance are to be experimentally tested, the plasmas must be tailored to accentuate the desired physics. Additionally, diagnostic access is commonly limited to views from the outboard, top or bottom of the tokamak. This results in two generic classes of observations; the up/down asymmetry, where n_z above and below the midplane are compared, and the in/out asymmetry where n_z on the low-field side and high-field side are compared. These asymmetries have been observed for a wide range of impurities using spectroscopy, SXR tomography and bolometry. In many cases, experimental ion flow or temperature profiles were not available, thus preventing quantitative comparisons to the neoclassical theory. Table 2.2 outlines the observations made, the type of asymmetry (I/O - in/out, U/D - up/down) studied, the impurity observed and diagnostic technique utilized. In the next sections, the up/down (2.4.1) and in/out (2.4.2) observations are described for other tokamaks

and the history of asymmetry experiments at Alcator C-Mod is reviewed (2.4.3).

Experiment					
	AUTHOR	YEAR	ASYM	Z	DIAGNOSTIC
Alcator A					
	Terry [72]	77	U/D	O,N	VUV Spec
Alcator C-Mod					
	Borras [73]	96	U/D,I/O	SXR	SXR Tomo
	Granetz [74]	97	U/D,I/O	SXR	SXR Tomo
	Rice [75]	97	U/D	Ar	SXR Spec
	Pedersen [76][77]	00,02	U/D,I/O	SXR	SXR Tomo
	Marr [78]	10	I/O	B	Visible Spec
ASDEX					
	Smeulders [79]	86	U/D,I/O	Fe	SXR Tomo
ASDEX-Upgrade					
	Dux [80]	99	I/O	Ar, Kr	SXR Tomo
COMPASS-C					
	Durst [81]	92	U/D	B,C	SXR Tomo
JET					
	Feneberg [82]	86	U/D	Ni	Bolometry
	Giannella [83]	92	I/O	Ni	SXR Tomo
	Alper [84]	96	I/O	Ni	SXR Tomo
	Ingesson [85][86]	98,00	U/D,I/O	Ni	SXR Tomo
	Chen [87]	00	I/O	Ni	SXR Tomo
PDX					
	Brau [50]	83	U/D	C, O	UV Spec
Phaedrus-T					
	Regan [88]	95	U/D	C, O	VUV Spec
PLT					
	Suckewer [89]	78	U/D	C,O	UV Spec
TdeV					
	Condrea [90]	1	U/D,I/O	B, C	Visible Spec
TEXT					
	Wenzel [91]	89	U/D	Ti	SXR Tomo
TFTR					
	Schivell [92][93]	86,87	U/D, I/O	PRAD	Bolometry

Table 2.2: Overview of the impurity asymmetry measurements organized by experiment

2.4.1 Up/Down

The up/down asymmetry has been observed more often than the in/out likely due to diagnostic access in tokamaks where wide-angle poloidal views from the LFS are easier to accomidate than those from the top the bottom. In most cases line-integrated profiles are not inverted to find local emissivity and the asymmetry is characterized by the peak brightness above and below the midplane.

The first observation of the up/down asymmetry was seen on Alcator-A [72] using VUV spectroscopy, scanning poloidally over a number of shots to form vertical brightness profiles of O VI and O V line emission. The brightness was observed to be higher on the side away from where the ion ∇B drift direction and was larger at higher densities. Separate poloidal scans were done with the B_T in both toroidal directions, thus reversing the sense of the ∇B drift direction. The asymmetry was observed to flip directions, helping to eliminate systematic errors in spatial alignment. Scans of line-averaged electron density over the range 5.0×10^{18} to 5.0×10^{19} m^{-3} and safety factor from $2.4 < q < 4.6$ showed the brightness ratio to scale like $n_e q^2$, increasing from unity to a factor of 4.

Using a poloidally scanning UV spectrometer, PLT [89] measured vertical profiles of main-ion (H I, He I and He II) and impurity (C II, C III, C V, O II and O V) line emission. Profiles ranged from symmetric to having brightness ratios of $\simeq 2$, with the main-ion species asymmetry typically opposite to that of the impurity, and a smaller asymmetry for higher impurity charge states. In contrast to the Alcator-A results, the asymmetry did not change when the ∇B direction was reversed. Instead, it was observed to change sense for similar repeated plasmas as well as during some discharges. The asymmetry was correlated to the position of the limiter and increased with higher edge temperature, and the conclusion was that localized plasma-wall interaction was creating a poloidally localized impurity source that was not yet symmeterized for low ionization states. The comparison of the Alcator-A and PLT results demonstrate the difficulty of interpreting measured asymmetries, due to the sensitivity to both localized sources and neoclassical transport.

On PDX [50], a poloidally scanning UV spectrometer measured profiles of C III, C V, O III and O V in circular, limited plasmas. Changes in the plasma positioning relative to the limiters resulted in dramatic changes to the C III asymmetry, even reversing its direction, with only minor changes in the magnitude of the C V asymmetry. Both the C V and O V were shown to only change orientation when the ∇B drift direction was reversed. The line-integrated profiles were used to constrain a 2-D emissivity reconstruction, $\varepsilon(r,\theta) = \varepsilon_0(r)(1+\eta\sin\theta)$, for 600 scans in Ohmic plasmas. The experimental asymmetries for C V, η_{exp}, were compared to (2.13) in the plateau and banana regime with better agreement for collisionless main-ions as shown in Figure 2-1 reproduced from [50]. Ion temperature profiles were not available and so T_i and ∇T_i, important drivers of the asymmetry, were held constant across the data set. A 2-D impurity transport code was written to evaluate the effect of neutral carbon and hydrogen source asymmetries on the asymmetry of C V . A neutral carbon asymmetry was shown to couple to H-like and He-like carbon, but only when the ion-ion collisionality was forced to be 10-100 times higher than the experiment, increasing $\tau_{\|}$. An assumed neutral hydrogen asymmetry did not couple to highly ionized carbon unless $n_0/n_e \simeq 5\%$ inside the confined plasma, an order of magnitude above that seen in the experiment. Anamalous radial diffusion was also included in the model and shown to have little effect on the asymmetry, $< 2\%$, unless it was increased to five times that observed in the experiment.

In the COMPASS-C tokamak [81], profiles from a toroidally viewing camera investigated up/down asymmetries in SXR emission from intrinsic boron and carbon in Ohmic plasmas. Characterizing the intensity profile as $I_z(r,\theta) = I_z^0(r) + I_z^1(r)\sin\theta$, the asymmetry factor, I_z^1/I_z^0, was shown to increase with collisionality up to the level of the inverse aspect ratio, $\varepsilon = 0.36$ for COMPASS-C, and reversed in orientation when the ∇B drift direction was changed. The data compared favorably to estimates using Feneberg [52] and Hsu and Sigmar [53], but lacked the accuracy to distinguish between the two. The absence of ion temperature and density profiles were cited as factors restricting further conclusions.

At the TEXT tokamak [91], SXR tomography was used to study the 2D emission

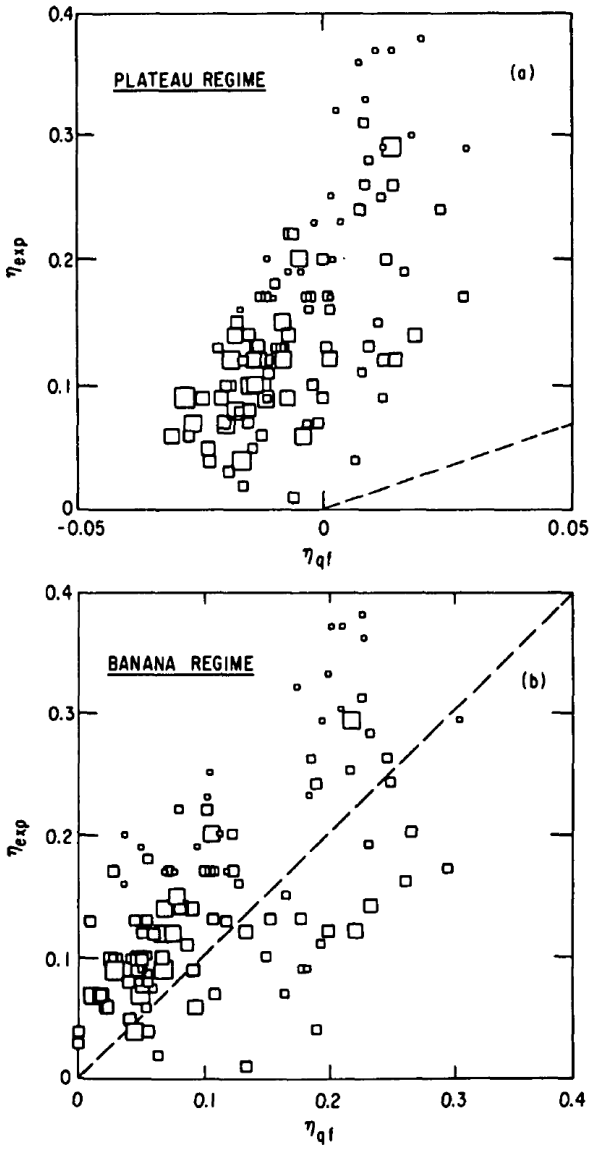

FIG. 7. Experimentally observed values of η for C V plotted versus different quantities. (a) Quasi-neoclassical fluid theory scaling, main ions assumed to be in plateau regime: $L_T = 10$ cm, $L_n = 12$ cm, (b) same as above, but main ions in banana regime.

Figure 2-1: Measurements of up/down asymmetries done on PDX (from [50]) showing good agreement to (2.13)

during Al injections into Ohmic plasmas. The asymmetry, $\Delta_x = (I_+ - I_-) / (I_+ + I_-)$, was determined to be on the order of the inverse aspect ratio and increased approximately linearly over the minor radius. Comparing the asymmetry in hydrogen, deuterium and helium main-ion plasmas, the level of the asymmetry was shown to scale like $\sqrt{m_i/Z_i}$. This is contrast to theory which shows the up/down asymmetry should scale with $Z_i^2/\sqrt{m_i}$ (2.13). For a decrease in plasma current at fixed B_t, Δ_x decreased, in contrast to the q^2 dependence found in prior experimental and theoretical work. No in/out asymmetry was observed during these experiments.

At Phaedrus-T [88], a multilayer-mirror spectrometer was used to measure the poloidal profiles of VUV He-like and H-like carbon lines in Ohmic and biased H-mode plasmas. Brightness profiles constrained an inversion to find the 2-D emissivity, $\varepsilon(r,\theta) = \varepsilon_0 (1 + \varepsilon_1 \sin\theta)$. The asymmetric term, ε_1 was observed to reverse with ∇B drift direction, was always higher in the direction oriented away from the drift and increased with electron density. According to Thomson scattering, n_e approximately doubled across the H-mode transition with little change in the T_e profile. The C^{4+} asymmetry was nearly invariant, $\varepsilon_1 \simeq 0.2$, between these two regimes in contrast to the C^{5+} which rose from zero to $\varepsilon_1 \simeq 0.15$ at mid radius. Comparison were made between Feneberg and Brau, and while there was no quantitative agreement between theory and experiment, the order of magnitude and orientation of the asymmetry was consistent.

Visible spectroscopy was used to measure poloidal variation of H-like boron using both a toroidally and poloidally viewing camera in TdeV [90]. At $r/a \sim 0.85$, ratios of reconstructed B V emissivity at the top and bottom, I_t/I_b, were measured in L- and H-mode plasmas to be from $1.4 < I_t/I_b < 2.3$. Changing the ∇B drift direction reduced the asymmetry, and in some cases reversed its direction with $0.66 < I_t/I_b < 1.5$. Emissivity also peaked at the poloidal location of the X-point, independent of the ∇B drift direction. The conclusion was that both a source asymmetry and neoclassical transport effects were at work. Despite having localized flow and temperature data simultaneously from B V Doppler spectroscopy, no attempt was made to compare these results quantitatively to theory.

At JET, 2D bolometry was used measure in/out and up/down asymmetries in the radiation profile for Ohmic plasmas [82] . Early JET discharges, prior to carbonization, were dominated by nickel and the intensity asymmetry, $\Delta_{UD} = (I_D - I_U) / (I_D + I_U)$ scaled with $\gamma = B_\phi n_e / I_p^2$ and grew to $\Delta_{UD} \simeq 0.4$. As γ increased further, Δ_{UD} returned to zero. This is the only empirical demonstration of the nonlinear nature of the up/down asymmetry discussed in Section 2.2.2, although this result is from a time-evolving I_p and n_e discharge. After carbonization, an up/down asymmetry in the radiation due to low-Z impurities was also shown to scale with γ, shown in Figure 2-2. This light impurity up/down asymmetry was shown to be strongly reduced and/or eliminated during NBI and ICRF-heated H-modes.

The presence of an up/down impurity asymmetry has been demonstrated across a number of tokamaks and in many cases observed to be consistent with neoclassical transport described in Section 2.2. In other instances, the asymmetry is driven by a poloidally asymmetric impurity source, highlighting the difficulty of designing a validation experiment. The work in PDX and JET have shown trends in up/down asymmetries which are qualitatively consistent with theory and what remains is a quantitative comparison using experimental ion flow and temperature measurements, an observation shared by a number of authors.

2.4.2 In/Out

The first experimental observation of an in/out asymmetry in impurity emission was seen on ASDEX [79] using SXR tomography to view the 2-D, (R,Z), emissivity due to a of a mix of bremsstrahlung and iron line emission. The reconstructions during a neutral beam heated ELM-free H-mode from [79] are shown in Figure 2-3. In the core, T_e =1.65 keV and v_ϕ =200 km/s or $M_i \simeq 0.5$ which for the Fe impurity results in $v_\phi / v_{th,Z} \simeq 4$. The asymmetries in the emissivity are claimed to be qualitatively explained by centrifugal force, and during ELMy H-modes, the ELMs were shown to promptly reduce the magnitude, but not eliminate, the in/out asymmetry.

On TFTR, strong emission irregularities in the bolometry brightness profiles were measured. This was explained [92][93] to be a MARFE moving poloidally around the

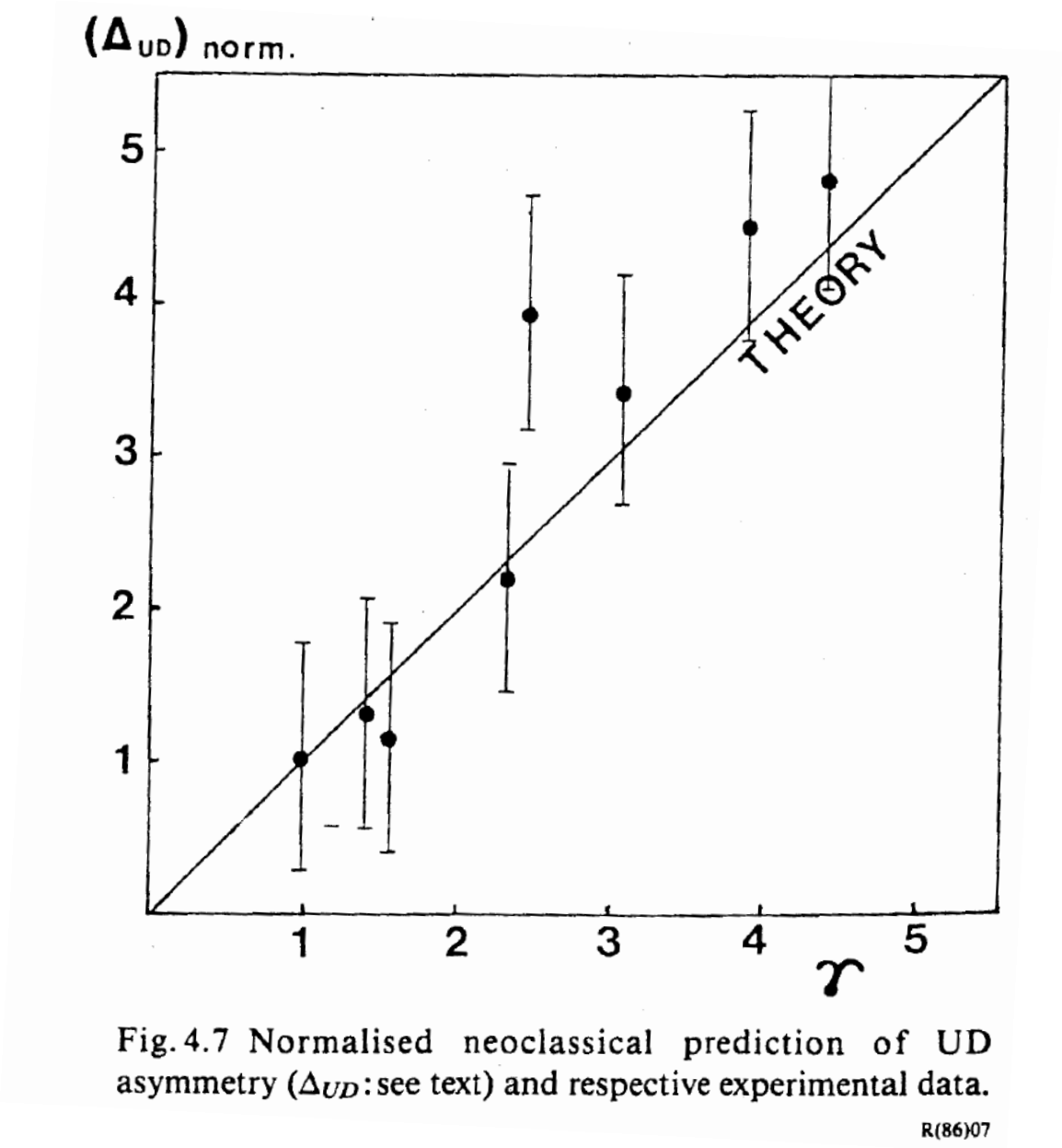

Figure 2-2: Measurements of up/down asymmetries in carbon found on JET, where $\gamma = n_e B_t / I_p^2$ (from [82]

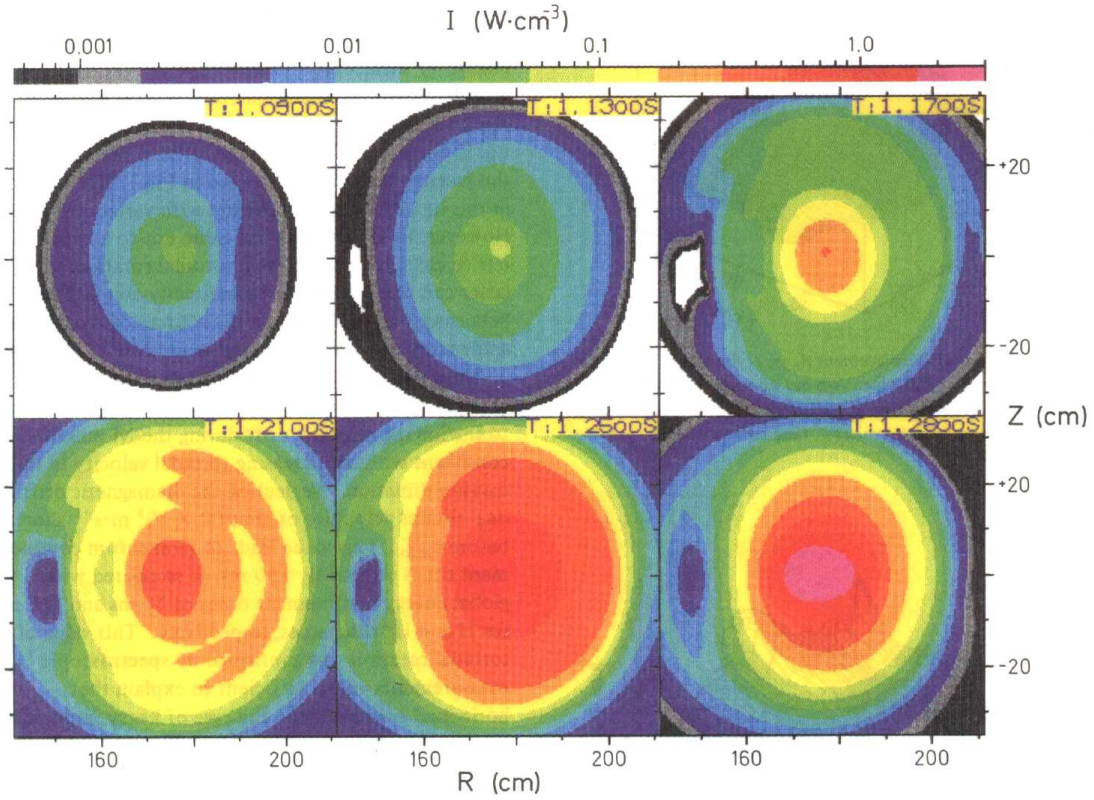

Figure 2-3: Reconstructions of soft x-ray emissivity from ASDEX (from [79]), the first measurement of in/out asymmetry due to centrifugal force

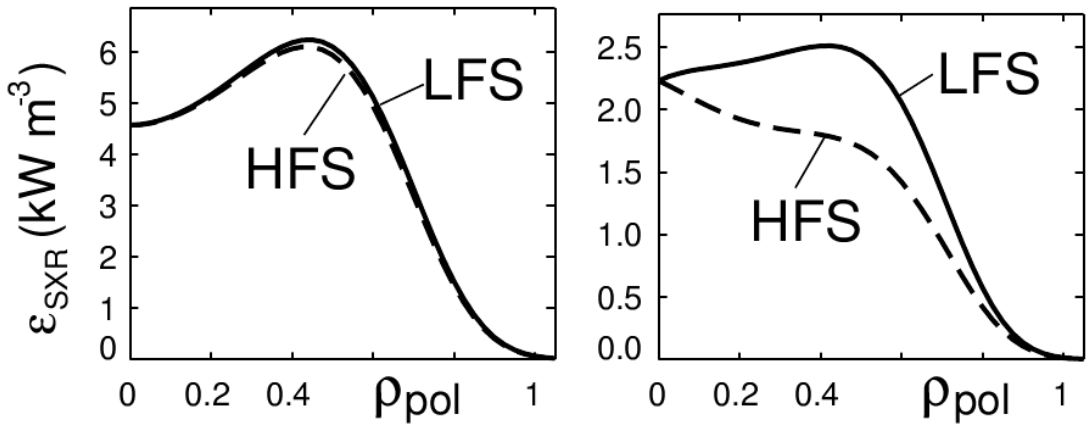

Figure 2-4: Soft x-ray emissivity profiles in ASDEX-U (from [80]), showing an asymmetry for Kr (right) but not for Ar (left)

HFS of the plasma. Despite having sufficient bolometric diagnostics and neutral beam heating to drive strong rotation, there is no record of in/out emissivity asymmetries being attributed to the centrifugal force.

An in/out asymmetry in SXR emission was shown in ASDEX-U (AUG) neutral beam heated ELMy H-mode discharges seeded with Kr. But, this asymmetry was not when seeding with Ar [80]. Although the explanation for the difference was the variation in centrifugal force, these results from do not agree with theory outlined in Section 2.2.1. Figure 2-4 from [80] shows that for Kr, the LFS emissivity is about 50% higher than that of the HFS, while for Ar, the emissivity on the LFS is, at most, a few percent above the HFS. The approximate symmetry for argon occurs even though $v_\phi/v_{Ar,th} \sim 1$.

The form of the emissivity in (2.9) has a exponential dependence on the ratio of the impurity to ion mass. For two trace high-Z impurities, which can be assumed to have the same temperature and toroidal rotation frequency, the mass scaling of the asymmetry, $\tilde{n}_z$, can be estimated by expanding the exponential,

$$\frac{\tilde{n}_{Ar}}{\tilde{n}_{Kr}} \sim \frac{m_{Ar}\left(1-\frac{Z_{Ar}m_i}{2m_{Ar}}\right)}{m_{Kr}\left(1-\frac{Z_{Kr}m_i}{2m_{Kr}}\right)} \leq \frac{m_{Ar}}{m_{Kr}} \tag{2.39}$$

assuming $T_i = T_e$. Based on the measured Kr results, (2.39) predicts that the LFS

argon emissivity should be about 20% above the HFS, much larger than observed in Figure 2-4.

JET has also used SXR tomography to investigate in/out asymmetries in impurity emission during beam-heated ELM-free [83] and hot-ion H-modes [84], as well as in optimized shear (OS) plasmas [87][85]. In ELM-free H-modes with $2 < \bar{n}_e < 5 \times 10^{19}$ m^{-3} and $3 < T_{e,o} < 5$ keV, Ni was injected using laser blow off (LBO), and viewed with a two-camera, 100 channel tomography system. Prior to the injection, the soft x-ray emissivity, dominated by bremsstrahlung from deuterium and low-Z impurities, was observed to be nominally flux-surface symmetric. After the Ni injection, the SXR emissivity showed a strong in/out asymmetry with the LFS emissivity higher then that on HFS of the same flux surface. For plasmas with *counter-current* neutral beam injection (NBI), the nickel asymmetry was shown to increase non-linearly with toroidal velocity, but roughly as $\sim M_i^2$, as shown in Figure 2-5 from [83], where $X = \epsilon m_z v_\phi^2/T$. The poloidal variation normalized to the flux surface average, $\tilde{\varepsilon}/\langle\varepsilon\rangle$, reached ~0.25 for toroidal velocities exceeding the Ni thermal velocity, $v_\phi/v_{th,z} \simeq 2.2$. For *co-current* NBI, the asymmetry scaled differently with rotation, and $\tilde{\varepsilon}/\langle\varepsilon\rangle \sim 0.1$ was achieved for $v_\phi/v_{th,z} \simeq 2.8$, nearly twice the rotation necessary for the same asymmetry during counter-current injection. Additionally, at lower velocities, $v_\phi/v_{th,z} \simeq 1.6$, the asymmetry reversed, $\tilde{\varepsilon}/\langle\varepsilon\rangle < 0$ for both Ni and Fe injections. This observation of a HFS abundance, shows that centrifugal force cannot be exclusively responsible for the JET in/out asymmetries.

Experiments at JET continued with an upgraded, six-camera, 210 channel soft x-ray tomography system, again utilizing Ni LBO but this time exploring hot-ion H-modes [84]. Strong, *co-current* neutral-beam heating in a low density H-mode predominately heats the ions, driving strong toroidal rotation and pushing T_i to over twice T_e. Line-integrated T_z and $v_{\phi,z}$ from x-ray spectroscopy of Ni^{26+} showed $T_z \sim 11$ keV and $v_\phi/v_{th,z} \simeq 3.1$. An in/out asymmetry of $\tilde{\varepsilon}/\langle\varepsilon\rangle$ between 0.5 and 0.66 was measured, roughly consistent with earlier *counter-current* heating experiments, extrapolated to higher Mach numbers.

The optimized shear plasmas of JET are formed by strong *co-current* beam and

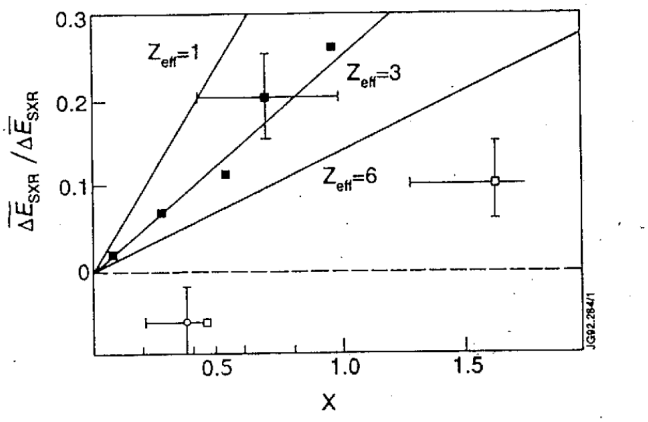

Fig. 4 Relative in/out modulation of the soft X-ray emissivity perturbation after metal injection in beam heated plasmas. ■ Ni, ctr.-inj.; [] Ni, co-inj.; ⊡ Fe, co-inj. The straight lines represent the prediction of eq.(1) for different values of Zeff in D plasma.

Figure 2-5: Initial measurements of in/out asymmetry for Ni and Fe injection into ELM-free H-modes (from [83])

minority ICRH in a low-density plasma, while the plasma current is slowly increasing, changing the magnetic shear, pushing $q_o > 1$ and, in some cases, exhibiting reversed shear. These plasmas have an L-mode edge and flat n_e profiles for $r/a \leq 0.5$, with large ion-temperature and rotation gradients. Core ion temperatures up to $T_i \simeq 30$ keV with $\nabla T_i/T_i \simeq 5$ m^{-1} and core rotation rates of $\simeq 35$ kHz are measured using carbon charge-exchange spectroscopy, shown to be consistent with line-integrated x-ray spectroscopy of He-like Ni. These radial profiles are shown in Figure 2-6 and the reconstructed midplane Ni density profile is shown in Figure 2-7, both from [87].

At $r/a \simeq 0.25$, the toroidal velocity is approximately three times the Ni thermal velocity and, $\tilde{\varepsilon}/\langle\varepsilon\rangle \simeq 0.6$. Prior to the Ni injection, the x-ray emissivity still shows an in/out asymmetry attributed to poloidal variation of C, Ne and Cl, all of which have toroidal rotation speeds exceeding their respective thermal velocities. Reconstructions of Ni injection in OS plasmas with a weak ITB show symmetric emissivity profiles despite similar input of external torque [85].

JET has also observed the asymmetries in highly-ionized Ni emission to be larger on the high-field side by 10-20% in plasmas with auxilliary heating provided only by

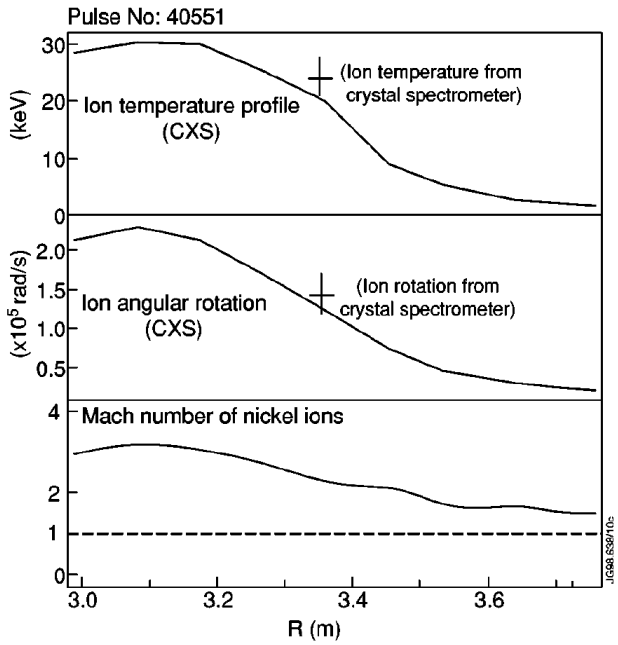

FIG. 3. Ion temperature and angular rotation profile measured by charge–exchange diagnostics for carbon ions. The measurements show good consistency with the crystal spectrometer measurement of nickel ions, shown as crosses. The Mach number of nickel ions is well above 1 across most of the plasma radius.

Figure 2-6: T_i, ω_ϕ and M_z profiles for JET optimized shear plasma

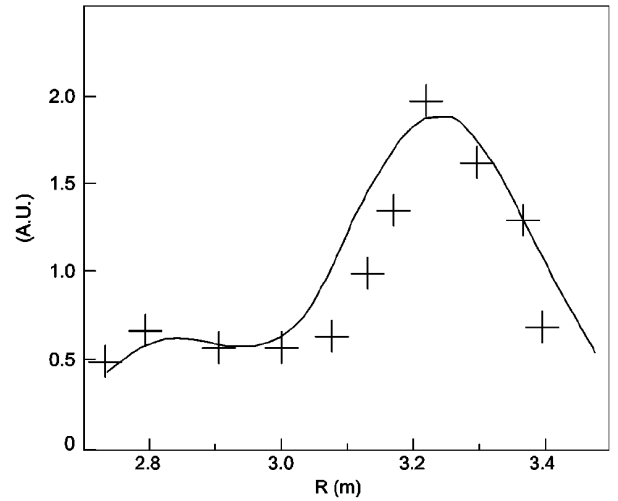

FIG. 4. Ni density derived from the soft x-ray emissivity at t=6.72 s (cross) and calculated Ni density at the same time (line).

Figure 2-7: Midplane emissivity from a JET optimized shear plasma (from [87]) showing a strong LFS abundance of Ni emission

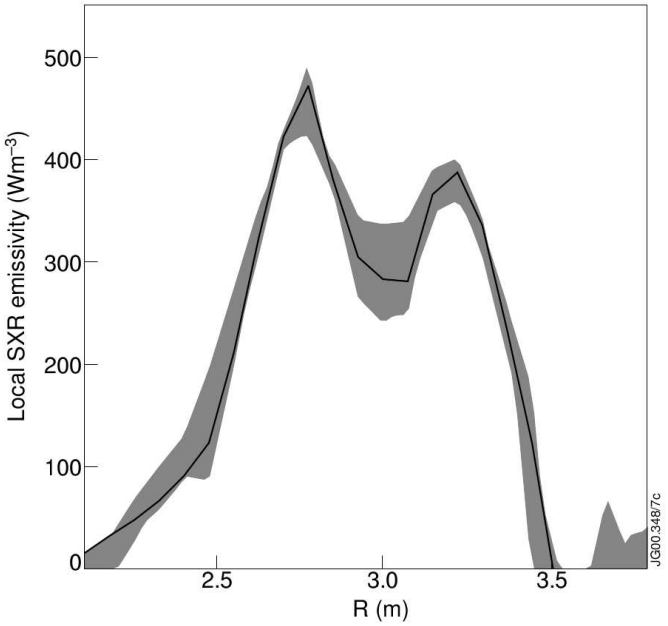

Fig.10: Soft X-ray emissivity in the middle plane, and the grey area represents the uncertainty from the tomographic reconstruction.

Figure 2-8: Midplane emissivity from a JET D(H) minority heated optimized shear plasma (from [86]) showing HFS abundance of Ni emission

3 MW of hydrogen minority heating. An example of this is shown in Figure 2-8 from [86]. Ion-impurity collisional effects are claimed to be insufficient, and the authors suggest a parallel electric field driven by a poloidal asymmetry of the minority ions as the cause. Initial modeling in [86] showed the amount of minority ion trapping is qualitatively consistent with this hypothesis, but detailed parallel transport analysis including inertial effects from self-generated flows was not included.

The experiments conducted on JET represent the most extensive tests of asymmetries driven by the centrifugal force and, prior to the research in this thesis, the only observation of a HFS impurity accumulation attributed to the use of ICRH. Still, there are internal inconsistencies in the data set as a whole indicating an incomplete picture of parallel impurity transport. The initial tests in [83] demonstrated both LFS and HFS abundance of Ni in ELM-free H-mode plasmas with NBI and no in/out asymmetry in SXR emission due to low-Z impurities. Later H-mode studies only reported a LFS abundance and described emission from low-Z elements to be

noticeably asymmetric. Ni injection into optimized shear plasmas have shown both asymmetric [87] (17 MW NBI, 6 MW ICRH) and symmetric (17 MW NBI, 8 MW ICRH) [85] distributions despite very similar momentum input. Additionally, the OS plasmas violate the ordering in which the parallel transport theory is derived, $\delta_{\theta,i} = \rho_{\theta,i}/L_\perp \ll 1$. Estimates from [87] reveal that $\delta_{\theta,i} \simeq 2$ close to the core, where the poloidal field is weak along with a strong ion thermal transport barrier. It is also unclear if any background impurities were included, thereby acknowledging the Z_{eff} dependency discussed in Section 2.2.1.

It is also worth noting that in addition to observed in/out asymmetries in impurity density, an asymmetry in electron density has been observed on the NSTX [94] and MAST [95] spherical tokamaks due to the centrifugal force. The ease of diagnostic access on these devices allows Thomson scattering measurements to be made across the entire midplane, and $n_e(r, \theta = 0)$ profiles can be compared to $n_e(r, \theta = \pi)$. Rotation profiles for neutral beam driven plasmas in MAST with $M_i \simeq 1$ show n_e greater on the LFS than the HFS. Similarly for NSTX $M_i \simeq 1$ plasmas, the electron density is shown to be asymmetric while the electron temperature shows no in/out asymmetry. Despite carbon fractions of a few percent, no information on poloidal impurity asymmetries have been reported for either experiments.

2.4.3 Alcator C-Mod

Flux surface asymmetries in impurity density have previously been observed on Alcator C-Mod, but a thorough comparison to theory has not been completed. The first asymmetry observations were made using the soft x-ray tomography diagnostic [73][74]. At that time, four 38 channel arrays viewed the core plasma and were used to construct 2-D (R,Z) contours of constant emissivity. The shape of these contours were then compared to flux surfaces derived from EFIT reconstructions and the discrepancies cataloged. The most dramatic was an over-prediction of κ for $0.3 < r/a < 0.7$, as shown in Figure 2-9. Detailed analysis of the calibration errors in the tomography diagnostics and the uncertainty in the EFIT reconstructions concluded that the differences were due to one or more of T_e, n_e, n_z or excitation physics not being constant

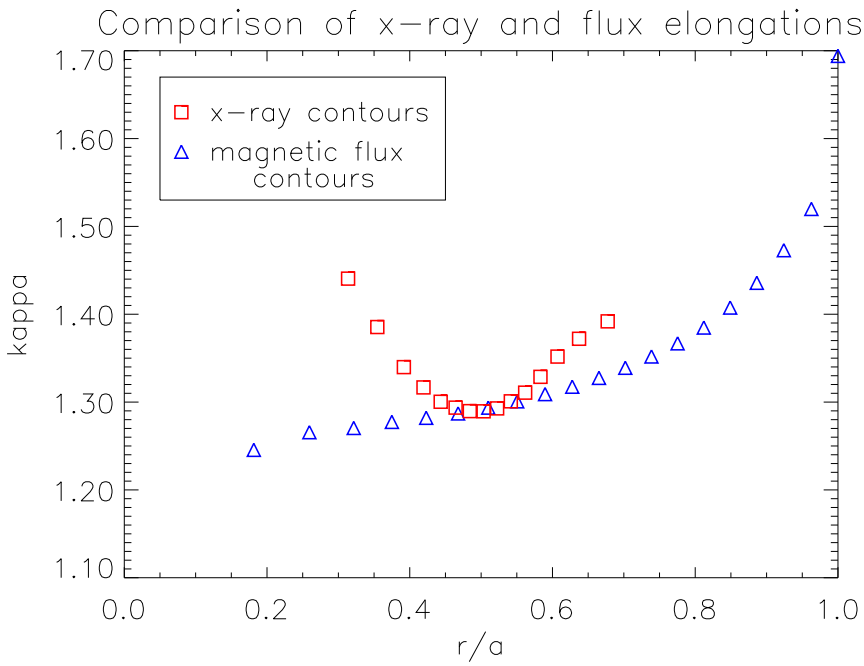

Figure 2-9: Disagreement between SXR-derived flux-surface elongation and EFIT reconstructions on Alcator C-Mod

on a flux surface.

A set of five, individually spatially scanning soft x-ray von Hamos spectrometers was used to examine the up/down asymmetry of lines in the He-like Ar spectrum. Repeatable plasmas were required to measure the spatial profile so only a single profile in forward (ion ∇B drift direction in the -$\hat{Z}$ direction) and reversed field were measured for the Ar^{16+} $1s^2$-1s2s transition as shown in Figure 2-10. The abundance of Ar was observed to be opposite of the ∇B drift direction as has been seen on most devices [75]. Measured $\tilde{n}_z/\langle n_z \rangle$ rose to $\sim$0.8 near the edge of plasmas and neither theory comparisons using [50] or [53] reproduced this result as shown in Figure 2-11.

Observations of poloidal impurity density asymmetries on Alcator C-Mod were also observed in the pedestal region of high confinement plasmas. Two of the soft x-ray tomography arrays, modified to look at K-shell emission from Ne and F, examined the emissivity profile in the pedestal of EDA H-mode plasmas at two different poloidal locations [76][77]. Emissivity at the top of the plasmas was much higher

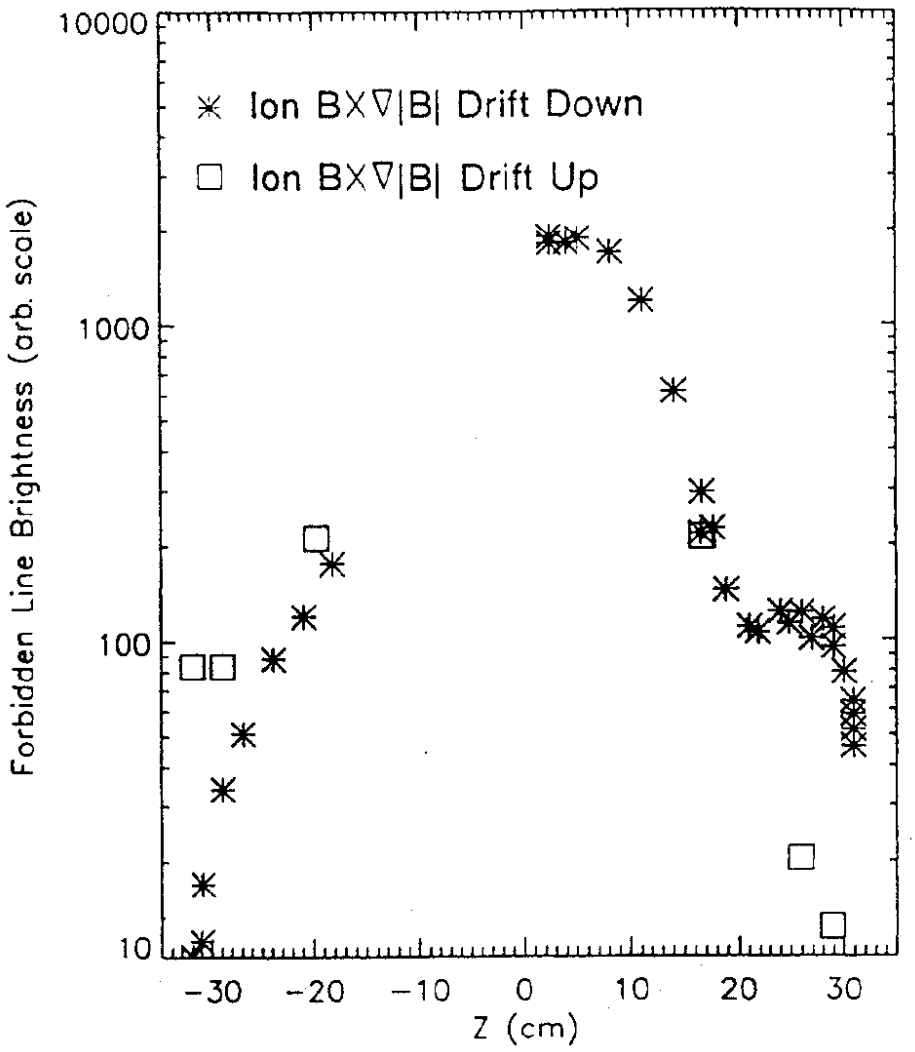

FIG. 6. Vertical brightness profiles for the forbidden line with the ion $\boldsymbol{B} \times \nabla|\boldsymbol{B}|$ drift downward (asterisks) and upward (boxes).

Figure 2-10: Demonstration of up/down asymmetry in He-like Ar emission (from [75])

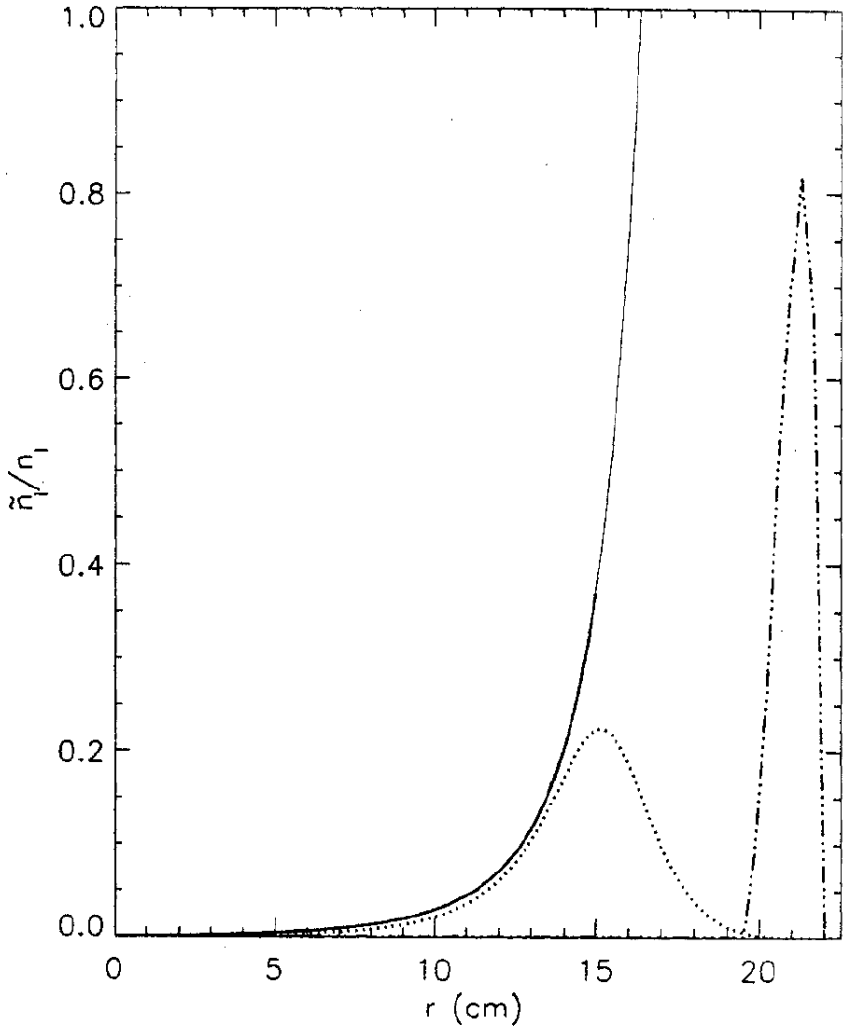

FIG. 13. Calculated $\tilde{n}_I/n_I$ from the treatment of Ref. [2] (solid curve) and the treatment of Ref. [8] (dotted curve), compared with the inferred impurity density perturbation (chain curve) of Fig. 10.

Figure 2-11: Comparison measured up/down asymmetry to theory showing disagreement (from [75])

than at the same flux surface on the outboard side, independent of the ∇B drift direction. Recent measurements of the in/out asymmetry of boron inferred from velocity measurements [78] indicate an abundance of boron on the high-field side, in qualitative agreement with [31]. For experiments examining the H-mode pedestal region, gradient scale lengths become short and the $\delta_{\theta,i} \sim 1$, violating the drift ordering In addition, uncertainties in EFIT, driven by unaccounted for bootstrap current, are larger, and using equilibrium reconstructions constrained by kinetic profiles is likely required.

2.5 Conclusions

The theoretical understanding and experimental demonstration of parallel impurity transport has made considerable advancements over the last few decades. The community has identified the fundamental forces at work; electrostatic, inertia and friction. In the limit where friction or inertia dominants, theory can predict direction and order of magnitude of the asymmetry, as well as match trends in important plasma parameters. For asymmetries driven by poloidal electric field the picture is not as clear and there exists room for advancement of both theory and experiment. When multiple forces are at work, a quantitative validation of the theory has not yet been completed. If a predictive capability can be demonstrated, then the 2-D impurity transport problem can be reduced back down to 1-D, assuming kinetic profiles are known to sufficient accuracy.

Chapter 3

Diagnostic Instrumentation and Interpretation

A number of diagnostics are utilized to study the poloidal variation of impurity density and compare measurements to theory. The 2-D structure of the local photon power loss density, commonly referred to as emissivity with units of power per unit volume, is found using a set of pinhole cameras. Those diagnostics to which significant contributions were made by the author during the completion of this work are described in detail in Sections 3.1 to 3.3. A brief overview of other diagnostic tools used is given in Section 3.4, and the reader is referred to more detailed sources for further information. Analysis and calibration routines that were developed during these investigations are also described in Sections 3.5 and 3.6 and expanded upon in Appendix B and C.

3.1 AXUV Tomography

3.1.1 Basic Design

The majority of the radiative power loss from C-Mod plasmas occurs in the vacuum ultraviolet (VUV) and soft x-ray (SXR) range, below the MgF_2 limit $\lambda \simeq 12$nm where lenses cannot be used and mirrors will only work in grazing incidence. This

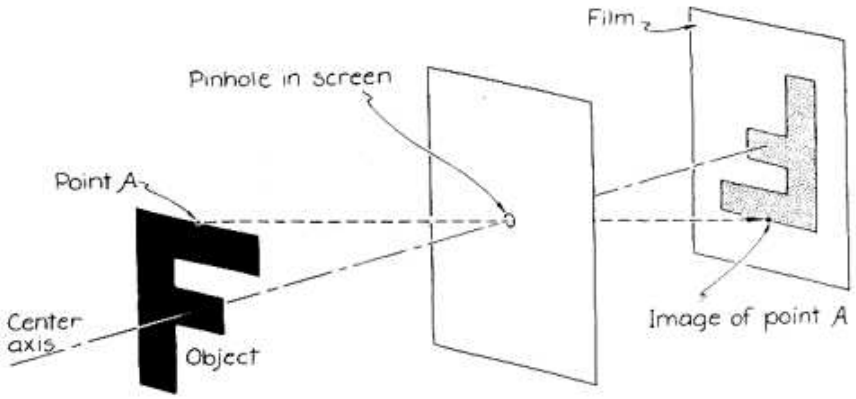

Figure 3-1: Schematic of the pinhole camera concept (http://www.wesjones.com/pinhole.htm)

makes the simple pinhole camera the most viable option for imaging the 2-D radiation structure. The basic design of this type of camera is shown in Figure 3-1, where a small aperture allows points in the image plane to be related to points in object plane. In such an instrument, the throughput and the resolution are linked and both increasing the size of the aperture or moving the film towards the pinhole degrade the spatial resolution. When using a pinhole camera to view a volumetric light emitter like a plasma, tomographic inversion techniques must be used to obtain local emission data and this is discussed in Section 3.1.4 and Appendix C.

For the C-Mod pinhole cameras, photodiodes are used in place of film as the detector and must operate remotely in the C-Mod vacuum chamber. Photocurrents generated by the diodes are carried to ultrahigh vacuum (UHV) feedthroughs using Microtech LN-3-30 coaxial cable [96], a 0.06 inch diameter Teflon jacketed/insulated cable with silver plated copper shield and center conductor. In order to reduce the amount of flange space needed to bring these signals out of the C-Mod vacuum vessel, Accu-Glass 25-pin D-SUB connectors [97] are used rather than conventional coaxial outputs, such as SMA connectors. This increases the noise while allowing for more channels and thus better spatial coverage of the plasma. Standard transimpedance amplifiers [98] are located within a few feet of the vacuum feedthroughs and utilize

gains on the order of 10^4 V/A, and have a 3 dB bandwidth of ∼100 kHz. Voltage time histories are digitized using 96-channel, 250 kHz, 16-bit D-tAcq ACQ196CPCI digitizers [99] supported by MDSPlus [100].

These cameras use Absolute eXtreme UltraViolet (AXUV) diodes from International Radiation Detectors [101] (IRD) which have been used on a number of tokamaks [102][103][104], including C-Mod [105], for measuring radiation in high-temperature plasmas. The AXUV-22EL, a standard 22-channel model, is used in all pinhole cameras, with photos and a schematic of this array shown in Figure 3-2. In most C-Mod plasmas, a substantial fraction of the radiated power is emitted in the vacuum ultraviolet and soft x-ray wavelength range where the non-grazing incidence reflectivity is several orders of magnitude below unity. To reduce the reflectivity in the visible, a black passivisation layer is applied to the stainless-steel camera housing and internal components. This adds a uniform, dull black finish maintaining vacuum compatibility while reducing coherent scattering.

The number of photodiodes deployed on C-Mod was substantially increased during the course of this research. Prior to the FY07 campaign, a single, 16-channel AXUV diode array viewed horizontally on the low-field side midplane. Over the FY07-FY10 campaigns, the number of photodiodes viewing the core increased to 132 in six, 22-channel arrays viewing on 5 different horizontal planes in 5 distinct enclosures [36]. Figures 3-3 and 3-4 show the in-vessel placement of the diagnostic enclosures containing the AXUV pinhole cameras.

The AXUV diode arrays viewing on the midplane, actually Z_o=1.25 cm, are inside the limiter enclosure located at the K horizontal port (KLIM) shown in Figure 3-3. Figure 3-5 shows the enclosure with the front limiter plate removed, revealing the three instrument plates full of detectors. The middle instrument plate has two AXUV-22EL arrays looking in different toroidal directions. AXJ looks from K towards J port, and AXA looks from K towards A port. The AXJ array views from the inner wall to the outer limiter, while AXA views just past the magnetic axis, its view restricted by a mirror incorporated into the KLIM enclosure used by the visible bremsstrahlung diagnostic. Also in the enclosure are the resistive bolometer arrays [106] on the top

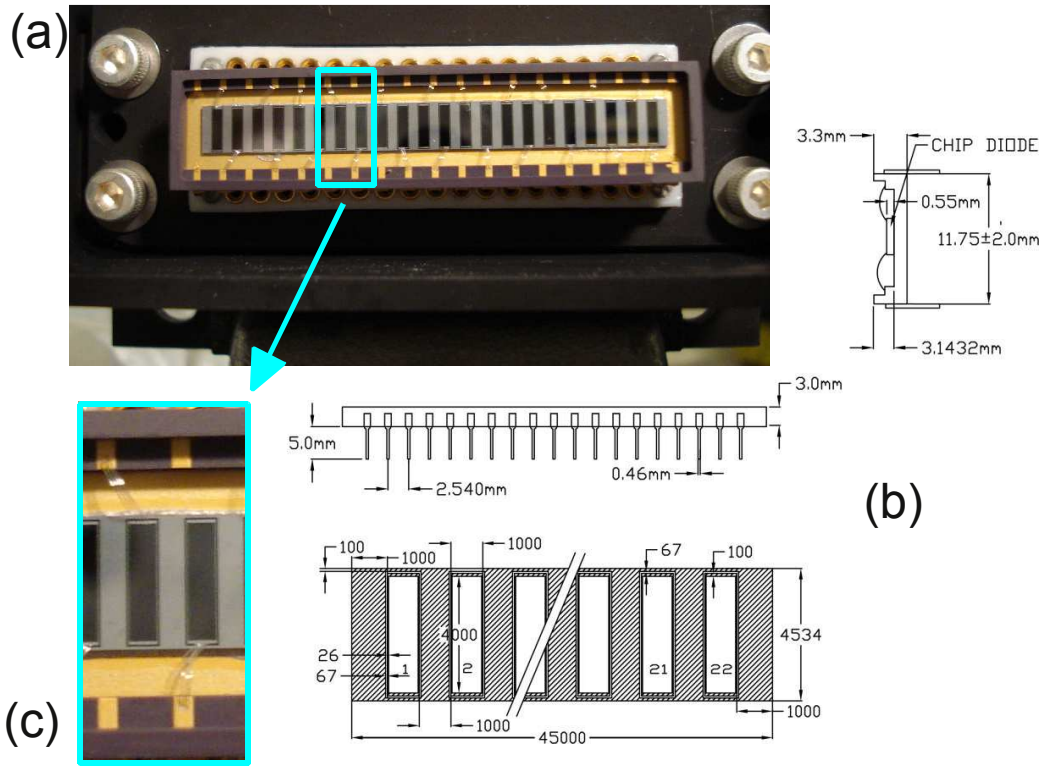

Figure 3-2: AXUV-22EL array installed in a wall box (a) and zoomed to show detail (c) specified in the engineering drawing (b)

Figure 3-3: Views of the KLIM enclosure inside Alcator C-Mod

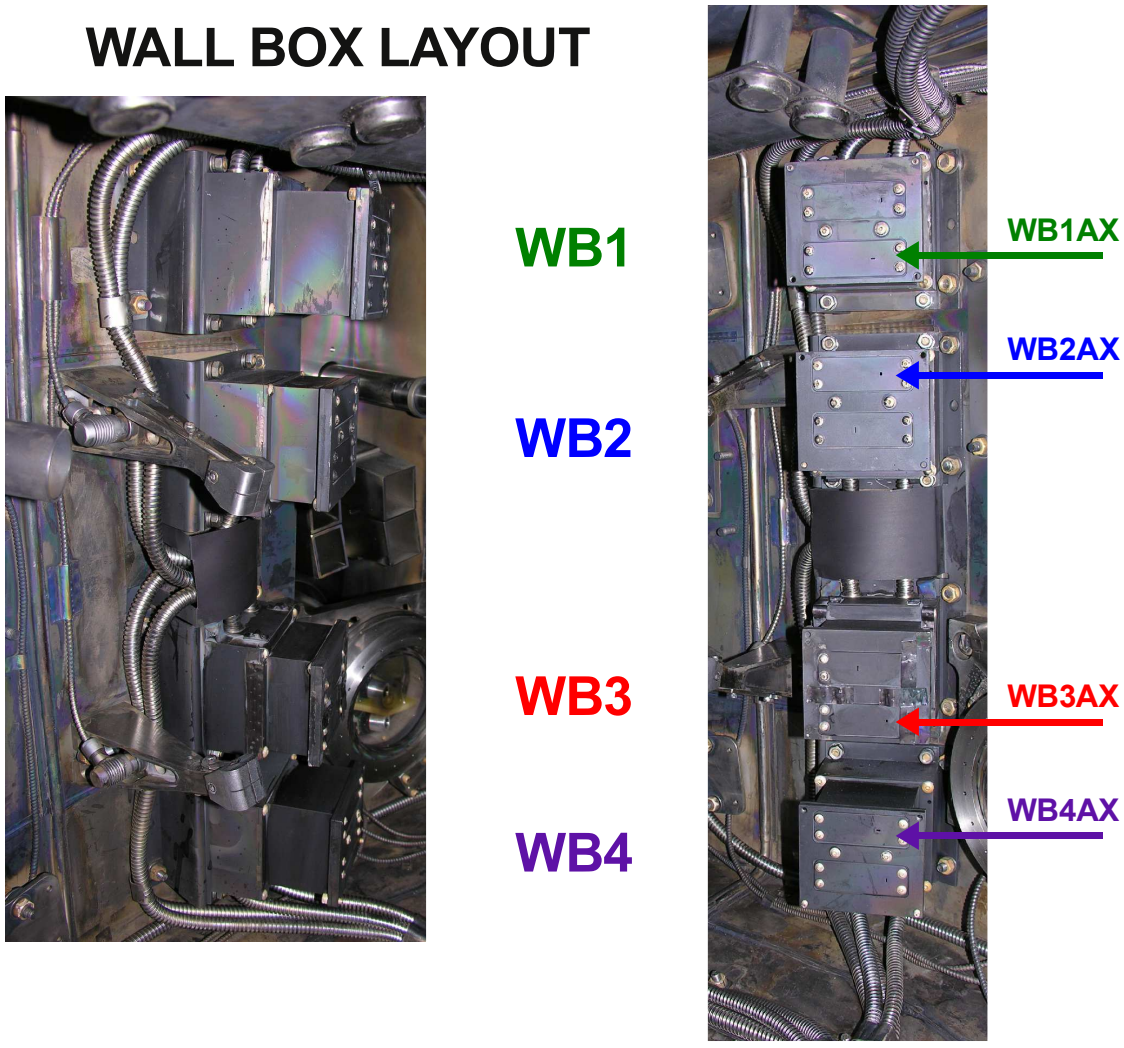

Figure 3-4: Views of the toroidally-viewing wall box enclosures inside Alcator C-Mod

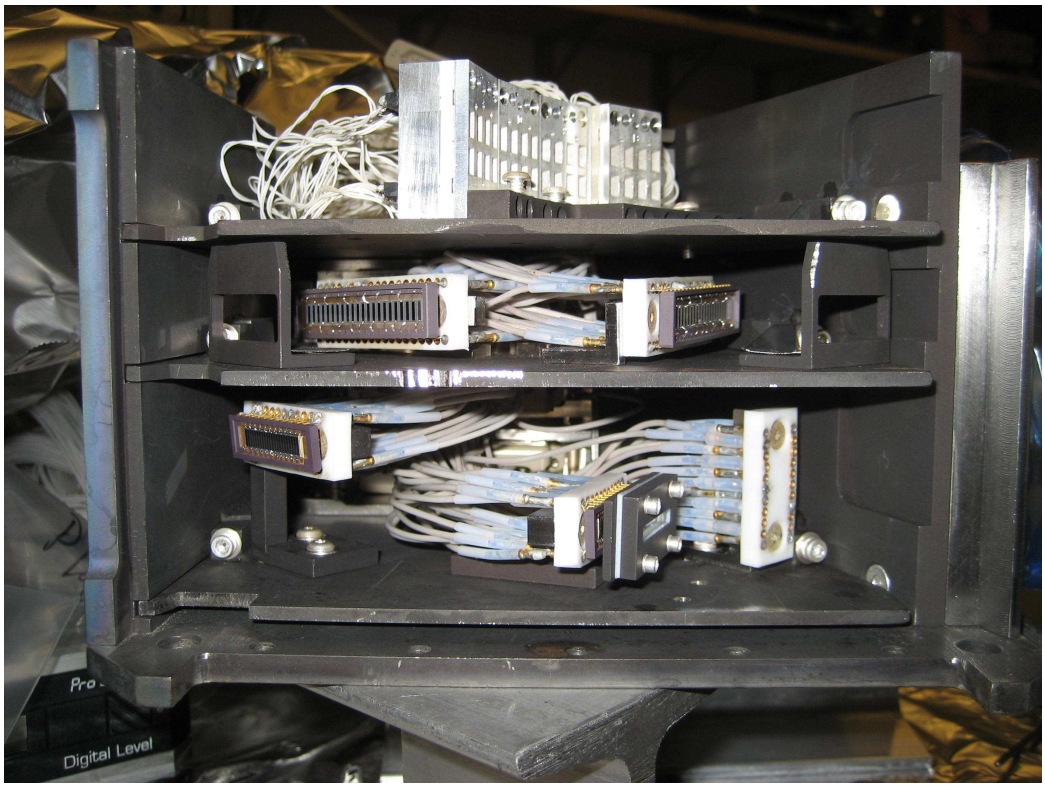

Figure 3-5: Internal view of the KLIM showing the midplane AXUV diode arrays AXJ (left) and AXA (right) on the middle instrument plate

instrument plate, and on the bottom, an AXUV-20EL array looks into the divertor, with another views Lyman-α emission from the edge.

Located to the K-side of the A horizontal port, there are four diagnostic enclosures referred to as the wall boxes, shown in Figure 3-4. In each box are two distinct pinhole cameras, a 22-channel AXUV diode array for core radiation and a 20-channel AXUV diode array for edge Lyman-α measurements. Figure 3-6 shows the internal construction of the lower wall box, WB4, typical of all four units. The 22-channel arrays are refereed to as WB1AX, WB2AX, WB3AX and WB4AX from top to bottom, viewing approximately on horizontal planes at Z_o=0.20, 0.125, -0.125 and -0.20 m, respectively. All wall box arrays view from the inner wall to the outer limiter.

Although the detectors measure radiation over a range of plasma volume and thus are not spatially localized, a useful characterization of the chords in each camera is the tangency radius, R_{TANG} or R_T. This refers to the major radius of closest

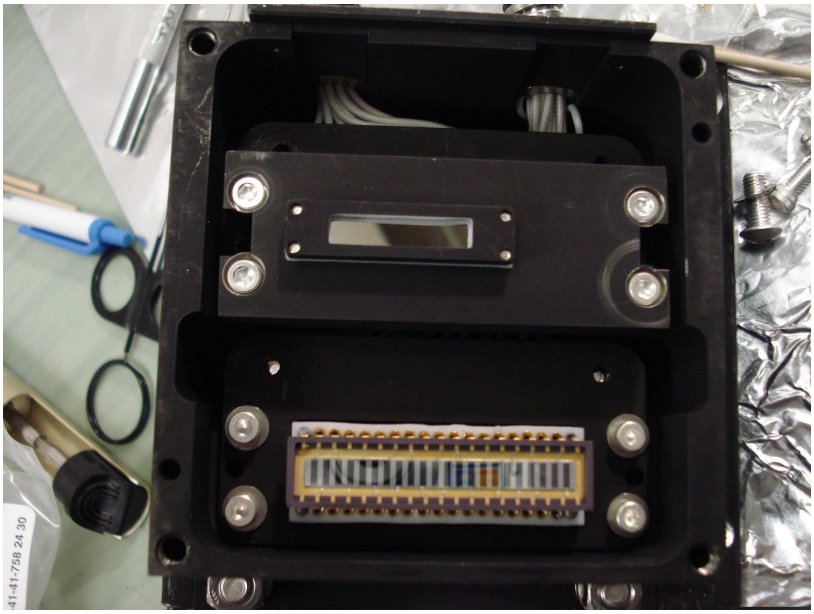

Figure 3-6: Internal view of WB4AX showing the AXUV-22EL and Lyman-α filter covering the AXUV-20EL detector

approach for the chord and identifies the region of the plasma which generally makes the largest geometric contribution to the line-integrated brightness. The tangency points, (R_T, Z_o) of the horizontally viewing arrays are shown in Figure 3-7 along with the flux surface contours of a typical diverted discharge. Noticeable gaps in the wall box coverage are due to the removal of broken/unused channels, and the AXA array has been offset from AXJ for clarity. Figure 3-8 shows a top-down view of the diagnostic layout, only showing a single wall box view (WB4AX) for clarity.

During the FY10 and FY11 campaigns (7/10-4/11), where all results from this thesis are derived, WB1AX was not functioning due to degradation of its in-vessel cabling. It is included here for completeness and was operational and calibrated, along with WB2AX, WB3AX and WB4AX, during the FY08 and FY09 campaigns, allowing future data mining. No calibrations or results from WB1AX will be discussed in the remainder of this work.

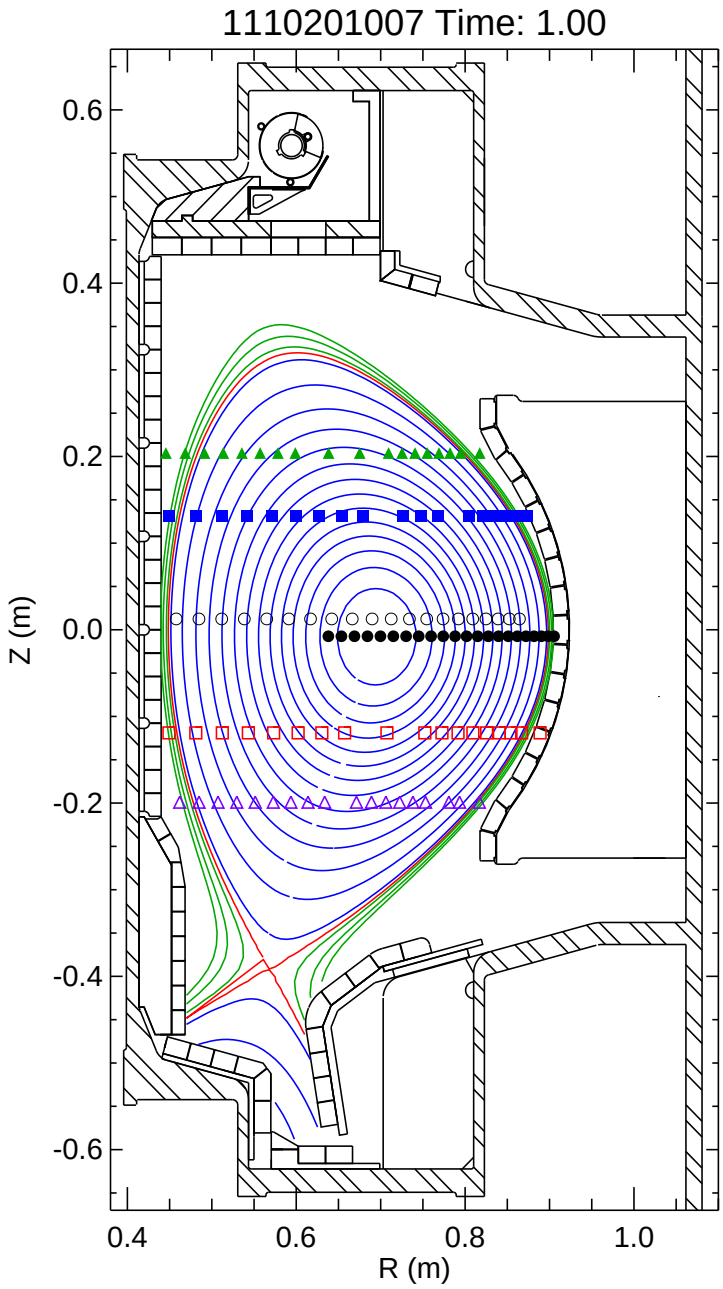

Figure 3-7: The tangency radii of the KLIM and wall box plotted over an H-mode equilibrium reconstruction; AXA (●), AXJ (○), WB1AX (▲),WB2AX (■), WB3AX (□) and WB4AX (△)

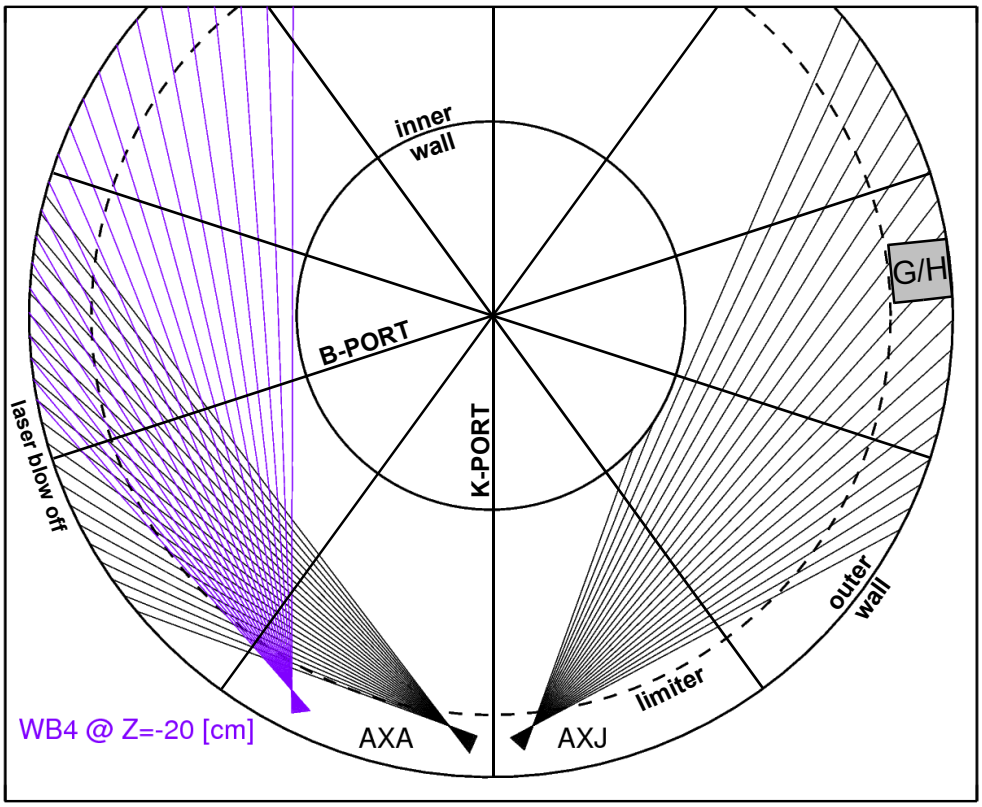

Figure 3-8: Top down view of the AXUV diode layout showing AXA and AXJ (black) and WB4AX (purple)

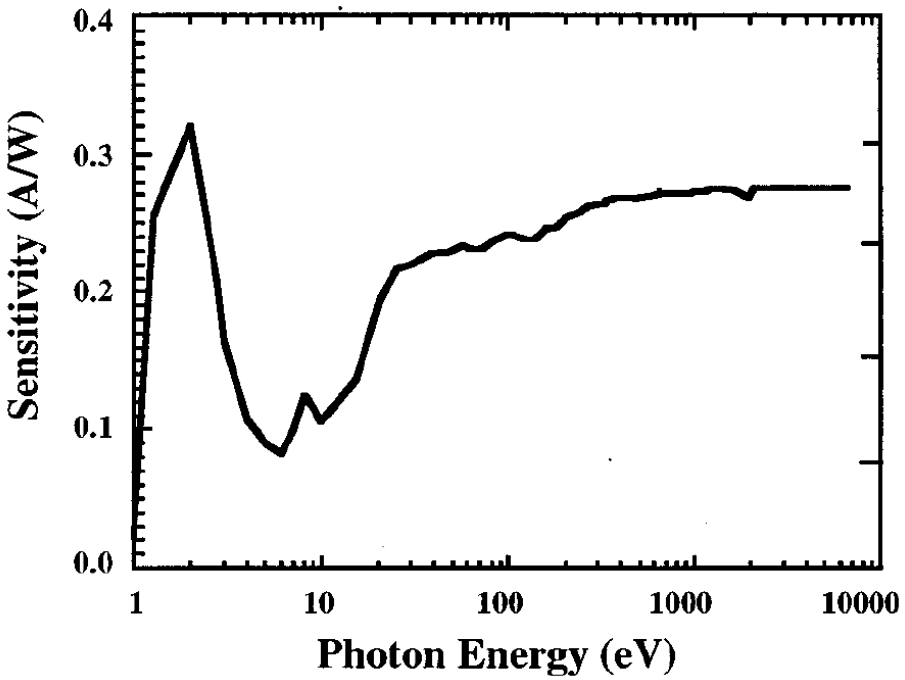

Figure 3-9: Sensitivity [A/W] of the AXUV photodiode versus input photon energy

3.1.2 Detectors

Although their operational principles are the same as a standard photodiode, the physical construction of AXUV diodes makes them well suited to studying plasma radiation. Photodiodes typically have a SiO_2 passivated layer of sufficient thickness so that weakly penetrating VUV photons are absorbed in the inactive region of the semiconductor. In AXUV diodes, this layer thickness is 3-7 nm compared to $\sim$100 nm found in other diodes such as those used in the C-Mod SXR tomography diagnostic. Figure 3-9 shows the sensitivity, the photocurrent generated per unit input power as a function of photon energy.

It is also known that these diodes may not perform exactly as specified, with neutron and photon induced damage reducing their spectral sensitivity [107][108][109]. Experiments in C-Mod have not demonstrated any significant, long-term degradation in the diodes that would impact the measurement of core radiation. The midplane emissivity profiles from the AXUV diode arrays are regularly compared to the emissivity derived from the resistive bolometers that have a flat spectral sensitivity and

are absolutely calibrated every campaign. In the plasma core, where the high electron temperatures lead to spectral emissivities weighted to the soft x-ray range, the AXUV diode and bolometer profiles agree for S_{diode}=0.28 (defined below). This indicates the diodes are resistant to degradation at photon energies where high-Z impurities tend to radiate. Additionally, the midplane emissivity profile is measured by both the AXA and AXJ arrays and a consistent result is obtained for most discharges. Due to the smaller aperture/detector distance for AXJ, photon fluxes are more than twice that of AXA, suggesting photon damage is negligible. The wall box arrays were not added at the same time as the midplane arrays yet they still produce emissivity profiles consistent with each other and the KLIM arrays, suggesting time integrated neutron damage is negligible. For these reasons, the effects of AXUV diode degradation are assumed to have no significant impact on this research.

3.1.3 Calibration

The line-integrated brightness, B [W/m^2], is determined from the measured voltage, V_m, and a variety of calibration constants by the relation,

$$B = \frac{4\pi V_m}{G_{amp} S_{diode} U_{ch}} \tag{3.1}$$

where G_{amp} is the transimpedance gain in [V/A], S_{diode} is the average sensitivity of the diode [A/W], and U_{ch} is the etendue of the view [m^2-str].

Techniques for calibrating the spatial position (R_T) and throughput (U_{ch}) of the pinhole cameras chords were developed as part of this research. Details of the techniques used for bench-top and in-vessel calibration are described in Appendix B along with the results of such calibrations for the FY10 and FY11 Alcator C-Mod campaigns. Two of the diode arrays, AXA and AXJ, both view the same (R_T, Z_o) points at different toroidal positions, allowing the quantitative accuracy of these calibrations to be demonstrated using steady-state plasmas where toroidal symmetry can be safely assumed. The results of these calibrations show that within an array, the relative throughput is known extremely well and channel-to-channel brightnesses should

be known to within 1-2%.

While this is sufficient to utilize an individual array to measure an in/out asymmetry, in order to constrain the 2-D radiation distribution, the relative calibration of one pinhole camera to another must be completed. Uncertainties in the manufactured size of the apertures or differences in the efficiency of the diode arrays must be accounted for by cross-calibrating each pinhole camera against a standard light source. Complications due to internal scattering of visible light, not an issue for VUV and SXR photons viewed from the plasma, limited the accuracy of the array-to-array calibration to $\sim$5%. This imparts a systematic uncertainty when studying up/down asymmetries.

3.1.4 Inversion

The AXUV diode arrays view toroidally on distinct horizontal planes, and by assuming toroidal symmetry, a discretized Abel inversion can be used to invert line-integrated brightness as a function tangency radius, $B(R_T)$, to find emissivity versus major radius, $\varepsilon(R)$. This is accomplished by breaking the plasma into concentric annuli, as shown in the top-down sketch in Figure 3-10, where ε is assumed to be constant in each layer.

Each of the chords is sensitive to the emission from layers whose outer boundary is greater then the tangency radius, $R_i \geq R_T$, with the increase in brightness from a layer depending on the length of inside that layer, $\delta B_j = L_j \varepsilon_j$. In this manner, the total brightness on the i-th channel can be expressed in terms of the lengths and the unknown emissivity in each layer.

$$B_i = \sum_j L_{ij} \varepsilon_j \tag{3.2}$$

The elements of the so-called length matrix, L_{ij}, can be determined geometrically as shown in Figure 3-10. For all layers except the inner-most,

$$L_{ij} = 2\left(\sqrt{R_j^2 - R_T^2} - \sqrt{R_{j+1}^2 - R_T^2}\right) \tag{3.3}$$

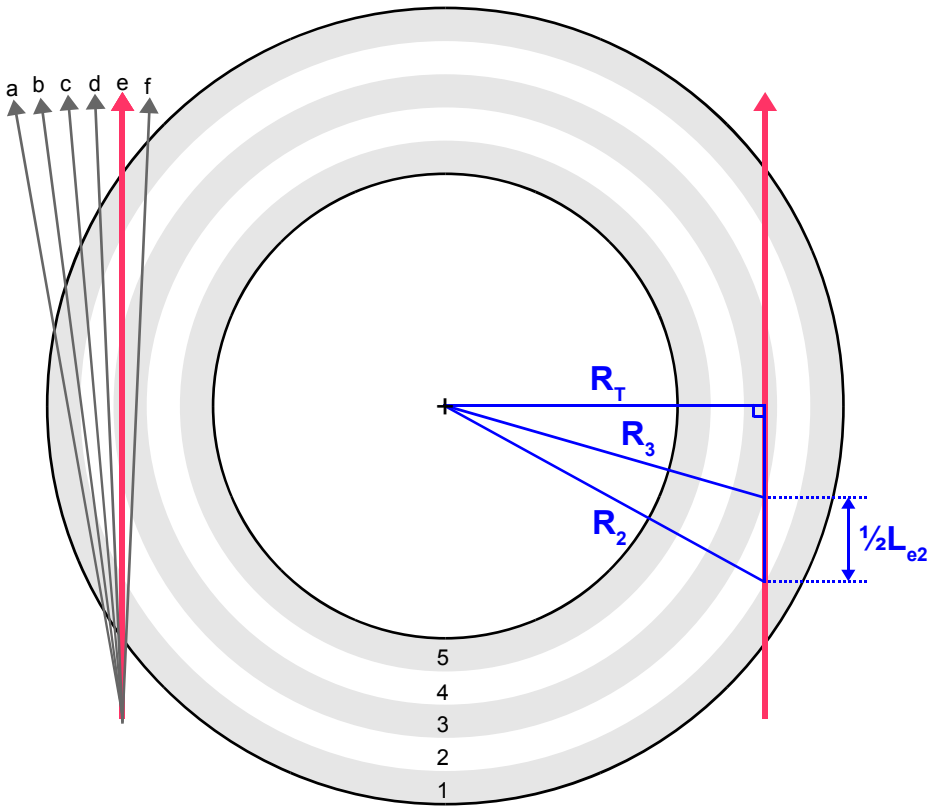

Figure 3-10: Sketch showing the the process in calculating the length matrix elements, L_{ij} for the discretized Abel inversion

while, the length in the inner most layer is simply $2\sqrt{R_j^2 - R_T^2}$. This results in the matrix equation relating the brightness and the emissivity,

$$\vec{B} = \mathbf{L} \cdot \vec{\varepsilon} \tag{3.4}$$

Solving this equation for $\vec{\varepsilon}$ can be done in a variety of ways. One common method is to define the radii of the emissive layers around the tangency radii. This makes $\mathbf{L}$ a triangular matrix, allowing it to be directly inverted to calculate the emissivity profile, $\vec{\varepsilon} = \mathbf{L}^{-1} \cdot \vec{B}$. If the number of layers is less then the number of chords, then (3.4) can be inverted in a least squares sense. The number of layers can be specified to be larger then the number of chords if regularization is included which adds *a-priori* information about the smoothness of the profile. This is done for the C-Mod arrays, where the regularization matrix, $\mathbf{D}$, works to minimize the second derivative of the radial profile. This acts to smooth the data concurrently with the inversion (3.5). The weighting of this matrix, ϵ, is set to 0.05 for the wall box arrays and 0.01 for the KLIM arrays, on the order of the elements of the length matrix.

$$\vec{\varepsilon} = \left(\mathbf{L}^T \cdot \mathbf{L} + \epsilon \mathbf{D}^T \mathbf{D}\right)^{-1} \cdot \mathbf{L} \cdot \vec{B} \tag{3.5}$$

The error propagation in this process can be calculated using a standard sensitivity analysis, allowing the uncertainties in derived emissivity profile to be found from those of the brightnesses, ignoring sensitivity due to ϵ assumptions. The SHELLINVERT procedure was written to implement this in IDL. The emissivity profile found using (3.5) is calculated in a least squares sense, including regularization, and can be reinserted into (3.4) to find the brightness profile that is consistent with the derived ε profile. This is refereed to as the brightness check or BRCHK profile, and is plotted along with measured brightness data as an indication of a reliable inversion.

This analysis make the assumption that views can be approximated by discrete chords when in reality they view a finite volume of the plasma. As part of a set of GENeric Impurity Emission (GENIE) analysis tools, a package of ray-tracing and

inversion codes, GENPOS, was developed in IDL, and is used to examine the impact of violating the so-called line-integral approximation. The specifics of how GENPOS handles ray-tracing is discussed in more detail in Section 3.5 and Appendix C.

To test the limits of the inversion algorithm, a poloidally symmetric emissivity profile is assumed, and GENPOS is used to determine the line-integrated brightnesses using the actual detector geometry, including finite sized apertures and detectors. Then, the SHELLINVERT procedure is used to determine the emissivity profile which can be compared to the assumed profile. In Figure 3-11 for AXA and 3-12 for AXJ, this is shown for three test emissivity profiles with an increasingly narrow feature size. In the right panels, "measured" data output from GENPOS (symbols) are plotted along with the BRCHK profile discussed above (dash-dot). In the left panels, the emissivity profiles calculated using SHELLINVERT (symbols plus dashed line), along with the assumed emissivity (green solid line). AXA is able to resolve features down to $\Delta(r/a) \sim 0.1$, while AXJ, due to larger magnification, can only resolve features to $\Delta(r/a) \sim 0.2$. Although not shown, this process is repeated for the wall box AXUV diode arrays with similar results.

In the left panels, the emissivity for the HFS (blue) and the LFS (black) are shown, mapped to minor radius. Despite the inboard/outboard degradation of spatial resolution for the AXJ array, no systematic in/out asymmetry is introduced by the inversion analysis in an otherwise symmetric plasma when using AXJ by itself. When combining AXJ profiles with data from the wall boxes and AXA in plasmas with narrow emissivity features, an in/out asymmetry would be found in an otherwise symmetric plasma due to the differences in spatial resolution. This sets lower limit on radial size of the emissive feature to be ~ 0.2 of r/a when all arrays are included.

3.1.5 Example Data

The AXUV diode pinhole cameras are a passive instrument that require no other diagnostic data to calculate $\varepsilon(R, Z_o)$. Only equilibrium reconstructions are needed to estimate the 2-D radiation profiles. Outside of isolated data acquisition problems, the KLIM profiles are available on every plasma shot. The availability of the wall

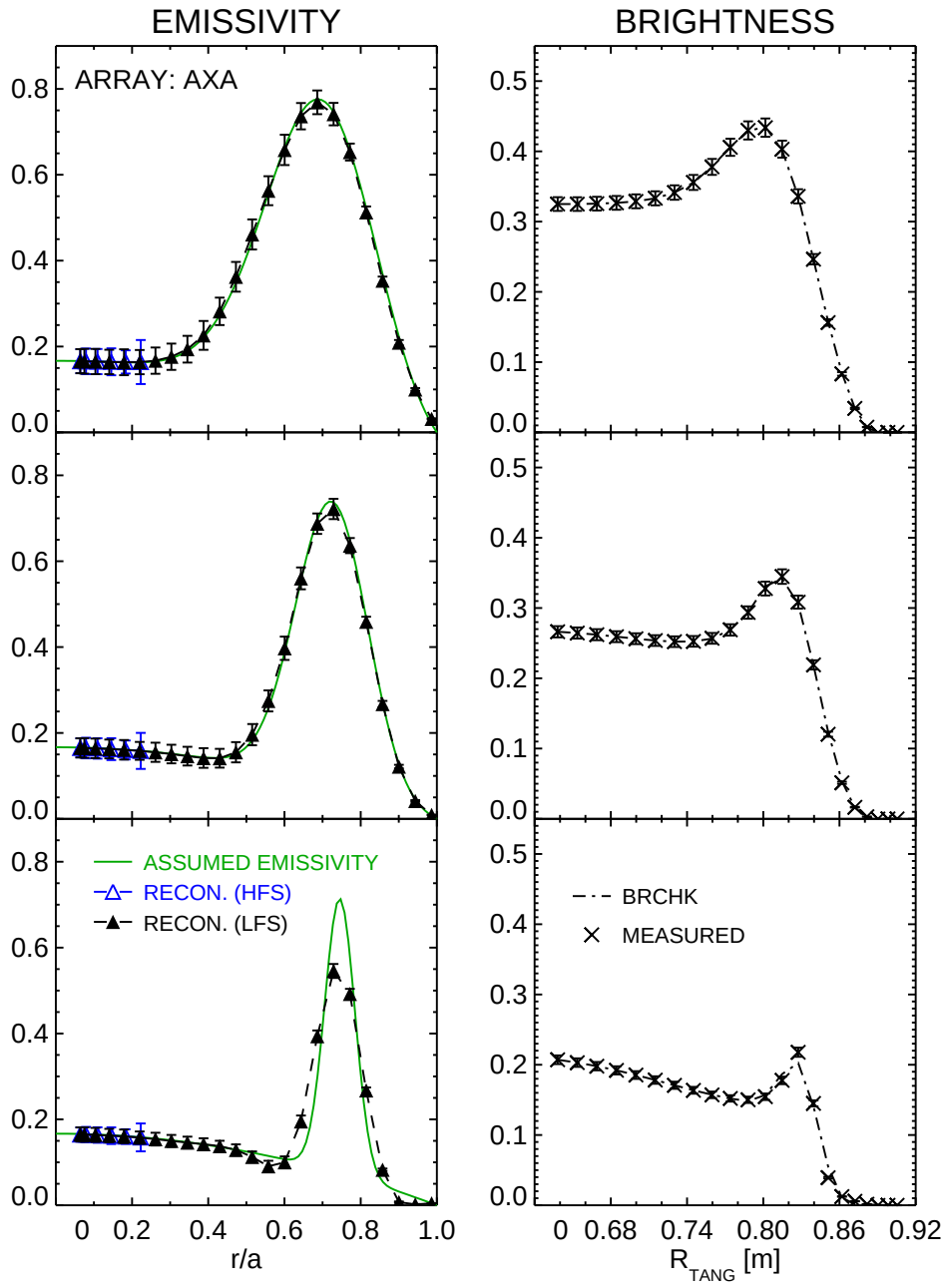

Figure 3-11: Comparison of assumed and reconstructed emissivity (left) and brightness (right) profiles for the AXA array wit

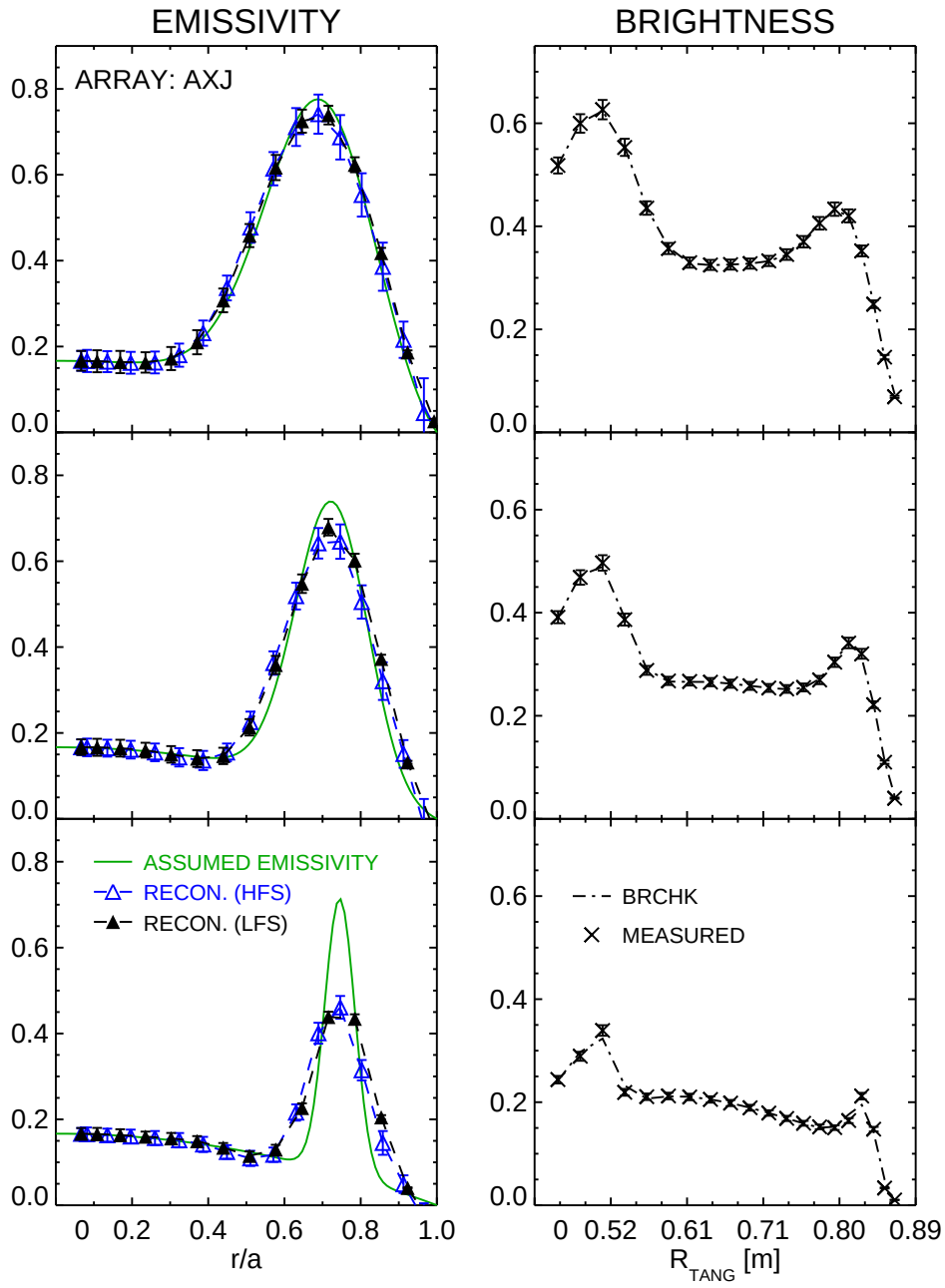

Figure 3-12: Comparison of assumed and reconstructed emissivity (left) and brightness (right) profiles for the AXJ array

box profiles is more limited due to pickup during ICRF operation, likely caused by their longer in-vessel cable runs. The wide variety of observations made using this diagnostic shows the emissivity profiles in C-Mod can exhibit flux surface symmetry (Figure 3-13), poloidal asymmetry with a significant in/out variation (Figure 3-14 and 3-15) and isolated, pathological cases of toroidal asymmetry (Figure 3-16).

In Ohmic plasmas, the emissivity profiles measured by the AXJ array are generally observed to be in out symmetric, $|\tilde{n}_z/\langle n_z\rangle| \leq 0.05$. The steady-state emissivity level is typically low, $\sim$100 kW/m^3, compared to $>$ 1 MW/m^3 in auxiliary heated plasmas, so to increase signal and accentuate any asymmetry, impurity injections are used. Figure 3-13 shows the line-integrated brightness (a) and inverted emissivity (b) profile just after a natural molybdenum injection in a 7.0 T, 1.05 MA, $\bar{n}_e$=1.0$\times$10^{20} m$-$3 Ohmic plasma. The AXA and AXJ agree with one another, and when the equilibrium reconstruction is used to map the $\varepsilon(R, Z_o)$ profiles to minor radius (c), the inboard (orange) and outboard (purple) profiles overlap.

In contrast to Ohmic plasmas, H-modes often exhibit a substantial in/out asymmetry with radiation higher on the outboard side of a flux surface. In Figure 3-14, the AXA and AXJ profiles are shown for an EDA H-mode plasma, and when mapped to r/a, the LFS emissivity is shown to be up to twice that calculated for the HFS. The radial emissivity profile is hollow, but the estimates from Section 3.1.4 show that AXJ should be able to accurately reconstruct the in/out asymmetry. The details of similar H-modes plasmas are explored in Chapter 4, where it is shown that this is due, primarily, to the centrifugal force.

In ion cyclotron resonance heated (ICRH) plasmas that do not transition into H-mode, an in/out asymmetry with increased radiation on the high field side of the flux surface can be observed. In most of these cases, the HFS abundance is localized to the core, $r/a < 0.3$ but in cases like that shown in Figure 3-15, this asymmetry extends over the inner half of the plasma. This discharge is a low density, $\bar{n}_e$=0.6$\times$10^{20} m^{-3} , plasma heated with 2 MW of ICRH power, where the resonance layer located off-axis at R=0.75 m. The physics of these types of plasmas are explored in more detail in Chapter 5, where it is shown that poloidal electric fields sustained by trapped

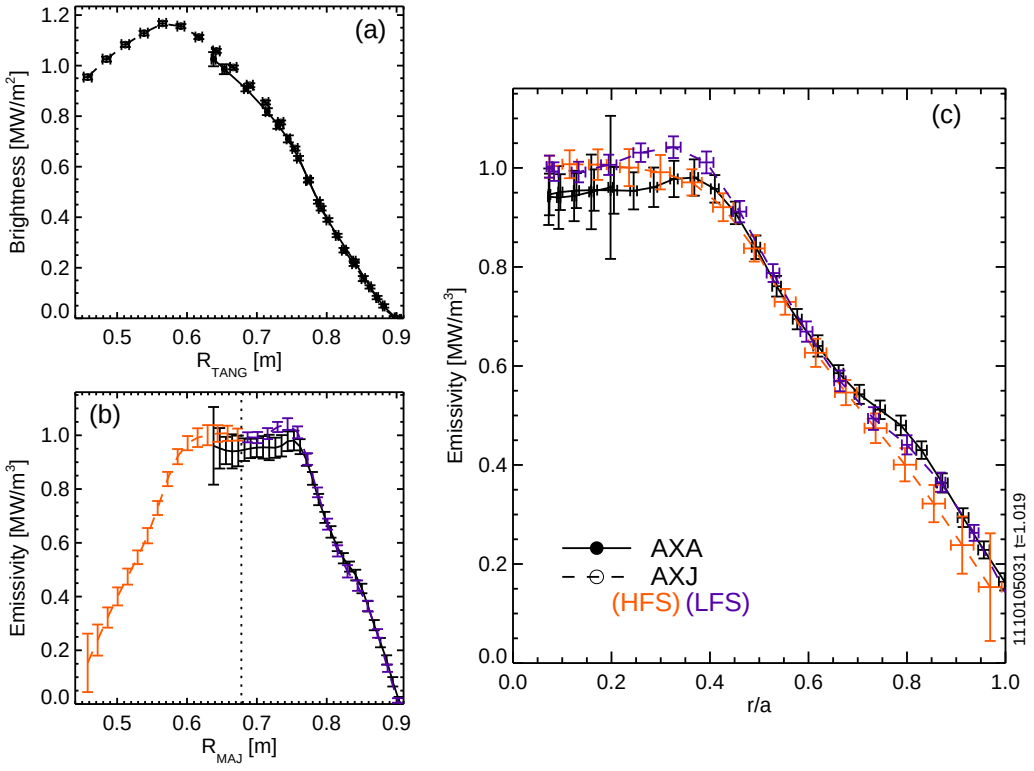

Figure 3-13: Measured brightness (a) profiles and inversions (b) for an Ohmic plasma showing nominally symmetric radiation distribution (c)

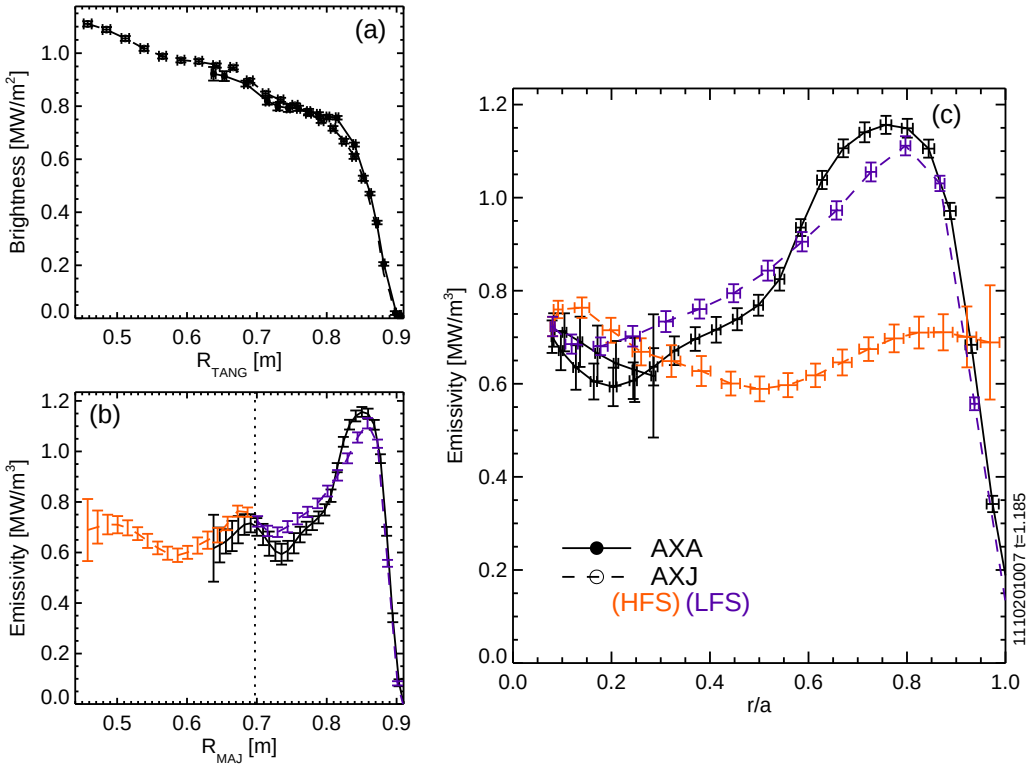

Figure 3-14: Measured brightness (a) profiles and inversions (b) for an EDA H-mode showing an outboard abundance of radiation (c)

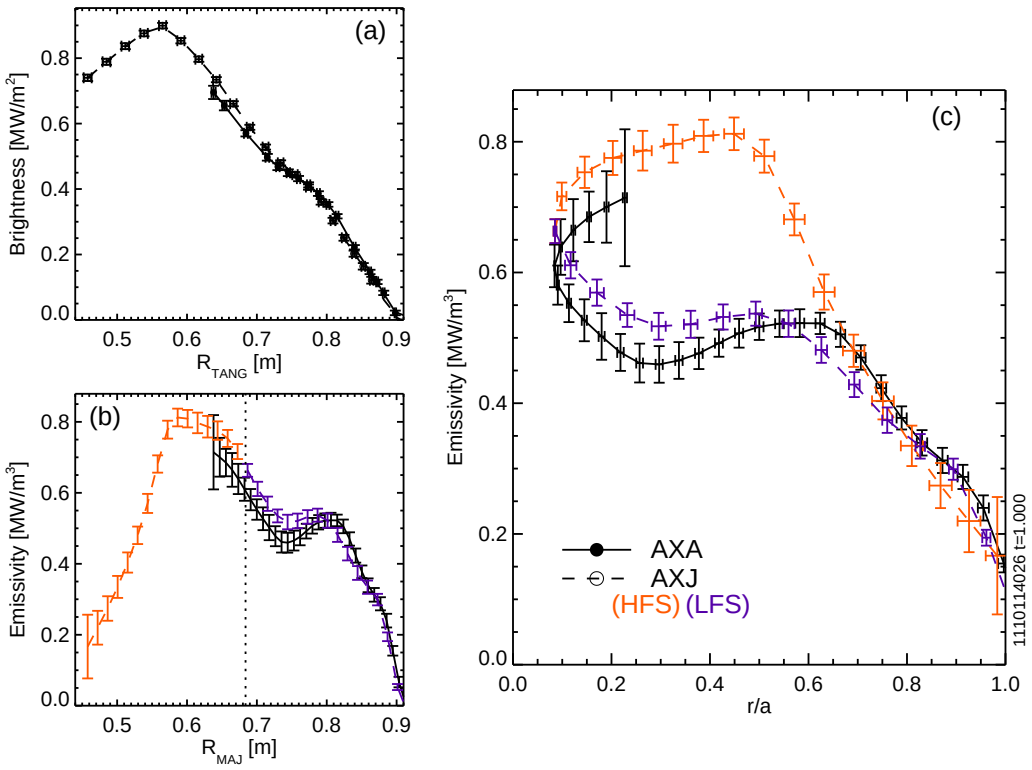

Figure 3-15: Measured brightness (a) profiles and inversions (b) for an ICRF-heated L-mode showing an inboard abundance of radiation (c)

minority ions drive the asymmetry.

In cases with substantial ICRH at low density and current, significant localized radiation is observed at or near the outboard limiters. Although the cause has yet to be proved conclusively, it is thought to be driven by losses of high energy fast ions at the outboard midplane. This radiative event, referred to as a TARFE (for Toroidally Asymmetric Radiation From the Edge), is troubling as the chords from middle of the AXJ array terminate on the G/H limiter as shown in Figure 3-8. Figure 3-16 shows the G/H limiter video camera view during the Ohmic (3-16a) and ICRF-heated (3-16c) parts of shot 1101202005, a 600 kA, $\bar{n}_e \sim 1.0{\times}10^{20}$ m^{-3} plasma with 3 MW of on-axis heating from the J-Port ICRF Antenna. The brightness profiles for the AXA and AXJ array are shown in Figure 3-16b where toroidal symmetry is seen during the Ohmic phase, but during the rf heating, a substantial difference of

$\sim$200 kW/m^2 is observed for views that terminate near the G/H limiter. Since this emission is toroidally localized, it breaks the axisymmetry assumption necessary for Abel inversion, and makes the resulting emissivity profile from AXJ unreliable. By comparing the AXJ and AXA brightness profiles, and viewing the G/H limiter video, TARFE cases can be avoided when investigating in/out asymmetries.

3.1.6 Other Applications

The upgraded AXUV diode diagnostic suite has also been used for research outside the scope of this thesis. Radiation near the active X-point during impurity seeded H-mode plasmas has been examined [110], and toroidally localized impurity injections from laser blow-off or vessel limiter and antenna structures have been identified. These diodes have also been utilized to investigate the 3-D nature of radiation during disruptions mitigated by massive gas injection (MGI), contributing to the physical understanding of disruption mitigation, and helping to constrain the design of the MGI system on ITER [111][112].

3.2 X-Ray Crystal Imaging Spectrometer: HIREXSR

A key tool used in these investigations is the HIgh REsolution X-ray spectrometer with Spatial Resolution (HIREXSR), which provides impurity flow and temperature profiles [37]. This instrument uses a spherically-bent crystal to reflect and focus soft x-ray radiation of a specific wavelength that satisfies the Bragg condition, $m\lambda = 2d\sin\theta$, where d is the spacing of layers in the crystal. Quartz crystals with $2d = 4.56216$ Å are used to view line emission from He-like and H-like argon, and its large resolving power, $\sim$10000, enables the Doppler shift and broadening to be measured. While the initial hardware was deployed prior to this thesis work [113], significant contributions were made to the calibration of the instrument and its analysis. A ray-tracing code was developed to recommend changes to the spectrometer layout to avoid vignetting, also allowing for more accurate spatial calibration and calculation of instrumental effects for finite sized, imperfect crystals. Spectral line fitting codes were upgraded

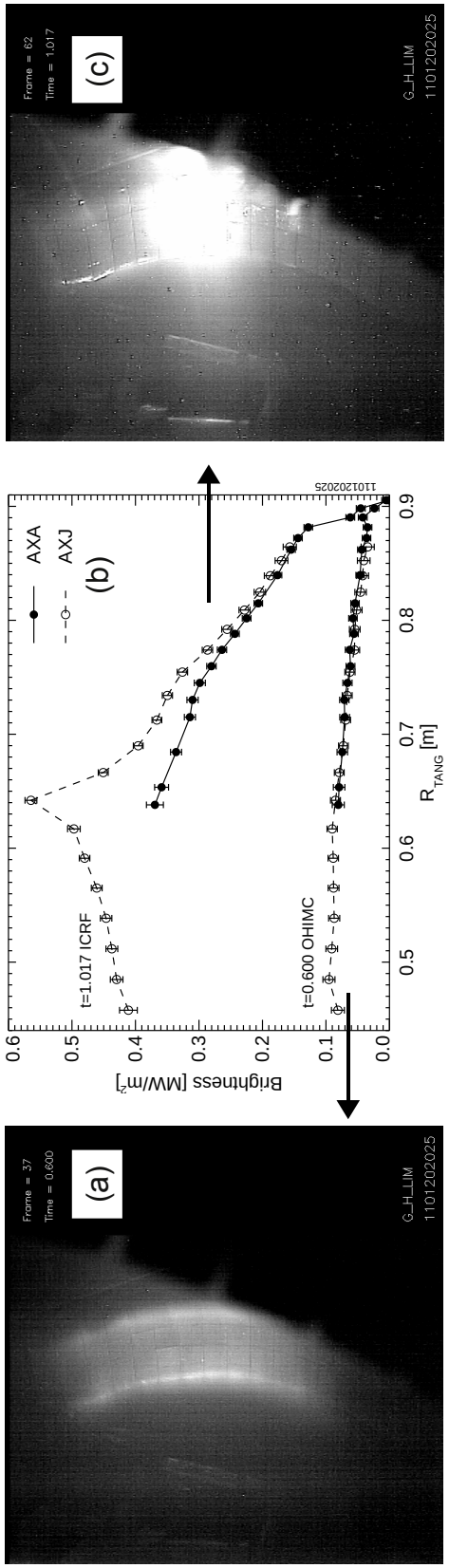

Figure 3-16: Comparison of AXA and AXJ during a TARFE, demonstrating a toroidal asymmetry due to emission from G/H limiter

to dramatically increase speed, and the accuracy was improved through the use of experimentally validated rest wavelengths. The Doppler tomography code used to invert line-integrated data was modified to include error propagation and enable time-evolving binning and inversion setup. This suite of codes, written in IDL and kept in a Mercurial database, is referred to as The HIREXSR Analysis COde (THACO), and has enabled measurements from HIREXSR to be used in a variety of transport experiments. The spatial coverage of the He-like and H-like views are shown in Figures 3-17a and 3-17b, respectively. In-depth details of the design, operation and validation of HIREXSR and THACO is beyond the scope of this research, but has been presented in the past [114][115], and will by included in the to-be-completed manual on THACO [116].

3.3 Impurity Spectroscopy

The AXUV and SXR diodes are sensitive over a wide range photon energies, but cannot determine the type of impurity responsible for the radiation. In order to interpret the calculated 2-D emissivity structures as poloidal variations of impurity density, other diagnostics must be used to identify strongly radiating impurities and to estimate their concentrations in the plasma. Spectroscopy in the VUV and SXR range over 1-15 nm is used to measured line-emission from incompletely ionized low-Z and high-Z impurities. Two instruments, along with the previously discussed HIREXSR spectroscopy are utilized.

3.3.1 Rowland Circle Spectrometer: McP

A 2.2 meter, grazing-incidence Rowland circle spectrometer, a McPherson Model 247, uses a 600 lines/mm grating to disperse VUV radiation in the 90-1030 Å range. The McPherson (McP) spectrometer is a mature diagnostic and is described in more detail in [117][118]. Contributions were made to data analysis for this diagnostic and effort was spent to improve the understanding of metallic impurities in C-Mod plasmas [119][120]. An analysis code was co-authored to automate shot-to-shot spectral fitting

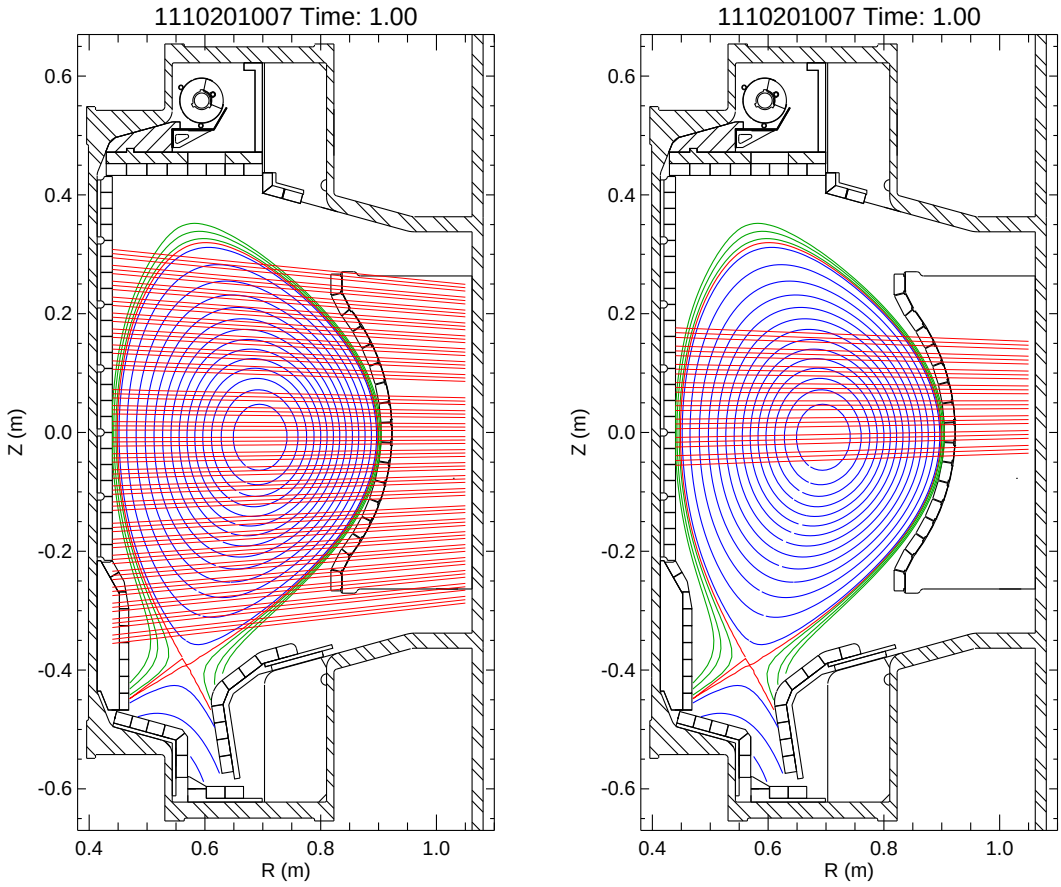

(a) (b)

Figure 3-17: Chordal views of the HIREXSR diagnostic looking at He-like Ar (a) and H-like Ar (b)

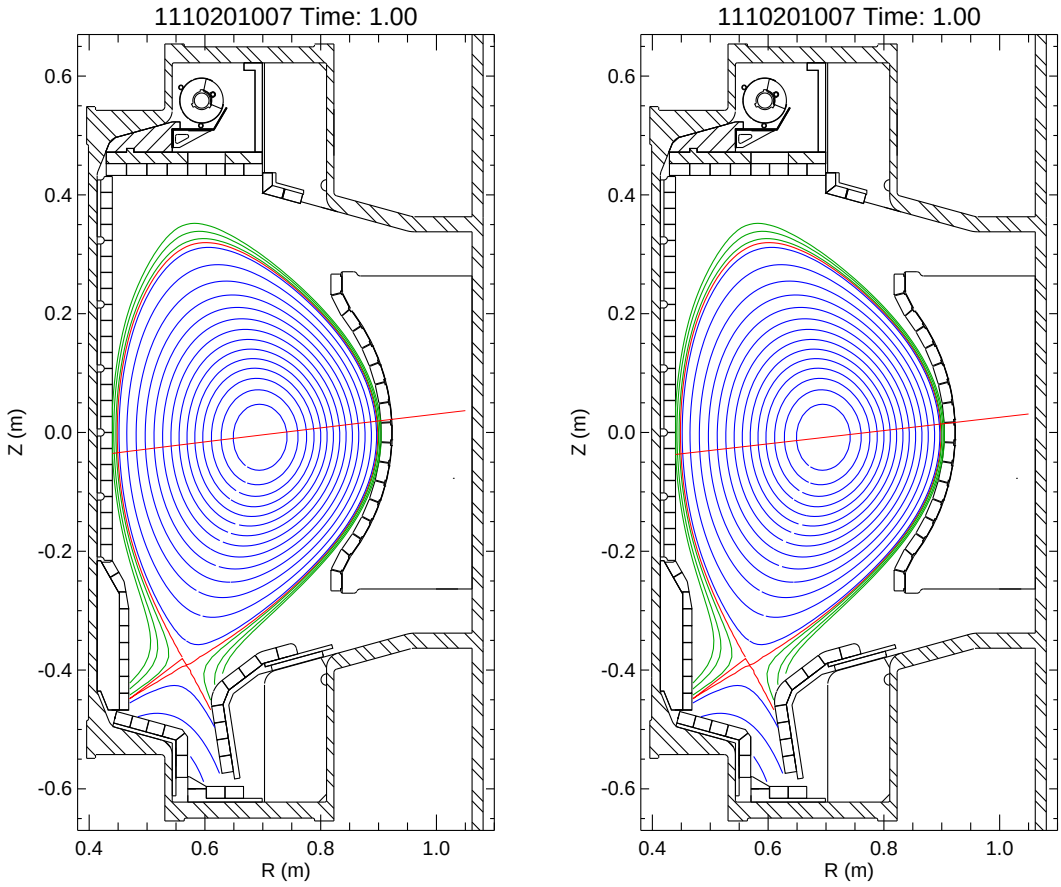

(a) (b)

Figure 3-18: Chordal view of the XEUS flat field spectrometer (a) and the McPherson Rowland circle spectrometer (b)

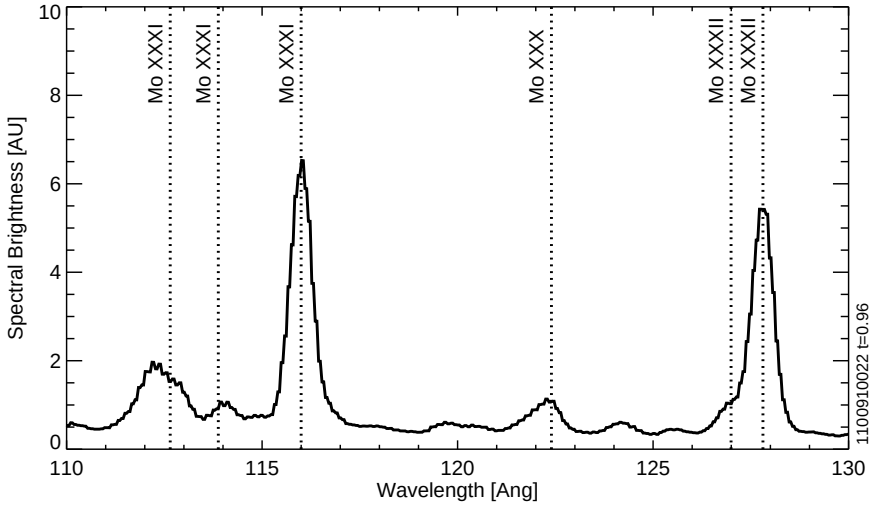

Figure 3-19: McPherson spectrum dominated by Mo during an I-mode plasma

and provide brightness time histories for a number of commonly observed impurity lines. This instrument is primarily responsible for measuring the amount of mid and high-Z elements in C-Mod plasmas and is critical in this research for determining when plasma radiation is dominated by molybdenum. It is also used to measure titanium, iron, nickel and copper injections from the vacuum vessel and ICRF antenna structures. While the McP line of sight can be scanned over the poloidal cross-section, a fixed core line of sight is used in this research, shown in Figure 3-20b. A typical molybdenum dominated spectrum is shown for an I-mode plasmas in Figure 3-19, with lines from various molybdenum charge states identified. The Mg-like (Mo XXXI, 115.9 Å) and Na-like (Mo XXXII 127.8 Å) charge states are used to characterize the molybdenum fraction.

3.3.2 Flat-Field Spectrometer: XEUS

A collaboration with LLNL was initiated giving C-Mod access to a flat-field X-ray Extended Ultraviolet Spectrometer (XEUS) [121] which was installed on C-Mod during the FY10 run campaign [118]. This instrument uses a 2400 lines/mm grating with varied line spacing (VLS), designed to focus the spectrum, normally on around the Rowland circle, onto a flat plane. The XEUS sensor was upgraded with a Princeton

Instruments PIXIS-XO 100B camera [122] which uses a 1340×100 back-illuminated charge-coupled device (CCD) designed to measure low-energy soft x-rays. VLS gratings have a nonlinear dispersion and to calibrate the wavelength scale, a second order polynomial is fit to pixel locations of known lines. The small height of the CCD, 33 kHz row shift rate and 2 MHz digitization rates allow spectra to be routinely collected with time resolution of ∼2.5 ms. The diagnostic line of sight is very similar to that of the McP spectrometer and is shown in Figure 3-20a. Example spectra from Ar and low-Z ions is shown in Figure 3-20.

3.3.3 Transfer Calibration Technique

Due to the lack of intense, portable sources in the 1-15 nm range it is difficult to photometrically calibrate either the McP or XEUS in order to use their data to find absolute impurity densities. The branching ratio technique [123] can be used at certain wavelengths, but this also requires the diagnostic to have an equivalent, calibrated visible view, which XEUS does not have. Instead, an *in-situ* calibration method was developed to transfer the absolute calibration from diagnostics such as resistive bolometry, soft x-ray tomography and Z_{eff}, to the VUV and SXR spectrometers. For plasmas where a single impurity is so abundant that it dominates the total radiated power and the dilution, the absolute density can be estimated from these non-spectroscopic diagnostics. In plasmas when the impurity fraction is smaller, the density can be found by comparing the ratio of the brightness measured to that of the severely polluted plasma. This technique is presented in more detail in [124].

3.4 Other Diagnostics

In order to demonstrate the poloidal variation of impurity density from AXUV measurements, the spatial contours of magnetic flux surfaces have to be determined. This is done using the EFIT code [125] constrained by external magnetic measurements. The estimated uncertainties in the location of the magnetic axis is $\delta R_o \simeq 6$ mm, with that of the elongation being $\delta\kappa \sim 0.05$ [126]. In most cases, asymmetry mea-

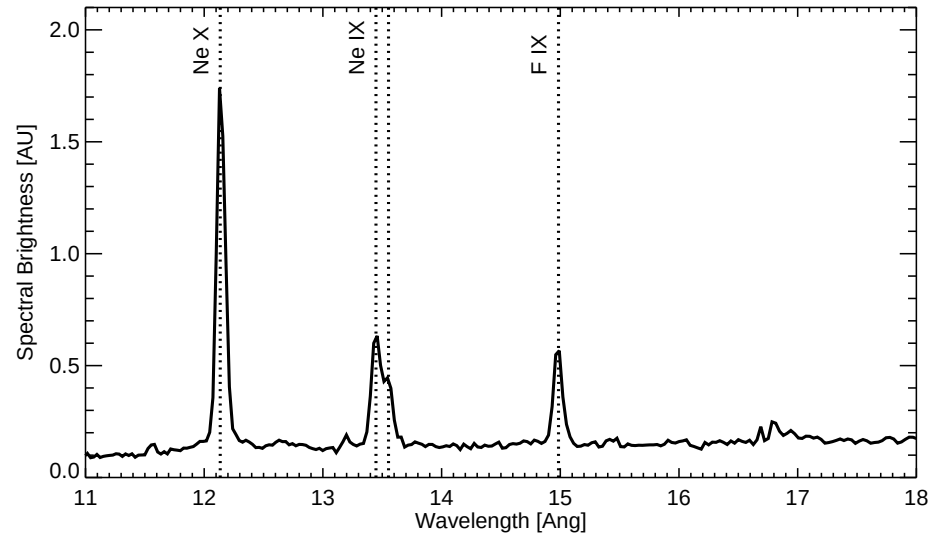

(a)

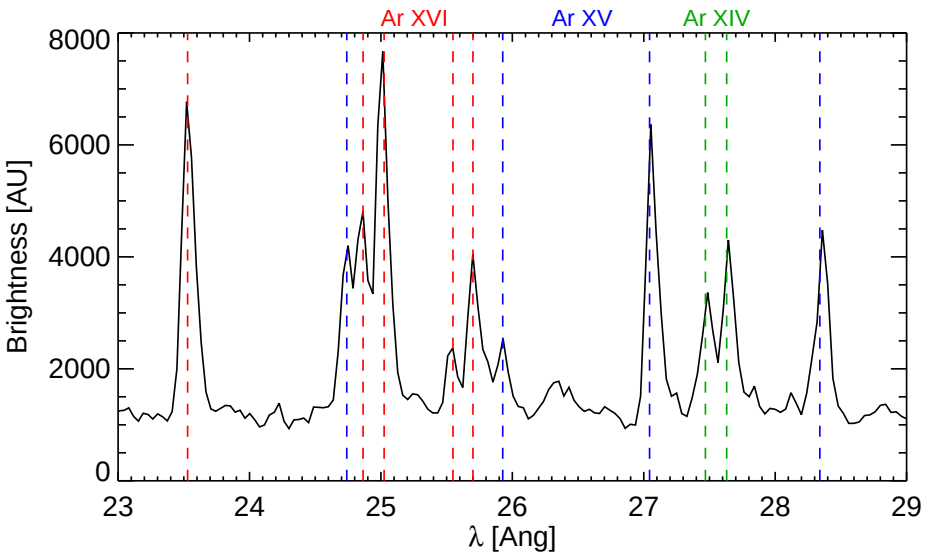

(b)

Figure 3-20: XEUS spectrum dominated by neon in an EDA H-mode plasma (a) and argon in an Ohmic plasma (b)

surements are based on wide radial emissivity features, making quoted δR_o of minor importance. In high performance plasmas, EFIT can be constrained further with experimental pressure profiles, which is explored in Section 4.3.2.

The time-dependent, radial electron density and temperature profiles are measured using proven diagnostic techniques. The local electron density and temperature are measured using Thomson scattering (TS) at various vertical points along a major radius chord at R=0.68 m. Two-color interferometry (TCI) measures line-integrated electron density along 10 vertical chords from $0.675 < \mathrm{R} < 0.810$ m. A number of electron cyclotron emission (ECE) diagnostics measure T_e from blackbody emission along the outboard major radius. Information regarding these and other general C-Mod diagnostics can be found in [127]

Impurities can be intentionally added to the plasma using laser blow-off (LBO) [128] and neutral gas puffs. Non-recycling impurities such as Ca, Mo and W are injected using LBO while recycling impurities, Ne, Ar, Kr and Xe are introduced using main chamber gas puffing. Both systems are localized at B-PORT and the AXUV diode system can be used to demonstrate when the emission has become toroidally symmetric.

3.5 2-D Tomography Tools

A novel tomography code was developed for use in design and interpretation of diagnostics used in these investigations. Previous tomography tools at C-Mod operated on a poloidal (SXR tomography, divertor bolometry) or horizontal planes (core bolometry, AXUV diodes), using this viewing geometry to simplify the inversion. When viewing on a horizontal plane and assuming the plasma has toroidal symmetry, the line-integrated brightness is only a function of tangency radius, $B(R_T)$. The local emissivity can be expressed as an integral transformation of the brightness profile using the well known Abel inversion. On a poloidal plane a general 2-D emissivity profile can be found similarly using the Radon transformation. A generic line of sight does not meet either of these criteria. Instead of parameterizing an arbitrary line of sight

through the tokamak and performing ray-tracing through a 3-D emitter, the toroidal symmetry is assumed which reduces the problem to tracing a hyperbola through a 2-D radiation distribution. The normal six degrees of freedom necessary for 3-D ray-tracing, $(R, \phi, Z)_1$ and $(R, \phi, Z)_2$, can be reduced to four parameters (R_1, Z_1, R_T, ψ) where R_T is the tangency radius and ψ is the declination angle of the line of sight. This way, when performing a line-integral through the tokamak, the emissivity only needs to be interpolated in two variables rather then three. Unfortunately, there is no known analogous method like the Abel or Radon transformations to expand the 2-D emissivity in terms of hyperbolic paths. The GENPOS codes allow arbitrary sets of views (horizontal, poloidal or mixed), to be grouped together to calculate emissivity profiles from line-integrated data.

The impact of violating the line-integral approximation can also be studied using the GENPOS tools. The aperture and detector area are both divided into sub arrays and each pair forms a discrete pinhole camera combination. As the density of the gridding is increased, the sum of the elements converges to an exact description. A more detailed explanation is outlined in Appendix C.

3.6 Calculating the Impurity Density Asymmetry

In the subsequent chapters the 2-D AXUV diode based emissivity measurements are used to infer poloidal variation of the high-Z impurity density. Two techniques are used, one which uses only the midplane arrays and the other which uses all horizontally viewing arrays. Both assume that the radiation is primarily from a single high-Z impurity species so that poloidal variations in emissivity, $\tilde{\varepsilon}/\langle\varepsilon\rangle$, directly correspond to poloidal variations in impurity density, $\tilde{n}_z/\langle n_z\rangle$. Since $\varepsilon = n_e n_z f(T_e)$, this assumes that the parallel heat transport forces poloidal symmetry in the electron temperature and electron density is relatively constant on the flux surfaces, an approximation valid for low main-ion Mach number plasmas, $M_i^2 < 0.1$. In practice, a fraction of the emissivity will be due to continuum radiation and/or line emission from other, more symmetric impurities, and a correction for this is shown.

3.6.1 In/Out Asymmetry Using KLIM Arrays

The AXA and AXJ arrays view close to the midplane, $Z_o = 1.25$ cm, and can be used to explore the in/out asymmetry independent of any up/down asymmetry. Using EFIT, the $\varepsilon(R, Z_o)$ data output from the inversion can be mapped to a common radial coordinate, either normalized minor radius, r/a, or the outboard midplane major radius, R_{MID}. With AXA, results are only available on both sides of the magnetic axis near the core, while using AXJ measures full HFS and LFS emissivity profiles. The poloidally varying component of the impurity density, $\tilde{n}_z/\langle n_z \rangle$, is found using,

$$\frac{\tilde{n}_z}{\langle n_z \rangle} = \frac{\varepsilon_{LFS} - \varepsilon_{HFS}}{\varepsilon_{LFS} + \varepsilon_{HFS}} \tag{3.6}$$

where ε_{LFS} and ε_{HFS} refers to the emissivity determined to be the outboard and inboard side of the same flux surface. If the impurity density varies like $n_z = \langle n_z \rangle + n_{cos} \cos\theta$ then using (3.6) with the KLIM arrays will be a measure of $n_{cos}/\langle n_z \rangle$, the amplitude of the $m = 1$ impurity density variation. Figure 3-21 shows the result of applying (3.6) to the AXJ data shown above in Figure 3-14.

In reality, the measured emissivity will not be due exclusively to the high-Z impurity. A correction to (3.6) can be estimated by assuming the total emissivity, $\varepsilon_{tot} = \varepsilon_z + \varepsilon_o$ to be comprised of a poloidally varying component due to the high-Z impurities, ε_z, and a more poloidally symmetric term due to main-ion bremsstrahlung and low-Z line emission, ε_o. The asymmetry in the measured emissivity, $\tilde{\varepsilon}/\langle \varepsilon \rangle$, is

$$\frac{\tilde{\varepsilon}}{\langle \varepsilon \rangle} = \frac{\varepsilon_{z,LFS} - \varepsilon_{z,HFS}}{\varepsilon_{z,LFS} + \varepsilon_{z,HFS} + 2\varepsilon_o} \tag{3.7}$$

where $2\varepsilon_o + (\varepsilon_{z,LFS} + \varepsilon_{z,HFS}) \simeq 2\varepsilon_{tot}$ when exploring in/out asymmetries.

$$\frac{\tilde{\varepsilon}}{\langle \varepsilon \rangle} = \frac{\varepsilon_z}{\varepsilon_{tot}} \frac{\varepsilon_{z,LFS} - \varepsilon_{z,HFS}}{\varepsilon_{z,LFS} + \varepsilon_{z,HFS}} \tag{3.8}$$

where $\varepsilon_z = (\varepsilon_{z,LFS} + \varepsilon_{z,HFS})/2$. This makes the derived $\tilde{n}_z/\langle n_z \rangle$ proportional the

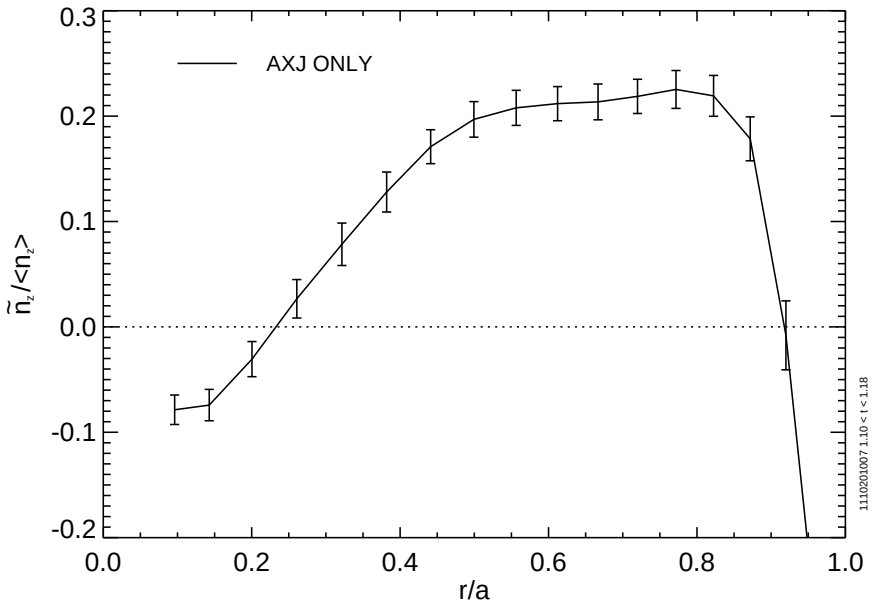

Figure 3-21: Poloidally varying component of the impurity density calculated from the AXJ data

purity assumption.

$$\frac{\tilde{n}_z}{\langle n_z \rangle} = \left(\frac{\varepsilon_{tot}}{\varepsilon_z}\right)\left(\frac{\varepsilon_{LFS} - \varepsilon_{HFS}}{\varepsilon_{LFS} + \varepsilon_{HFS}}\right) \tag{3.9}$$

3.6.2 2-D Profiles Using KLIM and Wall Box Arrays

When data are available from the wall boxes and the KLIM arrays, they can be used together to derive the 2-D emissivity profile. The discretized Abel-inversions are completed, as described in Section 3.1.4, to find $\varepsilon(R, Z_o)$ on the various horizontal planes. The EFIT equilibrium reconstruction is then used to map the profiles to minor radius, determining $\varepsilon(r/a)$. The output of the default (ANALYSIS) EFIT gives the (R, Z) points of each flux surface for 33 r/a locations evenly spaced in normalized poloidal flux, ψ_n. At each EFIT radial location, the inverted profile and the error bar are interpolated to find (θ_o, ε) points from each array. The emissivity on each flux surface is expanded in a low order Fourier series,

$$\varepsilon(\theta) = a_o + a_1 \cos\theta + a_2 \sin\theta + a_3 \cos 2\theta + a_4 \sin 2\theta \tag{3.10}$$

where θ is defined in the geometrical sense relative to the magnetic axis. The coefficients a_o-a_4 are determined by a linear-least squares fit of (3.10) to experimental (θ_o, ε) data. In regions of the plasma where only AXA and AXJ are available, only a_o and a_1 are used. When both WB2 and WB3 are available, a_o-a_2 are used, with the inclusion of the $m = 2$ terms being optional.

This process is first completed on test data to determine if an assumed asymmetry can be accurately reconstructed from the combination of AXA, AXJ, WB2AX, WB3AX and WB4AX data. As described in Section 3.5, the GENPOS tools can be used to find the line-integrated brightness for any defined $\varepsilon(R, Z)$ profile using using finite-sized detectors and apertures. The emissivity is defined to be $\varepsilon = \varepsilon_o + \varepsilon_c \cos\theta + \varepsilon_s \sin\theta$. Both peaked and hollow $\varepsilon_o(r/a)$ profiles are assumed, as shown in Figures 3-22a and 3-22a, while the $\varepsilon_c/\varepsilon_o$ and $\varepsilon_s/\varepsilon_o$ profiles are remain the same for both. Contour plots of the 2-D emissivity profiles are shown in Figure 3-23 along with EFIT flux surfaces. The $\varepsilon_s/\varepsilon_o$ profile monotonically increases towards the edge while $\varepsilon_c/\varepsilon_o$ profile is negative in the core, positive at larger r/a and returns to zero at the edge. A 3% uncertainty in the brightness in each channel is assumed and used in error propagation analysis to demonstrate the anticipated accuracy. The flux surface geometry of an actual USN plasma is used, and the SHELLINVERT code inverts the calculated brightness profiles in all cases.

Looking within one flux surface at a time, Figure 3-24 shows the results of fitting an $m = 1$ component to (3.10) for the peaked emissivity profile case, at various r/a. Poloidal profiles are normalized to the value at $\theta = 0$ in order to compare results from the output of the parallel transport code discussed in Chapter 2 and Appendix A. The black dotted lines represent the calculated uncertainties in the coefficients. In the core (3-24a), both AXA and AXJ are available and only the in/out asymmetry is fit. The data from WB2 and WB3 enter at mid radius (3-24b), allowing the small up/down asymmetry to be determined. Moving outward, the WB2 and WB3 data points move apart, and WB4 is included in the fit (3-24c). In this region, the $m = 1$ components are well constrained by having data at 8 different poloidal locations, making outliers indicators of higher order terms or non-Fourier poloidal variation. For larger minor

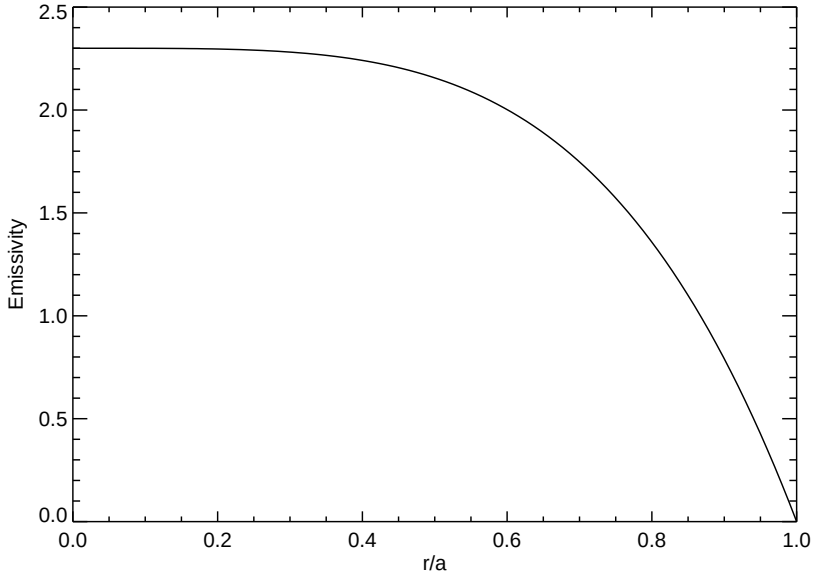

(a)

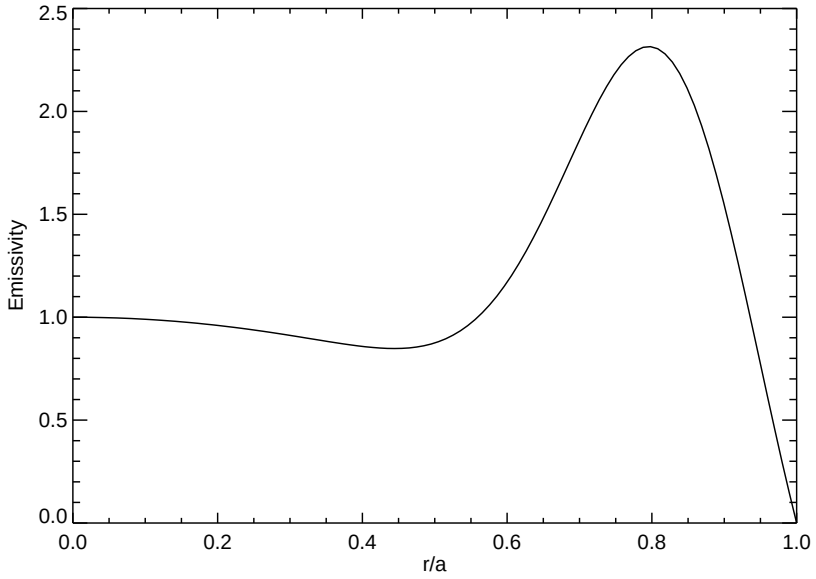

(b)

Figure 3-22: Peaked (a) and hollow (b) $\varepsilon_o(r/a)$ emissivity profiles used to test 2-D inversion code

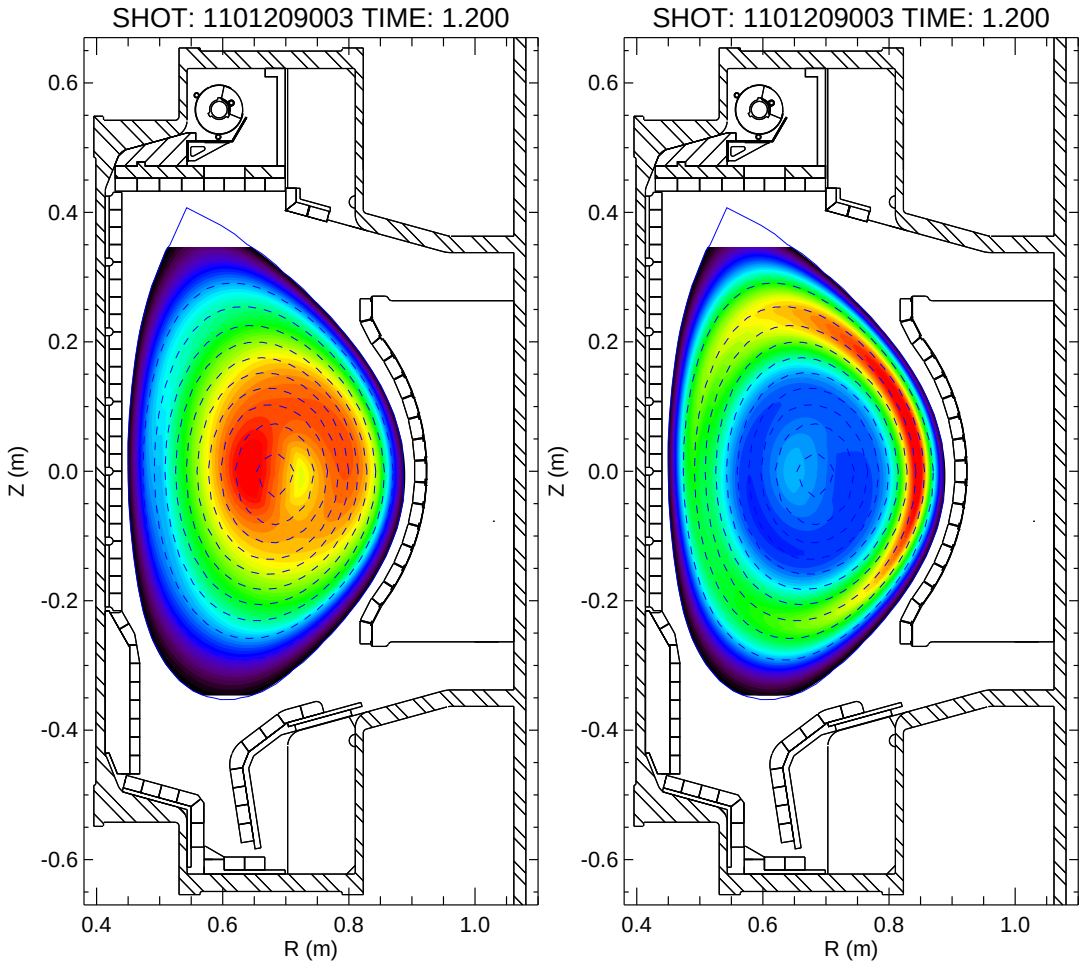

(a) (b)

Figure 3-23: 2-D emissivity contour plots for peaked (a) and hollow (b) profiles with specified up/down and in/out asymmetries

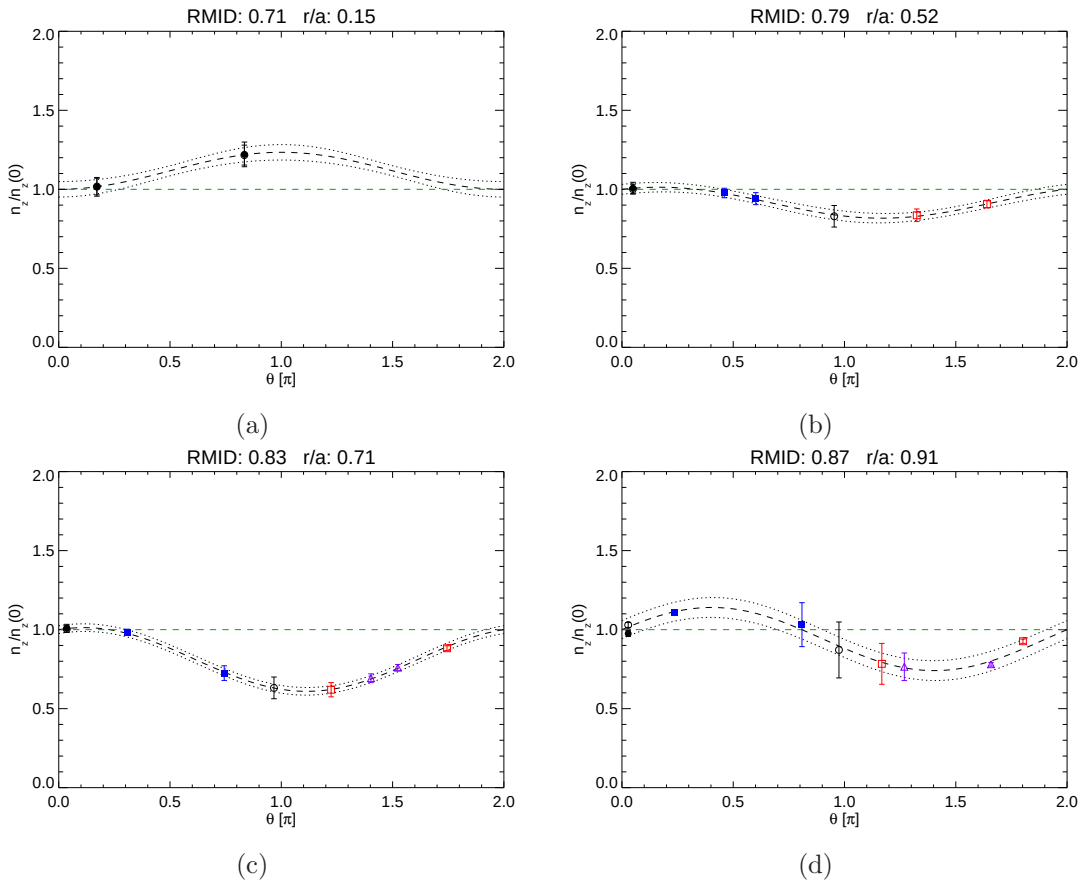

Figure 3-24: Plots of test emissivities and fit poloidal variation at various r/a using KLIM and wall box arrays; AXA (●), AXJ (○),WB2AX (■), WB3AX (□) and WB4AX (△)

radii (3-24d), the uncertainties in the data for $0.5 < \theta/\pi < 1.5$ become large due to propagation of error through the Abel inversion, and a slight difference in the AXA and AXJ data at $\theta \sim 0$ is apparent.

Figure 3-25 shows the reconstruction of the $\varepsilon_s/\varepsilon_o$ and $\varepsilon_c/\varepsilon_o$ profiles (EXP-black), demonstrating good agreement to the defined profiles (THEORY-green), independent of the peaked or hollow nature of the $m = 0$ profile. This is consistent with results from Section 3.1.4 that showed for relatively broad radial features, the diagnostics can accurately reconstruct the 2-D emissivity profile. Looking closer at the two up/down asymmetry profiles, there are noticeable discontinuities for the hollow emissivity case that are less pronounced or absent for the peaked emissivity reconstruction. When new wall box data is first included at $r/a = 0.52$ (WB2 added) and $r/a = 0.71$ (WB4

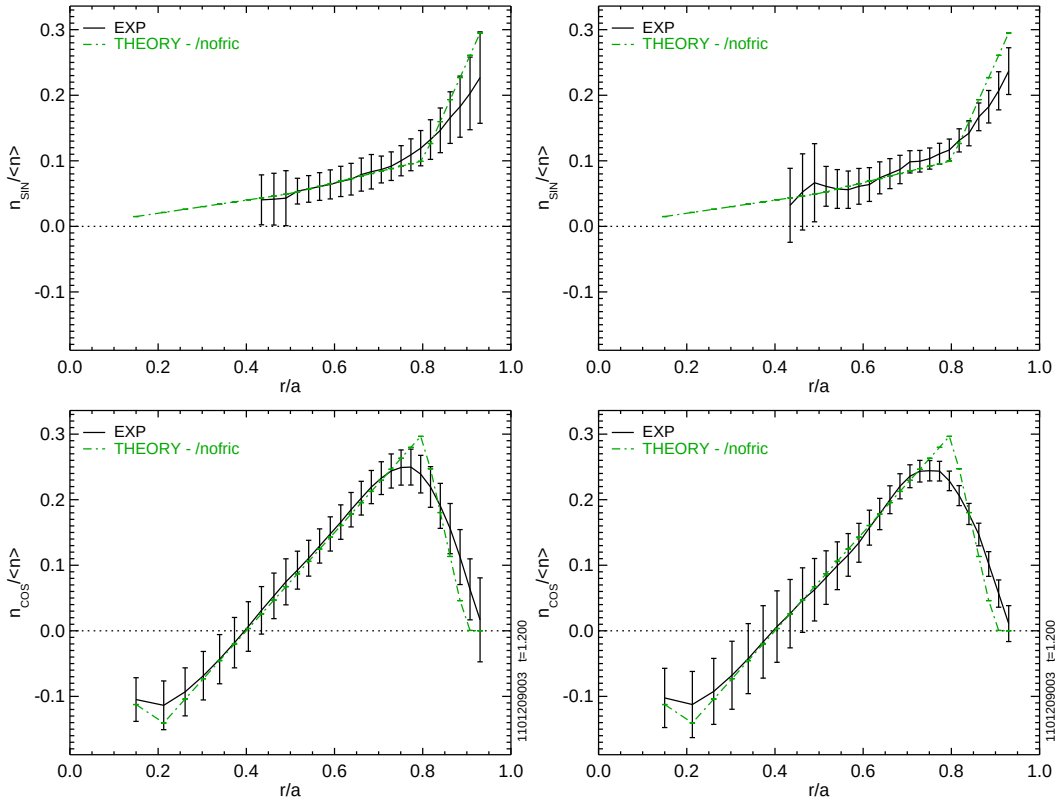

(a) (b)

Figure 3-25: Comparison of defined (dashed green - labeled theory) and reconstructed (solid black) asymmetry profiles for the peaked (a) and hollow (b) radial profiles

added), there is a noticeable break in slope. In contrast, the in/out asymmetry profiles change smoothly with respect to minor radius. Sharp changes at r/a =0.20 and 0.75 are not captured, but such features are unlikely to be present in experiments.

This analysis technique is applied to the EDA H-mode shot shown in 3-14, also analyzed using the method in Section 3.6.1. The AXA, AXJ, WB2AX, WB3AX and WB4AX are all used to find the $m = 1$ profiles, and in Figure 3-26, measured and fit profiles of $n_z(\theta)/n_z(0)$ are shown in at several minor radii. At mid-radius, 3-26a and 3-26b show that the strong in/out asymmetry seen by the AXJ array is also seen by the wall box arrays. Moving farther out, at $r/a = 0.8$ in 3-26c, AXJ starts to become an outlier with the wall boxes showing a smaller in/out asymmetry. This disagreement increases at $r/a = 0.9$, shown in 3-26c, and despite small error bars on the emissivity, no apparent low-order Fourier-type variation is evident. The fit $m = 1$ profiles are shown in Figure 3-27, and while a large in/out asymmetry is observed, a

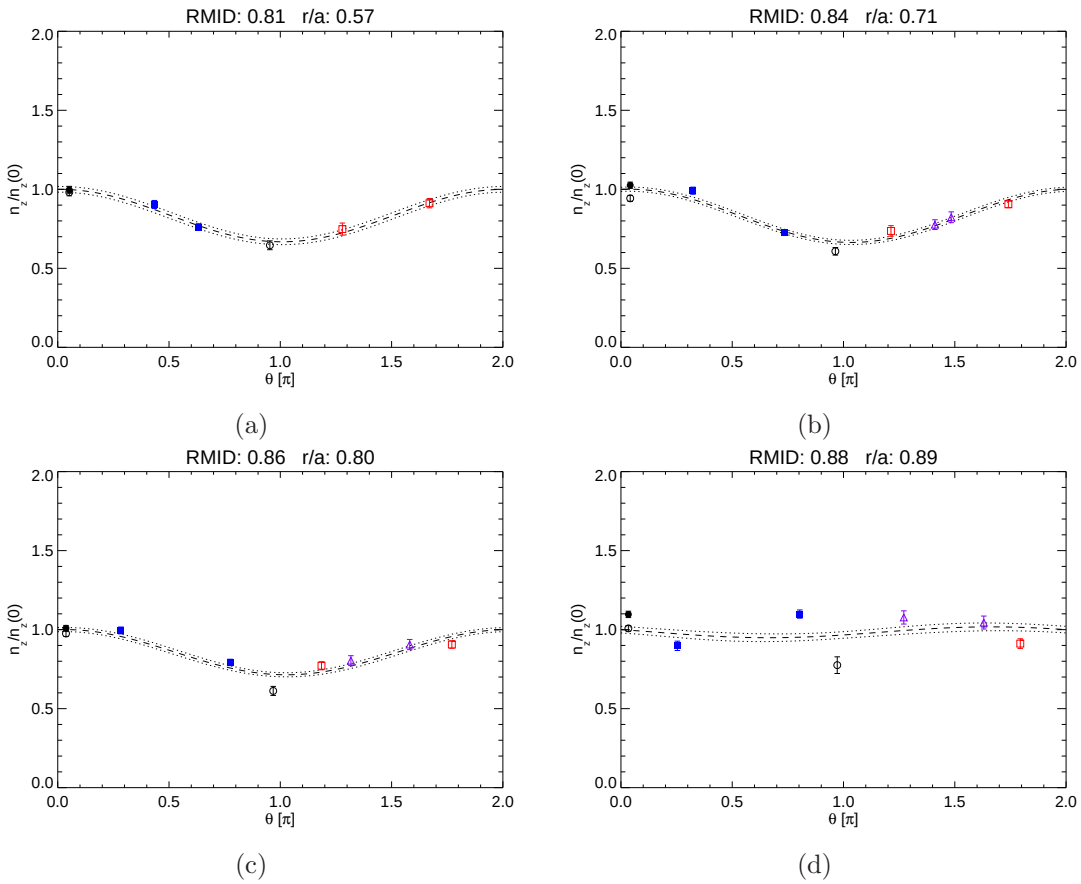

Figure 3-26: Plots of measured emissivities and fits of poloidal variation at various r/a; AXA (•), AXJ (○),WB2AX (■), WB3AX (□) and WB4AX (△)

much smaller up/down asymmetry is calculated.

In Figure 3-28, the output of the 2-D reconstruction is compared with the results using only AXJ, plotted in 3-21. For $r/a < 0.45$ only AXA and AXJ data are constraining the fit and the good agreement is not surprising. Between $0.45 < r/a <$0.7, WB2AX and WB3AX are also included, and both techniques find the same asymmetry within error bars. For $r/a > 0.7$, WB4AX is added, and the two techniques begin to disagree. But as plots in 3-26 showed, this is a disagreement between all the wall boxes and the AXJ data, and so for large minor radii r/a above 0.80-0.85, better asymmetry profiles can be found by removing AXJ.

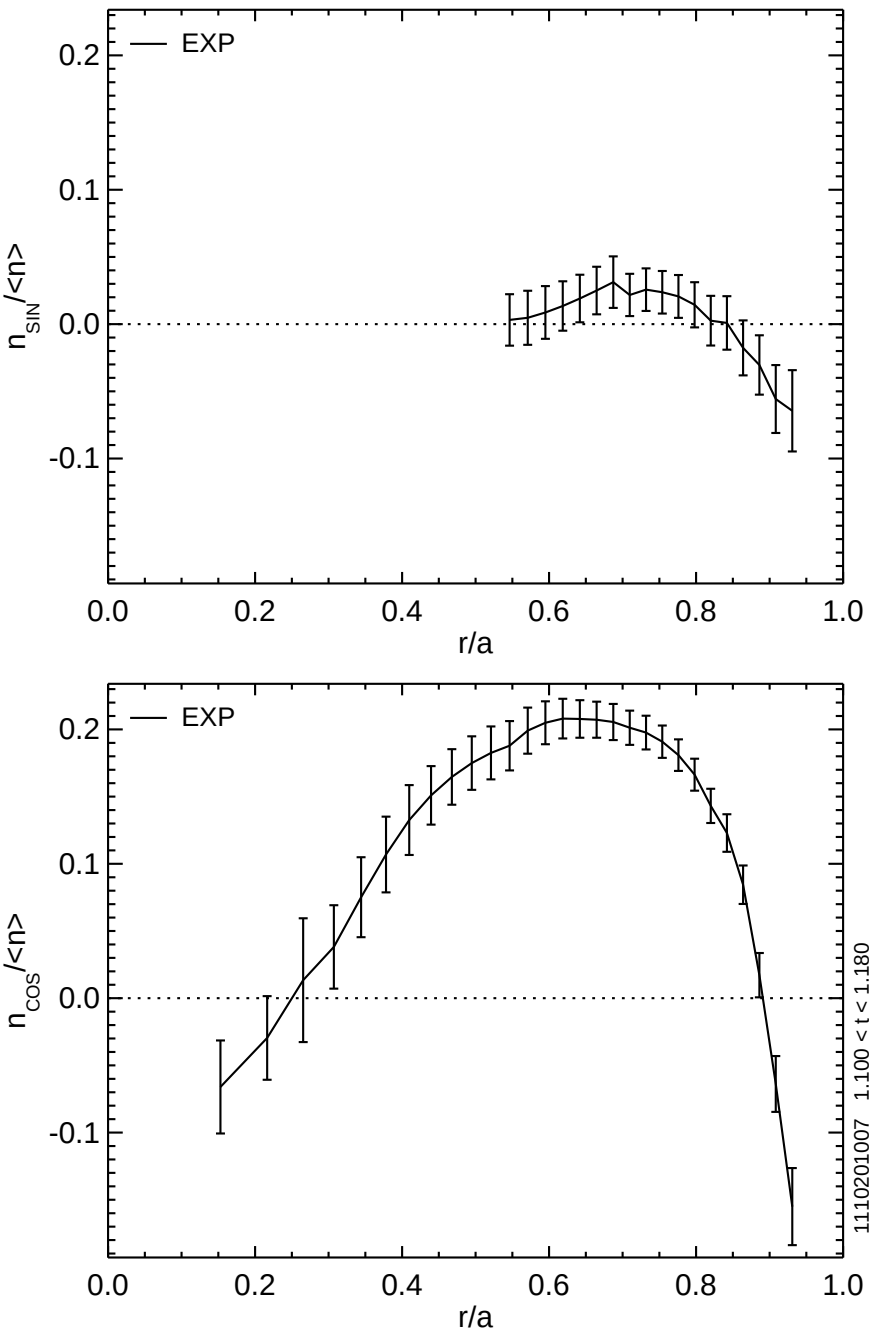

Figure 3-27: Up/down (top) and in/out (bottom) asymmetry profiles found from an EDA H-mode using the technique described in Section 3.6.2

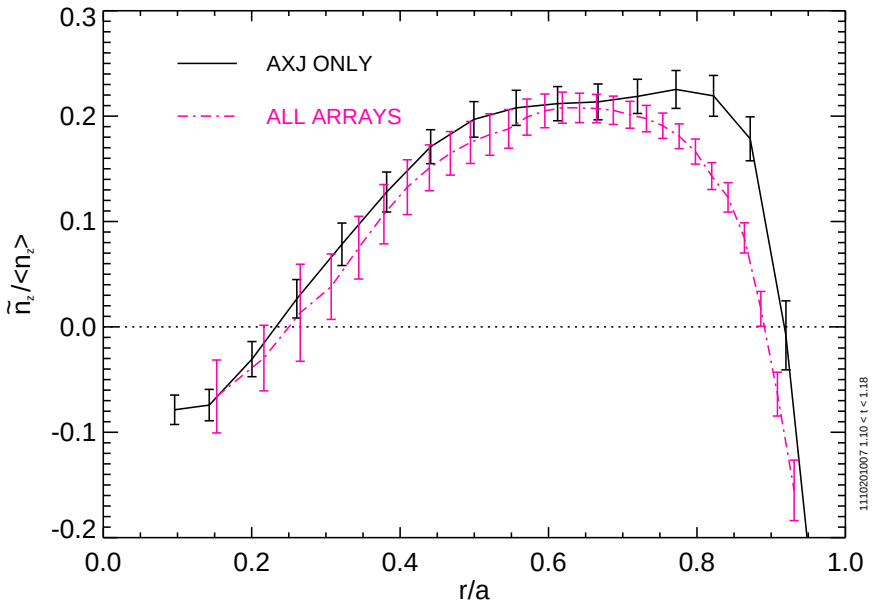

Figure 3-28: Comparison of methods to find the in/out asymmetry from AXUV measurements

3.7 Summary

This chapter discussed the design and calibration of set of diagnostic tools for measuring the poloidal variation of impurity density, as well as those necessary to compare such results to parallel impurity transport theory. Using the GENPOS codes, test brightness profiles were calculated, taking into account the finite resolution of the pinhole cameras, and the inversion tools demonstrated an ability to accurately reconstruct 1-D (Section 3.1.4) and 2-D (Section 3.6) emissivity profiles. Example diagnostic data demonstrate that both symmetric and asymmetric emissivity profiles have been observed in C-Mod. Additionally, in/out asymmetries with LFS and HFS accumulation have both been shown, foreshadowing the variety of forces will be explored in the next three chapters.

Chapter 4

Asymmetry Driven by Centrifugal Force

The most widely known cause of poloidal variation of impurity density is centrifugal force due to toroidal rotation. On the JET and ASDEX-U tokamaks, it has been shown to be responsible for observed enhancement of soft x-ray emission on the outboard side of a flux surface. These experiments utilized heating from neutral beams which also applies torque, driving toroidal rotation to speeds of up to 600 km/s on axis. Although there is no input of external momentum in the C-Mod plasmas explored in this research, so-called intrinsic rotation has been routinely observed, and speeds of H-like Ar have been measured up to $\sim$100 km/s. While the origin of this flow is not completely understood, the effect is easily reproducible and changes in rotation from Ohmic to both H-mode [129] and I-mode [130] are well characterized, allowing experiments that vary Mach number to be designed and executed.

In this chapter, the in/out asymmetry will be explored in Ohmic and ICRF-heated C-Mod plasmas over a range of densities, temperatures and currents. It will be demonstrated that the centrifugal force plays a primary, but by no means exclusive role in determining the in/out asymmetry of molybdenum density on Alcator C-Mod. While Chapter 5 will go on to show how some of these discrepancies can be explained by poloidal electric fields due to ion cyclotron heating, the large amount of data presented here is required to challenge the conventional wisdom that in/out

asymmetries of high-Z impurities are simply due to inertial effects. In Section 4.1, asymmetry measurements are explored, qualitatively highlighting the range of observations on C-Mod. In section 4.2 a detailed comparison between measurement and modeling is completed for an example Ohmic plasma and trends in the entire data set are analyzed. This is repeated for EDA H-modes and I/L-modes in Sections 4.3 and 4.4, respectively.

4.1 Demonstration of the In/Out Asymmetry

A collection of plasmas is analyzed in detail to examine trends in impurity asymmetries. This data set consists of 10 Ohmic plasmas with Mo LBO injection (1110204), 7 Enhanced D-Alpha (EDA) H-modes (1110201) and 7 L/I-mode plasmas (1101209), all with B_t in the forward field direction (ion B$\times\nabla$B drift pointing down). The specific H-mode and L/I-mode plasmas were chosen to avoid shots with neon or nitrogen seeding, which has recently seen widespread use in rf-heated C-Mod plasmas.

In Section 3.6, two techniques for finding the in/out asymmetry were discussed, one using only the midplane AXUV diode array, AXJ, the other incorporating additional data from the wall boxes to find the $m = 1$ in/out ($n_{z,cos}$) and up/down ($n_{z,sin}$) variations in $n_z/\langle n_z \rangle$. In Figure 4-1, the in/out asymmetries calculated from these two techniques are compared, demonstrating good agreement, with the AXJ-only method predicting marginally enhanced outboard accumulation. When a choice is available, the asymmetry derived from both the KLIM and wall box arrays will be the preferred method since it incorporates the most diagnostic information. Already, it is obvious that centrifugal effects cannot be completely responsible for parallel impurity transport on C-Mod since significant high-field accumulation, $n_{z,cos}/\langle n_z \rangle < 0$, is regularly observed by both methods.

The inclusion of the wall box data also allows the up/down asymmetry to be captured for $r/a > 0.5$. The character of the 2-D radiation asymmetry can be seen by examining scatter plots of $n_{z,cos}/\langle n_z \rangle$ versus $n_{z,sin}/\langle n_z \rangle$ shown in Figure 4-2. In Ohmic plasmas, 4-2a, the plasma is nominally symmetric within large error bars.

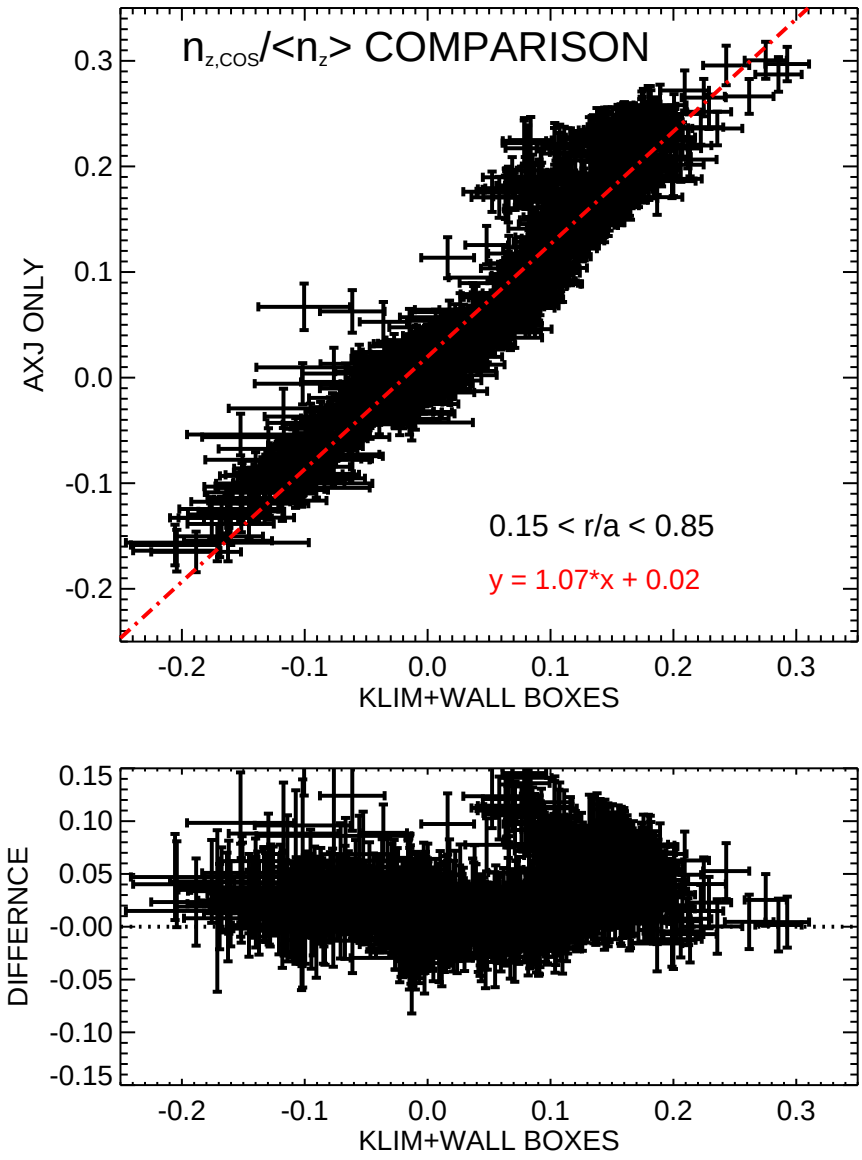

Figure 4-1: Comparison of the in/out asymmetry, $n_{z,cos}/\langle n_z \rangle$, calculated using all AXUV arrays (x-axis) and only the midplane AXJ array (y-axis)

For rf-heated plasmas, both EDA H-modes, 4-2b, and L/I-modes, 4-2c, a systematic outboard impurity accumulation is observed. This stands in contrast to Figure 4-1 which showed $-0.2 < n_{z,cos}/\langle n_z \rangle < 0.3$, indicating that inboard accumulation is localized to the inner half of the plasma. In all plasmas analyzed, an up/down asymmetry between $-0.05 < n_{z,sin}/\langle n_z \rangle < 0.10$ is seen, the details of which will be explored in Chapter 6.

For quantitative comparisons to theory, x-ray crystal spectroscopy is used to measure velocity and temperature profiles to find the radial variation of the Mach number. Even without that information, the order of magnitude of the measured asymmetries can be shown to be consistent with historical 0-D rotation measurements on C-Mod.

In an Ohmic plasma, molybdenum was injected into the plasma, and the asymmetry determined during the decay phase, as explained in further detail in Section 4.2. Figure 4-3 shows the midplane emissivity profiles, demonstrating good agreement between AXA and AXJ and the presence of a small low field side abundance. The $\tilde{n}_z/\langle n_z \rangle$ calculated from the AXJ data is shown in Figure 4-4 along with a simple estimate of the in/out asymmetry in the trace impurity limit with no ion-impurity friction (see Section 2.2.1), $n_{cos}/\langle n_z \rangle = 2\epsilon M_0^2$. For $T_i = T_e$, $M_0^2 \sim 2/3 m_z v_\phi^2 / 2T_i$, and the small Mo asymmetry, $0.1 < n_{cos}/\langle n_z \rangle < 0.2$, is consistent with $|v_\phi| < 20$ km/s routinely observed in C-Mod Ohmic plasmas [131].

For an EDA H-mode plasma, the in/out asymmetry is calculated from the steady-state emissivity profile which can be shown to be dominated by molybdenum. Figure 4-5 shows the midplane emissivity profiles, clearly demonstrating enhanced radiation on the outboard side, indicating a region of impurity accumulation. Figure 4-6 displays the $\tilde{n}_z/\langle n_z \rangle$ profile where for the outer half of the plasma this variation becomes of order the inverse aspect ratio, $\sim 1/3$. This level of asymmetry is consistent with M_o^2 between 0.50 and 0.75, indicating a core rotation of 60-75 km/s, in reasonable agreement with historical observations. For this shot, the sawtooth precursor oscillation is clearly visible on the magnetics at approximately 16 kHz, indicating a toroidal rotation speed of $\sim$70 km/s, assuming an $n = 1$ mode. Inside $r/a \sim 0.4$ the asymmetry drops faster than ϵ, inconsistent with modeling based only on the centrifugal force.

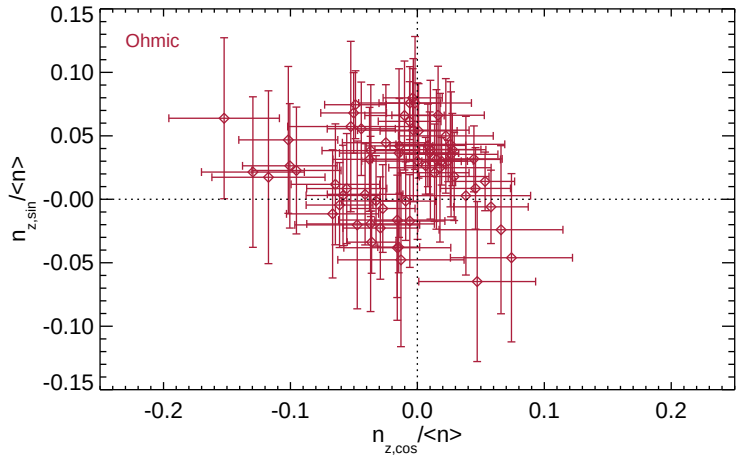

(a)

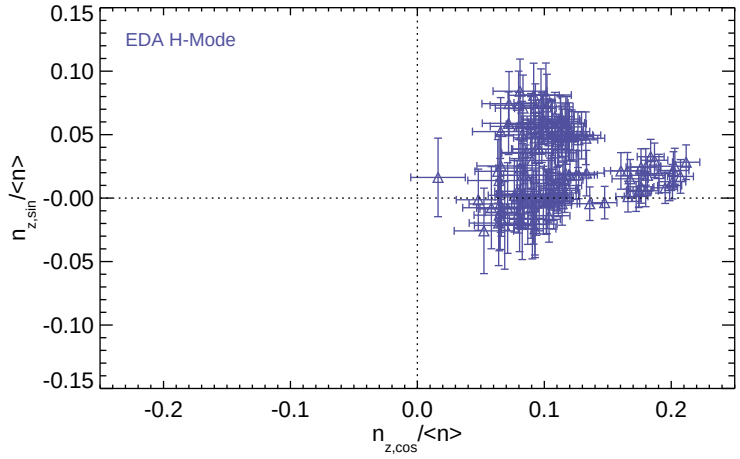

(b)

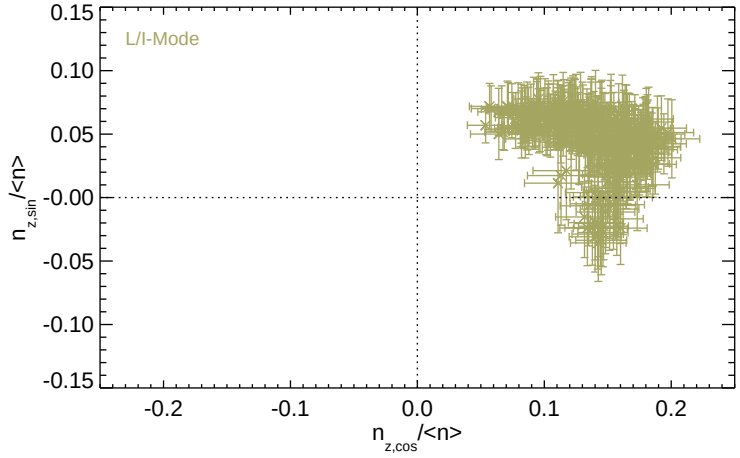

(c)

Figure 4-2: Plots of measured up/down ($n_{z,sin}$) and in/out ($n_{z,cos}$) asymmetries found for $r/a > 0.5$ in Ohmic (a), EDA H-mode (b) and L/I-Mode (c)

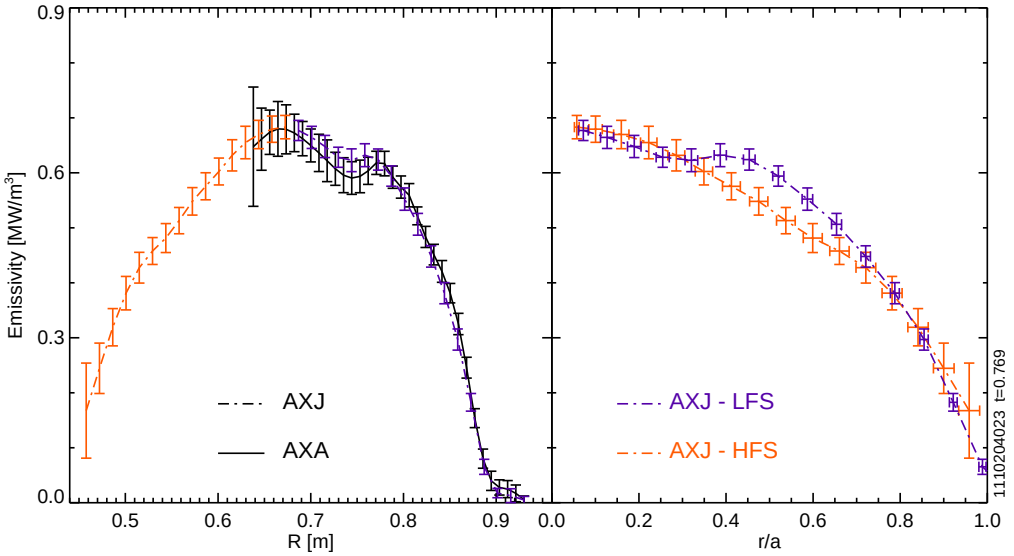

Figure 4-3: Measured midplane emissivity profiles during a Mo LBO injection into an Ohmic plasma, showing a small in/out asymmetry

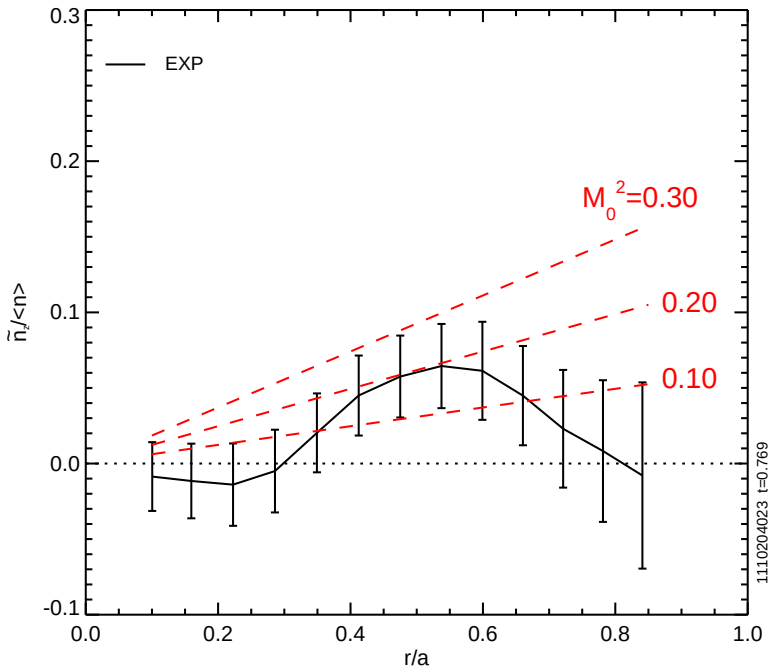

Figure 4-4: In/out asymmetry calculated from the Ohmic data (black) in Figure 4-3 shown to be consistent with low impurity toroidal rotation (dashed red)

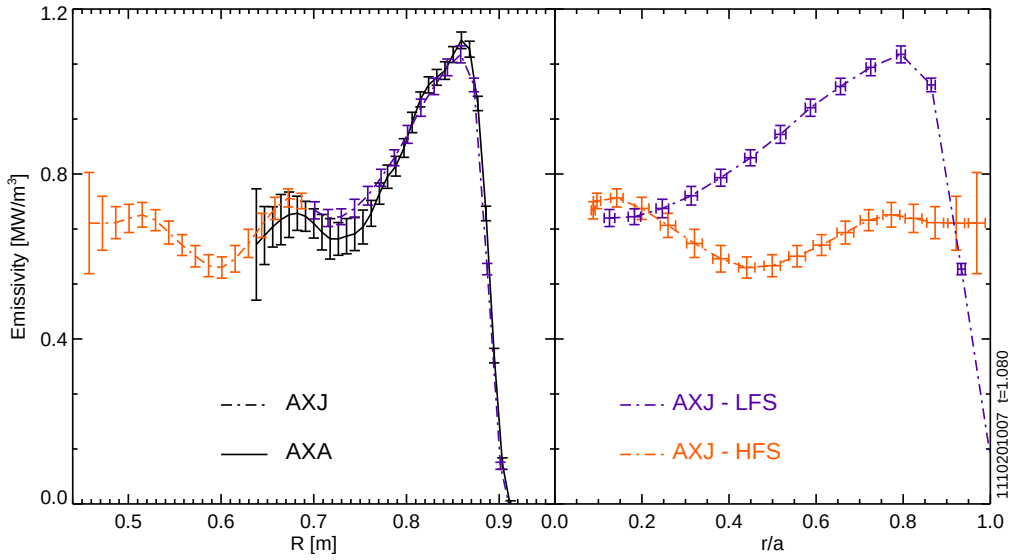

Figure 4-5: Measured steady-state midplane emissivity profiles during an EDA H-mode plasma showing a large in/out asymmetry

Inside of $r/a \sim 0.2$ the asymmetry reverses direction, which according to present theories [24] should only be possible for strong ion-impurity friction.

In the next three sections, the Ohmic, EDA H-mode and L/I-mode data displayed in Figures 4-1 and 4-2 are compared with centrifugal force impurity transport modeling using experimental profile and equilibrium data.

4.2 Ohmic Plasmas

The first set of experiments demonstrates that in cases of small toroidal rotation, $\omega \leq 5$ kHz, the impurity density has a small asymmetry, $\tilde{n}_z/\langle n_z \rangle < 0.1$, in reasonable agreement with parallel transport modeling including only inertial forces. For plasmas with a range of currents, toroidal fields and electron densities, molybdenum is introduced via laser blow-off into Ohmically-heated plasmas, also seeded with a small amount of argon to enable the measurement of rotation and ion temperature profiles. The LBO presents a transient, toroidally localized particle source at the plasma edge and a few milliseconds are required to allow for the radiation source to recover axisymmetry and establish equilibrium within a flux surface. As shown in

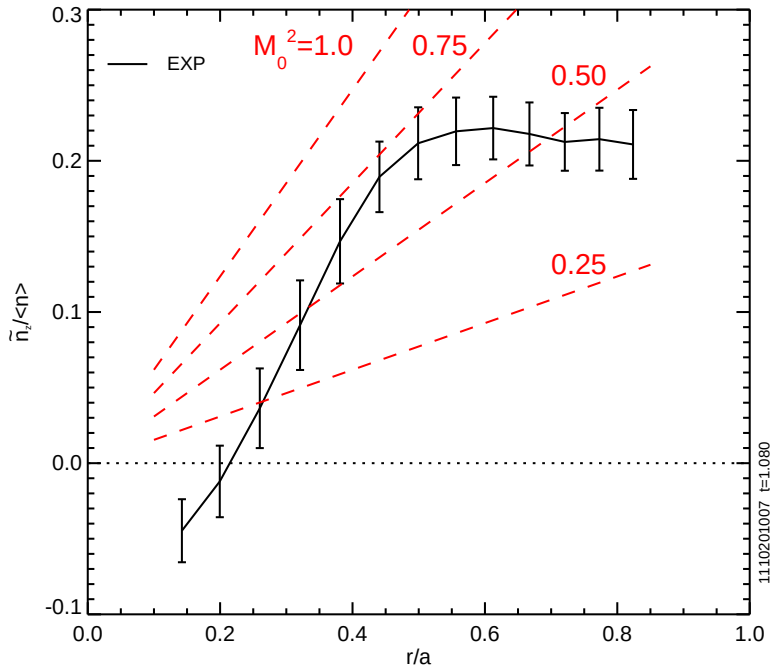

Figure 4-6: In/out asymmetry calculated from the H-mode data (black) shown in Figure 4-5 shown to be consistent with large impurity flow (dashed red)

earlier Figure 3-8, the AXA views terminate near B-port, the location of the LBO system, and can see the injection enter the plasma while AXJ view away from this region. By comparing the brightness between AXA and AXJ for chords with the same tangency radius, shown in Figure 4-7, this transient period can be identified and avoided. An even longer time is used in practice and the asymmetry is calculated during the decay phase of the injection, shown in the highlighted portion. In this time period, the radial profile of the emission does not change shape in contrast to the accumulating stage. The emissivity prior to the injection is not subtracted off before characterizing the asymmetry since there is no steady-state profile, due to the presence of sawteeth.

In Figure 4-8, the time evolving in/out asymmetry at two minor radii (f) are plotted over the time surrounding the injection at $t = 1.15$ seconds. In this shot, there is no ICRF power (a) and the density (b) and temperature (c) remain constant. Molybdenum is introduced via LBO, and an increase is seen in both the Na-like (Mo XXXII) line-brightness (e) and the radiated power calculated by voluming integrating

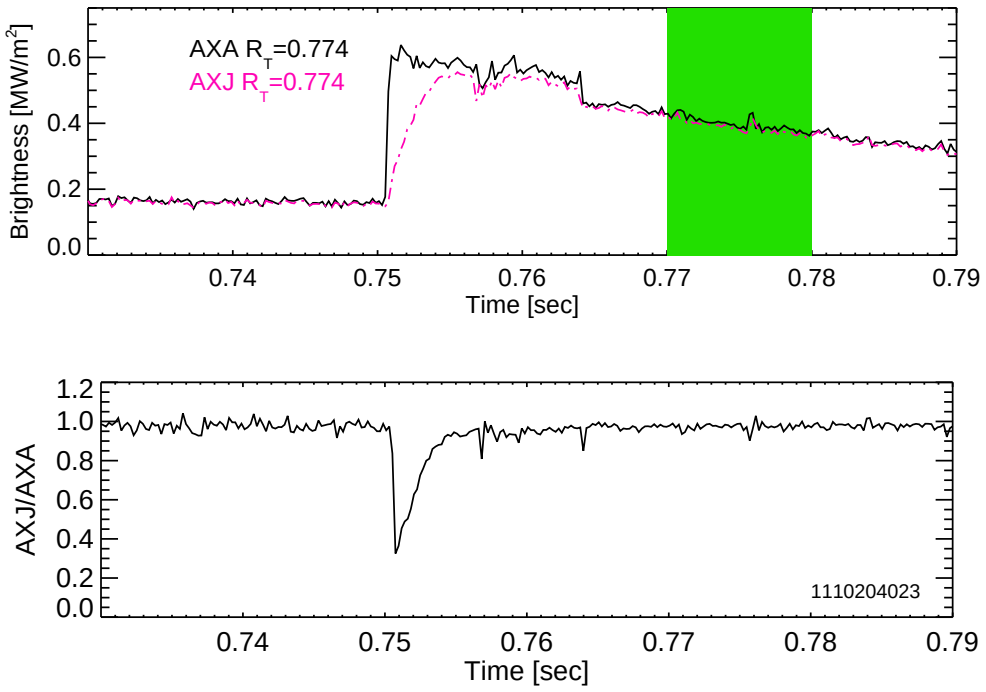

Figure 4-7: Comparison of AXA and AXJ chords at the same tangency radius after a Mo injection, showing timescale to establish parallel equilibrium

the AXA-based emissivity profile (d). Large changes in the in/out asymmetry are observed from $1.15 < t < 1.16$ when the radiation is toroidally asymmetric, and the radial profile is still hollow as the molybdenum density works its way into the core. There is a small, yet noticeable difference in the asymmetry prior to the injection, $t = 1.14$, and just after the injection, $t = 1.17$, that is assumed to be due the increase in the fraction of radiation due to molybdenum. Over $1.17 < t < 1.23$, the measured asymmetry decays slowly towards its pre-injection level as the molybdenum density drops on an impurity confinement time. Such changes are consistent with the smaller fractional increase in $P_{RAD,D}$ relative to the Mo XXXII line brightness, but is not significant relative to the error bars or modification in the core asymmetry across the sawtooth crash. While the LBO moves the radiation towards being dominated by molybdenum, it is likely that only 60-70% is due to Mo. But, this makes little difference in the interpretation since even after applying the correction discussed in Section 3.6.1, the result would remain within error bars. For simplicity, subsequent

Ohmic data are not corrected for a molybdenum fraction that is <100%.

4.2.1 Comparison to Theory

The in/out asymmetry driven by the centrifugal force is sensitive to the electron and ion temperature, as well as the toroidal rotation. Figure 4-9 shows the ion temperature (b) and toroidal rotation (c) profiles averaged over 120 ms, several sawtooth cycles for the 1.4 MA, 7.5 T plasma. Electron temperature (b) and density profiles (a) are taken near the peak of a sawtooth just prior to the Mo injection at 1.15 seconds. The parallel and perpendicular timescales discussed in Section 2.2.6 are shown in Figure 4-9d. The ion-impurity coupling timescale, τ_{zi} (2.6)(dotted line), is the shortest, indicating good collisional coupling between the ions and the impurities. The parallel diffusion timescale, $\tau_{\|,D}$ (2.34)(dashed line), is much shorter then all cross-field time scales out to $r/a \sim 0.9$, verifying that the approach in Chapter 2.2 of separated radial and parallel transport is valid. The neoclassical perpendicular time scales (solid lines) differ greatly ranging from the neoclassical diffusion time, $\tau_{\perp,D}$ (2.35), on order of the length of a C-Mod shot, to the time for cross-field drift, $\tau_{\perp,dr}$ (2.36), being from 1-10 ms. Here, as in subsequent plots, the anomalous timescales (dash-dot) are calculated assuming an impurity diffusivity of 1.0 m^2/s (2.37) and a convective velocity of 10 m/s (2.38), both on the order of empirical measurements [28]. All $L_\perp$ are calculated from the ion pressure profile.

The data from the midplane AXA and AXJ arrays are plotted in Figure 4-10 showing good agreement between the two measured brightness profiles (a) and a broad emissive feature (b) during the Mo injection. When mapped to minor radius (c), the high-field side and low-field side AXJ profiles overlap, indicating little in/out asymmetry. Including data from the wall box arrays, the up/down ($n_{sin}/\langle n_z \rangle$) and in/out ($n_{cos}/\langle n_z \rangle$) asymmetry profiles are calculated as described in Section 3.6.2 and plotted in Figure 4-11 (black solid). Here, as in the rest of Chapter 4 and Chapter 5, the $n_{sin}/\langle n_z \rangle$ profile is included for completeness despite the focus being on understanding the $n_{cos}/\langle n_z \rangle$ data. Also included are the asymmetries predicted by parallel neoclassical transport theory [24] (green dash-dot) ignoring ion-impurity

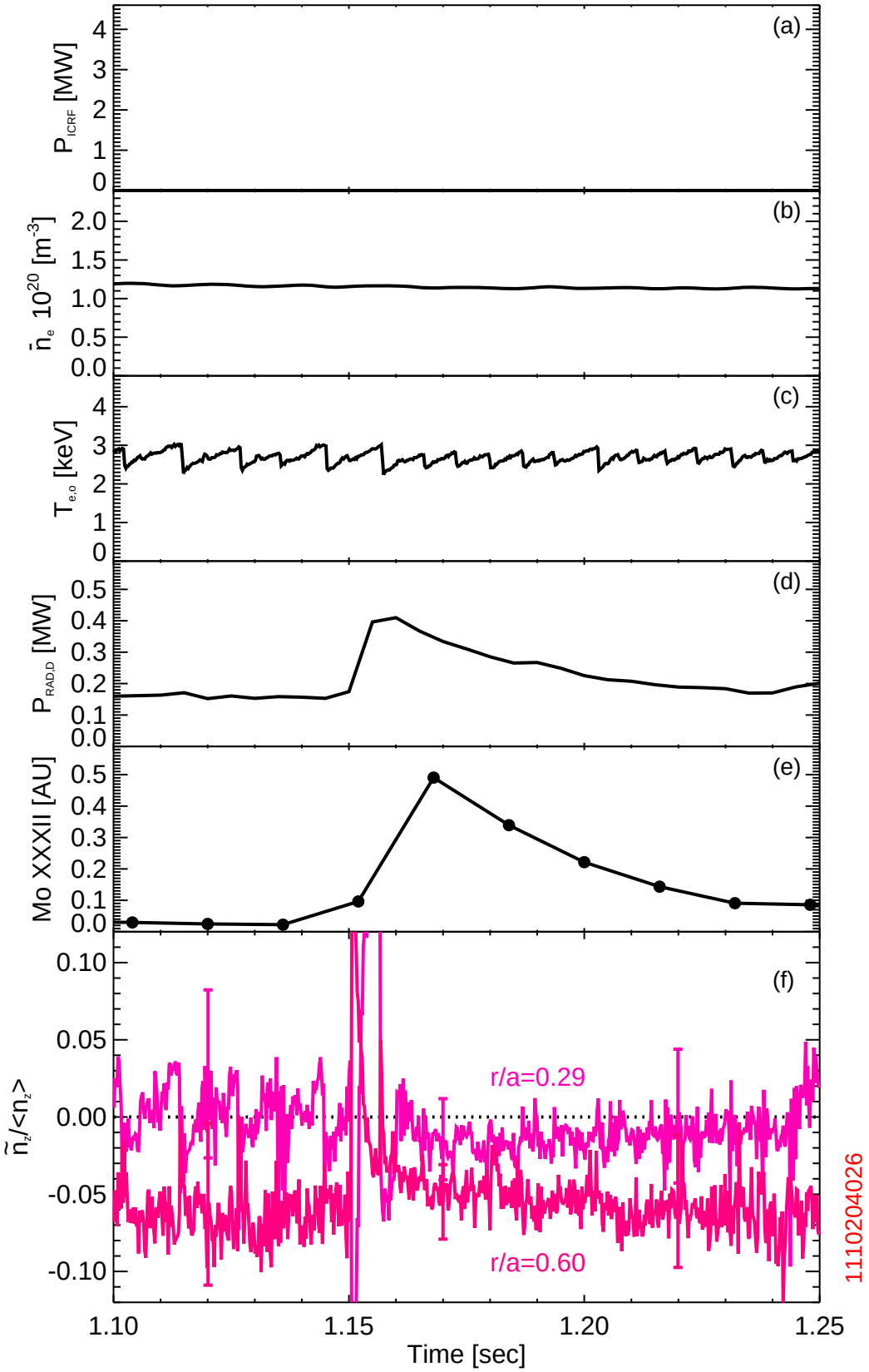

Figure 4-8: The time-evolving in/out asymmetry in an Ohmic plasmas over a Mo LBO injection

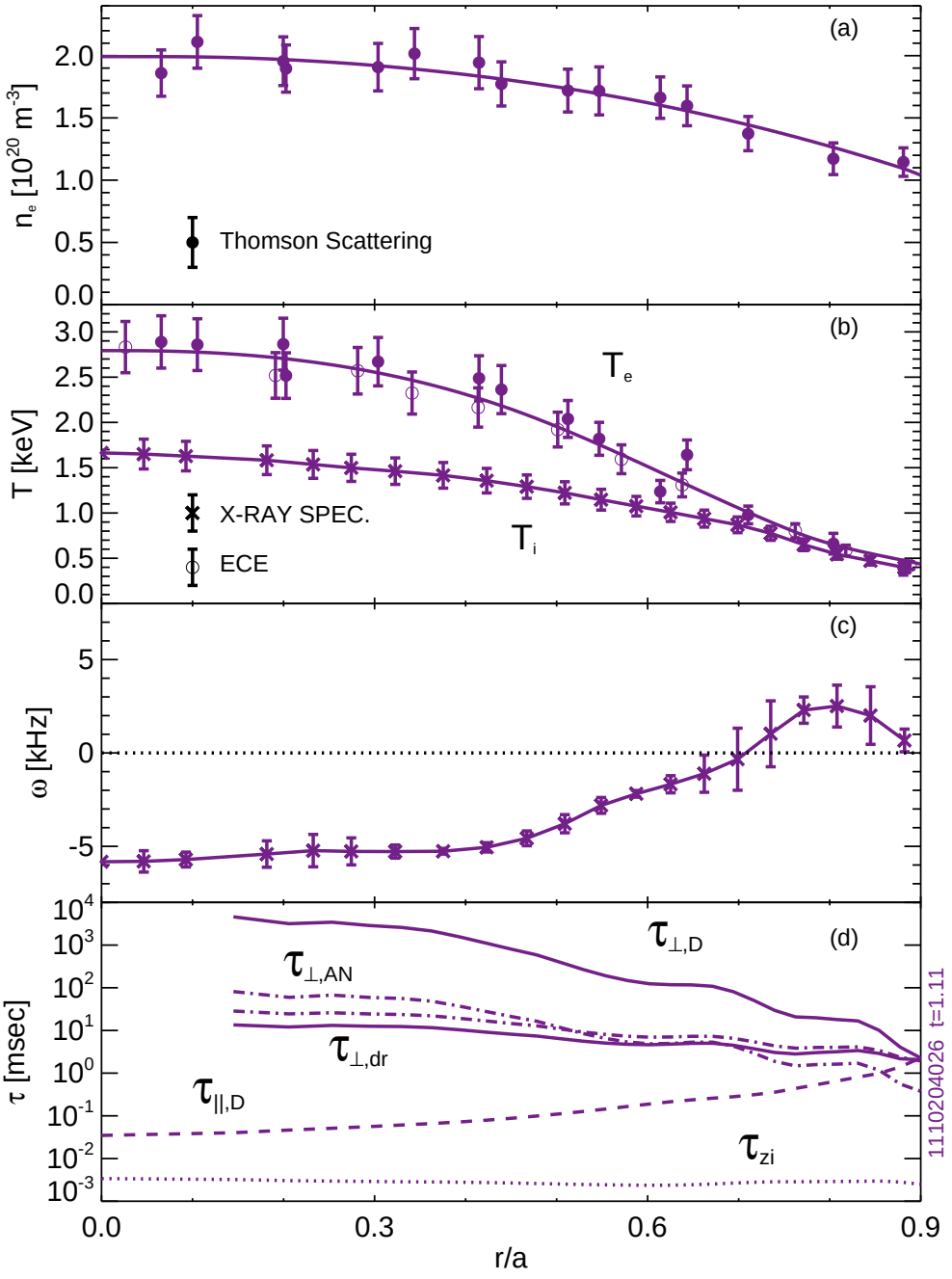

Figure 4-9: Radial electron density (a) ion and electron temperature (b) and rotation profiles (c) in an Ohmic plasma with relevant parallel and perpendicular time scales (d)

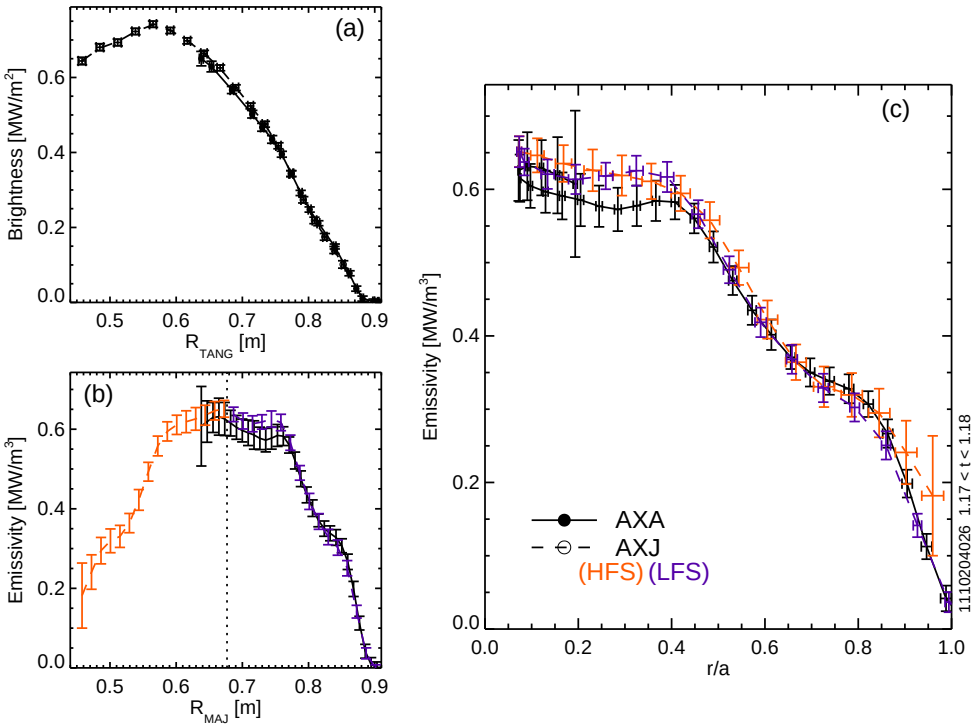

Figure 4-10: Example midplane AXUV diode profiles demonstrating the near symmetry of the radiation profile during a Mo LBO injection into an Ohmic plasma

friction, hence the absence of any predicted up/down asymmetry. It is worth noting that the shape of the measured and predicted asymmetries are very similar, yet are vertically offset from each other by ∼0.03. Although the two disagree outside the estimated error bars, both predict a small absolute magnitude of $n_{cos}/\langle n_z \rangle$.

This analysis procedure was repeated for all 9 laser blow off shots, and Figure 4-12 shows the comparison between measurement and modeling taken at 0.05 intervals in minor radius from $0.15 < r/a < 0.75$. The distribution of the data is more elongated vertically, indicating a wider variation of observed asymmetries than expected from inertial effects. A collection of measurements with $n_{cos}/\langle n_z \rangle < 0$ are found which cannot be explained by the centrifugal force. Regardless, no significant, systematic discrepancy between measurement and theory is observed.

4.3 ICRF Heated EDA H-Mode Plasmas

In Alcator C-Mod, the most commonly explored high-confinement regime [132] is the Enhanced D-Alpha or EDA H-mode [133]. Steady state is typically maintained for the duration of auxiliary heating, and the edge transport barrier is continually regulated via the quasi-coherent mode [134], in contrast to discrete edge localized modes (ELMs). While C-Mod is capable of running the so-called ELMy H-mode, the high-confinement regime common to most tokamaks, the operating space is severely limited in C-Mod [135]. The ELM-free H-mode can also be investigated, but the transient nature of the rotation and temperature profiles is difficult to capture with the HIREXSR diagnostic. On 1110201, a series of EDA H-mode plasmas was run to obtain detailed pedestal and core profiles for transport modeling. Plasma current and density were scanned shot-to-shot and a diagnostic level of argon was added to allow for core rotation and ion temperature profiles.

In Figure 4-13, the same time-evolving plots as shown in Figure 4-8 are shown for an EDA H-mode with a natural molybdenum injection at $t \simeq 1.08$. In this plasma, the steady-state Mo level is already high, typical of all shots used from 1110201. The injection increases the Mo XXXII line brightness (e) by nearly 50%, with the

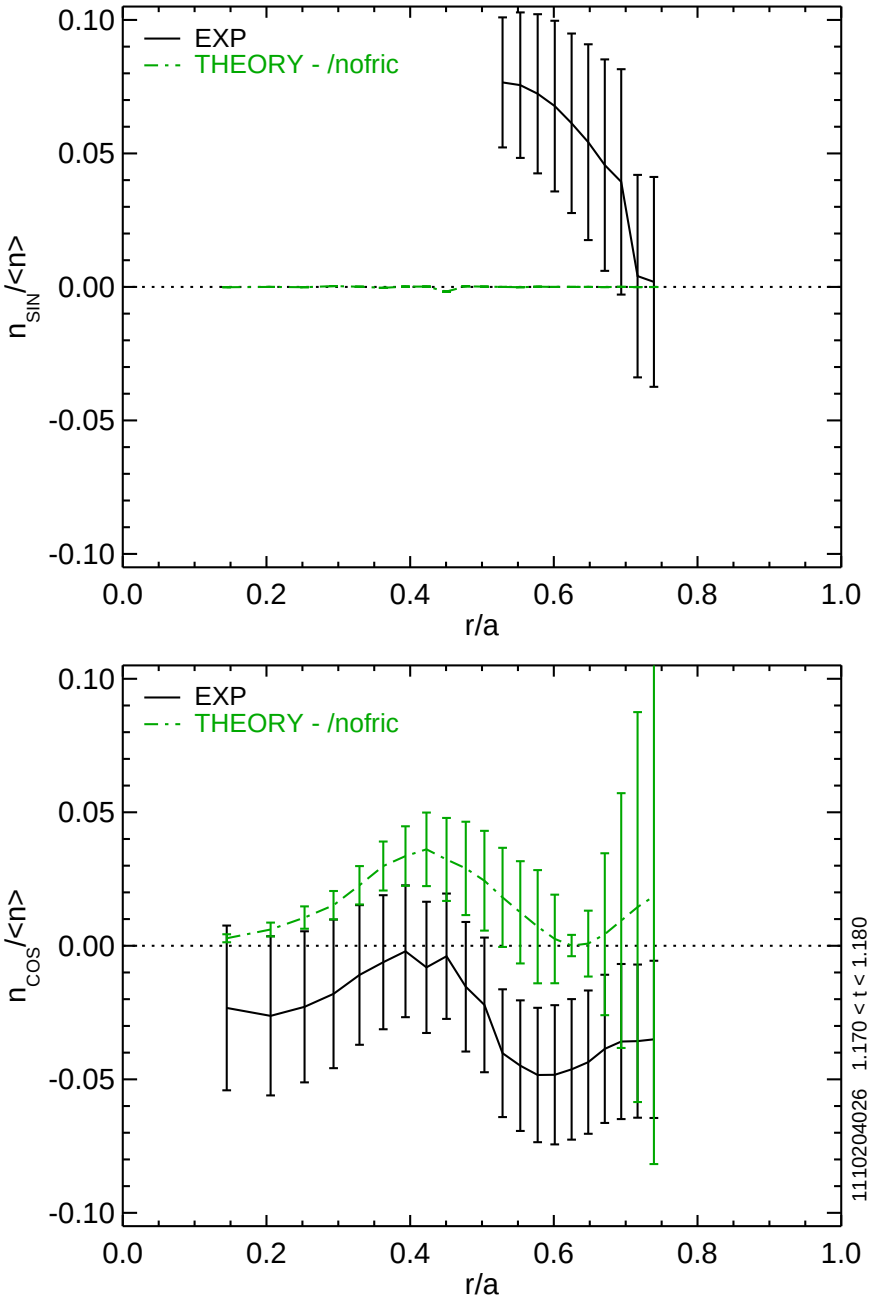

Figure 4-11: Comparison of measured (solid green) and modeled (broken black) radial asymmetry profiles for an Ohmic discharge, both showing small asymmetries

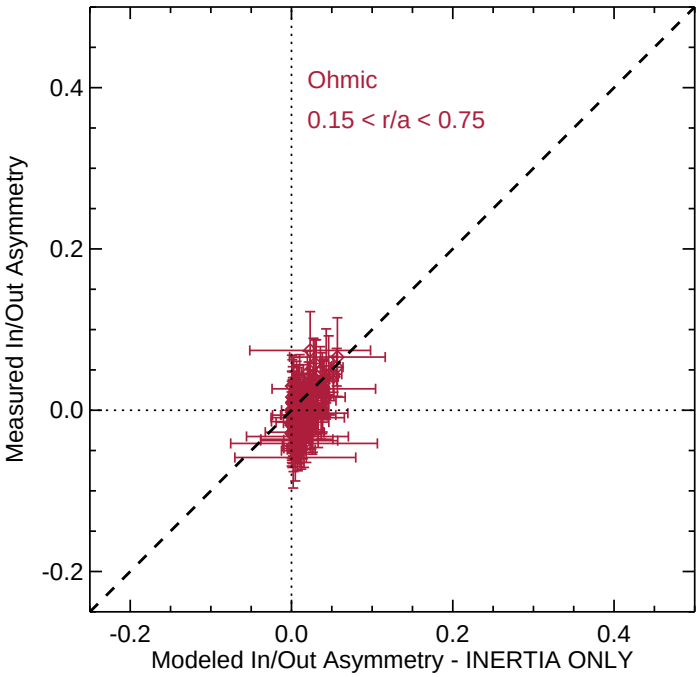

Figure 4-12: Comparison of measured in/out asymmetries to modeling using only inertia for Mo injections into Ohmic plasmas

increase in $P_{RAD,D}$ slightly lower (d). A prompt change in the asymmetry (f) on the ~10 ms timescale is once again observed. When comparing $t = 1.07$ and $t = 1.10$, the increase in molybdenum due to the injection does not change the asymmetry outside of error bars. A larger change is seen as the ICRF power (a) increases over $1.10 < t < 1.11$ seconds. Note the other abrupt changes in the core asymmetry at 1.05 and 1.12 seconds are correlated with incomplete sawtooth crashes as seen on the ECE temperature trace (c). This analysis indicates that the steady-state radiation asymmetries are already strongly dominated by molybdenum, and that corrections due to <100% Mo radiation are smaller then stated uncertainties. Thus, steady-state radiation profiles are used for EDA H-modes analysis.

4.3.1 Comparison to Theory

As in Section 4.2.1, detailed examples are shown before trends in the entire data set are analyzed. Two shots are examined, one which demonstrates reasonable agreement with modeling (1110201017) and another for which significant disagreement is initially

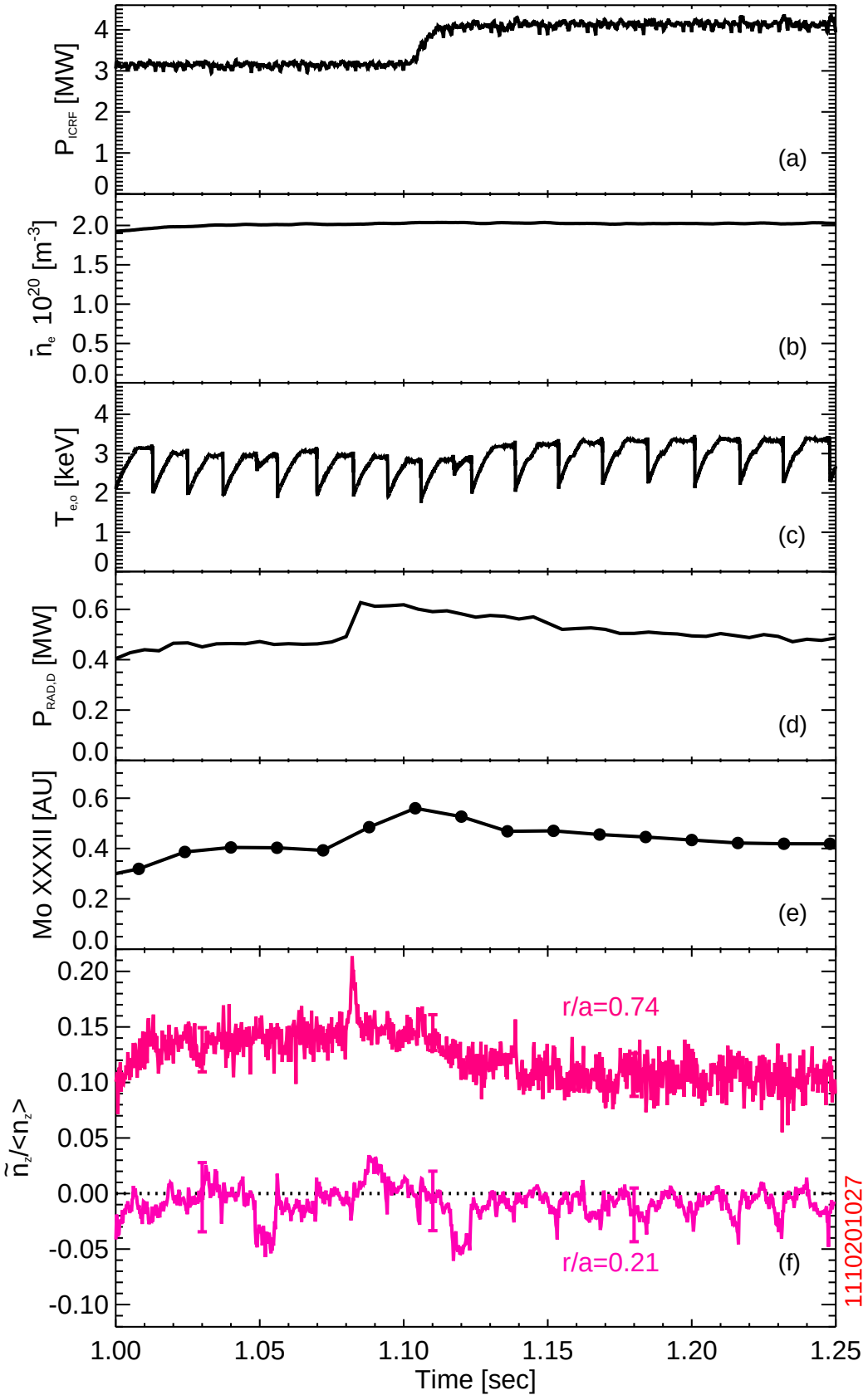

Figure 4-13: The time-evolving in/out asymmetry in an EDA H-mode plasma over a natural Mo injection

observed (1110201026). The relevant kinetic profiles are shown in Figure 4-14a-c, with the lower current, lower density shot (026) shown in teal and the higher current, higher density shot (017) shown in gold. The T_e profiles are plotted for times just prior to the sawtooth crash, while the T_i profiles are averaged over 40 ms. Measured rotation profiles are significantly higher than in Ohmic plasmas, and core rotation rates of 10-15 kHz are consistent with the frequency of the (assumed) $n = 1$ sawtooth precursor mode, observed using the soft x-ray diodes. As in the Ohmic plasma, the transport time scales are ordered such that parallel diffusion is faster than any cross-field transport inside of $r/a < 0.80$.

The midplane emissivity profiles for AXA and AXJ are plotted for shot 017 in Figure 4-15, and for shot 026 in Figure 4-16, averaging over a 20 ms time window during the time of peak molybdenum line brightness. The lower current shot (4-16) has a peaked radial profile with outboard accumulation for $r/a > 0.5$ but is nearly in/out symmetric in the inner half of the plasma. In the higher current shot (4-15), the radial profile is hollow and a measurable difference between AXA and AXJ is observed, attributed to the narrow emissive feature between $0.8 < r/a < 1.0$. In this discharge, outboard accumulation is seen in the outer two-thirds of the plasma.

Using both the KLIM and wall box arrays, the up/down and in/out asymmetries are calculated and compared to modeling using only the centrifugal force. For 017, the higher current and higher density shot, the measured in/out asymmetry profile agrees rather well with theory outside of $r/a \sim 0.3$, as shown in Figure 4-17, although inside of this radius, the two diverge and the measured data exhibit a small high-field side accumulation. The predicted asymmetry profile for 026 is similar to 017, as would be expected by comparing the rotation and temperature profiles from Figure 4-14, but, as shown in Figure 4-18, the measured in/out asymmetry profile is very different for the lower current shot. Near $r/a \sim 0.8$, agreement is close to being within error bars, but for smaller radii there is substantial disagreement in shape and magnitude of the asymmetry profile. The measured up/down asymmetry is weaker in the higher current shot where better agreement with theory is demonstrated.

In Figure 4-19, the measured and modeled asymmetries are compared at $r/a =$

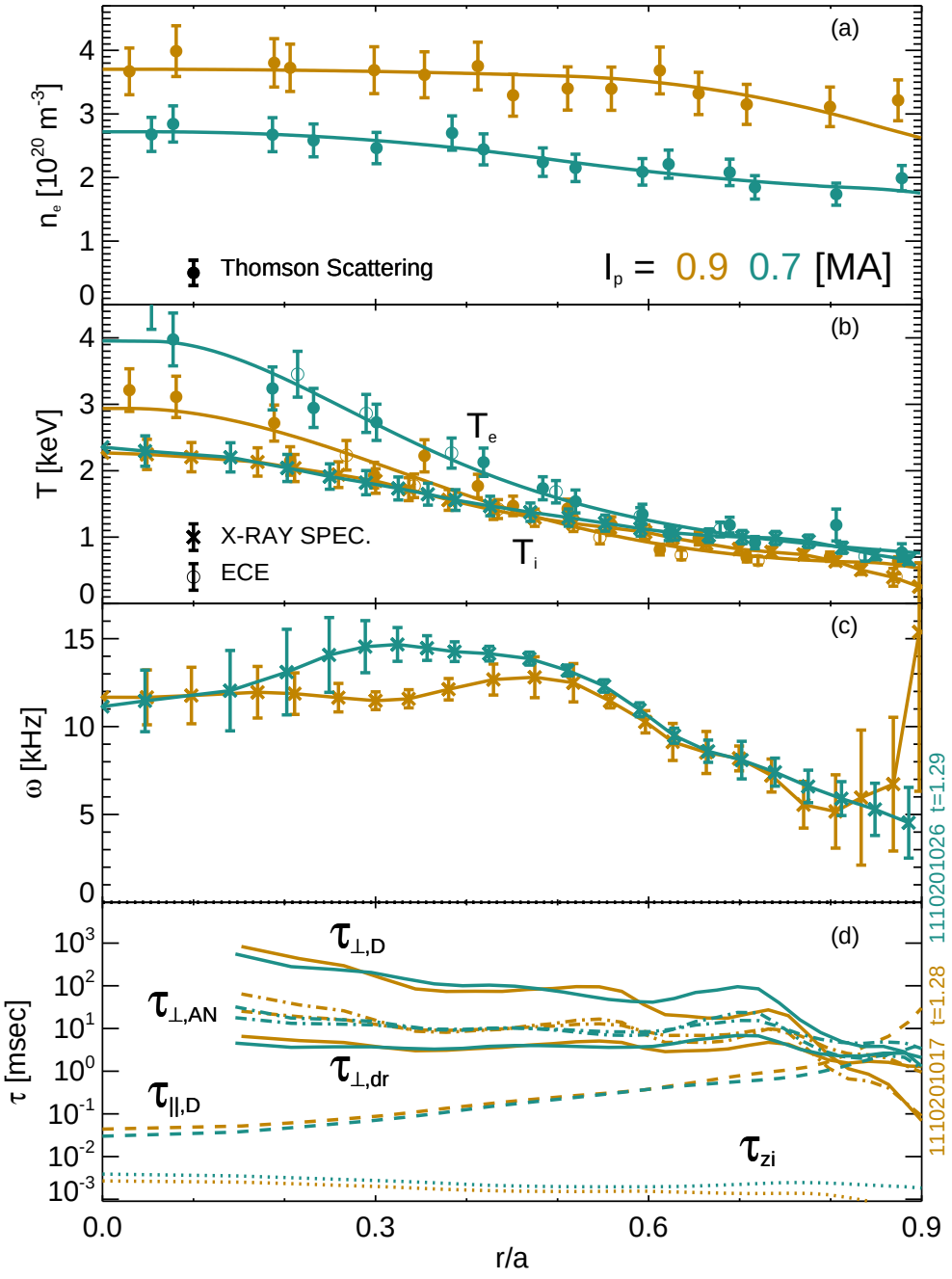

Figure 4-14: Radial electron density (a) ion and electron temperature (b) and rotation profiles (c) in two EDA plasma with relevant parallel and perpendicular time scales (d)

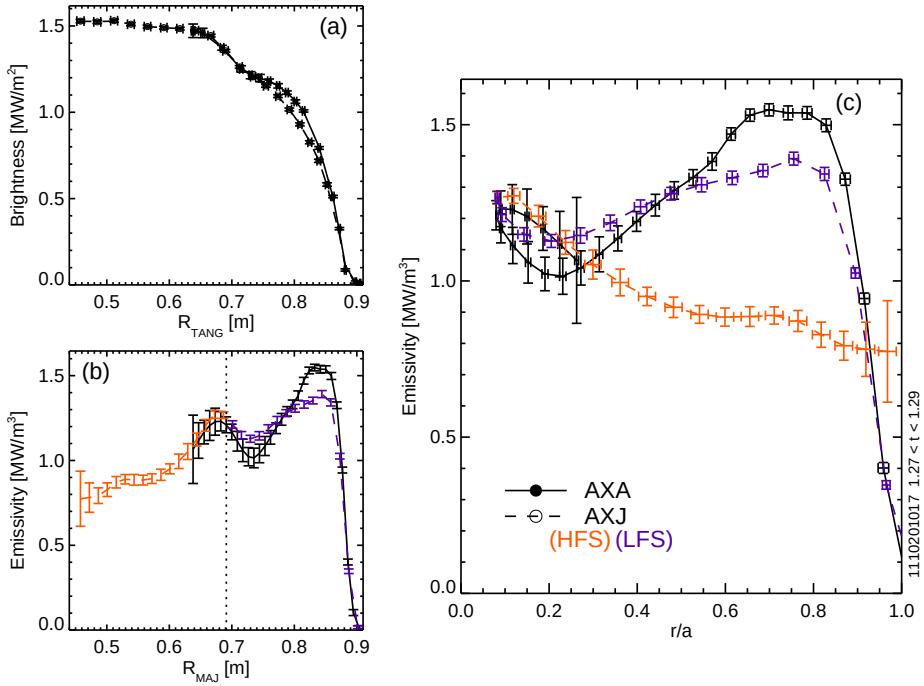

Figure 4-15: Example midplane AXUV diode profiles demonstrating the difference in the in/out asymmetry for the 0.9 MA EDA H-mode

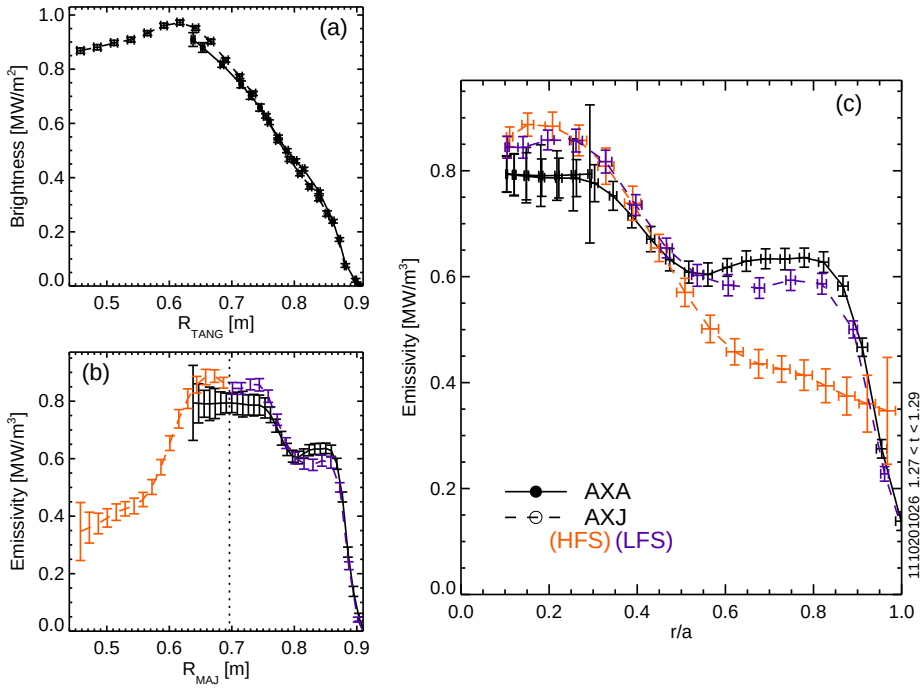

Figure 4-16: Example midplane AXUV diode profiles demonstrating the difference in the in/out asymmetry for the 0.7 MA EDA H-mode

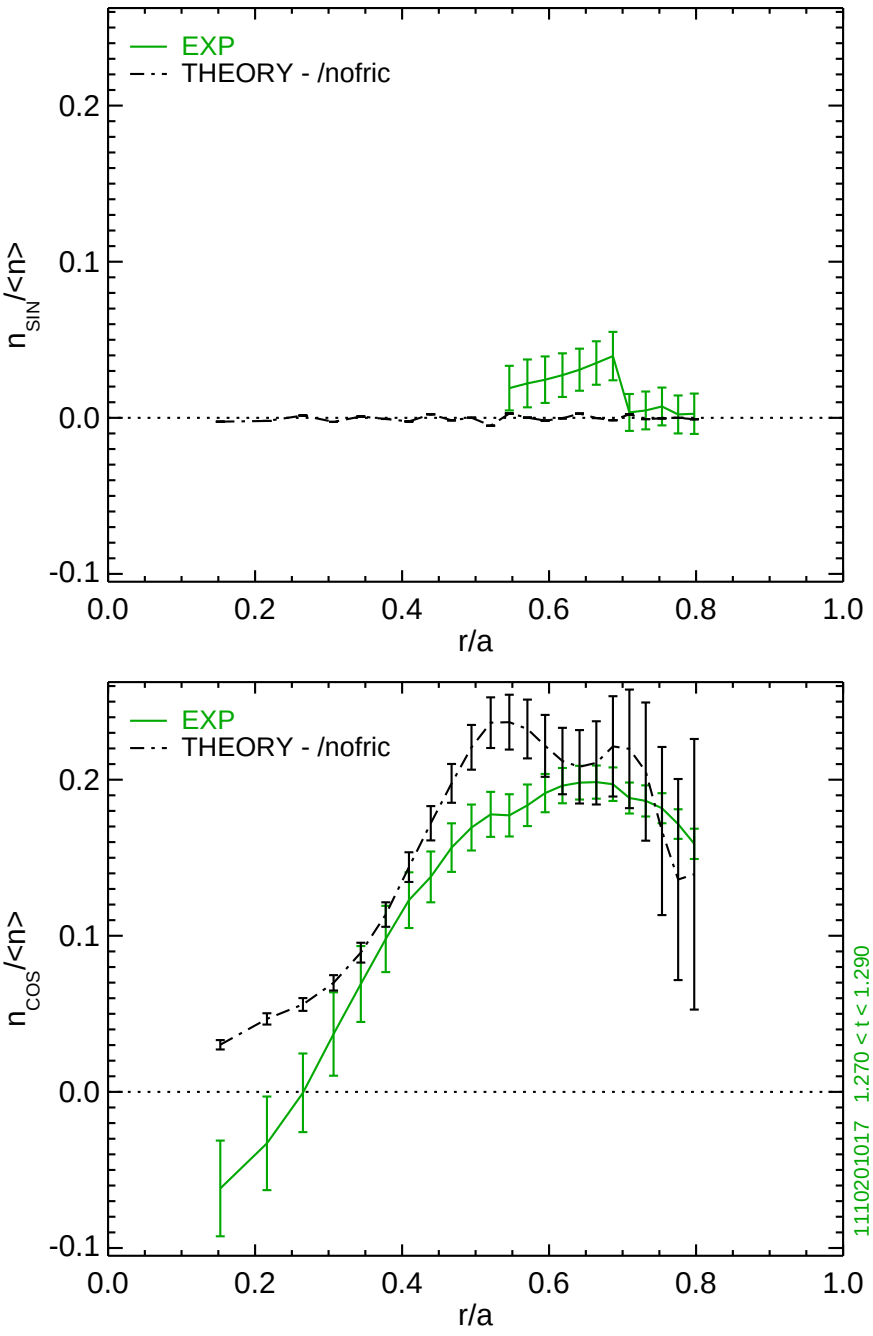

Figure 4-17: Comparison of measured (solid green) and modeled (broken black) radial asymmetry profiles for the 0.9 MA EDA H-mode

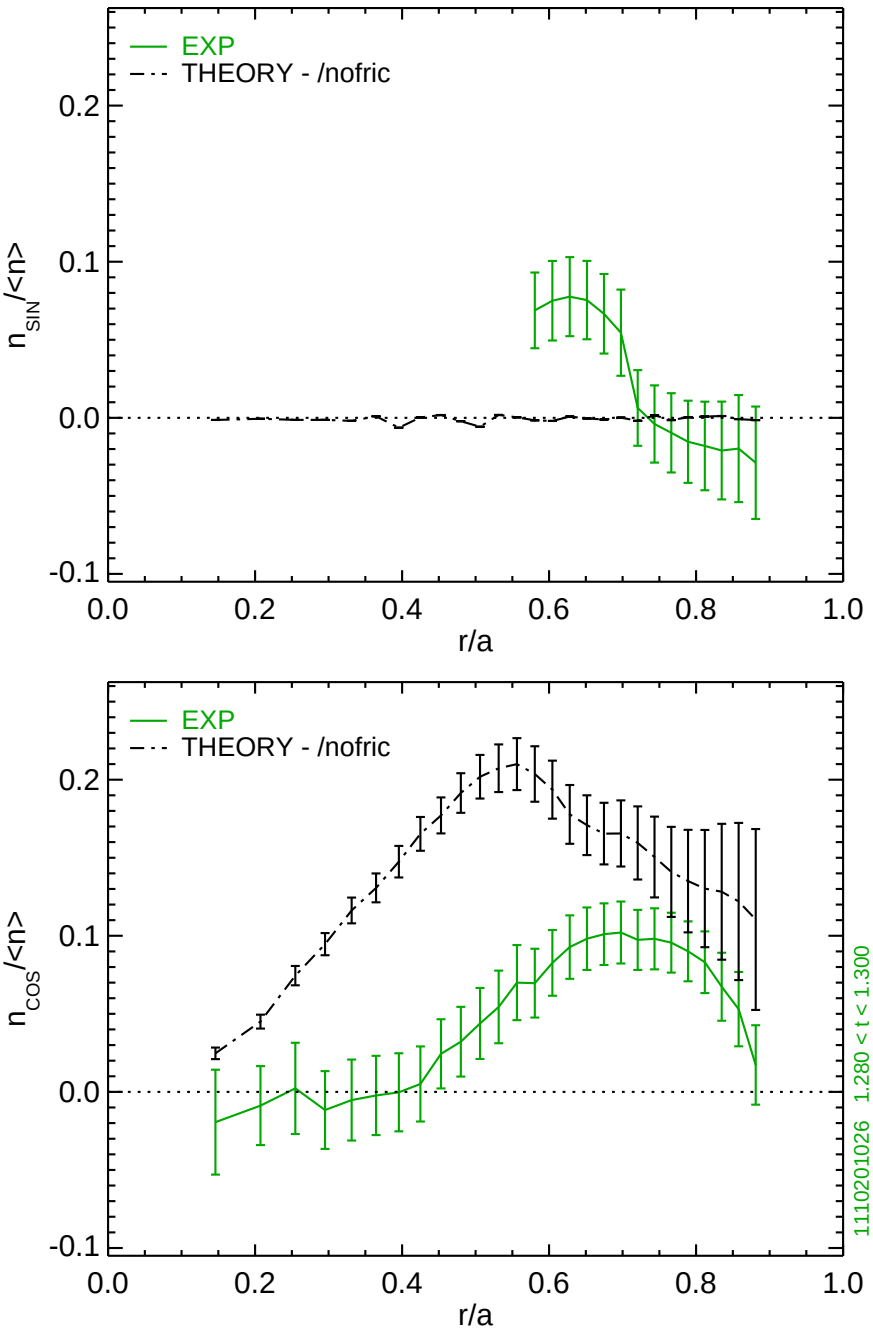

Figure 4-18: Comparison of measured (solid green) and modeled (broken black) radial asymmetry profiles for the 0.7 MA EDA H-mode showing disagreement in the core

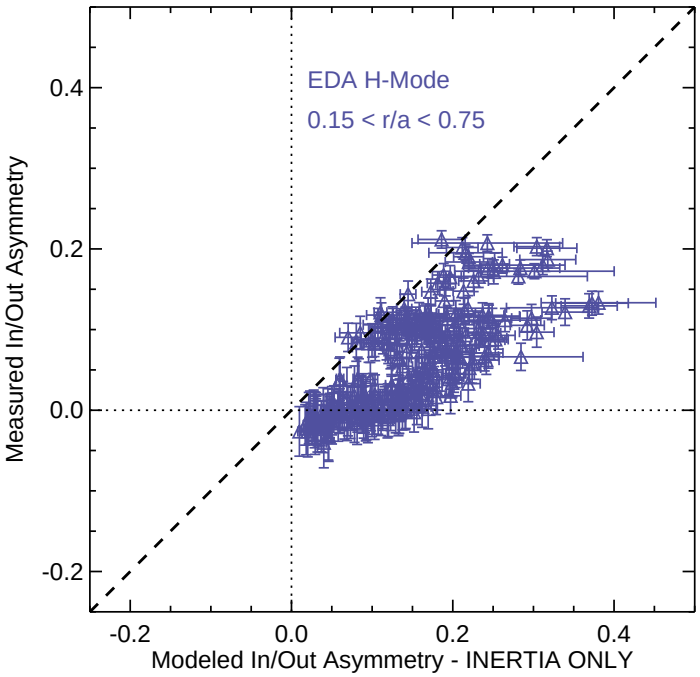

Figure 4-19: Comparison of measured in/out asymmetries to modeling using only inertia for steady-state molybdenum in EDA H-mode plasmas

0.05 intervals from $0.15 < r/a < 0.75$ for multiple time points in 7 EDA H-modes. The unity slope line (black dashed), implying agreement between observation and theory, acts as an upper bound for the measured asymmetry. Cases of inboard impurity accumulation, $n_{z,cos}/\langle n_z \rangle < 0$, are also seen. These trends are consistent with the two examples discussed above.

4.3.2 Sensitivity to Equilibrium Reconstruction

In order to test the sensitivity of these results to systematic errors in the magnetic equilibrium, kinetically constrained EFITs were completed for the two EDA H-modes. Measured electron density and temperature profiles from Thomson scattering and T_i from HIREXSR are used, with the ion density calculated from measured Z_{eff}, assuming an average ion, $< Z_I >= 8$. Fast-ion pressure, p_{fi}, calculated from TRANSP outputs, is included in the pressure profile with $p_{fi} = 3(p_\perp + p_\parallel)/2$, and a boundary condition of $T_e = 100$ eV is used [126].

Figures 4-20a and 4-20b show the magnetics only (ANALYSIS - black) and ki-

netic (EFIT02 - red) EFIT reconstructions for the higher current and lower current shots, respectively. Both find very similar stored energy, W_{MHD}, indicating that the measured kinetic and fast-ion pressure profiles are consistent with the magnetics measurements. In the 0.7 MA H-mode, the pressure profile in the kinetic EFIT is more peaked on axis, with a higher $\partial p/\partial \psi$, increasing the Shafranov shift. In Figure 4-21, the flux surface contours for both EFIT reconstructions for the 0.9 MA (4-21a) and 0.7 MA (4-21b) are plotted for various values of ψ_n. The relative difference in the contours, the separation between the black dashed (ANALYSIS) and red dash-dot (EFIT02), is larger for the 0.7 MA shot.. The slight upward shift in the magnetic axis results in a minor decrease in the magnitude of the up/down asymmetry.

In Figure 4-22, the emissivity profiles are shown for 0.7 MA shot using the kinetic EFIT data (4-22a) and the standard ANALYSIS EFIT (4-22b) to map the midplane emissivity profiles to minor radius. A noticeable difference in the in/out asymmetry is seen inside of $r/a < 0.5$ when using the kinetic EFIT to interpret the AXUV diode data, with the low-field side abundance seen much farther into the core.

In Figures 4-23 and 4-24, the $n_{cos}/\langle n_z \rangle$ profiles are compared for the two different EFIT reconstructions. The T_i, ω and T_e profile mapping that goes into the modeled asymmetry has not been recomputed with the new equilibrium so the predicted asymmetry remains unchanged. For the higher current shot (4-23), there are minor yet observable changes in the measured in/out asymmetry profile, the largest of which occurs for $r/a < 0.3$, likely due to the change in R_o. In the lower current case (4-24), changes in the asymmetry are seen out to $0.4 < r/a < 0.5$, where the emissivity profile changes from peaked to flat. The shape of the $m = 0$ radiation profile works to make the lower-current shots more sensitive to errors in the equilibrium.

Ideally, these results suggests that all asymmetry data should be recomputed using kinetically-constrained equilibrium reconstructions. Although the capability to run kinetic EFITs exists, developing this infrastructure to be used on many shots is outside of the scope of this research. Instead, shot and time slices are excluded that can be expected to be sensitive to pressure-induced changes in the equilibrium, such as those with high β_θ. In Figure 4-25, the difference between the measured and

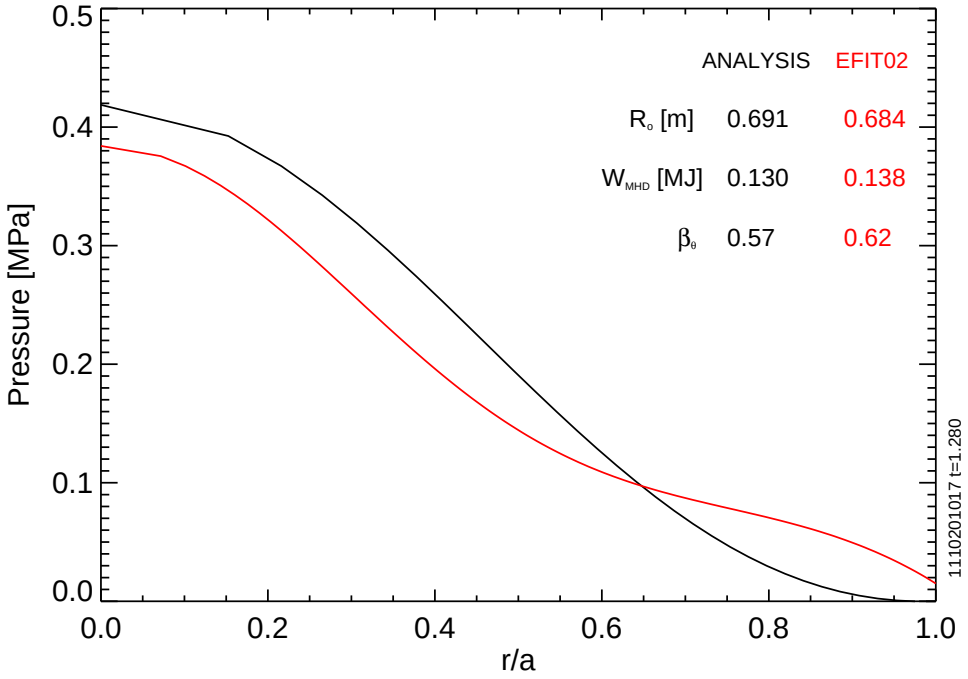

(a)

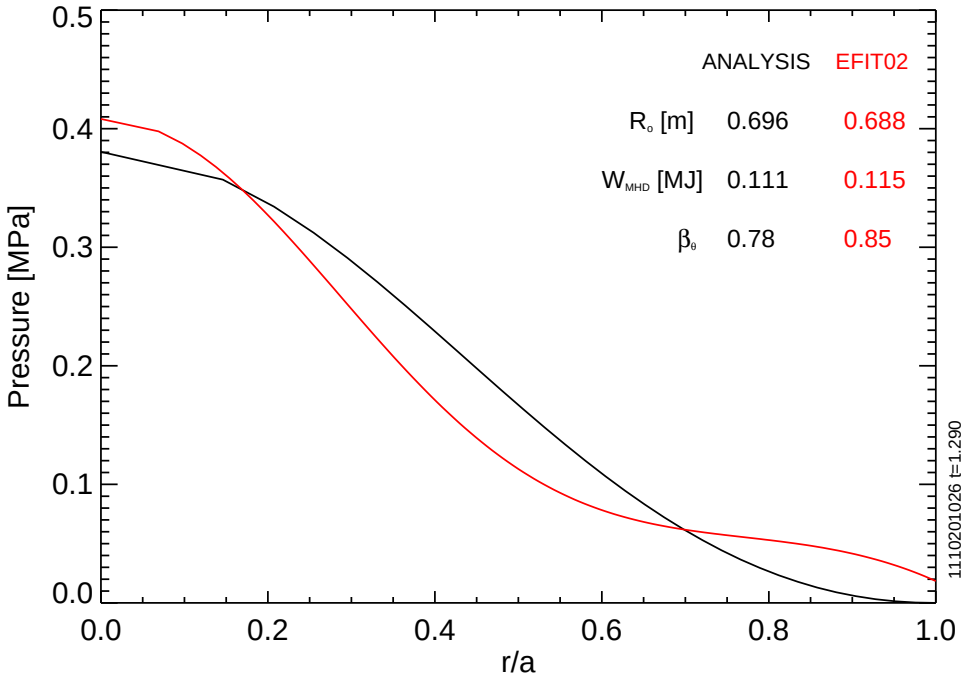

(b)

Figure 4-20: Comparison of magnetics only (ANALYSIS-black) and kinetically constrained (EFIT02-red) EFIT pressure profiles in the higher current (a) and lower current (b) EDA H-modes

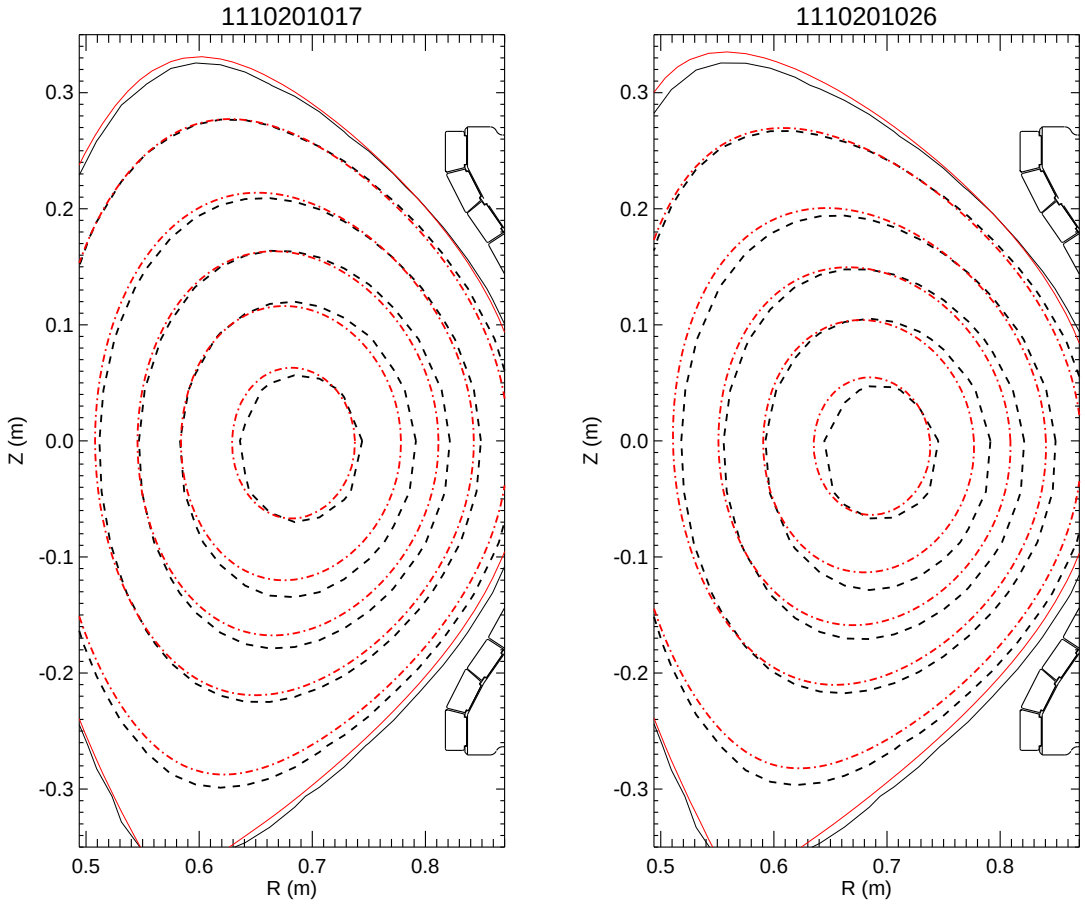

(a) (b)

Figure 4-21: Comparison of magnetics only (dashed,black) and kinetically constrained (dash-dot, red) EFIT flux-surface contours in the higher current (a) and lower current (b) EDA H-modes for ψ_n =0.1, 0.3, 0.5, 0.7, and 0.9

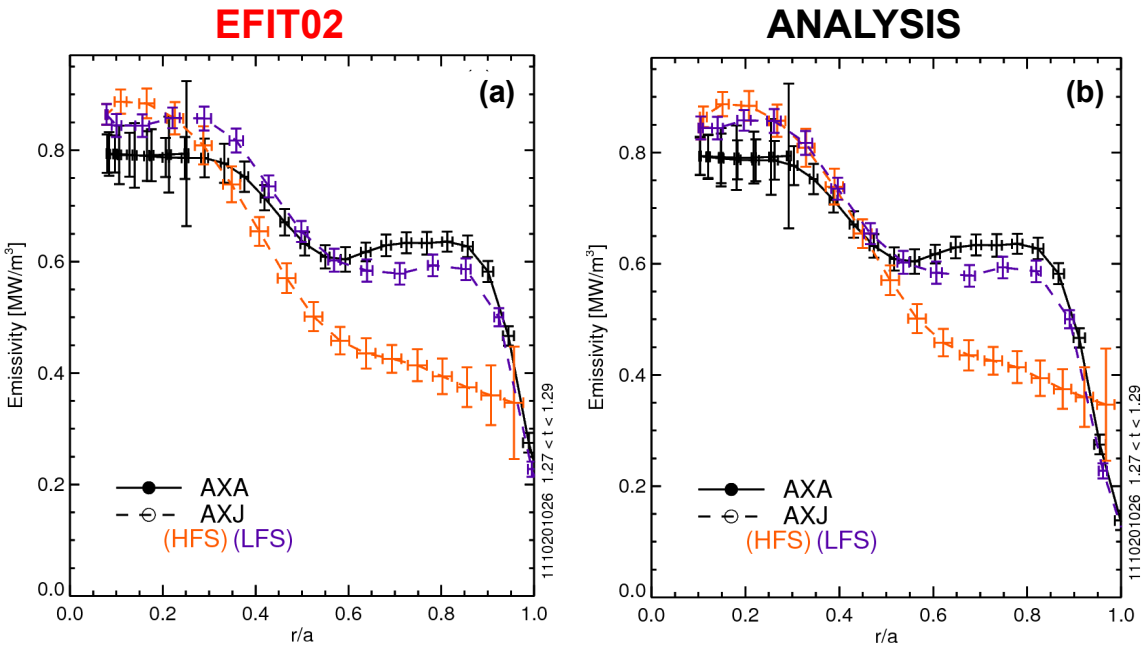

Figure 4-22: Midplane AXUV diode profiles for the 0.7 MA EDA H-mode using a kinetic EFIT (a) and the standard ANALYSIS EFIT (b)

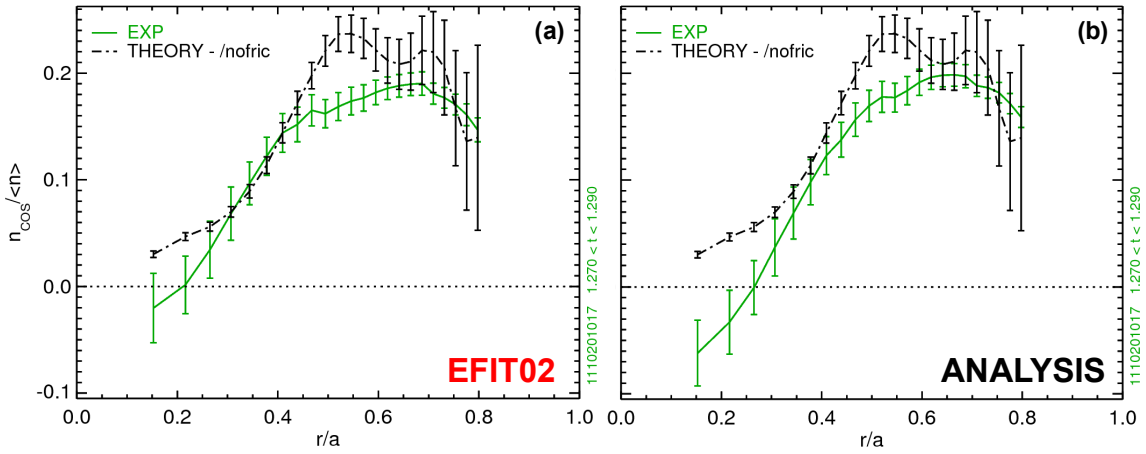

Figure 4-23: Comparison of measured (solid green) and modeled (broken black) radial asymmetry profiles for the 0.9 MA EDA H-mode using a kinetic EFIT (a) and standard ANALYSIS EFIT (b)

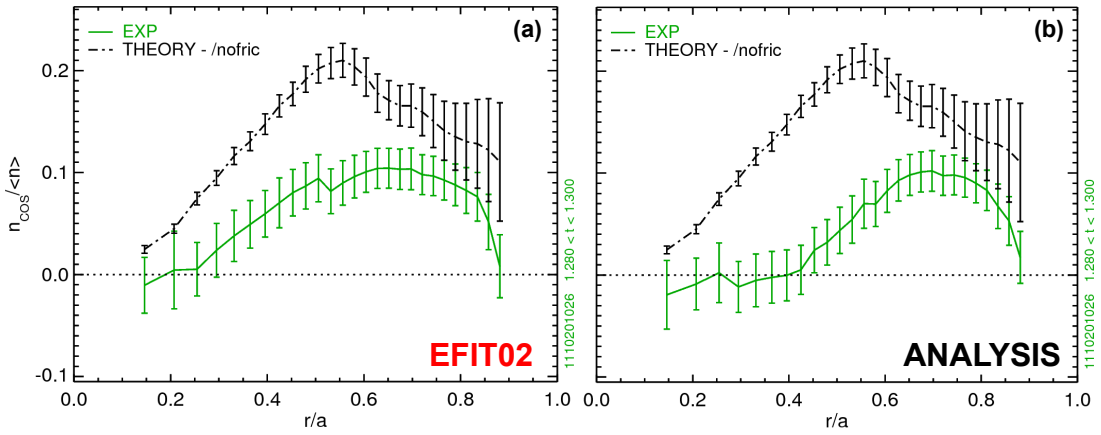

Figure 4-24: Comparison of measured (solid green) and modeled (broken black) radial asymmetry profiles for the 0.7 MA EDA H-mode using a kinetic EFIT (a) and standard ANALYSIS EFIT (b)

modeled asymmetry is at $r/a = 0.35$ is plotted against β_θ. For the EDA H-modes, this difference increases from close to zero at $\beta_\theta \sim 0.5$ to near 0.15 as β_θ approaches 0.8. The L/I-mode plasmas, discussed in Section 4.4, also show a large difference, but at a much lower β_θ. This discrepancy will be shown in Chapter 5 to be due to poloidal electric fields from magnetically trapped minority ions.

When shots with $\beta_\theta > 0.65$ are removed from the scatter plot comparing measured asymmetries to modeling based on the centrifugal force, as shown in Figure 4-26, results show better agreement between theory and experiment. This shows that in shots with narrow emissivity features at high β_θ, careful equilibrium reconstruction, possibly involving multiple iterations to recompute the kinetic profiles, is required before concluding any disagreement with theory.

4.4 ICRF Heated L/I-mode Plasmas

In plasmas where the auxiliary heating power is below the L-H threshold, the core electron and ion temperatures increase without a substantial change in electron density. Significant rotation is also observed due to self-generated flows. The L/I-mode plasmas exhibit similar Mach numbers as EDA H-modes, but at lower density and reduced collisionality. A series of I-mode plasmas was run on 1101209 with shot-to-shot

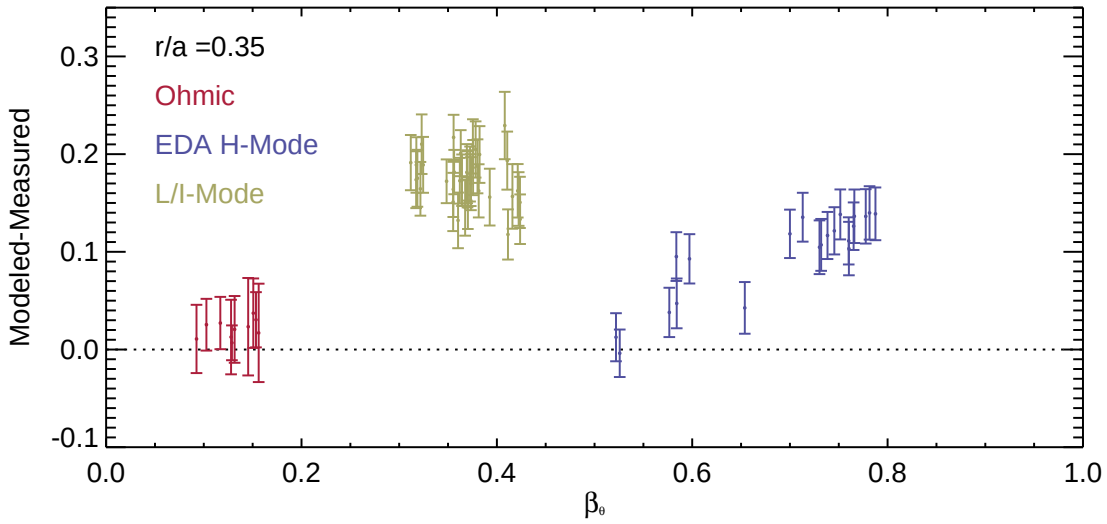

Figure 4-25: Relationship between the discrepancy between the predicted and measured asymmetry and β_θ, which impacts the Shafranov shift

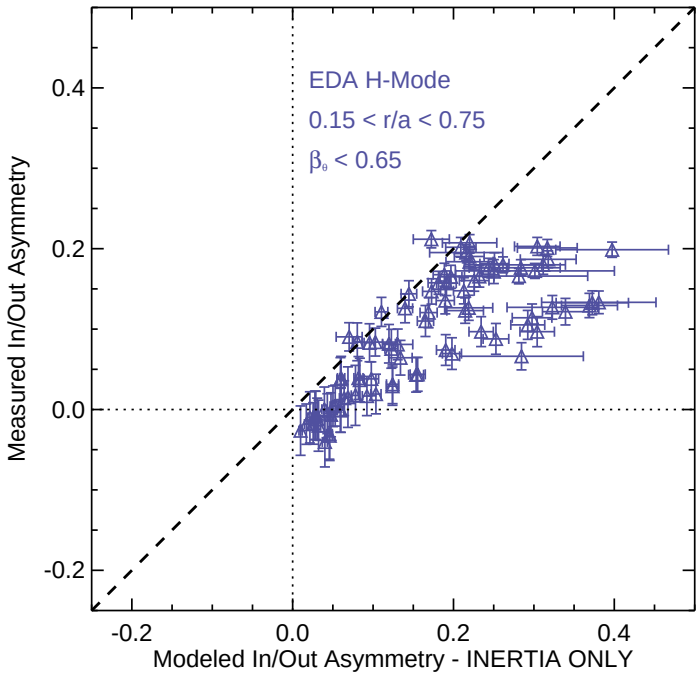

Figure 4-26: Comparison of measured and modeled in/out asymmetry for low β_θ EDA H-mode plasmas (compare with 4-19)

scans in plasma current and ICRF input power in order to study edge fluctuations and obtain detailed core profiles for transport analysis.

Significant radiation due to molybdenum allows asymmetry physics to be studied using steady-state radiation profiles. Figure 4-27, shows the time-evolution over a natural Mo injection at $t = 0.84$ seconds, as shown earlier for an Ohmic (4-8) and EDA H-mode plasma (4-13). As before, the increase in Mo XXXII brightness (e) and radiation (d) does little to change the in/out asymmetry (f), making $\varepsilon_z/\varepsilon_{tot} < 1$ corrections unnecessary.

4.4.1 Comparison to Theory

The asymmetry in a single ICRF-heated I-mode is analyzed in detail prior to presenting trends over the entire data set. In Figure 4-28, the kinetic profiles and time scales are plotted for an I_p=1.1 MA, B_t=5.6 T plasma heated with 3 MW of ICRH. The time scales again show that parallel and perpendicular transport are substantially disconnected over the plasma volume explored for in/out asymmetries.

The AXA and AXJ emissivity profiles shown in Figure 4-29 are in agreement with each other, peaked on axis, and reveal an in/out asymmetry that reverses direction for $r/a \leq 0.4$. Inside of this radius, there is large inboard accumulation which can be seen by both arrays while outside of $r/a \sim 0.4$ plasma exhibits accumulation on the outboard side of the flux surface. Looking closely at the shape of the profiles in 4-29b shows that equilibrium effects discussed in Section 4.3.2 are unlikely to be responsible. Radial shifts in the magnetic axis of 5-10 mm cannot eliminate the HFS abundance in the core.

The measured and predicted asymmetry profiles for the I-mode are shown in Figure 4-30, where a large, systematic disagreement of $\Delta n_{cos}/\langle n_z \rangle \sim 0.2$ is observed over the entire radial profile, even through the zero crossing at $r/a \sim 0.4$. Examining the structure of the radial profile in Figure 4-29, there is no reasonable change in the Shafranov shift that would eliminate the HFS abundance of impurity density. In addition, the β_θ for the higher current I-mode plasmas is far less then that of the lower current EDA H-mode case that necessitated more advanced equilibrium

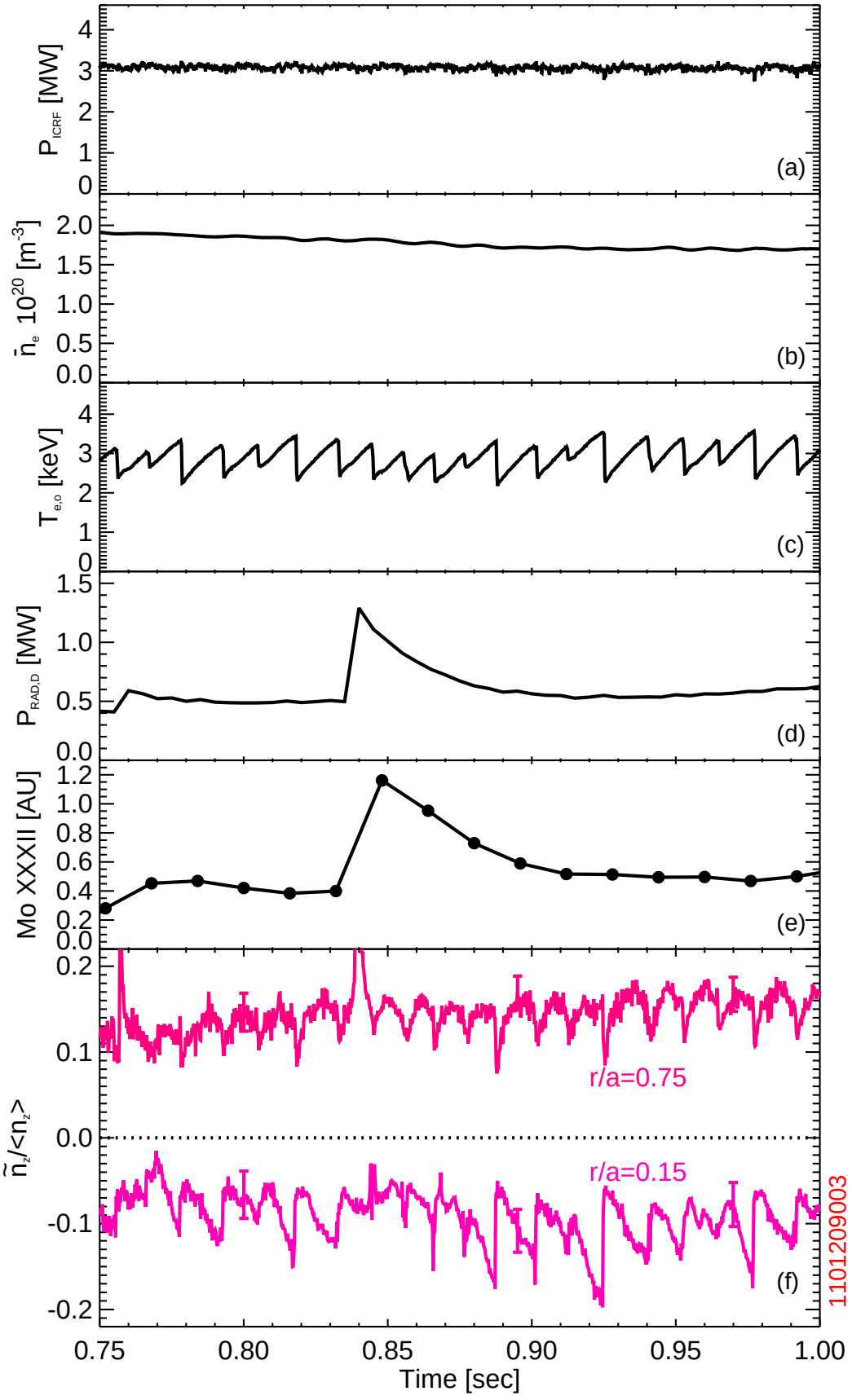

Figure 4-27: The time-evolving in/out asymmetry in an I-mode plasma over a natural Mo injection

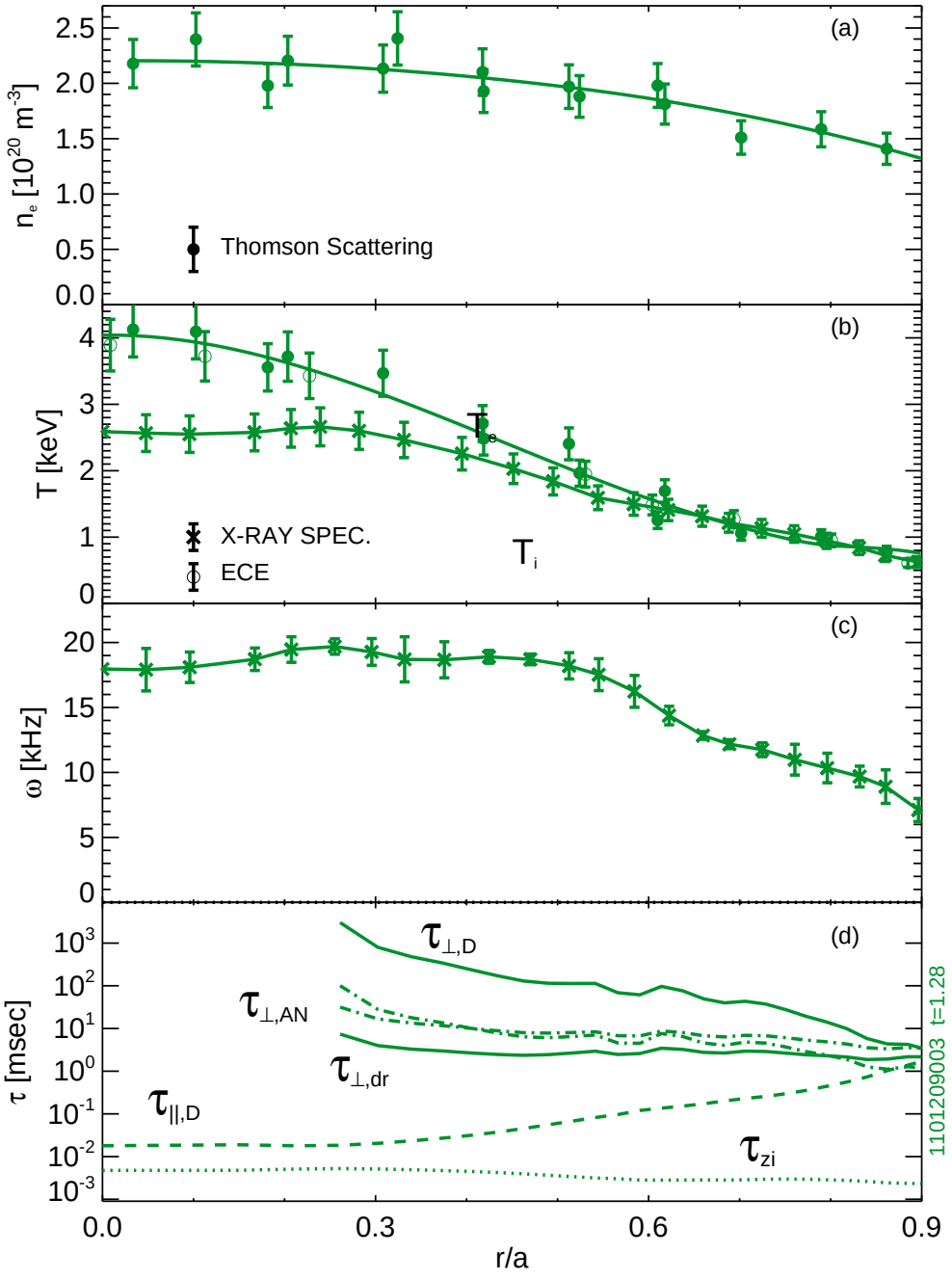

Figure 4-28: Radial electron density (a) ion and electron temperature (b) and rotation profiles (c) in an I-mode plasma with relevant parallel and perpendicular time scales (d)

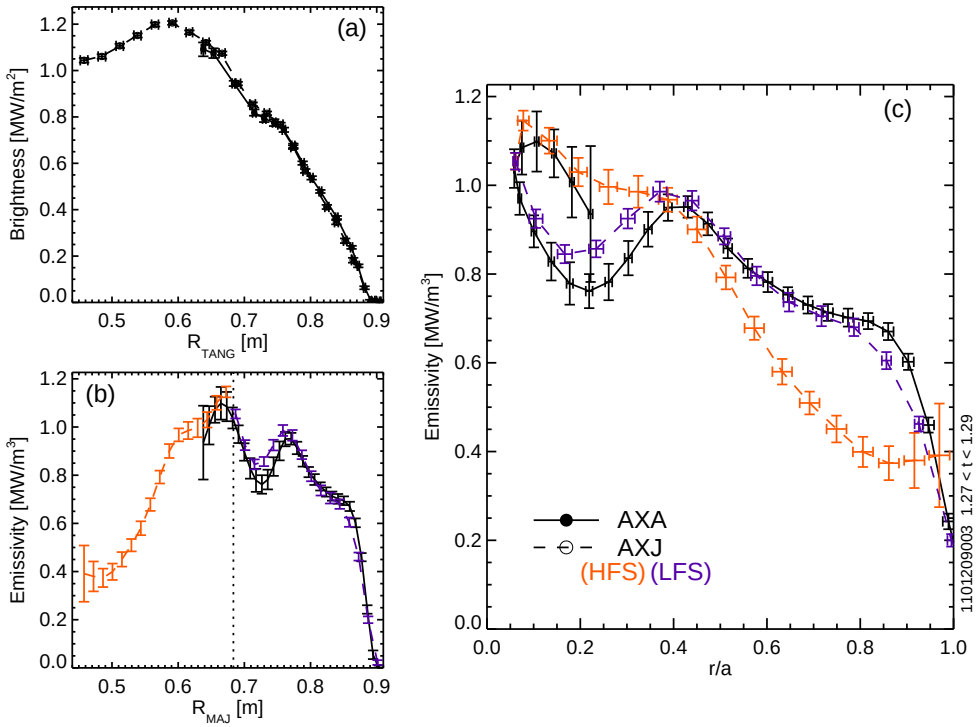

Figure 4-29: Example midplane AXUV diode profiles demonstrating both LFS and HFS accumulation in an I-mode plasma

reconstructions. This is a demonstration that more than just the centrifugal force is responsible for parallel impurity transport in the core of Alcator C-Mod plasmas.

In Figure 4-31, the measured in/out asymmetries are compared with modeling at $r/a = 0.05$ intervals from $0.15 < r/a < 0.75$, for multiple time points in 7 L/I-mode shots. Similar to H-mode comparisons, the unity slope line appears to be an upper bound, with most shots having reduced outboard accumulation or even significant inboard accumulation.

If the I-mode data set is further restricted to examine approximately just the inner half of the plasma, shown in Figure 4-32, then the measured asymmetries appear to be reasonably well correlated to the modeling, but at a negative offset of $n_{z,cos}/\langle n_z \rangle \sim 0.2$. Such a result cannot be achieved by uncertainties in the molybdenum fraction or the Mach number profile since the sense of the asymmetry is reversing. Additionally, the large difference is observed in all of the AXUV diode arrays as shown in Figure 4-33, where plots of measured and modeled $n_z(\theta)/n_z(0)$ profiles are displayed at various minor radii. These all show large disagreement with modeling while having an internal consistency. The large systematic error in the relative calibration necessary to force agreement in the I-mode plasmas would result in a significant asymmetry in the Ohmic and H-mode data set, and thus is an unlikely explanation for the difference seen in Figure 4-32. Explored in detail in Chapter 5, these I-mode plasmas have a large ICRH power per unit density, leading to increased magnetic trapping of minority ions, enhancing poloidal electric field effects on the impurity asymmetry, as discussed in Section 2.2.3.

4.5 Summary

In this chapter, measurements of the poloidal variation of the impurity density were compared with theoretical modeling that explains the in/out asymmetry as being driven by the centrifugal force. Ion temperature and toroidal rotation profiles, measured using x-ray crystal spectroscopy, were used to compute the magnitude of the in/out asymmetry expected for molybdenum. Ohmic plasmas exhibited nominally

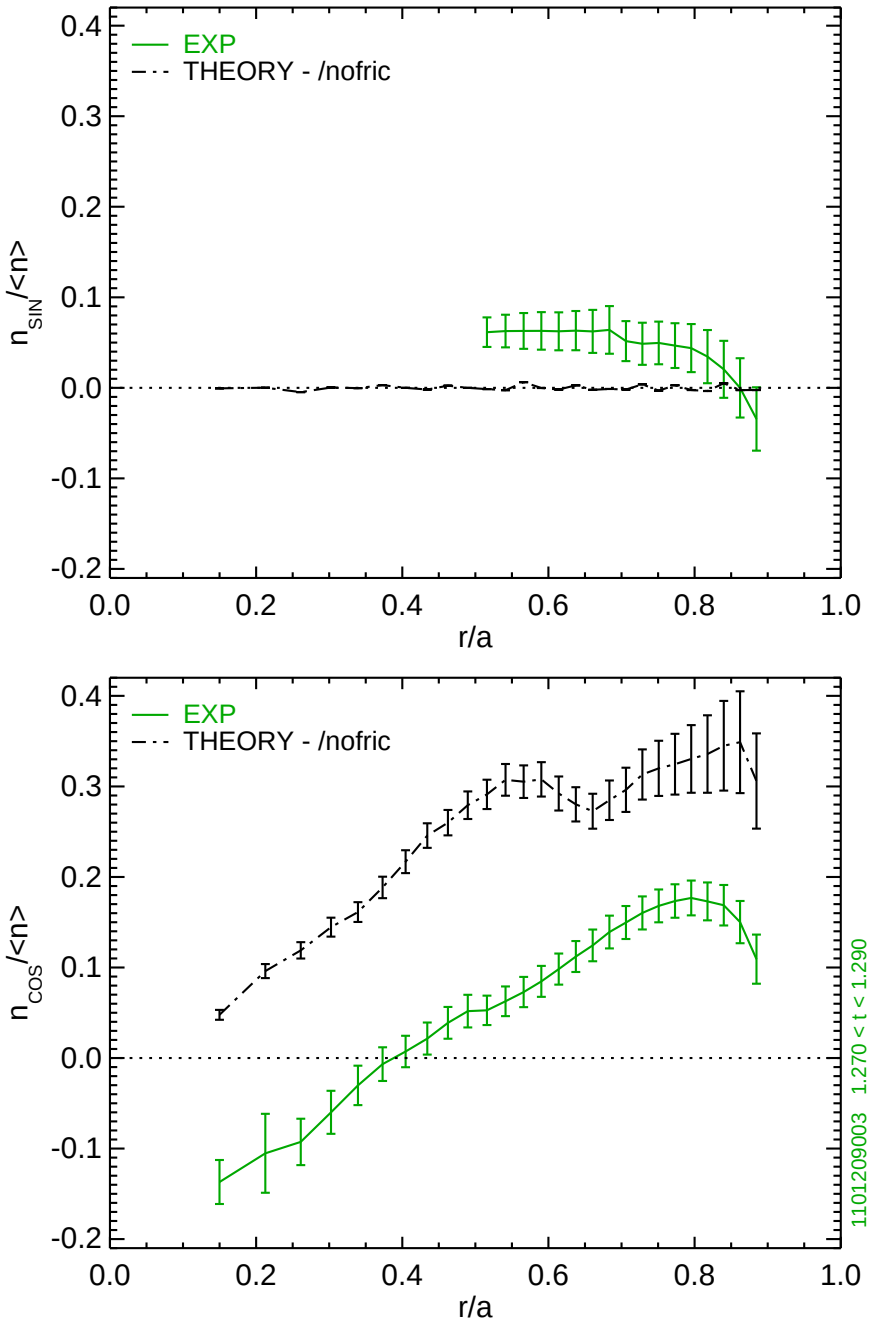

Figure 4-30: Comparison of measured (solid green) and modeled (broken black) radial asymmetry profiles for an I-mode discharge

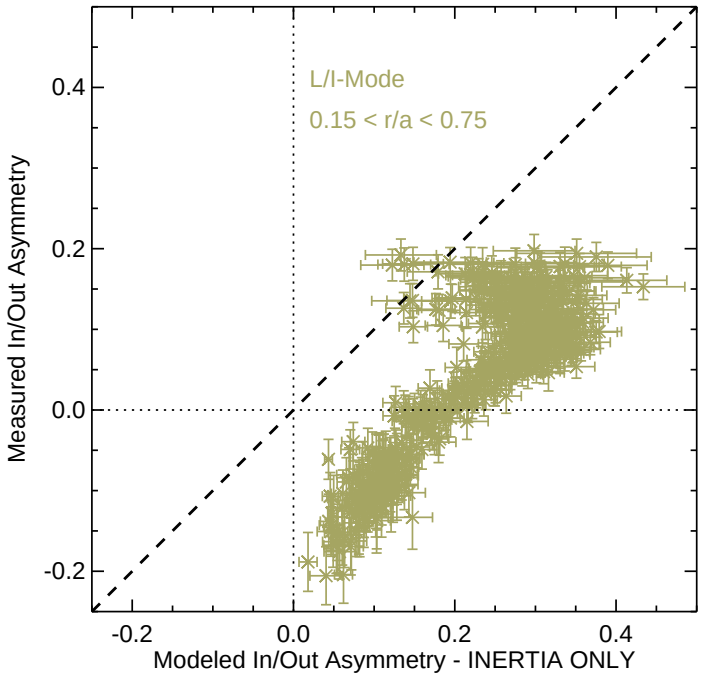

Figure 4-31: Comparison of measured in/out asymmetries to modeling using only inertia for steady-state molybdenum in L/I-mode plasmas

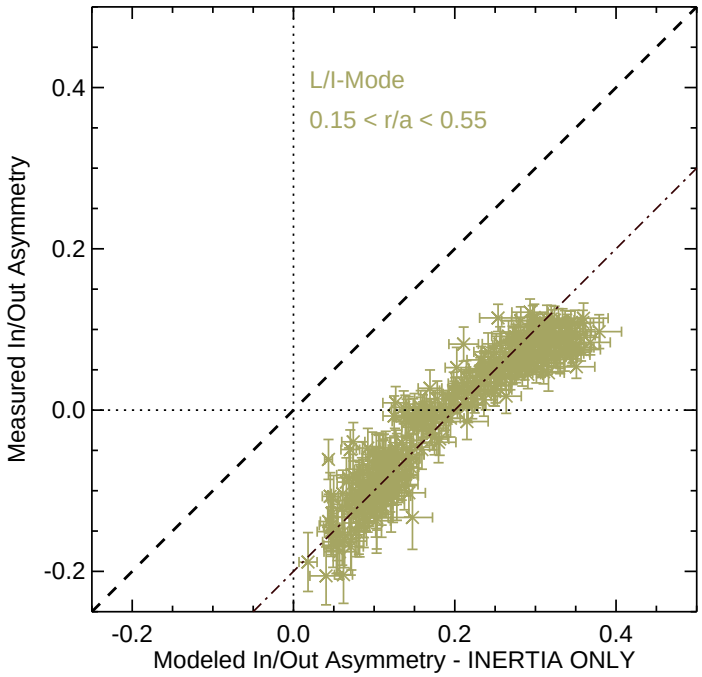

Figure 4-32: Measured and modeled in/out asymmetries in the core of L/I-mode plasmas agree but with a DC offset (black dash-dot)

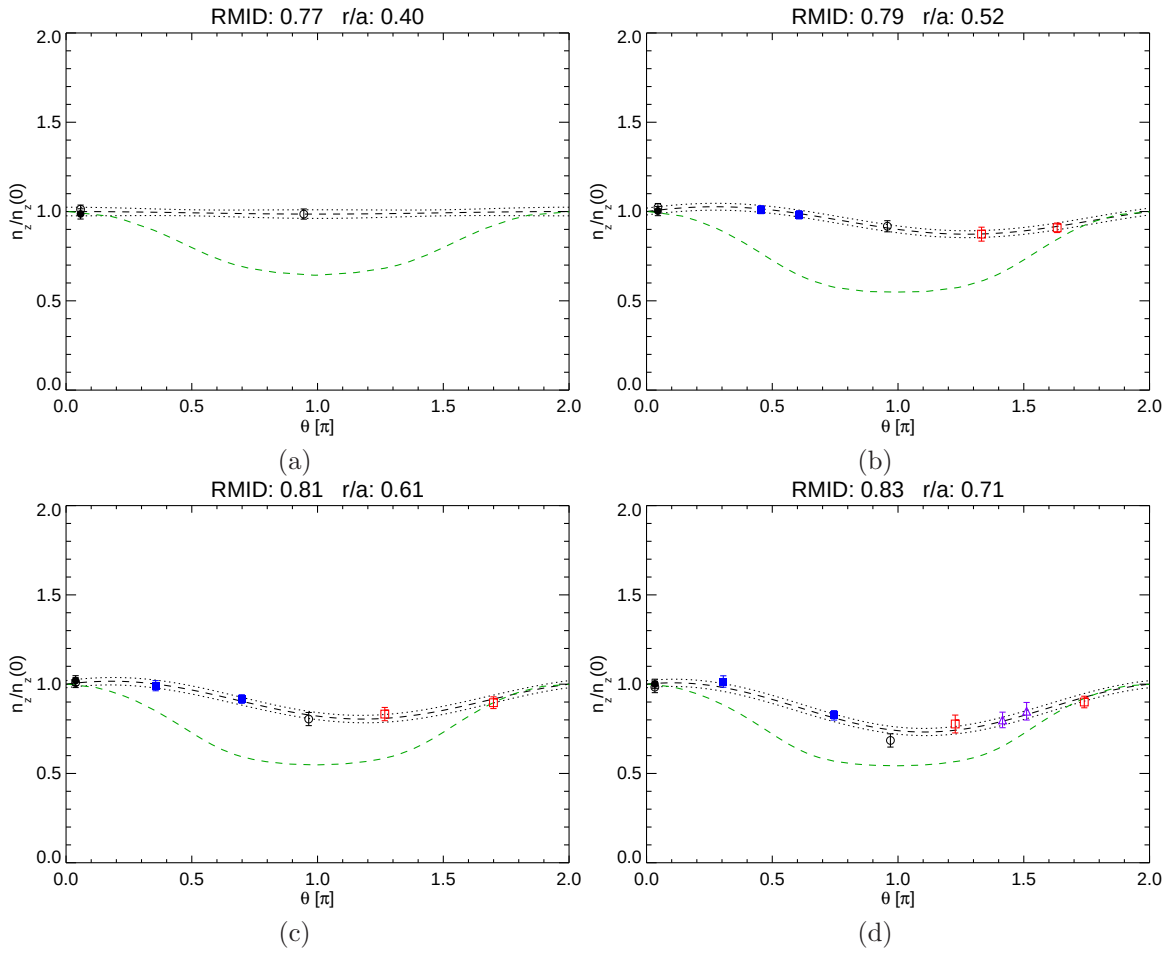

Figure 4-33: Measured poloidal variation of emissivity (symbols) compared to modeling (dashed green) showing significant disagreement for an I-mode plasma; AXA (●), AXJ (○), WB2AX (■), WB3AX (□) and WB4AX (△)

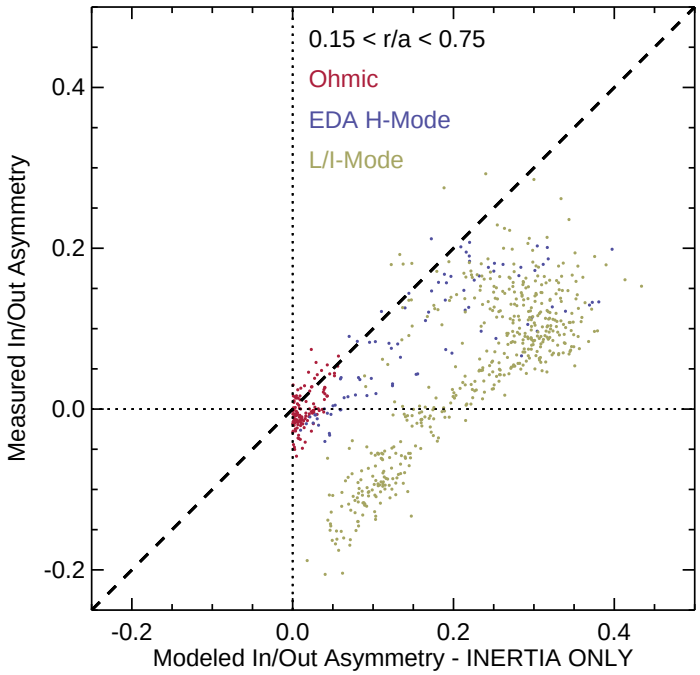

Figure 4-34: Comparison of measured and modeled in/out asymmetries in Ohmic, (low β_θ) EDA H-mode and L/I-mode plasmas.

symmetric radiation distributions during Mo injections, consistent with theory. Analysis in ion cyclotron heated plasmas, both EDA H-mode and L/I-mode, revealed that the centrifugal force represents an upper limit to the measured LFS impurity accumulation and that smaller magnitude LFS or even HFS accumulation is regularly observed. These results were shown to be sensitive to pressure-induced changes in the magnetic equilibrium reconstructions, and better agreement for EDA H-modes was found when excluding discharges with $\beta_\theta > 0.65$. Figure 4-34 shows a plot of this comparison in three operational regimes Ohmic (red) and rf-heated H-mode (blue) and L/I-mode plasmas (gold).

When including ion-impurity friction, discussed in more detail in Chapter 6, the predicted in/out asymmetry does not change substantially, as shown in Figure 4-35. This implies that existing parallel impurity transport theory is incomplete. One piece of physics missing from [24] that has been identified as a possible drive for flux surface variation of impurity density is the presence of a poloidal electric field sustained by cyclotron heating. The impact of this force is explored in Chapter 5 and is shown to lead to substantial inboard accumulation, as seen in the L/I-mode plasmas.

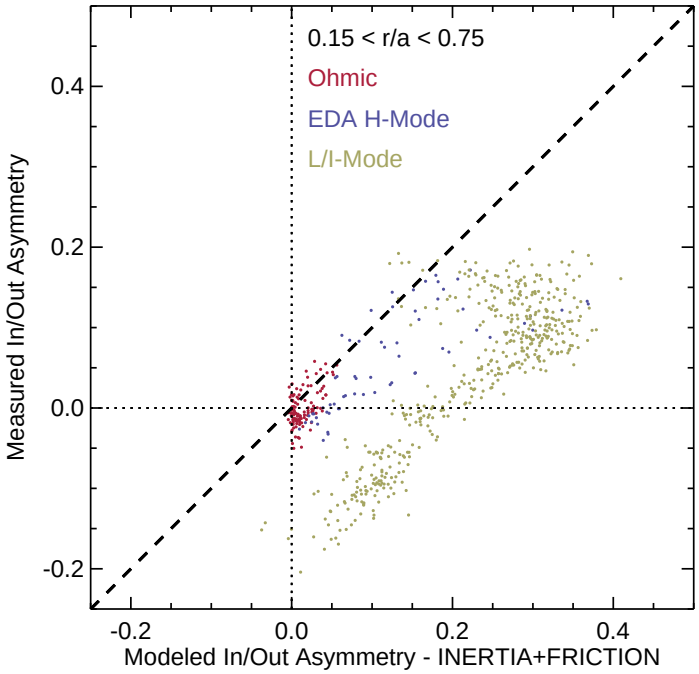

Figure 4-35: Comparison of measured and modeled in/out asymmetries in Ohmic, (low β_θ) EDA H-mode and L/I-mode plasmas including ion-impurity friction, showing little difference from 4-34.

Chapter 5

Asymmetry due to the Poloidal Electric Field

While impurity asymmetries have been examined in Ohmic and neutral beam heated plasmas, they have not been thoroughly investigated in electromagnetic wave heated discharges. The use of cyclotron heating is predicted to play a role in the parallel impurity force balance [51] via a poloidally varying electrostatic potential driven by electrons (ECRH) or ions (ICRH) magnetically trapped on the outboard side. The high charge of the impurities magnify these small potential variations, and the particles respond in Boltzmann-like manner, $\tilde{n}_z/\langle n_z \rangle \sim \exp(-eZ_z\tilde{\Phi}/T_z)$. In JET, Ni laser blow off into plasmas with hydrogen minority ICRH showed a $\sim$ 10 % HFS accumulation that was argued to be qualitatively consistent with this explanation [86]. But, a thorough demonstration of the impact of cyclotron heating on flux surface asymmetries of impurity density has not yet been completed.

In this chapter we extend the parallel transport theory discussed in Chapter 2 to include effects due to an ion species with an anisotropic pressure tensor, and compare predictions to molybdenum asymmetry measurements on Alcator C-Mod. Using toroidal field scans to modify the location of the minority resonance layer, experiments explore the link between ICRH and impurity asymmetries, and demonstrate quantitative agreement with the extended theory. When the resonance layer is located on the low-field side of the magnetic axis, inboard impurity accumulation is observed, while

during high-field side heating, only outboard accumulation due to the centrifugal force is seen. Increasing the plasma density is also shown to ameliorate this asymmetry. This effect is reduced, yet observable when using on-axis in ion cyclotron heated EDA H-modes.

5.1 Extending Parallel Transport Theory

Existing parallel impurity transport theories solve the coupled continuity and parallel force balance equations for a collisional high-Z impurity in an equilibrated background plasma. Experiments often employ auxiliary heating which can introduce distortions to the nominally Maxwellian distribution of a main or minority ion species. To evaluate the impact this has on the impurity asymmetry, an additional non-thermal ion species is included in quasi-neutrality when calculating the electrostatic potential variation on a flux surface, $\tilde{\Phi}$. As discussed in [62], a species heated by absorbing cyclotron waves increases its perpendicular energy, and can be modeled with a bi-Maxwellian distribution characterized by a temperature anisotropy, $T_\perp/T_\parallel > 1$. The parallel force balance equation for a species with an anisotropic but diagonal pressure tensor and a poloidally varying the electrostatic potential is given by,

$$\hat{b} \cdot (\nabla \cdot \mathbf{P_m} + n_m Z_m \nabla \Phi) = 0 \tag{5.1}$$

$$\nabla_\parallel p_\parallel + \frac{\left(p_\parallel - p_\perp\right)_m}{B} \nabla_\parallel B + n_m Z_m \nabla_\parallel \Phi = 0 \tag{5.2}$$

In most cases, $T_e/T_\parallel \ll 1$ and the effect of the potential is negligible, but it is included here for completeness. By assuming the temperatures to be constant on a flux surface, the minority density variation can be found from (5.2),

$$\nabla_\parallel \left(\ln\left(n_m\right) + \ln\left(B^\eta\right) - \frac{Z_m \Phi}{T_{m,\parallel}} \right) = 0 \tag{5.3}$$

$$\frac{n_m}{\langle n_m \rangle} = \left\langle \frac{1}{B^\eta} \right\rangle^{-1} \frac{1}{B^\eta} \exp\left(-\frac{Z_m \tilde{\Phi}}{T_{m,\parallel}} \right) \tag{5.4}$$

where n_m is the minority ion density, $\eta = T_\perp/T_\parallel - 1$ and B is the magnitude of the magnetic field. By assuming $\eta \sim 1$ and a circular plasma, the relation for the potential variation in [62] can be recovered from (5.4).

Before adding the effect of the minority into the generalized parallel impurity pressure balance discussed in Section 2.2, the poloidal variation can be derived for the case where only self-pressure and the electrostatic potential are included. In this case each thermalized species has a density variation of,

$$n_a = \langle n_a \rangle \exp\left(-\frac{Z_a e\tilde{\Phi}}{T_a}\right) \tag{5.5}$$

The minority species can be added into quasi-neutrality, $Z_m n_m + \sum_{j\neq m} Z_j n_j - n_e = 0$ and $e\tilde{\Phi}/T_e$ can be solved for by Taylor expanding the exponentials, which assumes the poloidal variation is relatively small. Summing over $j \neq m$ excludes the minority species and accounts for an arbitrary number and concentration of ion species. In cases of minority heating, $T_e/T_\parallel \ll 1$, and the potential term in 5.4 can be ignored.

$$\sum_{j\neq m} Z_j\langle n_j\rangle - \langle n_e\rangle + \langle n_m\rangle \left\langle \frac{1}{B^\eta}\right\rangle^{-1} \frac{Z_m}{B^\eta} = \frac{e\tilde{\Phi}}{T_e}\left(\langle n_e\rangle + \sum_{j\neq m} Z_j^2\langle n_j\rangle \frac{T_e}{T_j}\right) \tag{5.6}$$

By taking the flux surface average of both sides, assuming all (non-minority) ion species have the same temperature, $T_j = T_i$, and using $Z_{eff} - Z_m^2 f_m = \sum_{j\neq m} Z_j^2\langle n_j\rangle/\langle n_e\rangle$, (5.6) can be simplified to,

$$\frac{e\tilde{\Phi}}{T_e} = \frac{f_m Z_m}{1 + (Z_{eff} - Z_m^2 f_m)\frac{T_e}{T_i}}\left(\left\langle \frac{1}{B^\eta}\right\rangle^{-1} \frac{1}{B^\eta} - 1\right) \tag{5.7}$$

where $f_m = \langle n_m\rangle/\langle n_e\rangle$. Inserting (5.7) into (5.5) gives the density variation for an arbitrary, non-minority ion species.

$$\frac{n_a}{\langle n_a\rangle} = 1 - \frac{f_m Z_m Z_a T_e}{T_i + (Z_{eff} - Z_m^2 f_m)\, T_e}\left(\left\langle \frac{1}{B^\eta}\right\rangle^{-1} \frac{1}{B^\eta} - 1\right) \tag{5.8}$$

For $\eta > 1$, this makes the impurity density have an opposing flux surface variation

compared to the minority ions with an abundance on the inboard side where the magnetic field is strongest. The inclusion of impurities via Z_{eff} acts to short-circuit the potential developed by the minority species, collectively reducing the magnitude of the poloidal electric field.

The effect of the minority species can be added into quasi-neutrality when inertial forces are also included. In this case, the density of a thermalized ion species is,

$$n_a = \langle n_a \rangle \exp\left[-\frac{Z_a e\tilde{\Phi}}{T_a} + \frac{m_a\omega^2}{2T_a}\left(R^2 - \langle R^2\rangle\right)\right] \tag{5.9}$$

where E×B flow is assumed to be large, making all ion species have the same toroidal rotation, ω. Due to their lighter mass, the density of electrons is determined only by the potential, $n_e = \langle n_e\rangle \exp\left(e\tilde{\Phi}/T_e\right)$. Quasi-neutrality is again used to find the poloidal potential variation,

$$\frac{e\tilde{\Phi}}{T_e} = \left(\langle n_e\rangle + \sum_{j\neq m} Z_j^2\langle n_j\rangle\frac{T_e}{T_j}\right)^{-1}\left[Z_m\langle n_m\rangle\left(\left\langle\frac{1}{B^\eta}\right\rangle^{-1}\frac{1}{B^\eta} - 1\right) + \sum_{j\neq m} Z_j\langle n_j\rangle\frac{m_j\omega^2}{2T_j}\left(R^2 - \langle R^2\rangle\right)\right] \tag{5.10}$$

This general expression for the $\tilde{\Phi}$ can then be used in (5.9), yielding an accurate, but cumbersome expression for $n_z(\theta)/\langle n_z\rangle$. Further simplification can be made by assuming hydrogen minority heating in a deuterium plasma, with $T_j = T_i$. In this limit, $Z_m^2 f_m \ll 1$ and $m_j/m_i \simeq Z_j$ for fully-stripped, non-hydrogenic ions resulting in,

$$\frac{e\tilde{\Phi}}{T_e} = \frac{1}{1 + Z_{eff}\frac{T_e}{T_i}}\left[f_m\left(\left\langle\frac{1}{B^\eta}\right\rangle^{-1}\frac{1}{B^\eta} - 1\right) + Z_{eff}\frac{m_i\omega^2}{2T_i}\left(R^2 - \langle R^2\rangle\right)\right] \tag{5.11}$$

Using (5.11) to find the poloidal impurity density variation results in,

$$\frac{n_z}{\langle n_z\rangle} = 1 + \frac{m_z\omega^2}{2T_i}\left(1 - \frac{Zm_i}{m_z}\frac{Z_{eff}T_e}{T_i + Z_{eff}T_e}\right)\left(R^2 - \langle R^2\rangle\right) - Zf_m\frac{T_e}{T_i + Z_{eff}T_e}\left(\left\langle\frac{1}{B^\eta}\right\rangle^{-1}\frac{1}{B^\eta} - 1\right) \tag{5.12}$$

In the spirit of the transport theories derived in Chapter 2, it's useful to explore the circular, $\epsilon \ll 1$ limit to gain insight into the strength and orientation of the

asymmetry. Fourier expanding, $n_z/\langle n_z\rangle = 1 + n_c \cos\theta$ and the $m = 1$ cosine term including minority anisotropy, becomes

$$n_c = 2\frac{r}{R_o}\left[\frac{m_z\omega^2 R_o^2}{2T_i}\left(1 - \frac{Zm_i}{m_z}\frac{Z_{eff}T_e}{Z_{eff}T_e + T_i}\right) - Zf_m\frac{T_e}{Z_{eff}T_e + T_i}\left(\frac{T_\perp}{T_\parallel} - 1\right)\right] \quad (5.13)$$

For trace molybdenum in a rf-heated C-Mod deuterium plasma, $Z \sim 32$, and $Z_{eff} \simeq 1$. When $f_m \sim 5\%$, $T_e \sim T_i$, a temperature anisotropy of 2.7 in the minorities will have as much of an impact on the in/out asymmetry as a toroidal flow of order the thermal velocity. This will act opposite to the centrifugal force, pushing impurities to the high-field side. In the low-flow or high P_{rf}/n_e limit ($\eta \gg 1$), the effects of the the minority anisotropy can be expected to dominate the impurity asymmetry physics.

To include the effect of minorities in a general impurity parallel force balance equation, the procedure in Fülöp and Helander [24] is used, which has slightly modified notation. A single impurity species with a density of $Z^2 n_z \sim 1$ is included, with no assumption regarding the form of the poloidal variation, in contrast to (5.9). The main-ion Mach number, $M_i^2 = m_i\omega^2 R^2/2T_i$, is assumed to be small, making the n_i flux surface variation

$$n_i = n_{i,0}\left(1 - \frac{e\tilde{\Phi}}{T_i} + M_i^2\right) \quad (5.14)$$

where $n_{i,0} = \langle n_i\rangle/(1+\langle M_i^2\rangle)$ is a flux function. For the electrons, $n_e = n_{e,0}(1+e\tilde{\Phi}/T_e)$, where in this case, $n_{e,0} = \langle n_e\rangle$. Inserting, (5.14) into the quasi-neutrality equation that includes a fast-ion species and assuming $T_i/T_\parallel \ll 1$, the the electrostatic potential can be solved for using,

$$n_{i,0}\left(1 + M_i^2\right) + Zn_z + \langle n_m\rangle\left\langle\frac{1}{B^\eta}\right\rangle^{-1}\frac{Z_m}{B^\eta} - n_{e,0} = \frac{e\tilde{\Phi}}{T_i}\left(n_{i,0} + n_{e,0}\frac{T_i}{T_e}\right) \quad (5.15)$$

The parallel gradient of the potential is required for force balance (see (22) in [24]), which can be found from (5.15),

$$\nabla_\parallel\left(\frac{e\tilde{\Phi}}{T_i}\right) = \frac{T_0}{2n_0T_i}\left(n_{i,0}M_i^2 + Zn_z + \langle n_m\rangle\left\langle\frac{1}{B^\eta}\right\rangle^{-1}\frac{Z_m}{B^\eta}\right) \quad (5.16)$$

where, $2n_0/T_0 = n_{e,0}/T_e + n_{i,0}/T_i$, assuming $Z_m f_m \ll 1$. The form of the differential equation from [24] (2.27) does not change, but a new M^2 term is defined, which accounts for centrifugal force on the impurities and electrostatic potential effects from main-ions and the newly added minority species.

$$M^2 = \frac{m_z \omega R^2}{2T_i}\left(1 - \frac{Zm_i}{m_z}\frac{T_e}{T_e + T_i}\right) - Zf_m \frac{T_e}{T_i + T_e}\left(\left\langle \frac{1}{B^\eta}\right\rangle^{-1}\frac{Z_m}{B^\eta}\right) \tag{5.17}$$

In order to properly include the effect of other impurities in the limit of $Z_{eff} - 1 \sim 1$, a series of coupled 1-D differential equations would need to be solved. Using (5.11) to find the parallel gradient of the potential, an M^2 can be found which accounts for the effect of other impurities on the potential, but not the friction force.

$$M^2 = \frac{m_z \omega R^2}{2T_i}\left(1 - \frac{Zm_i}{m_z}\frac{Z_{eff}T_e}{Z_{eff}T_e + T_i}\right) - Zf_m \frac{T_e}{T_i + Z_{eff}T_e}\left(\left\langle \frac{1}{B^\eta}\right\rangle^{-1}\frac{Z_m}{B^\eta}\right) \tag{5.18}$$

For $Z_{eff} = 1$ and $f_m = 0$, this collapses to the standard M^2 term in [24].

5.2 ICRH Resonance Layer Scans in L-Mode Plasmas

In order to gain insight into the parallel impurity transport physics driven by ICRH, the flux-surface variation of the impurity radiation is characterized as the hydrogen minority, D(H), resonance layer is scanned shot-to-shot. Sufficient molybdenum allows the steady-state radiation asymmetry to be used as an accurate proxy for the flux surface impurity density variation. The mechanism thought to contribute to the high-field side accumulation is a poloidal electric field created by magnetically trapped minority ions whose non-thermal distribution function is sustained by absorption of cyclotron waves. For large power per particle, P_{rf}/n_e, resonance localization [136] should increase the perpendicular energy of the minority ions, further trapping them until their banana tips are at the D(H) resonance layer. As this layer is scanned from the LFS to the HFS by changing the toroidal field, the fast ion orbits will change

from deeply trapped (LFS-heating) to trapped orbits that are nearly passing (HFS-heating). It should be expected, qualitatively, that HFS heating would have less impact on parallel impurity transport, and this is shown empirically. Examining the dynamic behavior of the impurity asymmetries as the rf power drops to zero further establishes a clear link between measured in/out asymmetries and ICRH. Using the extended theory developed in the previous section, quantitative agreement between measurements and predictions is demonstrated.

5.2.1 Description of ICRH Experiments at 78-80.5 MHz

Upper single null plasmas in the unfavorable ∇B drift direction are used in order to avoid H-mode, thereby obtaining plasmas with high P_{rf}/n_e. The heating is provided by two, two-strap antennas at 80 and 80.5 MHz, and a single four-strap antenna at 78 MHz using heating phasing. A toroidal field of B_t=5.4 T places all frequencies nominally on-axis and over consecutive discharges, the toroidal field is scanned, at fixed plasma shape, from 4.2 T to 6.2 T, moving the resonance layer, R_{res}, from the HFS to the LFS, as shown in Figure 5-1. Resonance layer locations are calculated from the power weighted average of all antennas with diamagnetic corrections ignored.

The time evolution of selected shots used in the toroidal field scan are shown in Figure 5-2. The ICRH power (c), ∼3 MW, is applied from 0.6-1.42 seconds keeping the same antenna mix. The line-averaged electron density (a) is held fixed at $\simeq 1.8 \times 10^{20}$ m^{-3} using cryopumping. The plasma current is 1.1 MA in discharges with $B_t \geq 4.4$ T (e) and reduced to 1.0 MA in those with smaller toroidal field in an effort to maintain $q_{95} > 3$. For on-axis heating, I-mode plasmas are obtained, while for off-axis heating, plasmas remain in L-mode. All plasmas exhibit sawtooth activity and are therefore presumed to have $q_o < 1$.

As shown in Figure 5-2, when the D(H) resonance location is scanned, the core electron temperature (b) and toroidal rotation (f) change. The spatial profiles of plasma properties relevant for parallel impurity transport are shown in Figure 5-3 during the steady-state portion, $1.0 < t < 1.35$ of the selected shots. Profiles of

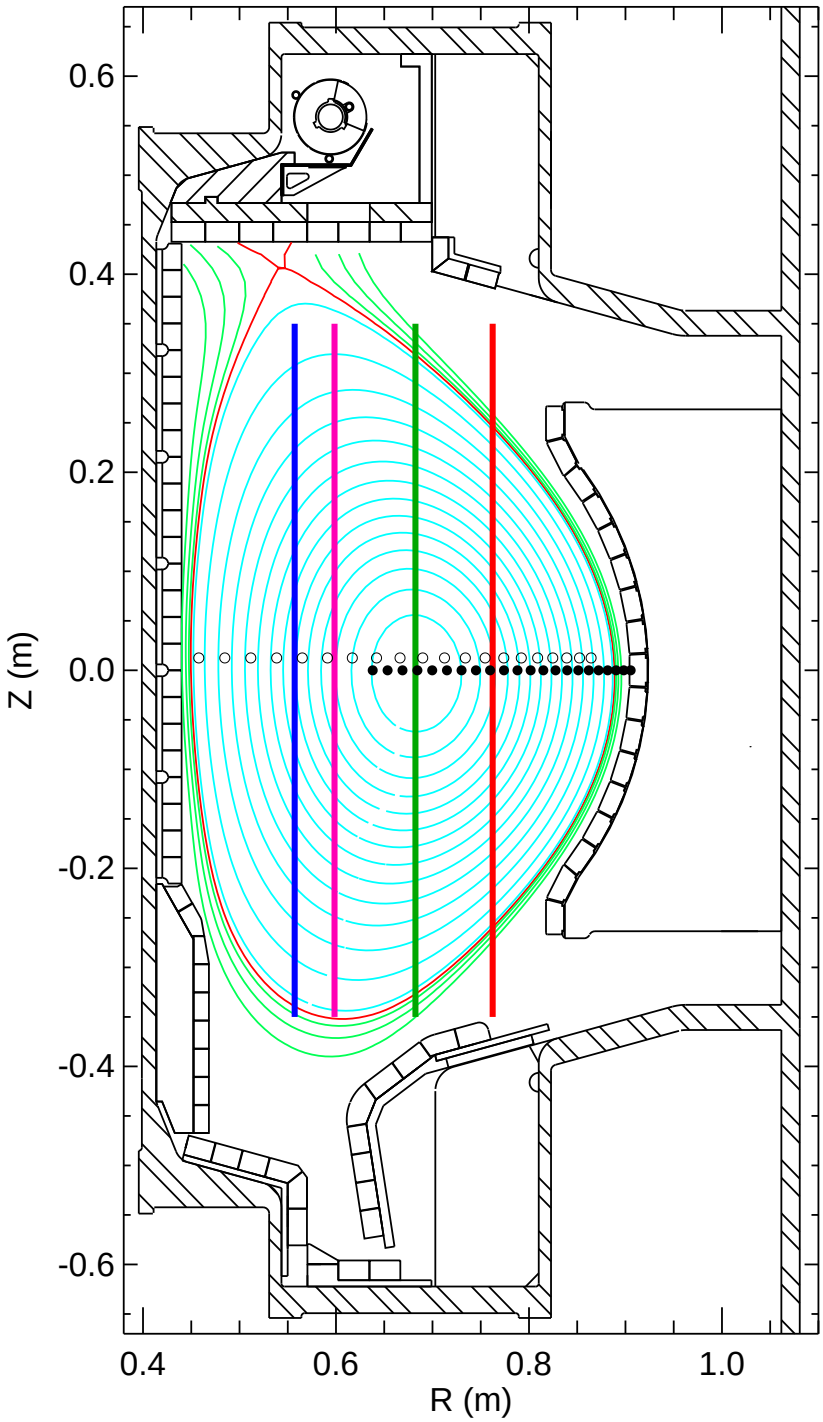

Figure 5-1: EFIT reconstruction of 78-80.5 MHz experiments showing the shot-to-shot scans of the resonance layer and including the AXA (•), AXJ (○) tangency radii

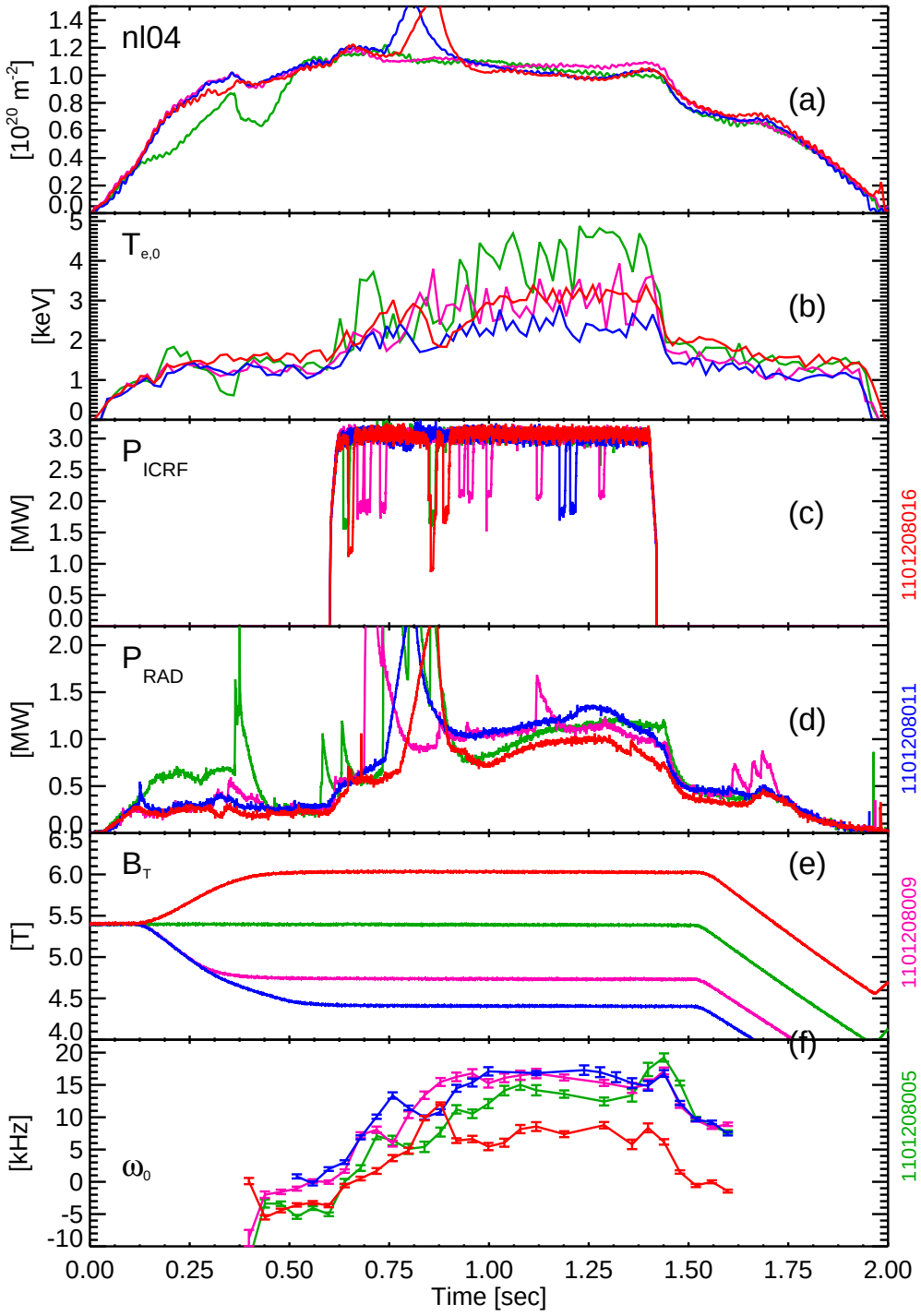

Figure 5-2: Time histories of relevant plasma parameters for the selected 1101208 shots

the electron density (a) and temperature (b), at the peak of the sawtooth cycle, are measured using Thomson scattering with additional T_e measurements from ECE. Line emission from Ar^{16+} averaged over 80 are used to calculate the ion temperature (c) and rotation profiles (d).

The pressure anisotropy of the minority ions is calculated via the TRANSP [137] suite of codes using spline fits to measured electron density and temperature profiles, and ion temperature profiles output from THACO. The ICRF modeling in TRANSP outputs the parallel and perpendicular stored energy, where $p_\perp/p_\parallel = E_\perp/2E_\parallel$ is assumed to be equal to $T_\perp/T_\parallel$. In Figure 5-4 the temperature anisotropy is shown during the steady-state portion of plasmas with the ICRH resonance layer on the HFS (R$\sim$0.56) and the LFS (R$\sim$ 0.76). Much larger temperature anisotropy is seen during LFS heating, in agreement with resonance localization arguments.

5.2.2 Results

The midplane emissivity profiles for these plasma are plotted in Figures 5-5 and 5-6 against major radius and normalized minor radius, r/a. Good agreement is demonstrated between the AXA and AXJ emissivity profiles in their region of overlap. When the resonance is located on the HFS (5-5a and 5-5b), the emissivity on the outboard side of a flux surface, $R > R_o$, is greater than that on the inboard side, $R < R_o$. As the resonance moves on-axis as shown in 5-6a, the difference shrinks, and for $r/a < 0.3$ the inboard emissivity is larger than the outboard. When the resonance is moved farther to the LFS side (5-6b) the outboard emissivity is below that of the inboard side up to $r/a \sim 0.6$.

The steady-state emissivity measurements from both the KLIM and wall box arrays are used to estimate the flux surface variation of the impurity density by assuming the emissivity is due to molybdenum radiation. As done in Chapter 4, this assumption can be confirmed by examining changes across a molybdenum injections as shown in Figure 5-7. In an otherwise stable background plasma, the radiated power (d) rise is approximately proportional to the rise in Mo XXXII line brightness (e). Except for the initial phase of the injection, the measured in/out asymmetries at two

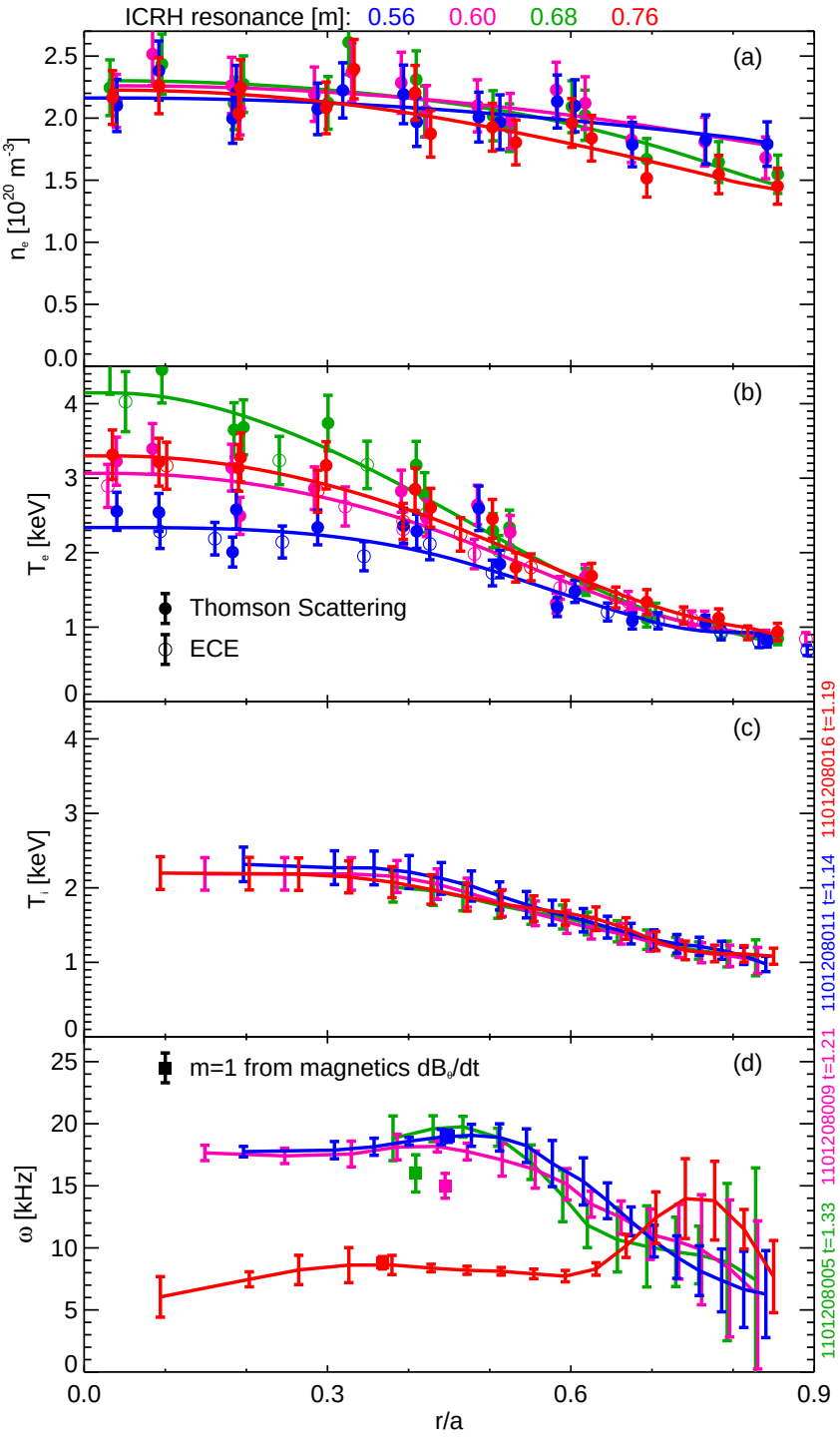

Figure 5-3: Spatial profiles of n_e (a), T_e (b) T_i (c) and ω (d) for the selected 1101208 shots

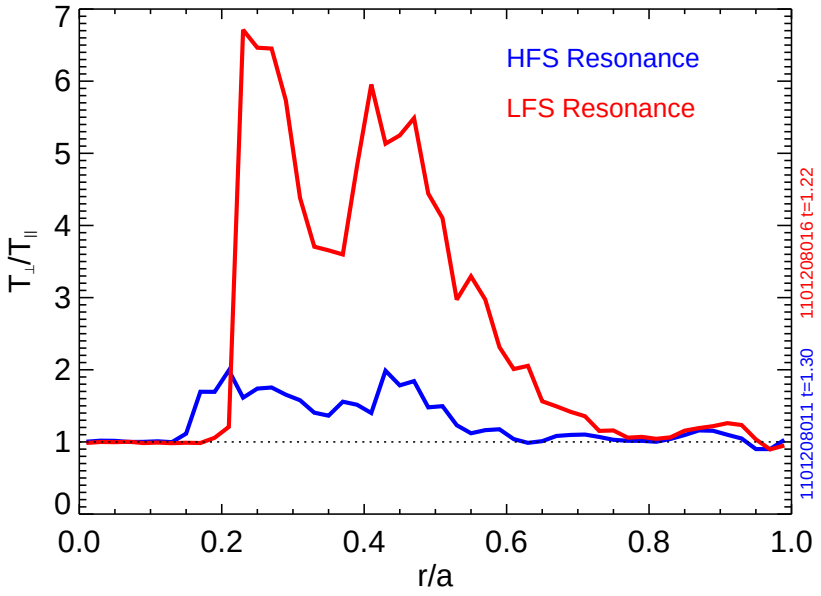

Figure 5-4: The TRANSP-predicted temperature anisotropy of the minority ions for HFS and LFS ICRH heating

minor radii (f) show little change, indicating the use of steady-state asymmetry data is reasonable.

The poloidal variation is fitted to the form $n_z/\langle n_z\rangle = 1 + n_{cos}\cos\theta + n_{sin}\sin\theta$, and the resulting profiles of $\tilde{n}_z/\langle n_z\rangle = n_{cos}/\langle n_z\rangle$ are plotted for the selected discharges in Figure 5-8. Differences in the measured asymmetry profiles are observed during the toroidal field scan, most notably when the D(H) resonance is on-axis ($R_{res} \simeq 0.68$) or the low-field side ($R_{res} \simeq 0.76$) and $n_{cos}/\langle n_z\rangle < 0$.

Predictions from parallel transport theory which include only inertial forces are compared to the measurements for the $R_{res} \simeq 0.56$ and $R_{res} \simeq 0.76$ plasmas, where real flux surface geometry is used, and differences in the background plasma, as shown in Figure 5-3, are accounted for. Inboard accumulation, $n_{cos}/\langle n_z\rangle < 0$, is allowed in cases of strong ion-impurity friction, but modeling using experimental profiles shows this to be negligible for these discharges and is omitted for clarity. The measured and modeled up/down and in/out asymmetry profiles for the B_t=4.4 T, HFS-heated plasma are shown in Figure 5-9. Qualitative agreement is found for $0.15 < r/a < 0.8$, with the predicted asymmetry about 0.05 larger than the measured asymmetry.

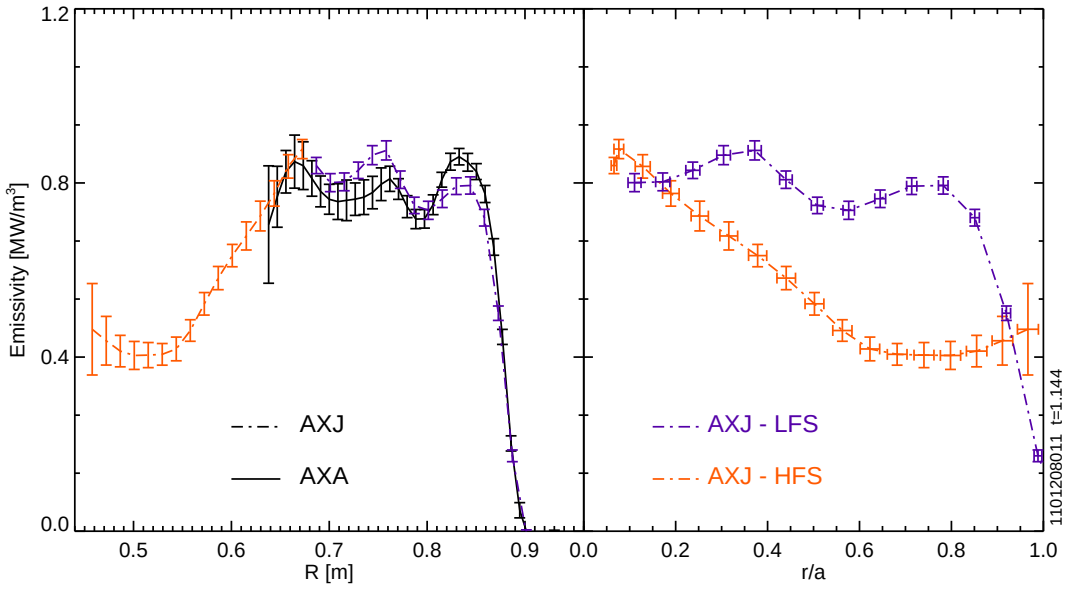

(a)

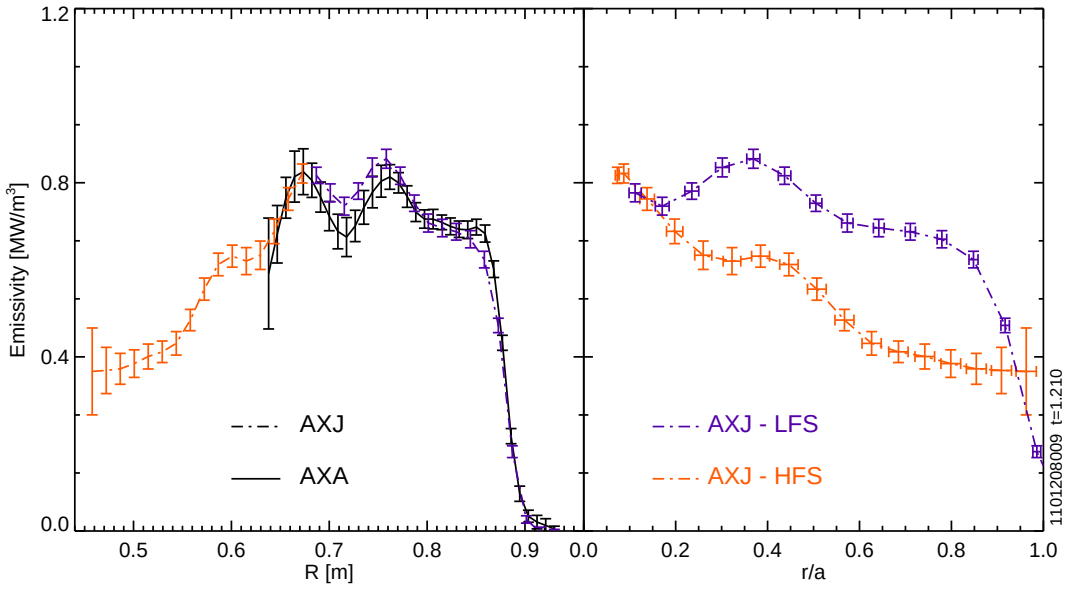

(b)

Figure 5-5: Midplane emissivity in HFS-heated plasmas. Profiles from AXA (solid) and AXJ (dashed) plotted against major radius (left) and AXJ for r/a (right) for resonance layer location of $R \sim 0.56$ (a), 0.60 (b)

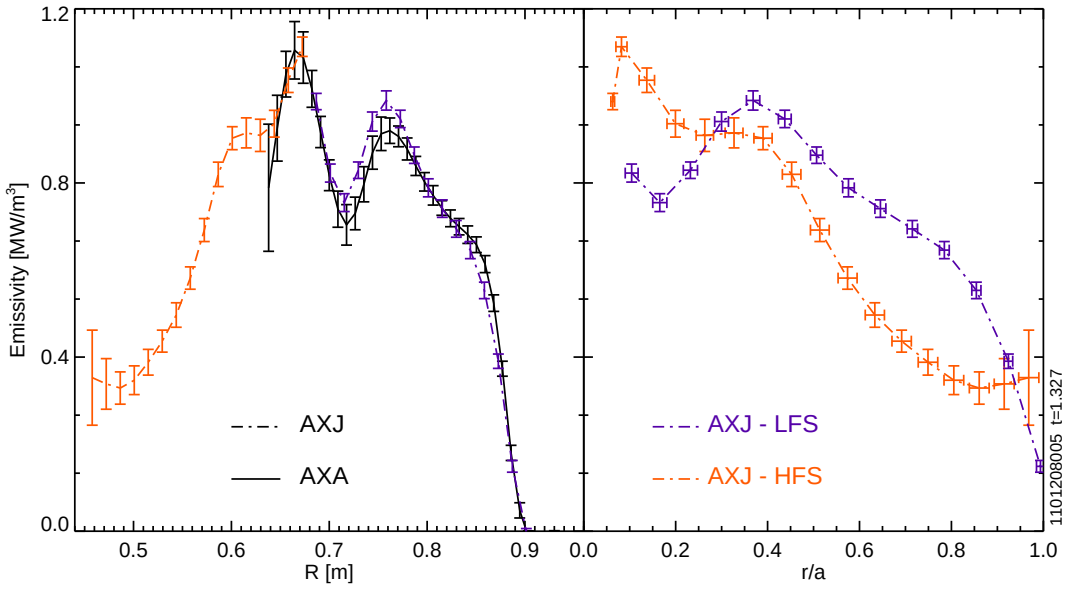

(a)

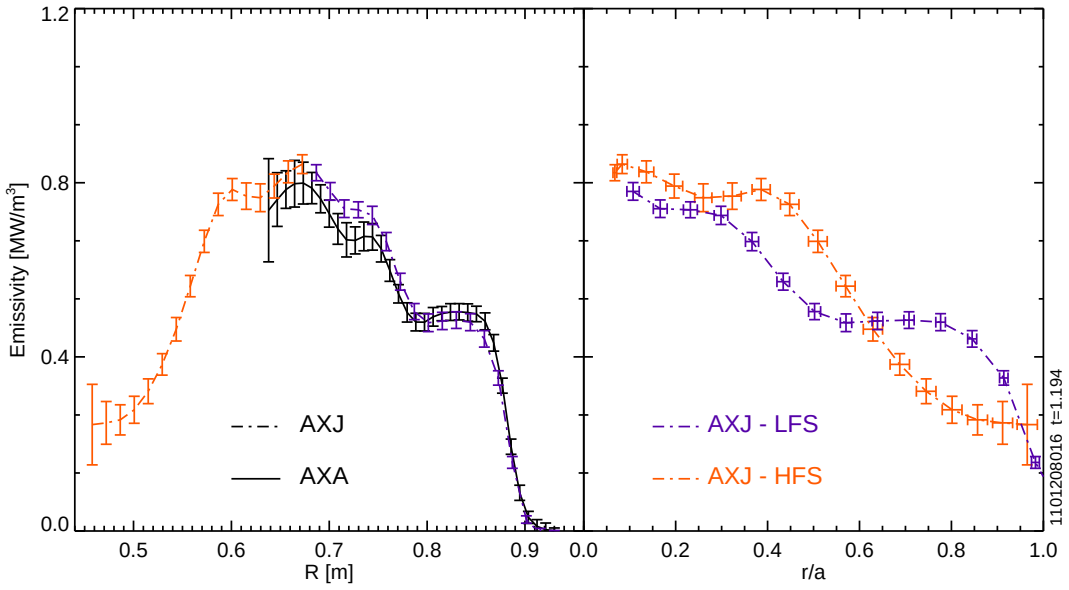

(b)

Figure 5-6: Midplane emissivity in on-axis and LFS-heated plasmas. Profiles from AXA (solid) and AXJ (dashed) plotted against major radius (left) and AXJ for r/a (right) for resonance layer location of $R \sim 0.68$ (a) and 0.76 (b)

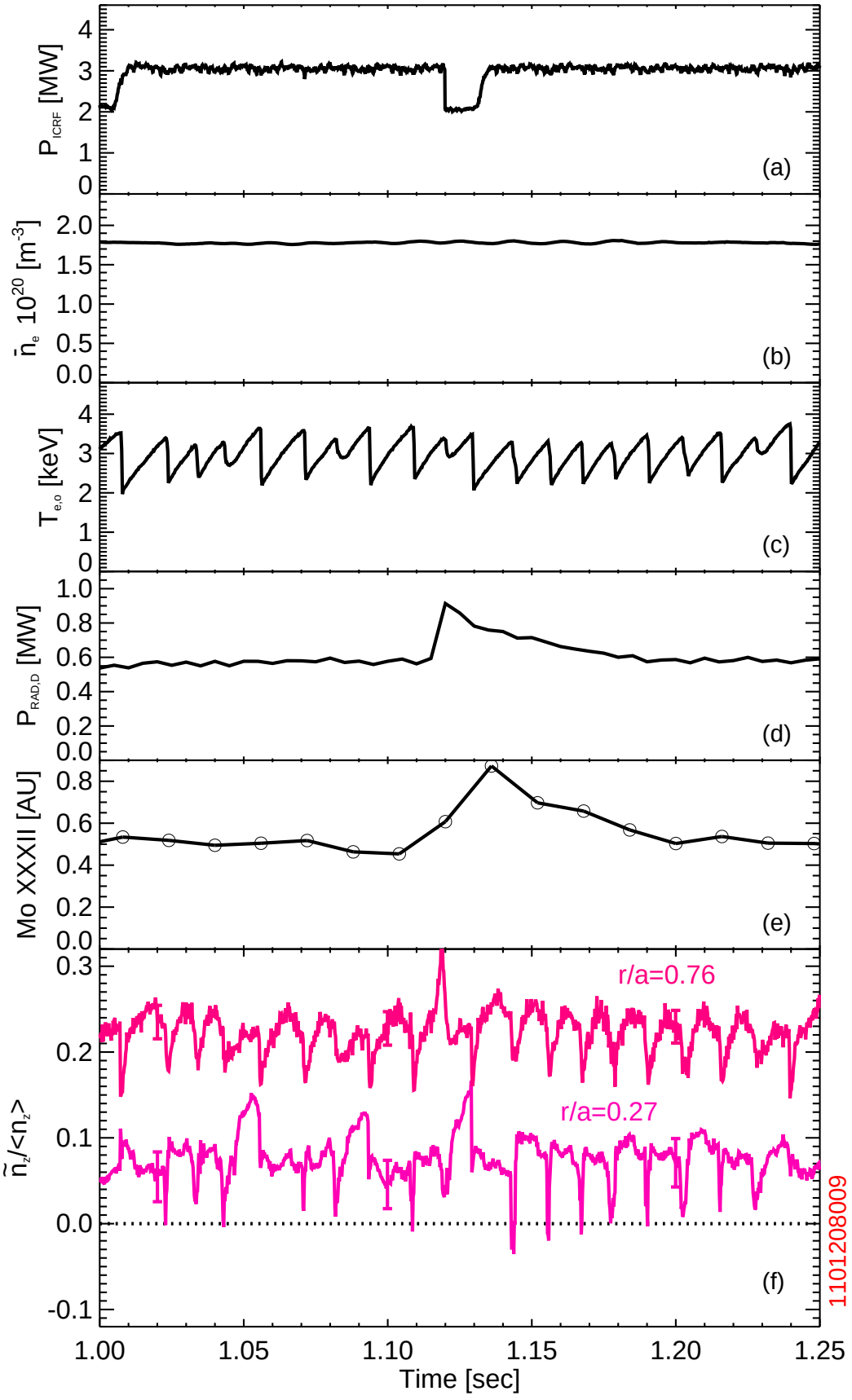

Figure 5-7: The time-evolving in/out asymmetry over a natural Mo injection

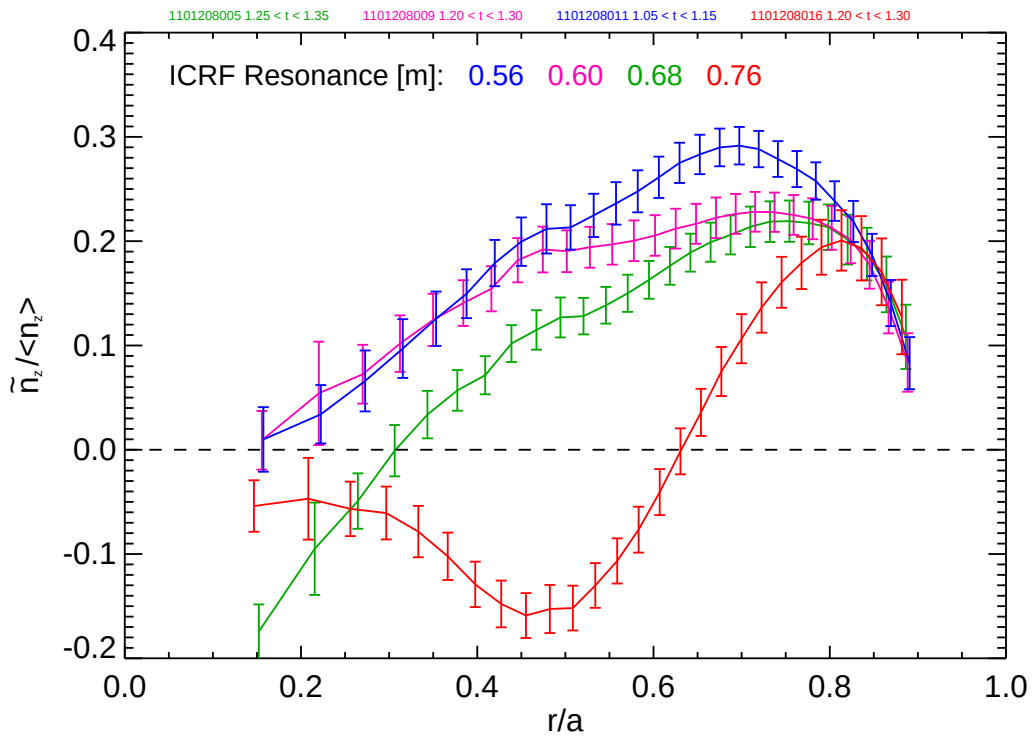

Figure 5-8: Radial profiles of the in/out asymmetry measured for different locations of the ICRH resonance layer

This same comparison is shown for the B_t=6.0 T, LFS heated plasma in Figure 5-10. While the experimental results agree with inertial-only modeling at $r/a \sim 0.7$, a large discrepancy is observed for $0.30 < r/a < 0.65$, where the ICRH power is expected to be deposited. Both also exhibit a small up/down asymmetry of $n_{sin}/\langle n_z \rangle \leq 0.1$.

In Figure 5-11, measured asymmetries at $r/a \sim 0.2$, 0.5 and 0.8 are plotted for the full toroidal field scan. Far off-axis, $r/a \sim 0.8$, the asymmetry is relatively independent of the resonance layer location and the small variation is likely due to shot-to-shot changes in ω, T_e and T_i. Near the magnetic axis, $r/a \sim 0.2$, the sign of $n_{cos}/\langle n_z \rangle$ is driven negative as the resonance layer is moved through this layer. Further off-axis, $n_{cos}/\langle n_z \rangle$=0 in the core for both LFS and HFS heated plasmas.. At mid radius, $r/a \sim 0.5$, the asymmetry response differs. As the resonance layer is scanned to the LFS, $n_{cos}/\langle n_z \rangle$ decreases, eventually becoming negative, similar to the response to on-axis heating. As the layer is scanned towards the HFS, $n_{cos}/\langle n_z \rangle$ becomes more positive, even as the resonance layer passes through $r/a \sim 0.5$. Such behavior is qualitatively consistent with resonance localization, as differences are found when the resonance layer is at the same minor radius but on different sides of the magnetic axis.

The discrepancy between the measured and modeled in/out asymmetries can also be linked to the ICRH dynamically. The input power is ramped down to zero over 1.40-1.42 seconds, prior to the start of the current and field ramp down at 1.5 seconds, and the measured asymmetry profiles change quickly, moving much closer to the ICRH-free modeling shown in Figures 5-9 and 5-10. Cross-field transport, $\tau_E \sim 30$ ms, is marginally slower than the fast-ion slowing down time, 20 ms, while the parallel impurity equilibration time is faster than both, ~ 1 ms. It is postulated that as the ICRH is removed, pitch angle scattering reduces $T_\perp/T_\parallel$, and the parallel impurity equilibrium is modified before the background plasma changes significantly, relaxing the asymmetry profiles back to their steady-state values.

Figure 5-12 shows the time history of $n_{cos}/\langle n_z \rangle$ (f) at $r/a \sim 0.16$ and 0.6 in the HFS-heated plasmas along with the background plasmas parameters. The line-averaged density (b) remains constant while the (ECE-based) electron (c) and ion

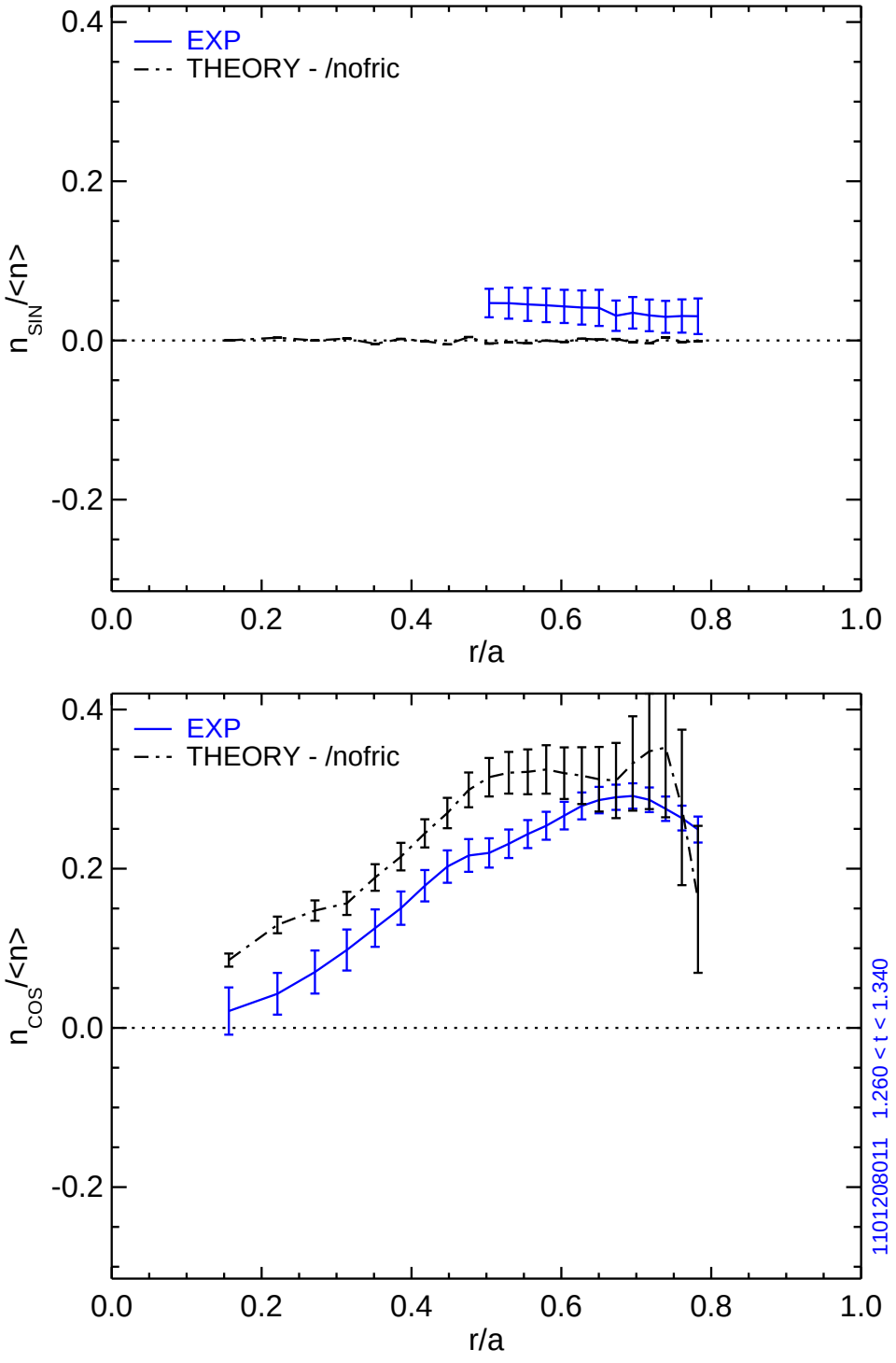

Figure 5-9: Comparison of $\tilde{n}_z/\langle n_z \rangle$ to inertial modeling for plasma with HFS heating

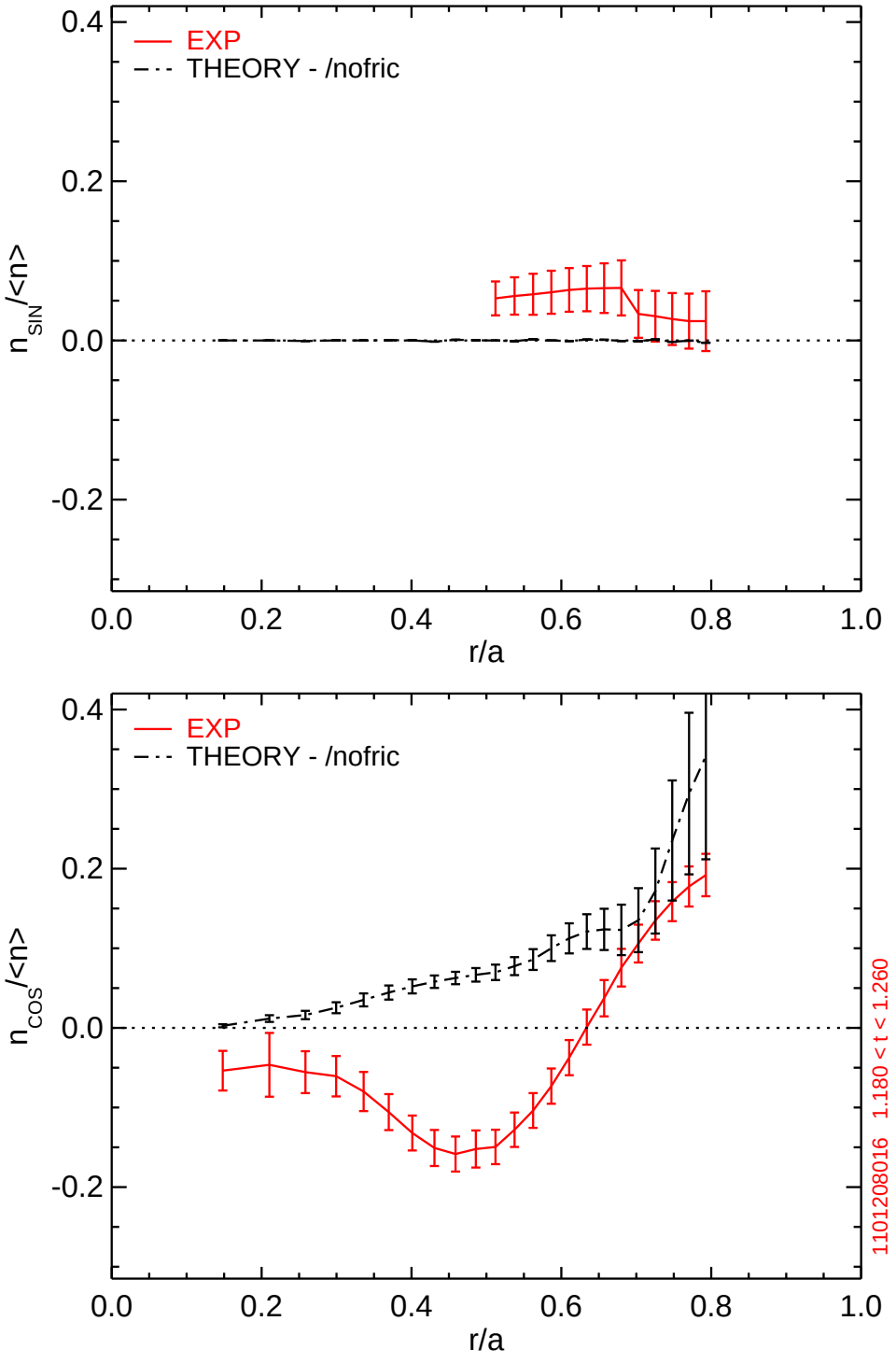

Figure 5-10: Comparison of $\tilde{n}_z/\langle n_z \rangle$ to inertial modeling for plasma with LFS heating

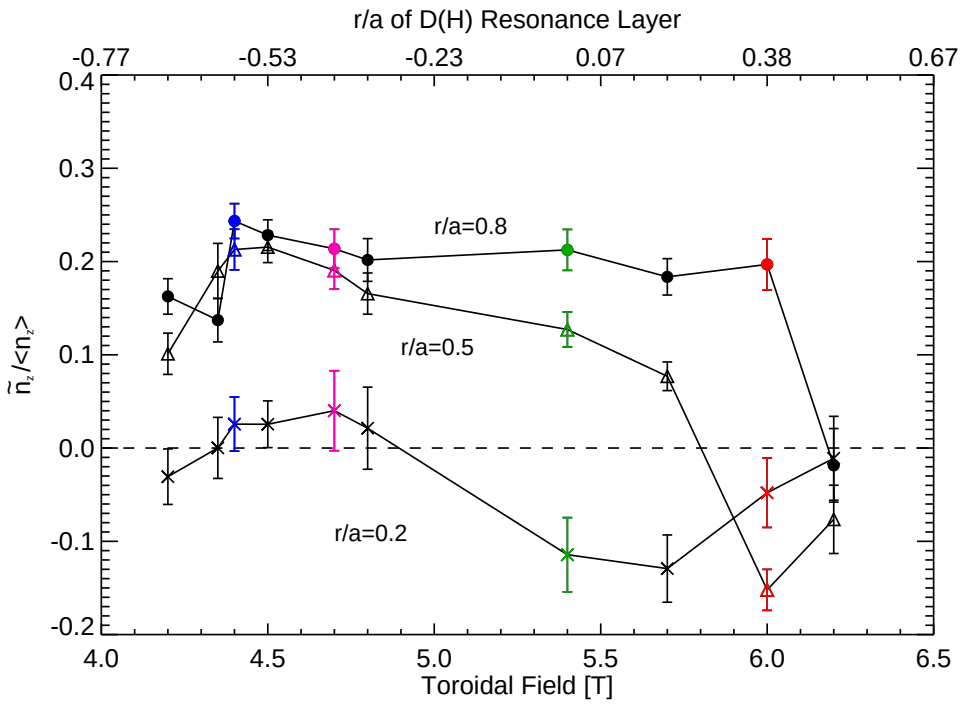

Figure 5-11: Asymmetry at various r/a over the field scan showing different response for LFS and HFS heating

temperature (d) drop on the energy confinement time scale when the ICRH power (a) is removed. The change in rotation (e) lags behind the temperature drop. Note that the ion temperature and rotation are from line-integrated core views of H-like Ar, and are used instead of inversions to obtain faster time resolution. Small changes, $n_{cos}/\langle n_z \rangle \sim 0.05$ occur in the asymmetry over $1.41 < t < 1.44$, and impurities move even further to the low-field side. These small changes lag behind the turn off of the ICRF power and thus could be due the increase in the Mach number as the ion temperature drops relative to the rotation. After $t \sim 1.435$, the asymmetry at $r/a = 0.6$ decays on the energy confinement timescale as the plasma begins to slow down. For the core asymmetry, the modulation by sawteeth is clearly evident, with the impurities becoming more localized on the outboard side after each sawtooth crash.

In Figure 5-13, the same plots are shown for the LFS-heated plasma for the in/out asymmetries at $r/a = 0.5$ and 0.7. The largest change is observed at $r/a = 0.5$, just outside of the resonance layer at $r/a = 0.38$, where an initial $n_{cos}/\langle n_z \rangle \simeq -0.15$ moves

quickly to $\simeq 0.04$ over 1.40 to 1.44 seconds. In comparison to the previous example, changes in the asymmetry profile occurs promptly following changes to the rf power level. The up/down asymmetry does not show a prompt response to changes in ICRH power.

These results show that centrifugal effects cannot explain the in/out asymmetry profiles in the LFS-heated plasma and that differences are closely linked to the presence of ion cyclotron heating. In contrast, the HFS-heated plasmas do not exhibit as much sensitivity to the ICRH and are in reasonable agreement with the centrifugal force-based models. These observations are consistent with the explanation of an asymmetry driven by minority-induced poloidal electric fields, and in order to provide quantitative evidence, measurements are compared to the extended parallel impurity transport theory derived in Section 5.1. The minority temperature anisotropies computed from TRANSP, shown in Figure 5-4, are used calculate $\eta = T_\perp/T_\parallel - 1$ and (5.18) is used in the parallel transport code as described in Appendix A. A $Z_{eff} = 2.0$ is calculated from neoclassical resistivity and included in the modeling along with a minority fraction of 4%, the same used in the TRANSP simulations.

Figure 5-14 compares measured and modeled $n_{cos}/\langle n_z \rangle$ profiles in the HFS-heated plasmas with the effect of ICRH heating included (b), showing little difference to modeling using only inertia (a). The agreement between theory and experiment is slightly improved and the change is consistent with the transient $\Delta n_{cos}/\langle n_z \rangle \sim 0.05$ seen when ICRH is removed.

For the LFS-heated plasma, the same comparison is shown in Figure 5-15 where substantially better agreement is observed when using the extended theory (b) in comparison to when ICRH effects are ignored (a). Remaining differences could possibly be explained by uncertainties in the modeling inputs such as the minority fraction or in the physics omitted from the TRANSP simulation. For example, the detailed structure in the anisotropy profiles shown in Figure 5-4 and reflected in 5-15 may be smoothed out when finite orbit effects are taken into account.

The sensitivity of the impurity asymmetry to the minority fraction is not monotonic despite the explicit dependence in (5.17), because a smaller minority fraction will

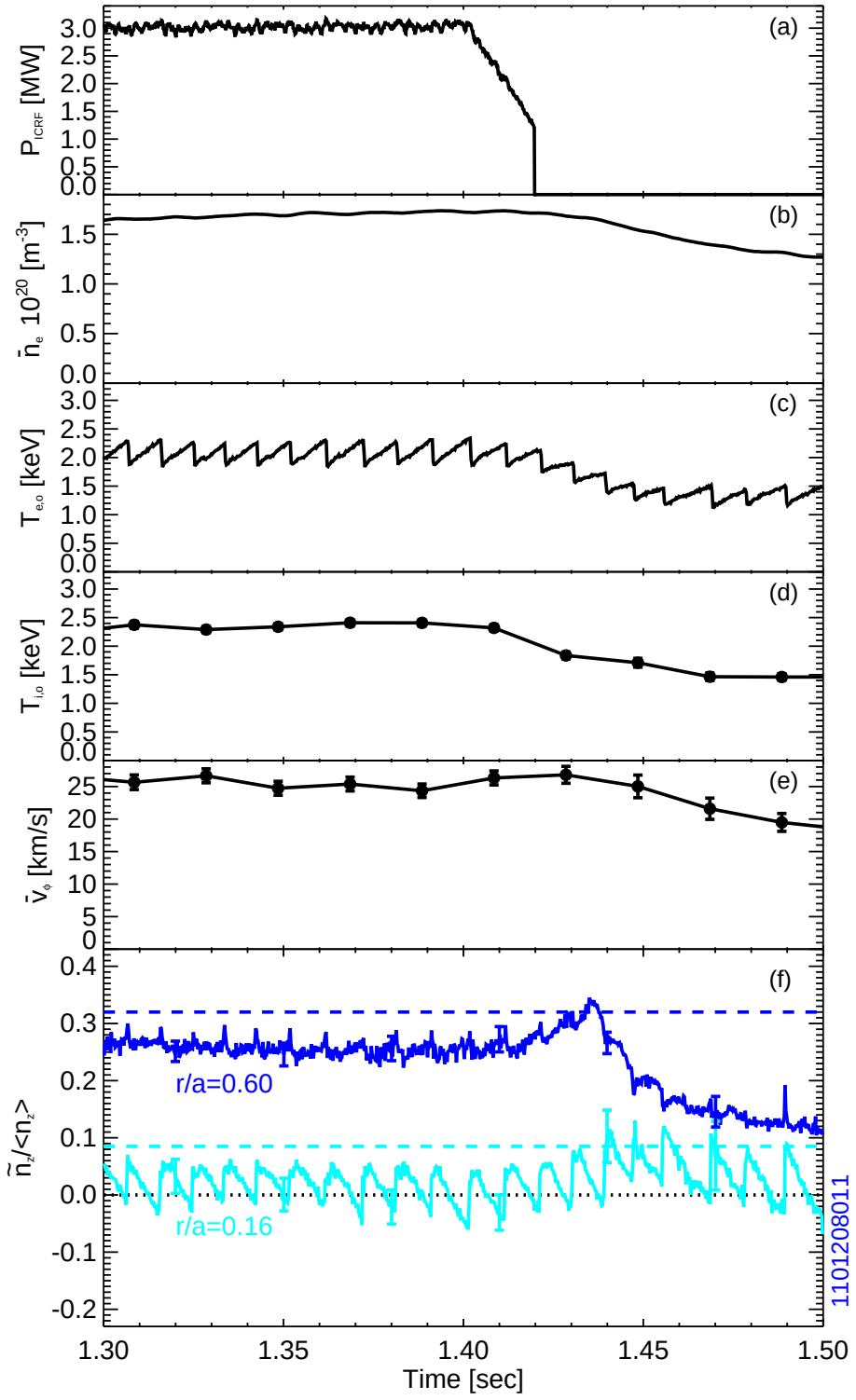

Figure 5-12: Prompt evolution of the asymmetry as HFS heating is removed

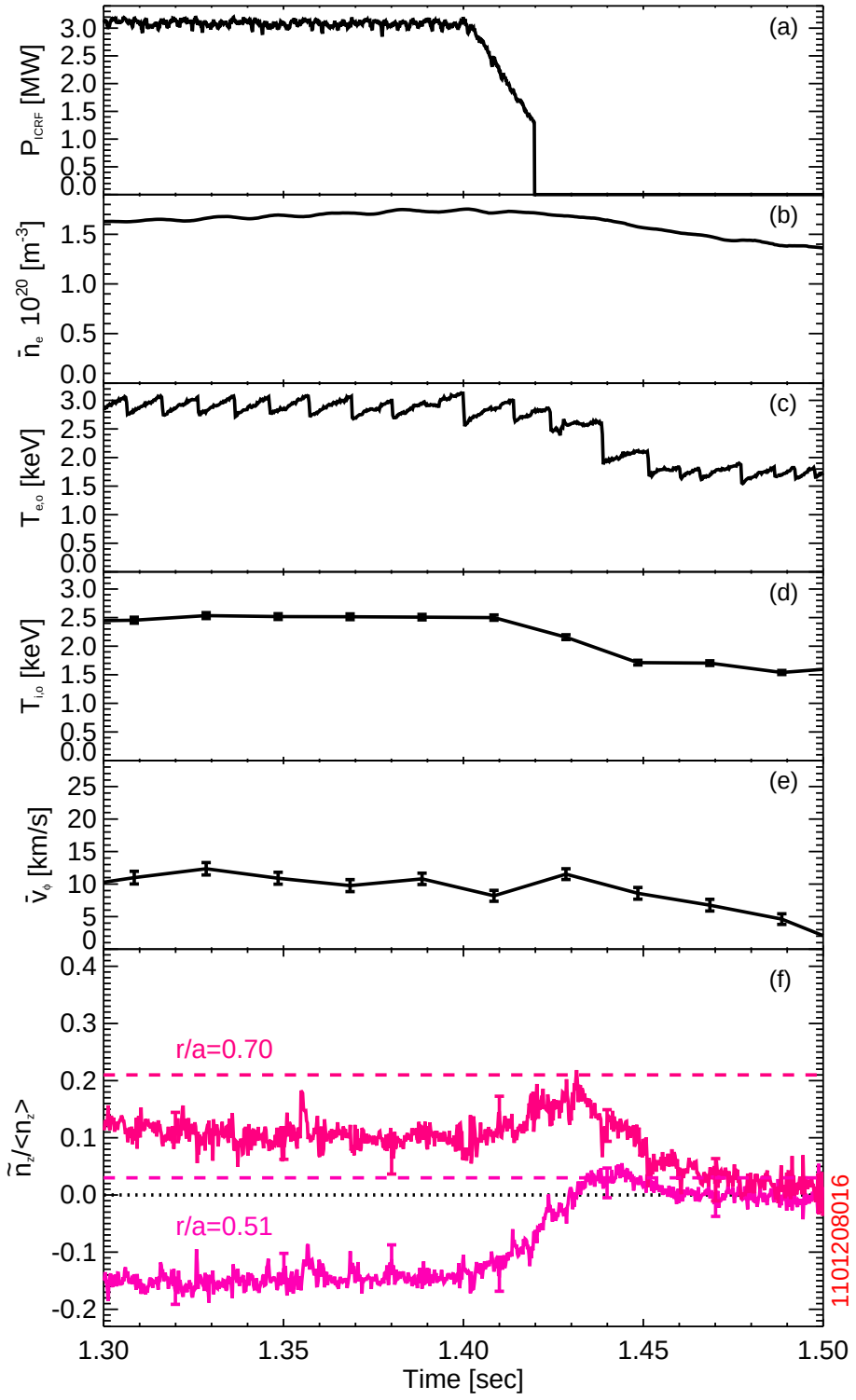

Figure 5-13: Prompt evolution of the asymmetry as LFS heating is removed

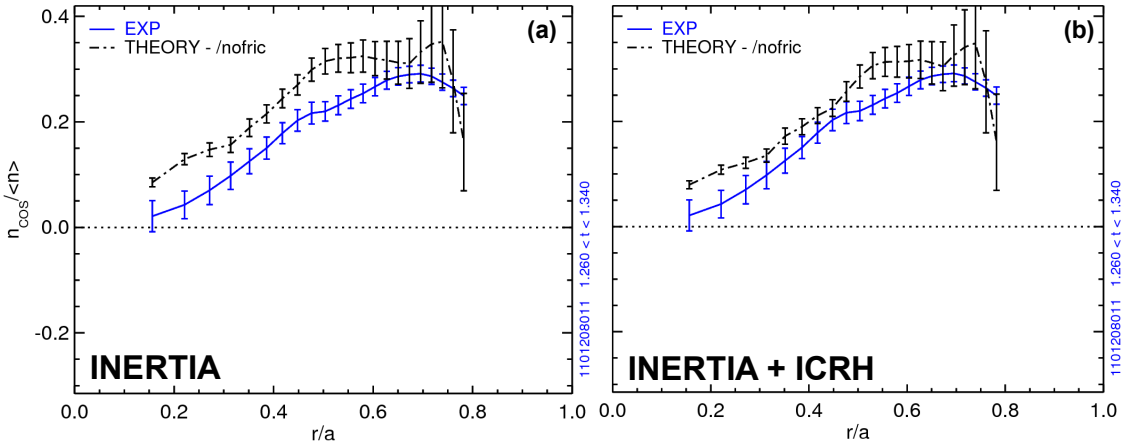

Figure 5-14: Comparison of $\tilde{n}_z/\langle n_z \rangle$ in HFS heating to modeling using only inertia (a) and extended theory including inertia and ICRH effects (b)

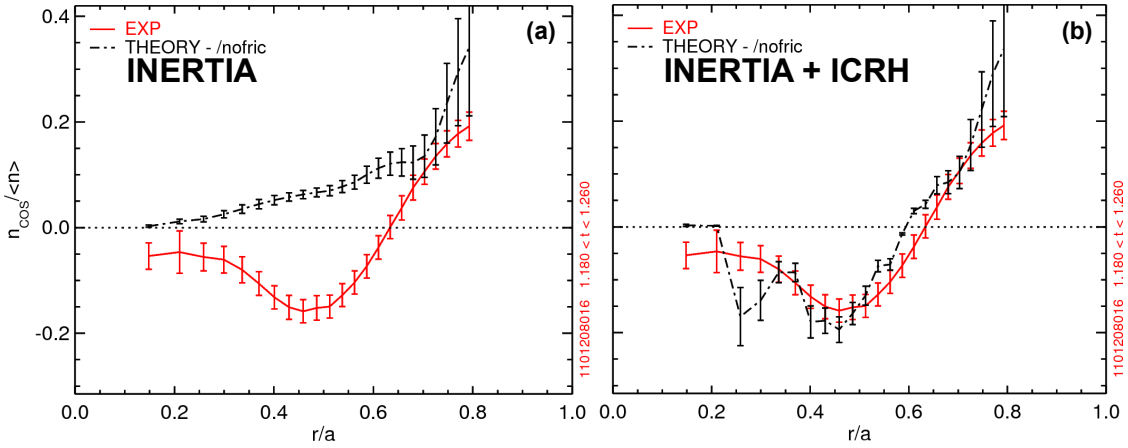

Figure 5-15: Comparison of $\tilde{n}_z/\langle n_z \rangle$ in LFS heating to modeling using only inertia (a) and extended theory including inertia and ICRH effects (b)

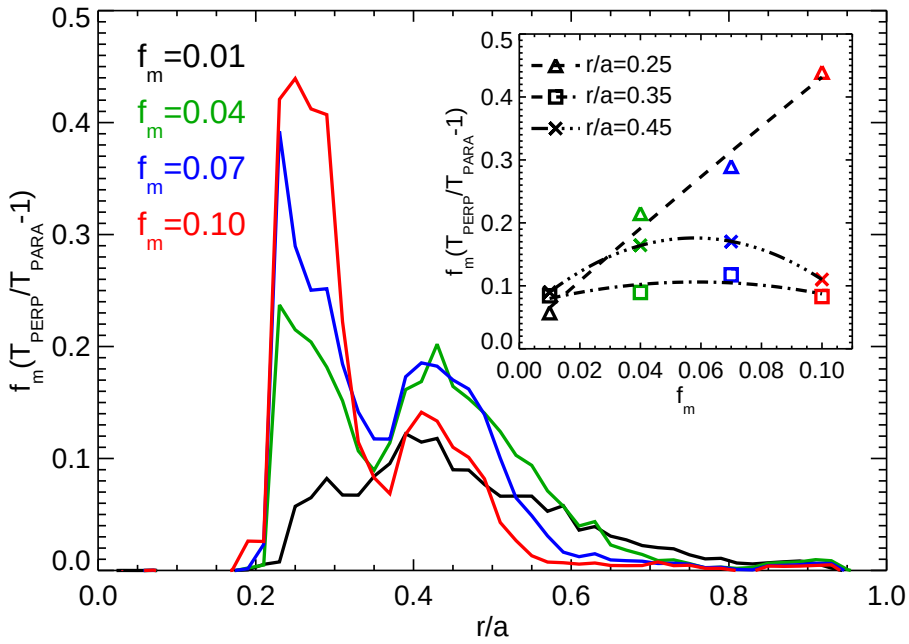

Figure 5-16: TRANSP predicted ICRH-induced asymmetry with different assumptions of the minority fraction, f_m, in the LFS-heated plasma

increase the anisotropy, η, due to increased power per particle. TRANSP simulations were completed varying the minority fraction from 1% to 10% in order to estimate the sensitivity to the assumed f_m (taken as 4% in the data shown in Figure 5-15). In Figure 5-16, the radial profiles of $f_m(T_\perp/T_\parallel - 1)$ are plotted for different minority fractions, with the inset showing its variation with f_m at fixed r/a. As derived in the circular, small inverse aspect ratio limit (5.13), the in/out asymmetry is proportional to $f_m(T_\perp/T_\parallel - 1)$. The feature at $r/a \sim 0.25$ is shown to grow nearly linearly with f_m, although only a factor of 5 change in asymmetry is predicted for a factor of 10 increase in f_m, indicating there is still an offset due to a reduction of $T_\perp/T_\parallel$ at higher minority fractions. In contrast, the $f_m(T_\perp/T_\parallel - 1)$ between $0.35 < r/a < 0.65$, where the largest in/out asymmetry is measured, is relatively insensitive to the assumed f_m, exhibiting a quadratic behavior.

It is also worth demonstrating the sensitivity of the modeling to Z_{eff}. As derived in Section 2.1, inclusion of non-trace impurities results in the reduction of the asymmetry by short-circuiting the poloidal electric field. The comparison between modeling and

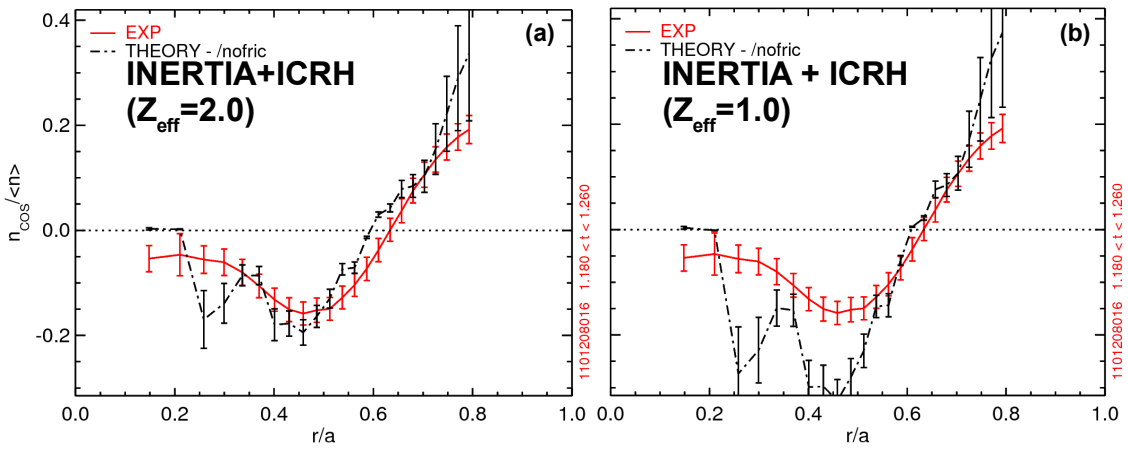

Figure 5-17: Comparison of $\tilde{n}_z/\langle n_z \rangle$ in LFS heating to extended theory using measured $Z_{eff} = 2$ (a) and $Z_{eff} = 1$ (b)

measurement is shown in Figure 5-17 where $Z_{eff} = 2$ (a) and $Z_{eff} = 1$ (b) are assumed. A substantially larger inboard accumulation of impurity density is predicted if the Z_{eff} contribution is omitted.

The extended theory also predicts the poloidal dependence of the minority density to vary smoothly like $1/B^{\eta}$ (5.4). For the LFS-heated plasma, Figure 5-15b shows that at $r/a = 0.51$, the magnitude of the modeled in/out asymmetry is in good agreement with measurements, and WB2AX and WB3AX can be used to investigate higher order poloidal variation. Figure 5-18 shows plots of $n_z(\theta)/n_z(0)$ from experimental data (discrete points), the fitted $m = 1$ variation (black lines) and the variation predicted by the extended theory (green line). Besides the small up/down asymmetry captured by the wall boxes, theory predicts a similarly shaped profile. Within their poloidal resolution, the wall boxes do not show any poloidally localized peaking, further validating the $1/B^{\eta}$ model.

5.2.3 Description of ICRH Experiments at 70 MHz

Another group of plasmas exhibiting strong in/out asymmetries was observed when exploring the sensitivity of the H-mode threshold power to the magnetic field at low densities, $\bar{n}_e \sim 0.6{\times}10^{20}$ m^{-3}. The threshold has been shown to increase strongly at low $\bar{n}_e$ [138] resulting in plasmas with a large rf power per particle. This increases

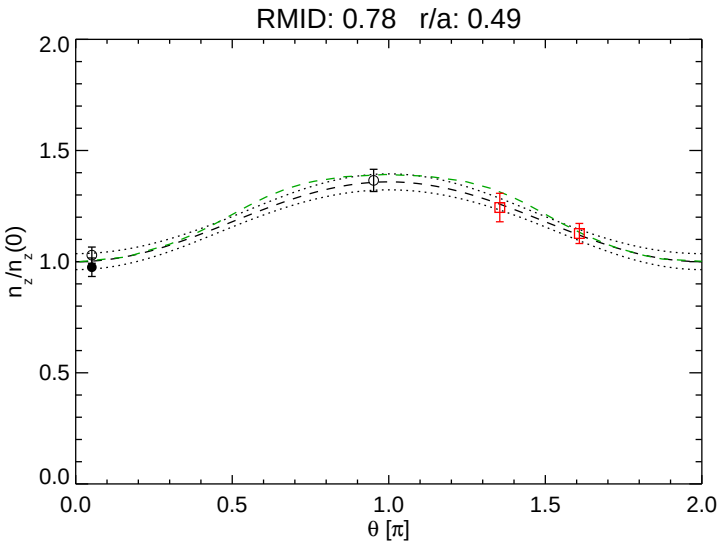

(a)

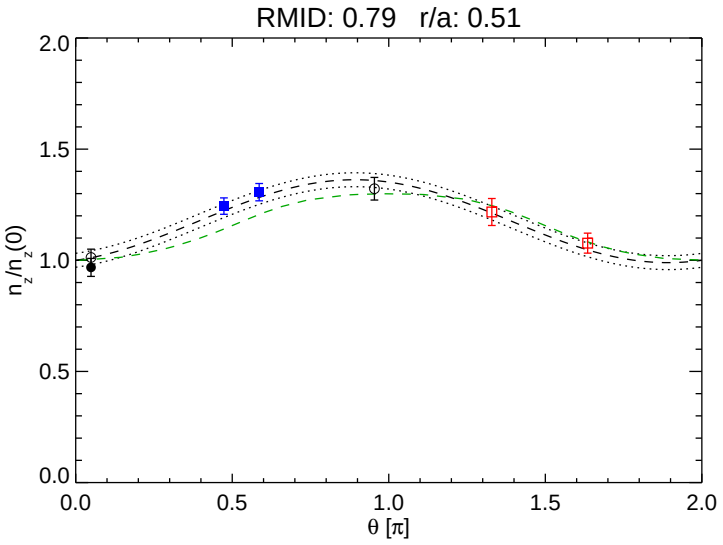

(b)

Figure 5-18: Comparison of $n_z(\theta)/n_z(0)$ to extended theory for plasma with LFS heating near the resonance layer; AXA (●), AXJ (○), WB2AX (■), WB3AX (□) and WB4AX (△)

$T_\perp/T_\parallel$ and, in C-Mod's case, also elevates the molybdenum content. In order to use hydrogen minority heating over a wider range of magnetic fields, the experiment used the J-ANT at 70 MHz to be able to heat inside $r/a \sim 0.5$ for $4.0 < B_t < 5.3$. Figure 5-19 shows the variation of the resonance layer with respect to the magnetic geometry.

The time history of the background plasma parameters are shown in Figure 5-20 where the line-averaged density (a) and the programmed ICRH power (b) are kept constant shot-to-shot. These low-density plasmas do not exhibit the same scaling of toroidal rotation (f) with stored energy as other regimes on Alcator C-Mod [129] and are observed to have low core rotation, < 5 kHz. Despite the presence of sawteeth, no precursor mode is seen on the magnetics or SXR arrays implying a low rotation frequency, in agreement with soft x-ray Doppler spectroscopy. A slowly rotating plasma with substantial off-axis ICRH provides a good test of the extended theory with only self-pressure and electric fields (5.8).

5.2.4 Results

Figure 5-21 shows the KLIM profiles in the $B_t = 5.3$ T, LFS-heated plasma where there is good agreement between AXA and AXJ, and a substantial, almost exclusive high-field accumulation. The KLIM and wall box data are used to determine the $n_{cos}/\langle n_z \rangle$ profiles for each shot shown in Figure 5-20, averaging over the $0.80 < t < 0.85$ when all discharges are still in L-mode. Figure 5-22 shows the asymmetry profiles demonstrating that the inboard accumulation is reduced as the resonance moves to the high-field side. Unlike plasmas discussed in Section 5.2.2, these discharges do not exhibit any significant core intrinsic rotation, so when ICRH effects are reduced by moving to HFS heating, only a small in/out asymmetry, $n_{cos}/\langle n_z \rangle \sim 0.05$ is observed.

This lack of rotation can also be used to demonstrate the density dependence of the ICRH effects on the asymmetry. At higher density, the rf power per particle is reduced, and the rate of energy transfer from fast-ions to the background plasmas is enhanced, both working decrease the high energy tail of the distribution function.

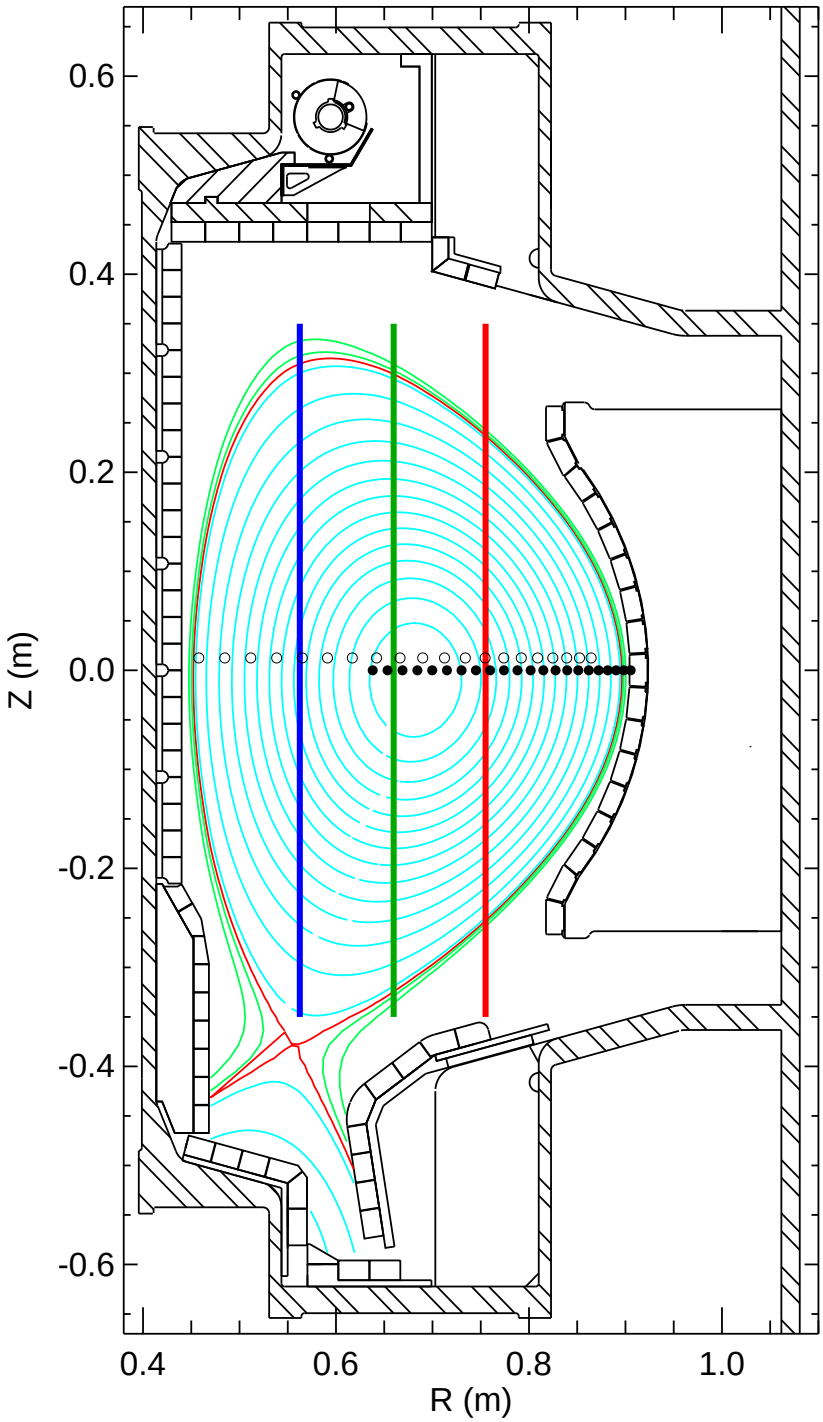

Figure 5-19: Plot of the equilibrium and resonance layer locations for the 70 MHz experiments including the AXA (•), AXJ (○) tangency radii

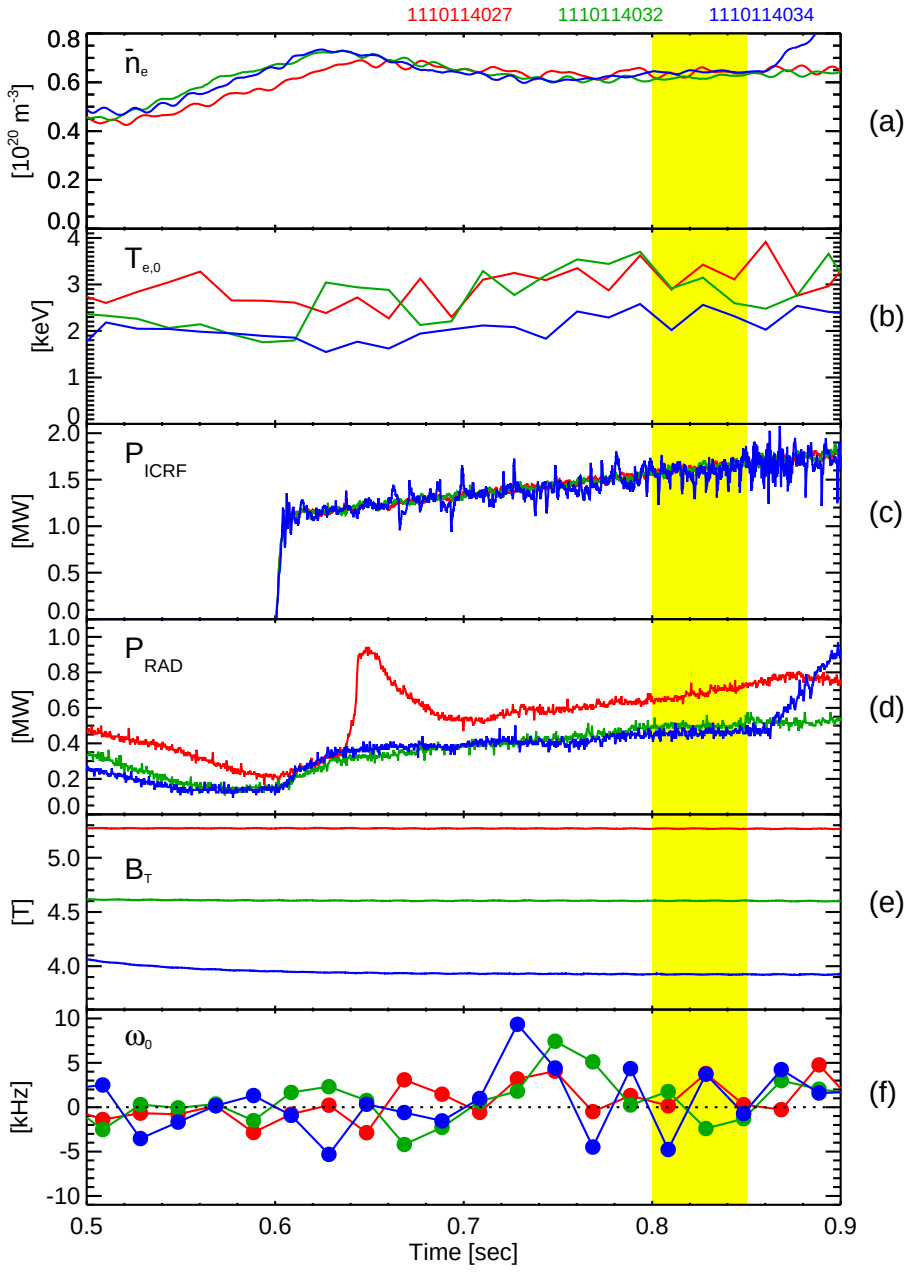

Figure 5-20: Time evolution of relevant plasma parameters for a resonance layer scan with J-ANT at 70 MHz

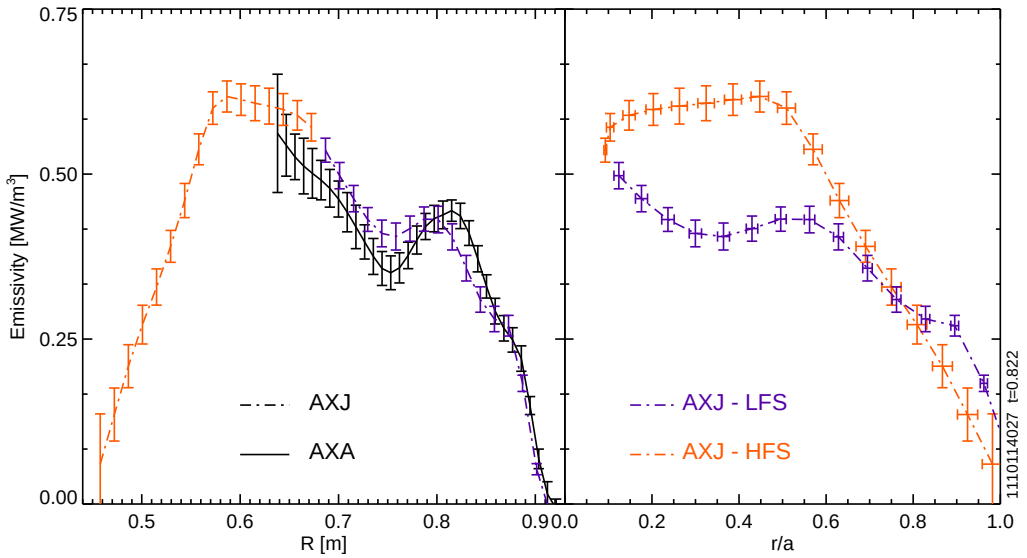

Figure 5-21: AXA and AXJ profiles from a LFS-heated slowly rotating plasma showing substantial inboard accumulation

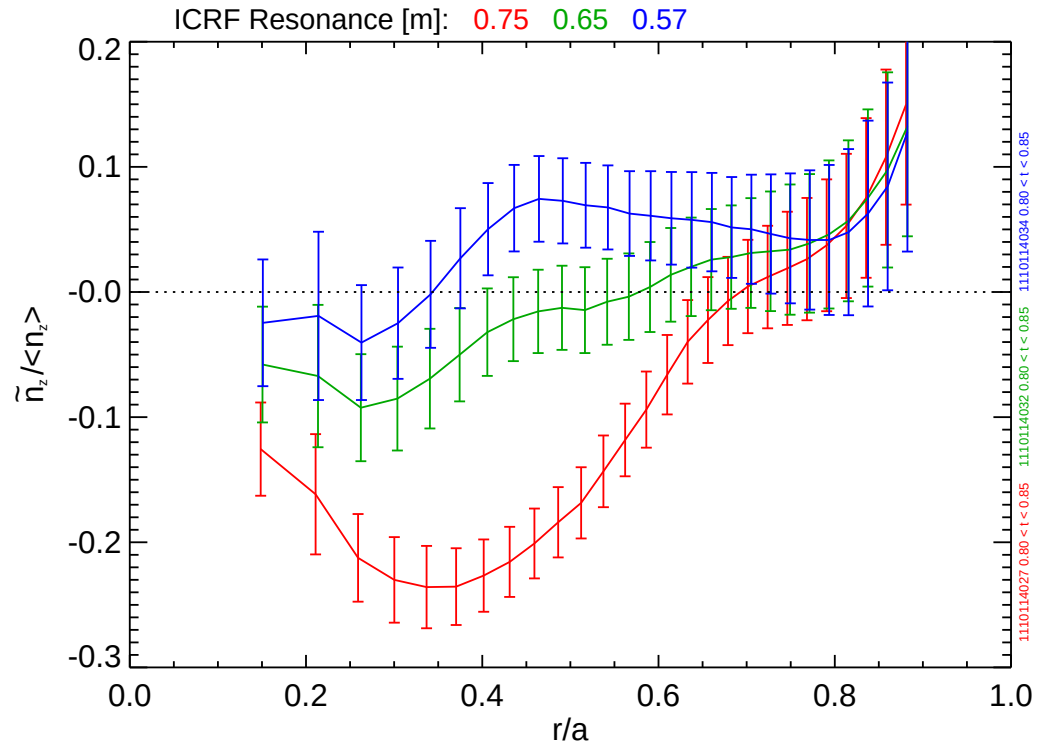

Figure 5-22: Comparison of $n_{cos}/\langle n_z \rangle$ profiles for the resonance layer scan at 70 MHz

Since this energy is input via ion cyclotron waves, and thus preferentially increases $E_\perp$, reducing the high energy tail also reduces the pressure anisotropy responsible for inboard impurity accumulation. Figure 5-23 shows the time evolution of the LFS-heated plasma across a transition into ELM-free H-mode occurring at t=1.20 seconds. At this time there is a break in slope in the line-integrated density (b) simultaneous with the prompt change in deuterium Balmer-α emission characteristic of the change in edge recycling. The electron (c) and ion (d) temperatures rise after the transition, but eventually begin to drop as the density continues to increase, leading to an H-L backtransition at 1.33. As during the L-mode phase, the core rotation (e) is observed to be small and does not respond according to the usual correlation of rotation with stored energy. The in/out asymmetries (f) near the resonance layer at $R \simeq 0.75$ ($r/a = 0.3$) and farther off-axis at $r/a \sim 0.6$ are shown to increase toward zero on the same time scale as the density rise.

While the trend during the H-mode is to reduce the core asymmetry, the prompt change in the asymmetry at the L/H transitions is somewhat puzzling. Immediately following the transition there is a break in slope in the asymmetry, and $n_{cos}/\langle n_z \rangle$ at $r/a = 0.3$ increases over the next 10 ms without any significant change in the core profiles. This time evolution is similar to changes shown in Figure 5-13 when the input power is ramped down. The KLIM profiles at $t = 1.193$ and 1.210, are shown in Figures 5-24a and 5-24b, respectively. While there is some time evolution of the asymmetry over the sawtooth, these profiles are from approximately the same phase in the cycle. The qualitative structure of the radial profile remains similar, but the prompt change in the in/out asymmetry is localized to $0.15 < r/a < 0.35$, near the resonance layer.

Based on the fast-ion physics thought to be responsible for the impurity asymmetry, this would imply a change in their distribution function without a significant change in local plasma properties. One possibility is that the large banana orbits of the magnetically trapped minority ions could be sampling other parts of the plasma that have responded to the H-mode transition. Increased collisional damping or pitch angle scattering of trapped ions would decrease $T_\perp/T_\parallel$, and thus reduce the asym-

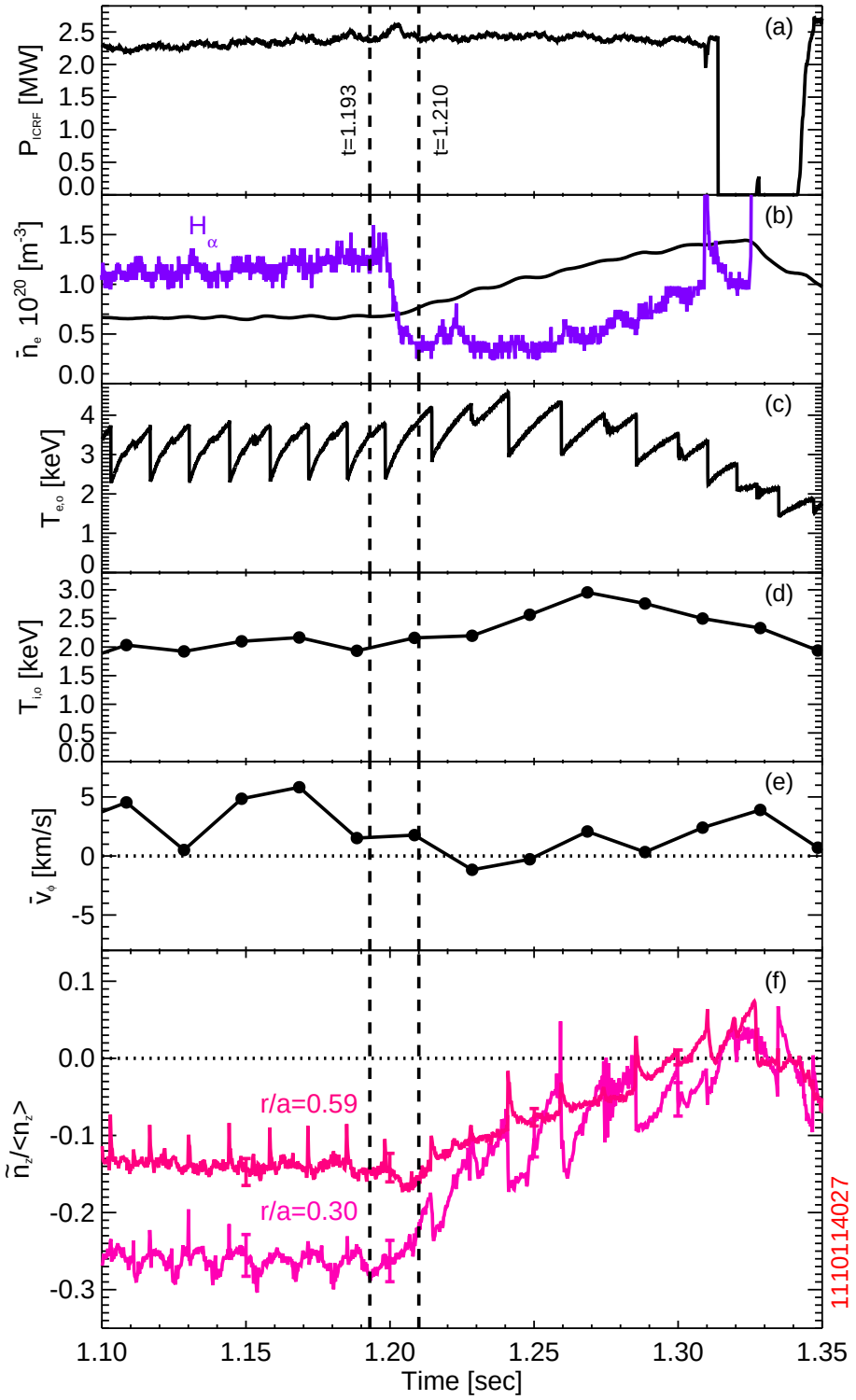

Figure 5-23: Prompt evolution of the asymmetry during HFS at L/H transition

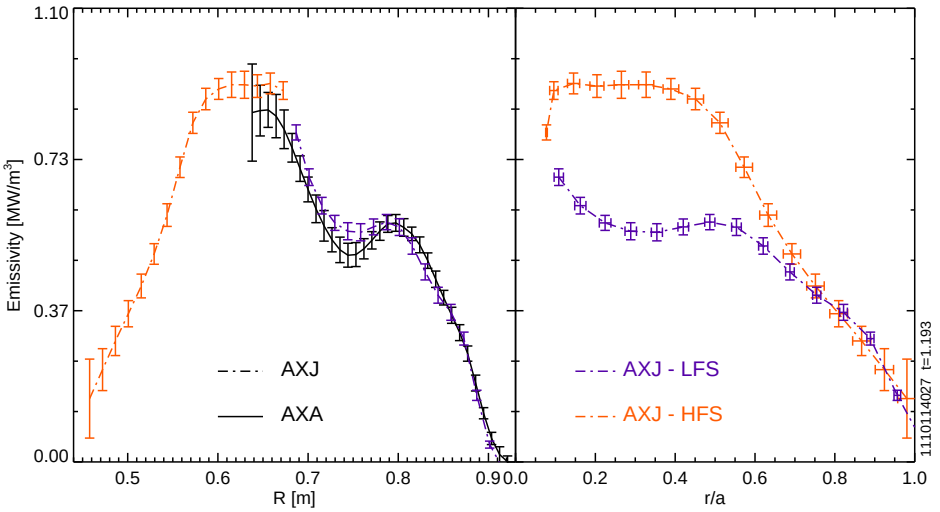

(a)

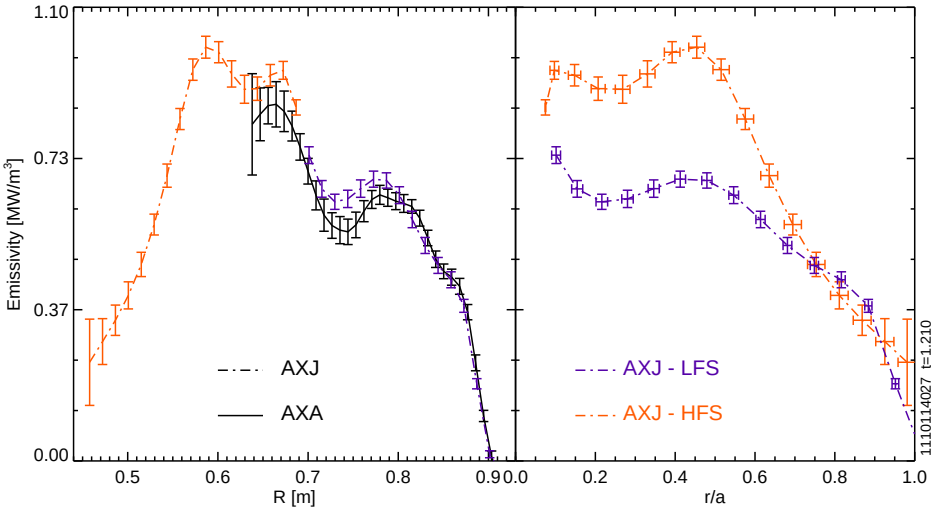

(b)

Figure 5-24: Comparison of KLIM profiles immediately before (a) and after (b) the L/H transitions showing a change near the resonance layer.

metry. Another explanation lies in the change of the wave propagation across the H-mode transition since the wave power must propagate through the edge plasma, the only region to have changed substantially in such a short time. The density change at the edge would need to reduce the cyclotron wave fields, dropping the rf power density in the core. A reduction in $T_\perp/T_\parallel$ would occur as energy is removed from the fast-ions via collisions but not replenished as fast as in the L-mode phase. This is consistent with the observation that the asymmetry near the resonance layer changes promptly. Initial TORIC runs suggest that if this is occurring, it must be in the SOL profiles [139].

Instead of comparing measured and modeled asymmetries as done in Section 5.2.2, the analysis will be worked in reverse with the measured asymmetry used to estimate the minority pressure anisotropy from (5.8), which assumes no inertial effects. This will then be compared to the $p_\perp/p_\parallel$ ratio calculated from TRANSP simulations. The asymmetry just prior to the L/H transition measured in the LFS-heated 70 MHz plasma is used, averaging over $1.14 < t < 1.18$. A $Z_{eff} = 3.5$, calculated from neoclassical conductivity, is assumed to be flat across the plasma and experimental T_e and T_i profiles are used. A flat minority fraction of 4% is also assumed, the same as for the TRANSP simulation. The poloidally varying emissivities at each r/a from the KLIM arrays and the wall boxes, where available, are normalized to the average of the AXA and AXJ emissivies on the low-field side to find $n_z(\theta)/n_z(0)$. Figure 5-25 shows the measured data against the predictions based on (5.8) for various values of $\eta = T_\perp/T_\parallel - 1$.

Values of η at various r/a are found via visual inspection, and the resulting radial profile of the temperature anisotropy is plotted in Figure 5-26, with estimated uncertainties. The calculation from experiment (red dashed line) shows the anisotropy extending farther into the core plasma, inside the resonance layer, while TRANSP (black lines) shows $T_\perp/T_\parallel$ dropping to unity inside of $r/a = 0.3$. At larger minor radii, the TRANSP prediction for $T_\perp/T_\parallel$ is higher then calculated from experimental asymmetry data. These two examples illustrate the possibility of the impurity density asymmetry being used as a tool for investigations into fast-ion physics.

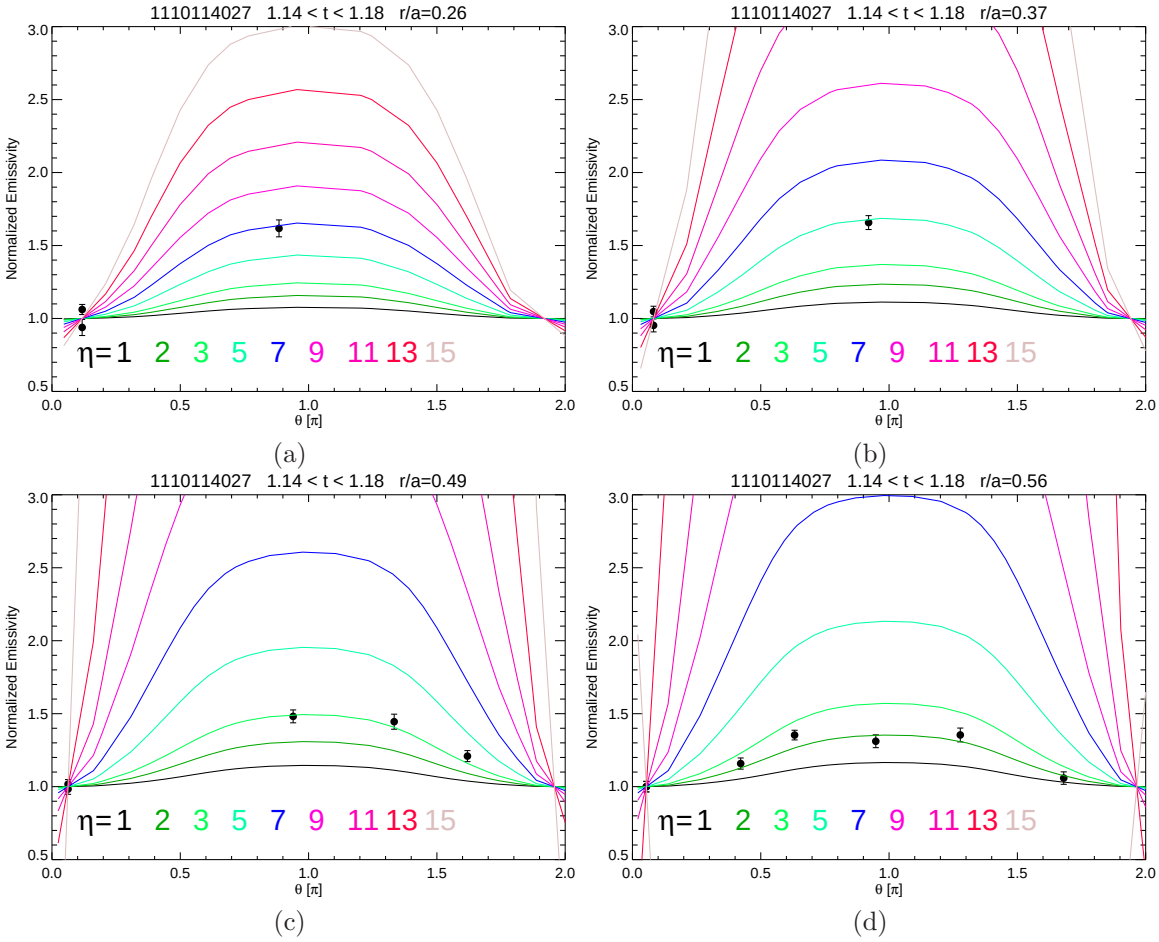

Figure 5-25: Normalized poloidal variation of emissivity computed for various anisotropies compared to measured variation

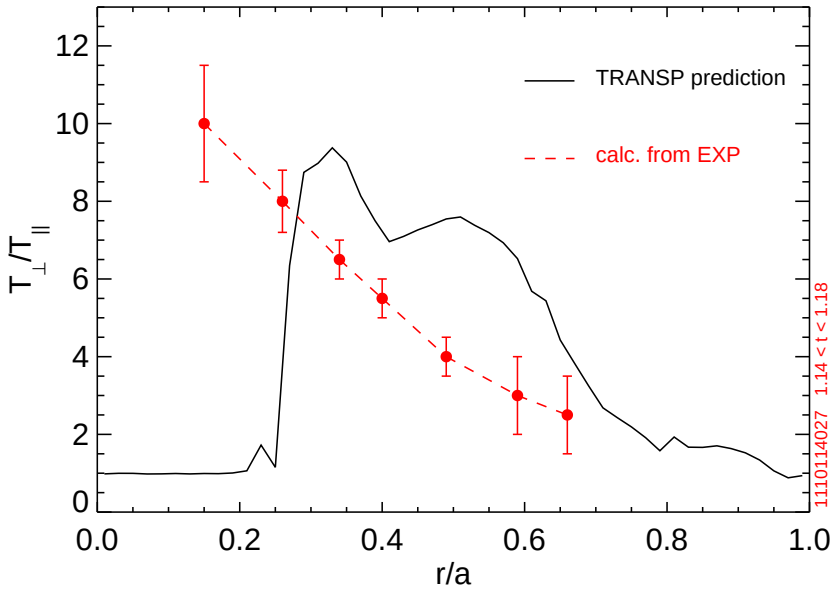

Figure 5-26: Comparison of measured and modeled minority pressure anisotropy profiles for the 70 MHz, LFS-heated plasma

5.3 On Axis Heating In EDA H-Mode Plasmas

In Chapter 4, comparisons between experiment and modeling using only centrifugal effects showed disagreement in the core of EDA H-mode plasmas. While Section 5.2.4 demonstrates that an increase in plasma density would substantially reduce the asymmetry, it is worth examining whether ICRH-effects can reduce any discrepancy in EDA H-modes. TRANSP simulations were performed on the higher current, higher density (1110201017) and lower current, lower density (1110201026) EDA H-modes. The measured $Z_{eff} = 1.8 - 2.0$ from bremsstrahlung, along with the standard 4% hydrogen fraction are used in the simulation. In Figure 5-27, the predicted energy anisotropy is sufficient to change the in/out asymmetry, and affects a slightly wider range of minor radii for the lower-current shot. The resulting $n_{cos}/\langle n_z \rangle$ profile for shot 017 is shown in Figure 5-28 where the inclusion of minority pressure anisotropy eliminates the disagreement between measurement and modeling inside of r/a ~0.3. For 026, shown in Figure 5-29, the core discrepancy is also reduced, but ICRH-effects cannot explain the large difference between modeling and experiment for $0.3 < r/a <$

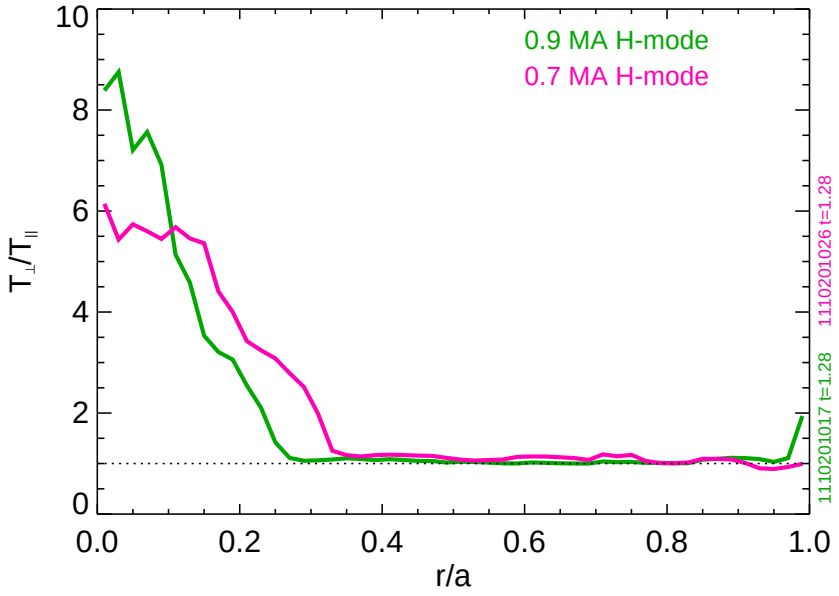

Figure 5-27: The TRANSP-predicted temperature anisotropy of the minority ions for on-axis ICRH heating in EDA H-mode

0.7. In the next chapter, the effect of ion/impurity friction will be added which increases the agreement between theory and experiment for both of these plasmas.

5.4 Summary

In this chapter, parallel impurity transport theory was extended to include the impact of a poloidal electric field driven by a pressure anisotropy in a fast-ion species. Experimental measurements of in/out asymmetries in C-Mod plasmas were shown to be sensitive to ion cyclotron resonance heating using both both 70 and 78-80.5 MHz minority heating schemes. With the resonance layer on the low-field side of the plasma, substantially larger inboard impurity accumulation is observed in comparison to high-field side heating which has little impact on the asymmetry. The link between the in/out asymmetry and ICRH was also demonstrated dynamically, with impurities being redistributed poloidally as the heating power is removed or as the power density is reduced during an ELM-free H-mode. Quantitative comparisons using the extended parallel transport theory compare favorably with measurements using TRANSP sim-

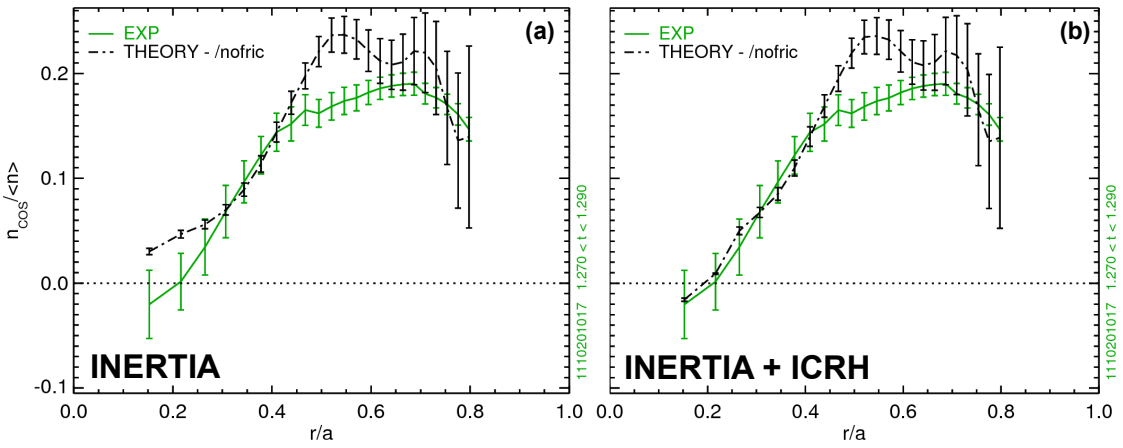

Figure 5-28: Comparison of $\tilde{n}_z/\langle n_z \rangle$ in 0.9 MA EDA H-mode to modeling using only inertia (a) and extended theory including inertia and ICRH effects (b)

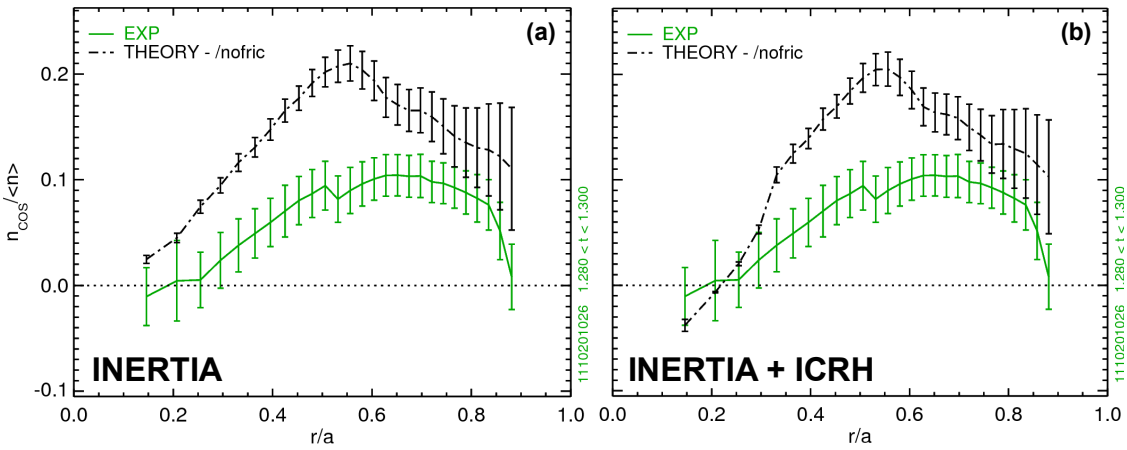

Figure 5-29: Comparison of $\tilde{n}_z/\langle n_z \rangle$ in 0.9 MA EDA H-mode to modeling using only inertia (a) and extended theory including inertia and ICRH effects (b)

ulations to calculate the minority temperature anisotropy, $T_\perp/T_\parallel$. The new theory correctly predicted the region in the plasma, and the approximate magnitude of the in/out asymmetry only when finite impurity density effects are included via Z_{eff}. In addition, the predicted θ-dependence within a flux surface was shown to be consistent with the measurements using the wall boxes. These experiments show conclusively that ICRH has an important impact on parallel impurity transport, and that a simple model based on pressure anisotropy can capture the basic physics.

Chapter 6

Asymmetry due to Ion/Impurity Friction

Friction between the main ions and the impurities is driven both by the difference in their diamagnetic flows, due to the 1/Z dependence, as well as the difference in their poloidal rotation. As discussed in Chapter 2, this force is responsible for determining the up/down asymmetry and, in cases of substantial friction, an in/out asymmetry with inboard accumulation. In Section 6.1 an example of high-field side impurity accumulation is shown to follow from assuming that the impurity and main ion flow along the magnetic field are equal. Section 6.2 compares the in/out asymmetries in the core of an Ohmic H-mode and ITB, while Section 6.3 documents observations of inboard accumulation at large minor radii in EDA H-modes. Both these results can be explained qualitatively by ion-impurity friction. Section 6.4 examines the up/down asymmetries measured in the Ohmic, EDA H-mode and L/I-modes plasmas discussed in Chapter 4, and shows that observations disagree with neoclassical parallel impurity transport theory in the trace limit. Section 6.5 discusses the link between the up/down asymmetry and poloidal rotation, suggesting future experiments which seek to validate neoclassical poloidal rotation theories must also include impurity density asymmetry comparisons and vice versa.

6.1 In/Out Asymmetries due to Friction

The basic form for the inboard accumulation follows directly from assuming that friction is large enough to force the parallel flow of a high-Z impurity to be equal to that of the main ions. From the leading order radial pressure balance, the perpendicular flow for any ion species has the form,

$$\mathbf{v}_\perp = \frac{\mathbf{B}\times\nabla\psi}{B^2}\left(\frac{1}{Zen}\frac{\partial p}{\partial\psi}+\frac{\partial\Phi}{\partial\psi}\right) \tag{6.1}$$

where $\mathbf{v} = v_\parallel\hat{b}+\mathbf{v}_\perp$. Taking the total flow to be divergence free, $\nabla\cdot(n\mathbf{v})=0$, and in steady state, the parallel velocity must be of the form,

$$v_\parallel = -\frac{I}{B}\left(\frac{1}{Zen}\frac{\partial p}{\partial\psi}+\frac{\partial\Phi}{\partial\psi}\right)+\frac{K(\psi)B}{n} \tag{6.2}$$

where $K(\psi)$ is an unspecified flux function, where $v_\theta = K/nB\theta$. By taking $v_{\parallel,i} = v_{\parallel,z}$ this constrains the poloidal impurity density variation to be,

$$n_z\left[\frac{K_i}{n_i}+\frac{I}{eB^2}\left(\frac{1}{Zn_z}\frac{\partial p_z}{\partial\psi}-\frac{1}{n_i}\frac{\partial p_i}{\partial\psi}\right)\right] = K_z \tag{6.3}$$

For a high-Z impurity, $Z\gg 1$, the $\partial p_z/\partial\psi$ term can be dropped, and the impurity density variation, n_z/n_i, is determined by flux functions and the magnetic field strength, B^2.

$$n_z/n_i = \frac{K_z/K_iB^2}{B^2-\frac{I}{eK_i}\frac{\partial p_i}{\partial\psi}} \tag{6.4}$$

If the neoclassical expression for $K_i = n_iu_i$ in the trace limit [24] is inserted into (6.4),

$$n_z/n_i = \frac{K_z/K_iB^2}{B^2+\frac{3}{f_c}\frac{\nabla\ln p_i}{\nabla\ln T_i}\langle B^2\rangle} \tag{6.5}$$

In general, ∇p_i and ∇T_i will have the same sign, and the impurities will accumulate where the magnetic field is strongest; on the inboard side of a flux surface. The parallel impurity force balance theory explored in 2.2.2 is derived with more rigor, but comparing (6.5) with the large gradient ($g\gg 1$) limit (2.22), the poloidal n_z

dependence on the magnetic field structure is very similar.

6.2 In/Out Asymmetry in the Core of Ohmic H-mode and ITB Plasmas

In Alcator C-Mod Ohmic H-mode plasmas with an internal transport barrier (ITB), enhanced gradients in core electron density and ion temperature profiles have previously been observed [140]. This is an ideal situation to explore in/out asymmetries driven by ion-impurity friction, since asymmetries driven by ICRH can be ignored, and the centrifugal force is generally reduced since there is no auxiliary heating. Additionally, the inertial effects become less important at smaller minor radii where ITB formation is seen. Rather than look for reductions in the low-field side abundance that could be caused by either friction or uncertainty in the flow and temperature profiles, the presence of a systematic, high-field side impurity accumulation would be straightforward evidence of a friction effect. The ITB also causes the radiation profiles to become more peaked on axis, and the asymmetry near the core becomes sensitive to uncertainties in the location of the magnetic axis as seen in Section 4.3.2. Again, using Ohmic ITBs is advantageous relative to ITBs in rf-heated plasmas due to the smaller β_θ which influences the Shafranov shift.

6.2.1 Example of Asymmetry

On 1110105, a series of Ohmic H-modes were created to study the transport properties of the H-mode at the onset of the ITB. Scanning the toroidal field down during the current flattop until an L/H transition is triggered and then ramping it back up has been a repeatable way to generate internal transport barriers in Ohmic plasmas on C-Mod [140] [141]. Line-averaged density prior the the L/H transition, $\bar{n}_e \sim 1.1$ 10^{20} m^{-3}, and plasma current, $I_p = 800$ kA, were kept constant while the target discharge was repeated, exhibiting strong shot-to-shot variations. Some plasmas stayed in ELM-free H-mode, others formed an ITB briefly during the H-mode, while many

developed strong ITBs only at the transitions from H-mode to L-mode. These so-called back-transition ITBs are avoided in this analysis due to their tendency to destabilize MHD modes and/or snakes, confusing calculations with radiation that is toroidally asymmetric in the lab frame. The strong inward radial impurity transport and the lack of reliable spectroscopy for the low, $\sim$1 keV, electron temperatures prevents a single impurity from being shown to dominate the radiation. Despite this obfuscation, results can still be used qualitatively by showing that the appearance of HFS impurity accumulation is linked to gradients in density and temperature that drive ion/impurity friction.

In Figure 6-1, the KLIM profiles are shown for a time slice late in the ELM-free Ohmic H-mode phase of shot 1110105002 in which an ITB has developed. The AXA and AXJ profiles agree very well, are peaked on axis and, when mapped to r/a, reveal a region of inboard radiation enhancement inside $r/a \sim 0.5$. This can be compared to the KLIM profiles in shot 1110105006 shown in Figure 6-2 for an Ohmic H-mode without an ITB. The emissivity profile is hollow, but only outboard peaking is observed, with AXA and AXJ agreeing within expected limits of spatial resolution. It is worth noting that this result qualitatively supports the work in Chapter 5, showing that in an H-mode without ICRH, no build-up of impurities on the high-field of a flux surface is seen.

Time histories during the ELM-free H-mode phase from these two plasmas are shown in Figure 6-3 for 002 and Figure 6-4 for 006. In the discharge with an ITB, 002, the electron density (b) rises steadily, along with the radiated power (d), while the core temperature (c) remains relatively constant. The peaking in the AXA emissivity profile (e), the ratio of the on-axis and off-axis values, rises continuously until the H/L back-transition at 1.112 seconds. The in/out asymmetry, calculated using both KLIM and wall box data (f), shows very different temporal behavior at $r/a = 0.45$ and 0.69. Initially after the L/H transition, there is substantial uncertainty due to the low absolute level of radiation. But, after $t \sim 1.05$ seconds, the impurities clearly begin to accumulate on the HFS at mid-radius as the emissive peaking crosses near unity. In the outer third of the plasma, a modest LFS accumulation, $n_{cos}/\langle n_z \rangle \sim 0.1$,

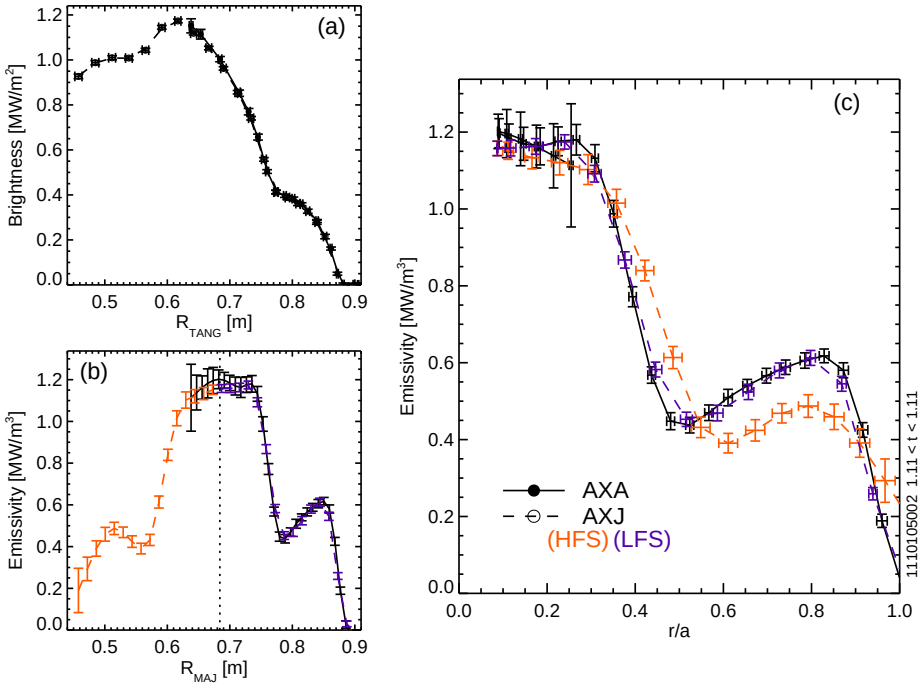

Figure 6-1: Profiles from AXA and AXJ during an Ohmic H-mode with an ITB, showing a region of HFS accumulation for $r/a < 0.5$

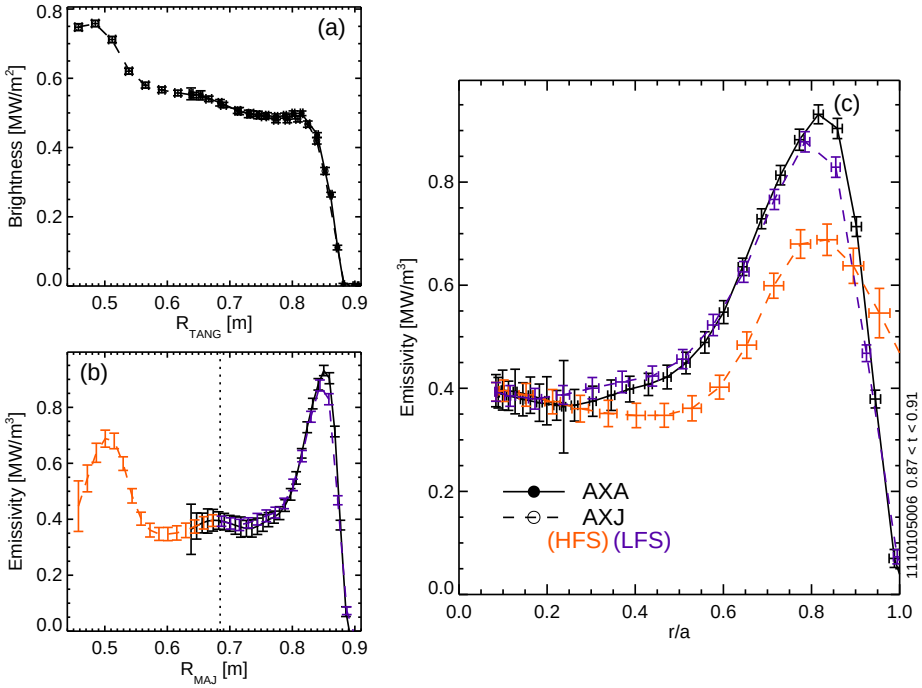

Figure 6-2: Profiles from AXA and AXJ during an Ohmic H-mode without an ITB, showing only LFS impurity accumulation

is maintained.

In the discharge with an ITB, 006, there is a similar trend in density, temperature and radiated power, but the in/out asymmetry decays to a relatively small, $n_{cos}/\langle n_z \rangle \sim 0.05$, low-field side abundance. The radial emissivity profile remains hollow for most of the H-mode, but begins to flatten out after 0.87 seconds, as evidenced by the change in peaking when dB_t/dt becomes positive.

6.2.2 Profile Analysis

To gain insight into the possibility of the asymmetry in the ITB plasma being driven by ion/impurity friction, the kinetic profiles are examined relative to the $n_{cos}/\langle n_z \rangle$ profiles. Due to the low-temperature, He-like Ar is not strongly excited and accurate HIREXSR temperature and rotation profiles are not available, but the high-collisionality allows $T_e = T_i$ to be a reasonable approximation.

In Figure 6-5, the radial profiles at two time points during 002 are plotted, one in the H-mode phase (light blue), the other in the ITB phase (gold). During the H-mode, the density profile (a) is flat while during the ITB, there is a strong gradient at $0.3 < r/a < 0.6$. In this region, the radiation asymmetry profile (c) is shown to drop below zero, but then increases back to $n_{cos}/\langle n_z \rangle \sim 0$ as the density gradient weakens. The temperature profile (b) is similar at both times and, along with n_e, is used to estimate the main-ion collisionality (d), $\nu_{ii}/\omega_{tr,i}$. This shows that during the H-mode, as the density rises, the core plasma transitions from the banana into the plateau regime, which has important consequences for the friction-induced asymmetry. As discussed in Section 2.2.2, the friction force responsible for HFS accumulation goes from being proportional to $\partial \ln n_i/\partial\psi - 0.5\partial \ln T_i/\partial\psi$ in the banana regime, to $\partial \ln p_i/\partial\psi$ when moving to the plateau regime.

Figure 6-6 shows the same radial profiles for two time slices in the H-mode which had no ITB, 006. The density profile remains relatively flat and the radiation asymmetry profile remains positive, showing no high-field side accumulation. Similar to 002, the plasma moves into the plateau regime during the H-mode, but without an ITB, it appears there is not a sufficient pressure gradient to lead to high-field side

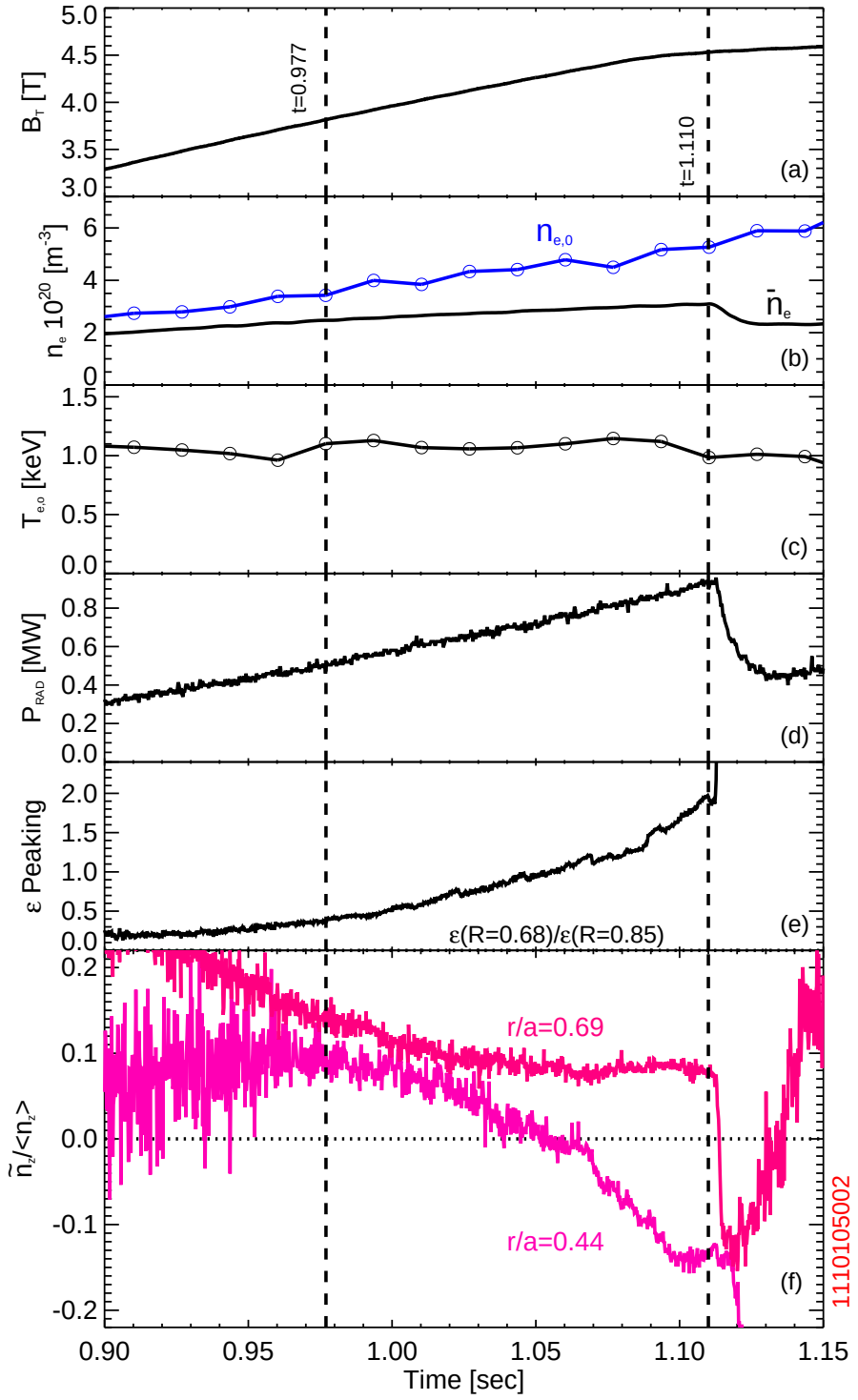

Figure 6-3: Time history of the in/out asymmetry during an ELM-free H-mode that develops into an ITB, showing $\tilde{n}_z/\langle n_z \rangle < 0$

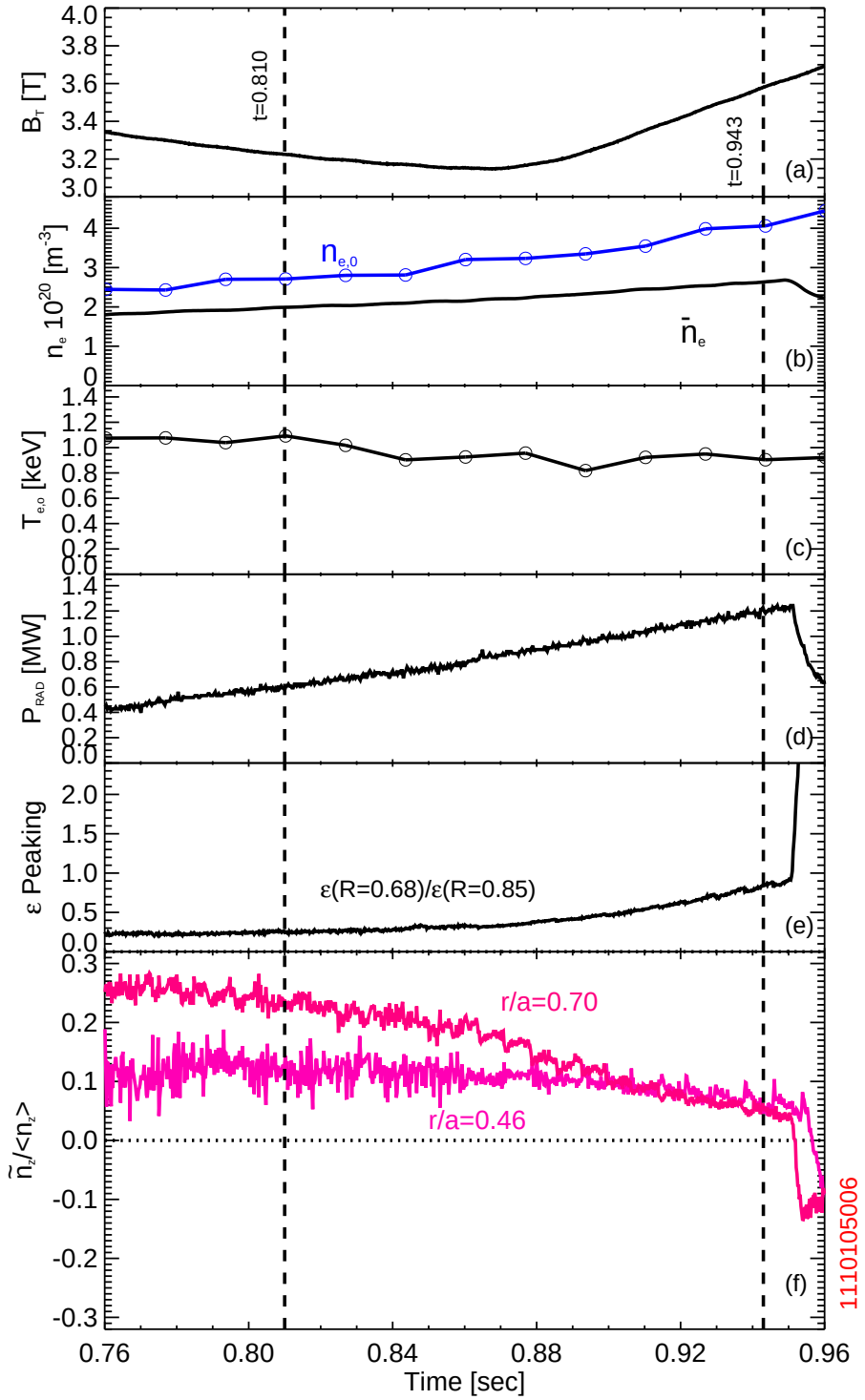

Figure 6-4: Time history of the in/out asymmetry during an ELM-free H-mode that does not develop an ITB, showing $\tilde{n}_z/\langle n_z \rangle$ remaining positive

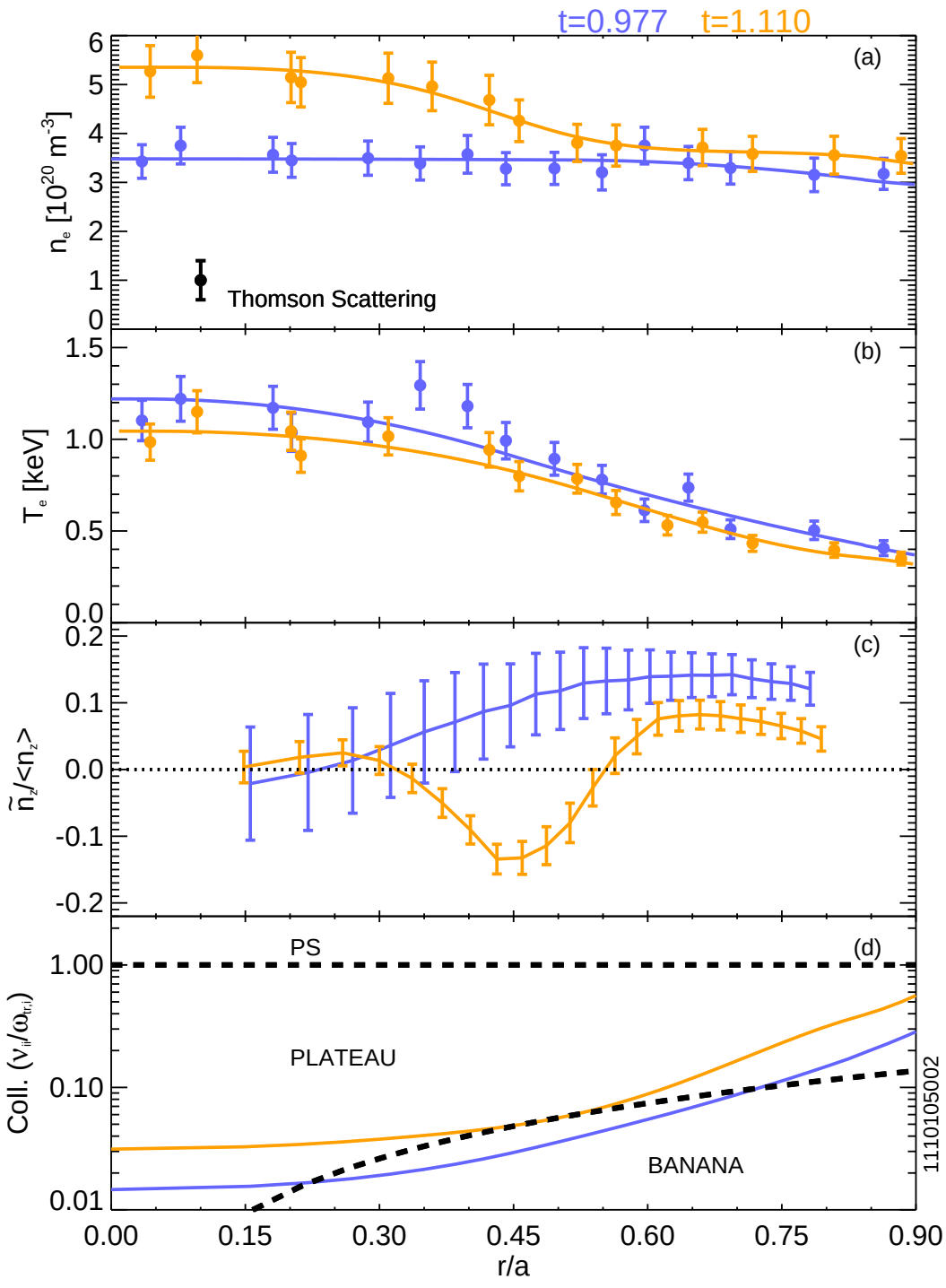

Figure 6-5: Radial profiles during an Ohmic H-mode with an ITB showing a region of HFS accumulation for $0.3 < r/a < 0.5$.

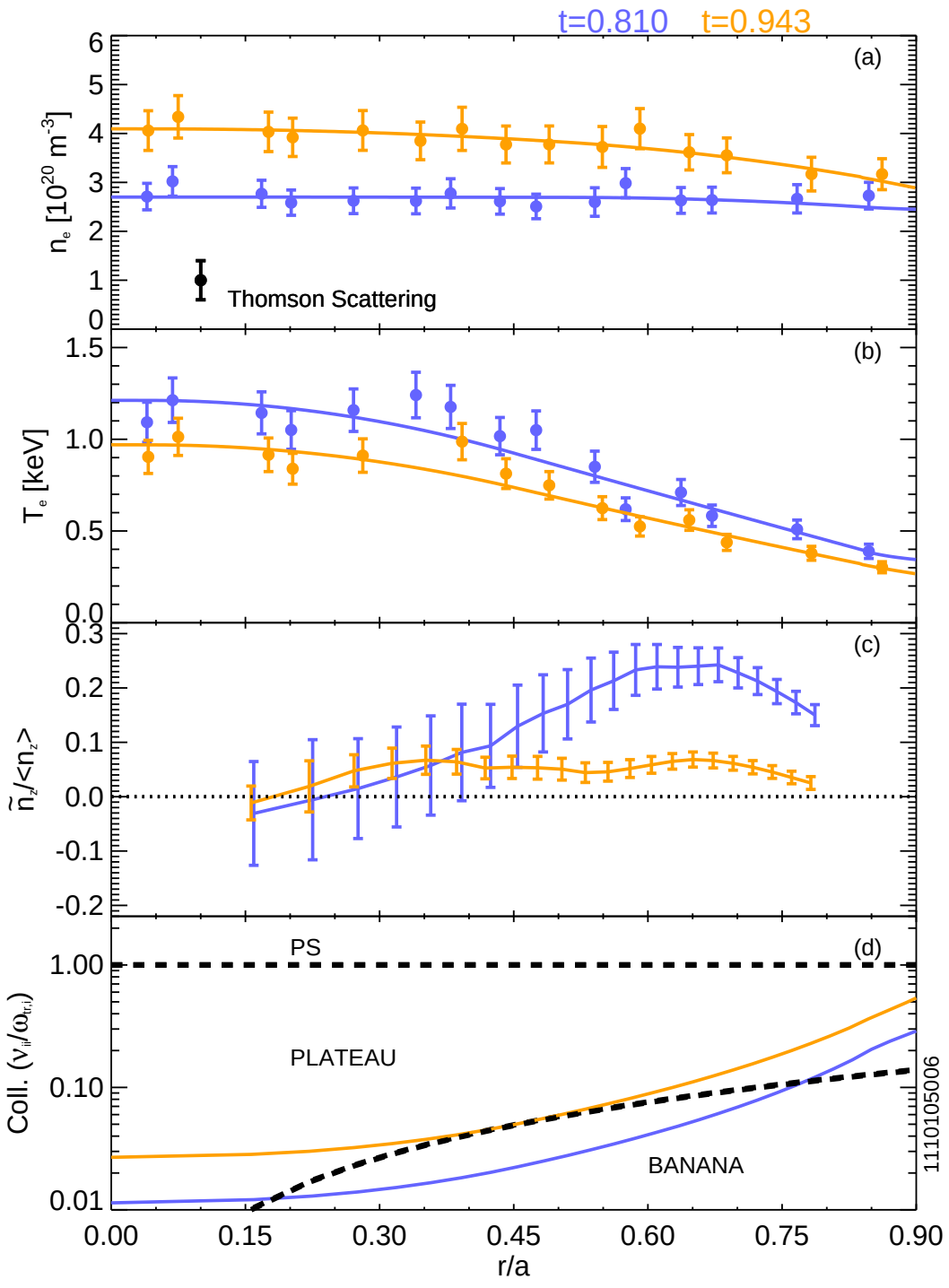

Figure 6-6: Radial profiles during an Ohmic H-mode without an ITB showing only LFS impurity accumulation

impurity accumulation.

The correlation between strong gradients in the emissivity and the impurity accumulation for 1110105002 and other ITBs during that run might still be explainable by systematic errors in the equilibrium reconstructions. Future experiments with better impurity spectroscopy, using kinetically constrained EFITs are required for proper validation.

6.3 In/Out Asymmetry in the Edge of EDA H-Modes

In the previous two chapters, the in/out asymmetry in the plasma core was explored using the KLIM and wall box arrays. Outside of $r/a \sim 0.8$, the in/out asymmetry is observed to go from strong low-field side accumulation due to the centrifugal force to strong high-field side accumulation and develop higher-order Fourier components. To analyze this edge region, AXJ is removed from the 2D asymmetry reconstructions due to its limited spatial resolution. The up/down and in/out asymmetries are calculated using $T_e = T_i$ where only the friction force is included. The centrifugal force will likely play a role in parallel force balance, but is excluded in this analysis to highlight the magnitude of the in/out asymmetry driven by friction as well as the region of the plasma where it plays a role. Thus, sections 6.3.1-6.3.3 provide qualitative evidence that ion-impurity friction is important when examining the in/out asymmetry at large minor radii in EDA H-modes.

Figure 6-7 shows time histories of electron density (a) and temperature (b) along with radiation (c)(d) and relevant line-emission (e)(f)(g) data in plasmas with strong molybdenum (black), argon (red) and neon (blue) radiation. All plasmas are at $I_p = 0.9$ MA and B_t=5.4 T with various levels of on-axis ICRH. In shot 1110201007 (black), the total radiation inside the LCFS from resistive bolometry, $P_{RAD,F}$ (c) is well correlated to the molybdenum time history (e) measured by McP, and no extrinsic impurities such as argon (f) or neon (g) were introduced. Section 6.3.1 discusses in/out

and up/down molybdenum asymmetries averaged over $1.06 < t < 1.16$ s, during peak Mo line emission. In shot 1110105005 (red), significant argon puffing during post-boronization ICRH conditioning led to colder plasma with reduced radiation, but the majority of which is due to argon (f). A small molybdenum injection just after 0.8 seconds, observable on the diode-based radiated power, $P_{RAD,D}$ (d), demonstrates the the small contribution due to Mo. Section 6.3.2 shows in/out and up/down argon asymmetries averaged over $1.10 < t < 1.30$ s. In shot 1101215012 (blue), strong neon seeding was intentionally introduced in order study EDA H-modes with a radiative divertor. Both $P_{RAD,F}$ and $P_{RAD,D}$ are well correlated to the neon line emission (g) measured by XEUS and a molybdenum injection just after 1.0 seconds indicates its minor contribution to the total radiation. Section 6.3.3 shows in/out and up/down neon asymmetries averaged over $1.30 < t < 1.40$ s.

6.3.1 Radiation Asymmetries due to Molybdenum

In Figure 6-8, the measured radial profiles for the up/down and in/out asymmetry (black) are shown for $r/a \geq 0.6$ using both $m = 1$ (solid) and $m = 2$ (dashed) components to find $n_z(\theta)$ from measurements. The modeled asymmetry, only ion-impurity friction, is also included (green dash-dot). The transition to strong inboard accumulation is predicted to occur in the same region as the measurements, but error bars on the modeling are too large to draw any solid conclusions. As will be discussed Section 6.4, a large accumulation at the bottom of the plasma, in the direction of the ion ∇B drift, is predicted from parallel transport theory while measurements show little to no up/down asymmetry. Note that the theory is calculated for the banana regime, while the transition into the plateau regime occurs outside of $r/a \simeq 0.85$.

In Figure 6-9, the measured poloidal variation (symbols) along with the fit (black) and theory prediction (green) are shown at two minor radii. In 6-9a, the $n_z(\theta)/n_z(0)$ profile is plotted at $r/a = 0.84$, near the region where the measured asymmetry goes from LFS to HFS accumulation. At this layer, theory predicts a strong up/down asymmetry, but AXA and all the wall boxes show the radiation is nearly poloidally symmetric. In 6-9b, the $n_z(\theta)/n_z(0)$ profile is plotted at $r/a = 0.93$ where consistent

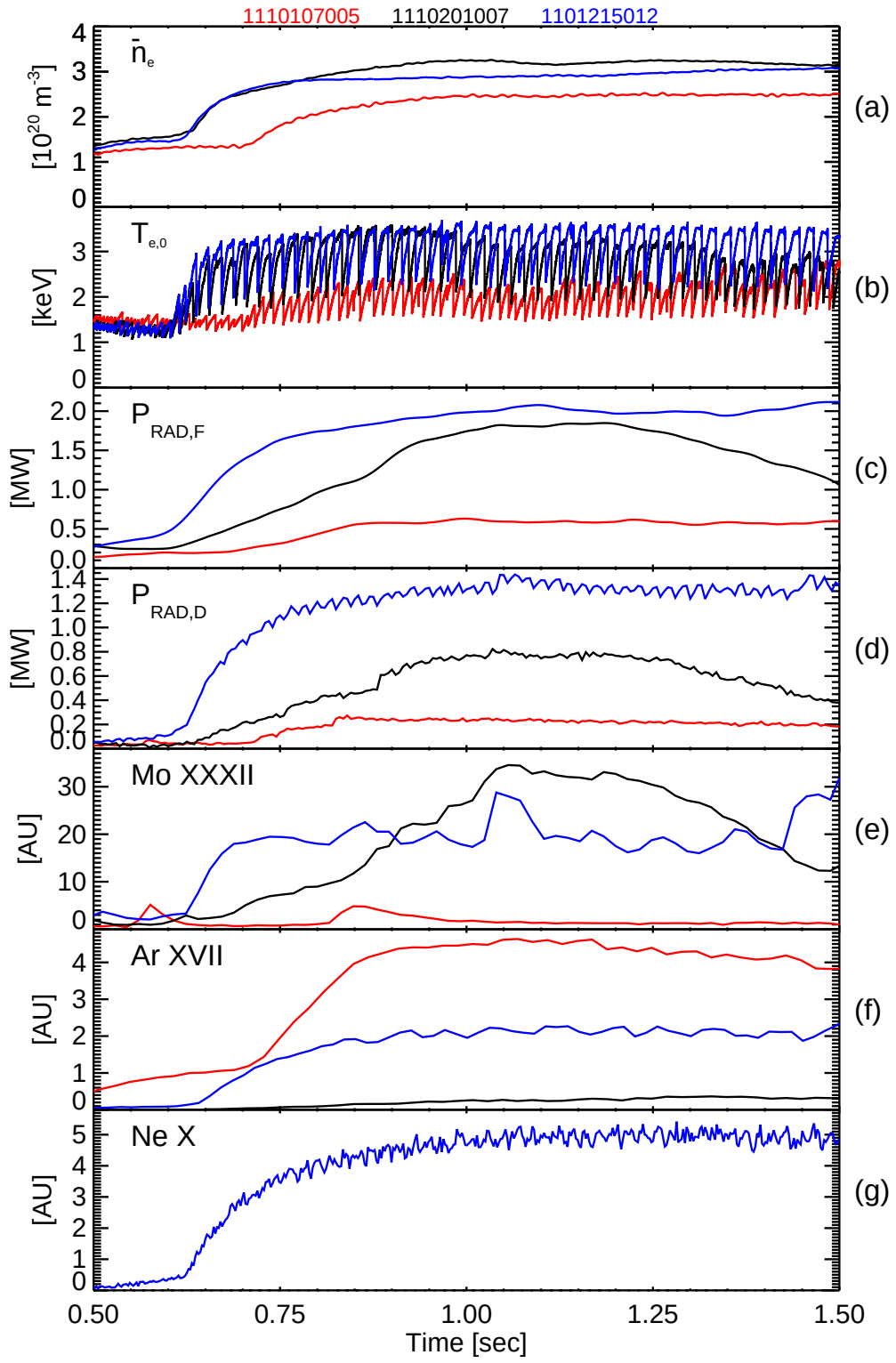

Figure 6-7: Time history of EDA H-modes demonstrating radiated power dominated by different impurities; molybdenum (black), argon (red) and neon (blue).

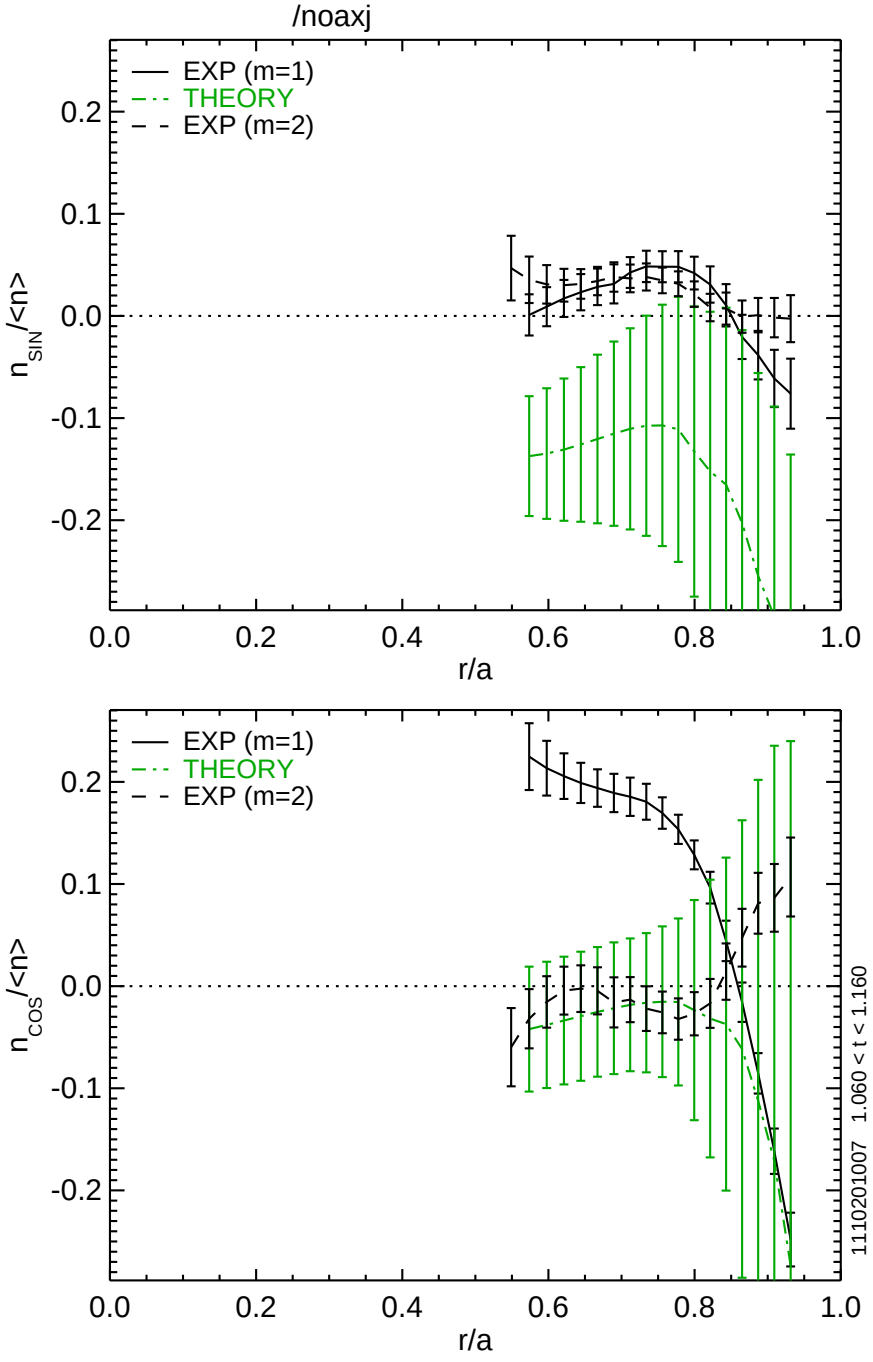

Figure 6-8: Measured asymmetry profiles (black) for an EDA H-mode plasma with strong Mo radiation compared to modeling only including friction (green)

measurements of inboard accumulation are found independently by both WB2AX (blue) and WB4AX (purple). The higher order Fourier components are apparent in both the experimental and theoretical profiles.

6.3.2 Radiation Asymmetries due to Argon

A similar analysis has been completed for the EDA H-mode with strong Ar radiation where Figure 6-10 compares the measured and modeled radial asymmetry profiles. While initially predicting a similar up/down asymmetry for $0.6 < r/a < 0.7$, the two diverge for larger minor radii, and show significant, $\Delta n_{sin}/\langle n_z \rangle \sim 0.2$, disagreement at $r/a \sim 0.9$. In this region, the inboard accumulation of argon due to ion-impurity friction is predicted to be at a level that is similar to experiment.

In Figure 6-11, the measurements and $n_z(\theta)/n_z(0)$ profiles are plotted along with theory prediction at $r/a = 0.79$ (6-11a) and $r/a = 0.88$ (6-11b). At both radii, a much stronger up/down asymmetry is once again predicted but not observed. Uncertainty in the emissivity due to the lower levels of radiation in this shot prevents $m = 2$ poloidal variation from being reliably constrained by the wall box measurements.

The measured inboard accumulation at large r/a is similar for both molybdenum and argon, raising the possibility of a systematic error in the analysis. In 6-12, the up/down and in/out asymmetry profiles are shown for an Ohmic plasma with substantial argon seeding (1110105027). For the outer half of the plasma, near symmetry in the radiation is demonstrated with the absolute magnitude of both $n_{cos}/\langle n_z \rangle$ and $n_{sin}/\langle n_z \rangle$ measured to be less then 10%. The absence of $n_{cos}/\langle n_z \rangle \sim -0.2$ as seen in the EDA H-modes indicates the relative calibration of the pinhole cameras are not to blame.

6.3.3 Radiation Asymmetries due to Neon

In Figure 6-13, the radial profiles for the up/down and in/out asymmetry profiles are shown for a plasma with significant neon radiation. Both $m = 1$ and $m = 2$ components are used, and friction-based asymmetry modeling assuming a dominant

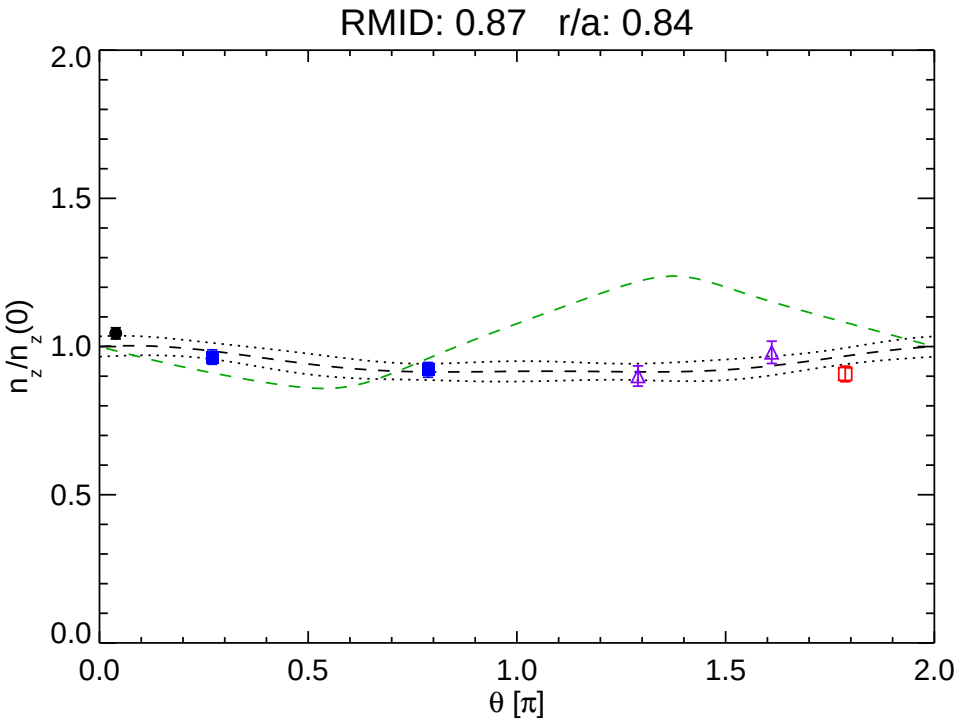

(a)

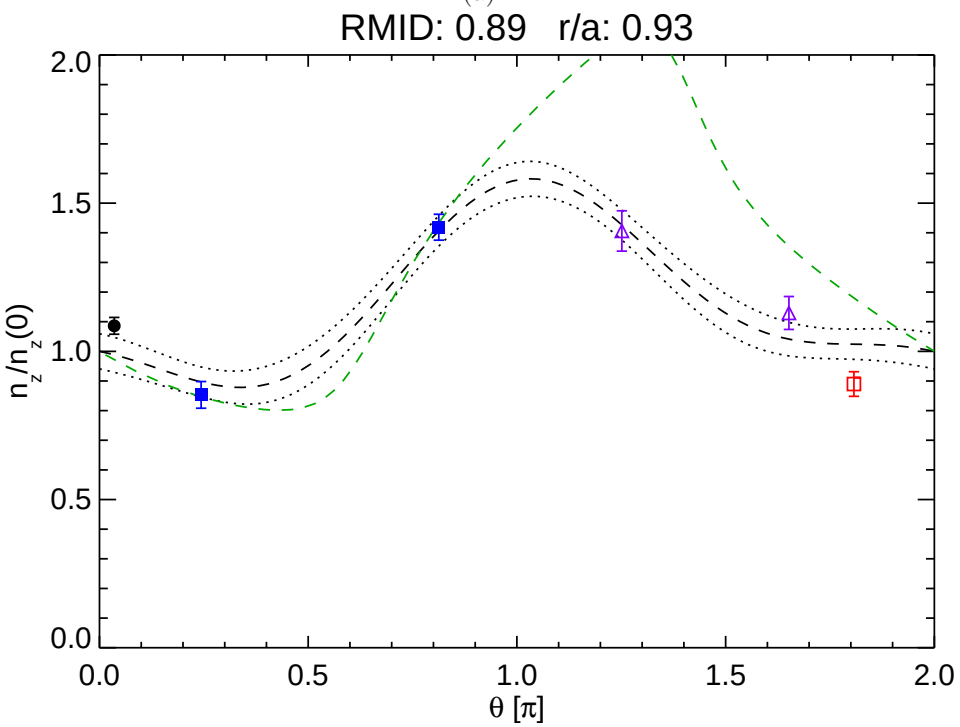

(b)

Figure 6-9: Poloidal variation in the impurity density for an EDA H-mode with strong molybdenum radiation; AXA (●), AXJ (○), WB2AX (■), WB3AX (□) and WB4AX (△)

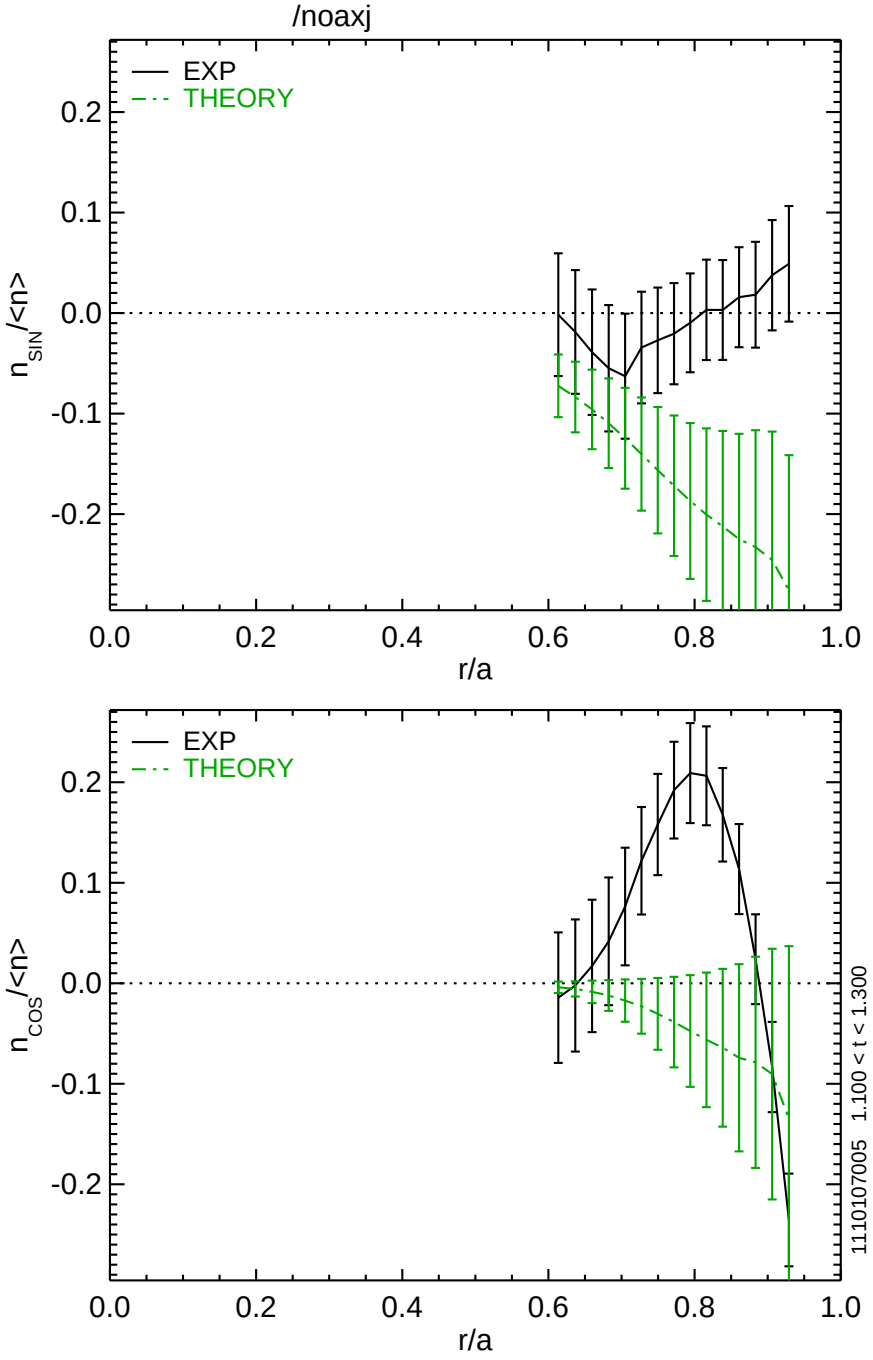

Figure 6-10: Measured asymmetry profiles (black) for an EDA H-mode plasma with strong Ar radiation compared to modeling only including friction (green)

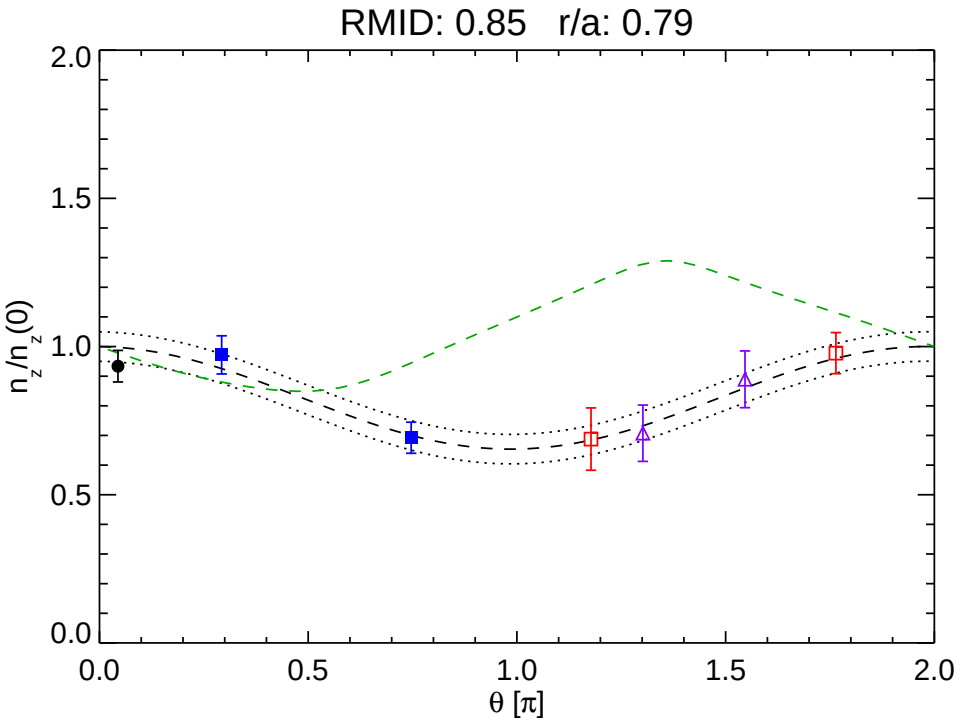

(a)

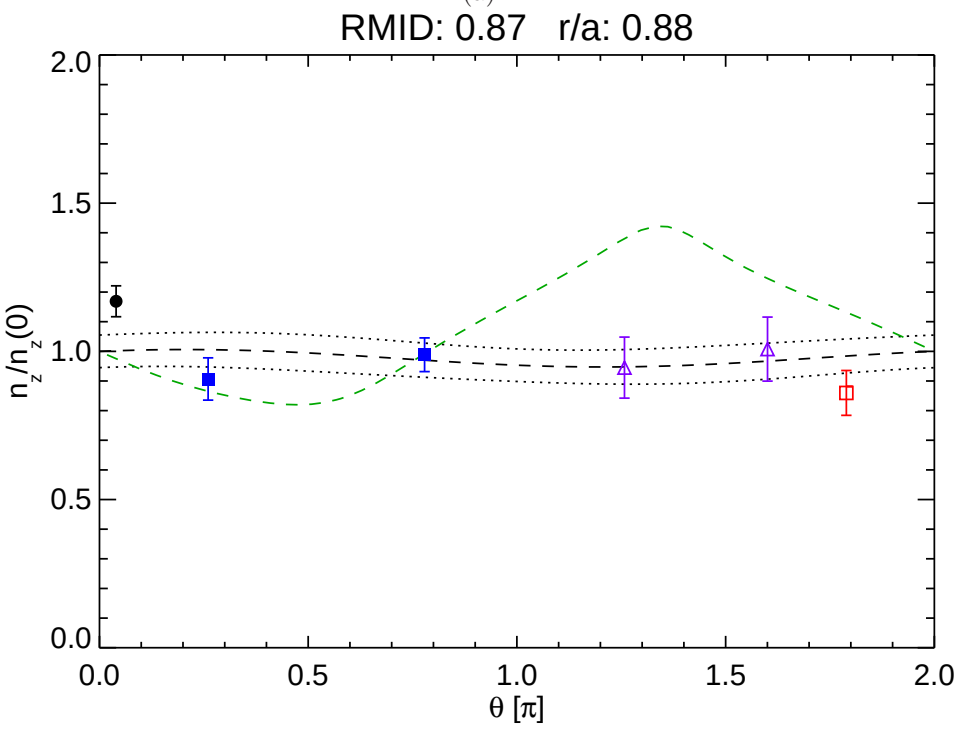

(b)

Figure 6-11: Poloidal variation in the impurity density for an EDA H-mode with strong argon radiation; AXA (●), AXJ (○), WB2AX (■), WB3AX (□) and WB4AX (△)

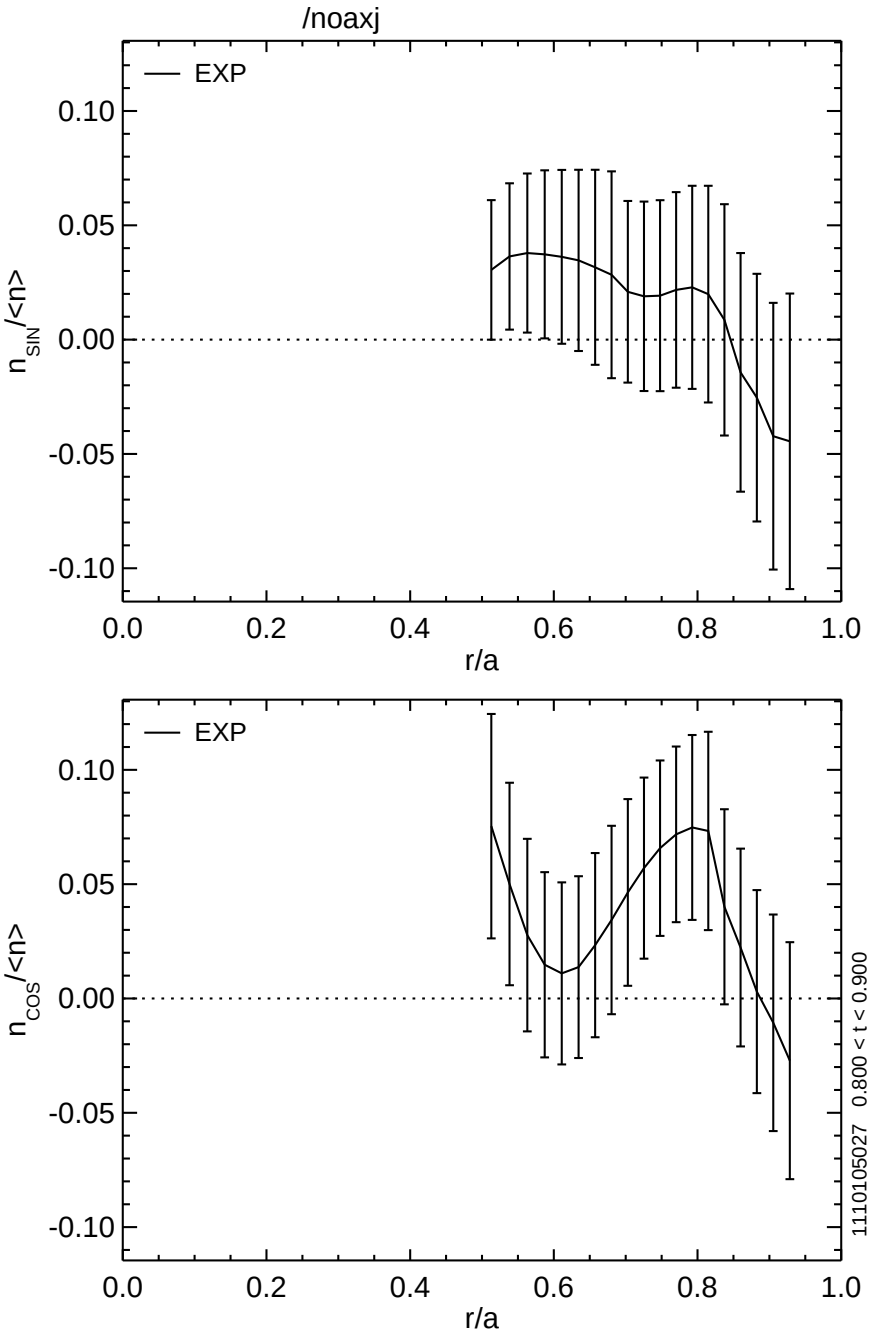

Figure 6-12: Radial asymmetry profiles for an Ohmic plasma with strong argon radiation

neon impurity predicts a much smaller level of inboard accumulation. Due to higher temperatures, the plasma is in the banana regime out to $r/a \simeq 0.9$ and so the modeling should be valid in this regime. In Figure 6-14, the $n_z(\theta)/n_z(0)$ plots show the $m = 2$ structure is consistent between all the wall box and KLIM profiles. By comparing Figure 6-9b (molybdenum) and Figure 6-14b (neon), there are striking similarities in the poloidal structure and even in the residual to the fit profile. This raises the possibility that low-Z intrinsics, such as fluorine and boron, might be playing a role in the AXUV diode-based asymmetry at large minor radii, even in so-called molybdenum dominated plasmas.

6.3.4 Discussion

For these EDA H-modes, the measured in/out asymmetry at large major radii was approximately the same, $\tilde{n}/\langle n_z \rangle \sim -0.2$, independent of the impurity thought to dominant the emissivity. Many of the assumptions that go into the asymmetry modeling may be violated in this region of an H-mode plasma. At this proximity to the separatrix, a poloidally localized impurity source could leave its footprint in the edge plasma, and lower-Z impurities, while fully stripped in the core, can contribute to the radiation. An additional source of friction due to neutral particles will likely impact the asymmetry physics, and, if the neutrals are poloidally asymmetric, could contribute via charge-exchange to the radiation asymmetry. Lastly, while these measurements are not at the steep-gradient layer of the edge transport barrier, the equilibrium reconstructions used do not take into account any bootstrap current generated in the pedestal region. Since the global β_θ values for these discharges are very different, 0.45, 0.65 and 0.85 for the Ar, Mo and Ne shots, respectively, pressure-induced changes in the equilibrium are unlikely to be exclusively responsible for observed $\tilde{n}/\langle n_z \rangle$.

Detailed investigation and validation of parallel impurity transport in this region of plasma is outside of the capability of the current techniques, tools and theory, and so will be left as future work. The results from this section will be very useful when scoping out the design and placement of any future pinhole cameras, or expanding parallel impurity force balance theory to include neutrals and/or impurity sources.

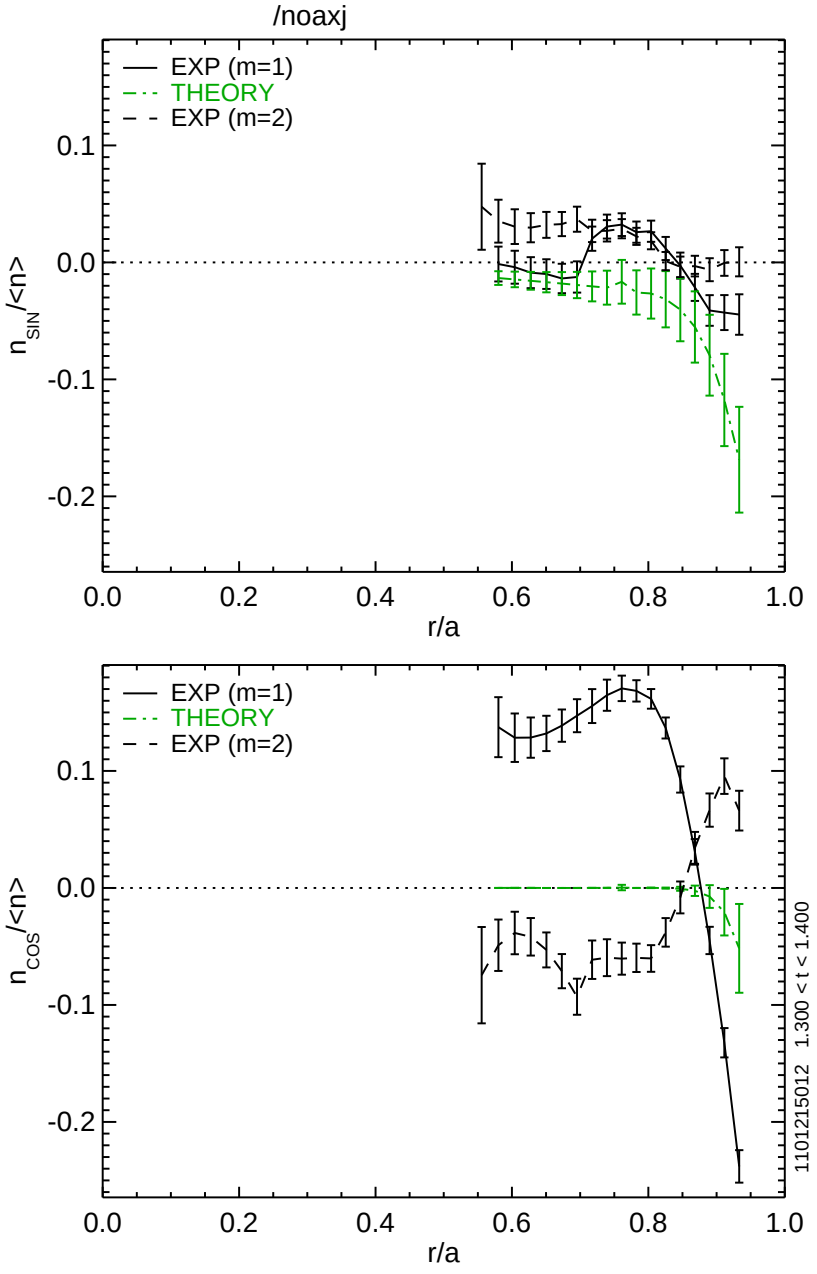

Figure 6-13: Measured asymmetry profiles (black) for an EDA H-mode plasma with strong Ne radiation compared to modeling only including friction (green)

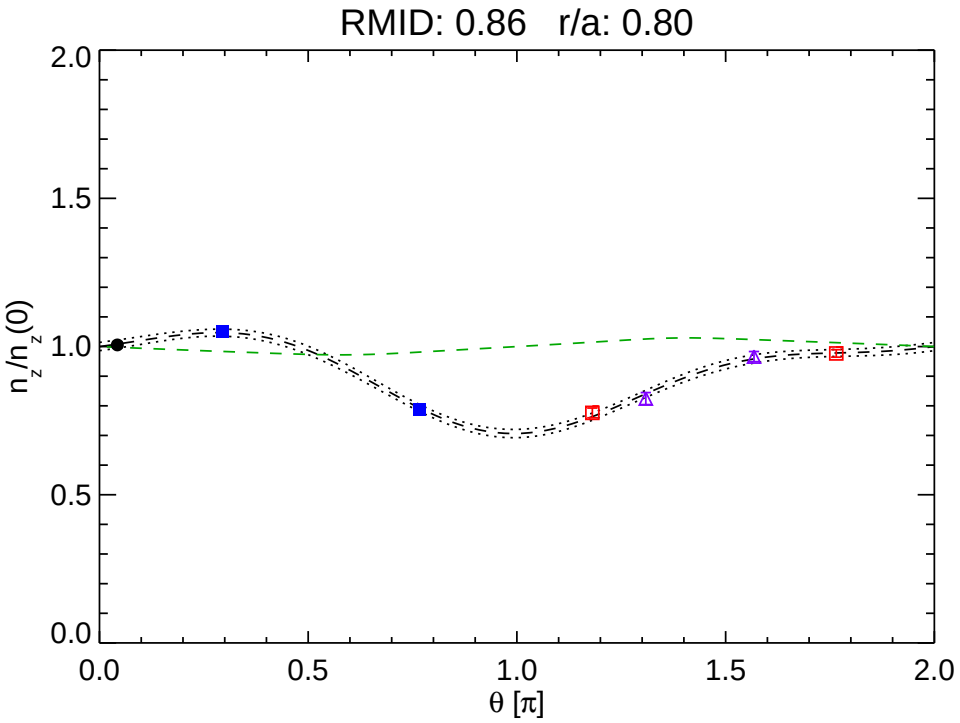

(a)

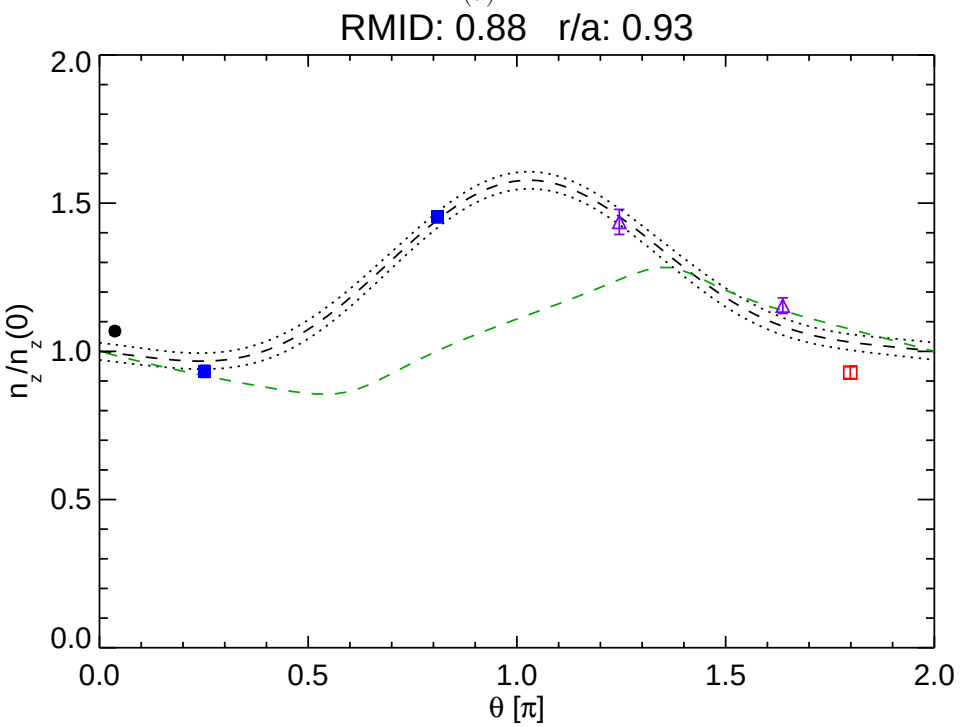

(b)

Figure 6-14: Poloidal variation in the impurity density for an EDA H-mode with strong Ne radiation; AXA (●), AXJ (○), WB2AX (■), WB3AX (□) and WB4AX (△)

6.4 Up/Down Asymmetry in the Core of EDA H-mode plasmas

The H-mode and I-mode plasmas discussed in earlier chapters showed significant in/out asymmetries that have been demonstrated to be driven, primarily, by the centrifugal force and the poloidal variation of the electrostatic potential. In these plasmas, a small, $\tilde{n}_z/\langle n_z \rangle \leq 0.1$, up/down asymmetry is also observed. As discussed in Section 2.2.4, comprehensive parallel impurity transport theory for the banana regime [24] predicts the up/down asymmetry is driven by ion/impurity friction but also depends on the toroidal rotation. This can be thought of qualitatively as friction smearing an in/out asymmetry driven by centrifugal force, causing a minor accumulation in the direction of the parallel flow.

For the higher current, higher density H-mode (1110201017) discussed in Chapters 4 and 5, the poloidal impurity variation and radial asymmetry profiles are calculated including ion-impurity friction, ICRH effects and the centrifugal force. In this case, the assumption of $T_e = T_i$ is made to reduce the uncertainty in the temperature profile going into the friction calculation since the difference between the density and temperature scale lengths are required. Figure 6-15 shows that between $0.5 < r/a < 0.8$, there is substantial disagreement between the predicted up/down asymmetry and the measurement. Because of the flat density and peaked temperature profile, $n_{sin}/\langle n_z \rangle < 0$ is predicted over the core plasma, while $n_{sin}/\langle n_z \rangle > 0$ is observed. As indicated by the scatter plots in Chapter 4 (compare 4-34 and 4-35), the inclusion of the friction does not substantially change the modeled in/out asymmetry. As shown in Figure 6-15, including friction marginally improves agreement between theory and experiment for $n_{cos}/\langle n_z \rangle$. Note that kinetic EFIT reconstructions discussed in Section 4.3.2 are used. Plots of $n_z(\theta)/n_z(0)$, shown in Figure 6-16, show that both the KLIM and wall box measurements (symbols) do not indicate any up/down asymmetry near the magnitude suggested by modeling (green dashed).

The same calculations are repeated for the lower current, lower density H-mode (1110201026) with the radial asymmetry profiles shown in Figure 6-17. Again, the

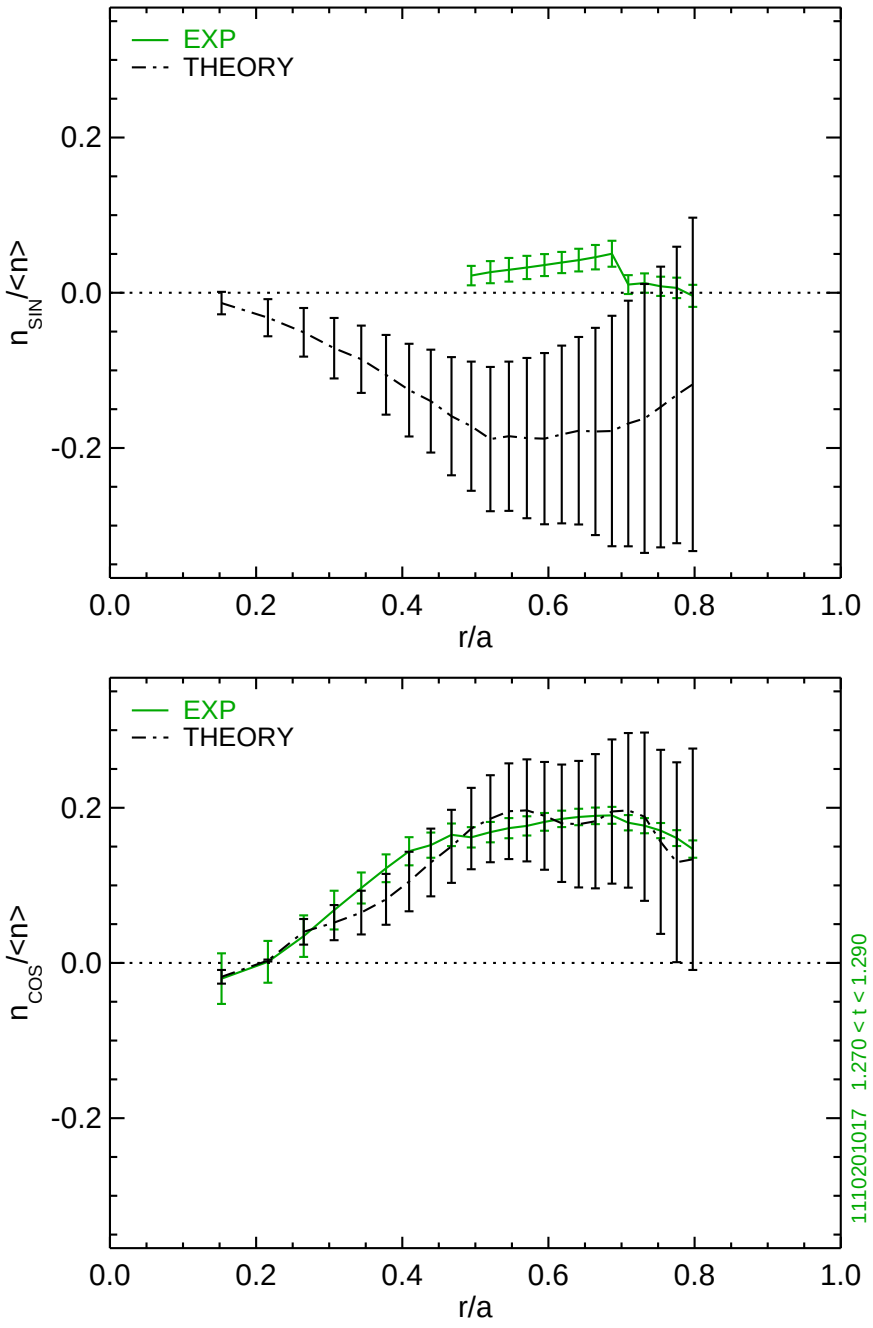

Figure 6-15: Profiles of experimental up/down and in/out asymmetry in the 0.9 MA EDA H-mode, compared to modeling including inertia, friction and ICRH effects

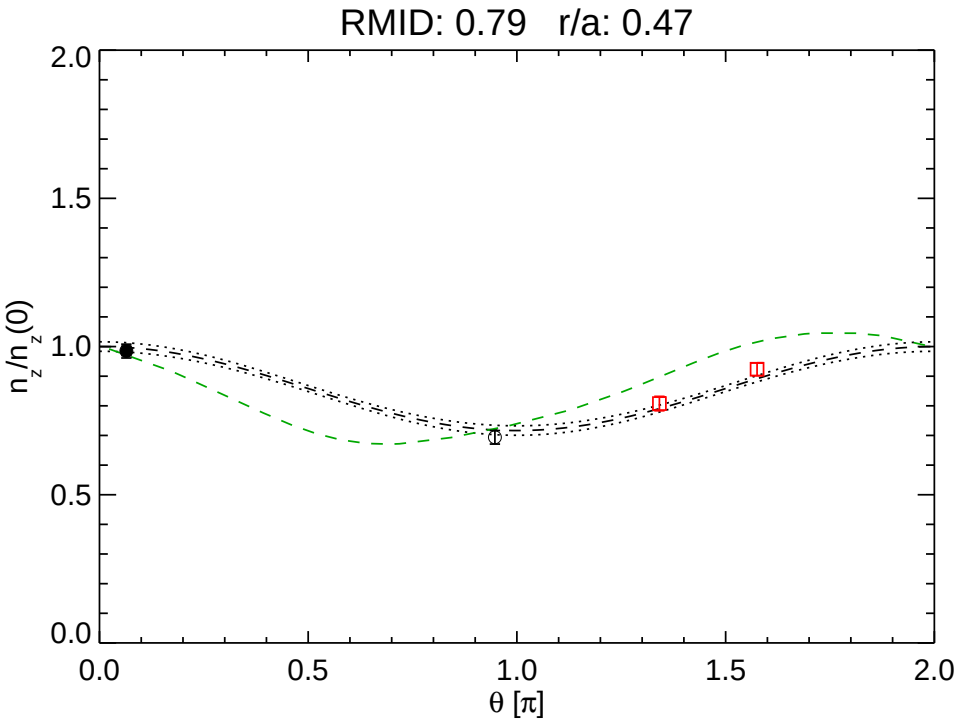

(a)

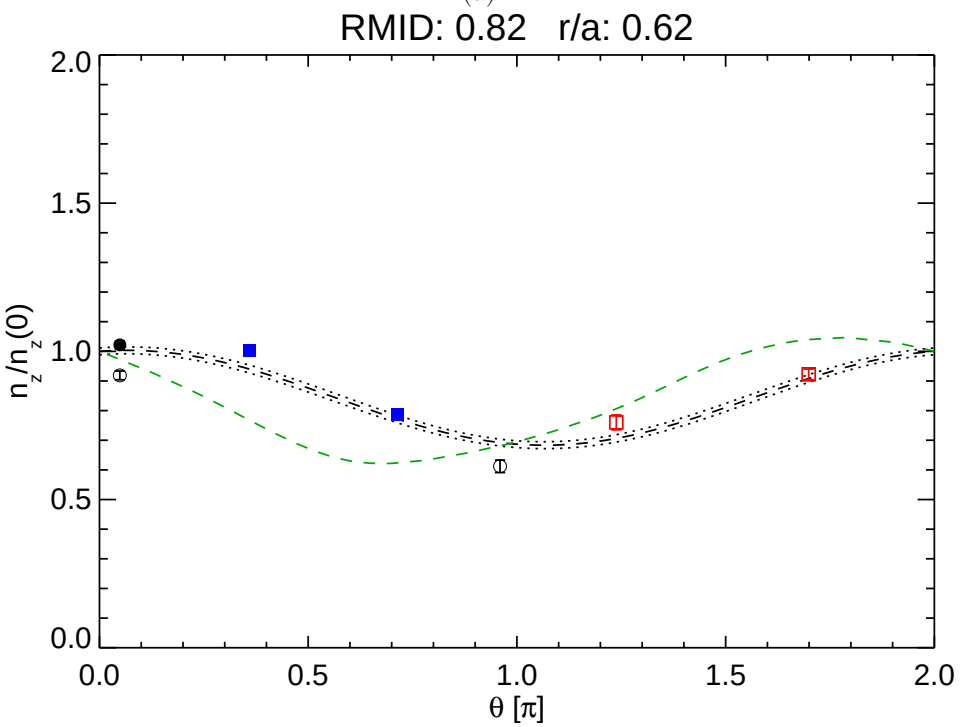

(b)

Figure 6-16: Poloidal variation of measured and modeled asymmetries at various r/a for the results shown in Figure 6-15; AXA (●), AXJ (○), WB2AX (■), WB3AX (□) and WB4AX (△)

measured and modeled up/down radial asymmetry profiles are in opposite directions, supported by the $n_z(\theta)/n_z(0)$ profile data, shown in 6-18. After including all physics thought to relevant in driving the in/out asymmetry, a discrepancy of only $n_{cos}/\langle n_z \rangle \sim 0.05$ for $0.3 < r/a < 0.6$ remains.

If just the in/out asymmetry profiles were measured, then results like those shown in 6-15 and 6-17 would indicate that existing neoclassical parallel impurity transport [24] when extended to include ICRH-effects as done in Section 5.1 does a good job in reproducing experiments and is likely complete. But, with such large discrepancies in the up/down asymmetry such conclusions must be approached cautiously. The ion-impurity friction effects which drive the up/down asymmetry also influence the in/out. If changes to theory or the inclusion of new physics is required to match measured and modeled $n_{sin}/\langle n_z \rangle$ profiles, this may alter the presently observed agreement in $n_{cos}/\langle n_z \rangle$.

6.4.1 Trends in Measured Up/Down Asymmetries

The collection of discharges discussed in Chapter 4 can be used to try and identify what is responsible for the disagreement in the up/down asymmetry data. In Figure 6-19, the measurement and modeling results are compared over $0.50 < r/a < 0.85$ for Ohmic (6-19a), EDA H-mode (6-19b) and L/I-mode (6-19c). In general, the measured asymmetries are much smaller and in the opposite direction relative to modeling. The large error bars are driven by the dependence of the banana regime friction on the difference between the density and temperature gradient scale lengths (2.20). For each of the plots in 6-19, the minimum and median error bars are plotted along with an example of disagreement between theory and experiment that is outside the error bars. These data show that systematic errors in the relative calibration between the wall boxes cannot be the cause of the discrepancy. If so, then the scattered data would organize to a line parallel to the unity-slope line (black-dashed) but be vertically offset.

In Section 2.2.2, two theories were presented that predict the up/down asymmetry in the circular low-aspect ratio limit. The work in [50] modeled $n_z(\theta, r) = n_{z,o}(r)(1 +$

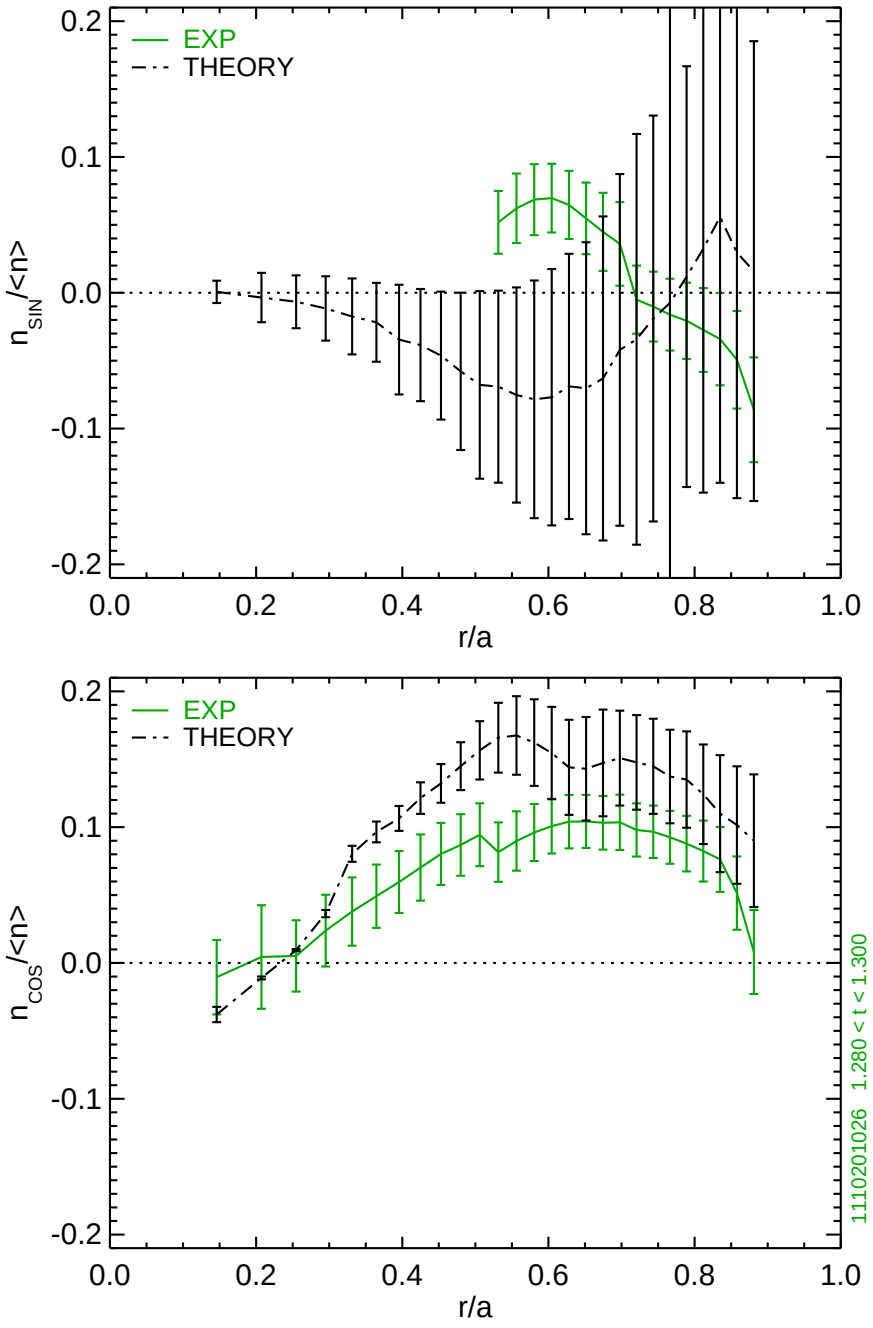

Figure 6-17: Profiles of experimental up/down and in/out asymmetry in the 0.7 MA EDA H-mode, compared to modeling including inertia, friction and ICRH effects

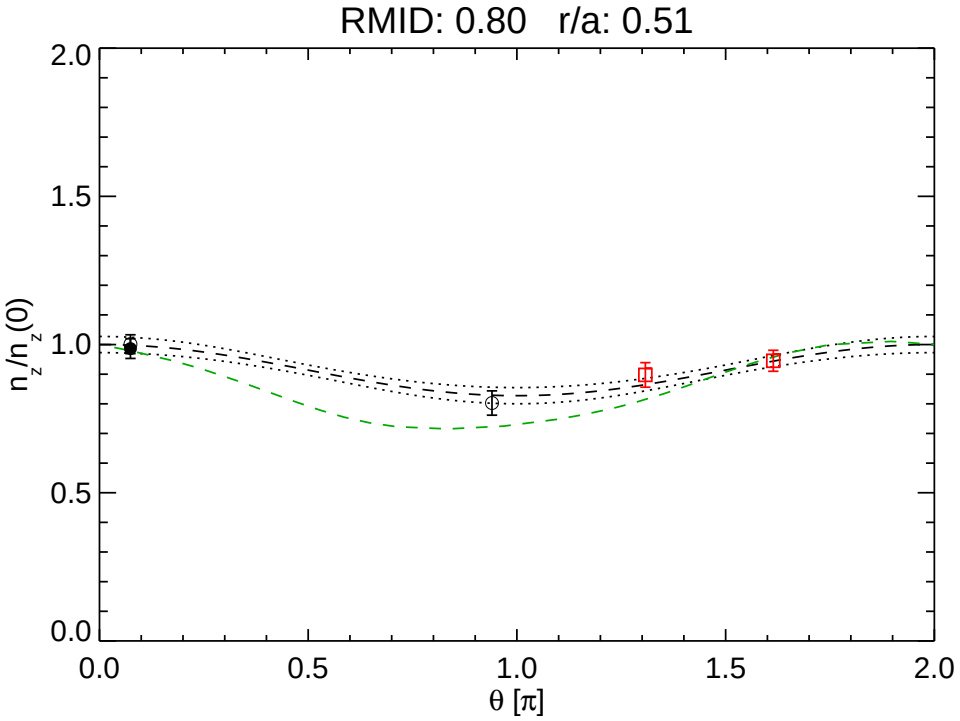

(a)

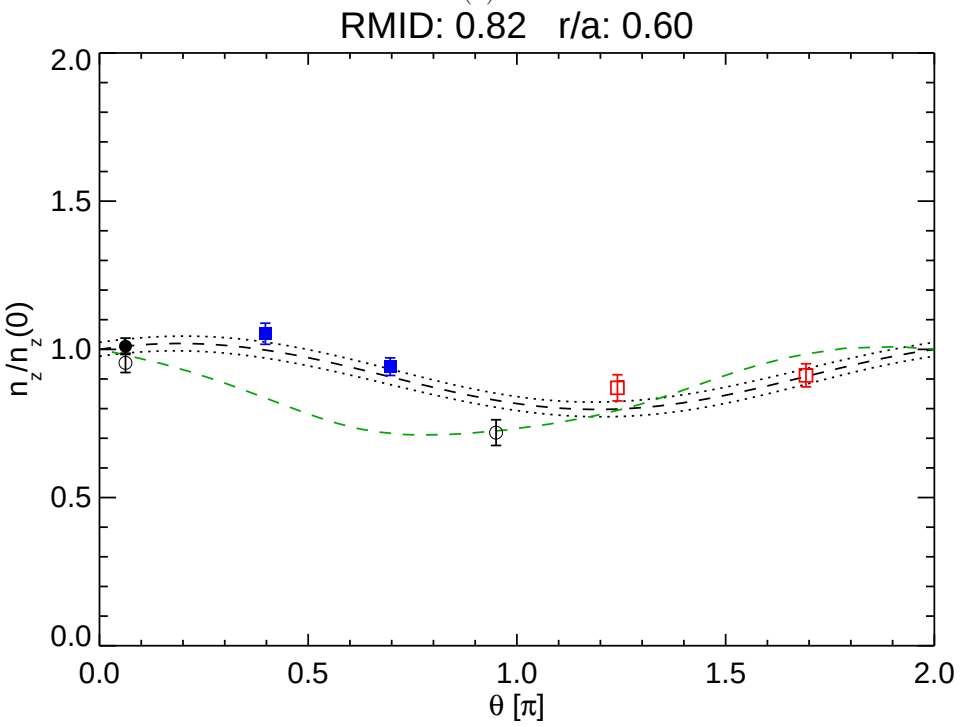

(b)

Figure 6-18: Poloidal variation of measured and modeled asymmetries at various r/a for the results shown in Figure 6-17; AXA (●), AXJ (○), WB2AX (■), WB3AX (□) and WB4AX (△)

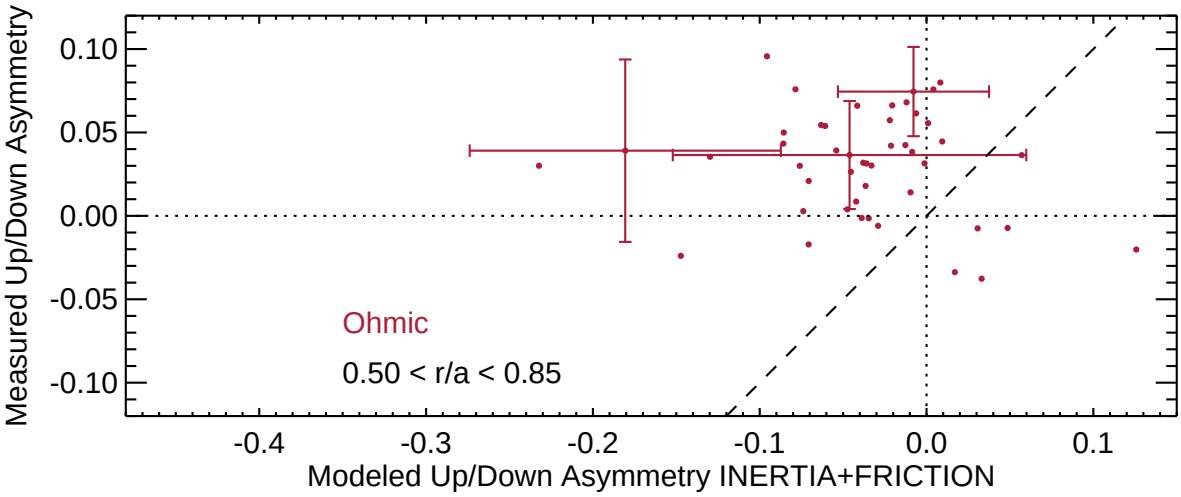

(a)

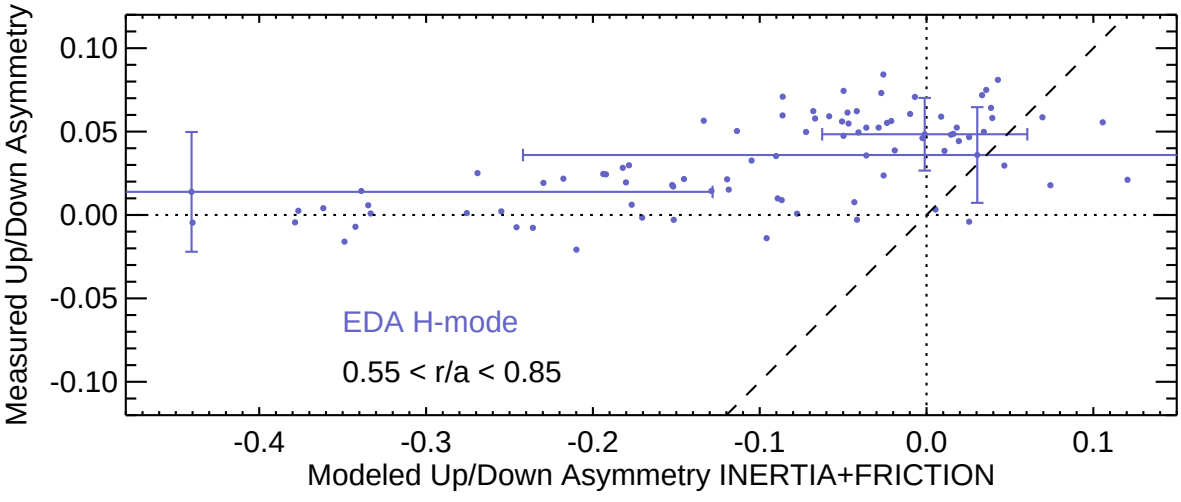

(b)

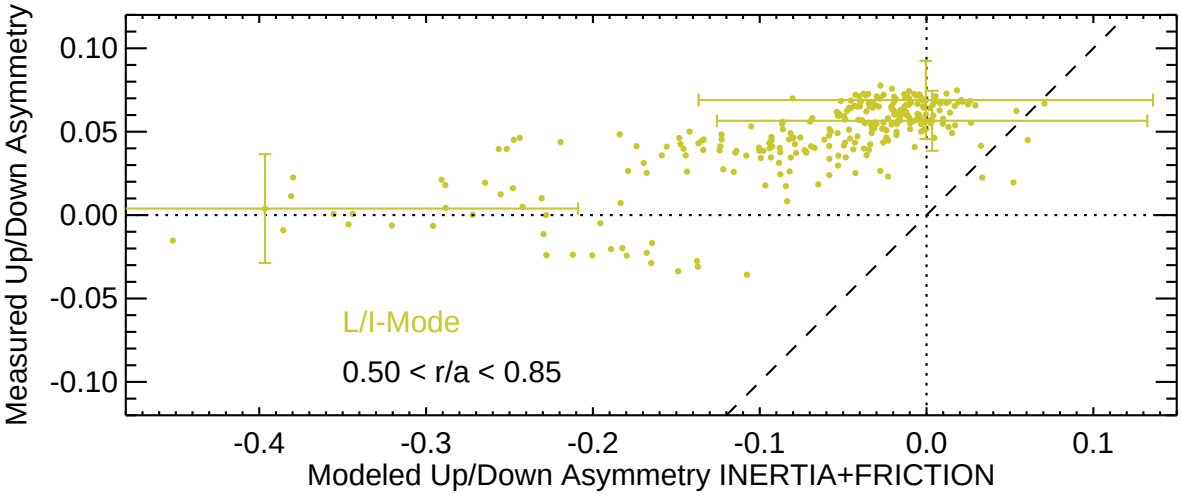

(c)

Figure 6-19: Comparison between measured up/down asymmetries with predictions from modeling including both inertial and friction forces for Ohmic (a) EDA H-mode (b) and L/I-mode (c) plasmas

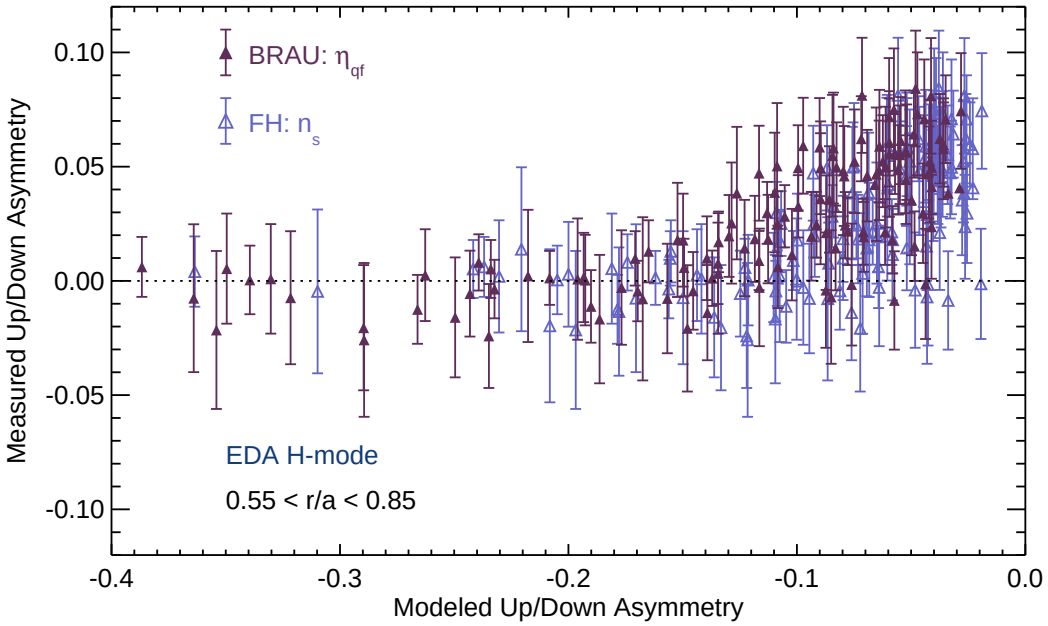

Figure 6-20: Comparison of the Brau (2.13) and Fülöp and Helander (A.19) models for up/down asymmetry, neither matching experiment.

$\eta_{qf} \sin\theta$), with η_{qf} given in (2.13). For the trace, circular-low aspect limit in [24], $n_s = 2\epsilon g(1+(1+\gamma)M_o^2)/(1+(1+\gamma)^2 g^2)$, with g (2.20) and $g\gamma$ (2.21) driven by radial gradients. As a consistency check, the measurements are compared to modeling using these simplified forms rather than the 1-D parallel transport code outlined in Appendix A. Data in Figure 6-19 were calculated using ion temperature profiles, but to reduce scatter, the temperature gradient terms for the circular limit comparison are calculated using spline fits to the T_e profiles. The data set is also restricted to EDA H-modes where the $T_e = T_i$ assumption is most accurate. A comparison of measurements to n_s and η_{qf} for $0.55 < r/a < 0.85$ is shown in Figure 6-20, where both trends overlap and predict substantial impurity accumulation in the direction of the ion ∇B drift direction. As the modeled asymmetry increases in magnitude, measurements show the plasma becoming more up/down symmetric, yet small, $n_{z,sin}/\langle n_z \rangle < 0.1$ accumulation opposite to the ion ∇B drift direction is observed in plasmas where n_s and η_{qf} are predicted to be near zero.

To gain insight into what could be driving the up/down asymmetry, the measured $n_{z,sin}/\langle n_z \rangle$ data are plotted against background plasma parameters. Data from all

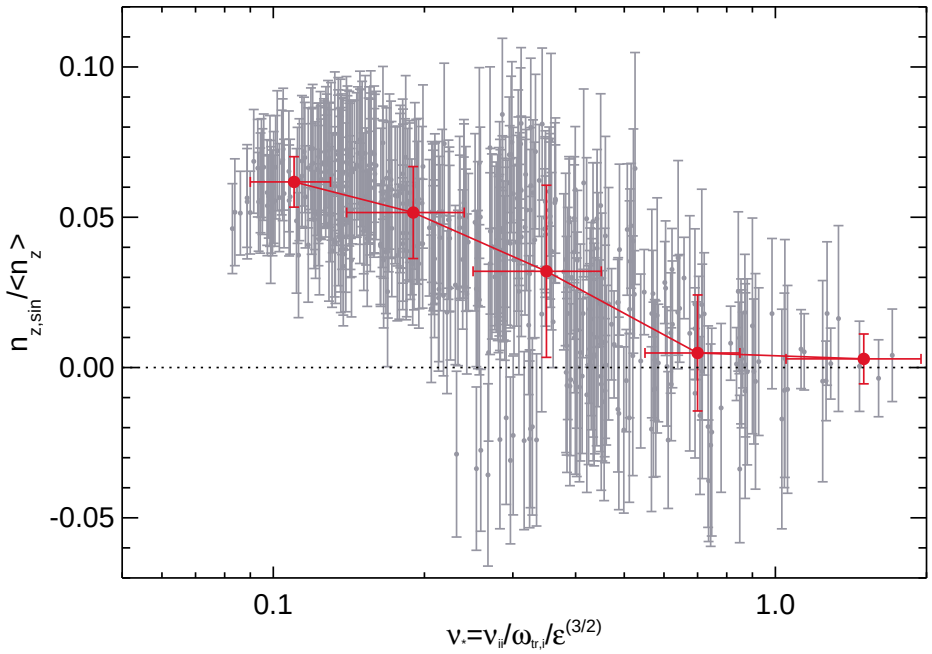

Figure 6-21: Weak correlation of the measured up/down asymmetry with collisionality, ν_*, with the full data set (gray) and binned and averaged data (red).

confinement regimes are used, but filtered to include only measurements with an uncertainty in the up/down asymmetry below 0.04. In Figures 6-21 to 6-24, the full data set is shown in gray with binned and averaged data shown in red. While somewhat limited due to uncertainties, the parametric dependencies of the measurements are shown to be inconsistent with modeling, suggesting an unaccounted for physical mechanism could be at work.

In Figure 6-21, the measured up/down asymmetry is plotted against the $\nu_* = \nu_{ii}/\omega_{tr,i}/\epsilon^{3/2}$, where $\nu_* > 1$ indicates a transition from the banana to the plateau regime. As the collisionality increases and approaches $\nu_* \simeq 1$, the weak impurity accumulation opposite the ion ∇B drift direction decreases and impurity density is measured to be more up/down symmetric. The larger asymmetries are well into the banana regime, confirming that comparisons between measurements and modeling shown earlier in Figure 6-19 were completed for the correct collisionality.

In Figure 6-22, the measured up/down asymmetry is plotted against the normalized electron temperature scale length, R_o/L_{T_e}, calculated from fits to measured Thomson scattering data, demonstrating the possibility of a weak trend. As the

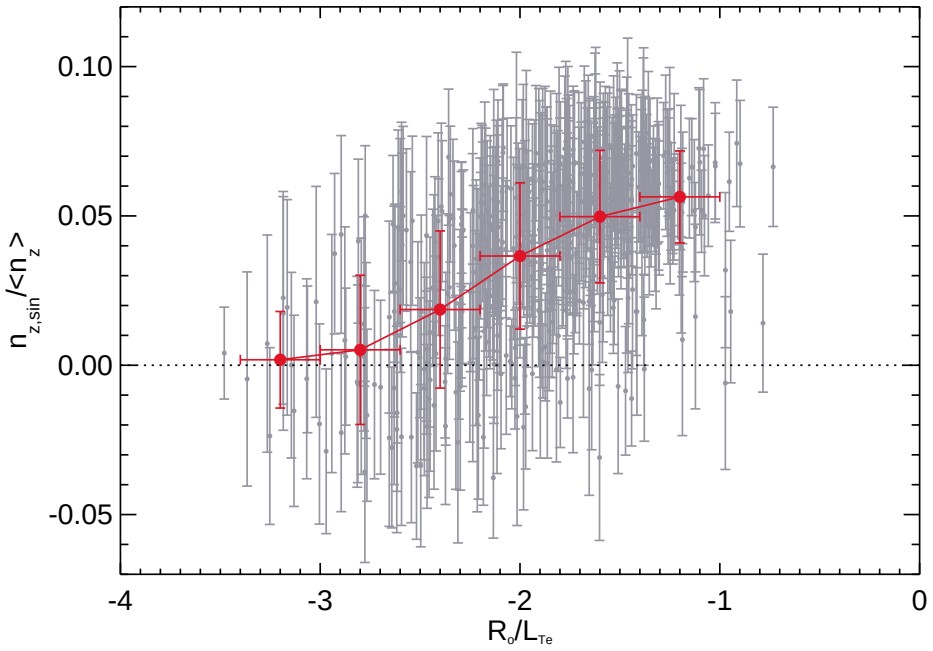

Figure 6-22: Weak correlation of the measured up/down asymmetry with the electron temperature gradient scale length, $L_{T_e} = \nabla T_e/T_e$, with the full data set (gray) and binned and averaged data (red).

gradient scale decreases, the up/down asymmetry moves from a small abundance opposite to the ion ∇B drift, becoming more up/down symmetric. Although T_e profiles are being used, the direction of the trend in the asymmetry is consistent with theory which predicts stronger accumulation in the ion ∇B drift direction as the ion temperature gradient increases. A stronger trend is observed when plotting the measured up/down asymmetry against the ion-ion collision time, τ_{ii}, shown in Figure 6-23, where the buildup of impurities away from the ion ∇B drift direction increases along with τ_{ii}. This is opposite to expectations, as the asymmetries should increase like $1/\tau_{ii}$ according to (2.20).

The parallel impurity transport modeling indicates that strong accumulation of impurities in the direction of the ion ∇B drift should be seen in C-Mod plasmas. Theory predicts this can only occur in the banana regime, only when the ion temperature gradients are stronger than the density gradient. In the Fülöp and Helander notation [24], the asymmetry is driven by the g parameter, $n_{sin}/\langle n_z \rangle \sim 2\epsilon g$, which can switch sign when $L_{T_i}^{-1} > 2L_{n_i}^{-1}$. That this occurs in C-Mod H-mode plasmas is consistent with

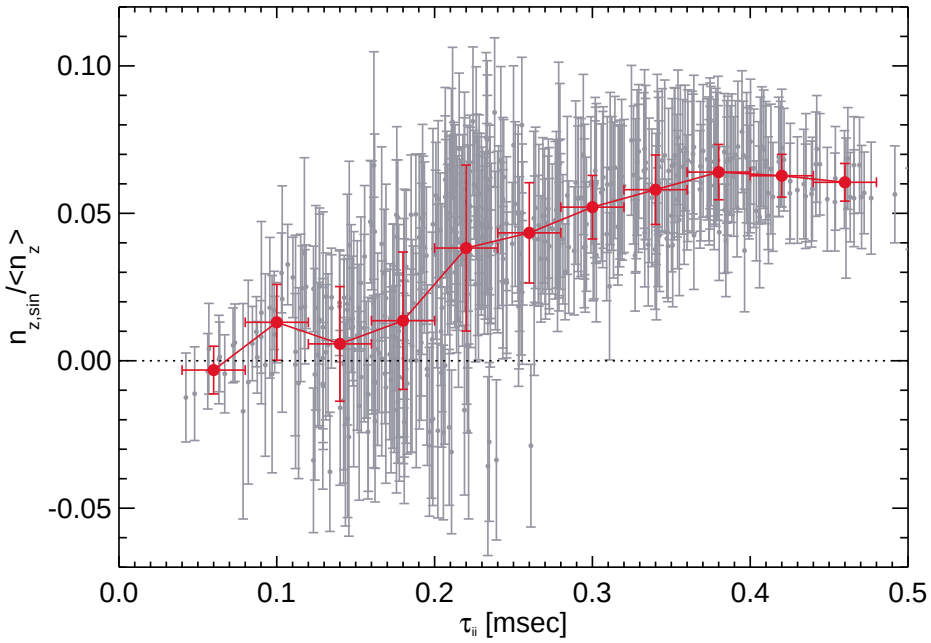

Figure 6-23: Correlation of the measured up/down asymmetry with the ion-ion collision time, τ_{ii}, with the full data set (gray) and binned and averaged data (red).

historical observations for EDA H-modes, where the electron density profiles are flat inside the pedestal, but temperature profiles are peaked on axis. In most cases, the observed asymmetries are in the opposite sense, $n_{sin}/\langle n_z \rangle > 0$, with trends indicating the largest positive values seen when the up/down asymmetry is predicted to be weaker. This indicates that another physical process may be at work to accumulate impurities away from the ion ∇B drift direction when ion-impurity friction is weak. This mechanism must also be large enough to balance or circumvent the ion-impurity friction in cases where predicted impurity asymmetries are large, $n_s/\langle n_z \rangle \sim -0.3$, while observations show them to be relatively small, $|n_{sin}/\langle n_z \rangle| \leq 0.05$.

One possibility is that turbulent cross-field transport is starting to become large enough to alter parallel transport. This hypothesis motivated by comparing the magnitude of the up/down asymmetry with a gyro-Bohm type diffusion coefficient [142], $\rho_{\star,\theta} T_e / eB_t$, as shown in Figure 6-24. Here, $n_{sin}/\langle n_z \rangle$ is shown to increase and saturate at $\sim$5%. Previous results in Chapters 4 and 5 showed that in the regions explored by the wall boxes, $0.50 < r/a < 0.85$, the parallel diffusive time-scale was much faster then any recognized cross-field diffusion. Additionally, neoclassical theory, when ex-

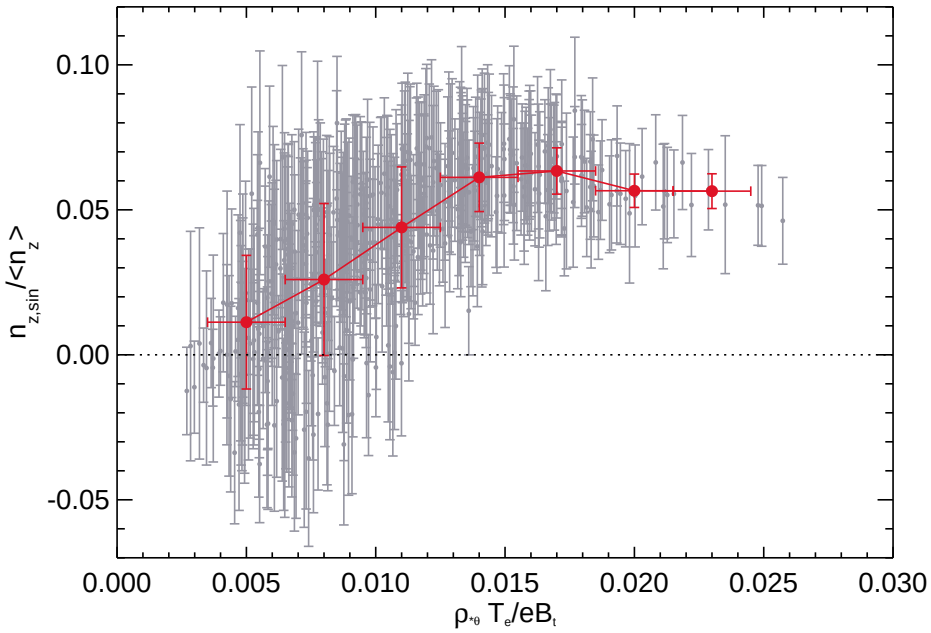

Figure 6-24: Correlation of the measured up/down asymmetry with gyro-Bohm diffusivity, $\rho_{\star,\theta}T_e/eB_t$, with the full data set (gray) and binned and averaged data (red).

tended to include ICRH effects, is demonstrated to be relatively accurate in describing the in/out asymmetry. This restricts any contribution to the asymmetry from turbulence to particle flux that is up/down asymmetric but remains relatively in/out symmetric. The impurity transport in this region of C-Mod plasmas is explored in [28], demonstrating flux-surface averaged, turbulent-driven radial convection on the order of 10 m/s. Drawing an analogy to the ∇B drift, the poloidally localized anomalous radial transport could be much larger than the measured flux surface average, resulting in much smaller perpendicular time scales then expected. The influence of turbulence on polodial rotation is also a possible mechanism [143]. This would influence the ion-impurity friction directly and thus have little impact on the in/out asymmetry. Establishing the existence of anomalous *parallel* transport would have important consequences for theory and simulation of impurity transport. Rather than draw firm conclusions using the limited data shown here, subsequent experiments on up/down asymmetries should work to simultaneously characterize the radial and poloidal transport and look for connections. This is discussed further in Appendix D for argon x-ray emission asymmetries observed in Ohmic plasmas.

6.5 Link Between the Up/Down Asymmetry and Poloidal Rotation

The friction is dependent upon the relative velocity between the ions and impurities, and in order to investigate the discrepancy between the measured and modeled up/down asymmetries, it is worth looking closer into the neoclassical prediction for impurity poloidal rotation. In the first order velocity equation,

$$\mathbf{V}_a = -\left(\frac{\partial \Phi}{\partial \psi} + \frac{1}{Z_a e n_a}\frac{\partial p_a}{\partial \psi}\right) R\hat{\phi} + \frac{K_a(\psi)}{n_a}\mathbf{B} \tag{6.6}$$

the field aligned flow term, $K_a(\psi)/n_a\mathbf{B}$, is found by solving the parallel force balance equation to find $u_a = K_a/\langle n_a \rangle$. This is accomplished by solving the same parallel transport equation being used to find the impurity density variation, and comes from the $n_z(0) = n_z(2\pi)$ constraint. The u_z profiles that are output from the code described in Appendix A are therefore self-consistent with the predicted poloidal asymmetry.

The toroidal velocity measured by HIREXSR has been assumed to be due entirely to solid-body rotation, ω, which is equivalent to assuming $u_z B_t \ll \omega R$. The diagnostic does have the ability to resolve poloidal rotation by comparing line-integrated velocity for chords at the same poloidal tangency radius above and below the midplane, but due to uncertainties in equilibrium reconstructions, the accuracy of the measurement is a few km/s, close to the expected poloidal flow speeds. Outside of isolated cases during so-called mode-conversion flow-drive [144], measurements of v_θ on C-Mod are limited by the noise floor of HIREXSR, estimated to be ∼1-2 km/s. Using u_z profiles computed from force balance, the expected poloidal flow, $v_\theta = u_z B_\theta$, and the toroidal flow, $v_\phi = u_z B_t + \omega R$, can be checked against the assumptions used in analyzing the rotation data. If v_θ predicted from force balance is large, ~ 10 km/s, but not observed experimentally, it has the same impact as a disagreement in $n_z(\theta)$ for validation of parallel impurity transport theory. If modeling shows v_θ is below the HIREXSR limit yet $u_z B_t \simeq \omega R$, then the experimental data has been interpreted incorrectly.

Poloidal rotation analysis for argon is shown for the previously analyzed 0.9 MA

EDA H-mode shot (1110201017) in Figure 6-25 where spline fits to experimental T_e data (a), rather than measured T_i, are used in calculating u_z (b) due to the sensitivity to L_T^{-1}. Error bars for u_z are estimated by solving for u_z for $T \pm \sigma_T$. The v_θ (c) profile is calculated for the outboard midplane, where positive velocity means flow away from the ion ∇B drift direction, and demonstrates the poloidal flow is below the estimated observational limit of HIREXSR. Two toroidal flow (d) profiles are plotted; the $u_z B_t + \omega R$ profile (black), which is the velocity that HIREXSR actually measures, and the solid-body rotation, ωR (red), calculated by subtracting off the predicted $u_z B_t$ component. Inside of $r/a \sim 0.5$, differences in the two profiles are shown to be outside of error bars, with the ωR 10-15% larger than what is, in practice, found from HIREXSR analysis by assuming $u_z B_t = 0$. Since ω is used to find the in/out asymmetry, this result indicates that predicted outboard accumulation for the core of 1110201017 should be increased. It is difficult to assign any systematic error since, like the up/down asymmetry, the actual v_θ could end up being the opposite sign. At the very least, the uncertainty in the predicted in/out asymmetry should be increased to reflect the absence of accurate poloidal rotation data.

The same analysis is performed for the 0.7 MA EDA H-mode (1110201026) and shown in Figure 6-26. The magnitude of the poloidal flow remains below 0.5 km/s, and the impact on the toroidal flow is negligible within stated uncertainty. Checking other shots from the Ohmic, EDA H-mode and L/I-mode data set shows that, in most cases, changes in the ω profile are minor, and results shown in Figure 6-25 represent more of an extreme case.

In the spatial region of largest poloidal flow, substantial disagreement between theory and experiment is seen in the up/down asymmetry. One aspect omitted from rotation and asymmetry analysis is the impact of impurities on the main ion poloidal flow. Throughout this research, u_i has been calculated assuming the trace impurity limit, fixing it at the conventional neoclassical prediction,

$$u_{i,NC} = -\frac{f_c}{3}\frac{I}{e\langle B^2 \rangle}\frac{\partial T_i}{\partial \psi} \tag{6.7}$$

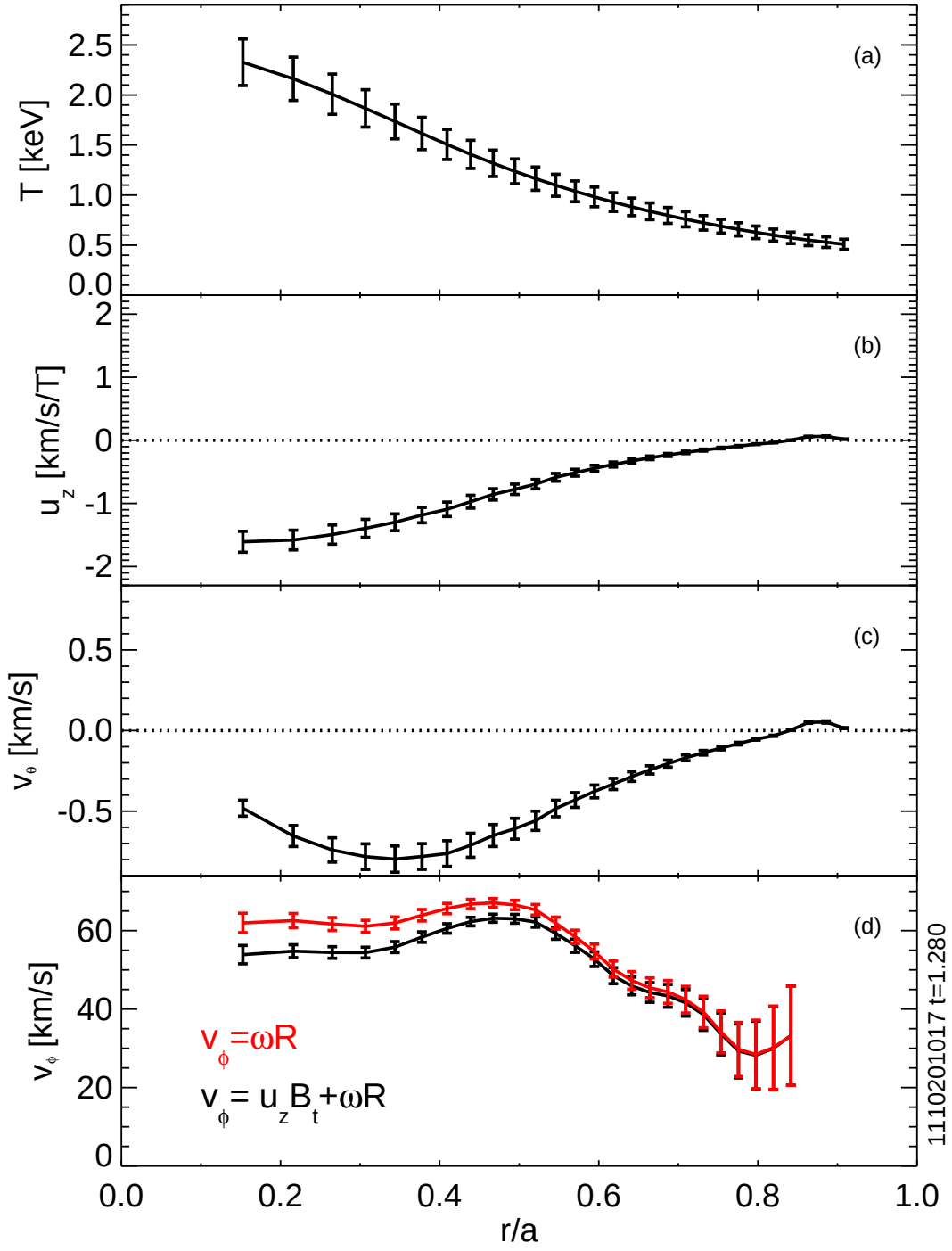

Figure 6-25: Poloidal rotation and modification to toroidal velocity predicted by theory for the 0.9 MA EDA H-mode

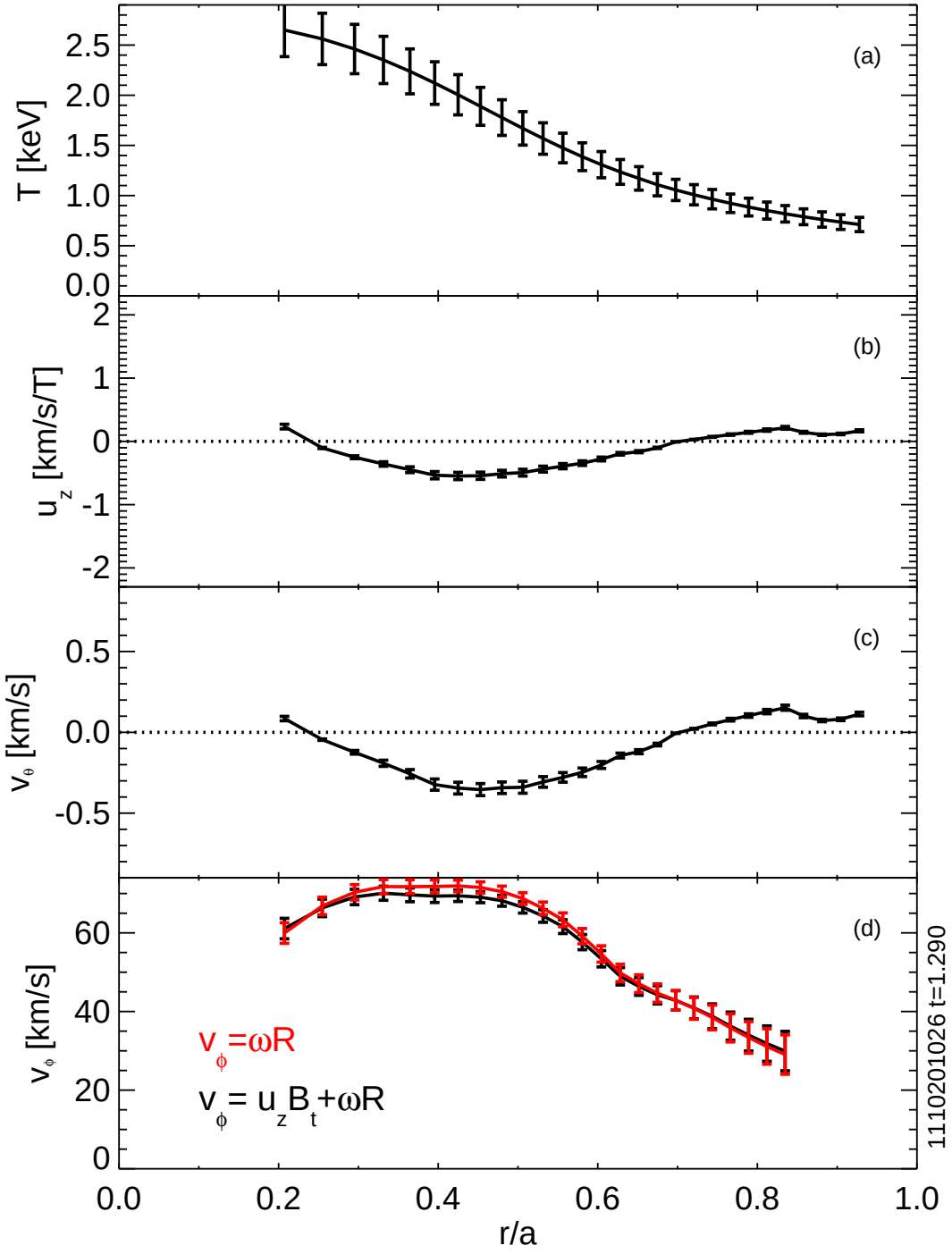

Figure 6-26: Poloidal rotation and modification to toroidal velocity predicted by theory for the 0.7 MA EDA H-mode

while theory predicts u_i to be modified for $n_z Z^2/n_i \sim 1$. Since the $g\gamma$ term in Fülöp and Helander [24],

$$g\gamma = \frac{m_i Z^2}{\tau_{ii}} \frac{\langle B^2 \rangle}{\vec{B} \cdot \nabla\theta} u_i \tag{6.8}$$

depends on u_i, the ion-impurity friction has a predicted dependence on the magnitude of n_z that is not currently captured by the modeling. Previously, for asymmetries driven by the centrifugal force and ICRH effects, the effect of background impurities could be included via Z_{eff}. For friction-based asymmetries, a separate force balance for the background impurities needs to be solved, and their effect on the main ion v_θ included. Thus, even when observing a trace-impurity, if $Z_{eff} \sim 2$, a trace-limit theory would be invalid. Note that if the background impurity is sufficiently high then impurity-impurity friction needs to included as well.

An alternate interpretation of the trends in Section 6.4.1 would be that small changes in the background plasma parameters such as L_{T_e}, $\nu_\star$ and $\rho_\star$ are responsible for changes in the main ion poloidal flow. The sensitivity of the asymmetry physics to main ion poloidal rotation can be studied by artificially changing the magnitude of the $g\gamma$ term. Although a weak constraint on the impurity poloidal rotation is provided by HIREXSR, no measurement of the main ion flow is available. Figure 6-27 shows the effect changes in u_i on the up/down and in/out asymmetries as well as for the poloidal rotation. This is completed for the 0.9 MA EDA H-mode (017) where the asymmetry is due to molybdenum, but the poloidal rotation is estimate from Ar^{16+} emission. For each $u_i/u_{i,NC}$ the parallel transport code is run for molybdenum to find the $n_{cos}/\langle n_z \rangle$ (a) and $n_{sin}/\langle n_z \rangle$ (b) profiles, and run again for argon to find $v_{\theta,z}$ (c), plotted for the outboard midplane. The up/down asymmetry is shown to change monotonically with u_i/u_{NC} in this range, while the in/out asymmetry increases and then decreases. This is due, numerically, to the non-linear dependence of $n_{cos}/\langle n_z \rangle$ on γ (A.18) and the fact that γ is negative. Physically, this could be interpreted as poloidal flow becoming so strong that is smears out any asymmetries driven by the centrifugal force.

It is clear from these results that both the up/down asymmetry and the impurity

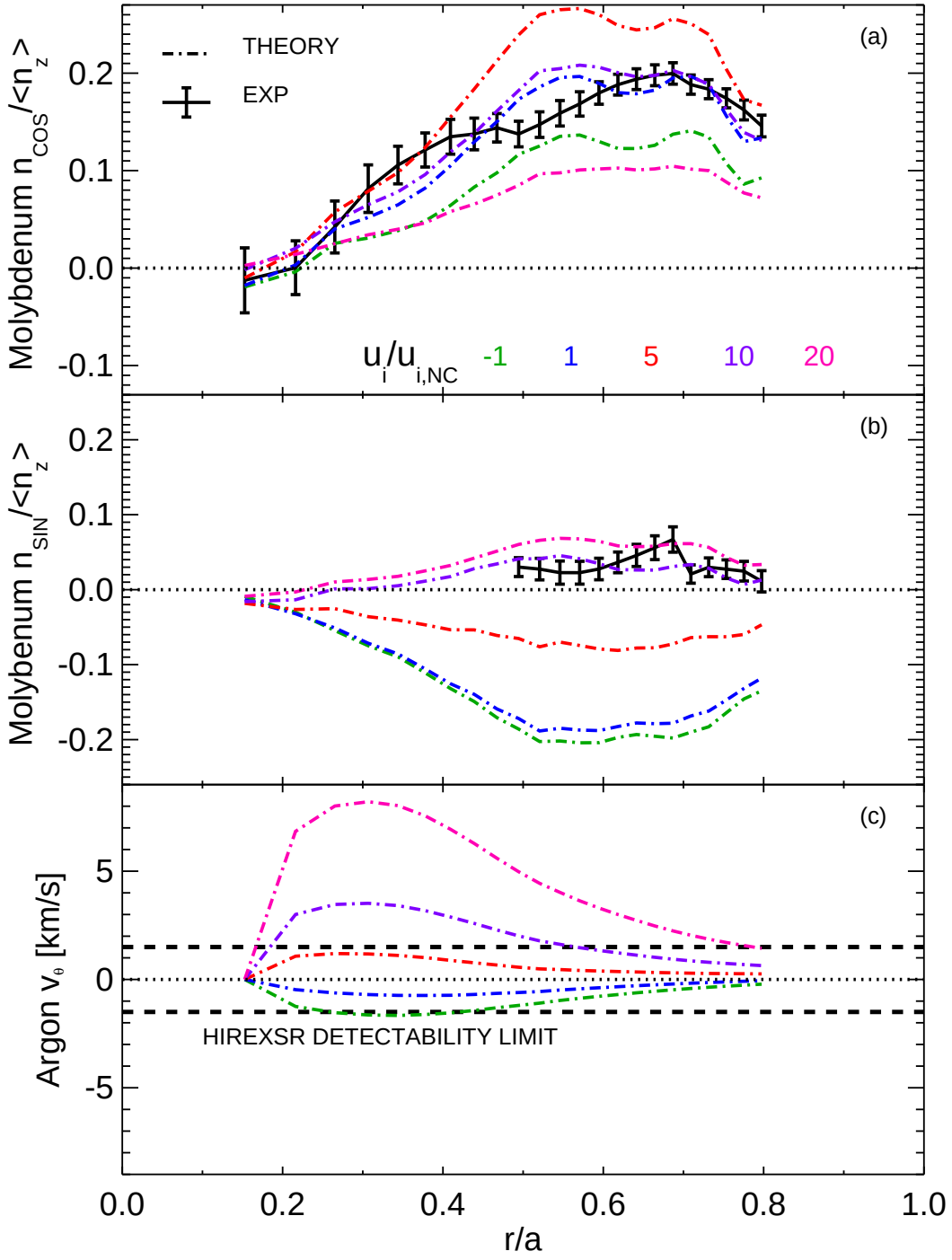

Figure 6-27: Change in the molybdenum asymmetry profiles and the argon poloidal rotation for various assumptions of the main ion poloidal flow

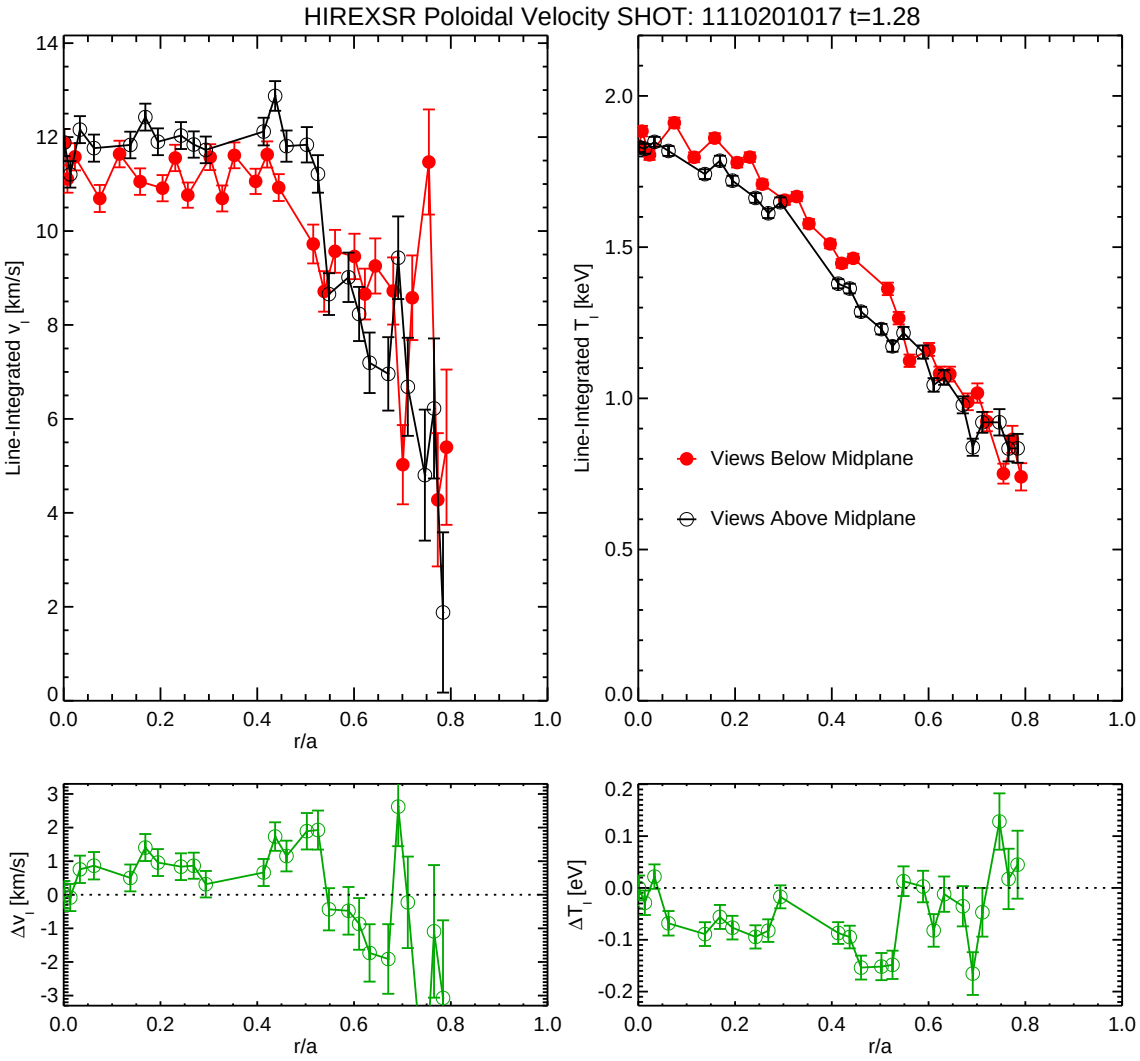

Figure 6-28: Estimate of argon poloidal rotation from HIREXSR by comparing chords above and below the midplane

poloidal flow are sensitive to the main ion poloidal rotation. The best agreement is found for $u_i/u_{i,NC} = 10$, where the modeled in/out and up/down asymmetries are both in reasonable agreement with measurement. But, forcing $u_i/u_{i,NC} = 10$ results in $v_{\theta,z}$ for argon of 3-4 km/s at $r/a \simeq 0.3$, speeds which should be observable on HIREXSR. Figure 6-28 shows an estimate of the argon poloidal rotation by comparing line-integrated velocity (left) and temperature (right) data against poloidal tangency radii. The inclusion of the temperature, which is expected to be up/down symmetric, increases confidence that the flux-surface mapping has been computed properly. The difference in the velocity profiles show that poloidal rotation is measured to be in the 1-2 km/s range for $r/a < 0.5$, in disagreement with predictions when using $u_i/u_{i,NC} \geq 10$

Previous experimental tests of poloidal impurity rotation [145] [146] [147] show that agreement between theory and experiment has not yet been consistently demonstrated in the core of collisionless tokamak plasmas. Comparisons with the best agreement was for carbon on NSTX [148] and MAST [149], showing good agreement between measured v_θ profiles for C^{6+} and those predicted by NCLASS and, for NSTX, GTC-NEO. Since both these experiments exhibit nearly sonic main ion flows, and $Z_{eff} - 1 \sim 1$ due to carbon, the influence of a non-trace, $\tilde{n}_z/\langle n_z \rangle \sim 1$ impurity would likely have an impact the neoclassical prediction for $v_{\theta,z}$. The link established between poloidal rotation and the density variation of an impurity shows that a much more stringent test would be to simultaneously demonstrate that both measured flows and up/down asymmetries agree with theory. The most widely used method to find $v_{\theta,z}$ is charge-exchange recombination spectroscopy using midplane neutral beams, a technique that is unable to meet this challenge.

6.6 Summary

In this chapter, measurements of in/out and up/down asymmetries thought to be driven by ion/impurity friction were compared qualitatively and quantitatively with parallel impurity transport modeling. Section 6.2-6.3 showed how in Ohmic ITBs and

in the edge of EDA H-modes, radiation enhancement on the inboard side of a flux surface was observed, consistent with friction dominating the in/out asymmetry physics. Uncertainties in experimental data and the absence of flow and ion temperature profiles prevented convincing quantitative comparisons to theory, but data collected will be useful in designing future experiments and diagnostics to study asymmetry physics in ITBs or the H-mode pedestal.

In Section 6.4 the up/down asymmetries measured in Ohmic, EDA H-mode and L/I-mode plasma were compared with modeling in the trace impurity limit. Significant disagreement between experiment and theory was demonstrated. In the modeling, large impurity buildup, $\tilde{n}_z/\langle n_z \rangle$ up to 0.3, in the direction of the ∇B drift direction is predicted, while modest accumulation, $\tilde{n}_z/\langle n_z \rangle \leq 0.1$, was regularly observed in the opposite direction. Two hypotheses were presented that could be the cause of the discrepancy. The magnitude of the up/down asymmetry did not scale with background plasma parameters as expected but instead was observed to increase as a gyro-Bohm like parameter, $\rho_{\star,\theta} T_e / eB_t$. This indicated the possibility of turbulence influencing the parallel transport, although in order to be consistent with in/out asymmetry measurements, severe restrictions on the nature of the turbulence are imposed. In Section 6.5, the sensitivity of the up/down asymmetry to assumptions of the main ion poloidal rotation, $v_{\theta,i}$, demonstrated the tight connection between the impurity poloidal rotation, $v_{\theta,z}$ and the up/down asymmetry. Artificial changes to the main ion flow in the modeling allowed agreement with measured up/down and in/out asymmetries in an EDA H-mode, but required a poloidal rotation for argon that is not observed by HIREXSR. Motivation for changes in $v_{\theta,i}$ are motivated by including the impact of a non-trace impurity on the main ion flow, which has not been accounted for in the current implementation of the parallel impurity transport code.

Chapter 7

Contributions and Consequences

The previous three chapters have shown how experiments conducted on Alcator C-Mod have led to a better understanding of parallel impurity transport. In this chapter we discuss the implications and results of this knowledge and how it impacts the tokamak community. The rigor exhibited in previous chapters is somewhat relaxed and the tone of the following sections is meant to indicate that these topics are open for further discussion. To begin with, the major accomplishments of this research are briefly summarized.

1. **Demonstrating a large $\tilde{n}_z/\langle n_z \rangle \sim 0.3$ in/out asymmetry due to intrinsic rotation**

   Previously, buildup of impurities on the LFS of a flux surface due to the centrifugal force has only been observed in neutral beam-heated plasmas where significant external torque drives toroidal flow above the impurity thermal speed. Chapter 4 shows that self-generated flows in C-Mod plasmas are sufficient to develop a strong in/out asymmetry in the molybdenum density. In Section 7.2, this results is discussed in the context of tungsten asymmetries on ITER and Section 7.4 investigates the impact of poloidal asymmetries on radial impurity transport.

2. **Establishing the impact of fast ion pressure anisotropy on parallel impurity transport**

In Chapter 5, existing parallel transport theory was extended to include effects from particle distributions exhibiting a pressure anisotropy like that expected during ion cyclotron minority heating. Measurements on C-Mod conclusively show a link between ICRH and inboard accumulation of impurities, and estimates using the extended theory agree well with experimental results. The strength of the fast ion contribution to the poloidal asymmetry calls into question prior in/out asymmetry validation efforts that used neutral beam heating, and this is discussed in Section 7.1. The sensitivity of the impurity asymmetry to small poloidal potential variations also demonstrates its effectiveness a novel diagnostic tool, as explored in Section 7.5.

3. **Defining a more rigorous experimental test of ion/impurity friction, linking asymmetries and poloidal rotation**
   Measurements of up/down asymmetries driven by ion/impurity friction are shown to disagree with theory in the trace impurity limit, $n_z Z^2/n_i \ll 1$ in Chapter 6. While more work remains to study the coupled parallel transport in the non-trace limit, the coupling between friction-driven asymmetries and poloidal rotation is demonstrated. Thus, to fully validate parallel impurity transport theory, the flux surface asymmetries and $v_{\theta,z}$ must be correctly predicted. While measured up/down asymmetries are found to be small, $\leq$10%, Section 7.3 shows how even these levels could impact future Doppler tomography diagnostics if left unaccounted for.

7.1 Fast Ion Anisotropy in Neutral Beam Heated Plasmas

In Section 5.1, the derivation of the poloidally varying electrostatic potential (5.10) did not assume that ion cyclotron heating was used to develop the pressure anisotropy. As Chang points out [64], perpendicular neutral beam injection will create an isotropy with $p_\perp > p_\parallel$ by launching particles into trapped orbits. Beams aligned toroidally will

also develop an anisotropy (both $p_\parallel > p_\perp$ and $p_\parallel < p_\perp$ are possible) [150][151][152], and when used for fueling will break the minority assumption, $\langle n_m \rangle / \langle n_e \rangle \ll 1$, used to derive (5.11). According to this model, if the fast ions have $T_\perp / T_\parallel < 1$, the addition of an anisotropic species in parallel force balance would act to increase the outboard accumulation, adding to the centrifugal force. The addition of finite orbit effects and differences in beam energy and injection geometry; on-axis, off-axis, co- and counter-current, can create an interesting zoology of fast ion distributions [153] making it not entirely straightforward to model the the effect on parallel impurity transport. It is also clear that contours of constant fast ion pressure are generally not equivalent to flux surface contours [154][155][156].

Important consequences follow from the possibility of a poloidal electric field due to a fast ion density asymmetry in a neutral beam-heated plasma. If $T_\parallel > T_\perp$ this effect could reconcile experimental inconsistencies pointed out in Section 2.4.2. JET observed differences in in/out asymmetries between co- and counter-current beam injection. Similar to the core asymmetry scaling shown in I-mode on C-Mod, asymmetries measured in Ni and Fe for JET co-current NBI plasmas scaled with Mach number, but were less than for counter-current, even reversing at low velocities as shown in Figure 7-1 from [83] (which was also shown in Chapter 2). This is a clear indication that even for neutral-beam heated plasmas, the centrifugal force is not the entire story. Additionally, the optimized shear plasmas JET used to validate centrifugal force models [87] had 6 MW of ion cyclotron minority heating and observed outboard accumulation of low-Z impurities prior to Ni injection. Both have the effect of reducing the outboard accumulation of a high-Z impurity, and so if measurements were observed to be consistent with theory based on centrifugal force, then some unaccounted for effect must be offsetting the reduction expected from minority heating and Z_{eff}.

Also mentioned in Section 2.4.2 is the inconsistency between Ar and Kr asymmetries in ASDEX-U beam heated plasmas. Published data show a much larger asymmetry for Kr than for Ar, more then a factor of 10 higher, despite the mass scaling of the centrifugal force suggesting a more modest difference for the two species.

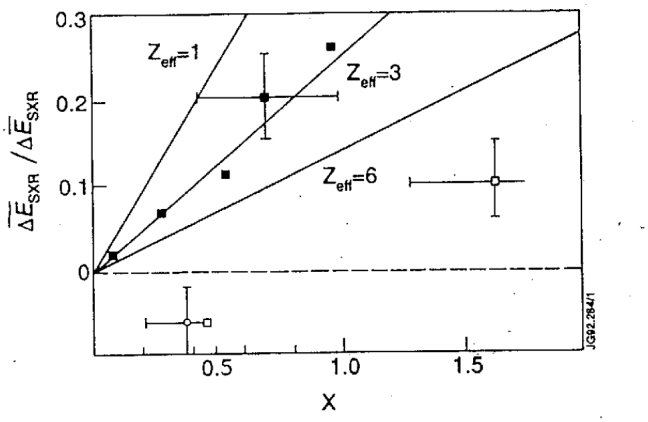

Fig. 4 Relative in/out modulation of the soft X-ray emissivity perturbation after metal injection in beam heated plasmas. ■ Ni, ctr.-inj.; [] Ni, co-inj.; ⊡ Fe, co-inj. The straight lines represent the prediction of eq.(1) for different values of Zeff in D plasma.

Figure 7-1: Initial measurements of in/out asymmetry for Ni and Fe injection into ELM-free H-modes (from [83])

If the fast ion distribution driven by beam heating caused inboard charge accumulation, then the asymmetry thought to be due exclusively to inertia would be enhanced. Since the electrostatic force depends on the absolute charge and not the charge to mass ratio, this would lead to a result like ASDEX-U where the higher-Z impurity (Kr) has a larger in/out asymmetry than would be expected from examining that of the lower-Z impurity (Ar).

These observations indicate that prior experimental results of in/out asymmetries in beam-heated plasmas should be re-evaluated in the context of the extended parallel transport theory presented in Section 5.1. Care must be taken to determine small poloidal potential variations, $e\tilde{\Phi}/T_e \sim \epsilon^2$, driven by any non-thermal population since these variations will be multiplied by Z when included into parallel impurity momentum balance.

7.2 Estimates of Tungsten Asymmetries on ITER

Currently envisioned designs for ITER and beyond will use tungsten as a divertor plasma facing material [157], and gases such as nitrogen, neon, argon and krypton for radiative mantles and divertors [158]. The results of molybdenum asymmetry studies on C-Mod can be used to estimate the behavior high-Z impurities on ITER. While the details of the kinetic profiles that will be achieved are a matter of some debate, the ITPA Integrated Operational Scenarios (IOS) teams have recently published estimates using transport modeling tools benchmarked against current experiments. Using the circular, $m = 1$ expansion (5.13), a rough idea of the in/out asymmetry can be found. Detailed flux-surface geometry unnecessary for this level of precision.

7.2.1 Centrifugal Force

Using existing transport modeling tools [159], IOS has published expected steady-state kinetic profiles on ITER where neutral beam heating is used to drive the toroidal rotation. In Figure 7-2, the impurity Mach number and $\tilde{n}_z/\langle n_z \rangle$ profiles are shown over the minor radius, assuming $v_i = v_z$ for simplicity. As with molybdenum, T_e-dependent average ionization curves are used to find the impurity charge. The TOPICS-based simulation shows tungsten which would result in $\tilde{n}_z/\langle n_z \rangle$ close to unity, much higher then has been observed on present experiments. TRANSP predictions are approximately a factor of two lower.

Intrinsic Rotation

In a large, high-density tokamak like ITER, the impact of beam-heating on core rotation will be lessened due to reduced penetration of low-energy, ~ 100 keV, beams or the reduced torque of high energy, ~ 1 MeV, beams. The observation of centrifugal effects on beam-heated plasmas is consistent with the concept of a tokamak driven by external momentum input. In contrast, this research demonstrates for the first time that these inertial effects can be accessed by entirely self-generated flows, the so-called intrinsic rotation, present in a tokamak plasma. While previous measurements

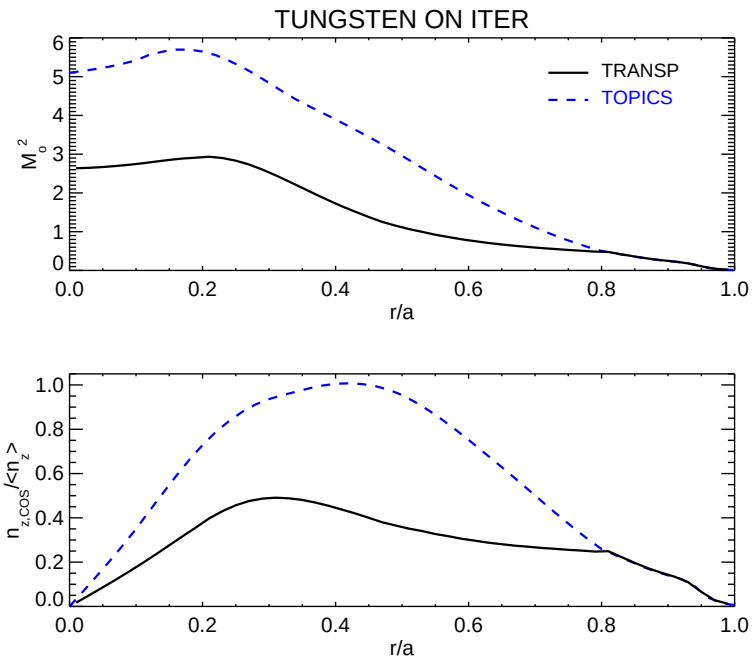

Figure 7-2: Expected asymmetry of tungsten on ITER due to centrifugal force (data from [159])

of rotation on Alcator C-Mod reveal that in/out asymmetries in molybdenum density should have been expected, the concept that the centrifugal force can play a role in transport in a plasma with no external momentum input is somewhat novel.

The origin of the intrinsic rotation is still not completely understood, but it has been observed on many tokamaks, enough to expect it will be present in ITER. This was not included in any of the IOS simulations mentioned above. Initial cross-machine scaling of the intrinsic rotation [160] showed some scaling of Mach number with β_N, as shown in Figure 7-3, although this did not unify the data set as well as other parameters. What is clear from these attempts is that main-ion Mach numbers, M_i, of 0.2-0.3 are commonly seen in other experiments, not just Alcator C-Mod. With asymmetries driven by the centrifugal force scaling like $M_i^2 m_z/m_i$, even modest flows can lead to large asymmetries of heavy impurities, making the intrinsic rotation an important unknown in predicting parallel impurity transport for ITER.

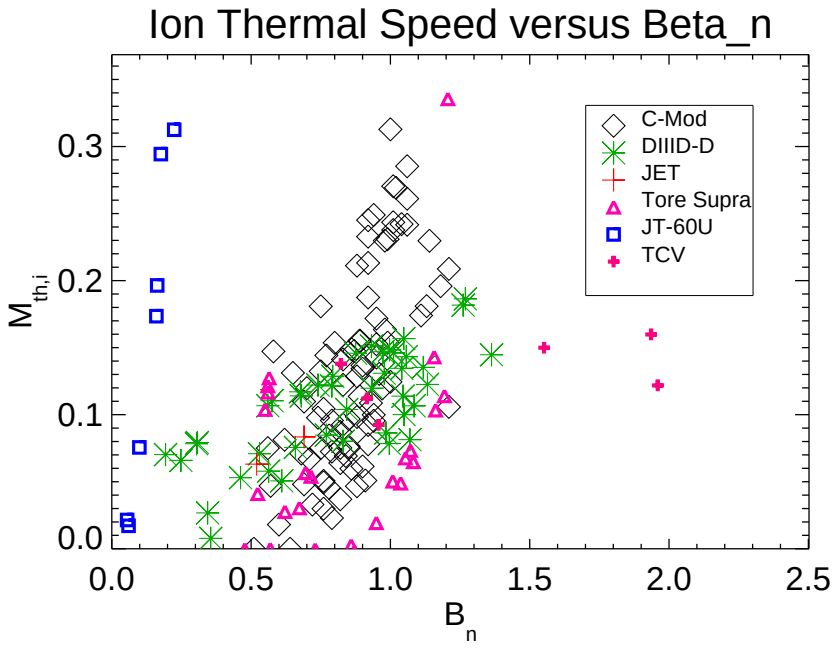

Figure 7-3: Main ion mach number due to intrinsic rotation (from [160])

7.2.2 Cyclotron Heating

The use of ∼20 MW of ion cyclotron heating is also planned for ITER, increasing the relevance of the C-Mod's experience with impurity asymmetries due to combined inertial and electrostatic forces. Benchmarking results of several full-wave codes for ITER used PTRANSP to determine the minority temperature anisotropy [161] for various planned heating schemes, with two of the cases shown in Figure 7-4. In 7-4a, results are plotted for a 2% ^{3}He minority in a DT H-mode at full field. In this instance, the heating is localized to the core, resulting in $\tilde{n}_z/\langle n_z \rangle \sim$ -0.1. In 7-4b, the results are plotted for 20% H minority heating in a ^{4}He H-mode at 2.7 T, a planned half-field, non-nuclear commissioning phase. In this instance, the heating is sufficiently off axis and the minority density large enough to expect a situation of almost complete HFS accumulation of tungsten. Comparing this with the asymmetry due to centrifugal force just discussed, it is clear that tungsten will have a complicated spatial distribution.

The planned heating for ITER will also include electron cyclotron heating, which is also predicted to contribute to poloidal impurity asymmetries. By trapping electrons

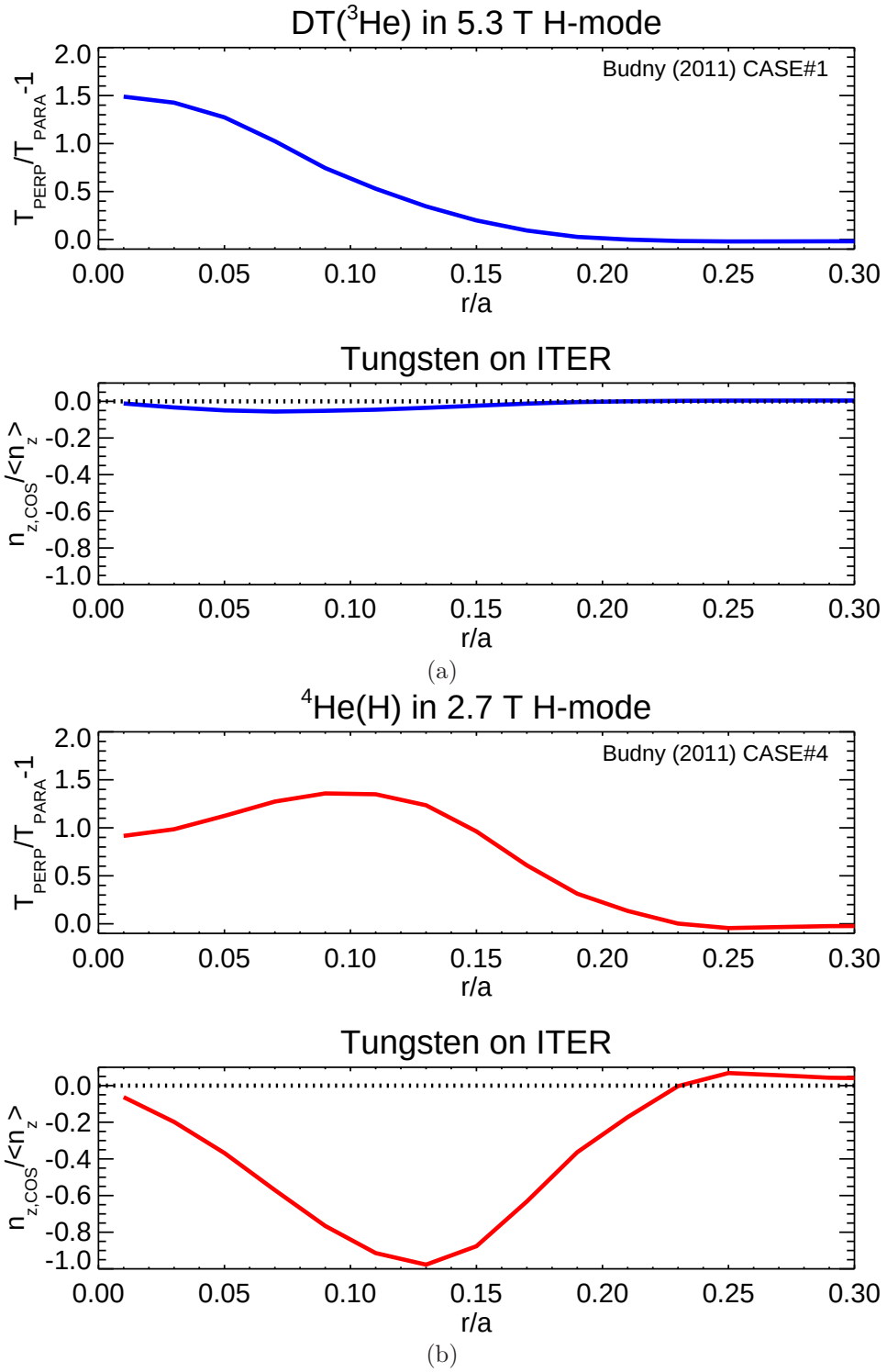

Figure 7-4: Expected asymmetry of tungsten on ITER due to ion cyclotron heating using ^{3}He minority in a DT plasma (a) and H minority in a ^{4}He plasma (b) (data from [161])

on the outboard side, a negative charge build-up will occur, creating a low-field side impurity accumulation. This should motivate explorations of the impact of ECRH on impurity asymmetries, since this effect has not been documented experimentally.

7.3 Impact of Asymmetry on Doppler Tomography

The HIREXSR diagnostic on C-Mod and the planned imaging x-ray crystal spectrometer for ITER view the plasma only from the outboard side, and cannot resolve any in/out asymmetries. For the He-like Ar emission, HIREXSR views above and below the midplane and so can resolve $m = 1$ up/down asymmetries. Current plans for the ITER x-ray crystal spectrometer [162] do not have a full poloidal view for all lines. The moment technique used in Doppler tomography calculates profiles of emissivity weighted flow and temperature, and must divide by the emissivity to get the local temperature and flow profiles [37]. It is not straightforward to see how an unresolved or unaccounted for poloidal asymmetry in the emissivity could impact the output of such inversions.

To gain insight into this problem, symmetric and both up/down and in/out asymmetric emissivity profiles are used to compute synthetic line-integrated spectra assuming flow, $\mathbf{v} = \omega(\psi)R\hat{\phi}$, and temperature profiles, $T_z(\psi)$, can be expressed by flux-functions. From these spectra, moment profiles are calculated and inverted assuming symmetric emissivity to find ω and T_z which can then be compared to the assumed profiles. No photon noise is included in order to demonstrate the systematic error caused by the asymmetry. Two extreme sets of viewing geometries are assumed, as shown in Figure 7-5. One has the crystal near the plasma (7-5a) and views the plasma at an angle, while the other places the crystal at infinity (7-5b) and views with parallel sight lines. Like HIREXSR, both views have a small toroidal angle to gain sensitivity to toroidal rotation.

Although not shown, both views are relatively insensitive to in/out asymmetries,

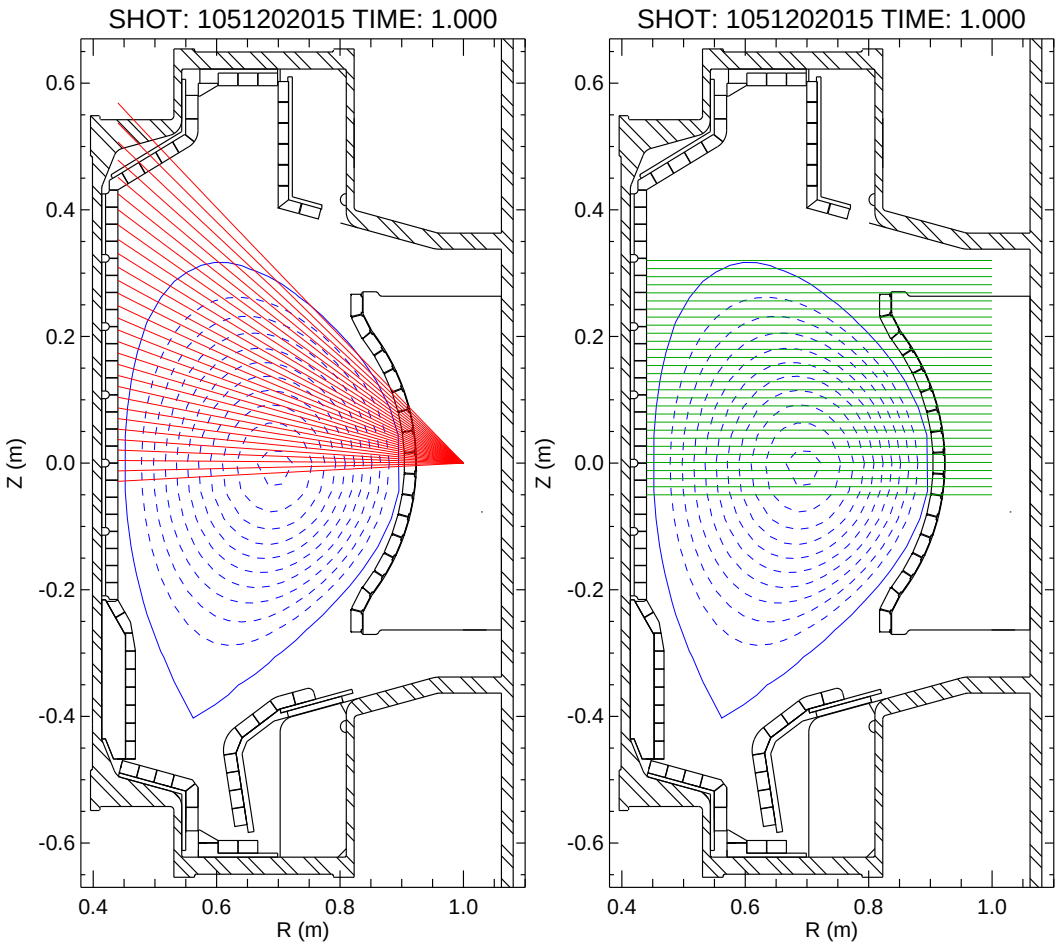

(a) (b)

Figure 7-5: Viewing geometries used to test sensitivity of Doppler tomography to unresolved emissivity asymmetries; one with an angled view (a) and another with parallel views (b)

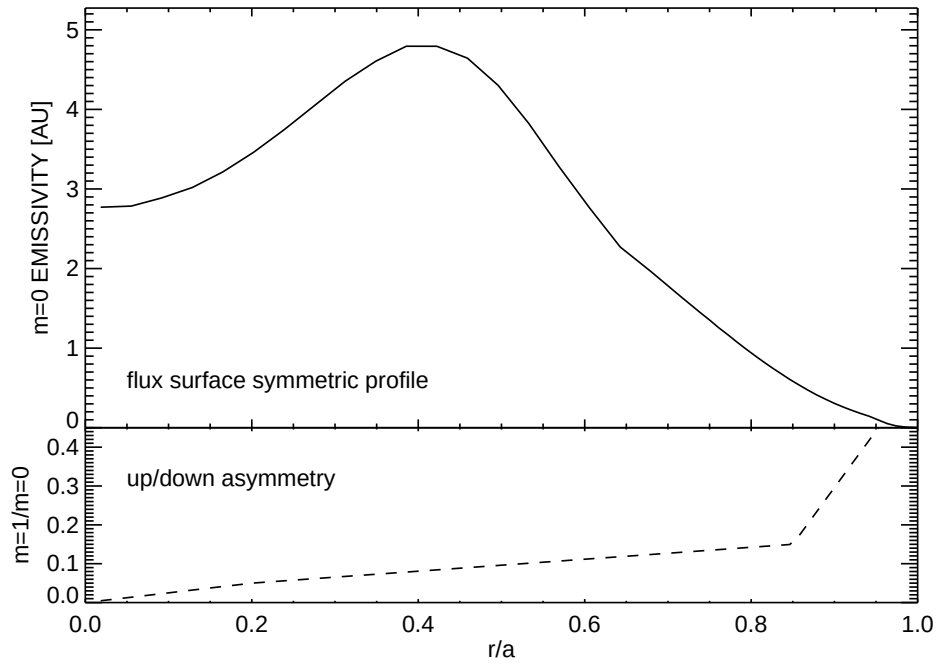

Figure 7-6: Assumed radial emissivity profiles and $m = 1$ up/down variation

even above the levels seen on C-Mod. Such a result is consistent with a LFS viewing geometry averaging over the in/out asymmetry. A larger sensitivity is found for the up/down asymmetry, explored using $\varepsilon(\psi, \theta) = \varepsilon_o(\psi) + \varepsilon_1(\psi) \sin\theta$, as shown in Figure 7-6. The $m = 1$ profile is based on C-Mod results demonstrating $< 10\%$ asymmetry for most of the core but increasing near the edge.

The reconstruction results are shown in Figure 7-7 and, despite the weak asymmetry, more significant changes in the profile are observed than for a larger in/out asymmetry. Inside of $r/a \sim 0.3$, when the $m = 0$ emissivity profile begins to hollow out, substantial differences in all three reconstructed profiles are predicted. These deviations are view-dependent, with the parallel viewing geometry being more robust in determining the magnitude of the profiles. However, neither viewing geometry satisfactorily captures the gradient scale length and using these data would result in systematic errors in impurity transport, E×B shear and χ_i.

These results should not be considered an exhaustive test of the influence of asymmetries on soft x-ray Doppler tomography. Many shapes of $m = 0$ and $m = 1$ profiles could combine to exacerbate or reduce errors in ω and T_z, as could higher order

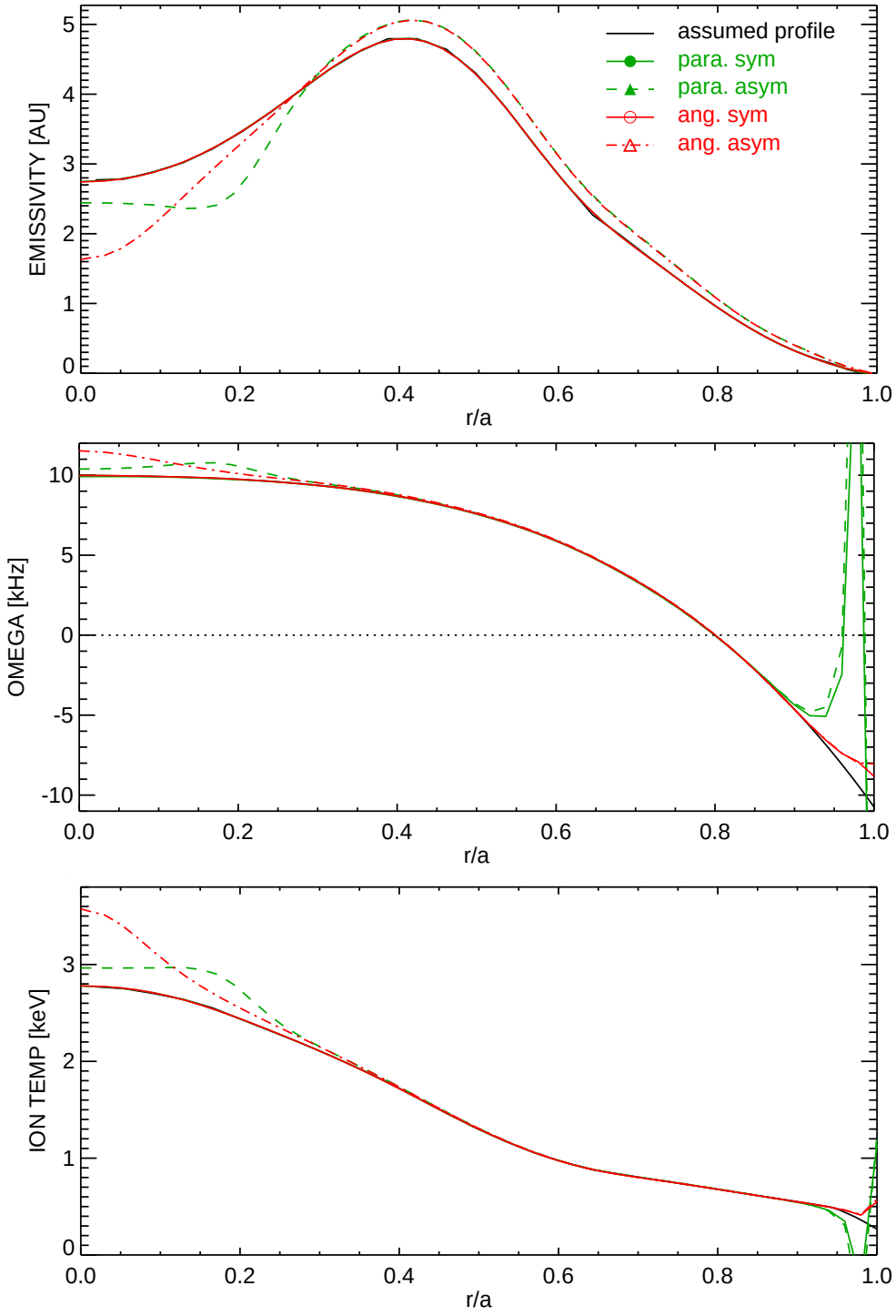

Figure 7-7: Reconstructed emissivity (a), rotation (b) and temperature (c) profiles with symmetric (solid) and asymmetric (broken) input emissivity profiles for a plasma with an up/down asymmetry. The red green traces correspond to different views shown in Figure 7-6

poloidal variations. Rather, these tests inform basic diagnostic design decisions showing that full poloidal coverage is extremely important when viewing from the LFS, and that the exact paths of such views makes little difference.

7.4 Influence of Asymmetry on Anomalous Transport

Recent work studying the effect of poloidal asymmetries on anomalous radial impurity transport [35][163] has shown that high-field side accumulation of impurities can lead to a reduction or even a reversal of the impurity density zero flux gradient scale length, L_z. The C-Mod measurements demonstrate asymmetries between $-0.25 < \tilde{n}_z/\langle n_z \rangle < 0.30$, suggesting the effect of asymmetries on turbulent cross-field transport might be important.

The poloidal variation of the impurity density in [163] is assumed to be of the form,

$$\frac{n_z}{n_{z0}} = \sum_n f_n P\left(\theta, \delta, n\right) = \sum_n \left[f_n \cos\left(\frac{\theta - \delta}{2}\right)\right]^{2n} \tag{7.1}$$

where an evenly distributed impurities would be described by $f_0 = 1$ and $f_n = 0$ for $n \neq 0$. For each n at various δ, the zero flux gradient scale length can be computed and the final result found from a weighted average of the f_n and $L_{z,n}$.

$$\frac{a}{L_z} \simeq \frac{\sum_n f_n \frac{a}{L_{z,n}}}{\sum_n f_n} \tag{7.2}$$

In Figure 7-8, calculations of $L_{z,n}$ for Ni asymmetries in JET-like plasmas are shown for variations in δ and n, while elsewhere in [163] a weak Z-scaling is demonstrated. For large n at $\delta = \pi$, the peaking factor can be driven negative, implying a hollow impurity density profile.

For the high-field side heated plasma discussed in Section 5.2.2, modeling using the extended impurity transport theory matched experiment reasonably well of $r/a \sim 0.45$. The predicted $n_z(\theta)/n_z(0)$ curve is decomposed by trial and error into the form

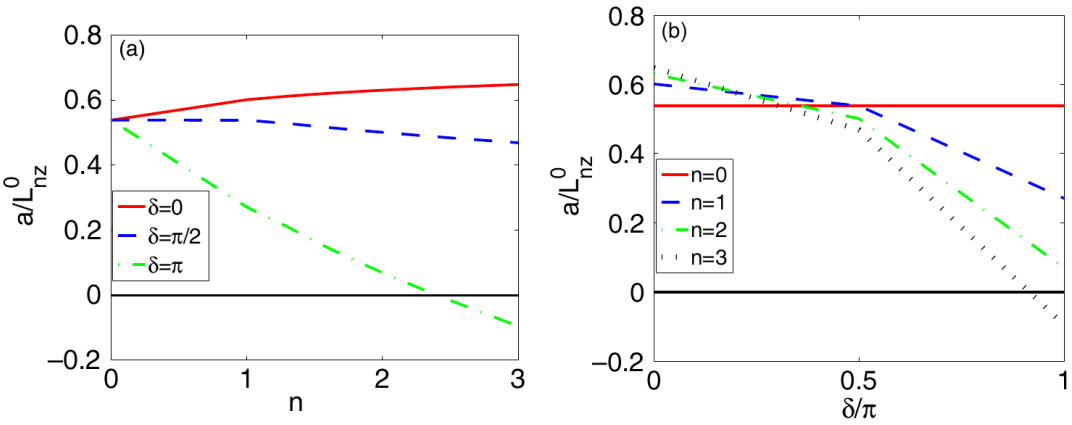

Figure 4. Peaking factor for nickel as a function of n (a) and δ (b). (a) symmetric impurity density (solid, red), up–down asymmetry (dashed, blue), and in–out asymmetry (dashed–dotted, green). (b) symmetric impurity density (solid, red), $n = 1$ (dashed, blue), $n = 2$ (dashed–dotted, green), and $n = 3$ (dotted, black).

Figure 7-8: Change in peaking factor caused by impurity asymmetries for various δ and n (from [163])

of (7.1), and the result is shown in Figure 7-9, where $f_0 = 1.0$, $f_1 = 0.494$, $f_a = 0.040$ and $f_b = 0.044$. Most of the asymmetry can be described by a $n = 1$, $\delta = \pi$ term (f_1), but significant residual needs to be accounted for by including $n \sim 5$ terms, (f_a, f_b), for δ above and below π. Based on results shown in Figure 7-8, at large n, even small values of f_n impact the calculated impurity peaking when $\pi/2 < \delta < 3\pi/2$.

The weighted average of a/L_z is estimated using the calculations for Ni for the (f_n, δ, n) found for the C-Mod plasma. A peaking factor of $\simeq 0.55$ for a symmetric impurity distribution is reduced to $\simeq 0.43$ when including poloidal asymmetries. While modest, a $\sim$20% reduction is sufficient to motivate further study into this topical area. More recent modeling results indicate an enhancement of the impact of asymmetries when including E×B drift [164]. Experiments should be completed to measure both radial and parallel impurity transport simultaneously, and calculations of $a/L_{z,n}$ made for molybdenum in C-Mod plasmas.

Although somewhat counter intuitive, it can be argued that it is easier to measure the poloidal variation of the high-Z impurity than the radial impurity density profile. This is due to the necessity of accurate electron density and temperature profiles, as well as atomic physics modeling to turn an emissivity into an impurity density, and

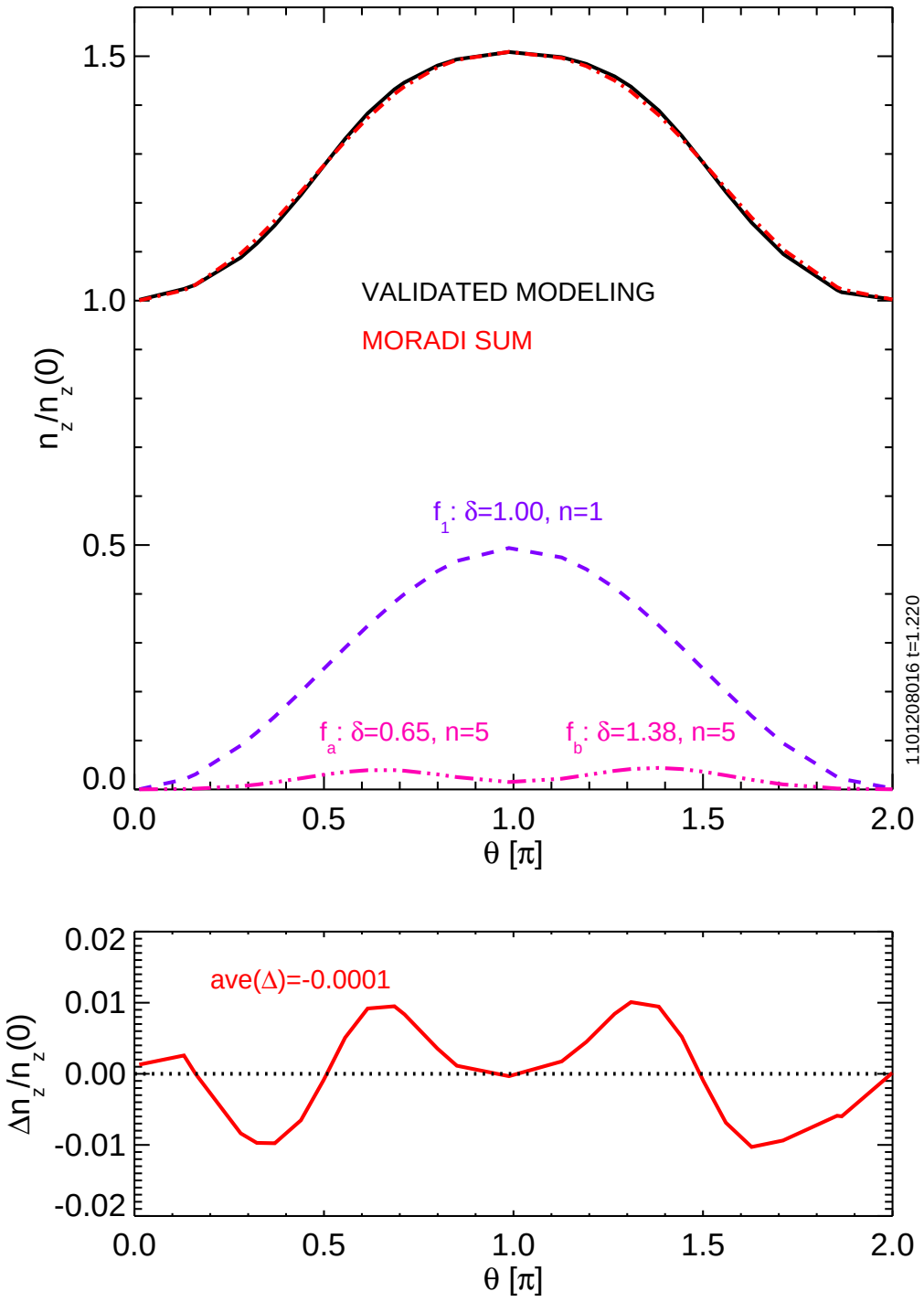

Figure 7-9: Experimentally-validated modeling of $n_z(\theta)/n_z(0)$ decomposed into the form based on (7.1)

then use it to constrain a 1-D impurity transport simulation. In contrast, the poloidal variation of the impurity emission should be able to be measured using tomography tools common to most tokamaks. It is suggested that future investigations into high-Z impurity transport include a characterization of the poloidal impurity density profile. Radial transport can be caused by a variety of mechanisms, but if large poloidal asymmetries are observed along with these changes, then it is an indication that parallel transport may be playing a role.

7.5 Utility of Poloidal Impurity Asymmetry Measurements

The results of Chapter 5 have demonstrated that the poloidal electric field can have a large impact on the flux-surface variation of high-Z impurities. This electric field, and what drives it, have implications beyond impurity transport, allowing the asymmetry data to be of wider use to the tokamak community. Several topics are discussed, showing the broad range of impact an asymmetry measurement can have. All of these topics are exploiting sensitivity to the same basic physics, but have different implications to different areas of research.

The Asymmetry as a Measurement of $E_\theta \times B_\phi$ Drift

The sensitivity of the parallel transport of high-Z impurities to the poloidal electric field suggests measurements of $n_z(\theta)$ can be used as a general diagnostic technique to infer E_θ. The radial force balance equation is often used in a similar manner to determine the radial electric field [165]

$$E_r = -\frac{1}{Zen_z}\frac{\partial p_z}{\partial r} - v_{z,\theta}B_\phi + v_{z,\phi}B_\theta \tag{7.3}$$

where n_z, $\partial p_z/\partial r$ and $v_{z,\theta}$ and $v_{z,\phi}$ are all measured. In this case the poloidal electric field can be found from the parallel force balance equation, ignoring ion-impurity

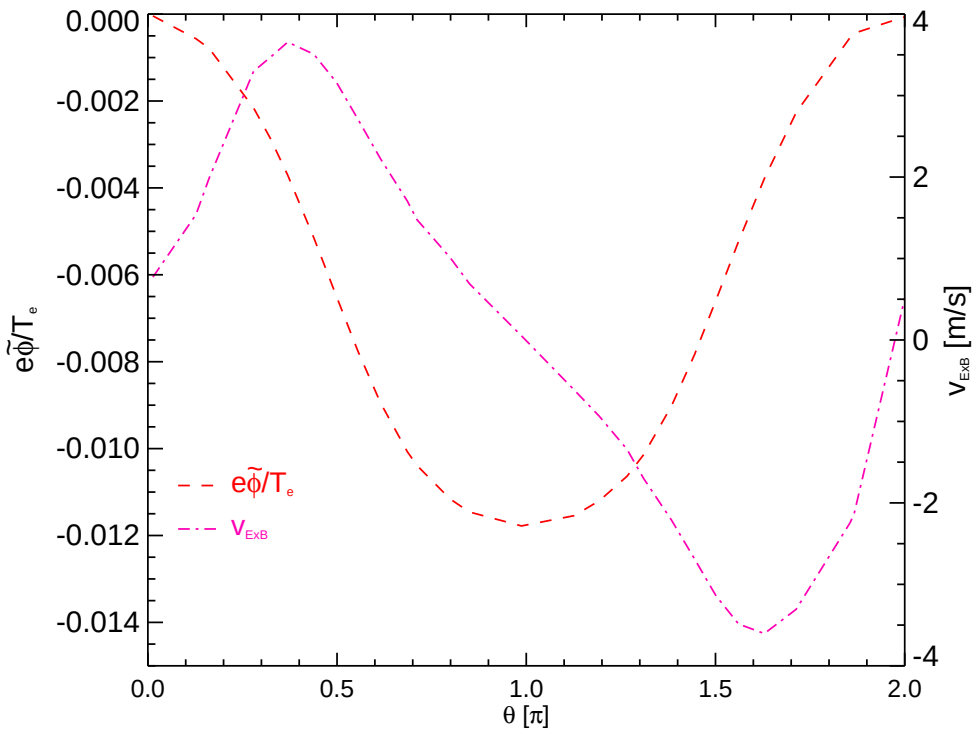

Figure 7-10: Experimentally-validated modeling of the poloidal potential variation (left axis) and the resulting $E_\theta \times B_\phi$ drift velocity.

friction,

$$E_\theta = \hat{b} \cdot \nabla\theta \frac{T_z}{e} \left(\frac{1}{Z n_z} \frac{\partial n_z}{\partial \theta} - \frac{m_z \omega_z^2}{2 Z T_z} \frac{\partial R^2}{\partial \theta} \right) \tag{7.4}$$

Instead of radial pressure gradients and $\mathbf{v}_z$ being measured to find E_r, the parallel gradients, $\partial n_z/\partial\theta$, and toroidal rotation, ω_z, can be measured to calculate E_θ.

The presence of a poloidal electric field could impact cross-field transport by imparting a radial $E_\theta \times B_\phi$ drift. Using the modeling for the LFS-heated plasma in Section 5.2.2 that includes both centrifugal force and ICRH effects results in drift velocity at $r/a = 0.45$ that varies over the flux surface. In Figure 7-10 this is shown to have the form $\sim v_d \sin\theta$ with $v_d \sim 3.5$ m/s. To have an impact on radial transport, an up/down asymmetry is necessary for the drift to survive the flux surface average. In the C-Mod experiments, the largest observed is $n_{sin}/\langle n_z \rangle \sim 0.1$ in the core plasma, indicating that any radial convection due to this effect is weak, < 1 m/s.

Neoclassical theories have shown that a poloidal potential variation of $e\tilde{\phi}/T_e \sim \epsilon$ can impact transport by causing electrostatic trapping, complementing the magnetic

trapping inherent to the tokamak. It was shown that radial electron transport can, in some cases, be enhanced by a factor of two as $e\tilde{\phi}/T_e$ rises to$\sim 4\epsilon$ [166]. The bootstrap current can also be influenced by this modification to trapping. Enhancement or reductions of the bootstrap current on the order of 20-30% are predicted depending on the sense of the asymmetry and impurity content [167]. For the C-Mod case described above, the potential variation, $e(\phi(\theta) - \phi(0))/T_e$ is plotted in Figure 7-10, where it is demonstrated to be much smaller than necessary to impact neoclassical transport.

These results demonstrate that high-Z impurity asymmetries can be used as a sensitive tool for measuring very small changes in the poloidal electric field and resulting $E_\theta \times B\phi$ drift. Large asymmetries, $\tilde{n}_z/\langle n_z \rangle \sim 1$, would act as a indicator of when neoclassical poloidal electric field effects need to be included in transport modeling.

The Asymmetry as a Novel Fast Ion Diagnostic

The link between the ICRH and the poloidal impurity variation can be explained reasonably well using an anisotropic pressure tensor for the minority ions. While it is not assumed that the simple model derived in Section 5.1 is complete, it is sufficient to demonstrate that the impurity asymmetry contains data relevant to fast ion physics. With more development it is conceivable that measuring impurity asymmetries could become a simple, routine way to probe the fast ion anisotropy as shown in Section 5.2.4.

A brief survey of fast ion diagnostic literature suggests that a robust measurement of the total pressure anisotropy would be a useful addition to existing tools. The use of the impurity asymmetry is a relatively inexpensive diagnostic requiring at a minimum a well-calibrated horizontally viewing pinhole camera. Feedback control using the asymmetry-based pressure anisotropy seems a possibility with the Abel inversion necessary for a horizontal view easily computed in real-time, and parallel equilibration time scales are only a few milliseconds. Ideally, existing bolometry and soft x-ray tomography tools common to most tokamaks could be used for the asymmetry measurements, but the inversion algorithms might need adjustment. After

all, such a large in/out asymmetry has likely been a feature of C-Mod plasmas for years but has remained undiagnosed despite the presence of a comprehensive SXR tomography diagnostic.

The Asymmetry as an Equilibrium Constraint

With sufficient ion cyclotron or neutral beam heating, the plasma pressure due to fast ions can grow to be as large as the thermal plasma pressure, influencing the equilibrium reconstruction. In the case of cyclotron heating, this pressure is also anisotropic, which requires either a modified version of EFIT [156] or a 3D equilibrium code such as VMEC [168]. The details of the pressure profile, and specifically the anisotropy, can have subtle but important impacts on tokamak plasmas.

The impurity density asymmetry could be used as a constraint for equilibrium reconstruction, or at least be used to identify cases where the anisotropy is significant and a more advanced reconstruction technique is required. The use of the asymmetry is not limited to cyclotron heating either. Strong toroidal rotation, flow speeds approaching the main-ion thermal velocity, adds an additional source of pressure that affects the magnetic equilibrium [155]. The in/out asymmetry of the impurities is once again a leading indicator of when this effect needs to be included. Additionally, the possibility of significant radiation asymmetries should prevent the use of soft x-ray emissivity contours from being used as a constraint in equilibrium reconstructions [169][170][171].

The Asymmetry as a Turbulence Diagnostic

After expounding on the sensitivity of the poloidal impurity equilibrium on small changes in the electrostatic potential, it seems natural to ask the question: can the asymmetry be used as a measure for potential fluctuations thought to be linked to turbulent plasma transport? The answer is most likely no because of the small spatial structures and short time scales involved in drift-wave turbulence. Since core parallel impurity equilibration is ~ 100 μs or more compared to typical electrostatic fluctuations frequencies above 100 kHz, time-evolving parallel impurity transport theory

would need to be derived. At low enough frequency and small enough wave number, the Boltzmann-like response of the impurities should allow for some insight into turbulence dynamics. It would be interesting to see where this resolution limit lies and what type of diagnostic layout would allow for observation of such structure.

7.6 Future Work

While this work represents a relatively thorough exploration of high-Z parallel impurity transport in tokamaks, there are topics which still remain to be completed and would benefit from future exploration.

In Chapter 5, the use of ion cyclotron heating was shown empirically to affect the poloidal variation of impurity density and initial estimates to model the magnitude of the effect were in good agreement. Much more comprehensive codes can couple wave propagation and damping to a Fokker-Planck equation evolving the fast ion distribution function. The GNET code [172], developed for use in stellerators, is a 5-D, finite-orbit-width code that solves for the minority ion distribution function in all 3 spatial dimensions and 2 velocity space dimensions. This can be used to determine more accurate $n_m(\theta)$ distributions and check for quantitative agreement with theories. Collaborations with S. Murakami to use GNET to model Alcator C-Mod plasmas are currently underway.

Electron cyclotron heating is also predicted to have a similar but opposite effect to ion cyclotron heating, causing high-Z impurity accumulation on the outboard side of the plasma due to trapped electrons. While C-Mod does not currently have an ECRH program, it represents the ideal testbed for any ITER system due to the similar range of toroidal field and electron density, making future deployment of ECRH not entirely surprising. Similar studies as completed in Chapter 5 using ECRH would be a natural experiment to complete. Collaborations with ASDEX-U which employs ECRH and studies tungsten transport, could also be an efficient research pathway in the near term.

As discussed in Section 7.1, this research has suggested more work remains to be

done in validating impurity asymmetries in beam-heated plasmas. With multiple, steerable high power beams and state of the art fast ion diagnostics, DIII-D is an ideal facility for such experiments. JET has recently been modified to test the ITER-like wall [173] and has recently begun operation with tungsten PFCs in the divertor. Based on the C-Mod experience with molybdenum, a comprehensive study of high-Z impurity asymmetries in beam heated plasmas could likely be completed without dedicated run time.

An exciting avenue of future work is to study the radial transport of molybdenum taking into account the poloidal asymmetry and determine empirically what role, if any, the latter has on the former. While the wall box diagnostic system has been retired, the AXA and AXJ arrays in the KLIM enclosure remain and can provide an accurate measure of the core in/out asymmetry. A miniproposal, MP 650, has already been approved to study differences in radial and parallel impurity transport in minority and mode-conversion heated plasmas and collaborations with T. Fülöp to model Mo on C-Mod have recently begun.

While this research has shown that parallel transport can be explained reasonably well by neoclassical theory, the impact of plasma turbulence cannot be ruled out as discussed in Section 6.4.1 and Appendix D. There has been no study of parallel transport coupled with non-linear gyro-kinetic codes to see how one can influence the other.

There are other regimes still described by the current theories that remain to be validated. The poloidal variation of low-Z impurities in the non-trace limit in the pedestal region is a topic of open investigations on Alcator C-Mod. The asymmetries that have been previously observed on C-Mod by Pedersen [77] and served as motivation for this research were not explored here, and part of the Future Work section of his thesis remains relevant. Marr [78] initially explored this regime for boron in H-mode plasmas, work that is being expanded upon by Churchill [174]. In C-Mod plasmas where low-Z impurity seeding is used to form radiative mantles and divertors, significant, 1-2%, amounts of N_2 and Ne are present in the pedestal region [175]. As part of an effort to better understand the interaction of these impurities with the

H-mode pedestal, exploration of low-Z impurity asymmetries in the steep-gradient region of Alcator C-Mod H-modes and I-modes is planned for the near future.

Appendix A

Verification of Asymmetry Code

The theories summarized in Chapter 2 are compared to each other in the circular limit, where the poloidally varying terms are expanded using a low-order Fourier expansion. Experiments use shaped plasmas where parallel derivatives cannot be computed analytically and the 1D inhomogeneous linear differential equation for $n_z\left(\psi\right)/\left\langle n_z\right\rangle$ must be solved numerically. In this Appendix, the specifics of this procedure are described and compared to theory in the appropriate limits.

The code is based on the work of Fülöp and Helander for a trace, $n_z Z^2/n_i \leq 1$, high-Z impurity in the collisional [58] and collisionless [24] main ion regimes with the following additions. First, the published work in the collisional regime does not include the effect of centrifugal force. As the form of the differential equation is the same for both regimes, it is straightforward to add. For the high-Z impurity, the toroidal rotation is assumed to be due to E×B flow, and including it does not change $v_{z,\|} - v_{i,\|}$ which drives the ion-impurity friction. Second, the effects of a minority species with an anisotropic pressure tensor are included as detailed in Section 5.1. Lastly, the ion and impurity toroidal rotation are assumed to be equal in [24] when there should actually be a difference due to in the diamagnetic flow. Including this will make the main-ion toroidal rotation slightly larger, increasing the electrostatic potential enhancement at the LFS.

The EFIT code is used to reconstruct the magnetic equilibrium by solving the Grad-Shafranov equation (1.3) to determine $\psi(R,Z)$. The axisymmetric magnetic

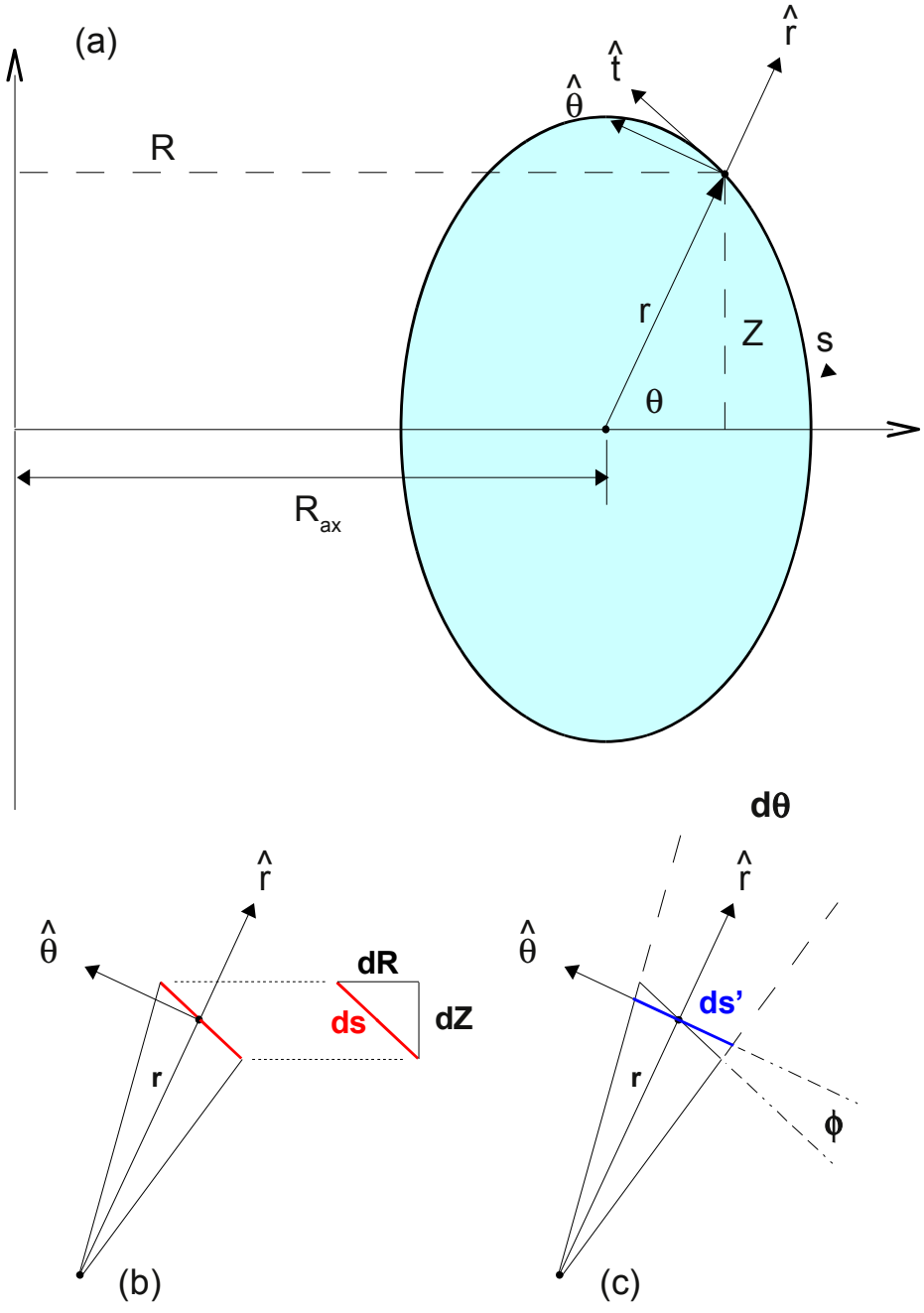

Figure A-1: Geometry used in calculating the solution to the 1-D parallel impurity transport equation

field is represented by

$$\vec{B} = I(\psi)\nabla\phi + \nabla\psi \times \nabla\phi \tag{A.1}$$

where $\nabla\phi = R\hat{\phi}$ and $I(\psi)$ is determined by EFIT. The standard (ANALYSIS) EFIT reconstruction solves for 33 points evenly spaced in poloidal flux between the magnetic axis and the last closed flux surface or $0 \leq \psi_n \leq 1$. At each ψ_n value, the (R,Z) points which describe the shape of the flux surface are provided. The poloidal angle, θ, is defined relative to the magnetic axis as shown in Figure A-1a.

$$r = \sqrt{(R - R_{ax})^2 + (Z - Z_{ax})^2} \tag{A.2}$$

$$\theta = \arctan\left(\frac{Z - Z_{ax}}{R - R_{ax}}\right) \tag{A.3}$$

with R_{ax} and Z_{ax} the location of the magnetic axis. The poloidal field, B_p, and the toroidal field, B_t, are known at each location along the flux surface. Note that even though the poloidal angle is defined in the naive, geometrical sense, the circular approximation is not being used and the flux surface shaping is kept in the $\vec{B} \cdot \nabla\theta$ term. This differs from the notation of [58] and [24]. From Figures A-1b and A-1c, $\vec{B} \cdot \nabla\theta$ can be derived to be

$$\vec{B} \cdot \nabla\theta = \frac{B_p \cos\phi}{r} \tag{A.4}$$

$$\vec{B} \cdot \nabla\theta = B_p \frac{\sin\theta - m(\theta)\cos\theta}{r\sqrt{m(\theta)^2 + 1}} \tag{A.5}$$

with $m(\theta) = dZ/dR$, the instantaneous slope along the flux surface. For a circular plasma, this reduces to B_p/r as expected. As described in Section 2.2.4, the 1-D inhomogeneous nonlinear differential equation for the parallel force balance on a flux surface is of the form

$$(1 + \alpha_z n)\frac{\partial n}{\partial \theta} = X(\theta)\, n + K_z Y(\theta) \tag{A.6}$$

where $n = n_z/\langle n_z \rangle$, $\alpha_z = Z^2\langle f_z \rangle/(T_i/T_e + n_i/n_e)$ and K_z is determined using the periodic boundary condition, $n(0) = n(2\pi)$. This can be reduced to a simpler linear

differential equation with the restriction that $\alpha_z \ll 1$.

$$\frac{\partial n}{\partial \theta} = X(\theta)\, n + K_z Y(\theta) \tag{A.7}$$

The largest impact of a finite impurity density is to reduce the magnitude of the asymmetry by including it in quasi-neutrality. This effect is kept in via Z_{eff} terms in $X(\theta)$, which also account for other background impurities. This limit ignores the impact on the ion-impurity friction that arises due to impurities modifying the main-ion flow as well as the possiblity of impurity-impurity friction.

The solution to (A.7) can be determined by using an integrating factor, $\exp(\mu) = \exp\left(\int_0^\theta X(\theta)\, d\theta\right)$ reducing (A.7) to

$$s\frac{\partial}{\partial \theta}\left[\exp(\mu(\theta))\, n(\theta)\right] = -K_z Y(\theta) \exp(\mu(\theta)) \tag{A.8}$$

Integrating and applying the periodic boundary condition allows $n(\theta)$ to be expressed as

$$\frac{n(\theta)}{n(0)} = \exp(-\mu(\theta)) \left(1 - \frac{1-\alpha}{\beta} \int_0^\theta Y(\theta) \exp(\mu(\theta))\, d\theta\right) \tag{A.9}$$

where $\alpha = \exp(-\mu(2\pi))$ and $\beta = \int_0^{2\pi} Y(\theta) \exp(\mu(\theta))\, d\theta$. The poloidally varying X function is determined separately for each main-ion collisionality regime, $\hat{\nu}_{ii} = \nu_{ii}/\omega_{tr,i}$, where the ion-ion collisionality is $\nu_{ii} = 3\sqrt{\pi}/4\tau_{ii}$ and the ion transit frequency is $\omega_{tr,i} = v_{th,i}/qR_o$. The low-collisionality or banana-regime is $\hat{\nu}_{ii} \ll 1$, and the high-collisionality or Pfirsch-Schlüter regime is $\hat{\nu}_{ii} \gg 1$. The $Y(\theta)$ term is the same for both

$$Y(\theta) = \frac{m_i Z^2}{\tau_{ii} T_i} \frac{B^2}{\vec{B} \cdot \nabla\theta} \tag{A.10}$$

where $B^2 = B_p^2 + B_t^2$ and $\vec{B} \cdot \nabla\theta$ is from (A.5). For both collisionalities $X(\theta)$ is broken into 4 parts, X_1, X_2, X_3 and X_4 where X_3 and X_4 are independent of $\hat{\nu}_{ii}$.

$$X_3 = -\frac{m_z \omega_z^2}{2T_i} \left[1 - Z\frac{\omega_i^2}{\omega_z^2}\frac{m_i}{m_z}\frac{Z_{eff}T_e}{Z_{eff}T_e + T_i}\right] \frac{\partial R^2}{\partial \theta} \tag{A.11}$$

$$X_4 = Z f_m \frac{T_e}{Z_{eff} T_e + T_i} \left\langle \frac{1}{B^\eta} \right\rangle^{-1} \frac{(-\eta)}{B^{-(\eta+1)}} \frac{\partial B}{\partial \theta} \tag{A.12}$$

with f_m being the minority ion fraction, n_m/n_e, $\eta = \left(T_\perp/T_\parallel - 1\right)$ is the minority's temperature anisotropy and $\langle ... \rangle$ is the standard flux surface average. The main ion toroidal rotation, ω_i, will always be slightly larger in the co-current direction relative to the impurity rotation due to diamagnetic flow but to quantitatively include this in the theory is beyond the scope of this work. In all cases, $\omega_i = \omega_z$ is assumed unless otherwise specified for purposes of exploring sensitivity to this assumption. For main ions in the banana regime,

$$X_1 = \frac{m_i I Z^2}{\tau_{ii} e} \left(\frac{n_i'}{n_i} - \frac{1}{2} \frac{T_i'}{T_i} \right) \frac{1}{\vec{B} \cdot \nabla \theta} \tag{A.13}$$

$$X_2 = \frac{f_c m_i I Z^2}{3 \tau_{ii} e \langle B^2 \rangle} \frac{T_i'}{T_i} \frac{B^2}{\vec{B} \cdot \nabla \theta} \tag{A.14}$$

where $f_c = 1 - 1.46\sqrt{\langle r \rangle / Ro}$ is the circulating fraction taken from [39] and prime denotes derivative with respect to ψ. The X_1 term is related to the g term and X_2 is related to the product of γ and g from the Fülöp and Helander papers. For simplicity, the trace-limit expression for γ is used in X_2 which avoids the need for velocity-space integrals in the main ion solution which would be needed to correct the ion-impurity friction for $\alpha_z \sim 1$. For main ions in the Pfirsch-Schlüter regime,

$$X_1 = \frac{m_i I Z^2}{\tau_{ii} e} \frac{n_i'}{n_i} \frac{1}{\vec{B} \cdot \nabla \theta} \tag{A.15}$$

$$X_2 = \frac{2.8 m_i I Z^2}{\tau_{ii} e \langle B^2 \rangle} \frac{T_i'}{T_i} \frac{B^2}{\vec{B} \cdot \nabla \theta} \tag{A.16}$$

The primary difference in the collisionalities is the weighting of the gradient scale length terms. For low $\hat{\nu}_{ii}$ plasmas, the ion-impurity friction is proportional to the difference between the density and temperature scale lengths. In practice, for $r/a < 0.9$, the kinetic profile scale lengths are of similar magnitude with L_n is less than L_T, so the X_1 from (A.13) is usually near zero. In contrast, these two terms add together for high collisionality plasmas making them more likely to impact force balance as $\hat{\nu}_{ii}$

is increased.

Solutions to (A.7) can be compared to analytic predictions in order to verify the code. For weak ion-impurity friction, $\alpha_z = 0$ and no minority effects, there exists an exact solution for the poloidal density variation with respect to major radius, R, for the trace impurity limit [56][29].

$$\frac{n\left(\theta\right)}{n\left(0\right)} = \exp\left[\frac{m_z\omega^2\left(R\left(\theta\right)^2 - R\left(0\right)^2\right)}{2T_z}\left(1 - Z\frac{m_i}{m_z}\frac{T_e}{T_e + T_z}\right)\right] \tag{A.17}$$

In Section 5.1, analytical solutions were derived for $n_z/\langle n_z\rangle$ sustained by a poloidal electric field due an anisotropic minority species (5.8), and the combination of the centrifugal force and an anisotropic species (5.12). For cases with combined inertial and ion-impurity friction forces Fülöp and Helander have expanded n in a Fourier series, in the $\epsilon \ll 1$ circular cross-section, limit to find the leading order $m = 1$ terms with $n = 1 + n_c\cos\theta + n_s\sin\theta$ [24].

$$n_c = 2\frac{r}{R_o}\frac{\left(1+\alpha_z\right)M_0^2 - \left(1+\gamma\right)g^2}{\left(1+\alpha_z\right)^2 + \left(1+\gamma\right)^2 g^2} \tag{A.18}$$

$$n_s = 2g\frac{r}{R_o}\frac{\left(1+\alpha_z\right) + \left(1+\gamma\right)M_0^2}{\left(1+\alpha_z\right)^2 + \left(1+\gamma\right)^2 g^2} \tag{A.19}$$

where equations for g, γ and M_0^2 can be found in [24] and [58] for low and high collisionality, respectively, and are also listed in Chapter 2. Fractional error is determined from (A.18) and (A.19) via standard error propagation assuming uncorrelated error in the input kinetic profiles, n_i, T_e, T_i and ω, and assumed to be the same for the in/out and up/down asymmetries derived from solutions using (A.7). In the limit of $g \gg 1$, or very large gradients, an approximate solution to order g^{-2} is found to be [58][31],

$$n_0 = \frac{\gamma}{1 - \left\langle\left(1+\gamma b^2\right)^{-2}\right\rangle}\frac{b^2}{1+\gamma b^2} \tag{A.20}$$

where $b^2 = B^2/\langle B^2\rangle$. In this limit, impurity density is accumulated where the magnetic field is strongest, at the inboard side.

To verify the code against these analytical solutions, we use experimental EFIT

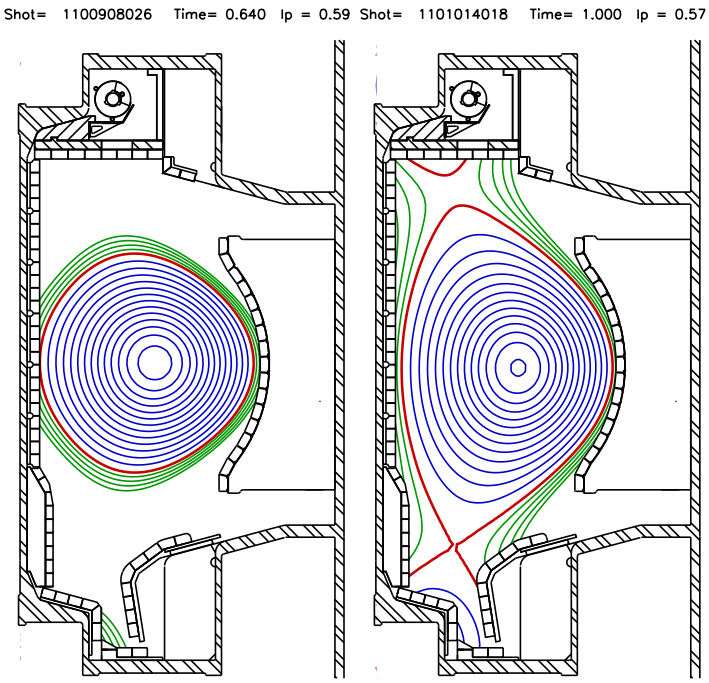

Figure A-2: EFIT reconstructions of C-Mod plasmas used for verification of the parallel transport code

reconstructions with arbitrary kinetic profiles, selected to highlight different physics. Two equilibria are used; one from shot 1100908026, a near-circular, Ohmic, low-β plasma ($\beta_p = 0.25, \beta_n = 0.5$) and one from shot 1101014018 an ICRF-heated EDA H-mode shaped plasma ($\beta_p = 0.8, \beta_n = 1.0$). Both are at the same current, 600 kA, and toroidal field, 5.4 T and their respective flux surface geometry are shown in Figure A-2. The $\alpha_z = 0$, $Z_{eff} = 1$ limits are assumed throughout.

The input profiles, shown in Figure A-3, are similar to typical C-Mod shots and are converted into the coefficients used in Fülöp and Helander, assuming a molybdenum impurity. The M_o^2, g and γg profiles are shown in Figure A-4a and Figure A-4b for low and high collisionality, respectively. Note that γg is used in the code to avoid a divide by zero error for flat profiles. Although the density and temperature profiles define a plasma that is deep into the banana regime for most of the volume, for the purposes of verification we can arbitrarily define the collisionality to be used in calculating the poloidal impurity density profiles.

We start by verifying the output against the analytical theory for the centrifugal

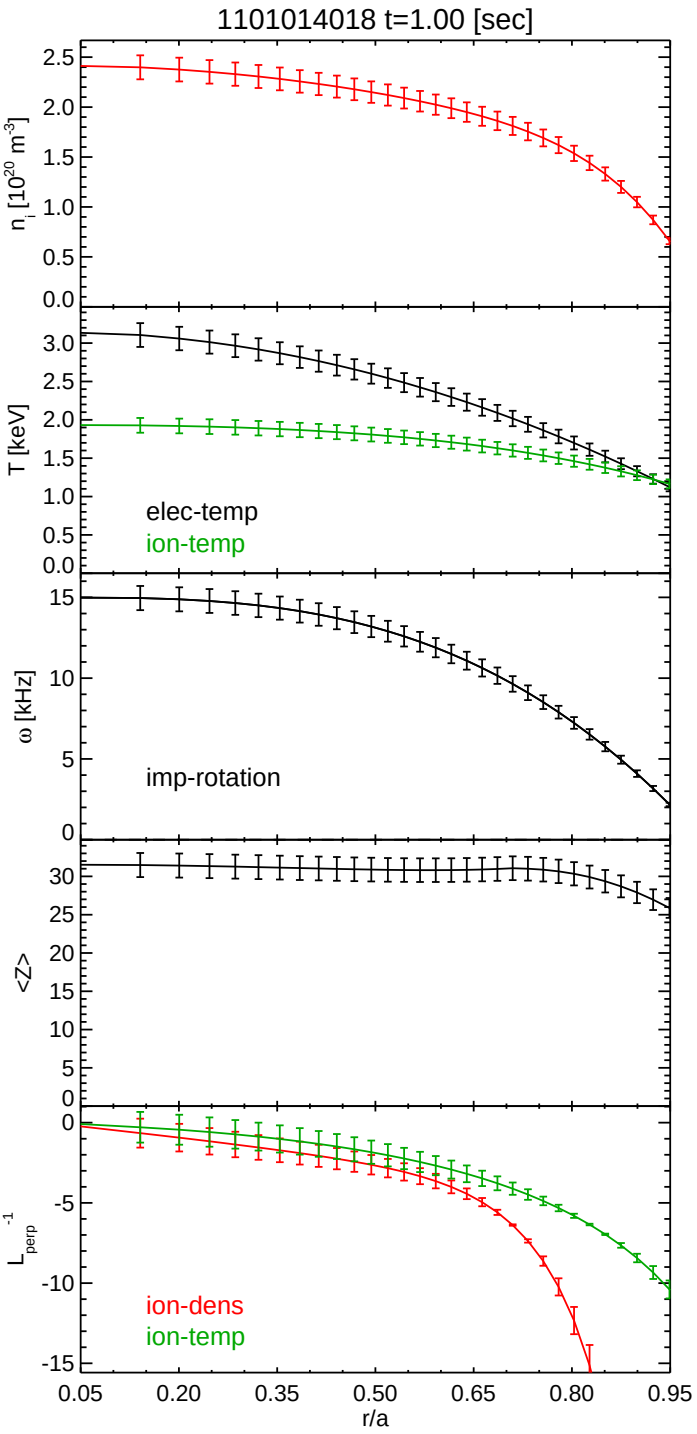

Figure A-3: Input profiles used for comparing 1-D asymmetry code to theoretical limits

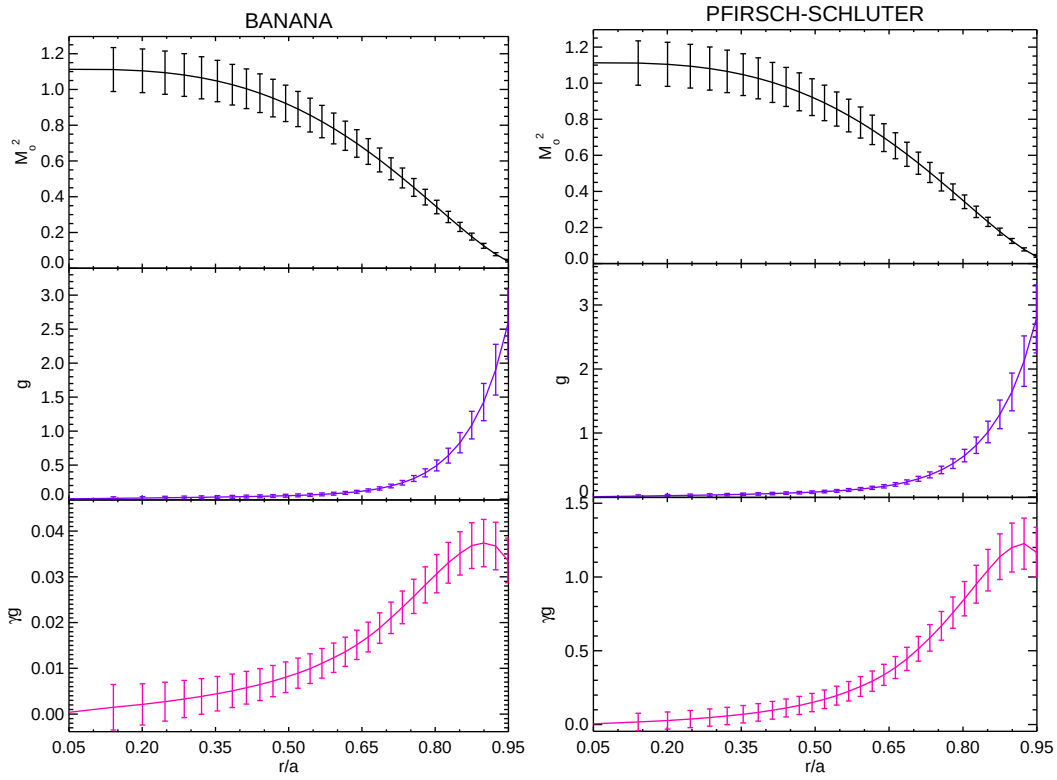

Figure A-4: Fülöp and Helander asymmetry parameters calculated from kinetic profiles for collisionless (a) and collisional (b) main-ions

force only (A.17) by artificially setting $g = 0$ in the code. The poloidal variation is plotted for the shaped plasma at $r/a \sim 0.5$ in Figure A-5a and the radial profiles of the asymmetry are shown in Figure A-5b. The radial asymmetry profiles are calculated from $n(\theta)/n(0)$ by defining $[n_z(0) - n(\pi)]/[n_z(0) + n(\pi)]$ to be the in/out asymmetry and $[n_z(\pi/2) - n(3\pi/2)]/[n_z(\pi/2) + n(3\pi/2)]$ to be the up/down asymmetry. In the $m = 1$ circular limit, these coefficients equal n_c and n_s, respectively. The code output, shown as the black solid line, matches the analytical result, red dash-dot line, very well and the $m = 1$ expansion, blue dashed line, has only a slight difference assumed to be due to shaping.

Next, the ion-impurity friction effects are added and the asymmetries are examined farther off axis at $r/a \sim 0.9$. Again Figure A-6a shows the poloidal variation and the radial profiles are shown in Figure A-6b. In this case, the asymmetry is not near either the strong rotation or strong ion-impurity friction, dotted green line, limits. The results are in good agreement with the $m = 1$ expansion, and by running the same case using the circular equilibrium, shown in Figure A-7, agreement between the code and the $m = 1$ expansion is improved. This highlights that realistic plasma shaping has a small, but observable impact on the poloidal variation.

In Figure A-8, the combined effects of the centrifugal force, minority anisotropy and ion-impurity friction are included in the analysis. Minority effects are artificially included by defining a Gaussian shaped $T_\perp/T_\parallel$ profile at mid radius, which would result in the asymmetry profile shown in light blue. At $r/a \sim 0.5$, the solution calculated by the 1-D simulation agrees very well with the analytical result, purple dash-dot, that combines centrifugal and minority effects.

Moving to the Pfirsch-Schlüter case shown in Figures A-9a and A-9b, agreement between output of the code and the $m = 1$ expansion is again observed. The radial profiles show that the asymmetry smoothly transitions from being dominated by the centrifugal force to being driven by ion-impurity friction and begins to approach the $g \gg 1$ limit even for $g \sim 3$.

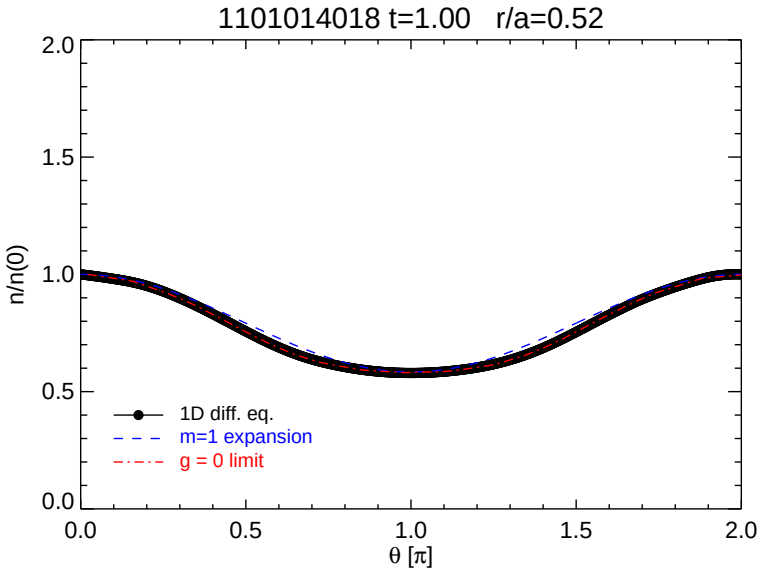

(a)

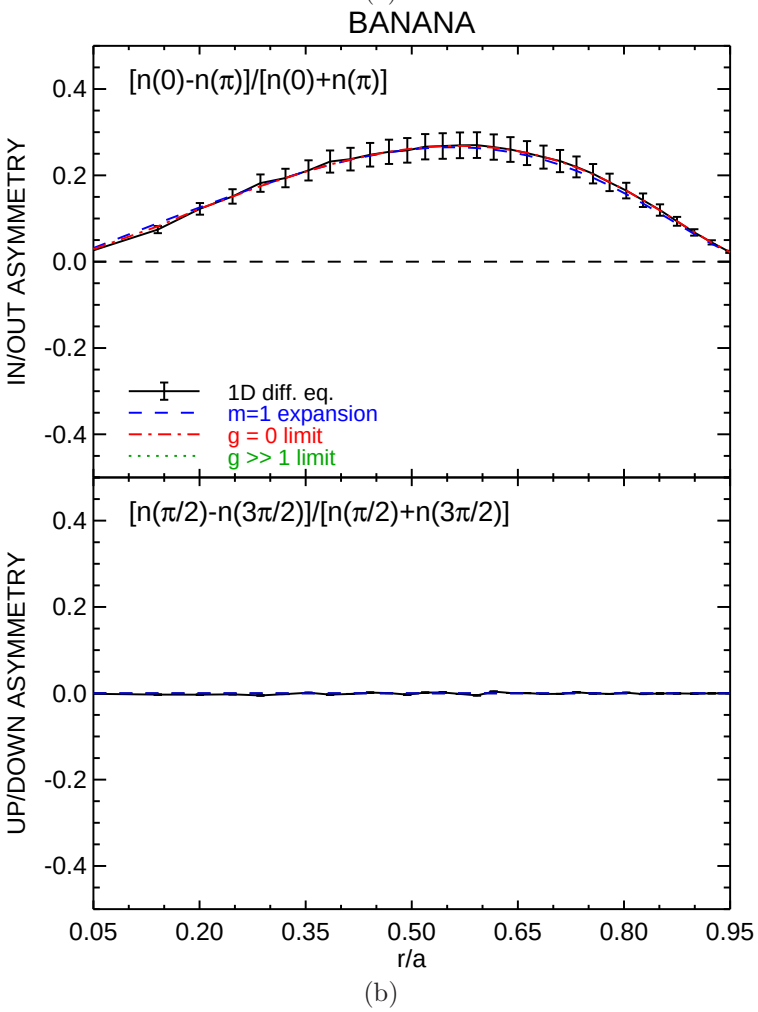

(b)

Figure A-5: Comparison of code against analytical limit assuming only toroidal rotation

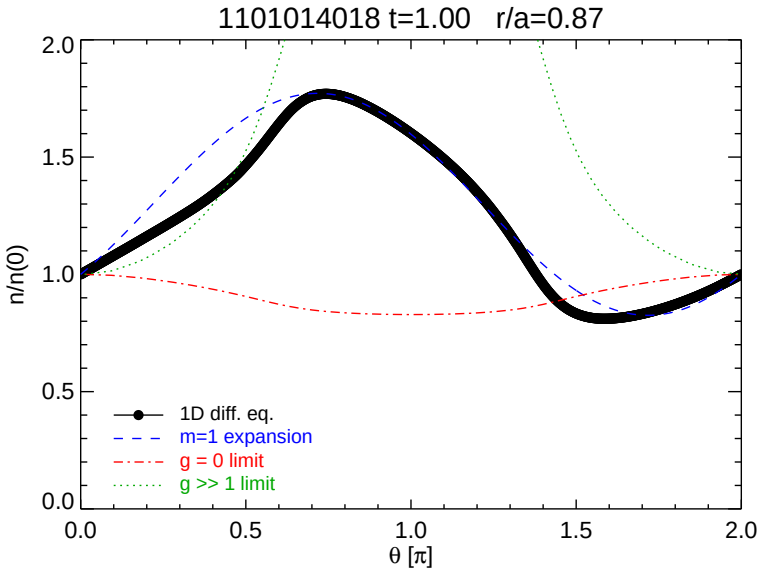

(a)

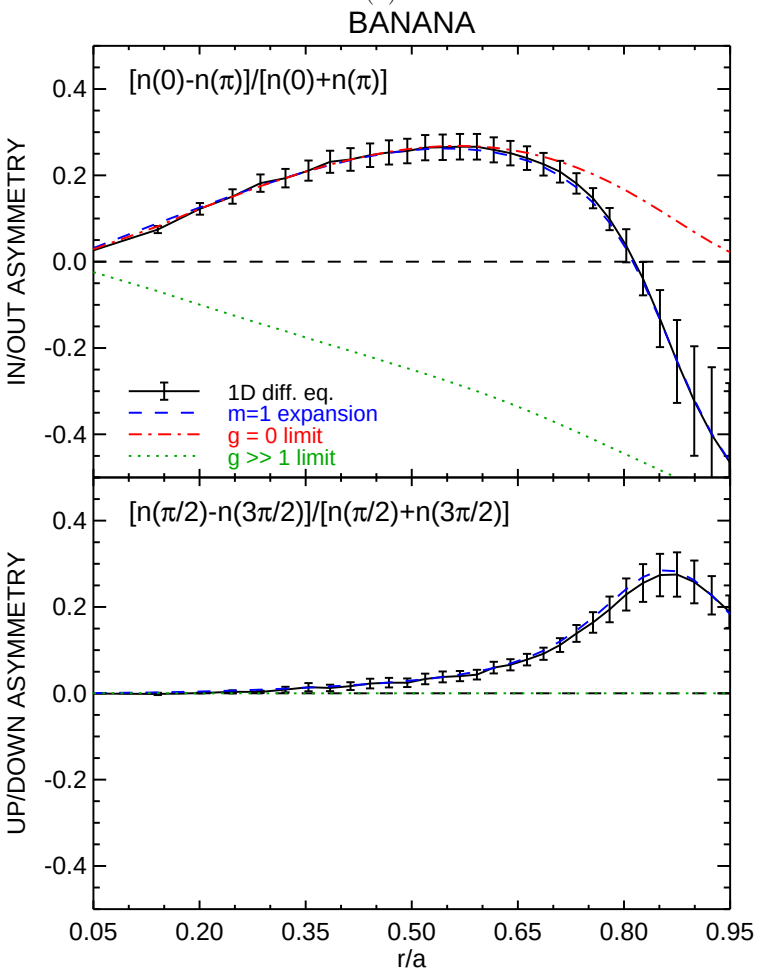

(b)

Figure A-6: Comparison of code against banana-regime theory for a shaped plasma including inertial and friction forces

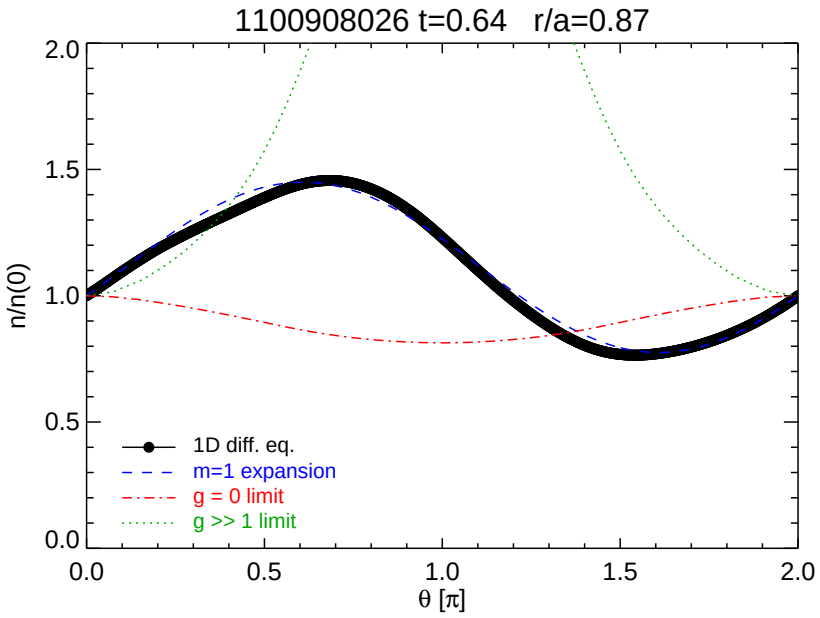

Figure A-7: Repeat of analysis shown in Figure A-9 using a circular plasma equilibrium

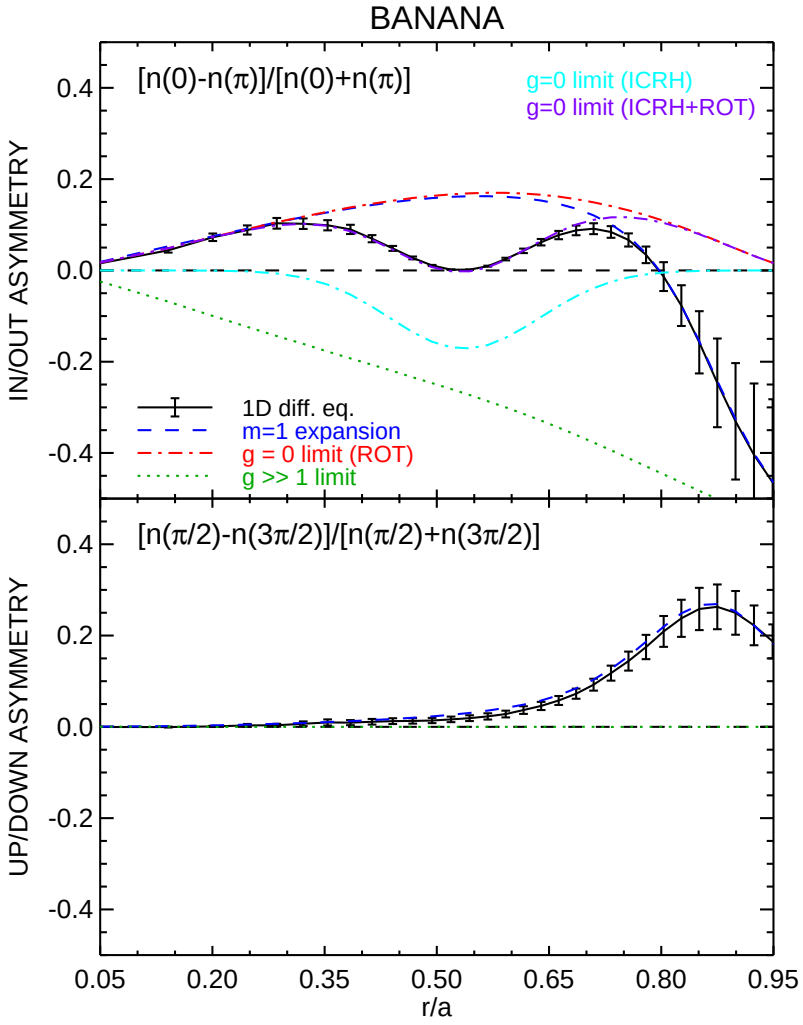

Figure A-8: Comparison of code against banana-regime theory for a shaped plasma including inertial, friction and minority heating effects

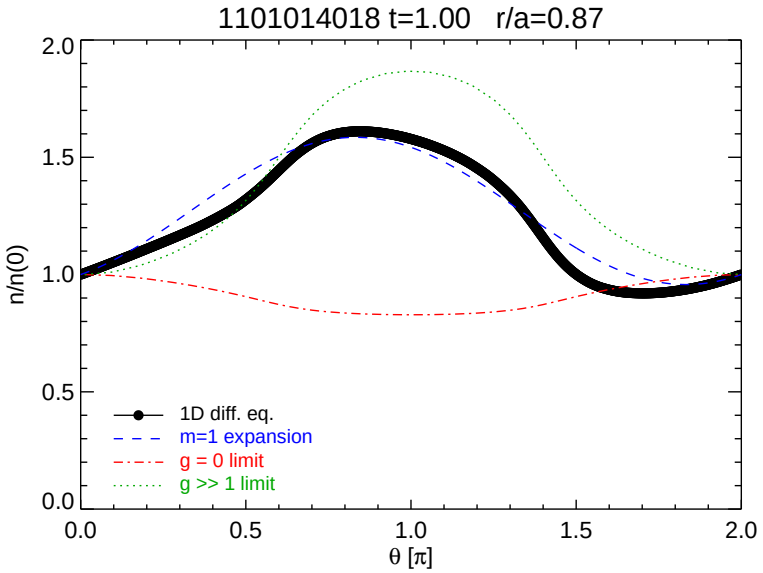

(a)

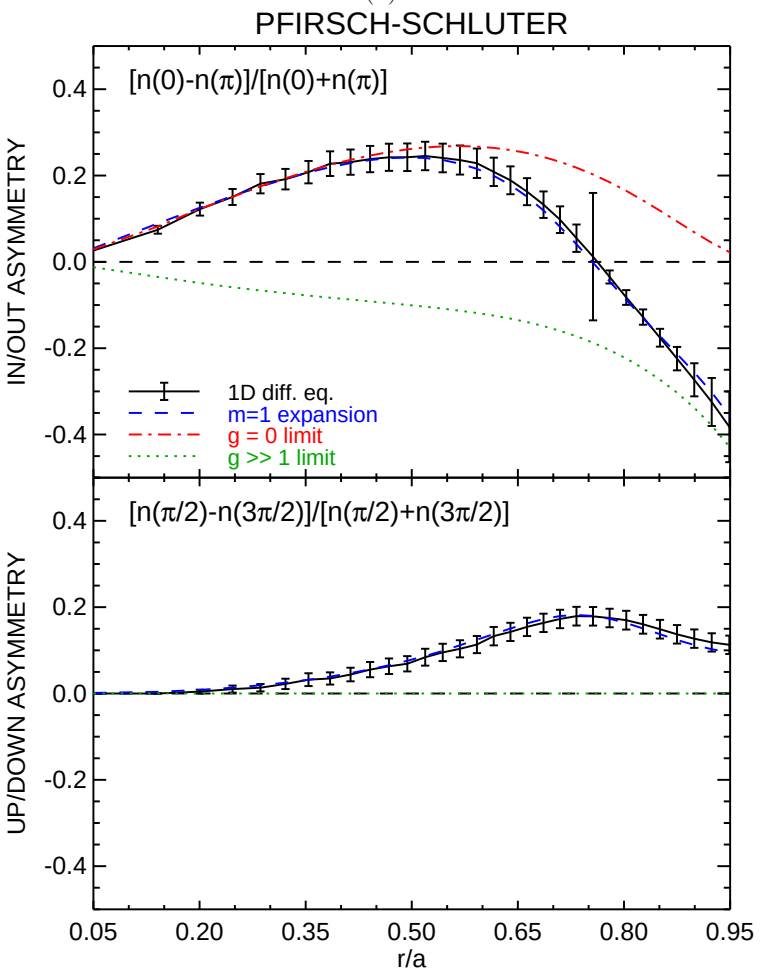

(b)

Figure A-9: Comparison of code against Pfirsch-Schlüter-regime theory

Appendix B

Calibration of AXUV Pinhole Cameras

The pinhole camera is the most basic optical system, composed simply of an aperture and a detector. Throughput and field of view are determined exclusively by the separation and orientation of these two elements. In C-Mod, these cameras view volumetric radiation and tomographic techniques are used to determine the local radiation power density from line-integrated brightness profiles. This research makes quantitative conclusions based on the poloidal distribution of the radiation, so accurate spatial and relative intensity calibrations are very important. The calibration scheme mirrors the thought process used in GENPOS described in Appendix C. First, the location of the detector with respect to the aperture coordinate system is determined, and then this aperture coordinate system is found relative to that of the tokamak.

B.1 Benchtop Laser Alignment

The C-Mod pinhole cameras are designed to have the normal of the detector array in the same plane as that of the aperture. Thus there are only three degrees of freedom that locate it relative to the aperture; x_o, y_o and α as sketched in Figure B-1. The center of the detector array is used as its fiducial, and the origin of the xyz coordinate system is at the aperture, with $\hat{x}$ being the normal of the aperture. The goal of the

laser calibration is to measure the distance between two points, $\Delta_1 - \Delta_2$, outside of the enclosure using rays that go through the aperture and impact the array a distance of $\delta_1 - \delta_2$ apart.

Since the diode array is manufactured from a single piece of silicon, the channel-to-channel spacing is known to within ± 5 μm according to the manufacturer [176], allowing δ_i to be measured accurately by shining a laser through the aperture and determining when the response peaks for a given channel. Using Figure B-1, the relationship between the desired degrees of freedom, x_o, y_o and α, the calibration measurements, Δ_i, δ_i, and the calibration setup, $\Delta_\perp, d_\perp$ can be shown to be,

$$-\frac{x_o + \delta_i \sin\alpha}{y_o + \delta_i \cos\alpha} = \frac{d_\perp}{\Delta_\perp - \Delta_i} \tag{B.1}$$

where it should be noted that values of x_o are negative since they are behind the aperture. The setup parameter, $d_\perp$ can be found very accurately, but $\Delta_\perp$ has a relatively large systematic uncertainty. Instead, the difference between channels is used,

$$\Delta_2 - \Delta_1 = -d_\perp \left(\frac{y_o + \delta_1 \cos\alpha}{x_o + \delta_1 \sin\alpha} - \frac{y_o + \delta_2 \cos\alpha}{x_o + \delta_2 \sin\alpha} \right) \tag{B.2}$$

Such a measurement does not uniquely place the detector behind the aperture if $\alpha \neq 0$, as multiple x_o and α values can account for the same data. In the next section, the benchtop etendue calibration is used to further constrain the position.

The layout of calibration setup is shown in Figure B-2 for the K-LIM enclosure and B-3 for a wall box. A precision protractor is used to align the translation stage and the diagnostic enclosure via a common fiducial, the vertically mounted bar seen in both photos. This allows the direction of motion of the translation stage to be mounted perpendicular to $\hat{x}$ in the aperture coordinate system to < 0.2 degrees. The distance between the aperture and the translation stage is measured using an inside micrometer and is known to < 0.01 inches.

The laser is defocused in order to fully illuminate the aperture and a $\sim$1 kHz square wave is used to pulse the laser. When moved along the translation stage, the orientation of the laser is adjusted using a rotational stage to maintain alignment

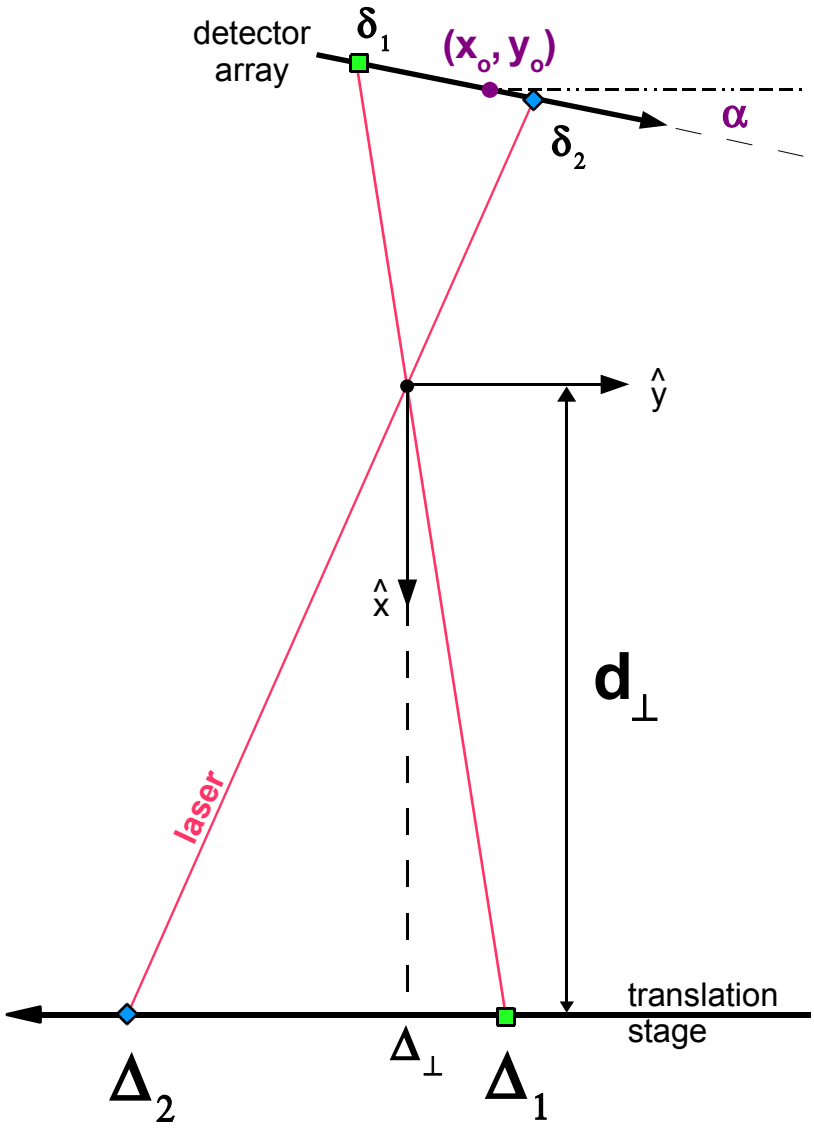

Figure B-1: Sketch showing how the variables measured in the benchtop laser calibration (δ_i, Δ_i and $d_\perp$) can be used to find x_o, y_o and α of the array

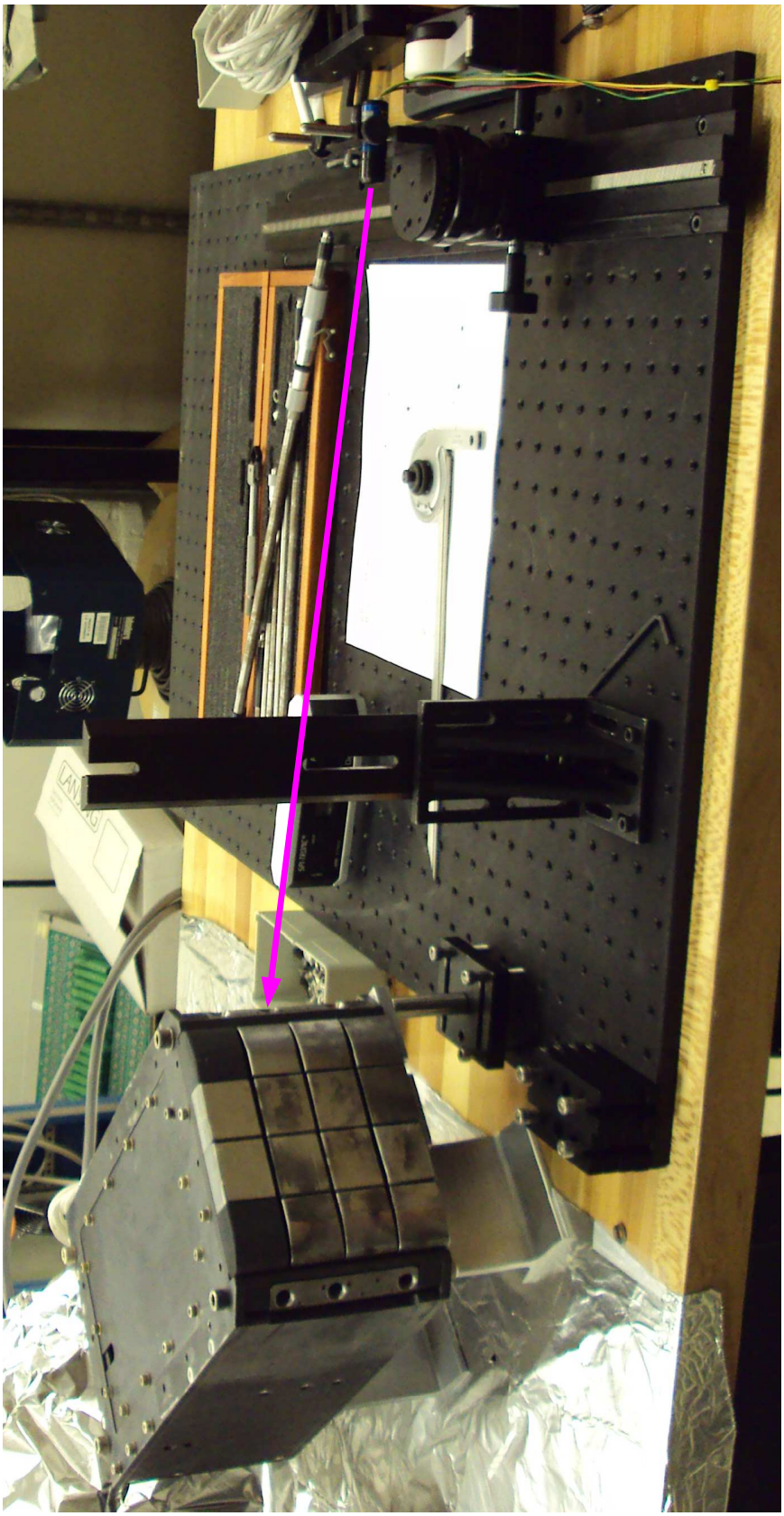

Figure B-2: Picture of the benchtop laser calibration setup for one of the AXA array in the KLIM enclosure

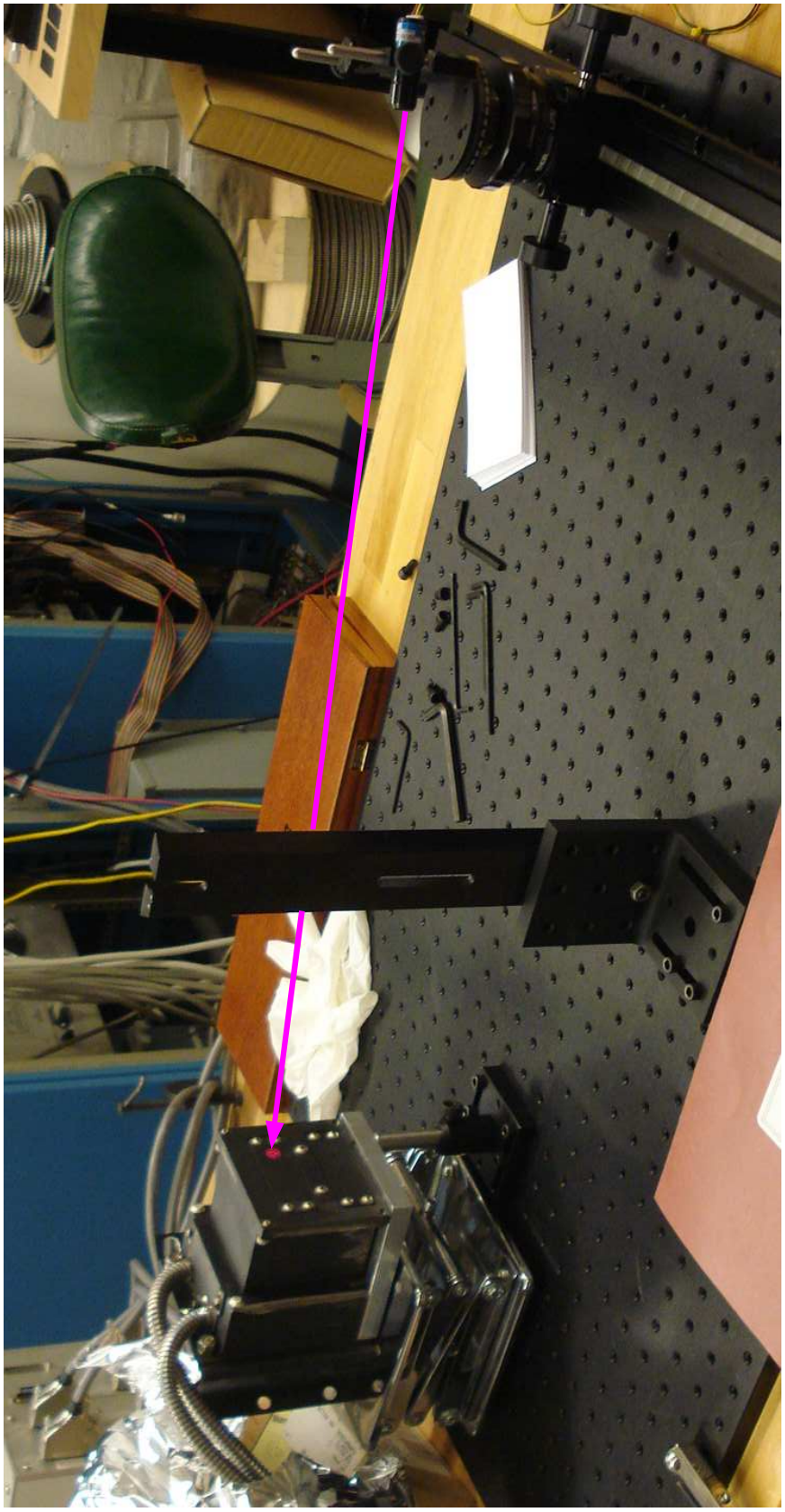

Figure B-3: Picture of the benchtop laser calibration setup for one of the wall box enclosures

with the aperture. This process works to convolve the aperture with the detector. Approximately 10-15 measurements are made for each channel, with the resolution of translation stage being 0.01 inches. The process is is then repeated for multiple channels in each array. Voltages are measured by the data acquisition system used for plasma operations. The results of the calibration are shown in Figures B-15 to B-19 in Section B.4. In the top half of each figure are the RMS voltage response for multiple channels plotted against stage position. Note the confusing notation of the x-axis where $x - x_o$ is stage distance from the center of fiducial channel, and does not have anything to do with distances in the xyz aperture coordinate system.

B.2 Benchtop Etendue Calibration

The etendue or throughput, U, in a pinhole camera is a function of the size, position and orientation of the detector and aperture. Since the area of the diodes, A_{det}, are constant across the AXUV-22EL array, the relative change in U across the array is only a function of x_o, y_o and α. Using the notation shown in Figure B-4, the etendue of a channel located δ_i from the center of the detector is,

$$U_i = \frac{A_{det} A_{ap} \cos\psi \cos\phi}{r^2} \tag{B.3}$$

where A_{ap}, is the area of the aperture, $x_i = x_o + \delta_i \sin\alpha$ and $y_i = y_o + \delta_i \cos\alpha$. The distance r_i^2, and the angle cosines, ψ and ϕ can be expressed as functions of the detector position, (x_i, y_i),

$$\begin{aligned} r_i^2 &= x_i^2 + y_i^2 \\ \cos\phi &= \sin\theta = -\frac{x_i}{r_i} \\ \cos\psi &= \sin\alpha\cos\theta + \cos\alpha\sin\theta = \sin\alpha\frac{y_i}{r_i} - \cos\alpha\frac{x_i}{r_i} \end{aligned} \tag{B.4}$$

although in practice the etendues are calculated using (C.20).

In order to accurately determine the relative etendue for an array, a correction

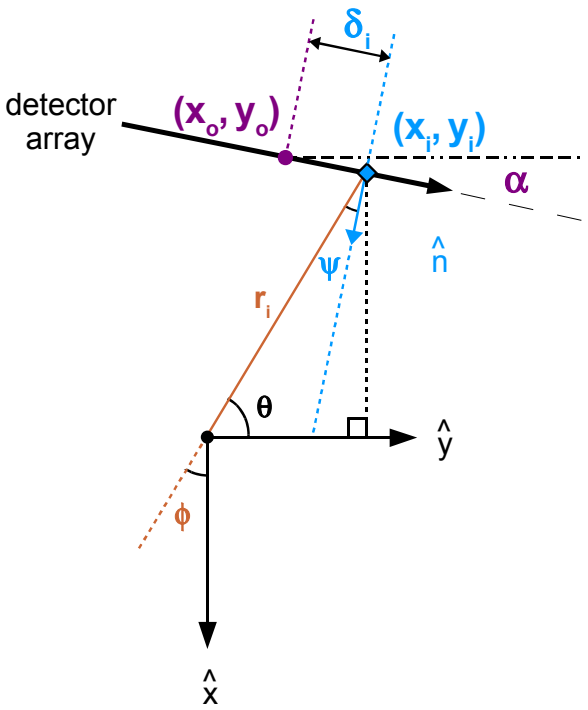

Figure B-4: Sketch showing the relationship between the calibration variables (x_o, y_o and α) and those used to calculated the etendue (ψ,ϕ,r^2)

must be made for the finite aperture thickness, t, which acts to vignette channels off the optical axis. Figure B-5 shows a sketch magnifying this effect which can be used to calculate the useful width, w', as a function of position behind the aperture (x_i, y_i), where $z_i = 0$ is assumed. The height of the detector is assumed to be close to the height of the aperture, making vignetting in that direction negligible.

Similar triangles with angle ϕ can be used to determine $\delta w = w - w'$ for $|y_i| > w/2$.

$$\tan\phi = \frac{|x_i| - t}{|y_i| - w/2} = \frac{t}{\delta w} \tag{B.5}$$

Assuming $x \gg w > t$, (B.5) reduces to $w' = w - t\,|y_i/x_i|$ which allows the functional area of the aperture, A_o to be calculated relative to the full area, A_{ap},

$$A_o = A_{ap}\left(1 - \frac{t}{w}\left|\frac{y_i}{x_i}\right|\right) \tag{B.6}$$

This effect can also be calculated by following rays between the aperture and detector, discounting those that would impact the sides of the aperture, a technique

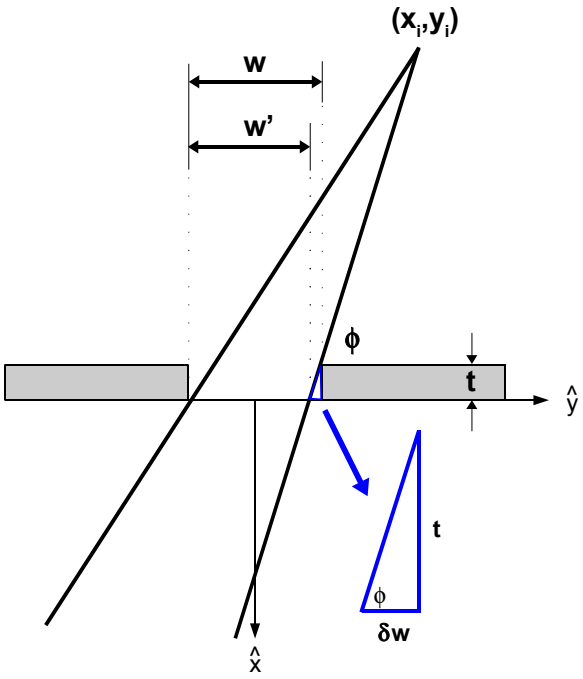

Figure B-5: Sketch exaggerating the finite aperture thickness effect which reduces the effective width of the aperture

that requires extremely fine gridding of the aperture. Figure B-6 plots etendue curves for the AXA (blue) and AXJ (black) arrays calculated using multiple techniques. The solid lines are found assuming an infinitely thin aperture, while the dashed lines include the correction for a 0.010 inch aperture using B.6. The solid symbols are the etendues calculated using GENPOS for very fine aperture and detector gridding. The analytical estimation provides accurate results with substantially less computational cost than the ray-tracing solution, and so it is used in practice.

To find the relative, channel-to-channel response of the diodes in each camera, a Labsphere URS-600 Uniform Radiance Standard is used to expose the array to a flat-field light source. The emitted power, $\sim$25 kW/m^2, is sufficiently large that calibrations can be performed with the apertures and amplifier gains used for plasma operations. The URS-600 has a 1.5 inch diameter aperture which doesn't allow the entire array to be calibrated simultaneously. If the Labsphere output is placed directly at the aperture, then the full 2π steradians surrounding the camera is indeed filled and all channels view light, but the source is non-uniform. This can be seen in Figure B-7, where, due to its construction, only the collimated view through the 1.5 inch

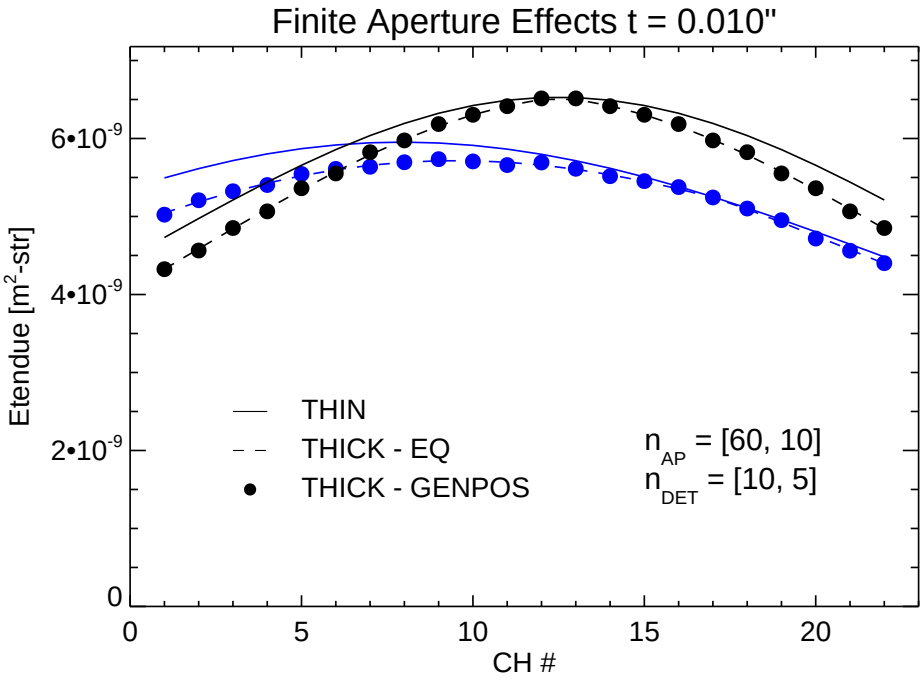

Figure B-6: Calculation of etendues for the AXA (blue) and AXJ (black) arrays for thick and thin apertures.

window can be used as a flat-field.

Instead, a composite response curve is found, as shown in Figure B-8, by rotating the pinhole camera at the aperture while keeping the light source stationary. This exposes each detector in the pinhole camera to the same portion of the Labsphere, and the relative voltage response proportional to the etendue. The wall box and KLIM enclosures are placed $\simeq$ 15 cm from the aperture to reduce scattered visible light, allowing $\sim$ 3 channels to be exposed simultaneously. The enclosure is rotated until all the channels have been exposed to the Labsphere. The relative response data are shown as the symbols in the bottom plots of Figures B-15 to B-19. Figure B-9 shows the summary of the combination of laser and Labsphere calibrations to measure the etendue of pinhole cameras.

The channel-to-channel etendue curves are all that is needed for an individual array to be used to look at in/out asymmetries. Combining the analysis from multiple arrays is necessary to explore the up/down asymmetries, and a camera-to-camera calibration is required. Quoted variation in detector efficiency from IRD as well as

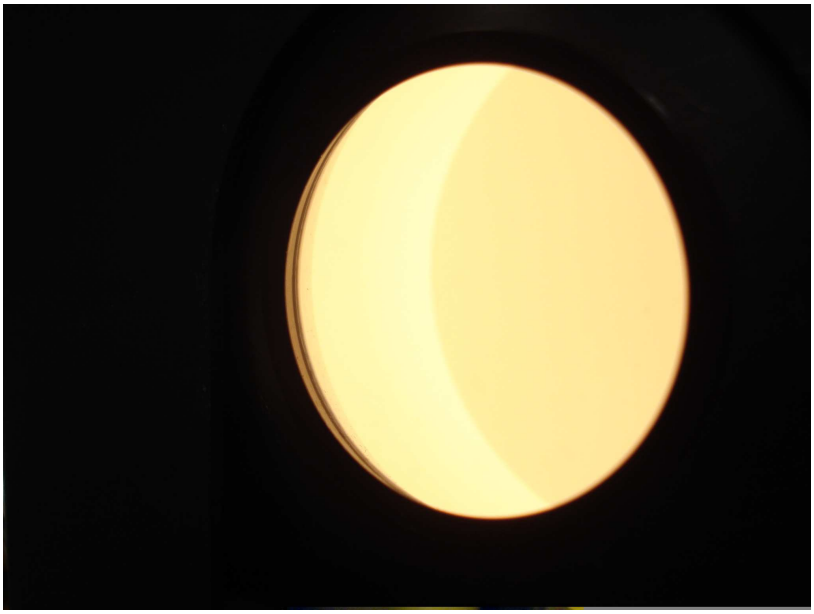

Figure B-7: Image of the Labsphere URS-600 showing internal non-uniformity

inaccuracies in the manufacturing of the apertures are expected to lead to a variation in the absolute brightness between arrays. Each camera is exposed to Labsphere during a single ∼30 minute use of the source, and the measured intensity compared to one another, as shown in Figure B-10. The WB4AX and WB2AX measurements measure the same brightness as one another, as due the AXA and WB3AX cameras, although the latter measure the brightness to be ∼ 10% lower then the former. The measurements define etendue "fudge-factors" used to calibrate out these differences.

If these results are applied to AXJ, then a systematic difference is measured between the AXA and AXJ brightness profiles, indicating an unphysical result of a steady-state, **toroidal** radiation asymmetry. If the arrays are exposed to visible light directly, bypassing the aperture, no difference in sensitivity is observed. The 15-20% error in the size of the aperture necessary to explain the AXA/AXJ difference in Figure B-10 is not found, either. It is thought that a small amount of internal reflections is causing this discrepancy, leading to AXJ measuring the labsphere to have an increased brightness. If this is the case, such an effect would not be seen in SXR and VUV plasma radiation where reflectivity is orders of magnitude below that of visible light. Thus, the benchtop results for the AXJ array are not used, instead trusting the

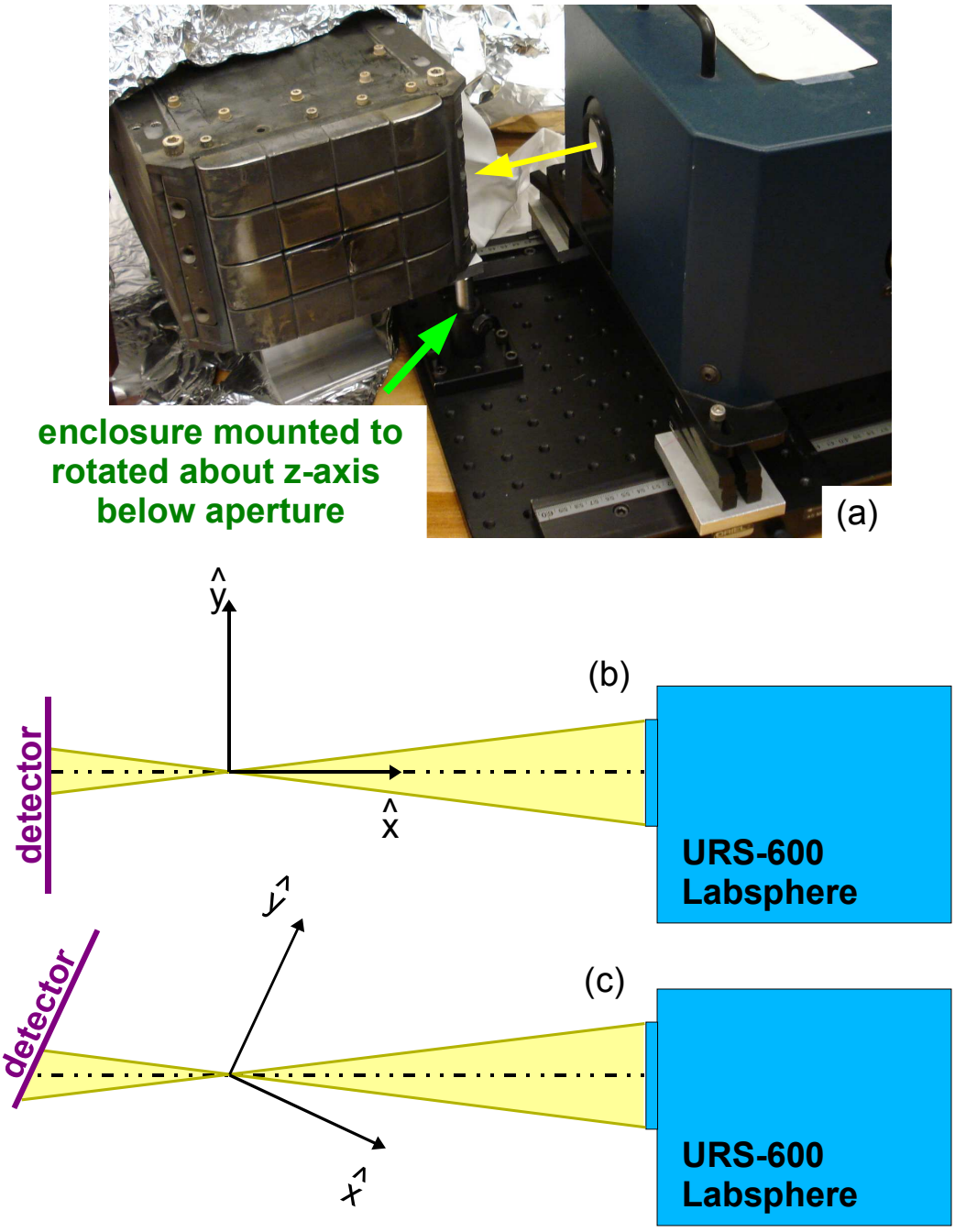

Figure B-8: Image of the Labsphere setup to calibrate AXA (a) with sketches (b),(c) showing the method of rotating the enclosure about a vertical axis going through the aperture

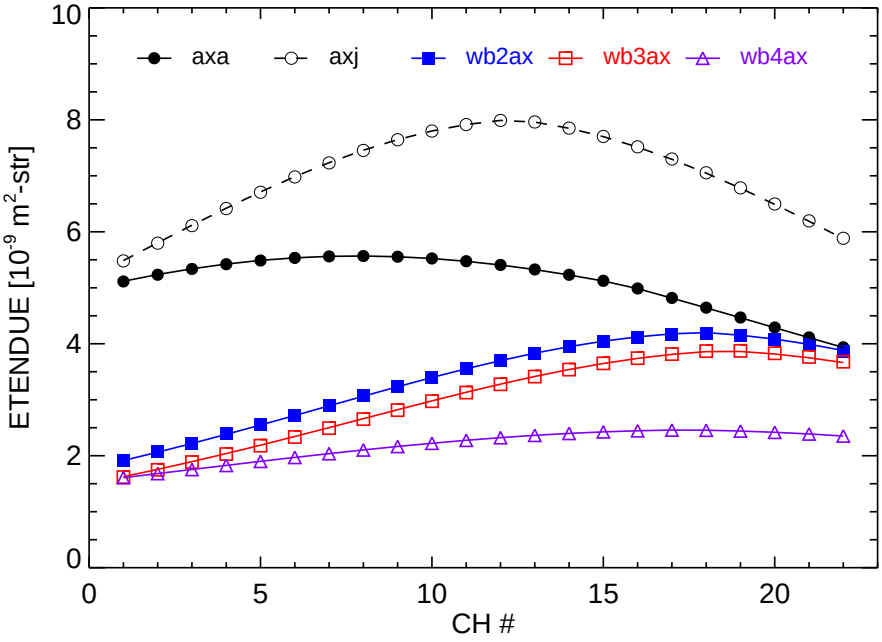

Figure B-9: Etendue of the AXUV diode arrays found from the benchtop calibrations

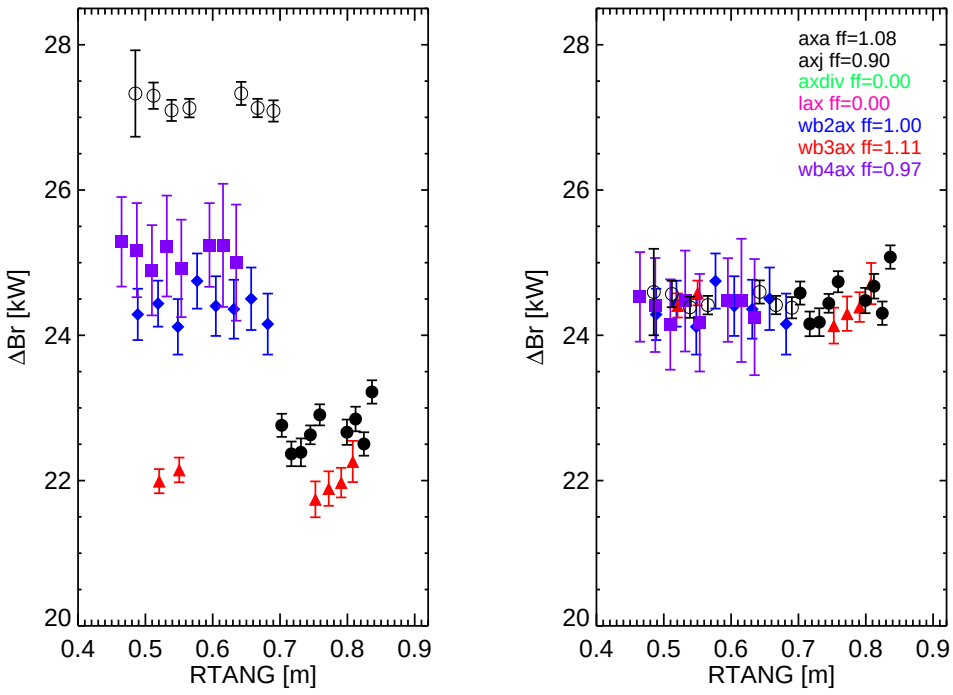

Figure B-10: Results of the relative calibration of the KLIM and wall box arrays

in-situ, empirical result that AXA and AXJ measure consistent brightness profiles when using etendues calculated from geometry. The construction of the wall boxes makes them less susceptible to scattered light, and the calibration results shown in Figure B-10 have been used throughout this research.

B.3 In-Vessel Positional Calibration

The benchtop calibrations accurately measure the position and orientation of the detector relative to the aperture, but when the enclosure is placed in the tokamak, the orientation of the aperture relative to the tokamak coordinate system must be found. A person without the Germanic heritage and Wisconsin upbringing of the author is necessary to go inside C-Mod to perform these calibrations. Figure B-11 shows an example of one of the many wonderful students and staff that assisted in in-vessel calibrations between 2007-2011. The degradation of the pleasant smile was observed to grow nonlinearly with duration of calibration. Sustained weekend calibrations often required the purchase of food and drink following the removal of the setup from the tokamak, an effort that proved useful in maintaining the availability of the apparatus.

In Alcator C-Mod, the inner wall is the known fiducial position, with the cylindrical surface being machined to be $R = 44.06$ [cm], and the midplane, $Z = 0.0$, defined by the tile geometry. An inside micrometer is used to find the minimum distance from the aperture to the inner wall, $R_{ap} - R_{wall}$. Its vertical offset is found relative to the inner wall midplane by using a conventional self-leveling laser to draw a line from the aperture to the inner wall, and then measuring the distance of this spot off the midplane. An estimate of the toroidal location of the arrays is made, but an accurate measurement this position is unimportant since toroidal symmetry is assumed.

For horizontally viewing cameras, the goal is to find the tangency radius, R_T, of each channel to be used in the Abel inversions. Since the x_o, y_o and α are known from the benchtop calibrations, the tangency radii of all the channels is fixed by a single R_T measurement, although in practice, the R_T of 3-4 channels are measured

Figure B-11: Example of critical calibration components deployed in-vessel

to increase the accuracy. Similar to the benchtop calibration, the defocused laser is scanned across the aperture using the translation stage, and positions on the stage recorded and the diode response measured.

Figure B-12 shows a sketch of the calibration layout, while pictures in Figure B-13 show the actual setup with the alignment variables labeled. The toroidal angle, θ, between the $\hat{R}$ of the calibration stage and that of the aperture is found by trilateration. The distances between the aperture and fiducial markings on the stage, a_m and b_m, are measured by an inside micrometer. Their horizontal projection, $a = \sqrt{a_m^2 - h^2}$ and $b = \sqrt{b_m^2 - h^2}$, respectively, are used to find θ, and require the measurement of the vertical offset between the fiducial plane and the laser line, h. The translation stage is aligned along a major radius, allowing stage positions, x_i to be related to major radii, $R_i = R_{wall} + x_o + x_i$, where x_o is the distance between $x_i = 0$ and the inner wall.

As shown B-12, in the value of θ can be found using $\sin\theta = d/R_{ap}$, with a, b and

c used to find d, accounting for the width of the stage, w.

$$d = \left(a^2 - \frac{(a^2 - b^2 + c^2)^2}{4c^2} \right)^{1/2} + \frac{w}{2} \tag{B.7}$$

Once R_i, R_{ap} and θ are known, then $R_{T,i}$ can be found using law of sines and law of cosines.

$$R_{T,i} = \frac{R_{ap} R_i \sin\theta}{\left(R_{ap}^2 + R_i^2 - 2R_{ap}R_i \cos\theta \right)^{1/2}} \tag{B.8}$$

The detailed results of this calibration are shown in Figures B-20 to B-24 in Section B.4. In the top half of each figure are the RMS voltage response for multiple channels plotted against major radius. The bottom plot of each shows the calculated tangency radii for these channels and the curve fit to the data. The listed γ value corresponds to one of the rotation angles discussed in Section C.2.3 used to connect an aperture coordinate system to that of the tokamak. In Figure B-14, the R_T curves for all of the pinhole cameras are shown. The reversal of AXJ is due to its viewing in a toroidal different direction then all of the other arrays.

B.4 Benchtop and In-vessel Calibration Results

The detailed on the benchtop (Figures B-15 to B-19) and in-vessel (Figures B-20 to B-24) calibration measurements are plotted below.

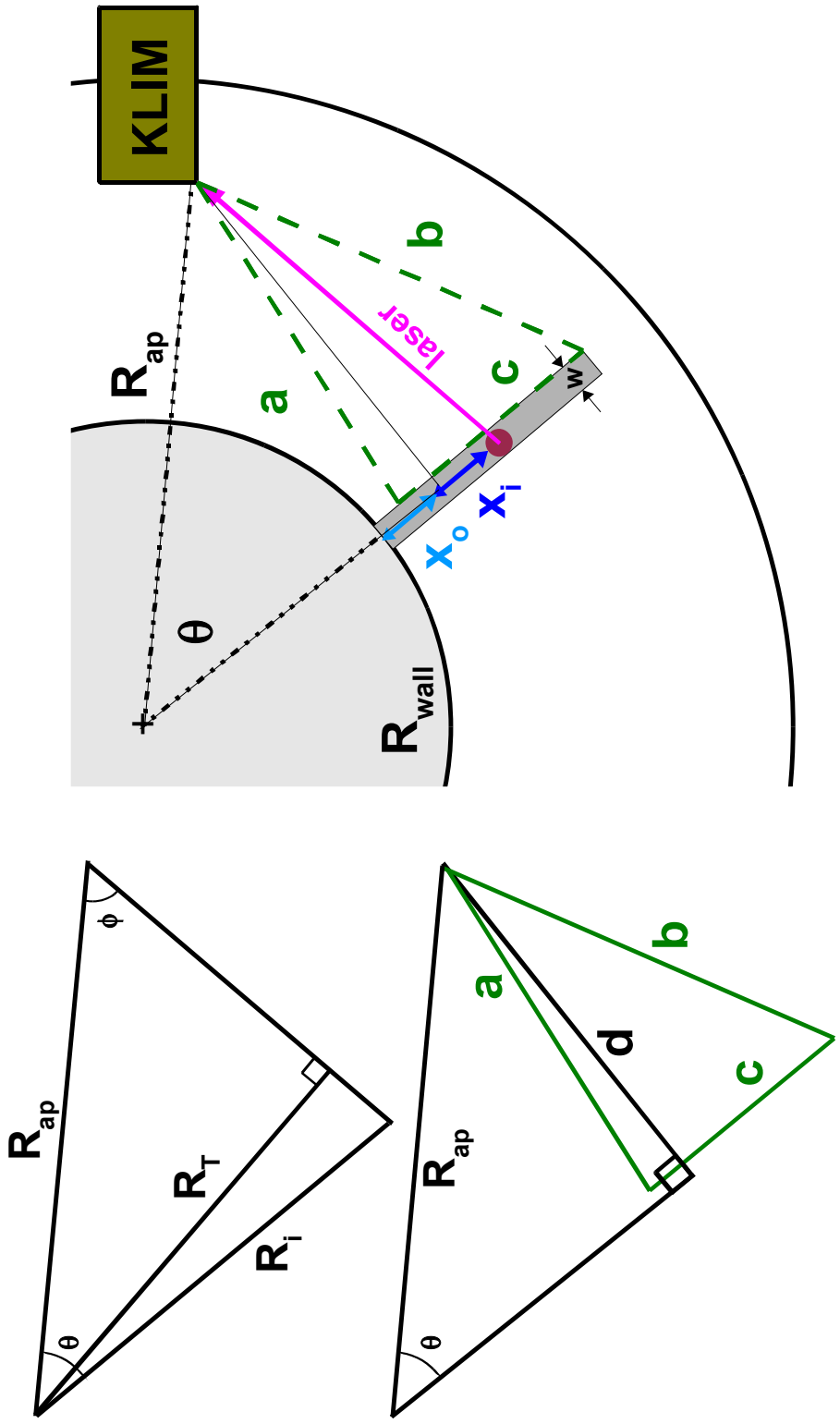

Figure B-12: Sketch of how the in-vessel calibration can be used to find a channel's tangency radius, R_T

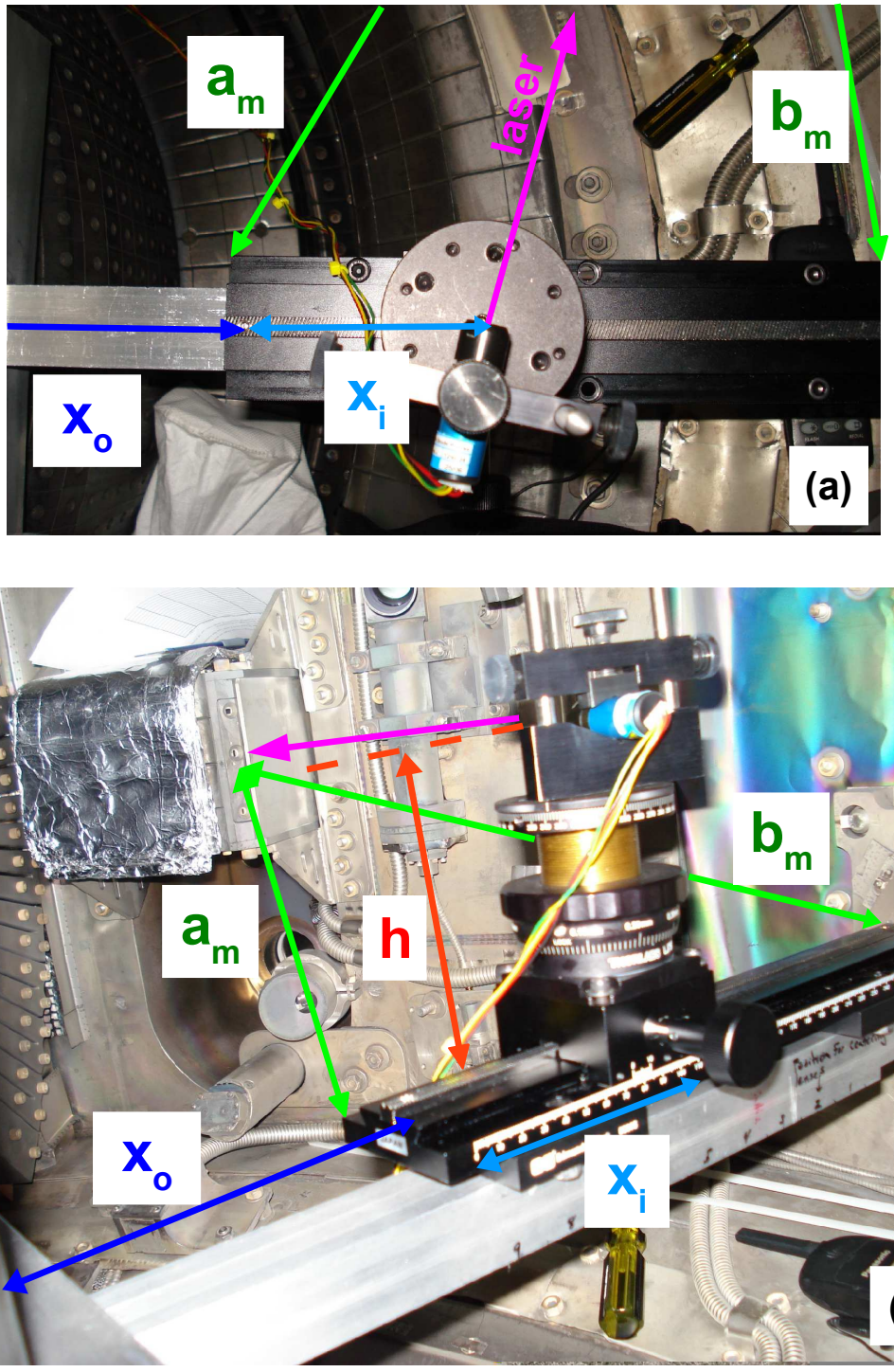

Figure B-13: Top (a) and side (b) views of the in-vessel laser calibration with the alignment variables (h, a_m, b_m and x_o) labeled

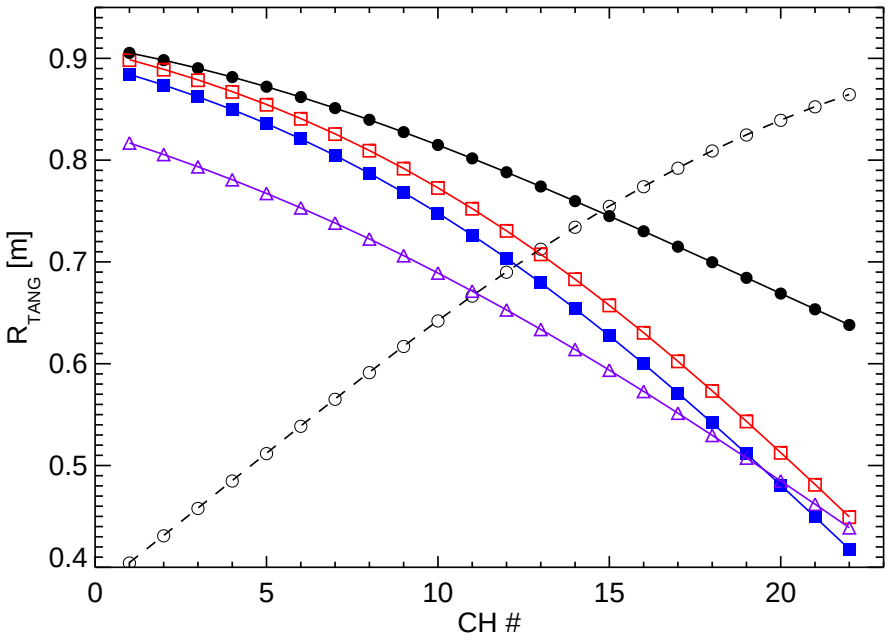

Figure B-14: Tangency radii of the AXUV diode arrays found from the in-vessel calibrations

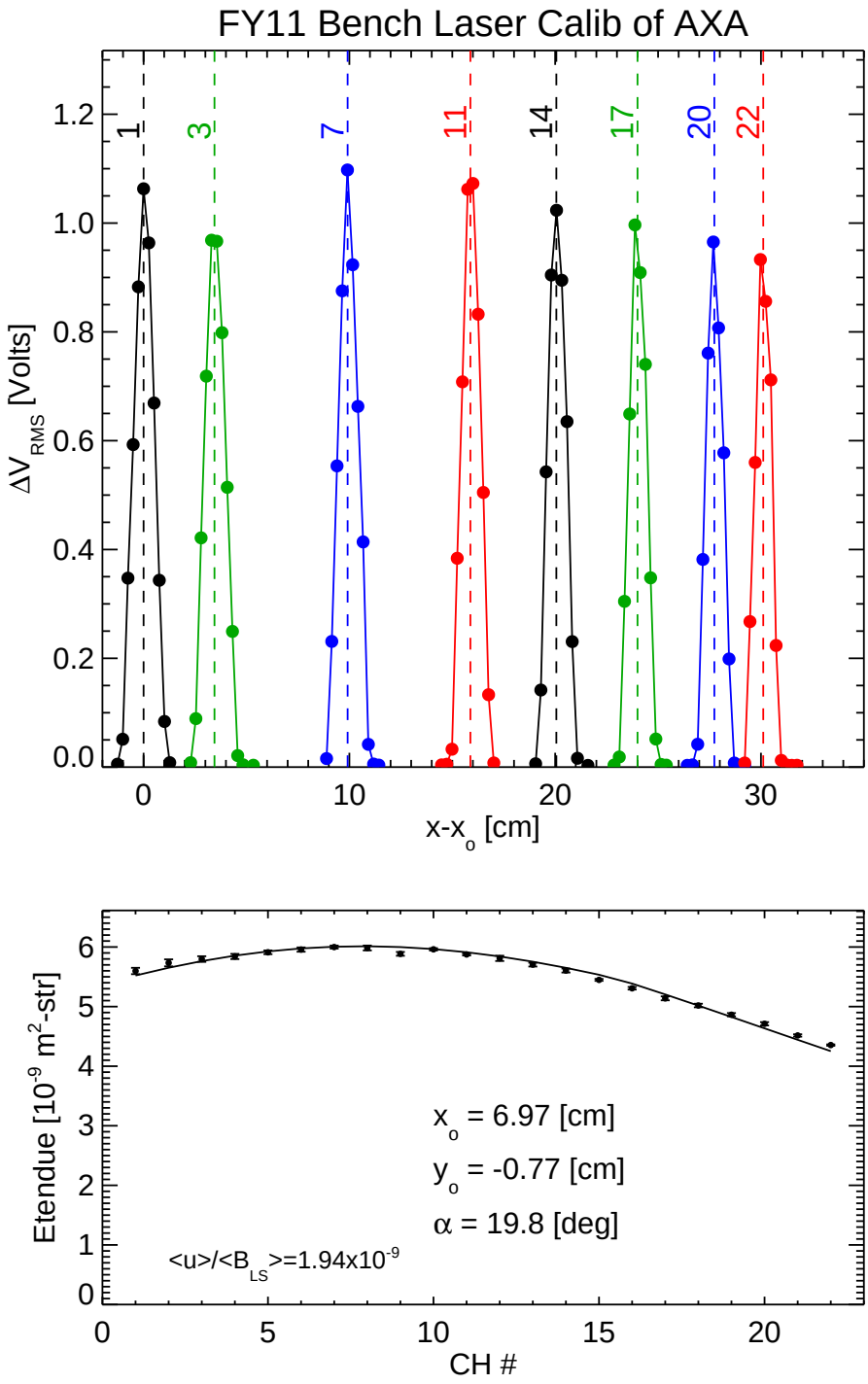

Figure B-15: Results of the AXA benchtop laser (top) and Labsphere calibrations (bottom) used to find x_o, y_o and α

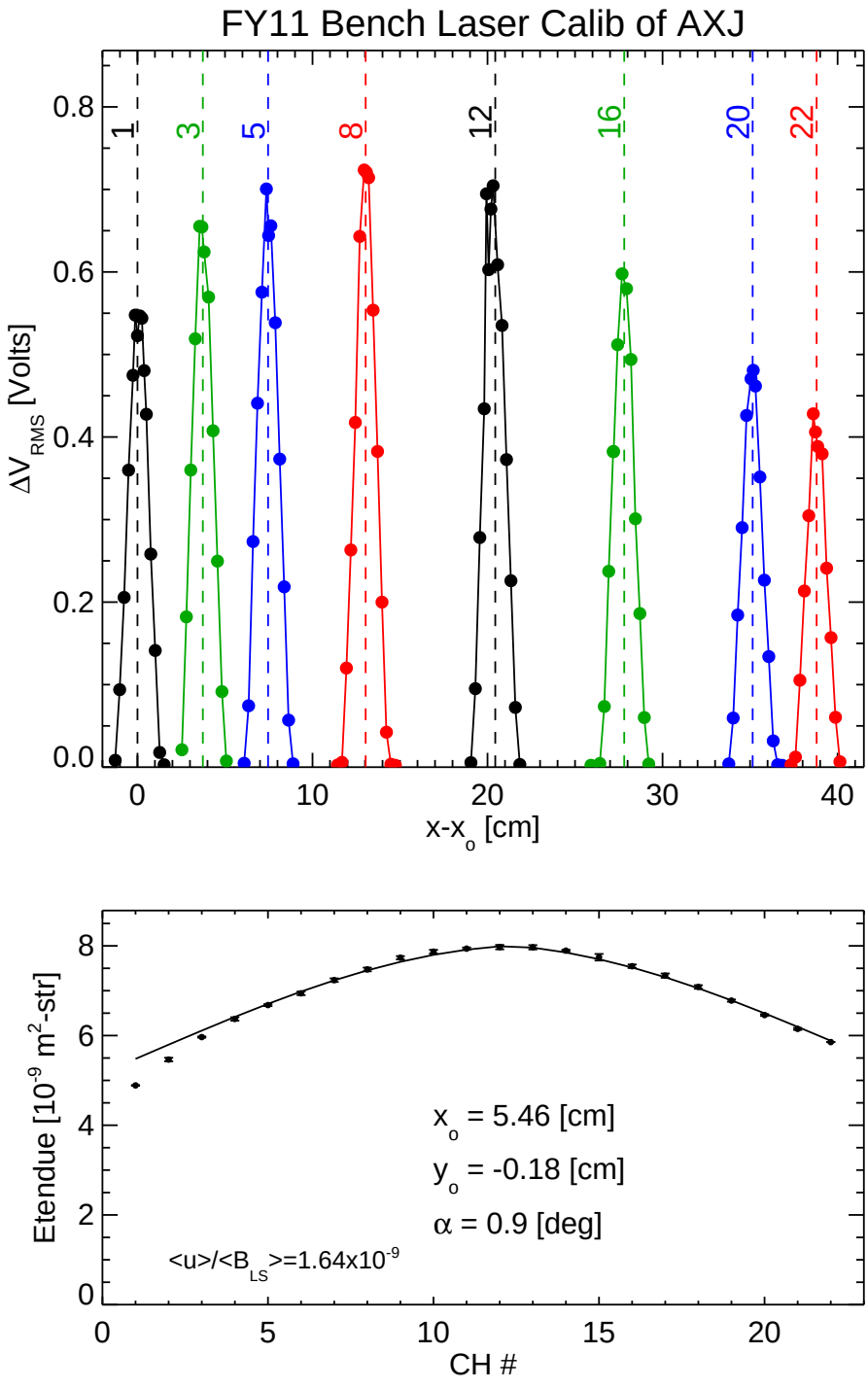

Figure B-16: Results of the AXJ benchtop laser (top) and Labsphere calibrations (bottom) used to find x_o, y_o and α

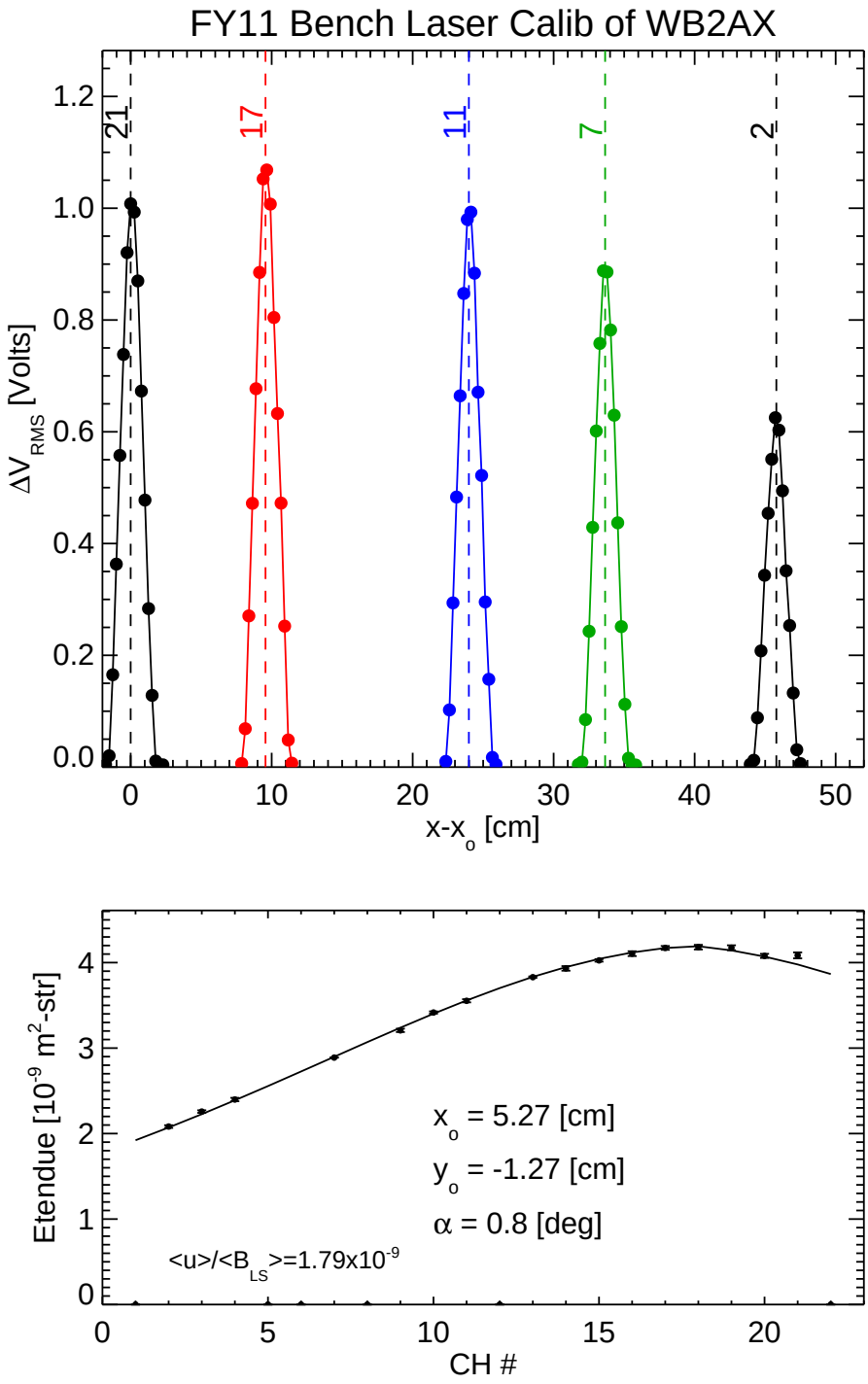

Figure B-17: Results of the WB2AX benchtop laser (top) and Labsphere calibrations (bottom) used to find x_o, y_o and α

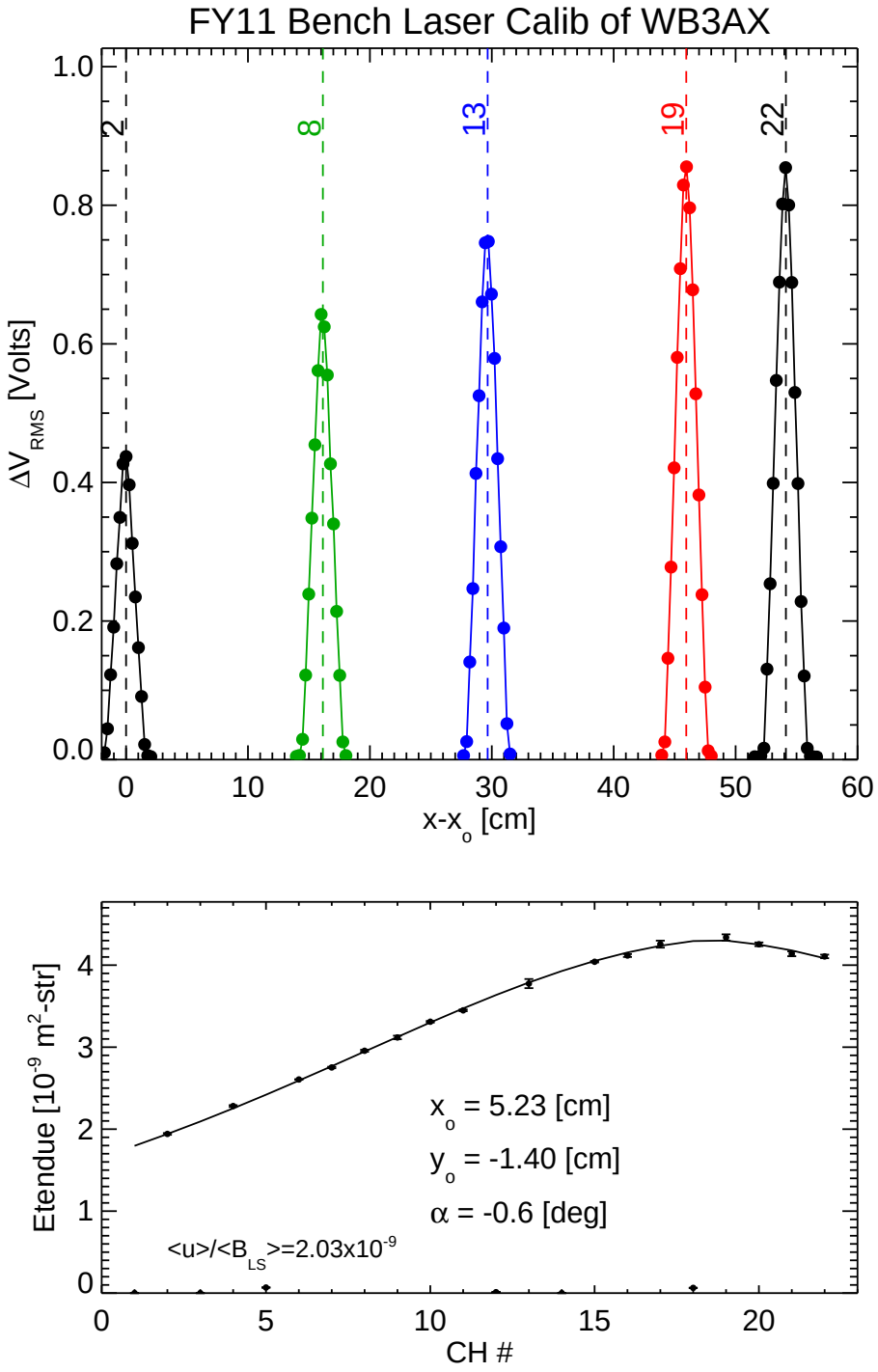

Figure B-18: Results of the WB3AX benchtop laser (top) and Labsphere calibrations (bottom) used to find x_o, y_o and α

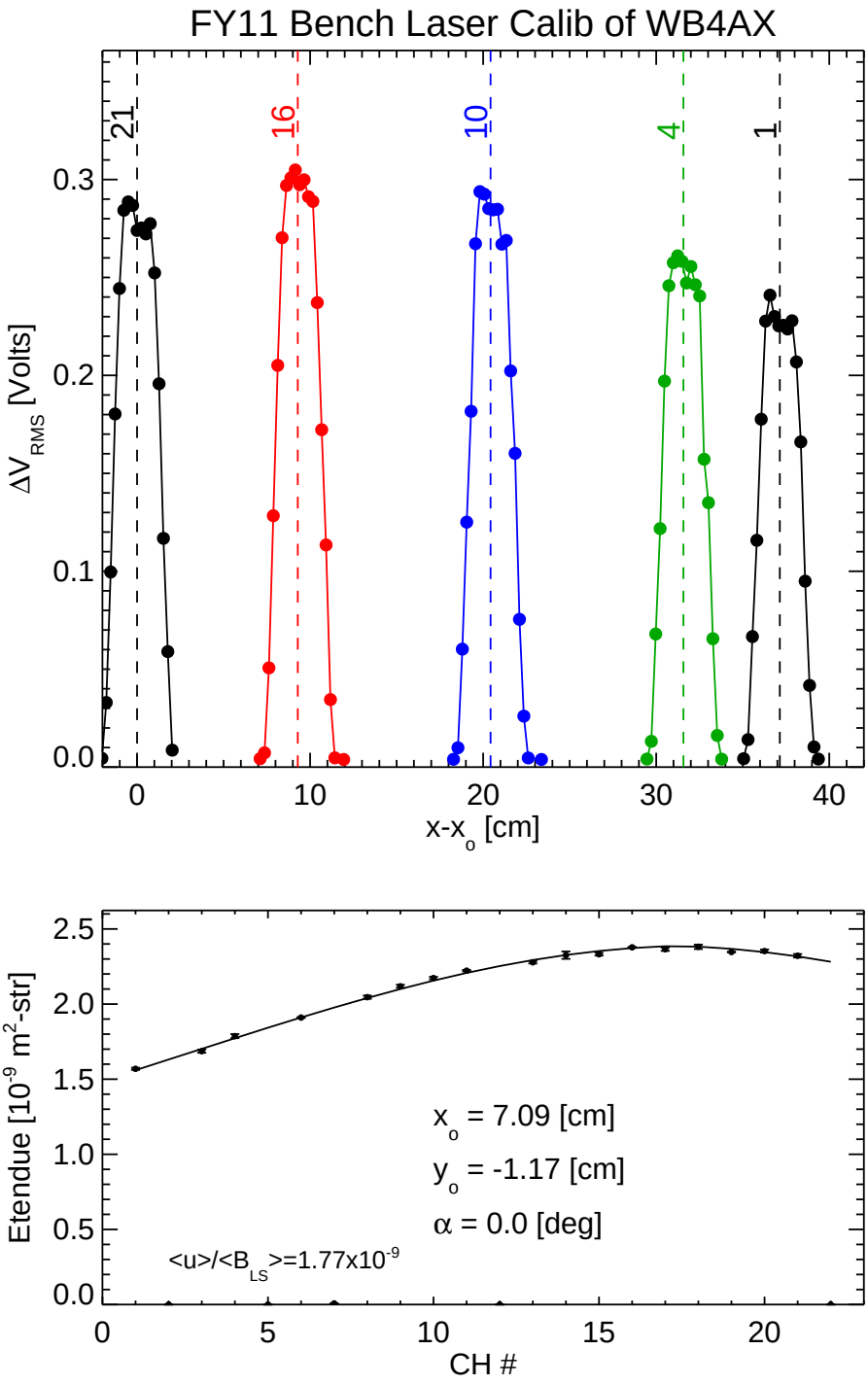

Figure B-19: Results of the WB4AX benchtop laser (top) and Labsphere calibrations (bottom) used to find x_o, y_o and α

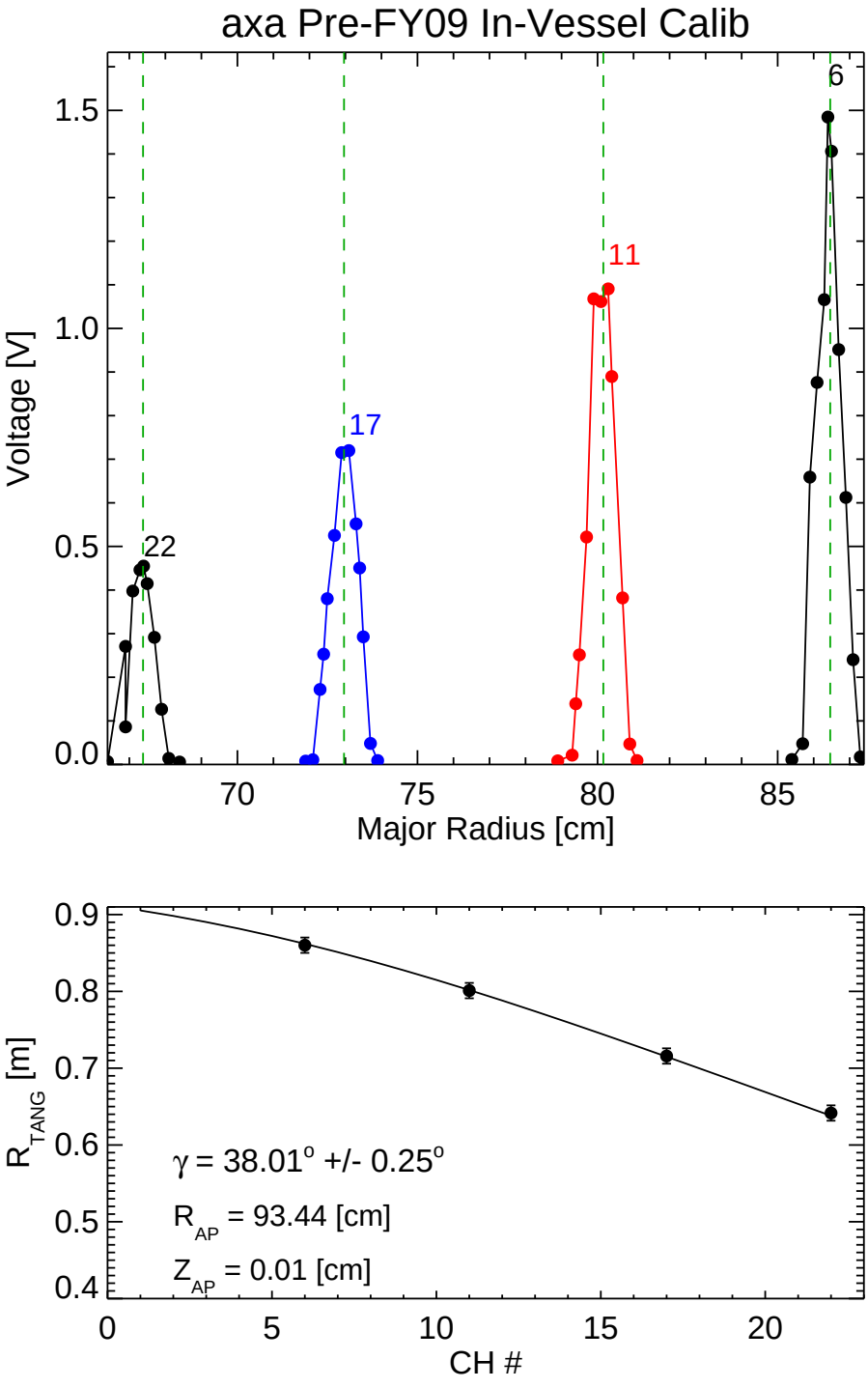

Figure B-20: Results of the AXA in-vessel laser calibrations to find R_T

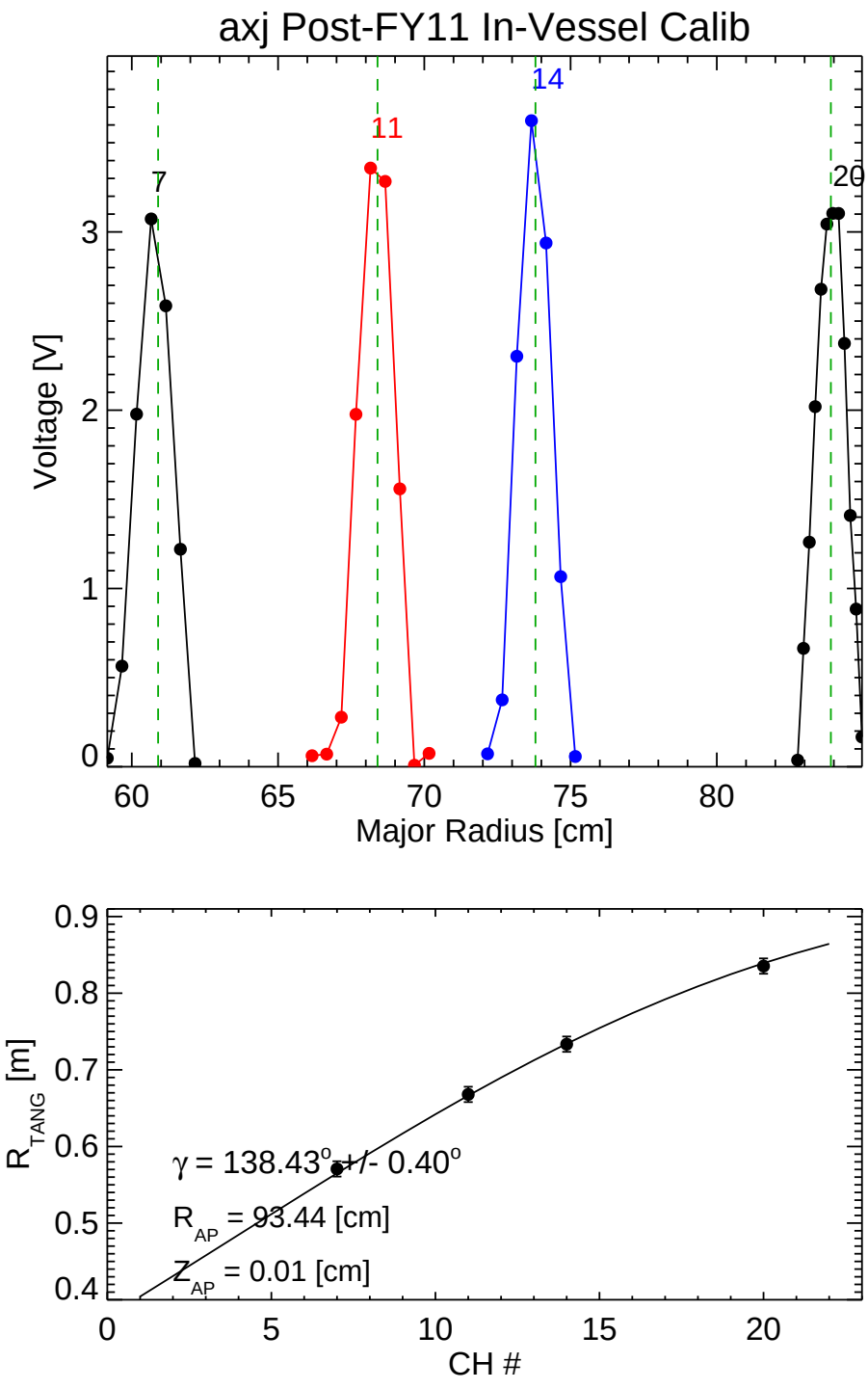

Figure B-21: Results of the AXJ in-vessel laser calibrations to find R_T

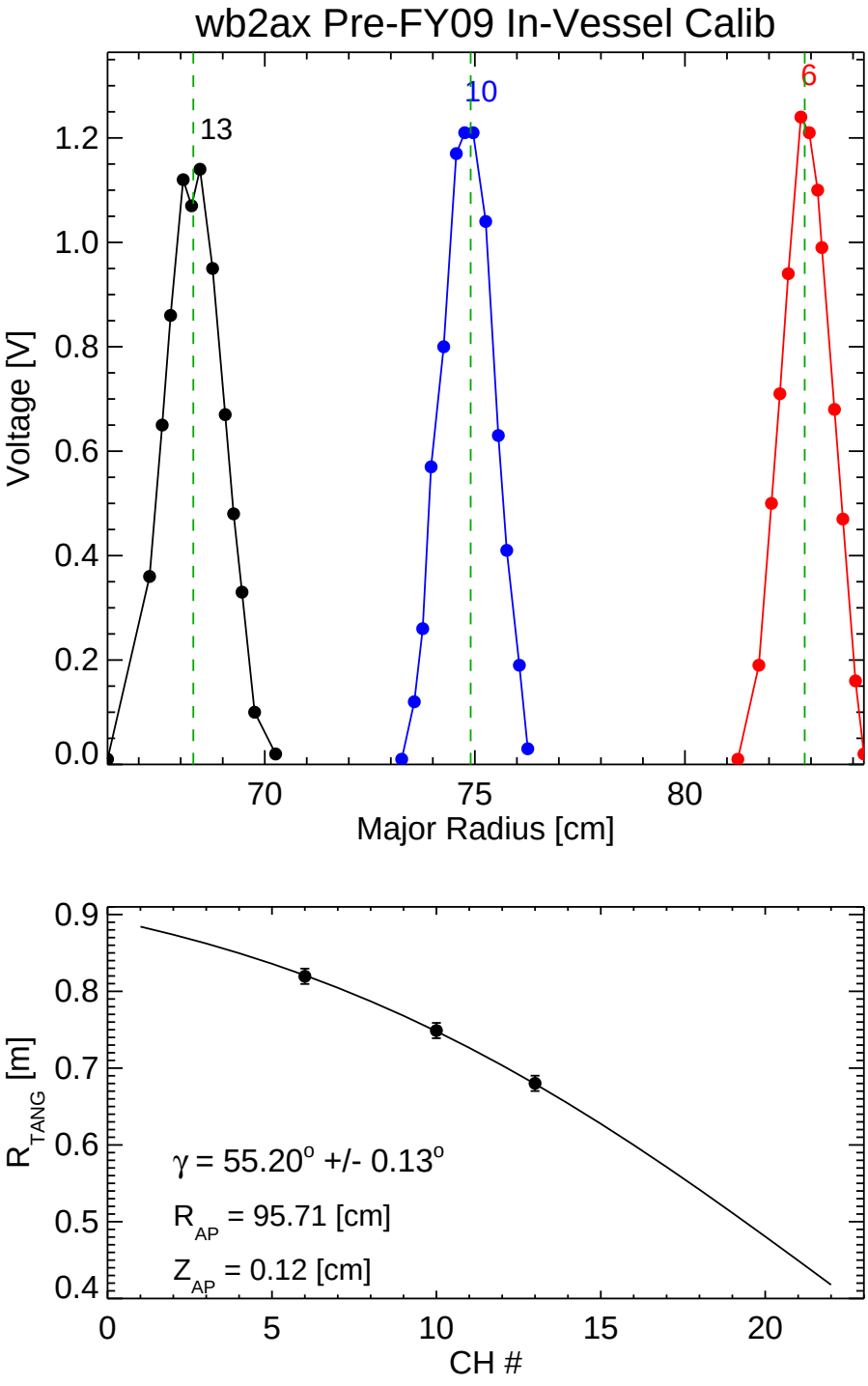

Figure B-22: Results of the WB2AX in-vessel laser calibrations to find R_T

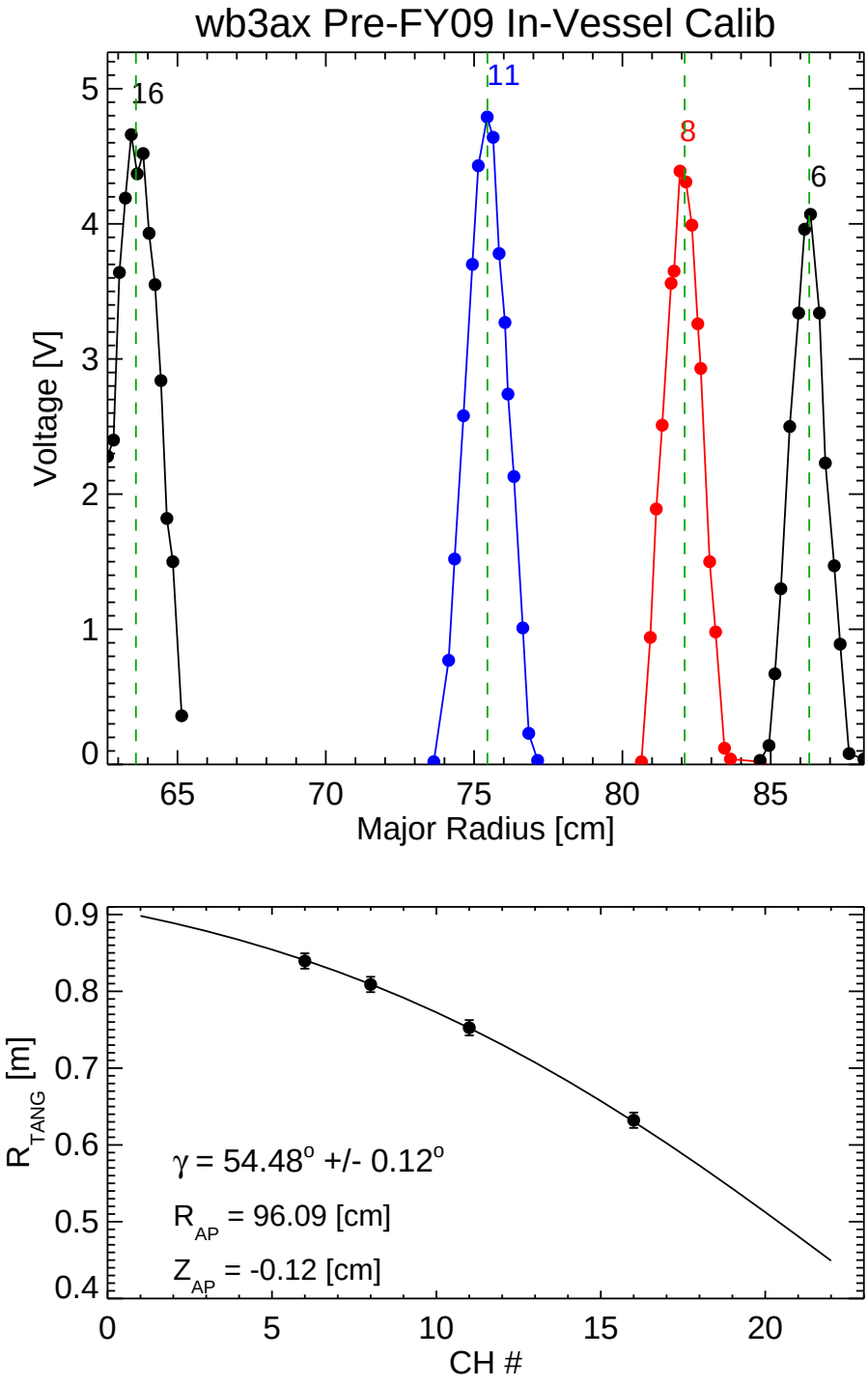

Figure B-23: Results of the WB3AX in-vessel laser calibrations to find R_T

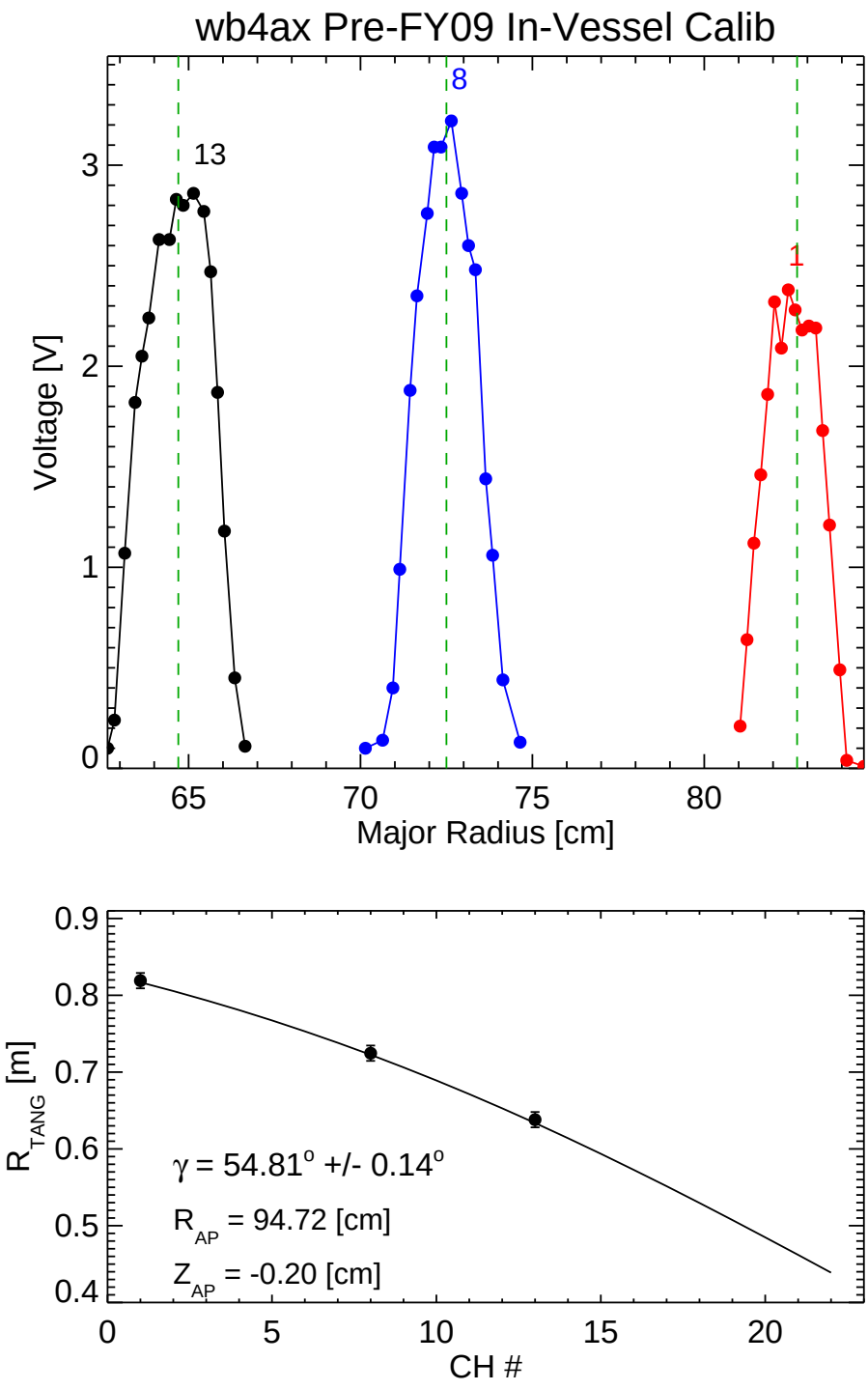

Figure B-24: Results of the WB4AX in-vessel laser calibrations to find R_T

Appendix C

The GENPOS Approach to Ray-Tracing

C.1 The 'Pinhole Camera'

The simplest camera possible is the pinhole camera, where a detector views a source of radiation through an aperture without the aid of filters, lenses or mirrors (see Figure C-1). The spectral sensitivity of the instrument is limited by the aperture diffraction ($\lambda \ll d_{ap}$) and the quantum efficiency, $Q(\lambda) = N_{\gamma,dec}(\lambda)/N_{\gamma,inc}(\lambda)$, of the detector. The aperture and a small area element of the detector, dA, define a viewing cone (dashed lines) with solid angle, Ω_{dA}, through a volumetric emission source with spectral emissivity, $\varepsilon_\lambda(\mathbf{r}, t, \lambda)$, with units of power per unit volume per unit wavelength. A volume element, dV' within this viewing cone will emit only a small fraction, $d\Omega/4\pi$ of its radiation, $\varepsilon_\lambda dV'$, through the aperture onto dA (solid lines). Most radiation sensors give response proportional to either the total energy or the rate of energy deposited onto the total detector area A_{det}.

$$dE_{det} = \frac{1}{4\pi} Q(\lambda)\, \varepsilon_\lambda(\mathbf{r}, t, \lambda)\, dV\, dt d\lambda d\Omega \tag{C.1}$$

The differential solid angle element can be expressed as $dA/|\mathbf{r}-\mathbf{r}_{dA}|^2$ and the integration over dV' must be restricted to the volume V', which is, itself, a function of

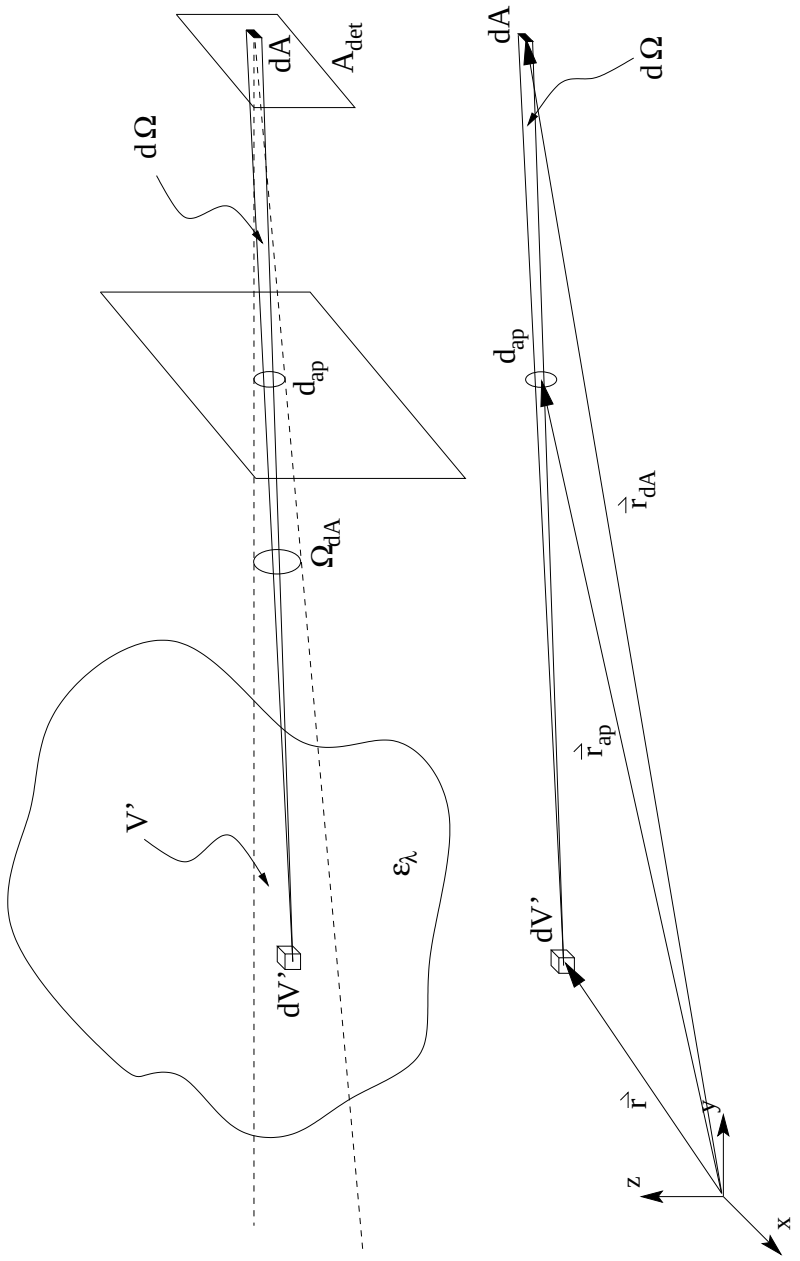

Figure C-1: Sketch of the relevant terms in the imaging of a volumetric source of radiation through an aperture. Vectors locating the volume element, aperture and detector element are labeled on a separate sketch.

$\mathbf{r}_{dA}$, $\mathbf{r}_{ap}$ and d_{ap}. Thus, if the problem were approached completely analytically, the integration must first be performed over dV' and then dA.

$$E_{det} = \frac{1}{4\pi}\int_{\Delta t} dt \int d\lambda \int_{A_{det}} dA \int_{V'} dV' \frac{1}{|\mathbf{r}-\mathbf{r}_{dA}|^2} Q(\lambda)\,\varepsilon_\lambda(\mathbf{r},t,\lambda) \tag{C.2}$$

Expressions for V' are dependent on source/aperture/detector geometry and no exact generalizations will be attempted here. The resulting integral equation is oppressive, yet computationally tractable, but major simplifications can be made if ε_λ is a weak function of $\mathbf{r}$.

C.1.1 The Line Integral Approximation

In most radiometric systems, there is the following ordering of length scales.

$$|\mathbf{r}-\mathbf{r}_{dA}| > |\mathbf{r}_{ap}-\mathbf{r}_{dA}| \gg d_{ap} \geq \sqrt{A_{det}} \tag{C.3}$$

This ordering represents, a point detector at a moderate distance behind a finite sized aperture. Note that the A_{det} is the area of a single detector element not the full detector size in the case of multichannel detector such as a photodiode array or CCD. In this limit, easily integratable expressions for V' and $|\mathbf{r}-\mathbf{r}_{dA}|$ can be found, and it will be shown that if the spatial variation length of ε_λ is not too small, then the (C.2) will reduce to a 1-D integral of ε_λ along the line of sight. If the detector size is small relative to $|\mathbf{r}_{dA}-\mathbf{r}_{ap}|$ and d_{ap} is not $\ll \sqrt{A_{det}}$ then the detector can be modeled as a point. This point and the aperture define a viewing cone through the volumetric source characterized by $\varepsilon_\lambda(\mathbf{r},t,\lambda)$. This arrangement is shown in Figure C-2. The volume element at a distance s from the detector is an annulus with $dV = 2\pi\rho d\rho ds$. Each point in this volume element has the same value of $|\mathbf{r}-\mathbf{r}_{dA}| = \sqrt{s^2+\rho^2}$. Inserting these expression into (C.2) gives

$$E_{det} = \frac{1}{4\pi}\int_{\Delta t} dt \int d\lambda \int_{A_{det}} dA \int ds \int d\rho \frac{2\pi\rho}{s^2+\rho^2} Q(\lambda)\,\varepsilon_\lambda(\mathbf{r},t,\lambda) \tag{C.4}$$

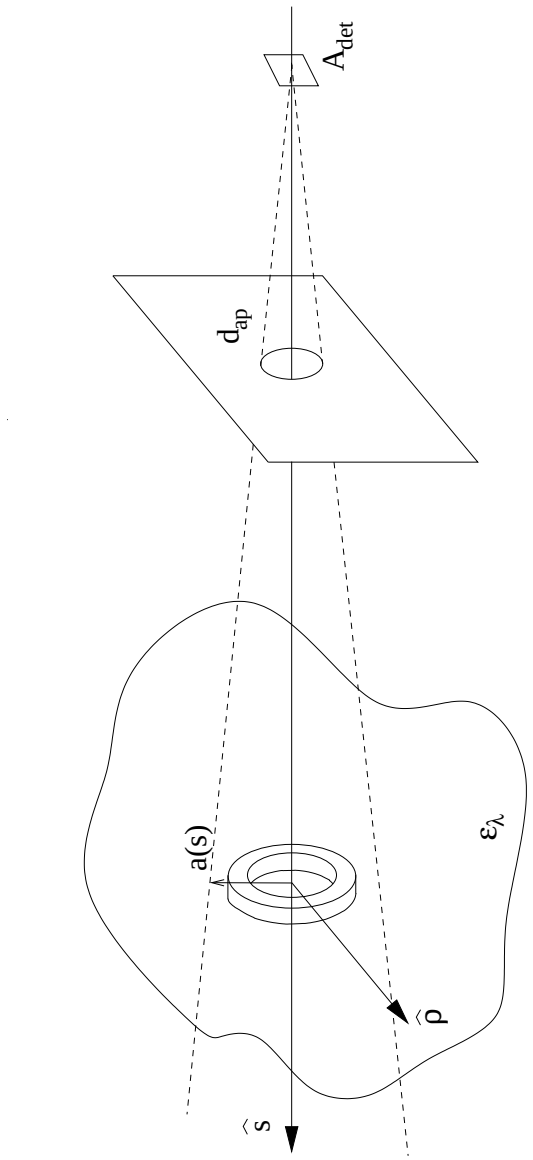

Figure C-2: Sketch of the setup under the line integral approximation. The volume element, dV, can be expressed as an annular volume element, $2\pi\rho d\rho dR$. Each point on this element has an equal value of $|\mathbf{r} - \mathbf{r}_{dA}| = \sqrt{R^2 + \rho^2}$.

Functions of t and λ remain unspecified, but the integration over dA can be done trivially since there are now no detector dependencies. Integration is done for $s > 0$ since ε_λ will go to zero outside of the emitting volume and the integral will not diverge. The integration limit for ρ is from 0 to $a\,(s)$, the radius of the cone at a distance s from the detector. This cone is defined by the detector/aperture pair with $a = sd_{ap}/2f$, where f is the distance between the aperture and detector. The emissivity is Taylor expanded about $\rho = 0$.

$$\begin{aligned} \varepsilon_\lambda\,(\mathbf{r}, t, \lambda) &= \varepsilon_\lambda\,(s, \rho, t, \lambda) \\ &= \varepsilon_\lambda\,(s, 0, t, \lambda) + \rho \frac{\partial}{\partial \rho} \varepsilon_\lambda\,(s, p, t, \lambda)\,|_{\rho=0} \\ &= \varepsilon_\lambda\,(s, t, \lambda) \left(1 + \frac{\rho}{L_\varepsilon}\right) \end{aligned} \tag{C.5}$$

This expansion introduces the derivative scale length, L_ε of the spectral emissivity. If $L_\varepsilon \gg a(s)$ then $\varepsilon_\lambda\,(\mathbf{r}, t, \lambda) = \varepsilon_\lambda\,(s, t, \lambda)$ can be used when integrating over ρ. Inserting this simplification in (C.4) and performing the integration gives,

$$E_{det} = \frac{A_{det}}{4} \ln\left(1 + \frac{d_{ap}^2}{4f^2}\right) \int_{\Delta t} dt \int d\lambda \int ds\, Q\,(\lambda)\, \varepsilon_\lambda\,(s, t, \lambda) \tag{C.6}$$

The ln term can be expanded about 1 since $d_{ap} \ll f$ and the aperture area can be inserted into the equation.

$$E_{det} = \frac{A_{det} A_{ap}}{4\pi f^2} \int_{\Delta t} dt \int d\lambda\, Q\,(\lambda) \int ds\, \varepsilon_\lambda\,(s, t, \lambda) \tag{C.7}$$

The energy absorbed by the detector is now in terms of macroscopic characteristics and the integral of ε_λ along the line of sight, significantly simplified from (C.2). Besides the ordering of scale lengths in (C.3) the main assumption is that the ε_λ does not change significantly in the plane perpendicular to the line of sight, $L_\varepsilon \gg a(s)$.

C.2 Parameterizing a Generic Tokamak View

From the results of the line integral approximation, it is clear that emissivity integrated along a an arbitrary line of sight will be necessary in analyzing experimental data. The view is defined by the detector and aperture locations and can be expressed by the set of parametric equations for a line in 3D Cartesian space as shown in Figure C-3. The parameter, l, can vary from $(-\infty,+\infty)$ to define the full line, while for $0 < l < 1$ the region between points **1** and **2** is described. Note that $l \neq s$, the effect of which will be discussed in the Section C.2.4.

$$\begin{aligned} x &= x_1 + l\,(x_2 - x_1) \\ y &= y_1 + l\,(y_2 - y_1) \\ z &= z_1 + l\,(z_2 - z_1) \end{aligned} \tag{C.8}$$

This set of equations can also be expressed in cylindrical coordinates which are more natural for tokamak geometry using $x_i = R_i \cos\theta_i$, $y_i = R_i \sin\theta_i$ and defining θ_2-θ_1=ϕ.

$$\begin{aligned} R^2 &= R_1^2\,(1-2l) + l^2\left(R_1^2 + R_2^2\right) - 2l\,(l-1)\,R_1 R_2 \cos\phi \\ \tan\theta &= \frac{\sin\theta_1 + l\left(\frac{R_2}{R_1}\sin\theta_2 - \sin\theta_1\right)}{\cos\theta_1 + l\left(\frac{R_2}{R_1}\cos\theta_2 - \cos\theta_1\right)} \\ Z &= Z_1 + l\,(Z_2 - Z_1) \end{aligned} \tag{C.9}$$

For most radiometry problems encountered in diagnosing tokamak plasmas, the assumption of axisymmetry means that the emissivity is independent of polar (toroidal) angle, making the parametric equation for θ unnecessary to find $\varepsilon_\lambda(l)$. If the 2-D emissivity, $\varepsilon_\lambda(R, Z)$, is then known, either numerically or analytically, then (C.9) can be used to find the expression for $\varepsilon(l)$ that is used in the line integral approximation.

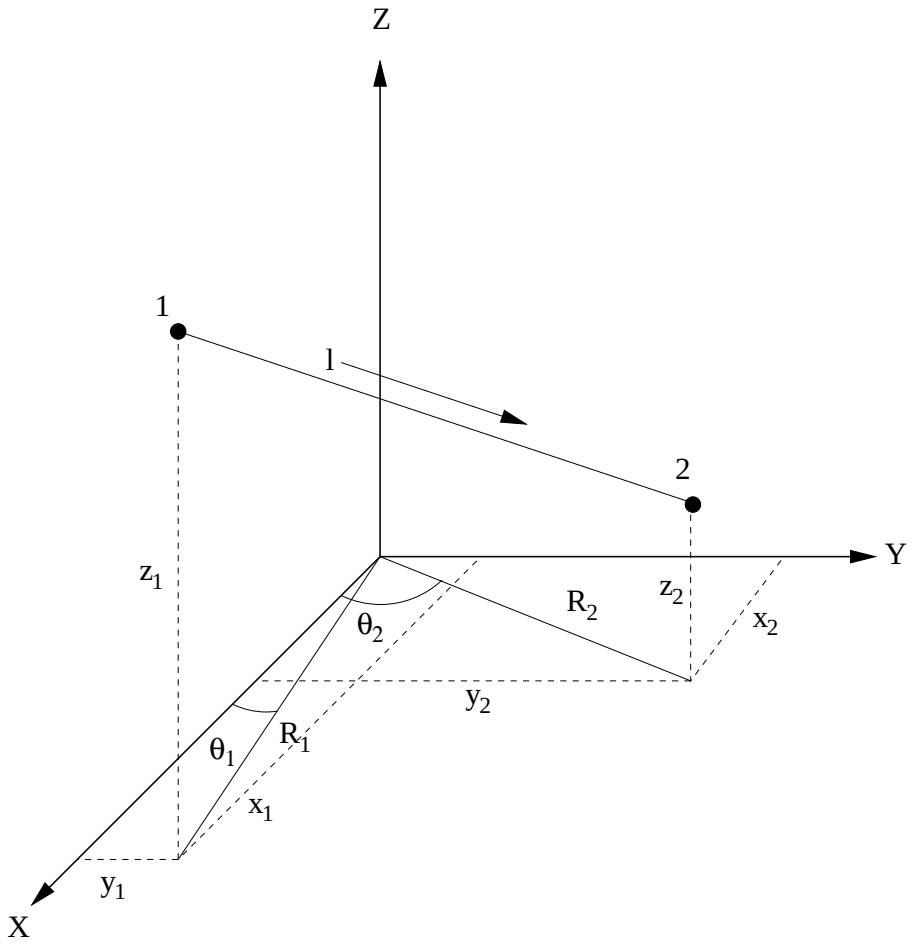

Figure C-3: A line in 3D space with the necessary Cartesian and cylindrical coordinates labeled.

C.2.1 Tokamak coordinates

The cylindrical parametric equations can be expressed in terms that are more physically relevant for tokamak applications. For any multichannel pinhole, the location of the aperture will be a common point, so it is useful to define this location as (R_1,Z_1). In the limit of tomography at a fixed toroidal location, another important parameter is the angle, ψ, the view makes with a constant Z plane. In the limit of tomography on constant Z plane, the radius of closest approach, defined as the tangency radius, R_T, is useful. It will be shown that this set of parameters, (R_1,Z_1,R_T,ψ), can fully describe an arbitrary view as well as be much less cumbersome than (R_1,Z_1,R_2,Z_2,ϕ). The apparent reduction in the number of free parameters comes from the assumption of an angle in defining the tangency radius. To form (C.9) in terms of these new variables let $R_2 = R_T$ and have R_T be normal to the projection in the polar plane of the line connecting **1** and **2**, $\overline{12}$ (see Figure C-4). The angle ψ is defined as the angle between $\overline{12}$ and its projection into a constant Z plane. Equations (C.9) for R^2 and Z can be rewritten using $R_2 = R_T$, $\cos\phi = R_T/R_1$ and $Z_2 = Z_1 - \tan\psi\sqrt{R_1^2 - R_T^2}$.

$$\begin{aligned} R^2 &= R_1^2 + l\,(l-2)\left(R_1^2 - R_T^2\right) \\ Z &= Z_1 - l\sqrt{R_1^2 - R_T^2}\tan\psi \end{aligned} \tag{C.10}$$

Note that solving for the l in $dR/dl = 0$ results in $l = 1$ which is consistent with the way the equation is defined. These equations can be easily inverted to give l values for given R or Z points.

$$\begin{aligned} l_R &= 1 \pm \sqrt{1 - \frac{R_1^2 - R^2}{R_1^2 - R_T^2}} \\ l_Z &= \frac{Z_1 - Z}{\sqrt{R_1^2 - R_T^2}\tan\psi} \end{aligned} \tag{C.11}$$

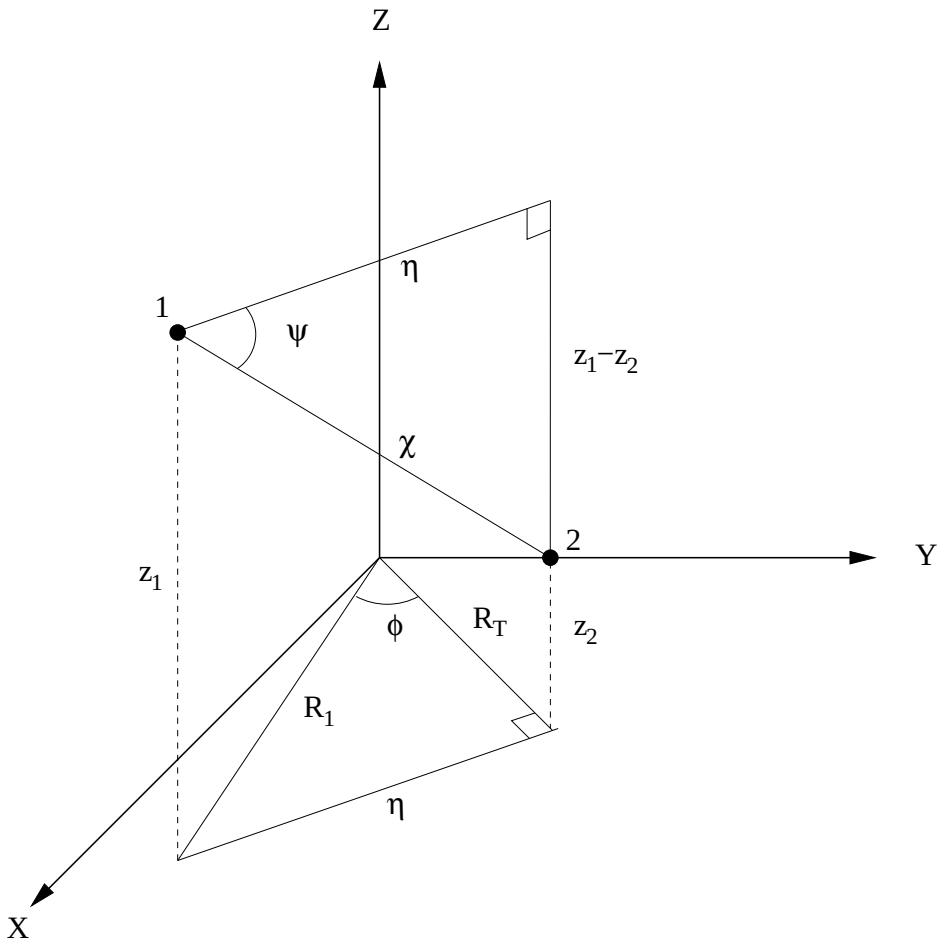

Figure C-4: A line in 3D space with the necessary tokamak coordinates labeled.

If l_Z in (C.11) is inserted into the equation for R^2 in (C.10), the result can be reorganized into the form of hyperbola.

$$\frac{R^2}{R_T^2} - \frac{(Z - Z_o)^2}{(R_T \tan\psi)^2} = 1 \tag{C.12}$$

The parameter Z_o which locates the origin $(0, Z_o)$ of the hyperbola, is

$$Z_o = Z_1 - \tan\psi\sqrt{R_1^2 - R_T^2} \tag{C.13}$$

and is a function of all four relevant parameters that define a view. For two views to have the same Z_o point, then both ψ and R_T would have to be the same, which for detectors which share an aperture is possible but unlikely unless the aperture normal is radial. This means that most detector arrays that share an aperture will have a unique set of hyperbola.

The parameters R_T and ψ used to describe are conceptual and not those that would be easily found from an *in-situ* calibration or engineering schematic of a detector. Values for R_T and ψ must be able to be found from the full set of five parameters. Figure C-5 shows their geometrical relationship and uses the variables η, α and β as placeholders in the derivation. Law of cosines for ϕ defines η, giving the following relation for ψ.

$$\tan\psi = \frac{Z_1 - Z_2}{\sqrt{R_1^2 + R_2^2 - 2R_1R_2\cos\phi}} \tag{C.14}$$

This equation reflects the arbitrary sign convention that positive ψ is a declination from a constant Z plane. To determine R_T, law of sines is used to show

$$\frac{\sin\beta}{R_1} = \frac{\sin\phi}{\eta} = \frac{\sin\alpha}{R_2} \tag{C.15}$$

The value of η can be determined from law of cosines on ϕ, and either α or β can be expressed in terms of R_T. Solving for R_T then gives,

$$R_T = \frac{R_2R_1\sqrt{1 - \cos^2\phi}}{\sqrt{R_1^2 + R_2^2 - 2R_1R_2\cos\phi}} \tag{C.16}$$

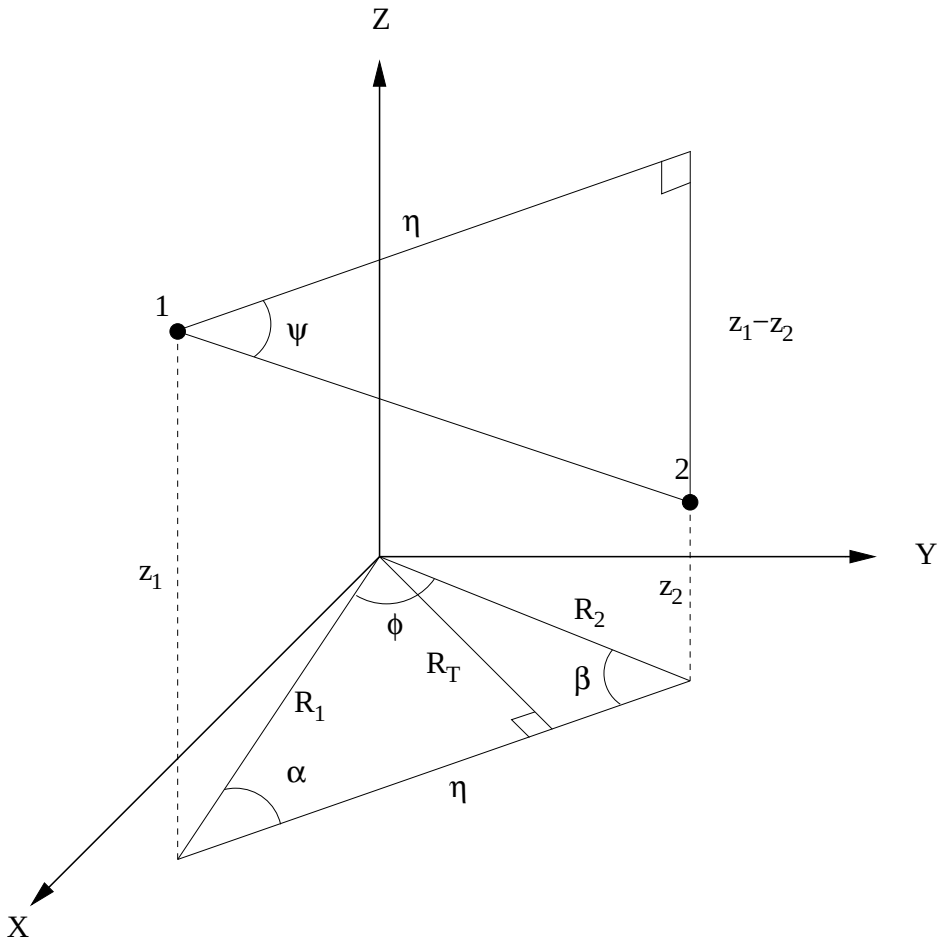

Figure C-5: A line in 3D space with the necessary cylindrical labels (R_1, R_2, Z_1, Z_2 and ϕ) and the reduced set of tokamak labels (R_1, R_T, Z_1, ψ).

Equations (C.14) and (C.16) can be used to form tokamak parameters from values defined by calibrations or design.

C.2.2 Aperture Coordinates

In addition to the line-integrated emissivity, the etendue, $U \sim A_{det}A_{ap}/f^2$, is the other important component of (C.7). For multichannel detectors U will vary smoothly, but for an arbitrary detector aperture combination, it can be algebraically messy. In this section, an expression for U will be formed for a location on a planar detector that has an arbitrary position and orientation relative to an aperture. The ordering in (C.3) is still assumed so that the detector can be well modeled by a single point. As will be discussed in the next section, a location in these aperture coordinates can be expressed in the tokamak coordinates, and the detector aperture pair can be used as points **1** and **2** in (C.14) (C.16).

Figure C-6 shows the layout of the relevant coordinate systems. An aperture is centered in the $y-z$ plane with a normal in the $\hat{x}$ direction. The detector plane with normal, $\hat{n}$, is positioned and orientated relative to the xyz coordinate system by $\mathbf{x}_0$, $\mathbf{x}_1$ and $\mathbf{x}_2$. From these three vectors the unit normal can be expressed as,

$$\hat{n} = \frac{(\mathbf{x_2} - \mathbf{x_0}) \times (\mathbf{x_1} - \mathbf{x_0})}{|(\mathbf{x_2} - \mathbf{x_0}) \times (\mathbf{x_1} - \mathbf{x_0})|} \tag{C.17}$$

The constraint $(\mathbf{x}_2\text{-}\mathbf{x}_0)\cdot(\mathbf{x}_1\text{-}\mathbf{x}_0)=0$ is used to create the Cartesian coordinate system $n\xi\zeta$. This makes $\mathbf{x}_0$ a reference point on the detector plane with $\hat{\xi}$ and $\hat{\zeta}$ aligned with a multichannel layout system such as rows and columns of pixels on a CCD. An arbitrary point, P, on the detector is located in the $\xi-\zeta$ plane by the vector $\mathbf{x}'=\xi'\,\hat{\xi} + \zeta'\,\hat{\zeta}$ where,

$$\hat{\xi} = \frac{(\mathbf{x_2} - \mathbf{x_0})}{|(\mathbf{x_2} - \mathbf{x_0})|} \tag{C.18}$$

$$\hat{\zeta} = \frac{(\mathbf{x_1} - \mathbf{x_0})}{|(\mathbf{x_1} - \mathbf{x_0})|} \tag{C.19}$$

This allows any point on the detector to be located by $\mathbf{x}=\mathbf{x}_0 + \mathbf{x}'$. The etendue can

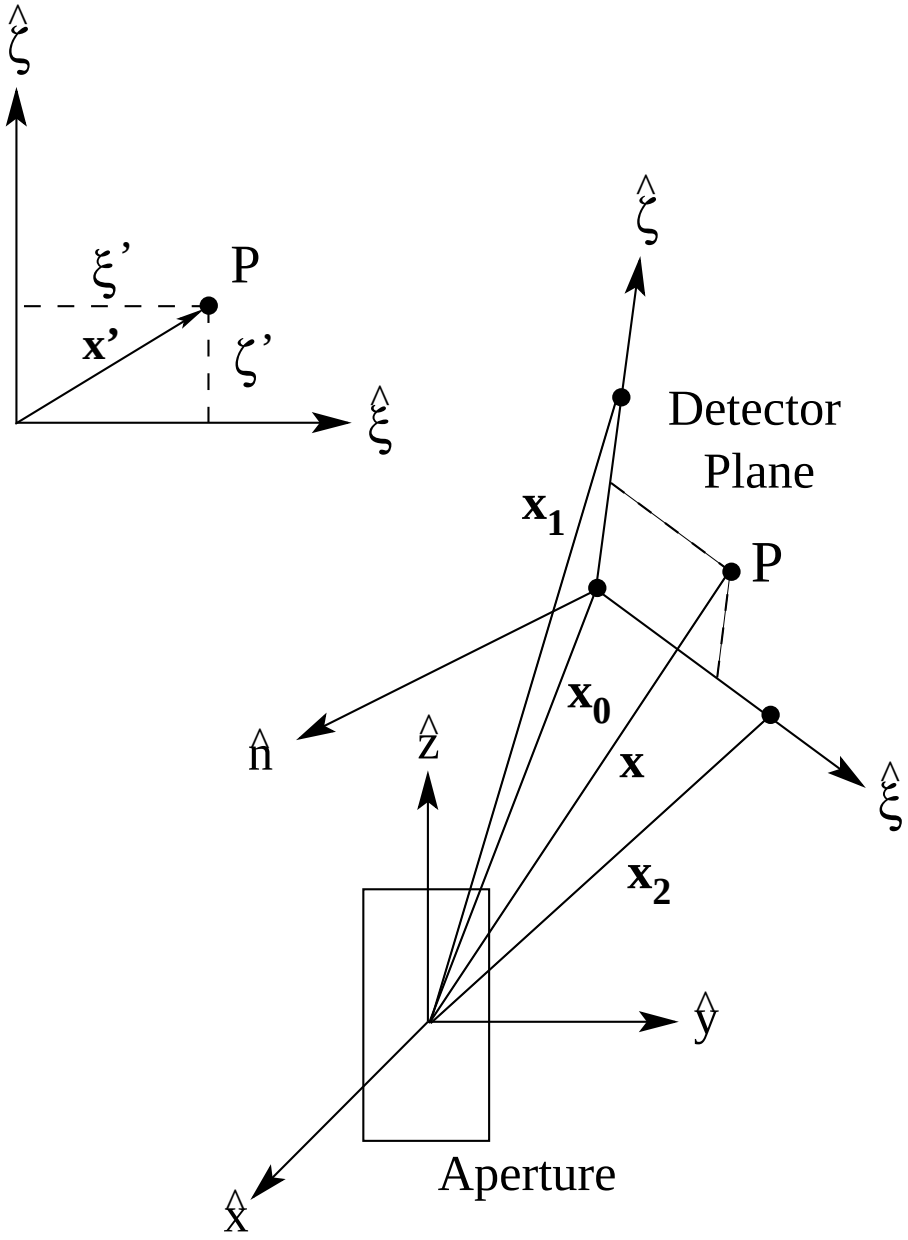

Figure C-6: An aperture is centered in the $y-z$ plane with a normal in the $\hat{x}$ direction. A detector plane with normal $\hat{n}$ is positioned and orientated relative to the xyz coordinate system by $\mathbf{x}_0$, $\mathbf{x}_1$ and $\mathbf{x}_2$ with the added constraint that these points form the Cartesian system $n\xi\zeta$. An arbitrary point, P, on the detector is located in the $\xi-\zeta$ plane by the vector $\mathbf{x}$'.

then be expressed as,

$$U = \frac{\frac{\hat{n}\cdot\mathbf{x}}{|\mathbf{x}|}A_{det}\frac{\hat{x}\cdot\mathbf{x}}{|\mathbf{x}|}A_{ap}}{|\mathbf{x}|^2} \tag{C.20}$$

The dominant term in U is the $1/|\mathbf{x}|^2$. The multipliers on A_{det} and A_{ap} represent the misalignment of the area normals with the line connecting them. These terms vary like cosine of this angular deviation and thus do not substantially affect the order of magnitude of the etendue for well aligned imaging systems. Although they can be ignored when estimating throughput for design purposes, these terms are imperative when tomographically inverting the results of a multichannel system.

C.2.3 Connecting the Aperture to the Tokamak

In Section C.2.2 an aperture coordinate system xyz was defined so that $\hat{x}$ was the aperture normal. A generic three angle rotation sequence is necessary to express $\mathbf{x}$ in the tokamak XYZ coordinates from which (R_2, ϕ, Z_2) can be determined. Figure C-7 illustrates the transformations where, in places the z-axes have been omitted and Z_1 is assumed to be zero for the sake of clarity. First, a rotation, α, is made about x, then a rotation, $-\beta$ about y' and lastly, a rotation, γ about z''. This sequence can be done analytically using three rotation matrices,

$$\mathrm{R}_\alpha = \begin{bmatrix} 1 & 0 & 0 \\ 0 & \cos\alpha & -\sin\alpha \\ 0 & \sin\alpha & \cos\alpha \end{bmatrix} \tag{C.21}$$

$$\mathrm{R}_\beta = \begin{bmatrix} \cos\beta & 0 & -\sin\beta \\ 0 & 1 & 0 \\ \sin\beta & 0 & \cos\beta \end{bmatrix} \tag{C.22}$$

$$\mathrm{R}_\gamma = \begin{bmatrix} \cos\gamma & -\sin\gamma & 0 \\ \sin\gamma & \cos\gamma & 0 \\ 0 & 0 & 1 \end{bmatrix} \tag{C.23}$$

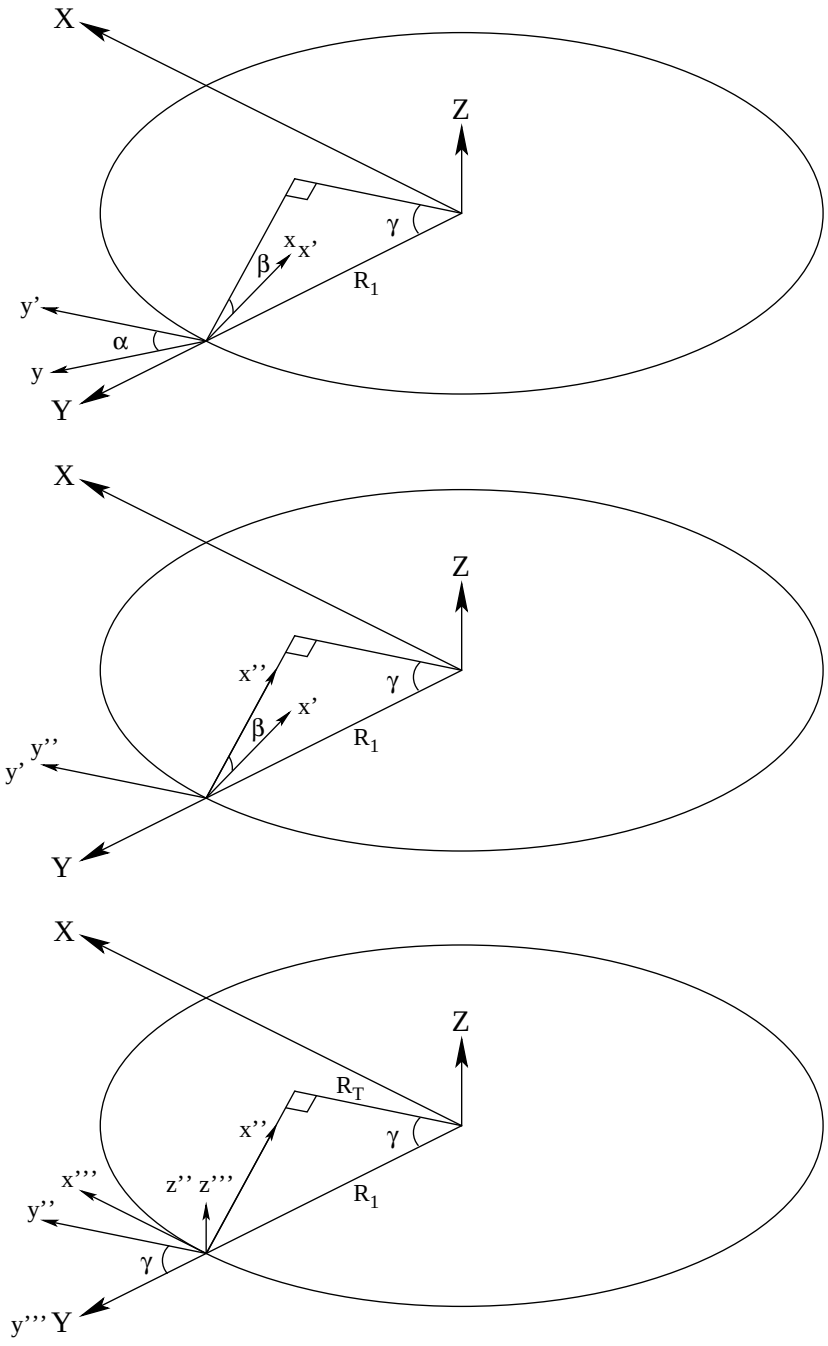

Figure C-7: Transformation from the xyz aperture coordinates to XYZ coordinates. First, a rotation, α, about x. Next, a rotation, $-\beta$ about y'. Lastly, a rotation, γ about z''.

It is worth noting that this transformation is not unique and other parameterizations maybe be optimal for specific viewing geometries. In purely toroidal or poloidal imaging, $\beta = 0$ and $\gamma = 0$, respectively. These matrices and the location of the pinhole are used to transform $\mathbf{x}$ to $\mathbf{X}$.

$$\begin{bmatrix} X \\ Y \\ Z \end{bmatrix} = \begin{bmatrix} 0 \\ R_1 \\ Z_1 \end{bmatrix} + \mathrm{R}_\gamma \mathrm{R}_\beta \mathrm{R}_\alpha \begin{bmatrix} x \\ y \\ z \end{bmatrix} \tag{C.24}$$

The tokamak coordinates can be obtained from the $\mathbf{X}$ by using,

$$\begin{aligned} R_2 &= \sqrt{X^2 + Y^2} \\ \cos\phi &= \frac{Y}{\sqrt{X^2 + Y^2}} \\ Z_2 &= Z \end{aligned} \tag{C.25}$$

Alternatively, two points in the aperture coordinate system can also be used to form a set of tokamak coordinates. A point $\mathbf{x}_i$ can be transformed into $\mathbf{X}_i$ using the rotation matrices and the aperture position via (C.24). Similar to (C.25) the cylindrical coordinates can be defined,

$$\begin{aligned} R_i &= \sqrt{X_i^2 + Y_i^2} \\ \theta_i &= \arcsin\left(\frac{X_i}{\sqrt{X_i^2 + Y_i^2}}\right) \\ Z_i &= Z_i \end{aligned} \tag{C.26}$$

and from there the tokamak coordinates can be found from (C.14) and (C.16) with $\phi = \theta_2 - \theta_1$. It is important to note that if the line of sight is defined in this manner, $l < 0$ will correspond to moving from **2** towards **1**, which for (C.25) is the detector $\rightarrow$ plasma direction. The identities of **1** and **2** can be switched by having $(R_2, Z_2) \rightarrow (R_1, Z_1)$ and $\tan\psi \rightarrow -\tan\psi$.

C.2.4 Discussion

The derived parametric equations (C.10) can be used to turn a known 2D emissivity, $\varepsilon_\lambda(R,Z)$, into an emissivity along the line of sight, $\varepsilon_\lambda(l)$. The parameter, l, is unit-less and describes the location relative to points **1** and **2**. To form the integral necessary in (C.7) a relationship between l and the absolute distance along the line, s must be found. From the initial parametrization it is known that $\Delta l = 1$ between **1** and **2** and their corresponding physical space separation, χ, is shown in Figure C-5. Thus a differential increase, ds, along the path in space is proportional to a differential increase, dl in the parameter l.

$$ds = \sqrt{(R_1^2 - R_T^2)(1+\tan^2\psi)}dl \tag{C.27}$$

This allows, the integration over ds in (C.7) to be expressed as an integral in dl,

$$E_{det} = \frac{U}{4\pi}\sqrt{(R_1^2 - R_T^2)(1+\tan^2\psi)}\int_{\Delta t} dt \int d\lambda\, Q(\lambda) \int dl\, \varepsilon_\lambda(l,t,\lambda) \tag{C.28}$$

$$E_{det} = \frac{A_{ap}A_{det}}{4\pi f^2}\sqrt{(R_1^2 - R_T^2)(1+\tan^2\psi)}\int_{\Delta t} dt \int d\lambda\, Q(\lambda) \int dl\, \varepsilon_\lambda(R(l), Z(l), t, \lambda) \tag{C.29}$$

where U is defined by (C.20).

C.3 Beyond the Line Integral Approximation

The results of Section C.2 can now be expanded to describe views which are not accurately described by the line integral approximation. Such deviations occur when the size of the detector or aperture becomes comparable to their separation. Instead of returning to (C.2) the detector and aperture can be broken into m and n respective sub-pixels, as shown in Figure C-8. For sufficiently large values of m and n, each ij pair can be made to satisfy the line integral approximation. At this point, the total

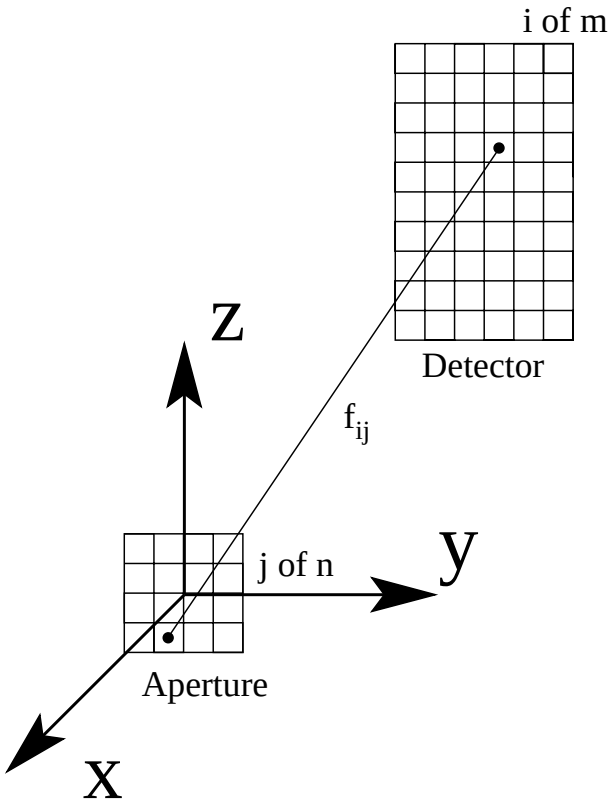

Figure C-8: When the line-integral approximation breaks down, the detector and aperture are split into m and n sub-units creating $m \times n$ views per detector. Each has a corresponding tokamak position vector $(R_1, Z_1, R_t, \psi)_{ij}$ and etendue, U_{ij}.

energy deposited on the detector becomes,

$$E_{det} = \sum_{i}^{m} \sum_{j}^{n} \frac{A_{det,i} A_{ap,j}}{4\pi f_{ij}^2} \int_{\Delta t} dt \int d\lambda \, Q(\lambda) \int_{ij} ds \, \varepsilon_\lambda (s, t, \lambda) \tag{C.30}$$

where each ij defines a different line integral. If regularly space grids in $y - z$ and $\xi - \zeta$ are used then generating the $m \times n$ sets of tokamak coordinates can be easily automated. If the (R, Z) space which is to be analyzed is then broken into p different pixels indexed by k, then the energy deposited onto the detector becomes,

$$E_{det} = \sum_{k}^{p} \sum_{i}^{m} \sum_{j}^{n} \frac{A_{det,i} A_{ap,j}}{4\pi f_{ij}^2} \int_{\Delta t} dt \int d\lambda \, Q(\lambda) \, L_k(i,j) \, \varepsilon_{\lambda,k}(t, \lambda) \tag{C.31}$$

where $L_k(i,j)$ is the length of the view defined by ij in pixel k.

As an example, (C.31) can be simplified by assuming that the power deposited onto the detector, P_{det}, is the measured quantity, and that $Q(\lambda) = 1$ for all wavelengths. This represents the conditions for an ideal bolometer, a diagnostic common to most tokamaks. For each ij view, the path length in pixel k, L_k, is proportional to an interval in the parameter l as shown in (C.27). These values, Δl_k, are determined using (C.11) by finding the intersection between the line of sight and the defined boundaries of pixel k. The etendue information can be folded into the L_k, creating volume weighting, V_k, for each pixel.

$$V_k = \sum_{i}^{m} \sum_{j}^{n} \frac{A_{det,i} A_{ap,j}}{4\pi f_{ij}^2} \left(\sqrt{(R_1^2 - R_T^2)(1 + \tan^2 \psi)} \right)_{ij} \Delta l_k (i,j) \, . \tag{C.32}$$

The power deposited on the detector is then,

$$P_{det}(t) = \sum_{k}^{p} V_k \varepsilon_k (t) \tag{C.33}$$

where $\varepsilon_k = \int d\lambda \varepsilon_{\lambda,k}$ with units of power per unit volume. The V_k terms can be determined for arbitrarily small meshing of the detector and aperture, and while this process quickly becomes computationally intensive as m and n are increased, the

values need only be computed once and can be stored for subsequent use. A set detectors viewing the (R, Z) space broken into k pixels can be represented by the matrix equation,

$$\vec{P} = \mathbf{V} \cdot \vec{\varepsilon} \tag{C.34}$$

where $\vec{P}$ is a vector of length h, $\mathbf{V}$ is an $h \times k$ matrix and $\vec{\varepsilon}$ is vector of length k. This method allows the emissivity to be determined from views that are neither on a constant Z or θ plane, and that trace hyperbolic paths through the (R, Z) plane. The inversion of the matrix equation, (C.34) can be addressed by many different techniques.

Appendix D

Argon Up/Down Asymmetries in Ohmic Plasmas

In Section 6.4, one of the hypothesis for the disagreement between modeled up/down asymmetries and those measured using the AXUV diode arrays was that turbulent cross-field transport was beginning to compete with parallel neoclassical transport. Up/down asymmetries in highly-ionized Ar emission have also been observed on C-Mod [75], and the HIREXSR diagnostic enables more comprehensive experiments to be completed than previously done using the 5 chord HIREX diagnostic [177]. Recent measurements show that neoclassical processes are unlikely to explain the Ar emissivity asymmetry. A threshold-type behavior is observed for $r/a > 0.85$, with the emissivity transitioning from a small asymmetry, $\tilde{n}_z/\langle n_z \rangle < 0.2$, to a large asymmetry, $\tilde{n}_z/\langle n_z \rangle \sim 0.6 - 0.8$, in plasmas where $B_t \bar{n}_e / I_p \simeq 4$. This phenomenology has similarities to the rotation reversal recently explored on Alcator C-Mod [131][178][179], thought to be linked to changes in the Ohmic confinement regime.

D.1 Origin of the Ar Line Emission

The $1s^2$-1s2s transition in He-like Ar, the z-line in Gabriel notation [180], is used in these investigations. Although the 1s2s state of He-like Ar is considered a metastable state, the transition probability is $\sim 10^6$ 1/s, allowing it still to be considered a

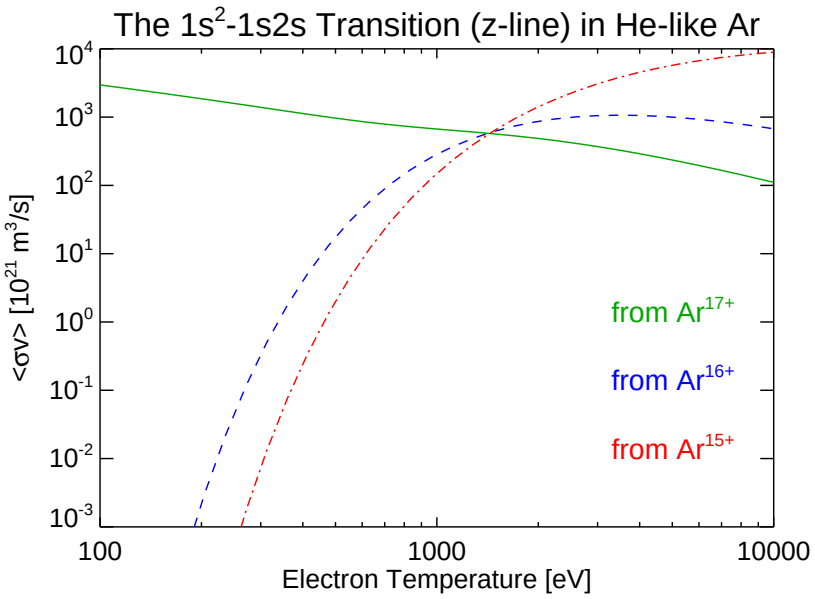

Figure D-1: Photon emission coefficients ($\langle \sigma v \rangle$), for the $1s^2$-1s2s transition in He-like Ar

probe of local plasma conditions. As discussed in prior work [75], this excited state can be populated by three different mechanisms, excitation from the ground state of Ar^{16+}, inner-shell ionization of Ar^{15+}, and recombination from Ar^{17+}. Both excitation and inner-shell ionization occur at high electron temperatures, $T_e \sim 1$ keV, while recombination from H-like Ar dominates at low temperatures. Figure D-1 shows the T_e dependent $< \sigma v >$ from all three charge states.

In Ohmic plasmas, the enhanced radial diffusion from the hotter core provides a source of H-like Ar at large minor radii where T_e is far below the temperature required for excitation or ionization. As will be shown, the Doppler broadening of the z-line demonstrates that the temperature of the impurity ion is closer to that of the local electron temperature, rather than the ion temperature in the core where the Ar^{17+} ion was created. This rules out ballistic or non-local transport, indicating that the H-like argon ion has had time to collisionally equilibrate with the background plasma, meaning the radial transport is likely diffusive. When the 2s excited state is populated only by recombination, it becomes a useful measure of the radially outward component of the impurity flux. As diagrammed in Figure D-2, the photons measured by HIREXSR are part of a one-way process of recombination, either directly into the

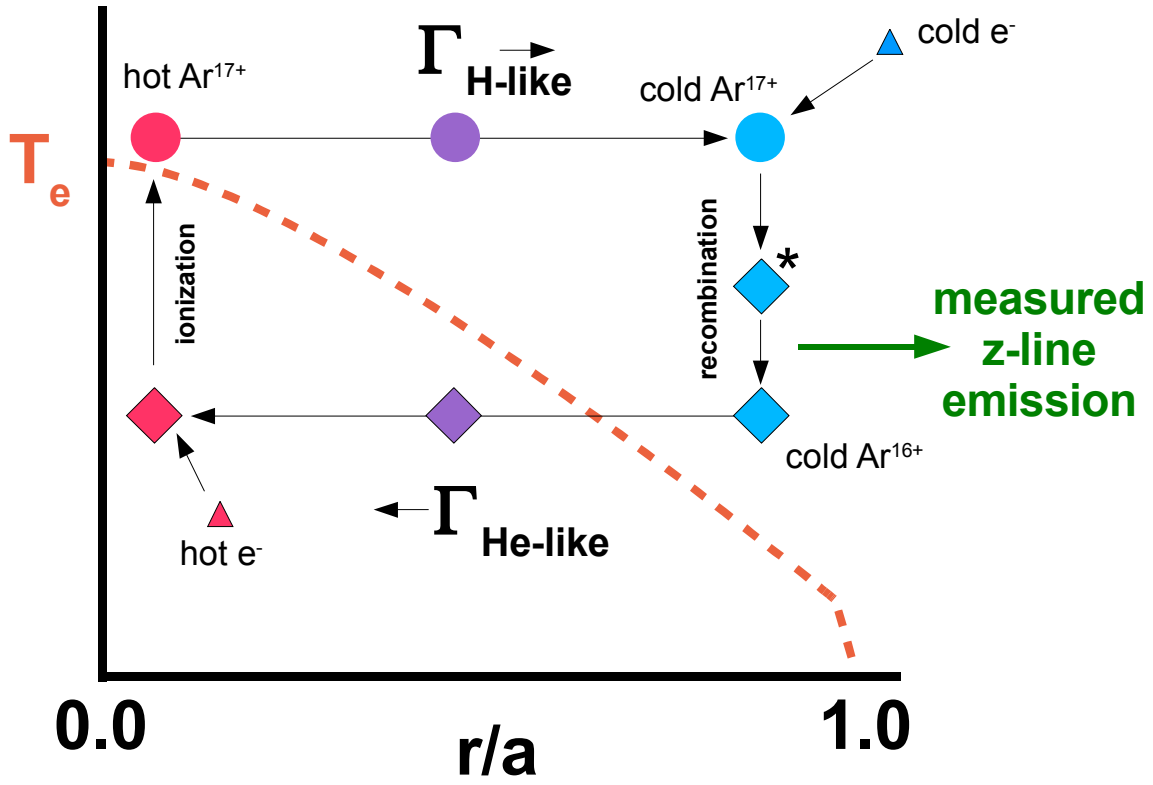

Figure D-2: Diagram of how the 1s2s excited state is populated via recombination

2s state or through cascades from higher n numbers. The total radial impurity flux, Γ_{Ar}, is the sum of the flux of all charge states, and so there must be a balancing inward transport of lower-ionization states in order to maintain steady-state.

D.2 Overview of Experiments

Prior up/down asymmetry experiments using the 5-chord spectrometers required several repeated discharges to scan the instrument over the poloidal cross-section to measure the full profile. With the addition of the HIREXSR spectrometer, a single time slice is all that is needed to gather an equivalent amount of data. In addition, the increased spectral resolution enables the local ion temperature and flow to be measured. In order to study the effect of ion-impurity friction on parallel impurity transport, the up/down asymmetry of soft x-ray emission from highly ionized Ar is measured over a large fraction of the Ohmic operating space of Alcator C-Mod. Impurity force balance along the field equilibrates on a time scale, $\sim$ 1 ms, much shorter than the duration

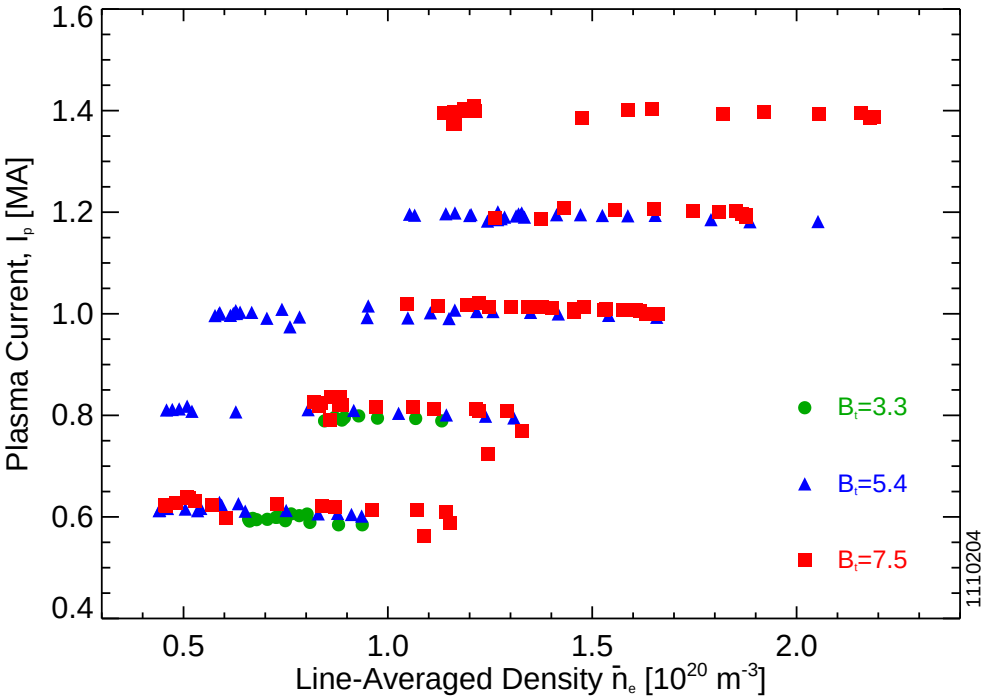

Figure D-3: The I_p, B_t and $\bar{n}_e$ operating space used in analyzing trends in the up/down Ar asymmetry

of the C-Mod current flattop, $\sim$ 1 s, allowing multiple data points to be collected per discharge. The electron density was scanned during the shot, and the plasma current and toroidal field were scanned shot-to-shot. Figure D-3 shows the operating space covered during the 1110204 run day dedicated to these experiments. Additionally, ohmic portions of plasmas from 1110218 were used for comparisons with the ∇B drift direction reversed. A typical plasma shape for 1110204 is shown in Figure D-4, along with the spatial coverage of HIREXSR. The normal configuration of the spectrometer was modified to enable these experiments. A cover was placed over the He-like argon viewing crystal to reduce its effective size, increasing spatial resolution and decreasing the instrumental broadening. The vertical alignment of the instrument was adjusted to ensure that the full poloidal profile was measured.

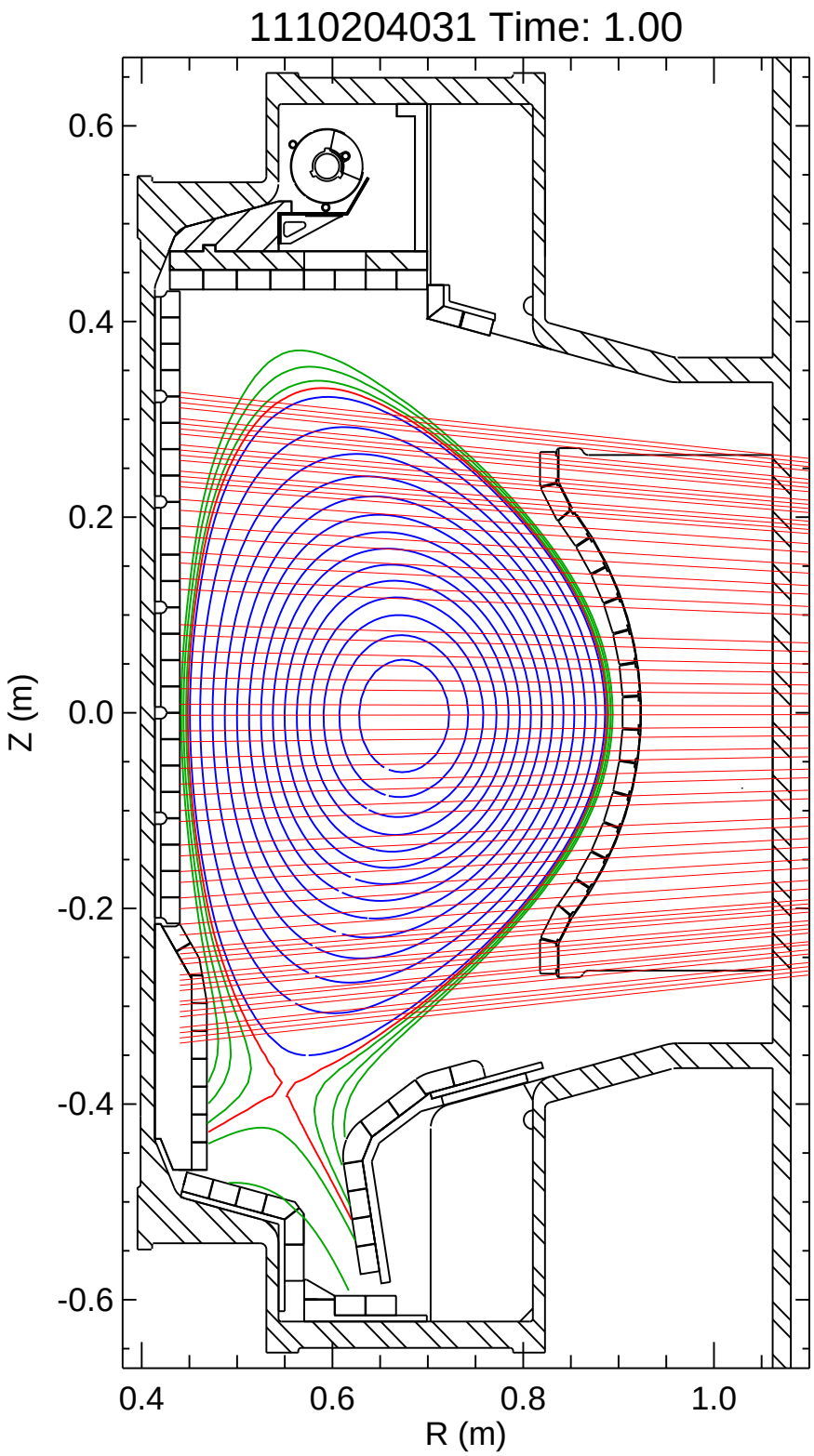

Figure D-4: Typical equilibrium used in the parameter scan with the HIREXSR lines of sight included

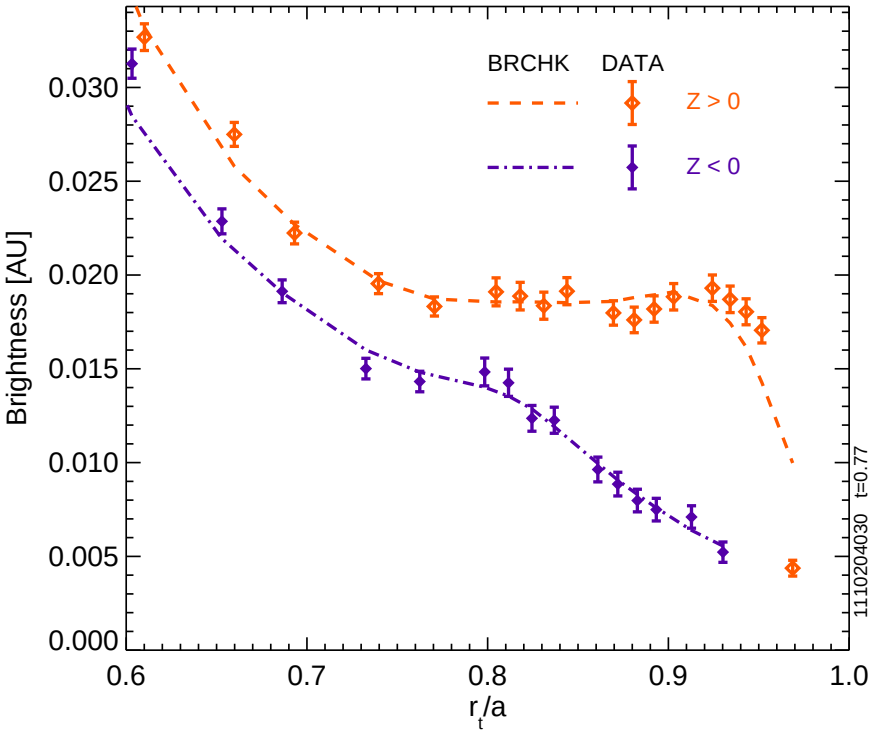

Figure D-5: Brightness profiles showing strong up/down asymmetry in a 0.6 MA, 5.4 T plasma at $\bar{n}_e \simeq 0.5 \times 10^{20}$ m^{-3}

D.3 Examples of the Up/Down Asymmetry

Measured line-brightnesses are plotted against poloidal tangency radius for two shots, the first shows an example of strongly up/down asymmetric radiation, Figure D-5, and second shows a nearly up/down symmetric radiation, Figure D-6. The dashed lines are the BRCHK profiles, representing the line-integrated brightness from the emissivity profiles calculated from these measurements.

Line-integrated spectra from the symmetric discharge are shown in Figure D-7, demonstrating that not only the brightness, but also line-width, and thus ion-temperature, is up/down symmetric. For the core view, D-7a, the width of the z-line at $\lambda \simeq 3.994$ is much wider than either of the views at $r/a \sim 0.9$ shown in D-7b. Additionally, the $n = 2$ satellite transitions between $3.980 < \lambda < 3.992$ that are populated by inner-shell ionization and dielectronic recombination, and are only seen in the core plasma. Both of these observations are typical of this data set, and support the discussion in Section D.1 that the z-line emission at large minor radii is due to

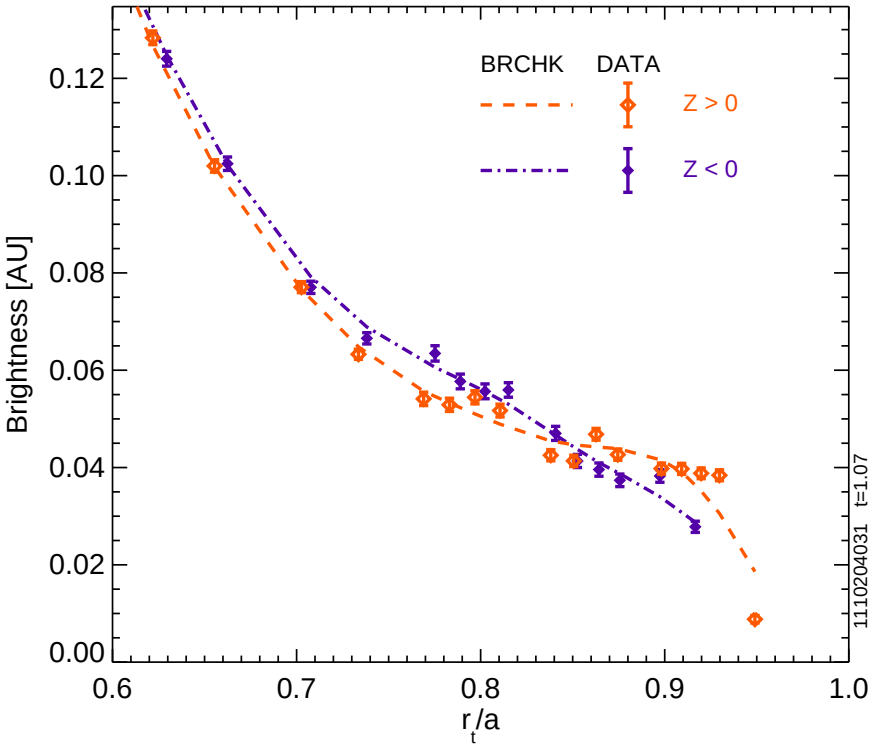

Figure D-6: Brightness profiles showing weak or negligible up/down asymmetry in a 1.0 MA, 5.4 T plasma at $\bar{n}_e \simeq 0.6 \times 10^{20}$ m^{-3}

recombination from H-like Ar that has diffused out from core.

The emissivity profiles for the asymmetric and symmetric plasmas are shown in Figures D-8a and D-8b, respectively. In the top panel of each plot, the $m = 0$ (solid) and $m = 1$ (dashed) profiles are plotted against minor radius, while the lower panel shows the ratio of the $m = 1/m = 0$, a measure of the up/down density asymmetry. Plotted error bars are only due to propagation of photon noise and do not account for any systematic calibration error. The grey highlighted region is an estimate of the flat-field calibration uncertainty, showing that up/down asymmetries of $\pm 15\%$ should be considered nominally symmetric. In Figure D-8a, the calculated up/down asymmetry is well outside of this shaded region and for $r/a > 0.8$, the profile moves from being nominally symmetric to having $\tilde{n}_z/\langle n_z \rangle \simeq 1$. This is in agreement with previous observations in [75] that showed the asymmetry rising to ~ 0.8 over the last 10% of the plasma.

The asymmetry is also demonstrated to reverse its orientation when the ∇B drift

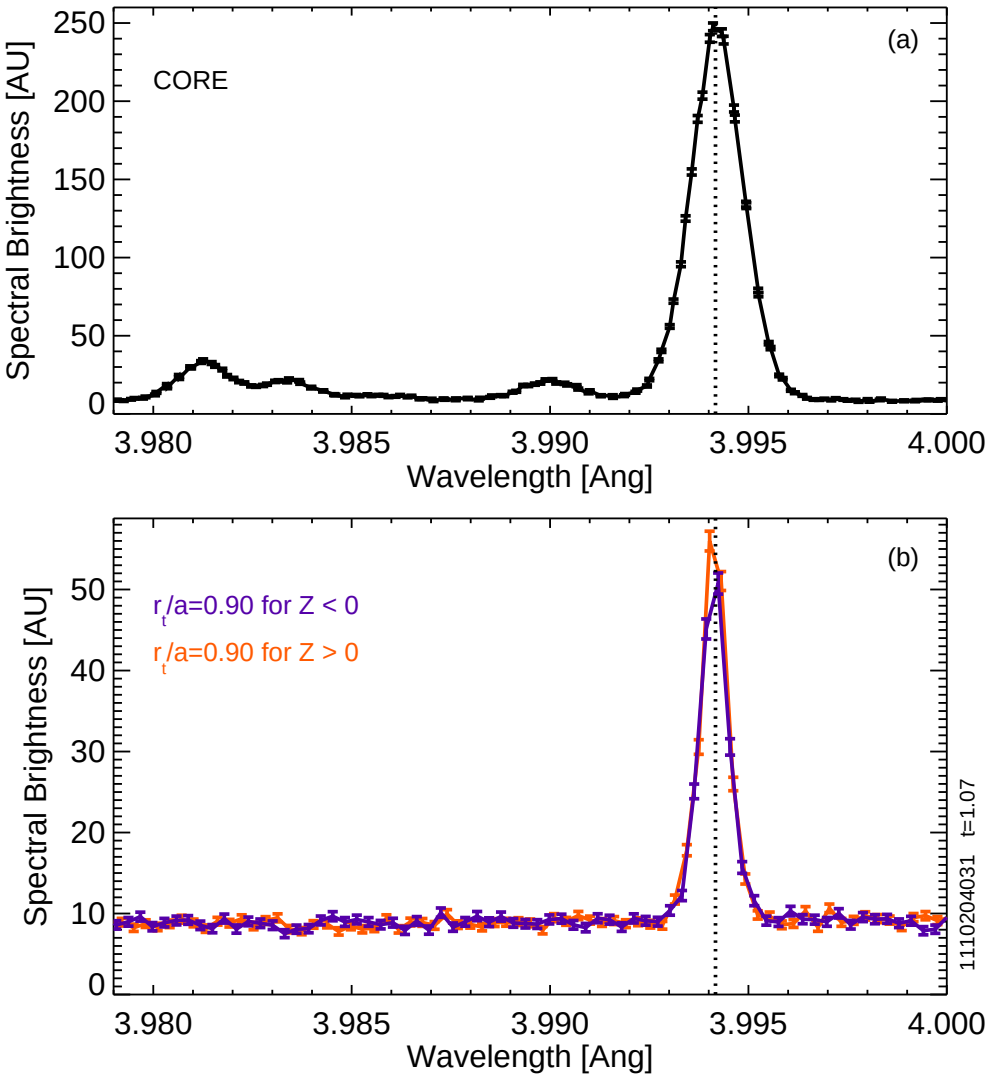

Figure D-7: Spectra for the core and chords at $r/a = 0.9$ for the up/down symmetric case shown in Figure D-6

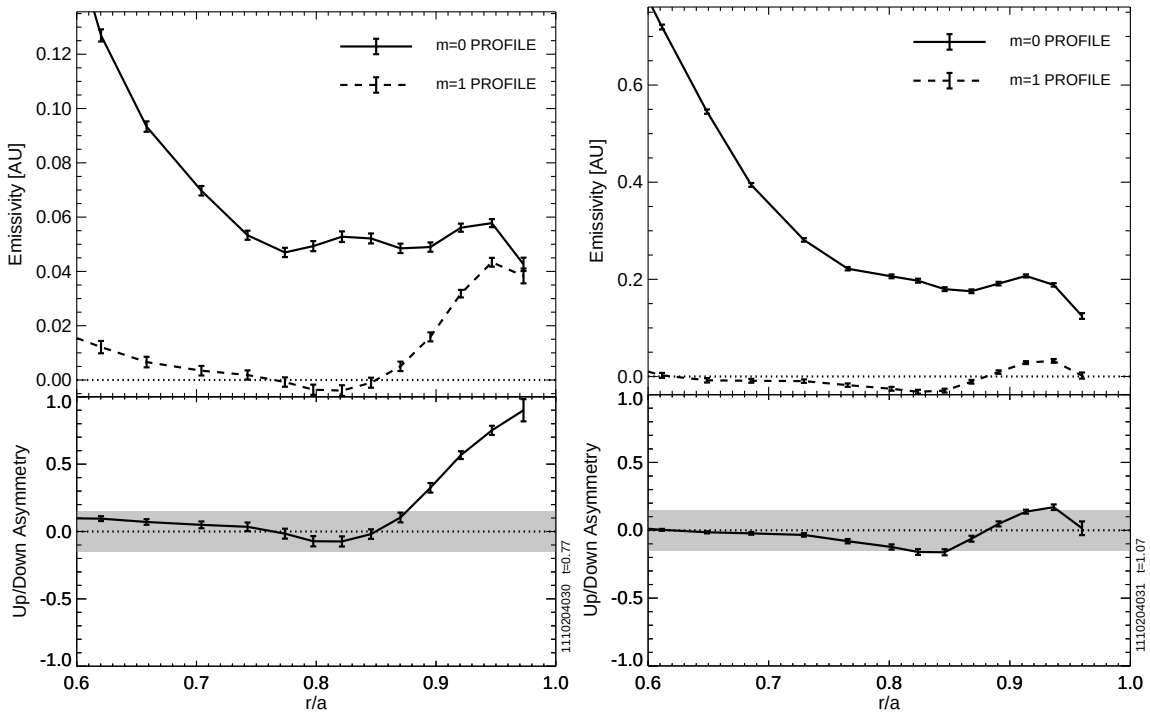

(a) (b)

Figure D-8: Emissivity profiles calculated from data shown in Figures D-5 D-6, showing a strong (a) and weak (b) up/down asymmetry

direction is reversed. Figures D-9 and D-10 show the brightness and emissivity profiles in forward and reversed field, respectively. This is for Ohmic plasmas with matched $I_p = 0.8$ MA and $B_t = 5.4$ T and similar electron density, $\bar{n}_e = 0.4 - 0.6 \times 10^{20}$ m^{-3}. Both discharges were lower single null plasmas. The magnitude of the up/down asymmetry is comparable, each showing $\tilde{n}_z/\langle n_z \rangle \sim 0.4$-$0.5$ in the outer region of the plasma. No dedicated up/down asymmetry experiments were run in reversed field, and so differences in alignment and spatial resolution may be responsible for the noticeable shape differences between the two asymmetry profiles.

D.4 Scaling of the Up/Down Asymmetry

The emissivity profiles for multiple time points in 17 discharges are used to determine the scaling of the up/down asymmetry with global plasma parameters over a large portion of the Ohmic operating space of Alcator C-Mod, as shown in Figure D-3. The

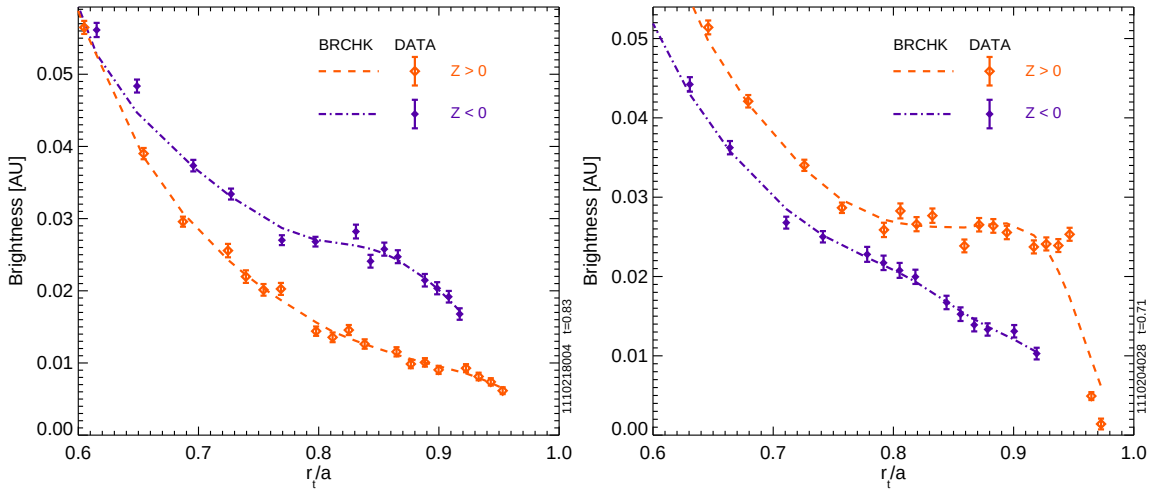

(a) (b)

Figure D-9: Comparison of brightness profiles in similar discharges (0.8 MA, 5.4 T plasma at $\bar{n}_e \sim 0.5 \times 10^{20}$ m^{-3}) in reversed (a) and forward (b) field

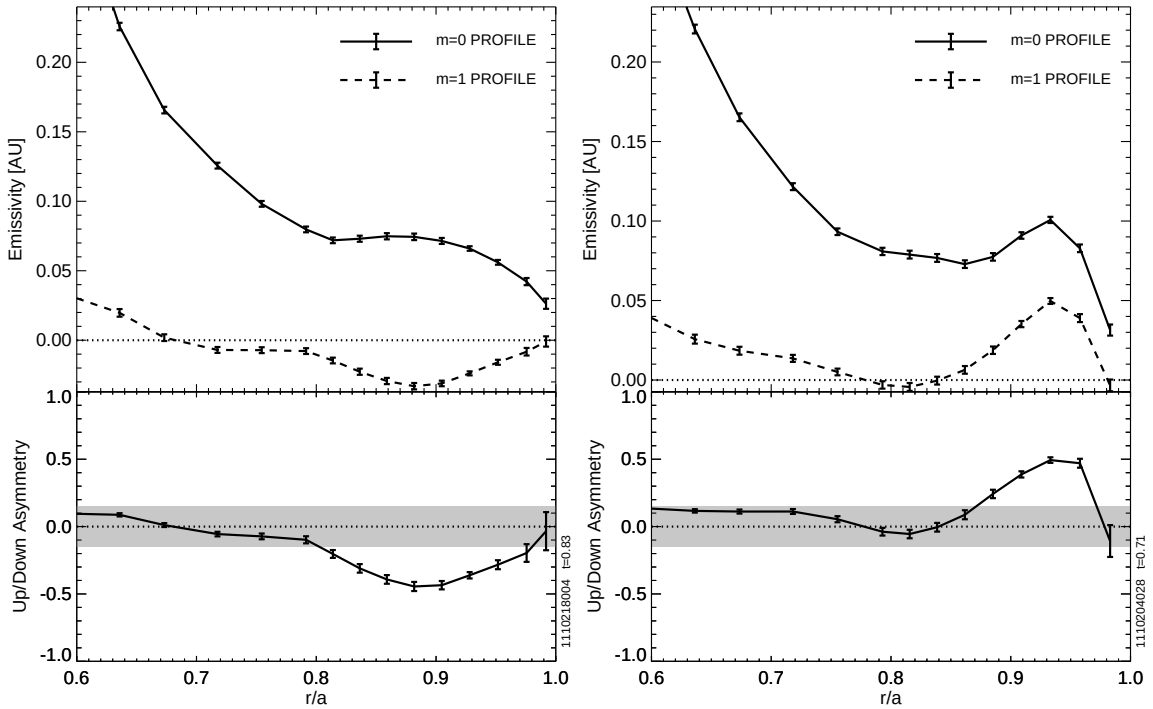

(a) (b)

Figure D-10: Comparison of emissivity profiles in similar discharges in reversed (a) and forward (b) field showing a flip in the direction and magnitude of the up/down asymmetry

radial location of $r/a = 0.92$ is used to characterize the edge asymmetry layer, which in prior work was unable to be reproduced by parallel neoclassical transport theory. In Figure D-11a, the up/down asymmetry data for $B_t = 5.4$ T plasmas are plotted against line-averaged density, $\bar{n}_e$, for various plasma currents, I_p. The differences are shown to be substantially reduced when plotting the up/down asymmetry versus $\bar{n}_e/I_p$, as shown in Figure D-11a. In this plot, the asymmetry is shown to have a threshold type behavior, increasing from near symmetry to a $\tilde{n}_z/\langle n_z \rangle \simeq 0.6$ between $0.6 < \bar{n}_e/I_p < 0.8$.

The same plot is shown in Figure D-12, now including data from all toroidal fields. The B_t=3.3 points (green) exhibit a similar type of threshold behavior as the 5.4 T shots (blue), although at a higher value of $\bar{n}_e/I_p$, while the high field shots (red) do not. The measured asymmetry is shown to decay back towards zero for larger values of $\bar{n}_e/I_p$, although with relatively large error bars.

In Figure D-13, the asymmetry is plotted against neutral pressure, p_{neut}, measured by a ratiomatic gauge at G-PORT, and the decay of the asymmetry at large $\bar{n}_e/I_p$ is shown to occur for $p_{neut} > 0.2$ mTorr. As the main-chamber pressure increases, the neutral density in the edge of plasma will also go up, increasing the rate of charge-exchange recombination. Similar to radiative or dielectronic recombination, this process will populate the 2s excited state in Ar^{16+}, and could influence the up/down argon density asymmetry if the neutral density is not poloidally symmetric. Prior measurements of both Lyman-α emissivity and neutral pressure show p_{neut} should be higher in the direction of the X-point [181]. Thus, the data in Figure D-13 suggest charge-exchange recombination adjusts the argon emission towards symmetry, or possibly an abundance in the direction of the X-point, as the neutral pressure increases. Note that $p_{neut} > 0.2$ mTorr is also where H-mode confinement began to show sensitivity to edge neutral pressure [175].

In Figure D-14, the asymmetry is plotted against $B_t\bar{n}_e/I_p$, restricting the data set for values of main-chamber pressure below $p_{neut} = 0.2$ mTorr. This is shown to unify the data for all toroidal field strengths and illustrates the up/down asymmetry increasing from near symmetry when $3 < B_t\bar{n}_e/I_p < 5$, saturating at a level of

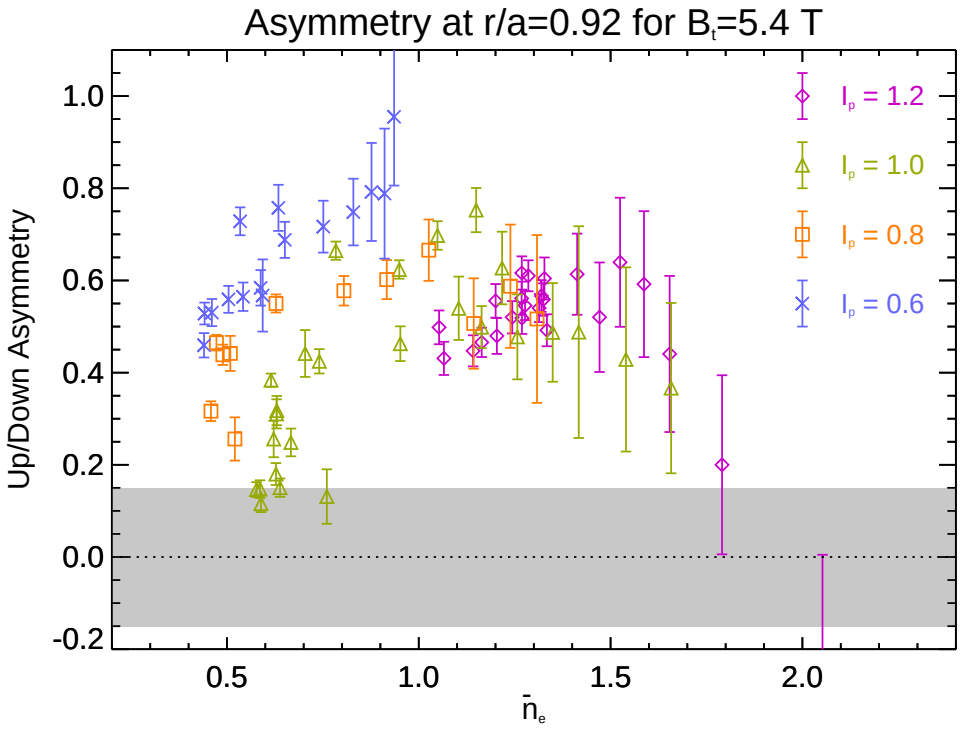

(a)

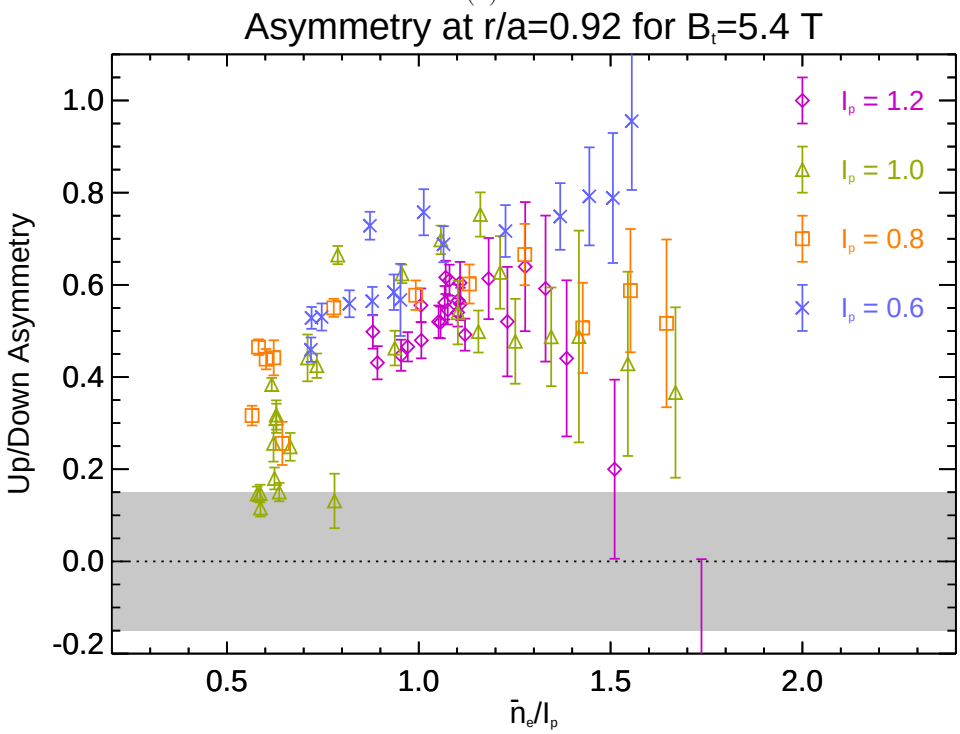

(b)

Figure D-11: At fixed toroidal field, up/down asymmetry scales differently with density at different currents (a), and shows much better scaling when plotted against $\bar{n}_e/I_p$ (b)

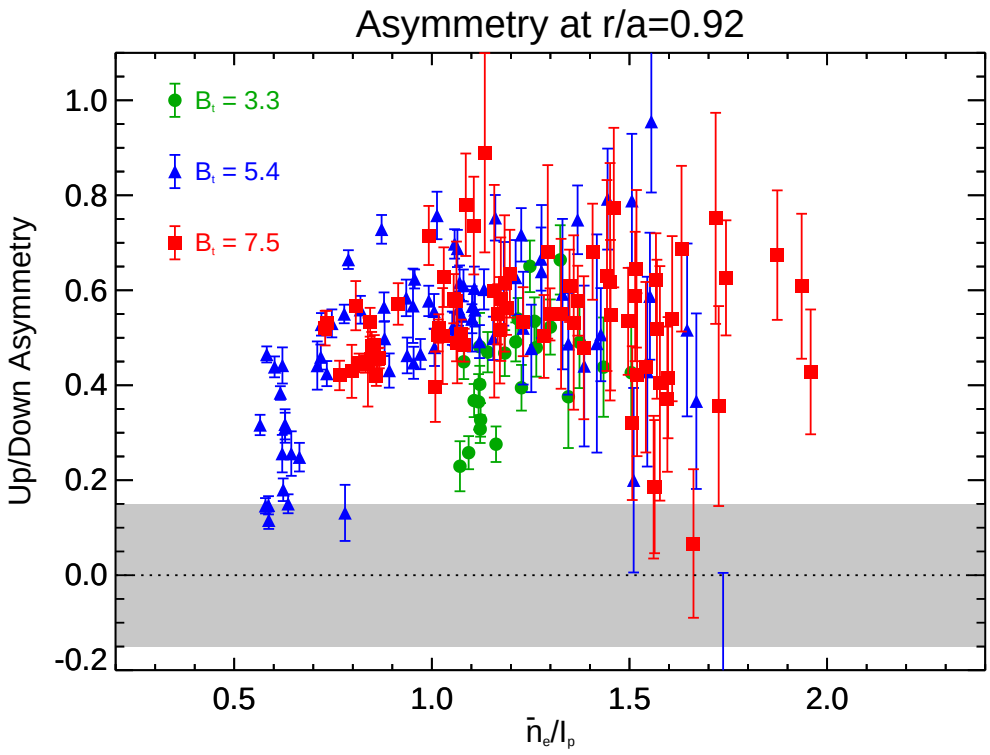

Figure D-12: Up/down asymmetry plotted against $\bar{n}_e/I_p$ for multiple toroidal fields

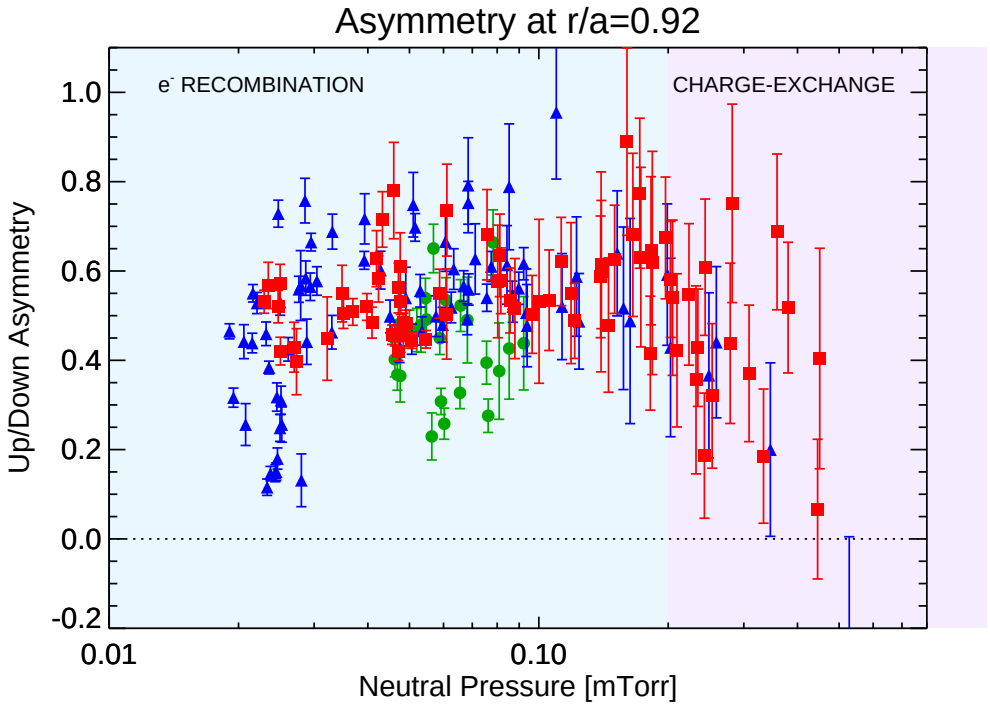

Figure D-13: The up/down symmetry is decreased at large values of main-chamber neutral pressure, p_{neut}

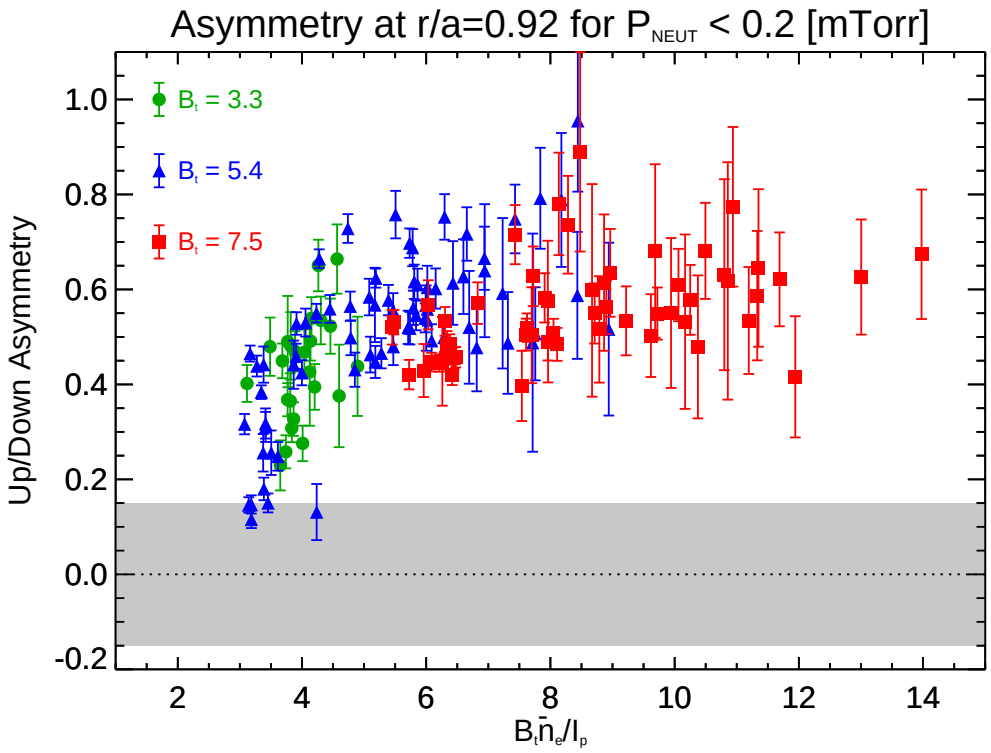

Figure D-14: Up/down asymmetry plotted against $B_t\bar{n}_e/I_p$ for time points where $p_{neut} \leq 0.2$ mTorr

$\tilde{n}/\langle n_z \rangle \sim 0.6$.

This behavior seems to have more in common with the rotation reversal phenomenon then with parallel neoclassical transport. In the former, core toroidal rotation is shown to abruptly change from co- to counter-current direct flow with very small changes in electron density [131]. For a wide range of currents and densities, the rotation reversal was shown to occur at $\bar{n}_e B_t^{0.6}/I_p = 2.8$, a similar scaling as demonstrated for the up/down asymmetry. For $B_t = 5.4$, this puts the threshold at $\bar{n}_e/I_p \simeq 1.0$, which, when comparing to data in Figure D-11b, is just after the argon emission has become strongly asymmetric.

The threshold behavior in relation to the rotation reversal can also be seen dynamically in a single discharge. Figure D-15 shows the time history of electron density (a) and temperature (b) in a $B_t = 5.4$ T and $I_p = 1.0$ MA plasma from the 1110204 run day. The core rotation (c) undergoes a reversal at $t \simeq 1.23$, while the up/down asymmetry (d) is shown to change promptly with the density increase near $t \simeq 1.15$.

Although the asymmetry data are averaged over 60 ms (3 frames), and thus cannot capture the details of the transition, they clearly show a change from a symmetric parallel equilibrium to one with a large up/down asymmetry just before the core rotation reversal. This is consistent with the trends shown in Figure D-14. In Figure D-16, the radial emissivity and asymmetry profiles are shown for time slices surrounding the transition, as highlighted in Figure D-15. Outside of $r/a \sim 0.8$, the asymmetry profile increases, reaching towards $\tilde{n}_z/\langle n_z \rangle \sim 1$ near the edge of the plasma.

D.5 The Ar Up/Down Asymmetry due by Strong Radial Transport

The previous section demonstrated that the strong up/down asymmetry in Ar^{17+} emission is unlikely to be explained by parallel impurity transport theory. Rather than show a smooth increase with $q^2\bar{n}_e$, as indicated by theory [50][24], the asymmetry at $r/a = 0.92$ exhibits a transition between a weak and strong asymmetry at $B_t\bar{n}_e/I_p \sim 4$. While the qualitative characteristics of this asymmetry are similar to up/down asymmetries explored on other tokamaks (see Section 2.4.1), there is an important difference in the origin of the line emission for the C-Mod case. Earlier experiments viewed resonance transitions from low-Z impurity ions [50] or broadband emission using bolometry [82]. As discussed in Section D.1, the Ar^{16+} 1s2s excited state is populated by recombination from H-like Ar ions at low temperatures. These ions must be transported from the core of the plasma, and so the very existence of measurable emission at large minor radii is tied to anomalous impurity transport. If this transport is shown to be strong enough to make $\tau_\perp < \tau_\parallel$, and the radial flux is up/down asymmetric, then the emission asymmetry could be explained by plasma turbulence.

The strongest argument for the argon asymmetry being driven by neoclassical transport is that it reverses sense with the ∇B drift direction. Alcator C-Mod is designed to be run with fixed helicity and must reverse the direction of the plasma current along with the toroidal field, keeping both parallel to one another. Changing

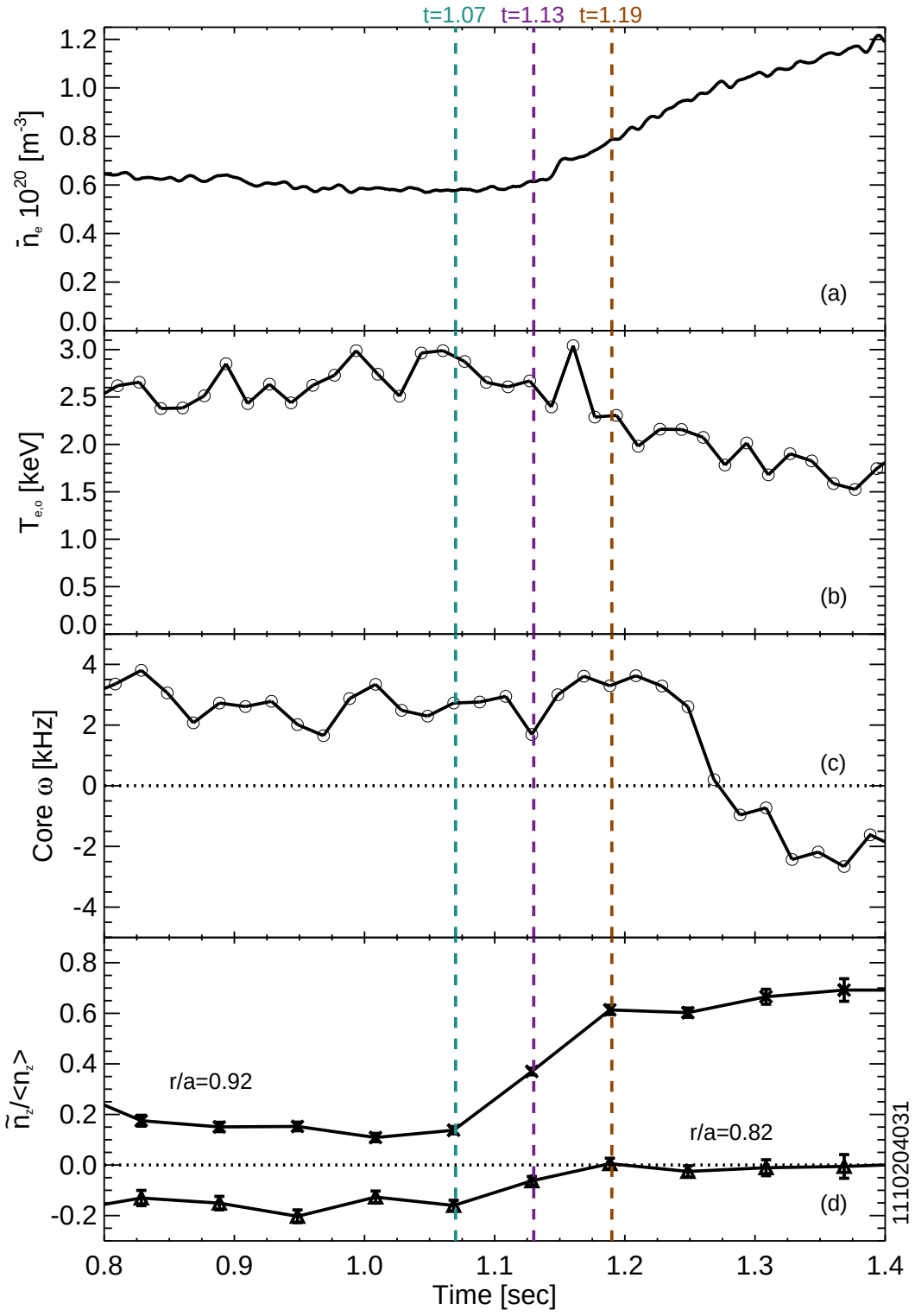

Figure D-15: Time history demonstrating the prompt change in the up/down asymmetry due to a small change in $\bar{n}_e$

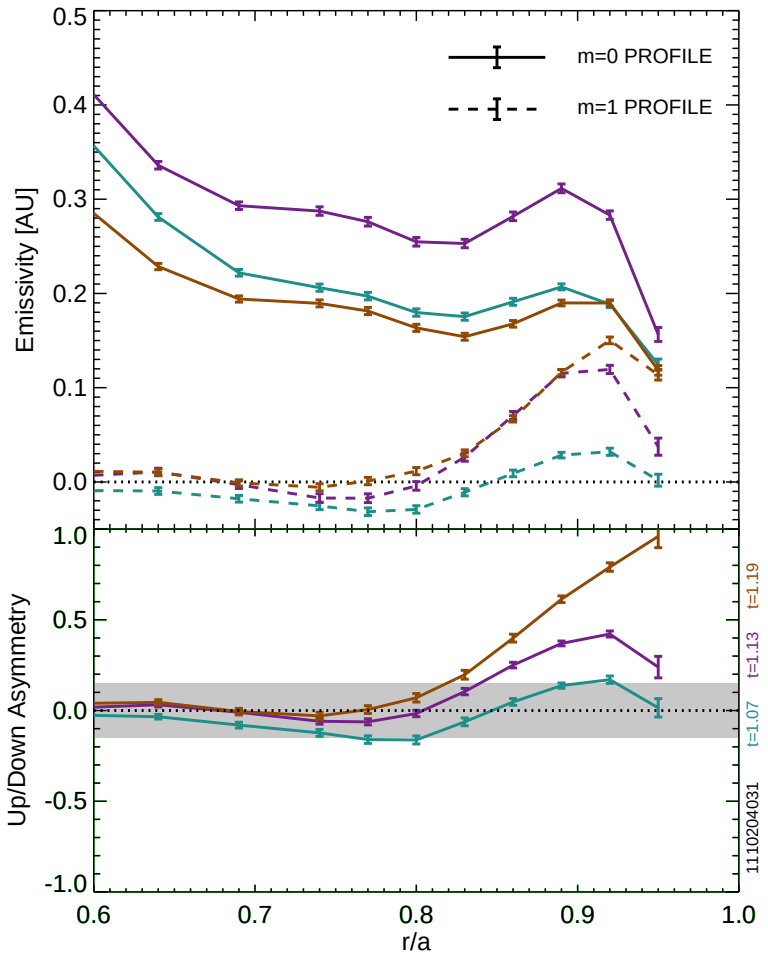

Figure D-16: Radial asymmetry profiles at the three time points highlighted in Figure D-15

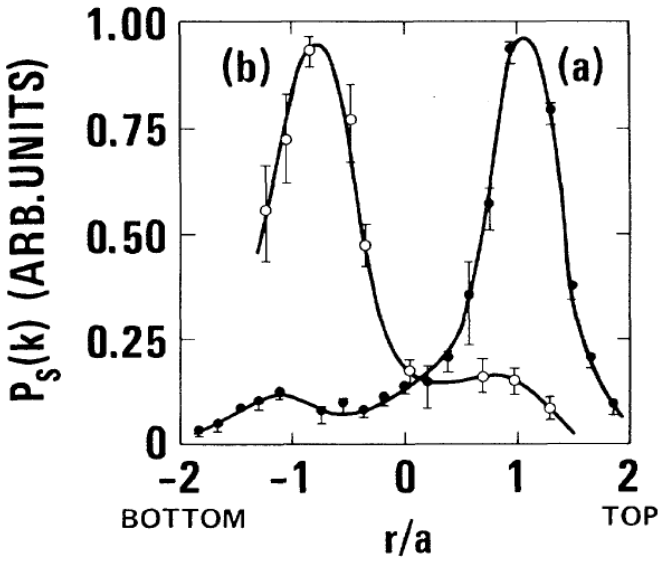

FIG. 2. The spatial distribution of the scattered power ($k_\theta = 9$ cm^{-1}) along a vertical chord through plasma center. Curve *a* I_p, B_T parallel; curve *b* I_p, B_T antiparallel. Note the large asymmetry which inverts with current reversal.

Figure D-17: Evidence of up/down asymmetry of density fluctuations measured in TEXT (from [34])

the current direction has been shown to reverse observed up/down asymmetries in fluctuation amplitude in laser scattering experiments [34]. In Figure D-17, results from an Ohmic plasma in the TEXT tokamak are shown, demonstrating this asymmetry is present in the spatial region $0.8 < r/a < 1.0$ explored for argon emission on Alcator C-Mod.

The capability to measure such an up/down asymmetry of fluctuations was not available for the 1110204 plasmas, although changes were observed in the density fluctuation amplitude measured by the O-mode reflectometer [127] at the outboard midplane. Similar changes in density fluctuation have been characterized across the rotation reversal [131]. This reversal has been linked to the transition between the linear Ohmic confinement regime (LOC) and the saturated Ohmic confinement regime (SOC) [178] postulated to be a changeover between trapped electron mode (TEM) and ion temperature gradient (ITG) dominated turbulence [179][182]. In this paradigm,

for the up/down asymmetry to be driven by poloidally asymmetric radial particle flux, TEM turbulence would need to be up/down symmetric, while ITG is up/down asymmetric. Such a hypothesis is highly speculative and requires further experimental and analytical scrutiny before reaching any conclusions.

D.5.1 H-like Ar Continuity Equation for Edge Plasma

Since C-Mod cannot break the degeneracy of the ∇B drift and I_p directions, the trivial experiment to test the connection between the asymmetry and turbulence cannot be performed. Instead, estimates of argon transport can be used to show that the $\tilde{n}/\langle n_z \rangle \sim 1$ up/down asymmetry occurs in regions of the plasma where $\tau_\perp$ and $\tau_\parallel$ become the same order of magnitude. In order to calculate the radial transport time scale from observed emissivity profiles, the continuity equation for H-like Ar is simplified for use in the cold outer regions where the asymmetry is observed. The full continuity equation includes ionization and recombination to and from neighboring charge states,

$$\frac{\partial n_H}{\partial t} + \nabla \cdot \vec{\Gamma}_H = n_e \left[I_{He} n_{He} - (R_H n_H + I_H n_H) + R_f n_f \right] + n_0 \left(C_f n_f - C_H n_H \right) \quad \text{(D.1)}$$

where the subscript f refers to the density of fully-stripped argon, H to hydrogen-like argon, and He to helium-like argon. The isoelectronic subscripts are used for clarity, but this equation can be generalized to any charge state of any ion. The ionization, I, and recombination, R, rates are known functions of electron temperature, while n_0 is the neutral density and C refers to the charge-exchange recombination rate. The time derivative is eliminated by observing the steady-state, and effects from fully-stripped argon, n_f, can be avoided by limiting the core T_e to prevent its production. In the outer layer of the plasma where the $\tilde{n}_z/\langle n_z \rangle$ starts to rise toward unity, ionization processes begin to turn off due to the low temperatures, and recombination rises as shown in Figure D-18 for R_H, I_H and I_{He}. These rates are plotted in units of 1/s, assuming a local electron density of 10^{20} m^{-3}, and indicate that timescales of ∼1 ms, on order of the parallel transport time scale, are possible.

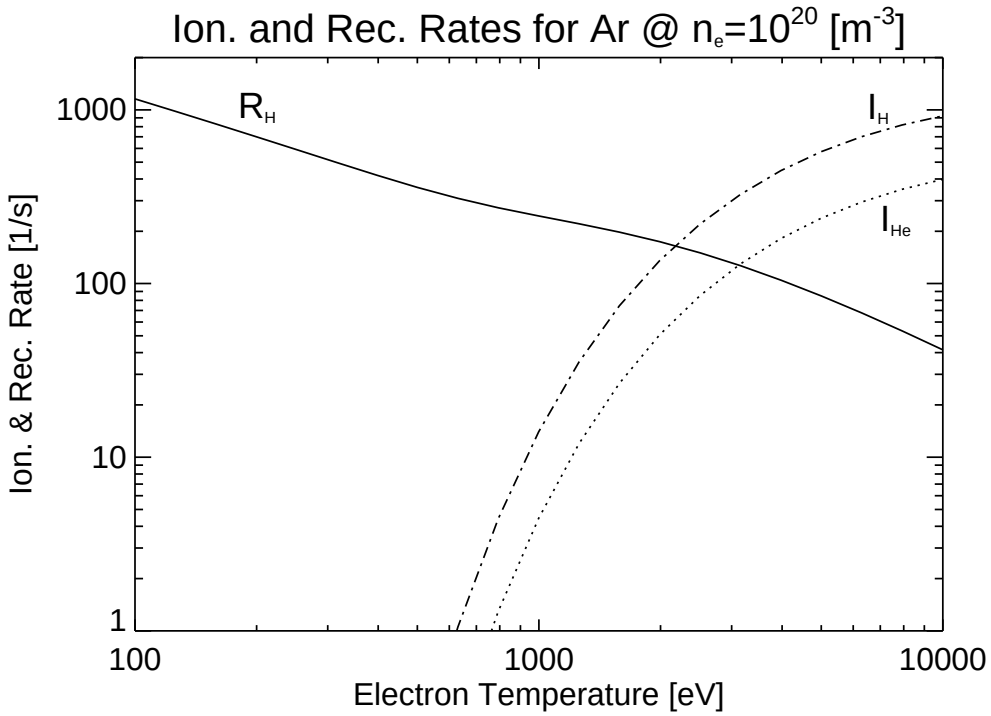

Figure D-18: Ionization and recombination rates into (I_{He}) and out of (R_H, I_H) the H-like argon charge state for $n_e = 10^{20}$ m^{-3}

For $T_e < 1$ keV, the strong loss term from the H-like charge state reduces the continuity equation to,

$$\nabla \cdot \vec{\Gamma}_H = -n_H \left(n_e R_H + n_0 C_H \right) \tag{D.2}$$

describing the change in the radial flux due to recombination. The measured z-line emissivity can be used to estimate n_H,

$$\varepsilon_z = n_H \left(n_e L_R \left(T_e \right) + n_0 L_C \left(T_i \right) \right) \tag{D.3}$$

where L_R is known from atomic physics modeling and n_e, T_e, and T_i are known. Measurements of neutral density, n_0, and atomic physics data for excitation via charge-exchange, L_C, are currently unavailable for these plasmas.

Figure D-19 shows the relative strength of both R_H and C_H against temperature ($T_e = T_i$ assumed), for various neutral density fractions. The electron recombination term likely represents a lower limit, with $n_0/n_e \sim 10^{-3}$ to 10^{-4} being reasonable

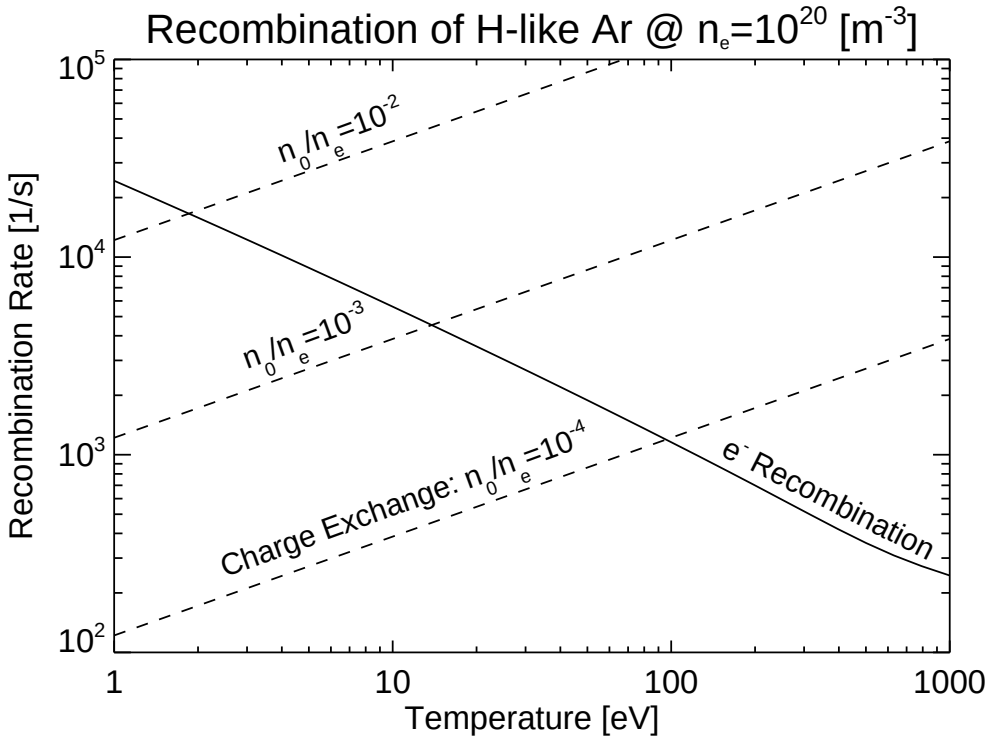

Figure D-19: Recombination rates at $n_e = 10^{20}$ m^{-3} for H-like argon due to electron impact (solid) and charge-exchange processes (dashed)

estimates for the neutral density so close to the edge of the plasma. More data are required to quantitatively estimate the perpendicular transport time scale from (D.2), but there is a reasonable expectation that H-like Ar recombination times are below 1 ms at large minor radii. In order to have a flat z-line emissivity profile, as shown in Section D.4, $\tau_\perp \ll \tau_{REC}$ in order to transport H-like argon across the field before it has a chance to recombine.

D.6 Future Experiments

The original experiments on 1110204 assumed that the up/down asymmetry could be explained by neoclassical parallel transport, while the results and analysis shows that this is unlikely to be the explanation. New experiments should be planned with more comprehensive diagnostic coverage, targeting the asymmetry transition region shown in Figure D-14. The neutral density should be measured, and, if possible, any poloidal variation in the neutral density captured by available diagnostics. Previous

measurements on Alcator-C showed that some high-n transitions in He-like Ar were more strongly populated by charge exchange than others. If HIREXSR can be re-configured to measure up/down asymmetry of these lines, simultaneous information on the up/down asymmetry due to both the recombination processes discussed in Section D.5 can be measured. In Section 4.1, the AXA and AXJ AXUV diode arrays were able to measure the parallel equilibration time after a laser blow-off injection. Calcium injections, regularly used to characterize radial impurity transport, could be used to measure $\tau_{\|}$ since Ca has a mass similar to argon. The measured $\tau_{\|}$ could then be compared to calculated $\tau_{\perp}$. Lastly, C-Mod's suite of turbulence diagnostics should be included. Specifically, the phase-contrast imaging diagnostic [127] has the ability to mask the detector, allowing fluctuations from the top and bottom half of the plasma to be viewed on separate shots [183]. Normally, this is used to investigate the propagation direction of the fluctuations, but this technique could be useful in seeing if the up/down argon asymmetry is correlated to any up/down density fluctuation asymmetry, as shown in Figure D-17.

Bibliography

[1] http://www.iter.org/proj/iterhistory.

[2] J. Freidberg. *Plasma Physics and Fusion Energy*. Cambridge University Press, 2007.

[3] http://www.merriam-webster.com/dictionary/tokamak.

[4] D. Meade. *Nucl. Fusion*, 50:014004, 2010.

[5] J. Wesson. *Tokamaks*. Oxford University Press, 3rd edition, 2004.

[6] J. Freidberg. *Ideal Magnetohydrodynamics*. Plenum Press, 3rd edition, 1987.

[7] E.S. Marmar and the Alcator C-Mod group. *Fusion Sci. Tech.*, 51:261, 2007.

[8] I.H. Hutchinson. *Principles of Plasma Diagnostics*. Cambridge University Press, 2nd edition, 2002.

[9] P.T. Bonoli *et al*. *Fusion Sci. Tech.*, 51:401, 2007.

[10] J. Irby *et al*. *Fusion Sci. Tech.*, 51:460, 2007.

[11] http://www.psfc.mit.edu/research/alcator/index.html.

[12] E. Hinnov *et al*. *Nucl. Fusion*, 18:1305, 1978.

[13] D. Pasini *et al*. *J. Nucl. Mater.*, 176-177:186, 1990.

[14] G. Fussmann *et al*. *J. Nucl. Mater.*, 162-164:14, 1989.

[15] J.E. Rice *et al*. *Fusion Sci. Tech.*, 51:357, 2007.

[16] D.E. Post *et al*. *Atomic Data and Nuclear Data Tables*, 20:397, 1977.

[17] S.P. Hirshman and D.J. Sigmar. *Nucl. Fusion*, 21:1079, 1981.

[18] T. Parisot *et al*. *Plasma Phys. Control. Fusion*, 50:055010, 2008.

[19] M.E. Puiatti *et al*. *Phys. Plasmas*, 13:042501, 2006.

[20] J.E. Rice *et al*. *Phys. Plasmas*, 4:1605, 1997.

[21] R. Dux. Technical Report IPP 10/27, Max-Plank-Institut für Plasmaphysik, 2004.

[22] M. Sertoli *et al*. *Plasma Phys. Control Fusion*, 53:035024, 2011.

[23] M. Greenwald. *Phys. Plasmas*, 17:058101, 2010.

[24] T. Fülöp and P. Helander. *Phys. Plasmas*, 6:3066, 1999.

[25] K.H. Burrell and S.K. Wong. *Nucl. Fusion*, 19:1571, 1979.

[26] C. Angioni *et al*. *Nucl. Fusion*, 51:023006, 2011.

[27] M. Valisa *et al*. *Nucl. Fusion*, 51:033002, 2011.

[28] N.T. Howard *et al*. *Submitted to Nucl. Fusion*, 2011.

[29] P. Helander. *Phys. Plasmas*, 5:1209, 1998.

[30] S.K. Wong. *Phys. Fluids*, 30:818, 1987.

[31] P. Helander. *Phys. Plasmas*, 5:3999, 1998.

[32] X. Garbet *et al*. *Nucl. Fusion*, 50:043002, 2010.

[33] J.L. Terry *et al*. *Nucl. Fusion*, 45:1321, 2005.

[34] D. Brower *et al*. *Phys. Rev. Letters*, 54:689, 1985.

[35] T. Fülöp and S. Moradi. *Phys. Plasmas*, 18:030703, 2011.

[36] M.L. Reinke and I.H. Hutchinson. *Rev. Sci. Instrum.*, 79:10F306, 2008.

[37] A. Ince-Cushman *et al*. *Rev. Sci. Instrum.*, 79:10E302, 2008.

[38] I.H. Hutchinson. *Monopolizing Knowledge*. Fias Publishing, 2011.

[39] P. Helander and D.J. Sigmar. *Collisonal Trasnport in Magnetized Plasmas*. Cambridge University Press, 2002.

[40] S.I. Braginskii. *Reviews of Plasma Physics*, 1:205, 1965.

[41] F.L. Hinton and R.D. Hazeltine. *Rev. Mod. Phys*, 48:239, 1976.

[42] J.W. Hughes *et al*. *Phys. Plasmas*, 9:3019, 2002.

[43] G. Kagan and P.J. Catto. *Plasma Phys. Control. Fusion*, 52:055004, 2010.

[44] T. Pütteich *et al*. *(in press) J. of Nucl. Mater.*, 2010.

[45] R. Dux *et al*. *Nucl. Fusion*, 44:260, 2004.

[46] R.D. Hazeltine and A.A. Ware. *Phys. Fluids*, 19:1163, 1976.

[47] M. Tendler. Impurity transport in a rotating toroidal plasma with cold-gas mantle. In *Proc. 8th Conf on Plasma. Phys and Controlled Fusion*, volume 1, page 765, 1980.

[48] C.S. Chang and R.D. Hazeltine. *Nucl. Fusion*, 20:1397, 1980.

[49] K.H. Burrell, T. Ohkawa and S.K. Wong. *Phys. Rev. Letters*, 47:511, 1981.

[50] K. Brau, S. Suckewer and S.K. Wong. *Nucl. Fusion*, 23:1657, 1983.

[51] W.M. Stacey. Technical Report GTFR-63, Georgia Institute of Technology, 1986.

[52] W. Feneberg. *Nucl. Fusion*, 29:1117, 1989.

[53] C.T. Hsu and D.J. Sigmar. *Plasma Phys. and Control. Fusion*, 32:499, 1990.

[54] W.M. Stacey. *Phys. Fluids B*, 4:3302, 1992.

[55] V. Rozhansky and M. Tendler. *Rev. of Plas. Phys.*, 18:147, 1996.

[56] J.A. Wesson. *Nucl. Fusion*, 37:577, 1997.

[57] M. Romanelli and M. Ottaviani. *Plasma Phys. and Control. Fusion*, 40:1767, 1998.

[58] T. Fülöp and P. Helander. *Phys. Plasmas*, 8:3305, 2001.

[59] W.M. Stacey. *Phys. Plasmas*, 9:3874, 2002.

[60] M. Landreman, T. Fülöp and D. Guszejnov. *Phys. Plasmas*, 18:092507, 2011.

[61] J.W. Connor *et al*. Technical Report PFC/JA-90-28, Plasma Fusion Center, 1990.

[62] W. Choe *et al*. *Phys. Plasmas*, 2:2044, 1994.

[63] V.S. Chan and S.K. Wong. *Phys. Fluids*, 30:830, 1987.

[64] C.S. Chang and R.W. Harvey. *Nucl. Fusion*, 7:935, 1983.

[65] H. Nordman *et al*. *Phys. Plasmas*, 15:042316, 2008.

[66] P. Helander . *Phys. Plasmas*, 8:4700, 2001.

[67] J.W. Connor *et al*. *Plasma Phys. Control. Fusion*, 29:919, 1987.

[68] J.W. Connor *et al*. *Plasma Phys. Control. Fusion*, 21:1475, 1989.

[69] W.A. Houlberg. *Phys. Plasmas*, 4:3230, 1997.

[70] E.A. Belli and J. Candy. *Plasma Phys. Control. Fusion*, 51:075018, 2009.

[71] R.A. Kolesnikov *et al*. *Phys. Plasmas*, 17:022506, 2010.

[72] J.L. Terry *et al*. *Phys. Rev. Letters*, 39:1615, 1977.

[73] M.C. Borras and R.S. Granetz. *Plasma. Phys. Control. Fusion*, 38:289, 1996.

[74] R.S. Granetz and M.C. Borras. *Fusion Eng. and Des.*, 34:153, 1997.

[75] J.E. Rice *et al*. *Nucl. Fusion*, 37:241, 1997.

[76] T.S. Pedersen and R.S. Granetz. *Rev. Sci. Instrum.*, 71:3385, 2000.

[77] T.S. Pedersen *et al*. *Phys. Plasmas*, 9:4188, 2002.

[78] K.D. Marr *et al*. *Plasma Phys. and Control. Fusion*, 52:055010, 2010.

[79] P. Smeulders. *Nucl. Fusion*, 26:267, 1986.

[80] R. Dux *et al*. *Nucl. Fusion*, 39:1509, 1999.

[81] R. Durst. *Nucl. Fusion*, 32:2238, 1992.

[82] W. Feneberg *et al*. Technical Report JET-R(86)07, JET Joint Undertaking, 1986.

[83] R. Giannella *et al*. In *Proc. 19th EPS Conf.*, volume 1, page 279, 1992.

[84] B. Alper *et al*. In *Proc. 23rd EPS Conf.*, volume A, page 051, 1996.

[85] L.C. Ingesson *et al*. *Nucl. Fusion*, 38:1675, 1998.

[86] L.C. Ingesson *et al*. *Plasma Phys. Control. Fusion*, 42:161, 2000.

[87] H. Chen *et al*. *Phys. Plasmas*, 7:4567, 2000.

[88] S.P. Regan. *Soft X-ray spectroscopy on the Phaedrus-T tokamak*. PhD thesis, Johns Hopkins Univerisity, 1996.

[89] S. Suckewer *et al*. Technical Report PPPL-1430, Princeton Plasma Physics Lab, 1978.

[90] I. Condrea *et al*. *Plasma Phys. Control. Fusion*, 43:71, 2001.

[91] K.W. Wenzel. *Measurements on injected impurity transport in TEXT (Texas Experimental Tokamak) using multiply filtered soft x-ray detectors*. PhD thesis, Massachusettes Inst. of Tech., 1990.

[92] J. Schivell and C.E. Bush. *Rev. Sci. Instrum.*, 57:2081, 1986.

[93] J. Schivell. *Rev. Sci. Instrum.*, 58:12, 1987.

[94] J.E. Menard *et al*. *Nucl. Fusion*, 45:539, 2005.

[95] R.J. Akers *et al*. *Plasma Phys. Control. Fusion*, 45:A175, 2003.

[96] http://www.mmm-microtech.com.

[97] http://accuglassproducts.com/.

[98] J.G. Graeme. *Photodiode amplifiers: op amp solutions*. McGraw Hill, 1996.

[99] http://www.d-tacq.com/.

[100] http://www.mdsplus.org.

[101] http://www.ird-inc.com.

[102] A.W. Degeling *et al*. *Rev. Sci. Instrum.*, 75:4133, 2004.

[103] A.W. Degeling *et al*. *Rev. Sci. Instrum.*, 75:4139, 2004.

[104] D. Yanmin *et al*. *Plasma Science and Technology*, 13:546, 2011.

[105] R.L. Boivin *et al*. *Rev. Sci. Instrum.*, 70:260, 1999.

[106] K.F. Mast *et al*. *Rev. Sci. Instrum.*, 62:744, 1991.

[107] R. Korde *et al*. *IEEE Trans. on Nucl. Science*, 36:2169, 1989.

[108] L. Werner *et al*. *Metrologia*, 35:407, 1998.

[109] L.R. Canfield *et al*. *Applied Optics*, 28:3940, 1989.

[110] A. Loarte *et al*. *Phys. Plasmas*, 18:056105, 2011.

[111] M.L. Reinke *et al*. *Nucl. Fusion*, 48:125004, 2008.

[112] M. Reinke *et al*. Implications of C-Mod disruption mitigation studies for ITER. American Physical Society, 51st Annual Meeting of the APS Division of Plasma Physics, 2009.

[113] A. Ince-Cushman. *Rotation studies in fusion plasmas via imaging x-ray crystal spectroscopy*. PhD thesis, Massachusetts Inst. of Tech., 2008.

[114] M.L. Reinke. On the accuracy of t_i measurements using x-ray crystal spectroscopy. Presented at the Fall 2010 NSE Seminar Series, 2010.

[115] M.L. Reinke. The other ions; dilution in the 1101209 i-mode plasmas. Presented at the Fall 2011 NSE Seminar Series, 2011.

[116] M.L. Reinke. Operation and validation of the hirexsr analysis code (thaco). Technical Report PSFC/RR-11-9, Massachusetts Inst. of Tech., 2012.

[117] H. Ohkawa. Determination of spectral sensitivity of a vacuum ultraviolet, grazing incidence spectrograph. Master's thesis, Massachusetts Inst. of Tech., 1994.

[118] M.L. Reinke *et al*. *Rev. Sci. Instrum.*, 81:10D736, 2010.

[119] B. Lipschultz *et al*. *Phys. Plasmas*, 13:056117, 2006.

[120] S.J. Wukitch *et al*. *J. Nucl. Mater.*, 363-365:491, 2007.

[121] P. Beiersdorfer *et al*. *Rev. Sci. Instrum.*, 79:10E318, 2008.

[122] http://www.princetoninstruments.com/.

[123] J.Z. Klose and W.L. Wiese. *J. Quant. Spectrosc. Radiat. Transfer*, 42:337, 1989.

[124] M.L. Reinke *et al*. Absolute calibration of a vuv/sxr spectrometer using bolometry. Poster presented at the 15th International Conference on Atomic Processes in Plasmas, 2007.

[125] L.L. Lao *et al*. *Nucl. Fusion*, 25:1611, 1985.

[126] S.M. Wolfe Private Communitcation (2011).

[127] N.P. Basse *et al*. *Fusion Sci. Tech.*, 51:476, 2007.

[128] N.T. Howard *et al*. *Rev. Sci. Instrum.*, 82:033512, 2011.

[129] J.E. Rice *et al*. *Nucl. Fusion*, 39:1175, 1999.

[130] J.E. Rice *et al*. *Phys. Rev. Letters*, 106:215001, 2011.

[131] J.E. Rice *et al*. *Nucl. Fusion*, 51:083005, 2011.

[132] M. Greenwald *et al*. *Nucl. Fusion*, 37:793, 1997.

[133] M. Greenwald *et al*. *Plasma Phys. Control. Fusion*, 42:A263, 2000.

[134] J.A. Snipes *et al*. *Plasma Phys. Control. Fusion*, 43:L23, 2001.

[135] R. Maingi *et al*. *Nucl. Fusion*, 51:063036, 2011.

[136] J.Y. Hsu *et al*. *Phys. Rev. Letters*, 53:564, 1984.

[137] http://w3.pppl.gov/transp.

[138] Y. Ma *et al*. *submitted to Nucl. Fusion*, 2011.

[139] Y.Lin Private Communitcation (2011).

[140] J.E. Rice *et al*. *Nucl. Fusion*, 42:510, 2002.

[141] C.L. Fiore *et al*. *Plasma Phys. Control Fusion*, 46:B281, 2004.

[142] M. Erba *et al*. *Plasma Phys. Control. Fusion*, 39:261, 1997.

[143] G. Dif-Pradalier *et al*. *Phys. Rev. Letter*, 103:065002, 2009.

[144] Y. Lin *et al*. *Phys. Rev. Lett.*, 101:235002, 2008.

[145] J. Kim *et al*. *Phys. Rev. Letter*, 72:2199, 1994.

[146] K. Crombe *et al*. *Phys. Rev. Letter*, 95:155003, 2005.

[147] W.M. Solomon *et al*. *Phys. Plasmas*, 13:056116, 2006.

[148] R.E. Bell *et al*. *Phys. Plasmas*, 17:082507, 2010.

[149] A.R. Field *et al*. *Plasma Phys. Control. Fusion*, 51:105002, 2009.

[150] W.A. Cooper *et al*. *Nucl. Fusion*, 20:985, 1980.

[151] E.V. Belova *et al*. *Phys. Plasmas*, 10:3240, 2003.

[152] I.T. Chapman *et al*. *Phys. Plasmas*, 16:072506, 2009.

[153] I.T. Chapman *et al*. *Plasma Phys. Control. Fusion*, 51:125001, 2009.

[154] N.A. Madden *et al*. *Nucl. Fusion*, 34:519, 1994.

[155] R. Iacono *et al*. *Phys. Fluids B*, 2:1794, 1990.

[156] W. Zwingmann *et al*. *Plasma Phys. Control. Fusion*, 43:1441, 2001.

[157] R.A. Pitts *et al*. *J. Nucl. Mater.*, 415:S957, 2011.

[158] A. Loarte *et al*. *Phys. Plasmas*, 18:056105, 2011.

[159] M. Murakami *et al*. *Nucl. Fusion*, 51:103006, 2011.

[160] J.E. Rice *et al*. *Nucl. Fusion*, 47:1618, 2007.

[161] R.V. Budny *et al*. Technical Report PPPL-4591, Princeton Plasma Physics Labratory, 2011.

[162] P. Beiersdorfer *et al*. *J. Phys. B: At. Mol. Opt. Phys.*, 43:144008, 2010.

[163] S. Moradi *et al*. *Plasma Phys. Control. Fusion*, 53:115008, 2011.

[164] A. Mollen *et al*. The effect of poloidal asymmetries on impurity transport driven by electrostatic microinstabilities. American Physical Society, 53nd Annual Meeting of the APS Division of Plasma Physics, 2011.

[165] K. Ida *et al*. *Plasma Phys. Control. Fusion*, 40:1429, 1998.

[166] C.S. Chang. *Phys. Fluids*, 26:2140, 1983.

[167] K. Indireshkumar and W.M. Stacey. *Phys. Fluids. B*, 5:1850, 1993.

[168] W.A. Cooper *et al*. *Nucl. Fusion*, 46:683, 2006.

[169] E.T. Powell *et al*. *Nucl. Fusion*, 33:1493, 1993.

[170] K. Tritz *et al*. *Rev. Sci. Instrum.*, 74:2161, 2003.

[171] J.P. Qian *et al*. *Nucl. Fusion*, 49:025003, 2009.

[172] S. Muakami *et al*. *Nucl. Fusion*, 46:S425, 2006.

[173] G. Matthews *et al*. *Phys. Scr.*, T128:137, 2007.

[174] R.M. Churchill *et al*. Inner-wall B^{5+} impurity density measurements using CXRS. American Physical Society, 52nd Annual Meeting of the APS Division of Plasma Physics, 2010.

[175] M.L. Reinke *et al*. *J. Nucl. Mater.*, 415:S340, 2011.

[176] R. Korde Private Communitcation (2011).

[177] J.E. Rice *et al*. *Rev. Sci. Instrum.*, 61:2753, 1990.

[178] J.E. Rice *et al*. *submitted to Phys. Rev. Letters*, 2011.

[179] J.E. Rice *et al*. *submitted to Phys. Plasmas*, 2011.

[180] A.H. Gabriel . *Mon. Not. R. astr. Soc.*, 160:99, 1972.

[181] B. Lipschultz *et al*. *Plasma Phys. Control. Fusion*, 44:733, 2002.

[182] C. Angioni *et al*. *Phys. Rev. Lett.*, 107:215003, 2011.

[183] L. Lin *et al*. *Rev. Sci. Instrum.*, 77:10E918, 2006.